Inverse Estimation for the Simple Earth System Model ACC2 and its Applications

Dissertation zur Erlangung des Doktorgrades der Naturwissenschaften
im Department Geowissenschaften der Universität Hamburg

vorgelegt von

Katsumasa Tanaka
aus Chiba, Japan

Hamburg 2008

Als Dissertation angenommen vom
Department Geowissenschaften der Universität Hamburg
auf Grund der Gutachten von Professor Dr. Richard S.J. Tol
und Professor Dr. Jochem Marotzke

Hamburg, den 30 April 2007

Professor Dr. Kay-Christian Emeis
(Leiter des Department Geowissenschaften)

Aggregated Carbon Cycle, Atmospheric Chemistry, and Climate Model (ACC2)

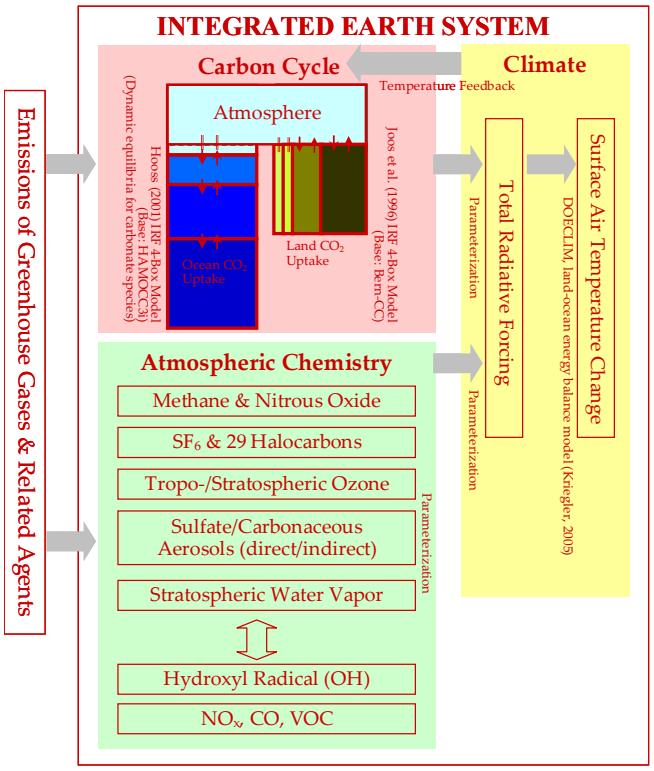

Characteristics

- Global-annual-mean computation
- Inverse estimation for integrated Earth system
- Future projections using multi-emission scenarios

Base Models

- NICCS (Hooss, 2001)
- ICLIPS Climate Model (Bruckner et al., 2003)
- DOECLIM (Kriegler, 2005)

Constants and Functional Relationships

- IPCC (2001) Climate Change 2001
- WMO (2003) Ozone Depletion 2002
- IPCC (2005) Safeguarding the Ozone Layer
- IPCC (2007) Climate Change 2007

Programming Language (optimization solver)

- GAMS (CONOPT3)

Applications

- Estimation of climate sensitivity (Tanaka et al., 2008)
- Evaluation of Global Warming Potentials (GWPs) (Tanaka et al., 2007b)
- Integrated Assessments

Uncertainty, far from being a barrier to progress, is actually a strong stimulus for, and an important ingredient of, creativity.

Henry N. Pollack (2005)

Table of Contents

ABSTRACT

The Aggregated Carbon Cycle, Atmospheric Chemistry, and Climate model (ACC2) (Tanaka and Kriegler et al., 2007a) describes physical-biogeochemical processes in the Earth system at a global-annual-mean level. Compared to its predecessors NICCS (Hooss, 2001) and ICM (Bruckner et al., 2003), ACC2 adopts more detailed parameterizations of atmospheric chemistry involving a set of agents (CO_2, CH_4, N_2O, O_3, SF_6, 29 species of halocarbons, sulfate aerosols (direct effect), carbonaceous aerosols (direct effect), all aerosols (indirect effect), stratospheric H_2O, OH, and pollutants NO_x, CO, and VOC). In contrast to the Impulse Response Function (IRF) approaches in the predecessor models, ACC2 uses DOECLIM (Kriegler, 2005), a land-ocean Energy Balance Model (EBM), to calculate temperature change. The carbon cycle is described by box models based on the IRF approach. A temperature feedback is newly implemented to ocean and land CO_2 uptake.

The most novel aspect of ACC2 is its inverse estimation, the first attempt to estimate uncertain parameters simultaneously for the carbon cycle, atmospheric chemistry, and climate system by taking their interactions into account. Theoretical underpinning of the ACC2 inversion is the probabilistic inverse estimation theory (Tarantola, 2005), which characterizes the ACC2 inversion as an integration of the existing Earth system knowledge. This includes parameter estimates, observational databases, reconstructions, and physical-biogeochemical laws. The inversion determines the best estimates of each single uncertain parameter and data (also those in time series) by optimization. This approach is complementary to the Probability Density Function (PDF) approach (e.g. Forest et al., 2002; Gregory et al., 2002; Knutti et al., 2002; Hegerl et al., 2006). Qualitative examinations indicate that the inversion results provide a plausible historical evolution of the Earth system in the years 1750-2000. The parameter estimates together with the model state for the year 2000 are then used for future projections and the differences with the projections in IPCC (2001) and WMO (2003) are discussed.

The ACC2 inversion setup is used for the following two applications (Tanaka et al., 2007b; Tanaka et al., 2008):

1) Climate sensitivity defined as the equilibrium response of global-mean surface air temperature to a doubling of the atmospheric CO_2 concentration from the preindustrial level is still not well constrained (IPCC, 2007; Gerald and Baker, 2007). This implies large uncertainties in projections of the future climate and difficulties in informing climate change policy. Here it is shown that the climate sensitivity is in fact even more uncertain than has been found by earlier studies (Andronova and Schlesinger, 2001; Gregory et al., 2002; Knutti et al., 2002; Forest et al., 2006; Hegerl et al., 2006). The results suggest that uncertainty in historical radiative forcing has not been sufficiently

considered. Also including the carbon cycle feedback, which in principle offers an additional constraint on climate sensitivity, does not reduce the uncertainty in climate sensitivity due to the poor knowledge of the global carbon budget before the year 1850.

2) Global Warming Potentials (GWPs) are indices to convert historical emissions of various GreenHouse Gases (GHGs) to equivalent CO_2 emissions. An analysis based on ACC2 inverse estimation reveals that for CH_4 and N_2O emissions indices higher than those used for the Kyoto Protocol (100-year time horizon) better reproduce the historical temperature evolution. The CH_4 GWP provides a best fit to historical temperature with a time horizon of 44 years. However, the N_2O GWP does not approximate the historical temperature with any time horizon. Therefore, a new exchange metric, TEMperature Proxy index (TEMP), is introduced that by definition provides a best fit to the temperature projection of a given period. By comparing GWPs and TEMPs, it is shown that the inability of the N_2O GWP to reproduce the course of historical temperature is a consequence of the GWP calculation methodology in IPCC, which includes only a coarse treatment of the background system dynamics and uncertain parameter estimation. Furthermore, the TEMP calculations demonstrate that indices have to be progressively updated upon the acquisition of new measurements and/or the advancement of our understanding of the Earth system processes.

PREFACE

In the past years the problem of global warming has witnessed enormous public awareness. The main cause of global warming is the human perturbation of the carbon cycle by fossil fuel combustion and land use change. The resulting CO_2 emissions together with the emissions of non-CO_2 GHGs and aerosols alter the Earth energy budget, which leads to a warming at the surface. This surface warming further influences the water cycle and affects the ocean and terrestrial carbon cycle. As a consequence of numerous feedbacks, global warming can be completely characterized only by an integrated Earth system approach. Feedbacks in the Earth system operate on various spatial and temporal scales. Therefore, to fully elucidate global climate change, the development of Earth system models with full complexity is underway in the Earth science community.

Why is *inverse estimation for a simple Earth system model* brought up now? One of the advantages of a simplified model lies in the feasibility of inverse estimation. Performing an inversion for state-of-the-art Earth system models requires prohibitively expensive computation. An inverse estimation gives insight into uncertainties. What are the best estimates of uncertain parameters by considering other uncertain aspects of the Earth system? It also provides advises for the modelling itself. Which processes should be included in the model given their associated uncertainties? The inverse calculation for the global-annual-mean model ACC2 (Tanaka and Kriegler et al., 2007a) considers a large number of uncertainties simultaneously in the three Earth system components: carbon cycle, atmospheric chemistry, and climate. Furthermore, the simplified integrated approach allows a novel way of looking at existing research questions.

Owing to the nature of this approach, the scope of this thesis is broad, requiring a substantial amount of documentation. For the sake of completeness, a first part of the thesis (Chapters 1 to 4) provides in-depth descriptions of the model ACC2 and its inversion and also presents the results of the standard past and future simulation. Then the following two parts of the thesis describe the applications of the ACC2 inversion: 1) estimation of climate sensitivity (Chapter 5), 2) estimation of exchange indices for non-CO_2 GHG emissions (Chapter 6). Each of the three parts is accompanied by additional material in Appendices A, B, and C, respectively.

More detailed structure of this thesis is given below. In Chapter 1, the history of the development of ACC2 and the improvements of ACC2 over the predecessors NICCS (Hooss, 2001) and ICM (Bruckner et al., 2003) are summarized.

In Chapter 2, each of the carbon cycle, atmospheric chemistry, and climate components is described including relevant issues where necessary. Assumptions in the carbon cycle modelling in ACC2 are extensively discussed at the end of the subsection for ocean CO_2 uptake and land CO_2

uptake. Note that the description for the climate component DOECLIM (Kriegler, 2005) in Section 2.3 has been provided by its developer Elmar Kriegler at Carnegie Mellon University/ Potsdam-Institut für Klimafolgenforschung (PIK).

Chapter 3 is devoted to the methodology of the inverse calculation for ACC2. This chapter starts with the generalization of uncertainty analyses (Section 3.1). The probabilistic inverse estimation theory (Tarantola, 2005) is discussed in Section 3.2, emphasizing that an inverse estimation synthesizes the information on parameter estimates, observations, and physical-biogeochemical laws. This theory is applied to the model with several assumptions – implications of such assumptions are discussed in depth at the end of Section 3.2.2. Then Sections 3.3 and 3.4 discuss the data and parameters in the ACC2 inversion. Section 3.5 describes the treatments of ENSO and volcanic eruptions in the inversion.

In Chapter 4, the past and future mode runs for ACC2 are shown. For the ACC2 past mode (Section 4.1), the results for the inverse calculation and the forward calculation (by fixing all the parameters at their prior estimates) are compared to clarify the effectiveness of the inversion. As this chapter is a part of the model description, only major aspects of the results are highlighted there. As for the ACC2 future mode (Section 4.2), projections obtained from ACC2 are compared with the corresponding projections in IPCC (2001) and WMO (2003). This chapter is concluded with the future perspectives for the development of ACC2.

Chapter 5 discusses the first application of ACC2 inversion: namely, estimation of climate sensitivity. Climate sensitivity is defined as an asymptotic surface air temperature response to a doubling of the preindustrial atmospheric CO_2 concentration. The uncertainty in climate sensitivity is one of the most important problems in climate science. First, it is demonstrated that the robustness of climate sensitivity estimation depends on how the uncertainty in radiative forcing is taken into account. The ACC2 inversion setup is fully utilized here to address a large number of uncertainties. Second, a question is posed as to whether the climate-carbon cycle feedback tightens the constraint for climate sensitivity estimation. The ACC2 approach takes account of the interaction of the climate system with the carbon cycle, which had not been addressed in previous inversion studies.

Chapter 6 discusses the second application of ACC2 inversion: estimation of exchange indices to convert non-CO_2 GHGs emissions to their CO_2 equivalences. First, it discusses GWPs, exchange indices used in Kyoto Protocol in spite of various criticisms. GWPs are evaluated by using the ACC2 inversion results as a historical basis. Such a historical evaluation was made possible as the inversion results provide a past evolution of the carbon cycle, atmospheric chemistry, and climate system by taking account of the associated uncertainties. Then TEMPs are proposed, new exchange indices that provide a best fit to the historical temperature evolution. The importance of the time-dependency of such indices is emphasized.

This thesis is concluded in Chapter 7, which provides some broad perspectives and general

lessons that I learned during the development of this thesis.

This thesis is cumulative as three publications are put together. Chapters 1 to 4 have originally been published as Tanaka and Kriegler et al. (2007a) but include minor changes to be consistent with the latest model (Version 3.1). Chapters 5 and 6 have been separately submitted to scientific journals and are currently under review (Tanaka et al., 2007b; Tanaka et al., 2008). Note that there are some overlaps in the materials as this thesis is a compilation of three different publications. Lastly, the GAMS code for ACC2 is made fully available for public to meet the interests from various institutes and universities around the world.

ACNOWLEDGMENTS

This thesis is a product of various interactions with people at several institutions and universities. The very start of my doctoral study was at the Carl von Ossietzky Universität Oldenburg. Dr. Georg Hooss introduced me to his model NICCS and its philosophy and brought me to his network of colleagues and friends to get my academic and private life in Germany started. Prof. Dr. Wolfgang Ebenhoeh provided me warm support for establishing the conditions to move my study forward. Most of my study has been conducted at Max Planck Institute for Meteorology, where I had stayed within the framework of International Max Planck Research School on Earth System Modelling (IMPRS-ESM). Prof. Dr. Richard S. J. Tol and Dr. Wolfgang Knorr were my principal advisors. Richard's support for my inversion approach at the early stage led to the following development. Several arguments in my thesis are the reflection of his criticisms at the later stage. Richard also supported my GWP evaluation approach to make it through the journal submission. Wolfgang always identified positive aspects of my work. I am influenced from his question-oriented thinking. As Wolfgang moved to the University of Bristol, Prof. Dr. Martin Claußen took over Wolfgang's position as my second advisor. The final draft of this thesis has been evaluated by Prof. Dr. Richard S. J. Tol and Prof. Dr. Jochem Marotzke.

Many useful interactions were outside of the formal supervisions. Dr. Thomas Raddatz has been supportive for the inversion approach and helped refine the methodology from the Earth science perspective. Thomas enthusiastically discussed with me the interpretation and implications of the inversion results at depth and at length. The core idea of the climate sensitivity study was developed with him. I owe Dr. Christian Reick for his mathematical and theoretical insights into the inversion methodology and results. Both Thomas and Christian kindly checked substantial portions of my thesis draft. Dr. Thomas Bruckner at Technische Universität Berlin introduced me to his ICLIPS Climate Model and offered me to work on it. Thomas supported me to extend my research activities. It was stimulating to work with Dr. Elmar Kriegler at Carnegie Mellon University and Potsdam-Institut für Klimafolgenforschung (PIK) for several tasks including the coupling of ACC2 with his model DOECLIM. I learned a lot from the discussion with him. The initial idea of the GWP study was developed under the supervision of Dr. Dmitry Rokityanskiy when I stayed at the International Institute for Applied Systems Analysis (IIASA) as a participant of the Young Scientists Summer Program (YSSP) in 2005. Later refinement of this study came under the guidance of Dr. Brian C. O'Neill at IIASA and National Center for Atmospheric Research (NCAR). Brian also contributed to the climate sensitivity study at all levels from fundamental mathematical underpinning to argumentation.

Specifically for the model development and its description, I am grateful to the following individuals for their respective contributions and supports (in alphabetical order):

Dr. John A. van Aardenne	Data provisions (historical non-CO_2 GHG emission uncertainties)
Mr. Arne Stolbjerg Drud	Technical advices (CONOPT3)
Dr. David M. Etheridge	Data provisions (historical halocarbon concentrations)
Dr. Jacqueline Flückiger	Data provisions (historical N_2O concentration with uncertainties)
Prof. Dr. Klaus Hasselmann	Review (results and conclusions section)
Dr. Ernst Maier-Reimer	Scientific advices (ocean carbon cycle component)
Dr. Sebastian Rast	Review (atmospheric chemistry section)
Dr. Christian Reick	Review (inversion and numerical integration sections)
Dr. Uwe Schneider	Technical advices (GAMS)

Furthermore, I would also like to express my thanks to Dr. Antje Weitz and Ms. Cornelia Kampmann for their warm supports throughout my study at IMPRS-ESM. I also thank the staffs at the departments of Bibliothek, CIS, Grafik, and Verwaltung for their extensive supports. Many other interactions with colleagues, conference participants, fellow researchers, and friends that are not specifically mentioned here were indispensable for the completion of my study. Last but not least, I thank my family for maintaining stable circumstances throughout my stay abroad.

I acknowledge Max Planck Institute for Biogeochemistry, European Commission (ENSEMBLES project), International Max Planck Research School on Earth System Modelling (IMPRS-ESM), Volkswagen Foundation (ECOBICE project), Max Planck Institute for Meteorology, and IIASA for their financial supports.

1. INTRODUCTION

A wealth of geophysical and biogeochemical observation databases indicate that the history of the Earth system has been radically changed by the onset of the anthropogenic CO_2 emission due to fossil fuel combustion in the 18th century, marking the beginning of the Anthropocene (Crutzen and Stoermer, 2000). There is a virtual agreement among scientists that present day human activities substantially influence various processes in the carbon cycle, atmospheric chemistry, and climate systems (Intergovernmental Panel on Climate Change (IPCC), 2007). These Earth system components are responding in a complex manner as they are strongly interdependent. Concerns over the fate of the Earth system are mounting and the scientific exploration of future climate projections is ever more important.

Recent years we developed the Aggregated Carbon Cycle, Atmospheric Chemistry, and Climate model (ACC2) describing major physical-biogeochemical processes in the Earth system on a global-annual-mean basis. ACC2 is a tool to advance understanding on the first-order interactions of Earth system processes and of the associated uncertainty estimates.

The development of ACC2 was motivated by its applications to multi-disciplinary investigation of the future natural and human Earth system co-evolution. This type of approach is called 'Integrated Assessment (IA),' in which several models ranging from climate and terrestrial biosphere models to land use and economy models are coupled (Hooss, 2004). ACC2 was implemented in IA models such as the Model of INvestment and technological Development (MIND) (Edenhofer et al., 2005) and the ECOnomy-BIosphere-ClimatE (ECOBICE) supermodel (Kemfert and Knorr, 2006).

The IA modelling approach relies on multiple long-term scenarios of future GreenHouse Gas (GHG) emissions (e.g. Special Report on Emissions Scenarios (SRES) (Nakićenović et al., 2000)), calling for computationally efficient models. The computational loads of the state-of-the-art General Circulation Models (GCMs) are prohibitively expensive for multi-scenario long-term runs. Only a tiny fraction of information obtained from GCM runs is meaningfully utilized by IA studies. In view of the need for dynamic yet concise representation of climate change, a reduced carbon cycle and climate model was developed in the framework of Structural Integrated Assessment Model (SIAM) (Hasselmann et al., 1997). It is based on the Impulse Response Function (IRF) approach, where the temporal evolution of a state variable (e.g. global-mean atmospheric CO_2 concentration) is extracted by perturbing the control run of a complex model. Hooss (2001) extended the applicability of the IRF-based carbon cycle model by describing the carbonate chemistry dynamically and established the Nonlinear Impulse-response representation of the coupled Carbon cycle-Climate

System model (NICCS). NICCS was utilized within the framework of the Multi-Actor Dynamic Integrated Assessment Model (MADIAM) (Weber et al., 2005). The IRF approach is a core methodology for NICCS and carried on in ACC2. Fixed spatial patterns (T21 resolution: 32 latitudinal and 64 longitudinal circles) of temperature change, cloud cover, precipitation, and sea level rise together with annual-global-mean characteristics are extracted from a 850-year quadruple CO_2 experiment of the coupled Atmosphere-Ocean GCM (AOGCM) European Centre HAmburg Model 3-Large Scale Geostrophic ocean model (ECHAM3-LSG) by the Empirical Orthogonal Function (EOF) approach. In NICCS, the fixed spatial patterns are superimposed on the global-mean projections that are computed separately.

The actual starting point of the ACC2 development was the Integrated assessment of CLImate Protection Strategies (ICLIPS) Climate Model (ICM) version 1.1 (Bruckner et al., 2003), which was used for the ICLIPS IA project (Toth, 2003). ICM deals with multi-gases (CO_2, CH_4, N_2O, halocarbons, SF_6, and SO_2) in contrast to NICCS dealing with only CO_2. The functional relationships and constants in ICM have been reviewed on the basis of IPCC (1996). ICM adopts the separation of the spinup mode (running from year 1750 to 1990) and the forward mode (running from 1990 onward) with a time step of 5 years to further reduce the computational burden for future multi-scenario analyses. ICM is programmed in the General Algebraic Modeling System (GAMS) while NICCS is programmed in Fortran 77. The optimization solver CONOPT2 provided with GAMS is utilized for coupling with economy models and calculating the emission corridors, within which permissible CO_2 emission pathways to satisfy certain climatic constraints are contained (Bruckner et al., 2003).

ICM has been progressively expanded to ACC2. ACC2 version 1.0 has been released in May 2005 (Tanaka et al, 2005), version 2.1 in March 2006 (Kriegler et al., 2006; Tanaka et al., 2006a), version 2.2 in September 2006 (Tanaka et al., 2006b), version 3.0 in March 2007 (Kriegler et al., 2007; Tanaka and Kriegler et al., 2007a), and version 3.1 in February 2008 (this thesis; Tanaka et al., 2007b; Raddatz and Tanaka, 2008; Tanaka et al., 2008). Major improvements of ACC2 version 3.1 over ICM are fivefold as follows:

1) Update of the physical and biogeochemical functional relationships and constants in accordance with IPCC (2001), Joos et al. (2001), WMO (2003), IPCC (2005), and other recent literature[1],
2) Implementation of the parameterization of atmospheric chemistry involving a set of radiative forcing agents (CO_2, CH_4, N_2O, SF_6, 29 species of halocarbons, tropospheric and stratospheric O_3, sulfate aerosols (direct effect), carbonaceous aerosols (direct effect), all aerosols (indirect effect), stratospheric H_2O, hydroxyl radical (OH), and pollutants (NO_x, CO, and Volatile Organic

[1] It is necessary to reflect the latest findings summarized in IPCC (2007) to ACC2. As far as we can see in the Summary for PolicyMakers (SPM), no major changes are necessary in the ACC2 model code (e.g. compare IPCC (2001, Figure SPM.3) and IPCC (2007, Figure SPM.2)).

Compound (VOC))) on the basis of IPCC (2001) and Joos et al. (2001) (Table 2.1),

3) Coupling with the Diffusion Ocean Energy balance CLIMate model (DOECLIM) (Kriegler, 2005), a land-ocean Energy Balance Model (EBM) to calculate the surface air temperature from the radiative forcing, as opposed to a physical interpretation of the IRF (Kriegler, unpublished) used in ICM version 1.1 and the original IRF (Hooss, 2001) used in ICM version 1.0,
4) Addition of the climate-carbon cycle feedback: the temperature dependency of the thermodynamic equilibria for marine carbonate species (Millero, 1995; Millero et al., 2006) and of the heterotrophic respiration using a Q10 factor, and
5) Development of an inverse calculation scheme to estimate uncertain properties in the Earth system at a global-annual-mean model.

The crucial new aspect of the ACC2 methodology is the inverse calculation scheme, where the values of the uncertain parameters in the coupled carbon cycle, atmospheric chemistry, and climate system are estimated by using various measurements between the year 1750 and 2000 (Table 3.1), other independent information on such parameters (Table 3.2), and physical-biogeochemical functional relationships. Currently an inversion for the Earth system is not operational for more complex models because of the requirement for prohibitively expensive computation.

The theoretical underpinning of the ACC2 inversion is the probabilistic inverse estimation theory (Tarantola, 2005), which formulates an inversion as an information synthesis (Figure 3.1). Assumptions in the ACC2 inversion approach are extensively discussed under the Tarantola's theory in Section 3.2.2. Our inversion scheme theoretically computes the maximum of the marginal posterior Probability Density Function (PDF) of all the parameters, which is equivalent to the minimum of the cost function (equation (3.2.14)). The cost function is the sum of the squared misfits for parameters and data weighted by respective prior uncertainty ranges. Our inversion produces an Earth system evolution between the year 1750 and 2000 and generates the best guess of uncertain parameters. The parameter estimates and model state for the year 2000 obtained from the inversion serve as a basis for future projections (Section 4.2). Such a consistent treatment of the uncertainties from the past to the future was not done in IPCC (2001).

Several inversion studies (e.g. Forest et al., 2002; Gregory et al., 2002; Knutti et al., 2002; Hegerl et al., 2006) estimated the marginal PDF of each of the uncertain climate properties. It is advantageous that PDFs present the extent of knowledge of uncertainties. Nevertheless, our one-point estimates of uncertain parameters obtained from the ACC2 optimization approach provide a distinct value. First, our approach deals with uncertain parameters in the Earth system simultaneously. Previous inversion studies neglected the fact that the interactions among different Earth system compartments provide additional constraints for the estimation of uncertain parameters. Second, it would not be possible to pick the peaks of posterior PDFs together as single estimates (e.g. aerosol forcing, ocean vertical diffusivity, and climate sensitivity) because of their interdependencies.

Our one-point estimates allow straightforward interpretation and appeal to different scientific applications (e.g. Chapters 5 and 6 of this thesis; Tanaka et al., 2007b; Tanaka et al, 2008). Third, the number of uncertain parameters considered in PDF studies is limited to several due to the computational requirement. Our optimization approach can account for a large number of uncertain parameters although a huge number of interdependencies in the uncertainty estimates are extremely complex to analyze and produce bias to the inversion solution. Based on the arguments above, the ACC2 inversion approach is complementary to the PDF approach.

The model operation is separated into the past mode (years 1750 – 2000) and the future mode (year 2000 onward). In the past mode, an inverse calculation is performed to estimate the uncertain parameters and model state for the year 2000, both of which are transferred to the future mode and used for the future projections. ACC2 is programmed in GAMS (Distribution 22.6) and the optimization is solved using solver CONOPT3 provided with GAMS (Section D.1). The optimization for the coupled Earth system is technically feasible because we restrict ourselves to global-annual-mean information. The numerical integration in ACC2 uses a variant of Heun's Predictor-Corrector method (Section D.2) with the time step of 1 year. The DOECLIM component uses an implicit two-stage Runge-Kutta method with maximum order 4 (Hammer and Hollingsworth method) (Section 2.3.4). The ACC2 model code contains a *switchboard* (Section D.3), an interface where one can control the parameters and data to be put into the inverse calculation and analyze the influence of particular information to the inversion results. In the switchboard one can also turn on and off the temperature feedback to the carbon cycle (Chapter 5 of this thesis; Tanaka et al., 2008).

This document aims at providing a complete description of the forward and inverse calculations of ACC2 at the level required for using the model. Discussions on relevant issues are also introduced where necessary. Assumptions in the model and their implications are explicitly stated. Some further details are directly written in the ACC2 model code. The cited references do not intend to serve as a comprehensive list of earlier works. We frequently cite IPCC (2001) and WMO (2003), which are the summary of the scientific findings in the respective fields and where further references can be found. Acronyms and abbreviations are listed in Appendix C. The main textbooks referred for the model documentation are Libes (1992), Schlesinger (1997), Zeebe and Wolf-Gladrow (2001), Mackenzie (2002), Fasham (2003), Mackenzie and Lerman (2006) and Millero (2006) for carbon cycle; Brasseur et al. (1999), Jacob (1999), Brasseur et al. (2003), and Seinfeld and Pandis (2006) for atmospheric chemistry; Wunsch (1996), Enting (2002a), and Tarantola (2005) for inverse estimation.

2. DESCRIPTION ON FORWARD MODELLING

2.1. CARBON CYCLE COMPONENT

2.1.1. Overview

CO_2 is the most important GHG regulating the Earth climate on the various time scales of the industrial period (IPCC, 2001), the glacial-interglacial cycle (Petit et al., 1999), and the Hothouse-Icehouse cycle (Fisher, 1984). Because of its substantial atmospheric abundance and particular molecular structure, CO_2 primarily interferes with the long-wave radiation emitted from the Earth surface and traps heat energy within the lower atmosphere. The very origin of carbon on the Earth dates back to the fusion reactions involving ^{4}He and ^{8}Be in the Earth interior during the planetary formation (Burbidge et al., 1957). At present, more than 99% of carbon on the Earth exists in sedimentary rocks in a form of organic carbon or carbonate minerals (Li, 2000, Table VIII-2; Mackenzie, 2002, Table 6.2), by far outnumbering the amounts stored in the ocean, the atmosphere, and the biosphere.[2]

On the time scale of ACC2 (typically between the year 1750 and 2100), the atmospheric abundance of CO_2 is largely controlled by the magnitudes of the CO_2 uptake from the ocean and the terrestrial biosphere and by the amounts of the anthropogenic CO_2 emission. These processes perturb an equilibrated state of the carbon cycle system assumed prior to 1750. Such an equilibrium-based approach conforms to the approach of GCMs that are tuned to produce zero net CO_2 exchange between the ocean and the atmosphere and between the land and the atmosphere in their control runs. Such an approach can also be taken as a 'first-cut' in view of the difficulty in modelling the riverine carbon transport in the temporal and spatial resolution of GCMs. However, the equilibrium assumption is not compatible with the accurate portray of the system even on shorter time scales

[2] On the geological time scale, the atmospheric CO_2 concentration is primarily controlled by the intensity of volcanism related to the plate tectonic activity; such geological processes are so drastic that the atmospheric CO_2 concentration reached as high as 5,000 ppm approximately 500 million years ago, according to geochemical evidences (Berner, 1991; Berner, 1997). The atmospheric CO_2 is removed by the weathering of limestone and calcium silicate, leaching dissolved carbon to the ocean. The dissolved carbon in the ocean is utilized to form body of life. A tiny fraction of dead body, detritus, and calcium carbonate is buried deeply in the ocean sediments. It is converted to oil and gas at elevated temperature and pressure on a time scale of million years; it is eventually returned to the mantle through subduction zones on a time scale of hundreds million years. Although such massive processes over the geological time horizon need to be remembered, the rates of these processes appear extremely slow on the annual to century time scale of ACC2 and are thus neglected here.

(Fred Mackenzie, personal communication, November 1, 2005) and is difficult to be justified in view of the constantly changing Earth system shown in various reconstructions. Thus, the particular preindustrial state assumed here is termed 'quasi-steady state' as coined in Ver et al. (1999).

In ACC2, the anthropogenic CO_2 emission is represented by the following two categories: the emission due to fossil fuel combustion and the emission due to land use change. The fossil fuel CO_2 emission originates from the combustion of all types of fossil fuel productions and consumptions, cement production, and gas flaring. The magnitude of the fossil fuel CO_2 emission became prominent at the onset of the Industrial Revolution, when energy-intensive machinery started to emerge. The global fossil fuel CO_2 emission is estimated to be about 7.3 GtC/year in 2003 (Marland et al., 2006). In all the 40 future emission scenarios of SRES, the fossil fuel CO_2 emission will continue to be dominant for the next one hundred years. The land use CO_2 emission means the net change in the carbon storage in terrestrial ecosystems due to human activities such as deforestation, afforestation (or reforestation), and the conversion of natural ecosystems to cultivated lands and pastures. The change in the terrestrial carbon storage due to the environmental factors is not included in the land use CO_2 emission and rather explained as the land CO_2 uptake as described later. In other words, the ecological processes of deforestation and afforestation are accounted for in the land use CO_2 emission and the physiological processes of photosynthesis and respiration in the land CO_2 uptake. The magnitude of the land use CO_2 emission has been considerable even earlier than the rise of the fossil fuel CO_2 emission. There is a hypothesis under debate that the Holocene CO_2 rise started 8,000 years ago is indeed driven by the land use CO_2 emission caused by the forest clearance in Eurasia (Ruddiman, 2003). Currently the land use CO_2 emission is the second largest human-driven CO_2 emission (2.1 GtC/year in 2000 according to Houghton and Hackler (2002)). However, the land use CO_2 emission is projected to approach zero or turn negative by 2100 in all six future emission scenarios of SRES, indicating an assumption on forest as a strong carbon sink. It should be noted that there is a speculation that the CO_2 emission due to soil erosion is substantial in magnitude (Lal, 2005). However, the soil erosion CO_2 emission is not included in ACC2 because its magnitude, even its sign, is not well-known due to the competing evidences from sedimentologists and soil scientists.

The CO_2 emission has been changing the atmospheric CO_2 composition, influencing the rates of the ocean and land CO_2 uptake. The disparity in the CO_2 partial pressure at the air-sea interface controls the rate of the oceanic CO_2 exchange. The atmospheric CO_2 concentration change directly affects the rate of photosynthesis of the terrestrial plants and indirectly controls the rate of heterotrophic respiration via the temperature change. The change in the water cycle and the nutrient availability are important factors controlling the terrestrial processes; however, these are not explicitly modelled in ACC2. The changes of ocean and land CO_2 uptake rates from the respective preindustrial levels are modelled using box model approaches as follows.

The ocean CO_2 uptake is described by an atmosphere-ocean box model. The parameters of the box model here are "back-calculated" from the output of a complex model by the IRF approach (Maier-Reimer and Hasselmann, 1987). The ocean uptake IRF (Hooss, 2001) is a mathematical substitute mimicking the ocean CO_2 uptake simulated by HAmburg Model of the Ocean Carbon Cycle (HAMOCC) 3i in response to an injection of a small amount of CO_2 into the atmosphere in the controlled state. The IRF can be interpreted as the solution of a system of differential equations that govern a four-layer atmosphere-ocean box model, allowing the estimation of the box model parameters.

The direct application of the box model obtained from the procedure above is valid only within the linear or quasi-linear range of the calibration; the validity of the atmosphere-ocean box model is limited to the cases with less than twice of the preindustrial CO_2 concentration (Hooss, 2001). The emerging nonlinear property with the departure from the calibration range stems from the fact that the atmospheric CO_2 concentration change influences the thermodynamic equilibria for the marine carbonate species such as CO_2(aq), HCO_3^-, and CO_3^{2-} (Pilson, 1998; Millero, 2006). As a result, the ocean takes up less CO_2 with increasing atmospheric CO_2 concentration. Such a linear limitation can be overcome by furnishing the box model equations with the thermodynamic equilibrium relationships. The modified box model is then good for applications even for cases with the quadruple of the preindustrial CO_2 level (Hooss, 2001). Furthermore, we adopted the relationships of the thermodynamic constants with in-situ temperature (Millero, 1995; Millero et al., 2006; other references therein), accounting for the temperature feedback to the ocean CO_2 uptake.

The formulation of the land box model is fairly straightforward relative to the oceanic counterpart. Under the quasi-steady state assumption, the Net Primary Production (NPP), defined as the difference between the rate of Gross Primary Production (GPP) and the rate of autotrophic respiration, is assumed to be constant and balanced with the heterotrophic respiration prior to 1750. The perturbation of NPP and the change in the heterotrophic respiration is described by the four-reservoir land box model. The departure of the atmospheric CO_2 concentration from the preindustrial level leads to the change in NPP, a process called CO_2 fertilization (or CO_2 fertilization effect), which is logarithmically parameterized with the beta factor (Gifford, 1980; Friedlingstein et al., 1995). CO_2 fertilization is caused by the fact that the higher partial pressure of CO_2 is exerted on stomata (microscopic leaf openings) distributed over plant leaves, which control the rate of photosynthesis.

The fertilized biomass is released back to the atmosphere by respiration, decay, and decomposition, which is parameterized by first-order kinetic equations. The parameters in the land box model are determined by comparing the *derivatives* of the box model solution with the IRF of Joos et al. (1996). Joos' IRF is a sum of exponential functions representing the heterotrophic respiration flux (not the reservoir size) simulated by the Bern Carbon Cycle model (Bern-CC) in

response to the additional sequestration of carbon. The temperature dependency of the heterotrophic respiration is parameterized using a Q10 factor, by which the rate of terrestrial respiration increases with a temperature increase of 10°C. The temperature dependency of the heterotrophic respiration is applied not only to the fertilized carbon but also to the preindustrial (or background) carbon. The land box model is coupled to the atmosphere-ocean box model.

In the average state of the preindustrial Earth system, there is a net CO_2 outgassing flux from the ocean (-0.48 ± 0.002 GtC/year) (Fred Mackenzie, personal communication, October 26, 2005; Mackenzie and Lerman, 2006, Figure 10.7) because of the combined effect of $CaCO_3$ deposition and organic metabolism (Smith and Mackenzie, 1987). This is counteracted by a net CO_2 uptake flux to the terrestrial biosphere (0.36 to 0.6 GtC/year) (Fred Mackenzie, personal communication, October 26, 2005; Mackenzie and Lerman, 2006, Figure 10.7). In ACC2, constant fluxes of preindustrial ocean CO_2 outgassing and preindustrial land CO_2 uptake are separately introduced. The magnitudes of these preindustrial fluxes are estimated in the inverse calculation. The addition of the preindustrial CO_2 fluxes partially resolves the drawback of the quasi-steady state assumption discussed earlier. These preindustrial fluxes are treated as if they were emissions in a sense that these fluxes directly affect the atmospheric CO_2 content but not the ocean and land carbon pools. Such a treatment does not lead to a serious error for the carbon budget on a time scale of the simulation because preindustrial fluxes are almost negligible relative to the gigantic carbon storages in the ocean (38,000 GtC (IPCC, 2001, Figure 3.1)) and over land (2,000 GtC (IPCC, 2001, Figure 3.1)).

The preceding discussion summarizes the carbon cycle modelling in ACC2. Detailed and technical explanations on the ocean and land CO_2 uptake follow. The explanation of the ocean CO_2 uptake is in particular devoted to the following two complications. First, the differential equations of the ocean box model are decoupled by being expressed in the eigen-system so that the decoupled differential equations are comparable with the IRF. In contrast, the conversion to the eigen-system was not needed for the land box model due to its reservoir configuration that all the four reservoirs are directly connected to the atmosphere without any flow between the reservoirs. Second, the thermodynamic equilibria among the marine carbonate species are described to adjust the ocean CO_2 uptake with increasing atmospheric CO_2 concentration. Our approach is simple relative to other approaches centering on the carbonate system (e.g. Andersson et al., 2006). Justification of our approach requires argumentation from a wider perspective of the ocean carbon cycle (subsection on limitations on ocean CO_2 uptake in ACC2).

2.1.2. Ocean CO_2 Uptake

- Atmosphere-Ocean Box Model

The ocean CO_2 uptake is represented by a four-layer box model. The uppermost layer represents a composite layer consisting of the atmosphere and the ocean mixed layer, while the three subsequent layers represent the ocean's inorganic carbon storage capacity. The mixed layer is characterized as being isothermally uniform due to the wind mixing and insolation, usually up to a depth of 50 to 150 m (Tomczak and Godfrey, 1994, p.56). The composite layer approach is justified because the model's numerical time step (= 1 year) is larger than the equilibrium time of the atmosphere-mixed layer system with respect to CO_2 (about 240 days in Zeebe and Wolf-Gladrow (2001, pp.80–81)). Note that only inorganic carbon is modelled in this atmosphere-ocean box model.

When the CO_2 emission is exogenously added to the atmosphere in an equilibrated system, the perturbed amounts of carbon in the reservoirs over time are described in the following dynamic equation.

$$\dot{\mathbf{c}}_{atm-ocn} + \mathbf{D}\mathbf{c}_{atm-ocn} = \mathbf{e}\,, \tag{2.1.1}$$

$$\text{with} \quad \mathbf{c}_{atm-ocn} = \begin{bmatrix} c_{cmp,1}(t) \\ c_{ocn,2}(t) \\ c_{ocn,3}(t) \\ c_{ocn,4}(t) \end{bmatrix}, \quad \mathbf{e} = \begin{bmatrix} e_1(t) \\ 0 \\ 0 \\ 0 \end{bmatrix}, \tag{2.1.2}$$

$$\text{and} \quad \mathbf{D} = \begin{bmatrix} \eta_{1,2}/h_1 & -\eta_{1,2}/h_2 & 0 & 0 \\ -\eta_{1,2}/h_1 & (\eta_{1,2}+\eta_{2,3})/h_2 & -\eta_{2,3}/h_3 & 0 \\ 0 & -\eta_{2,3}/h_2 & (\eta_{2,3}+\eta_{3,4})/h_3 & -\eta_{3,4}/h_4 \\ 0 & 0 & -\eta_{3,4}/h_3 & \eta_{3,4}/h_4 \end{bmatrix}. \tag{2.1.3}$$

$c_{x,i}(t)$ denotes the amount of perturbed inorganic carbon stored in reservoir i $(i = 1,2,\cdots,4)$ at time t. Note that $c_{x,i}(t)$ does not include the preindustrial (or background) inorganic carbon, which was present prior to the perturbation. The reservoir designation is assigned from top to bottom. $e_1(t)$ denotes the time-dependent anthropogenic CO_2 emission in the atmosphere. The inventory of the perturbed carbon is controlled through Newtonian fluxes across the boundaries. $\eta_{i,i+1}$ denotes the Newtonian transfer coefficient between reservoir i and reservoir $i+1$. h_i denotes the water-column depth of reservoir i; in particular, h_1 is a fictitious depth of the composite layer including the water-column-equivalent depth for the atmosphere in terms of the carbon content. By expressing the dynamic equation in the eigen-system, the four-dimensional dynamic equation is 'disentangled' to a set of decoupled differential equations as follows:

$$\sum_{k=1}^{4} \dot{x}_k(t)\mathbf{g}_k + \mathbf{D}\sum_{k=1}^{4} x_k(t)\mathbf{g}_k = \sum_{k=1}^{4} r_k(t)\mathbf{g}_k\,, \tag{2.1.4}$$

$$\Leftrightarrow \sum_{k=1}^{4} \dot{x}_k(t)\mathbf{g}_k + \sum_{k=1}^{4} \lambda_k x_k(t)\mathbf{g}_k = \sum_{k=1}^{4} r_k(t)\mathbf{g}_k \tag{2.1.5}$$

$$\text{with} \quad \mathbf{c}(t) = \sum_{k=1}^{4} x_k(t)\mathbf{g}_k \quad \text{and} \quad \mathbf{e}(t) = \sum_{k=1}^{4} r_k(t)\mathbf{g}_k \ . \tag{2.1.6}$$

$\mathbf{g}_k$ and λ_k are the *k*th eigenvector of matrix $\mathbf{D}$ and the corresponding eigenvalue, respectively.

We now consider a case with a pulse emission at time 0, that is $\mathbf{e}_\delta(t) = \delta(t) \cdot \begin{bmatrix} e_{\delta,init,1} \\ 0 \\ 0 \\ 0 \end{bmatrix}$,

where $\delta(t)$ and $e_{\delta,init,1}$ denote the Dirac's delta function and the initial magnitude of the pulse emission, respectively. The differential equation $\dot{x}_{\delta,k}(t) + \lambda_k x_{\delta,k}(t) = r_{\delta,k}(t)$, $k = 1,2,\cdots,4$, a special case of equation (2.1.5), has the following solution: $x_{\delta,k}(t) = r_{\delta,init,k} \exp(-\lambda_k t)$, where $\mathbf{r}_\delta(t) = \delta(t) \cdot \begin{bmatrix} r_{\delta,init,1} \\ r_{\delta,init,2} \\ r_{\delta,init,3} \\ r_{\delta,init,4} \end{bmatrix}$.[3] Now, using equation (2.1.6), the solution for the composite layer is given as

$$c_{\delta,cmp,1}(t) = \sum_{k=1}^{4} x_{\delta,k}(t) g_{k,1} = \sum_{k=1}^{4} r_{\delta,init,k} \exp(-\lambda_k t) g_{k,1} \ . \tag{2.1.7}$$

In the following, the parameters in the box model are conversely obtained from the IRF, opposite to the conventional way of establishing a box model (Garrels et al., 1975).

- IRF for Ocean CO_2 Uptake

Hooss (personal communication) found that, after a pulse injection in the amount of 1% of the preindustrial CO_2 concentration, a sum of four exponential functions with different lifetimes is the best least-square model that fits the temporal attenuation curve representing the amount of CO_2

[3] More generally, a perturbation driven by *continuous* emissions is expressed by the convolution of the IRF: $\int_{-\infty}^{t} e(t') IRF_{ocn}(t-t')dt'$, where $e(\cdot)$ denotes the time series of CO_2 emissions. The IRF convolution can be interpreted as the Green's function solution of the following system of *n* decoupled first-order differential equations:

$$\dot{x}_k = -\frac{x_k}{\tau_{ocn,k}} + A_{ocn,k} e(t), \quad k = 1,2,\cdots,4 \ . \tag{2.1.8}$$

The solutions for the individual differential equations are summed up to

$$\sum_{k=1}^{4} x_k(t) = \int_{-\infty}^{t} e(t') \cdot IRF_{ocn}(t-t')dt' \tag{2.1.9}$$

and each of the individual solutions is

$$x_k(t) = \int_{-\infty}^{t} e(t') \cdot A_{ocn,k} \exp\left(\frac{-t}{\tau_{ocn,k}}\right) dt' \ . \tag{2.1.10}$$

remained in the atmosphere as it is absorbed to the ocean (based on HAMOCC 3i) (Figure 2.1). The normalized IRF for ocean CO_2 uptake (R01 experiment[4] in Hooss (2001, Figure 3.1)) is given as follows:

$$IRF_{ocn}(t) = \sum_{i=0}^{4} A_{ocn,i} \exp\left(\frac{-t}{\tau_{ocn,i}}\right), \tag{2.1.11}$$

$$\text{with } \sum_{i=0}^{4} A_{ocn,i} = 1, \begin{bmatrix} A_{ocn,0} \\ A_{ocn,1} \\ A_{ocn,2} \\ A_{ocn,3} \\ A_{ocn,4} \end{bmatrix} = \begin{bmatrix} 0.095 \\ 0.209 \\ 0.253 \\ 0.311 \\ 0.132 \end{bmatrix}, \text{ and } \begin{bmatrix} \tau_{ocn,0} \\ \tau_{ocn,1} \\ \tau_{ocn,2} \\ \tau_{ocn,3} \\ \tau_{ocn,4} \end{bmatrix} = \begin{bmatrix} 1.271 \\ 12.17 \\ 59.52 \\ 236.5 \\ \infty \end{bmatrix}, \tag{2.1.12}$$

where t is time in year. $\tau_{ocn,i}$ is the time constant for each of the four dominant decaying modes. $\tau_{ocn,0}$ can be interpreted as the time constant for the ocean mixed layer. $A_{ocn,4}$ indicates the asymptotic fraction of the initial perturbation i.e. what eventually remains in the atmosphere.

- Parameter Estimation of Atmosphere-Ocean Box Model

In order to estimate the box model parameters, we associate the box model solutions with the IRF under the simplified case of a pulse emission. One of the box model solutions (equation (2.1.7)) represents the temporal decay of the perturbation in the composite layer whereas the IRF describes the perturbation decay only in the atmosphere. The IRF can be modified to be comparable directly with the composite layer solution by making use of the equilibrium condition for the atmosphere-mixed layer carbon transfer. $A_{ocn,0}$ (equation (2.1.12)) can be interpreted as the fraction of perturbed carbon immediately absorbed into the mixed layer after the pulse emission. Thus, the ratio of the carbon content in the atmosphere to that in the mixed layer is maintained at $\frac{A_{ocn,0}}{1-A_{ocn,0}}$ as long as the pulse emission is sufficiently small. The corresponding lifetime $\tau_{ocn,0}$ in equation (2.1.12) confirms that the atmosphere-mixed layer equilibrium assumption is justified for the 5-year-mean NICCS and ICM. It can be also justified for the annual-mean ACC2 as long as one does not particularly look into the short-term ocean response to interannual atmospheric CO_2 variations.

Thus, the IRF (equation (2.1.11)) can be modified to express the perturbed carbon in the composite layer as follows:

$$e_{\delta,init,1} \cdot \frac{1}{1-A_{ocn,0}} \sum_{j=1}^{4} A_{ocn,j} \exp\left(\frac{-t}{\tau_{ocn,j}}\right), \tag{2.1.13}$$

[4] The sediment interaction is not included in the R01 experiment (Georg Hooss, personal communication).

where the scaling term $\frac{1}{1-A_{ocn,0}}$ is simply obtained from $\frac{(1-A_{ocn,0})+A_{ocn,0}}{1-A_{ocn,0}}$ and the highest turnover term corresponding to $A_{ocn,0}$ has been dropped. By comparing the modified IRF (equation (2.1.13)) with the box model solution for the composite layer (equations (2.1.7)), the following relationships can be derived:

$$\lambda_j = \frac{1}{\tau_{ocn,j}}, \text{ with } j = 1,\cdots,4, \tag{2.1.14}$$

$$r_{\delta,init,j} \cdot g_{1,j} = e_{\delta,init,1} \cdot \frac{A_{ocn,j}}{1-A_{ocn,0}}. \tag{2.1.15}$$

Equation (2.1.14) indicates $\lambda_4 = 0$.

At this point, only the relative relationships among the unknowns can be obtained. To complete the analogy between the box model solutions and the IRF, we must fix one more unknown, namely the depth of the mixed layer as follows. CO_2 dissolved in the ocean exists in different chemical forms (CO_2(aq), H_2CO_3, HCO_3^-, and CO_3^{2-}), the sum of which is collectively termed the Dissolved Inorganic Carbon (DIC). The fractional change in the atmospheric CO_2 partial pressure can be related to the fractional change in the DIC concentration in the mixed layer by using the Revelle factor, ξ, as follows:

$$\frac{c_{atm}(t)}{\bar{c}_{atm}^{pre}} = \xi \cdot \frac{[\mathrm{DIC}(t)]_{mix} - [\overline{\mathrm{DIC}}]_{mix}^{pre}}{[\overline{\mathrm{DIC}}]_{mix}^{pre}}. \tag{2.1.16}$$

The denominators express the preindustrial (or background) amounts while the numerators express the perturbed amounts. $\bar{c}_{atm}^{pre}$ and $c_{atm}(t)$ denote the preindustrial (594 GtC in equation (37) of Hooss et al. (1999)) and perturbed fractions of the atmospheric carbon load, respectively. $[\overline{\mathrm{DIC}}]_{mix}^{pre}$ and $[\mathrm{DIC}(t)]_{mix}$ denote the DIC concentrations during the preindustrial period (2.0809 mol/m^3 in equation (37) of Hooss et al. (1999)) and at time t, respectively. Note that $[\mathrm{DIC}(t)]_{mix}$ is the total DIC including its preindustrial fraction. Here the Revelle factor is assumed to be a preindustrial constant value (= 9.25401 in equation (37) of Hooss et al. (1999)). This assumption is valid under a small perturbation (subsection on carbonate chemistry). $[\mathrm{DIC}(t)]_{mix}$ is expressed as

$$[\mathrm{DIC}(t)]_{mix} - [\overline{\mathrm{DIC}}]_{mix}^{pre} = \frac{c_{mix}(t)}{Area_{ocn} \cdot h_{mix}}, \tag{2.1.17}$$

where $c_{mix}(t)$, $Area_{ocn}$, and h_{mix} are the perturbed carbon amount in the mixed layer, the area of the world ocean (= 3.62×10^{14} m^2 in equation (37) of Hooss et al. (1999)), and the global-mean depth of the mixed layer, respectively. Under a small perturbation, the atmosphere-mixed layer equilibrium condition leads to

$$\frac{c_{mix}(t)}{c_{atm}(t)} = \frac{A_{ocn,0}}{1-A_{ocn,0}}. \tag{2.1.18}$$

Based on equations (2.1.16), (2.1.17), and (2.1.18), the following relationship can be derived:

$$h_{mix} = \frac{\xi \cdot \bar{c}_{atm}^{pre}}{Area_{ocn} \cdot [\overline{\mathrm{DIC}}]_{mix}^{pre}} \cdot \frac{A_{ocn,0}}{1 - A_{ocn,0}} . \tag{2.1.19}$$

With a different expression of the equilibrium condition, $\frac{h_{mix}}{h_1} = A_{ocn,0}$, one can derive the following:

$$h_1 = \frac{\xi \cdot \bar{c}_{atm}^{pre}}{Area_{ocn} \cdot [\overline{\mathrm{DIC}}]_{mix}^{pre}} \cdot \frac{1}{1 - A_{ocn,0}} . \tag{2.1.20}$$

Now h_1 can be directly computed from equation (2.1.20).

Therefore, equations (2.1.14), (2.1.15), and (2.1.20) are used to compute 7 unknowns ($h_1, h_2, h_3, h_4, \eta_{1,2}, \eta_{2,3}, \eta_{3,4}$) in the box model dynamic equation (equation (2.1.4)). Once the 7 unknowns are estimated, λ_j, $r_{\delta,init,j}$, $g_{1,j}$ can be determined. The solutions are numerically computed by iteration as no explicit analytical relationships between the IRF and box model solutions can be derived (Hooss et al., 1999, Appendix E). The parameter values adopted in ACC2 (corresponding to R01 NA in Table 3.2 of Hooss (2001)) are as follow:

$$\begin{pmatrix} h_1 \\ h_2 \\ h_3 \\ h_4 \end{pmatrix} = \begin{pmatrix} 768 \\ 479 \\ 1{,}299 \\ 2{,}723 \end{pmatrix} \text{ in m,} \tag{2.1.21}$$

$$\begin{pmatrix} \eta_1 \\ \eta_2 \\ \eta_3 \end{pmatrix} = \begin{pmatrix} 19.30 \\ 10.33 \\ 7.23 \end{pmatrix} \text{ in year}^{-1}. \tag{2.1.22}$$

h_{mix} is estimated to be 73 m.

The atmosphere-mixed layer equilibrium assumption has been extensively used because the shortest lifetime in the IRF requires the box model to combine the atmosphere and the mixed layer. If the model run time step is further reduced, the atmosphere and the mixed layer have to be separated and the equilibrium assumption would no longer be valid.

- Carbonate Chemistry

In estimating the box model parameters by using the IRF, the Revelle factor is assumed to be constant, implying that the relative abundances of the carbonate species are kept unchanged and ensuring that the atmospheric CO_2 concentration change always affects the ocean CO_2 uptake linearly. However, in reality, the rate of ocean CO_2 uptake is saturated with rising atmospheric CO_2 concentration because the ocean buffers against the pH drop (Figures 2.3 and 2.4). This buffering mechanism is provided by the dissociate carbonate species functioning as weak acids. In the following, we dynamically describe the thermodynamic equilibria for the carbonate species. The addition of the explicit thermodynamic equilibria extends the validity of the model beyond the linear range of the calibration with IRF; the valid upper range has been extended from the doubling to the

quadruple of the preindustrial CO_2 concentration (Hooss, 2001).

When a CO_2 molecule in the atmosphere (CO_2(g)) is dissolved in the seawater, H_2O molecules cluster around the CO_2 molecule, a process termed electrostriction, resulting in the production of CO_2(aq). Approximately 0.1% of CO_2(aq) is turned into carbonic acid (H_2CO_3) but both are collectively expressed as CO_2(aq) for convenience below.

$$CO_2(g) \leftrightarrow CO_2(aq) \tag{2.1.23}$$

CO_2(aq) progressively dissociates to aqueous ions of HCO_3^- and CO_3^{2-} as described in the following chemical equations.

$$CO_2(aq) + H_2O \leftrightarrow H^+ + HCO_3^- \tag{2.1.24}$$

$$HCO_3^- \leftrightarrow H^+ + CO_3^{2-} \tag{2.1.25}$$

DIC is defined as

$$[DIC] = [CO_3^{2-}] + [HCO_3^-] + [CO_2(aq)]\,. \tag{2.1.26}$$

The particular CO_2 molecular structure and the resulting affinity to H_2O molecules explain why CO_2 accounts for a disproportionately large fraction of gases dissolved in the seawater relative to the fraction in the atmosphere. These also explain the large capacity of CO_2 storage in the ocean, but the multiple dissociation of CO_2(aq) is another important factor. The CO_2 dissociation allows more than 90% of the carbon in the seawater to be present as aqueous ions, which are not directly bounded by the CO_2 pressure equilibrium at the air-sea surface. However, this ocean's carbon storage capacity is not without limit; increasing CO_2 concentration acidifies the ocean, resulting in less CO_2 dissociation (in other words, the reactions in equations (2.1.24) and (2.1.25) are pushed to backward) (Figure 2.2). The chain of the chemical equations (equations (2.1.23) – (2.1.25)) provides the buffering effect of the ocean pH ($=-\log_{10}[H^+]$) against the change in the atmospheric CO_2 concentration. Thus, the sensitivity of the ocean CO_2 uptake to the air-sea CO_2 pressure difference becomes low under rising atmospheric CO_2 concentration. Dissolution of calcium carbonate does play a role in the buffering by providing CO_3^{2-} to lock additional H^+, but this process is not included in ACC2 and its implication is discussed in the last subsection of this section.

The following reactions also contribute to the buffering against the pH change:

$$H_2O \leftrightarrow H^+ + OH^-\,, \tag{2.1.27}$$

$$B(OH)_4^- + H^+ \leftrightarrow B(OH)_3 + H_2O. \tag{2.1.28}$$

Thus, the Total Alkalinity (TA), essentially expressing the buffering ability of the seawater against the change in pH, can be written as

$$[TA] = 2[CO_3^{2-}] + [HCO_3^-] + [B(OH)_4^-] + [OH^-] - [H^+]\,. \tag{2.1.29}$$

Weak acids containing phosphate, silicate, ammonia, and others are omitted because of their low concentrations.

Now, the thermodynamic equilibria for the foregoing reactions (equations (2.1.23) – (2.1.25), (2.1.27), and (2.1.28)) can be written as follows:

$$\mathrm{pCO_2} = \frac{1}{K_0^*}[\mathrm{CO_2}(aq)], \tag{2.1.30}$$

$$[\mathrm{H^+}][\mathrm{HCO_3^-}] = K_1^*[\mathrm{CO_2}(aq)], \tag{2.1.31}$$

$$[\mathrm{H^+}][\mathrm{CO_3^{2-}}] = K_2^*[\mathrm{HCO_3^-}], \tag{2.1.32}$$

$$[\mathrm{H^+}][\mathrm{OH^-}] = K_w^*, \tag{2.1.33}$$

$$[\mathrm{H^+}][\mathrm{B(OH)_4^-}] = K_B^*[\mathrm{B(OH)_3}]. \tag{2.1.34}$$

$\mathrm{pCO_2}$ denotes the partial pressure of atmospheric $\mathrm{CO_2}$.[5] The shift in the thermodynamic equilibria for $\mathrm{CO_2}$(aq), $\mathrm{HCO_3^-}$, and $\mathrm{CO_3^{2-}}$ under changing pH is shown in Figure 2.2.

K_0^* is the inverse of the Henry's constant (3.265×10^{-2} mol/kg/atm in Hooss (2001, p.95)). K_1^*, K_2^*, K_w^*, and K_B^* are the associated thermodynamic equilibrium constants (9.709×10^{-7} mol/kg, 6.903×10^{-10} mol/kg, 6.152×10^{-15} mol^2/kg^2, and 1.835×10^{-9} mol/kg, respectively, in Bacastow (1981, p.101) obtained from Keeling (1973)). The preceding values are used to compute $[\overline{\mathrm{DIC}}]_{mix}^{pre}$ and the Revelle factor for the box model parameter estimation ($h_1, h_2, h_3, h_4, \eta_{1,2}, \eta_{2,3}, \eta_{3,4}$) (Hooss et al., 1999, p.19). Note that the actual values implemented in the GAMS code are scaled with different units. The current estimates of the thermodynamic constants are somewhat different. The examples of the estimates today for K_0^*, K_1^*, K_2^*, and K_w^* are 3.746×10^{-2} mol/kg/atm, 1.119×10^{-6} mol/kg, 7.970×10^{-10} mol/kg, and 2.380×10^{-14} mol^2/kg^2, respectively, at 15°C at the salinity of 35 in Mackenzie and Lerman (2006, Table 5.2) calculated based on Zeebe and Wolf-Gladrow (2001, pp.255-258, 266-267). The current estimate of K_w^* in particular is larger by a factor of 4 than the old estimate. The actual thermodynamic constants used in ACC2 to characterize the carbonate system are temperature dependent and shown in the next subsection.

The asterisks in superscript mean that the effects of electrostatic interactions among charged solutes, which are important in solution with high ion concentrations such as seawater, are taken into account in the these constants. The well-hydrated strong electrolytes have only long-range nonspecific electrostatic interactions while the not-well-hydrated weak electrolytes have short-range specific interactions resulting in the formation of ion pairs and complex ions (Millero, 2006, Chapters 4 and 7). The effective concentrations influencing the chemical reactions, called activities, are smaller in seawater than the ideal stoichiometric concentrations. Because the ion species are defined in stoichiometric concentrations in ACC2, the effects of the electrostatic interactions must be

[5] Although the partial pressure is a term used interchangeably with the mole fraction here, the mole fraction is a more consistent property with altitude. To be precise, $\mathrm{pCO_2}$ represents the fugacity of atmospheric $\mathrm{CO_2}$. The relationship between the partial pressure and the fugacity is similar to that between the concentration and the activity (or effective concentration) in aqueous solutions. The fugacity approaches the partial pressure in dilute mixtures as the activity approaches the concentration in dilute solutions. The fugacity of the atmospheric $\mathrm{CO_2}$ at present is smaller than the partial pressure by merely 0.7% (Zeebe and Wolf-Gladrow, 2001, pp.61–67). Thus, the distinction between the partial pressure and fugacity is not critical in the discussion here.

reflected in the equilibrium constants.

The total boron concentration is assumed to be constant (= 4.09×10^{-4} mol/liter in Bacastow (1981) and Hoffert et al. (1981))[6], based on the fact that the rate of main Boron removal due to oceanic mineral-water reactions has been balanced with the rate of Boron input from the continents on our time scale (Harriss, 1969). That is,

$$[\mathrm{B(OH)_4^-}]+[\mathrm{B(OH)_3}]=4.09\times10^{-4}\,(\mathrm{mol/liter})\,. \qquad (2.1.35)$$

So far the carbonate system has a total of ten variables: pCO_2, [DIC], $[CO_2(aq)]$, $[HCO_3^-]$, $[CO_3^{2-}]$, $[H^+]$, $[OH^-]$, $[B(OH)_3]$, $[B(OH)_4^-]$, and TA with eight constraints (equations (2.1.26) and (2.1.29) – (2.1.35)).[7] Additional two constraints to characterize the carbonate system come from the specifications for pCO_2 and TA. First, the atmospheric CO_2 concentration is fixed at 277 ppm in 1750 (Etheridge et al., 1996) and iteratively computed in the following years in the model. Second, as a first order assumption, the mean total alkalinity is maintained at a constant value of 2.435×10^{-3} mol-equivalent/liter (Bacastow, 1981; Hoffert et al., 1981)[8] because a significant amount of carbonate precipitation or dissolution or addition of alkalinity from land did not occur during the historical period of the model run (Mackenzie and Lerman, 2006, p.136) and is assumed negligible for next hundreds of years. An implication of the TA assumption can be seen from the condition of electroneutrality that the electrical charges of the ions susceptible to H^+ (that is, TA) must be balanced with those not susceptible (that is, major ions) in the following.

$$\begin{aligned}&2[\mathrm{CO_3^{2-}}]+[\mathrm{HCO_3^-}]+[\mathrm{B(OH)_4^-}]+[\mathrm{OH^-}]-[\mathrm{H^+}]\\&\quad=[\mathrm{Na^+}]+[\mathrm{K^+}]+2[\mathrm{Mg^{2+}}]+2[\mathrm{Ca^{2+}}]-[\mathrm{Cl^-}]-2[\mathrm{SO_4^{2-}}]\end{aligned} \qquad (2.1.36)$$

Equation (2.1.36) shows that the constant TA assumption confirms the conservation of the major ions. Conversely it also indicates that the concentration of the total major ions determines TA, in which the composition of the alkalinity species is allowed to change. Thus, the TA assumption greatly simplifies the characterization of the carbonate system (see carbonate pump in subsection on limitation).

With pCO_2 and TA fixed, [DIC] and pH are numerically calculated in ACC2 using equations (2.1.37) and (2.1.38). This approach is essentially the same with the predecessor model ICM, but ACC2 implements the simpler equations (equations (2.1.37) and (2.1.38)). pH is given

[6] The thermodynamic equilibria of the carbonate species in ACC2 are not so sensitive to the total boron concentration when it changes ±10% (results not shown).

[7] It is commonly known that characterization of the carbonate system requires the estimates of two of the following four measurable quantities: pH, TA, [DIC], and pCO_2 (Park, 1969; Millero, 2006, Chapter 7).

[8] This value above is consistent with the box model parameter estimation. This value is slightly larger than 2.29 to 2.38×10^{-3} mol-equivalent/liter (Takahashi, 1989) and the global alkalinity distribution as functions of Sea Surface Temperature (SST) and Sea Surface Salinity (SSS) (Lee et al., 2006). However, a separate analysis indicated that the thermodynamic equilibria of the carbonate species in ACC2 are not so sensitive to the assumed representative value of the alkalinity when it is within the literature range (results not shown).

from the solution of $[H^+]$ of the following equation:

$$[\mathrm{TA}] = \mathrm{pCO}_2 K_0^* \left(1 + \frac{K_1^*}{[\mathrm{H}^+]} + \frac{K_1^* K_2^*}{[\mathrm{H}^+]^2} \right) + \frac{[\mathrm{B(OH)}_4^-] + [\mathrm{B(OH)}_3]}{1 + \frac{[\mathrm{H}^+]}{K_B^*}} + \frac{K_w^*}{[\mathrm{H}^+]} - [\mathrm{H}^+]. \quad (2.1.37)$$

The solution for [DIC] is then expressed as a function of $[H^+]$ as follows:

$$[\mathrm{DIC}] = \mathrm{pCO}_2 K_0^* \left(1 + \frac{K_1^*}{[\mathrm{H}^+]} + \frac{K_1^* K_2^*}{[\mathrm{H}^+]^2} \right). \quad (2.1.38)$$

The foregoing results are implemented to the atmosphere-ocean box model in Section 2.1.4.

- Temperature Feedback to Ocean CO_2 Uptake

In the section above, the thermodynamic dependence on the ocean buffering effect is introduced. We now implement the temperature dependence by redefining the thermodynamic constants as functions of the mixed layer temperature. The thermodynamic constants are sensitive to in-situ temperature (Figure 2.3) and pressure but the pressure dependence is not important in the mixed layer. ACC2 adopted the following dissociation constants based on a number of laboratory experiments and field measurements (Millero, 1995; Millero et al., 2006; other references therein).

$$\ln K_0^* = \ln K_0^0 + A_0 \cdot S_{mix} \quad (2.1.39)$$

$$\ln K_0^0 = -60.2409 + 93.4517 \cdot \left(\frac{100}{T_{mix}} \right) + 23.3585 \ln \left(\frac{T_{mix}}{100} \right)$$

$$A_0 = 0.023517 - 0.023656 \left(\frac{T_{mix}}{100} \right) + 0.0047036 \left(\frac{T_{mix}}{100} \right)^2$$

$$\mathrm{p}K_1^* - \mathrm{p}K_1^0 = A_1 + B_1 / T_{mix} + C_1 \cdot \ln T_{mix} \quad (2.1.40)$$

$$\mathrm{p}K_1^0 = -126.34048 + 6320.813 / T_{mix} + 19.568224 \ln T_{mix}$$

$$A_1 = 13.4191 \cdot \sqrt{S_{mix}} + 0.0331 \cdot S_{mix} - 5.33 \times 10^{-5} \cdot {S_{mix}}^2$$

$$B_1 = -530.123 \cdot \sqrt{S_{mix}} - 6.103 \cdot S_{mix}$$

$$C_1 = -2.06950 \cdot \sqrt{S_{mix}}$$

$$\mathrm{p}K_2^* - \mathrm{p}K_2^0 = A_2 + B_2 / T_{mix} + C_2 \cdot \ln T_{mix} \quad (2.1.41)$$

$$\mathrm{p}K_2^0 = -90.18333 + 5143.692 / T_{mix} + 14.613358 \ln T_{mix}$$

$$A_2 = 21.0894 \cdot \sqrt{S_{mix}} + 0.1248 \cdot S_{mix} - 3.687 \times 10^{-4} \cdot {S_{mix}}^2$$

$$B_2 = -772.483 \cdot \sqrt{S_{mix}} - 20.051 \cdot S_{mix}$$

$$C_2 = -3.3336 \cdot \sqrt{S_{mix}}$$

$$\ln K_B^* = A_B \cdot \frac{1}{T_{mix}} + B_B + C_B \cdot \ln T_{mix} + D_B \cdot T_{mix} \tag{2.1.42}$$

$$A_B = 8966.90 - 2890.51 \cdot \sqrt{S_{mix}} - 77.942 \cdot S_{mix} + 1.726 \cdot S_{mix}^{1.5} - 0.0993 \cdot S_{mix}^{2}$$

$$B_B = 148.0428 + 137.194 \cdot \sqrt{S_{mix}} + 1.62247 \cdot S_{mix}$$

$$C_B = -24.4344 - 25.085 \cdot \sqrt{S_{mix}} + 0.2474 \cdot S_{mix}$$

$$D_B = 0.053105 \cdot \sqrt{S_{mix}}$$

$$\ln K_w^* = \ln K_w^0 + A_w \cdot \sqrt{S_{mix}} + B_w \cdot S_{mix} \tag{2.1.43}$$

$$\ln K_w^0 = 148.9802 - 13847.26 / T_{mix} - 23.6521 \ln T_{mix}$$
$$A_w = -5.977 + 118.67 / T_{mix} + 1.0495 \ln T_{mix}$$
$$B_w = -1.615 \times 10^{-2}$$

$\ln x$ is a logarithmic function of x having natural base. px is defined as $\mathrm{p}x = -\log_{10} x$ (just as pH). S_{mix} denotes the average salinity of the mixed layer, the value of which is fixed at a representative global-mean estimate of 34.76 (Hoffert et al., 1981). The fixed salinity assumption is consistent with the fixed TA assumption discussed previously because TA is equivalent to the charge balance of the conservative ions (equation (2.1.36)) (Zeebe and Wolf-Gladrow, 2001, p.48). Note that the thermodynamic constants are also not so sensitive to the salinity when it is varied between 1.02 and 1.03 (results now shown). T_{mix} is a representative temperature of the ocean mixed layer (in Kelvin), parameterized with the preindustrial temperature of the mixed layer, T_{mix}^{pre}, and a damping factor, γ, to attenuate the change in surface air temperature change over the ocean, $\delta T_{ocn-air}(t)$, to the mixed layer temperature change as follows:

$$T_{mix}(t) = T_{mix}^{pre} + \gamma \cdot \delta T_{ocn-air}(t) . \tag{2.1.44}$$

The value of $\delta T_{ocn-air}(t)$ is computed by the climate component DOECLIM (Section 2.3). If the IRF is rather employed for temperature calculation, the global-mean temperature change computed from IRF is instead used in equation (2.1.44) (First paragraph of Section 2.3). The values of the preindustrial mixed layer temperature T_{mix}^{pre} and the temperature damping factor γ are estimated in the ACC2 inverse calculation.

The concentration quantities in ACC2 are defined with the molar units of mol/L while the thermodynamic constants are preferably defined with the gravimetric units of mol/kg because they are not dependent on the temperature and pressure. Conversions between the units to define concentrations and thermodynamic constants are made by using the average seawater density of 1.025 kg/L (Hoffert et al., 1981). One should not be confused between molality (or *molal*

concentrations; mol/kg-H_2O) and molarity (or *molar* concentration; mol/L) (Zeebe and Wolf-Gladrow, 2001, pp.251-253; Mackenzie and Lerman, 2006, p.124).

The functions for K_1^* and K_2^* above are taken from Millero et al. (2006) and the others from Millero (1995) and other references therein. The functions for K_1^* and K_2^* in Millero et al. (2006) were obtained from the measurements in real seawater. They are the replacements for the earlier functions in Millero (1995) based on artificial seawater, which would require further corrections on ion pairing to use as thermodynamic constants (F. Millero, personal communication, September 28, 2006). The functions for K_B^* and K_w^* (Millero, 1995) are also obtained from artificial water, but the corrections for ion pairing are not necessary because the reactions of Mg^{2+} and Ca^{2+} with $B(OH)_4^-$ and OH- are include in the artificial seawater measurements (F. Millero, personal communication, October 13, 2006). The K_1^* and K_2^* functions appearing in the abstract in Millero et al. (2006) should be used. The same functions in Millero et al. (2006, Table 5) contain some editorial errors (F. Millero, personal communication, October 13, 2006). Although different functions for K_1^* and K_2^* are shown in Millero (2006, Chapter 7.3), the functions in Millero et al. (2006) should be used (F. Millero, personal communication, September 28, 2006). There are various different estimates of the thermodynamic constants available, which are extensively discussed in Zeebe and Wolf-Gladrow (2001, pp.251-270). The largest factor giving rise to the differences in the thermodynamic constant values is the different pH scales[9] (Zeebe and Wolf-Gladrow, 2001, Table 1.1.4).

- Limitations for Ocean CO_2 Uptake in ACC2

Of the three major mechanisms of the ocean's control on the atmospheric CO_2 content (solubility pump, carbonate pump, and soft tissue pump) (Mackenzie and Lerman, 2006, pp.305-309), the solubility pump is partly modelled and the soft tissue and carbonate pumps are not at all modelled in ACC2. Although it was shown that describing only the thermodynamic equilibria of carbonate species as we modelled is a valid first-order approach (Maier-Reimer et al., 1996), it is worth discussing the implication of neglecting the other mechanisms, in the high time of mounting concern over the thermohaline circulation collapse[10], ocean acidification, and coral bleach[11]. Care must be

[9] Note that three different pH scales are in operation in aquatic chemistry, leading to the situation where the absence of the scale specification would give rise to a large uncertainty in [DIC] (Zeebe and Wolf-Gladrow, 2001, pp.53–61). Here the seawater scale pH is used for consistency with the functions of the thermodynamic constants discussed in the section of temperature feedback (Millero, 1995; Millero et al., 2006). Technically, the seawater scale pH is defined as $-\log_{10}\left([H^+]_F + [HSO_4^-] + [HF]\right)$. Also note that $[H^+]_F$ represents H_3O^+ and $H_9O_4^+$ (bonded to a water molecule) as virtually no free protons present in aqueous solutions.

[10] A partial or complete paucity of the thermohaline circulation in the future is projected in various modelling studies although the level of the threshold is not well-known. The simplified thermohaline circulation model (Zickfeld and Bruckner, 2003) can be readily coupled with ACC2 although the change in the thermohaline circulation needs to be reflected to the ocean CO_2 uptake.

taken when one uses $[H^+]$ for ocean acidification studies – one needs to be aware of the relevant assumptions of the modelling approach of the ocean carbon cycle in the following.

The solubility pump is the ocean CO_2 uptake driven by the partial CO_2 pressure difference between the atmosphere and the ocean. The rate of the solubility pump depends on the atmospheric CO_2 concentration and its rate of change (Stocker and Schmittner, 1998). The solubility pump is more intense over the cold water. ACC2 accounts for the influence of the solubility pump from the temperature change by calculating the thermodynamic equilibria explicitly, but it cannot resolve the influence from the thermohaline circulation and the ocean ventilation (Falkowski et al., 2000). As a significant portion of ocean CO_2 uptake occurs in the North Atlantic and the Southern Ocean, the rate of the large scale circulation, if it were to change abruptly in the future, is an important factor controlling the ocean CO_2 uptake.

The carbonate pump is the downward transport of calcium minerals, which are formed by calcifying organisms at the surface[12] accompanied with the evasion of atmospheric CO_2. In ACC2, the dissolution and precipitation of carbonate mineral are neglected, but such an approach is justifiable on our spatial and time scale (Ernst Maier-Reimer, personal communication, November 21, 2006). Over the longer time scale, limestone rocks play a role of stabilizing the pH of the global ocean. When CO_2 is invaded from the atmosphere (equations (2.1.23) and (2.1.24)), H^+ is generated. Then H^+ is locked up with CO_3^{2-} (equation (2.1.25)), resulting in a production of HCO_3^- (backward reaction of equation (2.1.25)). CO_3^{2-} is supplemented from the dissolution of limestone as follows:

$$CaCO_3(s) \leftrightarrow Ca^{2+} + CO_3^{2-}. \tag{2.1.45}$$

The net reaction is summarized in the following buffering reaction (Holland, 1978):

$$CO_2 + CaCO_3(s) + H_2O \rightarrow Ca^{2+} + 2\,HCO_3^-. \tag{2.1.46}$$

---

[11] The atmospheric CO_2 increase leads to more CO_2 invasion to the ocean, resulting in the ocean acidification. The intensification of the ocean acidification is reported for low latitude regions (Kleypas et al., 1999) and high latitude regions (Orr et al., 2005) by modelling approaches. It has also been shown by laboratorial studies that elevated atmospheric CO_2 concentration results in decreased calcification of coccolithophorids (Riebesell et al., 2000). The acidification is projected to penetrate substantially below the mixed layer beyond 2150 (Caldeira and Wickett, 2003). The impacts of the ocean acidification to coral reef and calcifying organisms are reported in Ruttimann (2006).

[12] In actuality, the thermodynamic equilibrium, $[Ca^{2+}][CO_3^{2-}] = K_{sp}^*$, is far from attained by the biogenical formation of calcium carbonate occurring in two different crystalline forms: 'calcite' produced by coccolithophorids and foraminifera and 'aragonite' produced by pterpods. As a result, the surface ocean is substantially supersaturated with respect to both calcite and aragonite. The state of supersaturation is maintained down to a depth of some hundreds meter with respect to aragonite and some thousands meter with respect to calcite (Mackenzie and Lerman, 2006, Figure 5.5D). Coccolithophorid blooms affect the surface pCO_2 as suggested by observations (Denman and Pena, 2000) although the mechanism leading to the onset and collapse of the blooms is not well-known from modelling studies (Tyrrell and Taylor, 1996). Their responses to climate change are different across calcifying species and their global implication is uncertain (Ridgwell et al., 2006).

Therefore, upon CO_2 invasion from the atmosphere, calcium carbonate is dissolved because of the drop in pH; calcium carbonate provides an additional buffering mechanism against the pH change. However, the provision of such a negative feedback would lead to merely a few percent change in the carbon flux (Maier-Reimer et al., 1996) and would not be consistent with the constant alkalinity assumption in ACC2.

Furthermore, the precipitation of calcium carbonate (equation (2.1.46)) competes with the primary production (equation (2.1.47)) because both of the processes consume CO_2.

$$CO_2 + H_2O \rightarrow CH_2O + O_2 \qquad (2.1.47)$$

The soft tissue pump is the downward transport of Particulate Organic Carbon (POC), which is originally formed by photosynthesis in the euphotic zone accompanied with the invasion of atmospheric CO_2.[13] The soft tissue pump is important on the millennium or longer time scale. It is estimated that, without the soft tissue pump, the atmospheric CO_2 concentration would be 150 to 200 ppm higher at present (Falkowski et al., 2000). The soft tissue pump is implicit in the atmospheric CO_2 concentration calculated in ACC2 although the marine biota itself is not modelled. The metabolism of the marine ecosystem is comparable in size with the terrestrial ecosystem (Field et al., 1998). Thus, the influence of the future climate change to the marine ecosystem metabolism is expected to have a significant implication for the global carbon cycle. In fact, satellite observations between 1997 and 2005 demonstrate that, in the midst of the warming accompanied with the reduction in surface ocean mixing, the ocean biological productivity decreased in the tropics and mid-latitudes because of the nutrient limitation (Bahrenfeld et al., 2006; Doney, 2006). However, on the time scale of ACC2, there is no evidence to suggest the relationship between the climate change and the biological productivity.

The role of the coastal zone (up to a depth of 200 m) is significant for the competition between calcium carbonate dissolution and primary production because 10 to 30% of the marine primary production and 45% of the carbonate accumulation occurs in the coastal zone (Mackenzie et al., 2004).[14] The coastal zone is not treated as a separate entity in ACC2 and even GCMs. The

[13] Because of the mineralization all the way to the deep ocean, the bottom waters are supersaturated by approximately 30% with respect to CO_2. Such a disequilibrium is maintained by vertical stratification of the ocean. The trapped CO_2 in the deep ocean returns back to the surface mainly in the Equatorial Pacific by being conveyed through the thermohaline circulation. The pCO_2 in the upwelling region is higher than other ocean (Maier-Reimer and Hasselmann, 1987)

[14] Highly complex carbonate chemistry takes place in the coastal zone, influenced by the deposition of organic carbon and inorganic nutrient from land, calcification in coral reef, pelagic and benthic ecosystem, and the water exchange with the open ocean. The coastal zone is susceptible to the mobilized carbon due to soil erosion and the nutrient discharge from fertilized land. Owing to these activities of mankind, the metabolism of the coastal zone has been shifted from net autotrophy to net heterotrophy. Although the distinct biogeochemistry in the coastal zone has a sizable impact on the ocean carbon cycle, even the state-of-the-art coupled Earth system model has no provision in treating the costal zone as a separate entity. Dynamical modelling of the marine ecosystem in the coastal zone is a difficult task due to the insufficient data and knowledge on the relevant processes

coastal zone together with the river system has been studied more in the biogeochemical approach (e.g. Andersson et al., 2006). The spatial inhomogeneity of the river system and coastal zone hardly reconciles with the GCM approach.

The arguments above are convoluted as processes involving the ocean carbon cycle are highly interlinked. To summarize, the ocean carbon cycle approach in ACC2 does not describe the change in the large-scale ocean circulation, the dissolution/precipitation of the calcium carbonate, and marine biota. Nevertheless, ACC2 describes the inorganic carbon chemistry in the ocean including its temperature dependence, the most important oceanic mechanism for determining the atmospheric CO_2 concentration. Thus, the characterization of the carbonate system (including pH) in ACC2 serves as first-order estimates.

2.1.3. Land CO_2 Uptake

- Land Box Model

ACC2 uses a box model approach to describe the CO_2 uptake associated with the NPP and the CO_2 release associated with the heterotrophic respiration; i.e. the Net Ecosystem Production (NEP) of the global terrestrial biosphere is modelled here. In ACC2, the NPP is controlled by the atmospheric CO_2 concentration and the heterotrophic respiration controlled by the surface air temperature over land. While only the fertilized carbon was modelled in the predecessor model ICM, both the background (preindustrial) and fertilized carbon is modelled in ACC2 because the temperature dependence of the heterotrophic respiration should apply for both the background and fertilized carbon.

First, we discuss the land box model without considering the temperature dependence. Thus we discuss only the fertilized carbon in this subsection. In the land box model, all the reservoirs are directly connected to the atmosphere. Thus, the governing equations for the land reservoirs are as follows:

$$\dot{c}_{ter,l}(t) = k_{ter,l} \cdot \delta f_{NPP}(t) - \frac{1}{d_{ter,l}} c_{ter,l}(t) , \tag{2.1.48}$$

$$c_{ter}(t) = \sum_{l} c_{ter,l}(t) . \tag{2.1.49}$$

$c_{ter,l}(t)$ is the amount of the fertilized carbon in reservoir l. l is the index of a land reservoir. The first term of the right side of equation (2.1.48) describes the fertilized NPP (due to the increase in the atmospheric CO_2 concentration). $\delta f_{NPP}(t)$ denotes the global fertilized NPP. $k_{ter,l}$ is a coefficient to relate the global fertilized NPP to the fertilized NPP of each reservoir l. The second term of the right side of equation (2.1.48) describes the release of carbon accumulated due to fertilized NPP. $d_{ter,l}$ is a decay time constant of each of the land reservoirs.

(Tanaka and Mackenzie, 2005).

The fertilized NPP, $\delta f_{NPP}(t)$, is further defined as:

$$\delta f_{NPP}(t) = \bar{f}_{NPP}^{pre} \beta_{NPP} \ln\left(\frac{\mathrm{pCO}_2(t)}{\mathrm{pCO}_2^{pre}}\right). \tag{2.1.50}$$

$\bar{f}_{NPP}^{pre}$ denotes the global preindustrial NPP and is assumed to be 60 GtC/year (Joos et al., 1996) under the quasi-steady state assumption. The CO_2 fertilization effect is parameterized with the beta factor, β_{NPP}, which logarithmically scales the fractional change in the atmospheric CO_2 concentration relative to its preindustrial level (277 ppm). The parameterization above is one of the standard practices in simple terrestrial biosphere models (Gifford, 1980; Friedlingstein et al., 1995). The value of the beta factor is highly uncertain (Table 3.2 for existing estimates) and is estimated in the inverse calculation. The actual response of plants to the atmospheric CO_2 concentration change varies with species and other environmental conditions (see subsection on the limitation on for land CO_2 uptake in ACC2).[15]

Equation (2.1.48) has a Green's function solution as follows:

$$c_{ter}(t) = \int_{-\infty}^{t} \delta f_{NPP}(t') \sum_l k_{ter,l} \exp\left(-\frac{t-t'}{d_{ter,l}}\right) dt' . \tag{2.1.51}$$

Under a special circumstance where a pulse change in the atmospheric CO_2 concentration is imposed at the time 0, equations (2.1.48) and (2.1.49) have the following simpler solution:

$$c_{ter}(t) = \left[\sum_l k_{ter,l} \exp\left(-\frac{t}{d_{ter,l}}\right)\right] \cdot \delta f_{NPP}(0) . \tag{2.1.52}$$

The parameters $k_{ter,l}$ and $d_{ter,l}$ are determined based on the IRF explained below.

- IRF for Land CO_2 Uptake

The temporal trajectory of the respiratory release of the fertilized biomass is expressed in the following IRF based on the Bern-CC model (Joos et al., 1996) (Figure 2.5):

$$\delta f_{NPP}(0) \cdot IRF_{ter}(t) = \delta f_{NPP}(0) \cdot \sum_{j=1}^{4} A_{ter,j} \exp\left(-\frac{t}{\tau_{ter,j}}\right), \tag{2.1.53}$$

where the values for the coefficients in the IRF (equation (2.1.53)) are given as

[15] The CO_2 fertilization effect is demonstrated both theoretically and experimentally (Free-Air CO_2 Enrichment (FACE)), but the plant response to the CO_2 concentration change depends on the functional group (trees > legumes > C_3 grasses in Ainsworth and Long (2004)), photosynthetic pathway (C_3 > C_4 in Ainsworth and Long (2004)), growth conditions (Körner, 2006), other limiting factors (water, temperature, light, and nutrients), and the experimental setup (Long et al., 2004).

$$\begin{bmatrix} A_{ter,1} \\ A_{ter,2} \\ A_{ter,3} \\ A_{ter,4} \end{bmatrix} = \begin{bmatrix} -0.71846 \\ 0.70211 \\ 0.013414 \\ 0.0029323 \end{bmatrix} \quad \text{and} \quad \begin{bmatrix} \tau_{ter,1} \\ \tau_{ter,2} \\ \tau_{ter,3} \\ \tau_{ter,4} \end{bmatrix} = \begin{bmatrix} 2.18 \\ 2.86 \\ 20 \\ 100 \end{bmatrix}. \tag{2.1.54}$$

The values of the coefficients, $A_{ter,j}$, in equation (2.1.54) are normalized such that the evaluation of the integral of the IRF (equation (2.1.53)) between 0 and ∞ is unity. Note that the maximum release of CO_2 from the terrestrial biosphere is delayed by approximately 2.7 years from the point of perturbation (Figure 2.5).

The time constants, $\tau_{ter,j}$, are chosen to be the equivalent to the overturning time constants of the reservoirs in the parent model (Bern-CC model), which are detritus, ground vegetation, wood, and soil organic carbon, respectively (Joos et al., 1996). However, each of the terms in the IRF can no longer be *physically* interpreted as a biospheric reservoir. In the IRF expression, all the reservoirs can be interpreted to be directly connected to the atmosphere. On the contrary, in the original Bern-CC model, only the vegetation and wood reservoirs are directly connected to the atmosphere; the detritus and soil reservoirs are connected to the vegetation and wood reservoirs. The reservoirs of the land box model are configured to be the same as the IRF, avoiding cumbersome matrix conversion that was necessary for the ocean counterpart. Mathematically, in the IRF expression, the matrix is made diagonal whereas, in the parent model, it would not be so. The difference in the reservoir configuration explains why a negative coefficient $A_{ter,1}$ appears in the IRF (Fortunat Joos, personal communication, January 25. 2007). The same can be seen in the High-Resolution terrestrial Biosphere Model as implemented in the Community Terrestrial Biosphere Model (HRBM/CTBM) (Meyer et al, 1999, Figure 3).

- Parameter Estimation of Land Box Model

Equation (2.1.53) is equivalent to the *time derivative* of the box model solution (equation (2.1.52)) except for the sign being opposite because equation (2.1.52) describes the carbon contents (not fluxes) of the terrestrial reservoirs. Then, by comparison, the following relationships are derived:

$$d_{ter,l} = \tau_{ter,l}, \tag{2.1.55}$$

$$k_{ter,l} = A_{ter,l}\tau_{ter,l}. \tag{2.1.56}$$

The number of the reservoirs in the box model is now chosen to be four. Therefore, the box model governing equation is

$$\dot{c}_{ter,l}(t) = A_{ter,l}\tau_{ter,l}\delta f_{NPP}(t) - \frac{1}{\tau_{ter,l}} c_{ter,l}(t), \quad l = 1,2,3,4. \tag{2.1.57}$$

One can confirm that $\sum_{l=1}^{4} A_{ter,l}\tau_{ter,l}$ is approximately equal to one (compare with equation (2.1.48)). The temperature dependence of the heterotrophic respiration is implemented to equation (2.1.57) in the next subsection.

The land box model can also be expressed as

$$\dot{c}_{ter}(t) = \delta f_{NPP}(t) - \int_{-\infty}^{t} \delta f_{NPP}(t') \sum_{j=1}^{4} A_{ter,j} \exp\left(-\frac{t-t'}{\tau_{ter,j}}\right) dt' , \qquad (2.1.58)$$

where the second term of the right side of the equation has the Joos' IRF within the integral. However, because the IRF convolution in equation (2.1.58) cannot be directly implemented to the GAMS code, the box model expression of equation (2.1.57) has been derived.

Note that the predecessor models NICCS and ICM make a further equilibrium assumption for the two short-term land reservoirs because their model time steps (5 years) are longer than the lifetimes of these short-term reservoirs (τ_1 and τ_2) (Hooss et al., 1999). The equilibrium assumption is needed to ensure numerical stability in NICCS and ICM. However, the trouble is that the assumption requires an additional term $\frac{dc_{atm}}{dc_1}$ (Hooss et al., 1999, equation (88)), leading to complication in the model implementation. Such an equilibrium treatment is not necessary for ACC2 because of the finer time step of 1 year.

- Temperature Feedback to Land CO_2 Uptake

The temperature feedback is applied to both the preindustrial and fertilized carbon. The preindustrial (or background) carbon needs to be modelled here. The following conditions can be derived from equation (2.1.57):

$$A_{ter,l}\tau_{ter,l}\bar{f}_{NPP}^{pre} = \frac{1}{\tau_{ter,l}}\bar{c}_{ter,l}^{pre} , \quad l = 1,2,3,4 . \qquad (2.1.59)$$

Because the preindustrial NPP, $\bar{f}_{NPP}^{pre}$, is fixed at 60 GtC/year, the preindustrial carbon storage of each reservoir, $\bar{c}_{ter,l}^{pre}$, can be determined from equation (2.1.59). Then, the addition of equations (2.1.57) and (2.1.59) gives:

$$\dot{c}_{ter,l}(t) = A_{ter,l}\tau_{ter,l}\left(\bar{f}_{NPP}^{pre} + \delta f_{NPP}(t)\right) - \frac{1}{\tau_{ter,l}}\left(\bar{c}_{ter,l}^{pre} + c_{ter,l}(t)\right)q(t) , \quad l = 1,2,3,4 , \qquad (2.1.60)$$

$$q(t) = Q_{10}^{\frac{\delta T_{land-air}(t)}{10}} . \qquad (2.1.61)$$

Q_{10} is a factor, by which the rate of terrestrial respiration increases with a temperature increase of 10°C, assumed to be 2 in many modelling studies. The parameterization using Q10 is often used in physiological studies. In ACC2, the value of the Q10 factor is determined by the inverse calculation. Further discussion on the Q10 parameterization is provided in the next subsection. $\delta T_{land-air}(t)$ is the change in surface air temperature change over land and is computed by the climate component DOECLIM (Section 2.3). If the IRF is employed to calculate the air temperature, the global-mean

temperature change calculated from the IRF is used here. Note that, when $\delta T_{land-air}(t)$ is equal to 0, equation (2.1.60) is equivalent to equation (2.1.57).

- Limitations for Land CO_2 Uptake in ACC2

Although NPP is determined solely by the atmospheric CO_2 concentration in ACC2, various other factors such as the Photosynthetically Active Radiation (PAR), temperature, water availability, nutrient availability, and species composition come into play in reality (Melillo et al., 1993; Goldewijk et al., 1994). The stomata conductance (i.e. openness) is adjusted by the surrounding soil moisture to maintain proper water holding in the plants, influencing the rate of CO_2 uptake. Nitrogen supply is an important factor among others controlling NPP. It is demonstrated by observations that NPP is significantly affected by variations in diffuse radiation (Gu et al., 2003). The geometry of radiation is important for plant productivity because of the light saturation of photosynthesis (Farquhar and Roderick, 2003).

The effect of temperature on NPP is not modeled in ACC2. The relationship between NPP and surface temperature is highly uncertain as indicated by the results of recent coupled GCMs and Earth system Models of Intermediate Complexity (EMIC) intercomparison experiments (Coupled Climate-Carbon Cycle Model Intercomparison Project (C^4MIP)) (Friedlingstein et al., 2006).[16] If the highly uncertain temperature dependence on NPP would be included in the inverse calculation, other factors controlling NPP discussed above would be explained wrongly by temperature. Therefore, we describe only the CO_2 concentration control on NPP.

Although the heterotrophic respiration in ACC2 is controlled only by the temperature, the actual heterotrophic respiration also depends on the property of the organic matter, the substrate availability, and the soil moisture. Modelling of the temperature sensitivity to soil carbon decomposition is currently under debate (Davidson and Janssens, 2006). Both observations (Tjoelker et al., 2001; Chen and Tian, 2005) and theories (Davidson and Janssens, 2006) indicate that the value of Q10 decreases with increasing soil temperature. Process-based models such as the Lund-Potsdam-Jena Dynamic Global Vegetation Model (LPJ-DGVM) introduce the temperature dependency of Q10 for the soil respiration and the autotrophic respiration (Sitch et al., 2003). However, the temperature-dependency of Q10 is not so important in the global-mean studies such as ACC2 because the large temperature gradient between the tropics and the high latitudes is not

[16] A recent ECHAM5/MPIOM simulation indicates a negative correlation between surface temperature and NPP in the tropics (between 0 and 30 degree in latitude). In the tropics, an increase in temperature leads to higher autotrophic respiration, resulting in a reduction of NPP. In the mid latitudes, on the contrary, the correlation is positive but not strong enough to offset the negative correlation in the tropics. Thus, on a global scale, there is a negative correlation between NPP and surface temperature (Raddatz et al., 2007). On the contrary, Meyer et al. (1999) estimate an increase in NPP by 1.6% per 1°C increase in surface temperature. However, both of the results are well within the range of different coupled GCM/EMIC projections (Friedlingstein et al., 2006).

modelled.

Note that the importance of the carbon cycle interaction with other element cycles of nitrogen, sulfur, phosphorus, and oxygen are addressed in Ver et al. (1999), demonstrating that an omission of the interactions among element cycles on land leads to a significant underestimate in the future projection of atmospheric CO_2 concentration. However, multi-element cycles are beyond the scope of ACC2 and have not so far been incorporated in the state-of-the-art coupled GCMs.

2.1.4. Coupling of the Atmosphere-Ocean and Land Box Models

The atmosphere-ocean box model and the land box model have been derived above. Now they are coupled in such a way that the four-reservoirs of the land box model are connected to the composite layer of the atmosphere-ocean box model as follows:

$$\dot{c}_{cmp,1}(t) = e(t) - \frac{\eta_2}{h_{mix}} c_{mix}(t) + \frac{\eta_2}{h_2} c_{ocn,2}(t) - \sum_{l=1}^{4} \dot{c}_{ter,l}(t), \tag{2.1.62}$$

$$\dot{c}_{ocn,2}(t) = \frac{\eta_2}{h_{mix}} c_{mix}(t) - \frac{\eta_2 + \eta_3}{h_2} c_{ocn,2}(t) + \frac{\eta_3}{h_3} c_{ocn,3}(t), \tag{2.1.63}$$

$$c_{ocn,3}(t) = \frac{\eta_3}{h_2} c_{ocn,2}(t) - \frac{\eta_3 + \eta_4}{h_3} c_{ocn,3}(t) + \frac{\eta_4}{h_4} c_{ocn,4}(t), \tag{2.1.64}$$

$$c_{ocn,4}(t) = \frac{\eta_4}{h_3} c_{ocn,3}(t) - \frac{\eta_4}{h_4} c_{ocn,4}(t), \tag{2.1.65}$$

$$\dot{c}_{ter,l}(t) = A_{ter,l}\tau_{ter,l}\bar{f}_{NPP}^{pre}\left(1+\beta_{NPP}\right)\ln\left(\frac{\mathrm{pCO}_2(t)}{\overline{\mathrm{pCO}}_2^{pre}}\right) - \frac{1}{\tau_{ter,l}}\left(\bar{c}_{ter,l}^{pre} + c_{ter,l}(t)\right)\cdot Q_{10}\frac{\delta T_{land-air}(t)}{10}. \tag{2.1.66}$$

We elaborate the expression of the anthropogenic carbon content in the mixed layer, c_{mix}, as a function of the anthropogenic carbon content in the composite layer, $c_{cmp,1}$.

Under a small perturbation, fixed thermodynamic equilibria (in other words, a constant Revelle factor) can be assumed. Thus, by using the equilibrated fraction in the mixed layer, $A_{ocn,0}$, indicated from the IRF (equation (2.1.12)), the following expression can be derived.

$$c_{mix} = A_{ocn,0} \cdot c_{cmp,1} \tag{2.1.67}$$

c_{mix} can be described as a function of [DIC] as follows:

$$\bar{c}_{mix}^{pre} + c_{mix} = Area_{ocn} \cdot h_{mix} \cdot [\mathrm{DIC}]. \tag{2.1.68}$$

Recall that [DIC] represents the background as well as perturbed carbon concentration. With equations (2.1.38), [DIC] in equation (2.1.68) is replaced with $[H^+]$ and pCO_2 as follows:

$$\bar{c}_{mix}^{pre} + c_{mix} = Area_{ocn} \cdot h_{mix} \cdot \mathrm{pCO}_2 \cdot K_0^* \cdot \left(1 + \frac{K_1^*}{[\mathrm{H}^+]} + \frac{K_1^* K_2^*}{[\mathrm{H}^+]^2}\right). \tag{2.1.69}$$

Similar to equation (2.1.68), c_{atm} can be described as a function of pCO_2 by using equation (2.1.30) as follows:

$$\bar{c}_{atm}^{pre} + c_{atm} = Area_{ocn} \cdot h_{atm} \cdot \mathrm{pCO}_2 \cdot K_0^* . \tag{2.1.70}$$

The conservation in the amount of carbon in the atmosphere-mixed layer subsystem is trivially

$$\bar{c}_{cmp,1}^{pre} + c_{cmp,1} = \left(\bar{c}_{atm}^{pre} + c_{atm}\right) + \left(\bar{c}_{mix}^{pre} + c_{mix}\right). \tag{2.1.71}$$

Finally, from equations (2.1.69) – (2.1.71), the expression for c_{mix} can be derived as follows:

$$\bar{c}_{mix}^{pre} + c_{mix} = \frac{f([\mathrm{H}^+])}{1 + f([\mathrm{H}^+])}\left(\bar{c}_{cmp,1}^{pre} + c_{cmp,1}\right), \tag{2.1.72}$$

where $f([\mathrm{H}^+]) = \left(1 + \frac{K_1^*}{[\mathrm{H}^+]} + \frac{K_1^* K_2^*}{[\mathrm{H}^+]^2}\right) \cdot \frac{h_{mix}}{h_{atm}}$. Equation (2.1.72) can be substituted into c_{mix} in equation (2.1.62). The estimate of $[\mathrm{H}^+]$ is provided by solving equation (2.1.37) with respect to $[\mathrm{H}^+]$. Equation (2.1.37) together with equation (2.1.38) are key equations to compute the carbonate system variables in ACC2.

2.1.5. CO_2 Radiative Forcing

The atmospheric CO_2 abundance is sufficiently high in our time scale such that the saturation of the absorption bands with increasing CO_2 concentration needs to be taken into account. In ACC2, the CO_2 radiative forcing is estimated using the following logarithmic parameterization (IPCC, 2001, Table 6.2):

$$RF(\mathrm{CO}_2)_t = RF_{2\times c(\mathrm{CO}_2)_{pre}} \cdot \frac{\ln\left(c(\mathrm{CO}_2)_t / c(\mathrm{CO}_2)_{pre}\right)}{\ln 2}. \tag{2.1.73}$$

$RF_{2\times c(CO_2)_{pre}}$ denotes the $2\times CO_2$ forcing, that is, the change in the forcing by doubling the atmospheric CO_2 concentration from the preindustrial level, $c(\mathrm{CO}_2)_{pre}$ (= 277 ppm in ACC2). In ACC2, the $2\times CO_2$ forcing is fixed at 3.7 W/m^2 (IPCC, 2001, p.357). The parameterization used here is derived from radiative transfer calculation with three-dimensional climatological meteorological input data (Myhre et al., 1998).

2.2. ATMOSPHERIC CHEMISTRY COMPONENT

2.2.1. Overview

A fairly comprehensive set of forcing agents and the parameterization of their atmospheric chemistry (IPCC, 2001; Joos et al., 2001; WMO, 2003; IPCC, 2005) are implemented in ACC2 as summarized

in Table 2.1. Importance of implementing atmospheric chemistry is suggested by the strong feedback of the CH_4 concentration on the CH_4 lifetime associated with OH oxidation (IPCC, 2001, p.250) and also by the photochemical production of tropospheric O_3 from CH_4 oxidation (Brasseur et al., 1999, pp.527-528; IPCC, 2001, p.365). The direct CH_4 radiative forcing is 0.33 W/m^2, with an indirect forcings of 0.11 W/m^2 due to OH feedback and an additional indirect forcing of 0.11 W/m^2 due to tropospheric O_3 production (Lelieveld et al., 1998). The parameterization of CH_4 (lifetime of 8.4 years (IPCC, 2001, p.248)) is better reproduced in ACC2 than in the predecessor model ICM because of the finer temporal resolution of ACC2.

In ACC2, each of the emissions of GHGs, aerosol precursors, and pollutants is separated into the anthropogenic and natural emissions. The historical anthropogenic emissions of CH_4 and N_2O are estimated in the inverse calculation (Section 3.4). The anthropogenic emissions are fixed at zero in 1750 in accordance with the preindustrial quasi-steady state assumption (Section 2.1). The historical natural emissions of CH_4 and N_2O are assumed to be constant over time and estimated in the inverse calculation. Such estimates are also used as the natural emissions of CH_4 and N_2O for future projections. For halocarbons and SF_6, the historical emission in the literatures is not used in ACC2 – respective concentrations are directly prescribed to the model. The historical anthropogenic emissions of CO, NO_x (NO and NO_2), VOC, and SO_2 are based on EDGAR-HYDE 1.3 (van Aardenne et al., 2001). The future anthropogenic emissions of all of these gases (further separated into energy-related and non-energy-related emissions) use SRES (Nakićenović et al., 2000). The new future emission estimates of IPCC (2005, Chapter 11) is not so far utilized here.

In both the past and future modes of ACC2, the concentrations of CH_4 and N_2O are dynamically calculated by single-reservoir box models. The change in the concentration of each of these gases is generally described as

$$\dot{c} = \frac{e}{\upsilon} - \frac{c}{\tau}, \qquad (2.2.1)$$

where c, e, υ, and τ are the global-annual-mean atmospheric concentration, the sum of the anthropogenic and natural emissions, the unit conversion factor between mass and concentration, and the lifetime of a gas, respectively. The concentrations of SF_6 and halocarbons are also dynamically calculated using equation (2.2.1) in the future mode but they are simply prescribed in the past mode (references in Sections 2.2.5 and 2.2.6). The unit conversion factors υ for these gases are estimated from a linear function of their molecular weights[17] and such estimates are shown in Table 2.2.

[17] The estimates of υ in equation (2.2.1) for various GHGs are compiled in Fuglestvedt and Berntsen (1999, Table 2), most of which are taken from IPCC (1996). These estimates were not updated in IPCC (2001). Fuglestvedt and Berntsen's estimates suggest that the unit conversion factors have a linear relationship with the respective molecular weights as follows: $\upsilon(\mathrm{A}) = 0.1716 \times mw(\mathrm{A})$. $mw(\mathrm{A})$ denotes the molecular weight for gas A.

The expression for the lifetime τ in equation (2.2.1) is different among the gases. For SF_6 and halocarbons without containing any H atom, their lifetimes are simply expressed as constants (Table 2.2) because their removal processes are virtually independent of OH. On the contrary, for halocarbons containing at least one H atom, their lifetimes are scaled with the OH concentration because they are predominantly depleted by OH (equation (2.2.11)) (IPCC, 2005, p.167). For CH_4 and N_2O, which influence the background chemical processes in complex manners, their lifetimes[18] are given as functional forms (equations (2.2.3) and (2.2.6)). Note that, when a gas has multiple sinks, its lifetime with respect to each of the sinks $\tau_k \quad (k = 1,2,\cdots,n)$ holds an inverse relationship with the total lifetime τ_{total} as follows:

$$\frac{1}{\tau_{total}} = \frac{1}{\tau_1} + \frac{1}{\tau_2} + \cdots + \frac{1}{\tau_n}. \tag{2.2.2}$$

Equation (2.2.2) is used to define the lifetime of CH_4 in equation (2.2.3).

In both the past and future modes of ACC2, the concentration of OH is directly related to the CH_4 concentration and the pollutant emissions without using dynamic relationships (IPCC, 2001, Table 4.11). Such a treatment is owing to the fact that the OH consumption by oxidizing CH_4 and CO and the OH formation from NO_x (via O_3 production) are very fast reactions. In the future mode, the concentration of the tropospheric O_3 is similarly treated because of the fast O_3 production from NO_x and the O_3 consumption to yield OH (IPCC, 2001, Table 4.11). The lifetimes of OH and tropospheric O_3 are in the order of minutes and weeks, respectively (Brasseur et al., 1999, Table 13.3; IPCC, 2001, Table 4.1(a) and p.361). In the past mode, the concentration of the tropospheric O_3 is not explicitly provided – the radiative forcing of the total O_3 (Hansen and Sato, 2004) is prescribed.

The relationships between the concentrations and the radiative forcings of the GHGs are parameterized differently depending on their atmospheric concentrations and radiative interferences. The radiative forcings of SF_6 and halocarbons are linearly related to their atmospheric concentrations by scaling with their radiative efficiencies[19] (equations (2.2.12) and (2.2.13)) (IPCC, 2005, p.158 and 163). On the other hand, because CH_4 and N_2O take substantial fractions of the atmospheric gas composition and significantly perturb the Earth's radiation budget, the saturation and overlap effects of the absorption bands for CH_4 and N_2O have to be taken into account to describe their radiative forcings.[20] The saturation effects for CH_4 and N_2O are parameterized as square root functions of the

[18] More precisely, it is the perturbation time (IPCC, 2001, Tables 4.3 and 4.5) and the adjustment time (Seinfeld and Pandis, 2006, p.1048), which is the lifetime taking account of the chemical feedbacks.

[19] A radiative efficiency is a radiative forcing per concentration unit, typically $W/m^2/ppb$.

[20] O_3 and H_2O also play a pivotal role in the saturation and overlap effects of absorption bands in particular when one looks at the natural greenhouse effects. However, such effects for O_3 have not been parameterized (Sections 2.2.8 and 2.2.9). H_2O is not taken as a radiative forcing agent (IPCC, 2001, Appendix 6.1)and rather considered as a feedback (Section 2.2.11).

associated concentrations (equations (2.2.4) and (2.2.7)) (IPCC, 2001, Table 6.2).[21] The overlap effects for CH_4 and N_2O are parameterized in an elaborated function shown in equation 2.2.5 (IPCC, 2001, Table 6.2). Although the overlap effects with the other GHGs (IPCC, 2005, Figure 2.6) are not parameterized, the overlap effect with HFC-134a may become important in the future as the concentration of HFC-134a is projected to rise in SRES. Both the past and future modes of ACC2 use the same parameterizations consistently for the radiative forcings of CH_4, N_2O, SF_6, and halocarbons.

In ACC2, the total aerosol forcings are represented by three types of aerosol forcings: 1) direct forcing due to sulfate aerosols of anthropogenic origin, 2) direct forcing due to Organic Carbon (OC) and Black Carbon (BC) emitted from biomass burning and fossil fuel burning, and 3) indirect forcing due to all the anthropogenic aerosols. In both the past and future modes of ACC2, these aerosol forcings are parameterized as functions of the emissions of SO_2 and pollutants (equations (2.2.30) – (2.2.32)).

The radiative forcing is separated further into the radiative forcing over land and the ocean. They are used in the climate component DOECLIM. The land-ocean separations of the radiative forcing involve different assumptions depending on the spatial distributions of the individual radiative forcings. The details and assumptions for such land-ocean separations are discussed in Section 2.3.5, together with the description of DOECLIM.

In the following, the non-CO_2 GHGs and other radiative agents are discussed in detail. Below, IPCC (2001) and WMO (2003) are mainly referred, where further references are found.

2.2.2. CH_4

CH_4 has been the second most important GHGs after CO_2 during the Anthropocene in terms of the radiative forcing. The IPCC estimate of the CH_4 radiative forcing is 0.48 W/m^2 in the year 2005 (IPCC, 2007, Figure SPM.2). The atmospheric observation indicates that the CH_4 concentration has stabilized for the past several years. Although the exact reason is unknown, this can be caused by the decrease in the natural emission and/or the increase in the atmospheric OH concentration offsetting the persisting rise in the anthropogenic CH_4 emission. The recently debated CH_4 emission from plants (Keppler et al., 2006) influences the budgetary calculation. SRES showing the future increase in the CH_4 emission indicates that CH_4 will continue to be an important radiative agent for the next one hundred years. If a proper mitigation strategy is put into place, the atmospheric CH_4 concentration in principle decreases quickly because of its atmospheric lifetime time (8.4 years (IPCC, 2001, p.248)). However, a growing concern lies in a possible large-scale CH_4 emission from

[21] CO_2 also plays a substantial role in the atmospheric radiative interference. The radiative forcing for CO_2 is parameterized as a logarithmic function of the CO_2 concentration (Section 2.1.5).

the permafrost and ocean sediments depositions.[22]

CH_4 has various emission sources such as waste treatment, energy use, biomass burning, termites[23], landfills, rice paddies, CH_4 hydrate, ruminants[24], natural wetlands, and ocean (IPCC, 2001, Table 4.2; Lowe, 2006). The literature estimates of the natural CH_4 emission encompass a substantial range.[25]

Such diversified sources are collectively represented as anthropogenic and natural emissions in ACC2. The time series of the historical anthropogenic CH_4 emission is obtained from the inverse calculation. SRES is used as the anthropogenic CH_4 emission in the future mode. In ACC2, the magnitude of the natural CH_4 emission is assumed to be constant over time and is estimated by the inverse calculation. Such an estimate is transferred from the past mode to the future mode and used as the future natural emission of CH_4.

Much simpler are the CH_4 sinks, which are reaction with OH, lost to the stratosphere, and soil uptake (diffusion and microbial oxidation (Ridgwell et al., 1999)). The lifetime of CH_4 is estimated to be 9.58 years with respect to OH depletion[26], 120 years with respect to stratospheric

---

[22] CH_4 hydrate is stored in the Siberia permafrost and in the ocean sediments. The CH_4 hydrate deposit in the ocean sediments is estimated to be as enormous as 10^7 TgC (Suess et al., 1999). The current emission from CH_4 hydrate is merely 10 Tg/year (Lelieveld et al., 1998) because most of the methane is oxidized before reaching the surface (Dickens, 2001). However, there are carbon isotopic records suggesting the occurrence of a gigantic CH_4 release from marine hydrate, resulting in 5 to 10°C warming in the surface temperature during the initial Eocene thermal maximum, approximately 55 million years ago (Dickens, 2004). This CH_4 release is triggered by submarine volcanoes indicated by seismic observations (Svensen et al., 2004). A gigantic CH_4 release can also be triggered by large-scale submarine landslides (Nisbet and Piper, 1998). The CH_4 emission from the permafrost hydrate is expected to rise as the global warming affects the polar region in an amplified manner.

[23] Termites are white ants relying on bacteria in their stomachs for digestion and producing CH_4 as a by-product of their digestive processes.

[24] Ruminants are hooved animals such as cows, goats, sheep, camels, and antelope that digest their foods in two steps, first by eating the raw material and regurgitating a semi-digested form known as cud, then eating the cud.

[25] The estimate of the CH_4 emission from natural wetlands has a large uncertainty (IPCC, 2001, Table 4.2; Lowe, 2006). The global distribution of natural wetlands is still not well-known although efforts have been made by various workers initiated by Matthews and Fung (1987) performing an extensive observational campaign. Soil moisture data such as the output of the BIOME4 model (Kaplan, 2001; Kaplan, 2002) can be in principle combined with digital terrain models such as Global DTM5 by GETECH and GTOPO30 by US Geological Survey to infer the global wetland distribution. Kaplan formulates the following criteria for a grid cell to be 'qualified' as a wetland: 1) Grid cell slope is less than 15%, 2) Soil moisture is more than 65%. However, this approach is criticized by the ignorance of the soil texture (Stefan Hagemann, personal communication). There are substantial discrepancies among model simulations in soil moisture. Furthermore, there are no general patterns in the temporal changes in soil moisture, according to the Global Soil Wetness Project (Dirmeyer et al., 1999, Figure 13), and no long-term reliable observation-based global soil moisture dataset (Zhao and Dirmeyer, 2003, p.1). The estimate of wetland area by using passive microwave techniques has yet to be available. At present, the Global Soil Wetness Project II does not show a global compilation of remotely sensing wetland area.

[26] This lifetime estimate with respect to OH depletion refers to the CH_4 concentration of 1745 ppb in

loss, and 160 years with respect to soil uptake (IPCC, 2001, p.248).

In the ACC2 past and future modes, the CH_4 lifetime is described as follows (compare equation (2.2.2)):

$$\frac{1}{\tau(\mathrm{CH_4})_t} = \frac{r(\mathrm{OH})_t}{\tau(\mathrm{CH_4})^{\mathrm{OH}}} + \frac{1}{\tau(\mathrm{CH_4})^{strastophere}} + \frac{1}{\tau(\mathrm{CH_4})^{soil}} . \qquad (2.2.3)$$

$\tau(\mathrm{CH_4})^{stratosphere}$ and $\tau(\mathrm{CH_4})^{soil}$ in equation (2.2.3) correspond to the last two CH_4 sinks and have the values of 120 and 160 years, respectively. The first term on the right side of equation (2.2.3) is the parameterization of the dominant CH_4 sink due to reaction with OH, having an inverse relationship with the *relative* concentration of OH, $r(\mathrm{OH})_t$, that is, the ratio of OH concentration in year *t* to that in year 2000. The CH_4 lifetime with respect to OH depletion, $\tau(\mathrm{CH_4})^{\mathrm{OH}}$, is estimated in the inverse calculation (Table 3.2).

The expression of the CH_4 lifetime (equation (2.2.3)) is put into the dynamic equation (equation (2.2.1)) to calculate the CH_4 concentration in both the ACC2 past and future modes. The unit conversion factor between mass in $Tg(CH_4)$ and concentration in ppb, $\upsilon(\mathrm{CH_4})$ in equation (2.2.1), is 2.746 $Tg(CH_4)$/ppb.

The first term in equation (2.2.3) and equation (2.2.10) (OH concentration defined as a function of the CH_4 concentration) are combined to express the feedback of the CH_4 concentration on its own lifetime as follows. An increase in the CH_4 concentration is quashed by its oxidation reaction with OH, leading to the formation of CO. Both CO and CH_4 suppress OH, which is the major sink of CH_4. As a result, the CH_4 lifetime lengthens when the CH_4 concentration increases (e.g. Seinfeld and Pandis, 2006, pp.1048-1049). The adjustment time is 12 years in contrast to the lifetime with respect to OH depletion being 9.58 years (IPCC, 2001, pp.251-252; Seinfeld and Pandis, 2006, p.1048). This CH_4 feedback adds 25% to 35% more to the direct CH_4 forcing (IPCC, 2001, p.365). The additional CH_4 feedback to the production of tropospheric O_3 (Section 2.2.1) is accounted for directly in the parameterization of the tropospheric O_3 radiative forcing (equation (2.2.21)).

The radiative forcing for CH_4 is parameterized as follows:

$$RF(\mathrm{CH_4})_t = 0.036 \cdot \left(\sqrt{c(\mathrm{CH_4})_t} - \sqrt{c(\mathrm{CH_4})_{pre}} \right)$$
$$- Overlap\left(c(\mathrm{CH_4})_t, c(\mathrm{N_2O})_{pre}\right) - Overlap\left(c(\mathrm{CH_4})_{pre}, c(\mathrm{N_2O})_{pre}\right). \qquad (2.2.4)$$

Note that 0.036 in equation (2.2.4) is a coefficient for the parameterization and different from the radiative efficiency of CH_4. The overlap function, $Overlap(M, N)$, in equation (2.2.4) is defined in the following:

---

the year 1998 (IPCC, 2001, p.248, Figure 4.1, and Table 4.3), based on contemporary CTMs in OxComp showing the rage from 6.5 to 13.8 years (IPCC, 2001, p.250 and Table 4.3).

$$Overlap(M,N) = 0.47 \cdot \ln\left(1 + 2.01\times10^{-5}(M\cdot N)^{0.75} + 5.31\times10^{-15}M(M\cdot N)^{1.52}\right). \quad (2.2.5)$$

$c(CH_4)_{pre}$ and $c(N_2O)_{pre}$ are the respective concentrations in 1750 (710 ppb and 273 ppb, respectively) (Table 3.1). The square roots of the right side of equation (2.2.4) take into account the saturation effect of the CH_4 absorption bands with increasing atmospheric CH_4 concentration. The overlap function parameterizes the radiative effects of the absorption bands that are shared by CH_4 and N_2O between wavelengths of about 10 μm and 7.5 μm.[27] The above parameterization of the CH_4 radiative forcing is taken from IPCC (2001, Table 6.2) based on radiative transfer calculations of Myhre et al. (1998).

2.2.3. N_2O

N_2O is currently the fourth important GHG after CO_2, CH_4, and CFC-12 in terms of the radiative forcing. The IPCC estimate of the radiative forcing due to N_2O in the year 2005 is 0.16 W/m^2 (IPCC, 2007, Figure SPM.2). N_2O plays a role in the stratospheric O_3 chemistry as a source of NO_x.

The sources of N_2O are cattle and feedlots, industrial sources, biomass burning, agricultural soils, natural soils, ocean (denitrification performed by some specific heterotrophic bacteria in the anoxic environment respiring large amounts of organic matter with the use of nitrate as the electron acceptor), and NH_3 oxidation (IPCC, 2001, Table 4.4). The literature estimates of natural N_2O emission are in a better agreement than those of the anthropogenic N_2O emission – in particular, the emission from agricultural soil due to nitrogen fertilizer applications are quite uncertain.[28]

---

[27] It should be noted that the overlaps of the absorption bands for HFC-134a, CFC-12, HCFC-22, CH_4, and N_2O can significantly affect the associated radiative forcings in future projections; however, they are not parameterized in ACC2, or in any simple model that exists at present. Computation of such effects of absorption band overlaps on the radiative forcing require a sensitivity analysis using a radiative transfer model such as MODTRAN.

[28] The agricultural N_2O emission occurs from microbial nitrification and denitrification in the soil (Conrad, 1996) and in the ocean sediments (Shaffer and Rönner, 1984). High N_2O production is associated with denitrification. Denitrification rates are spatially and temporally highly variable across ecosystem types, whereas nitrification is a relatively constant process in many ecosystems. The importance of the agricultural emission suggested from the isotopic N data in Arctic ice cores (Bernard et al., 2006). The future N_2O emission from agricultural sources is expected to increase drastically particularly from the tropics where the terrestrial ecosystem is often phosphorus-limited (Hall and Matson, 1999). A first-order emission model is developed by Bouwman (1996): $E = 1 + 0.0125\times F$, which relate the nitrous oxide emission (E) from fertilized fields to the N fertilizer applied (F) with E and F in kg(N)/ha/yr. This equation consists of background emission of 1 kg(N)/ha/yr with a range from –0.6 to +3.2 kg(N)/ha/yr and fertilizer-induced emission of 1.25% of fertilizer application rate with a range from 0.25 to 2.25%. This equation was statistically derived from observational dataset and is adequate for global analysis. Note that the sample database excludes data on leguminous crops because these crops usually do not receive N fertilizer but take up N through symbiotic N fixation. The equation above is independent of fertilizer types. Bouwman's equation does not account of the factors controlling the rate of denitrification: soil

In ACC2, similar to the treatment for CH_4, the past anthropogenic N_2O emission is obtained from the inverse calculation. The future anthropogenic N_2O emission adopts SRES. The magnitude of the natural N_2O emission is assumed to be constant and is estimated by the inverse calculation. Such an estimate is transferred from the past mode to the future mode and used as the future natural emission of N_2O.

The sink of N_2O is known to be lost to the stratosphere and photodissociation. The N_2O concentration has a negative feedback on its own lifetime (IPCC, 2001, Table 4.5) although it is weaker than the similar feedback for CH_4. An increase in the N_2O concentration leading to an increase in the production of stratospheric NO_y[29] results in a catalytic destruction of O_3, letting more ultraviolet radiation reach the troposphere, which eventually destroys N_2O (Prather, 1998; Seinfeld and Pandis, 2006, p.1048). The N_2O negative feedback in the N_2O-NO_y-O_3 system is assessed by using 2-D stratospheric chemical models and parameterized in the expression of the N_2O lifetime used in ACC2:

$$\tau(\mathrm{N_2O})_t = \tau(\mathrm{N_2O})_{2000} \cdot \left(\frac{c(\mathrm{N_2O})_t}{c(\mathrm{N_2O})_{2000}} \right)^{-0.046} . \qquad (2.2.6)$$

$\tau(\mathrm{N_2O})_{2000}$ is estimated in the inverse calculation (110 years in IPCC (2001, Table 4.5, Prather's estimate)) (Table 3.2). The sensitivity coefficient of -0.046 (IPCC, 2001, Table 4.5, Prather's estimate) implies that the N_2O lifetime systematically decreases by about 0.5% with increasing N_2O concentration by 10%. $c(\mathrm{N_2O})_{2000}$ is fixed at 330 ppb as equation (2.2.6) is calibrated in the sensitivity experiment (IPCC, 2001, Table 4.5). Note that the expression above is different from that of Joos et al. (2001) using emission rather than concentration and with a different lifetime and sensitivity coefficient.

The expression of the N_2O lifetime (equation (2.2.6)) is substituted into the dynamic equation (equation (2.2.1)) for both the past and future modes. The unit conversion factor $\upsilon(\mathrm{N_2O})$ is 4.8 Tg(N)/ppb in the dynamic equation.

The radiative forcing for N_2O is described in ACC2 as follows:

$$RF(\mathrm{N_2O})_t = 0.12 \cdot \left(\sqrt{c(\mathrm{N_2O})_t} - \sqrt{c(\mathrm{N_2O})_{pre}} \right)$$
$$- Overlap\left(c(\mathrm{CH_4})_{pre}, c(\mathrm{N_2O})_t\right) - Overlap\left(c(\mathrm{CH_4})_{pre}, c(\mathrm{N_2O})_{pre}\right). \qquad (2.2.7)$$

Note that 0.12 in equation (2.2.7) is a coefficient for the parameterization and different from the radiative efficiency of N_2O. $c(\mathrm{CH_4})_{pre}$ and $c(\mathrm{N_2O})_{pre}$ are the respective concentrations in 1750 (710 ppb and 273 ppb, respectively). Similar to the formulation of CH_4 forcing, the square roots of

---

moisture and temperature, the amount of mineralizable organic carbon, soil oxygen availability, concentrations of nitrate and ammonium, and soil pH. The rate of denitrification is also affected by the availability of O_2, NO_3, and organic-C.

[29] Odd-nitrogen gases (NO, NO_2, NO_3, N_2O_5, HONO, HO_2NO_2, and HNO_3) in the stratosphere (e.g. Prather, 1998)

the right side of equation (2.2.7) express the saturation effect of the N_2O absorption bands with increasing N_2O concentration. The parameterization of the N_2O forcing above is based on IPCC (2001, Table 6.2).

2.2.4. OH

OH is the main cleansing agent in the atmosphere; it oxidizes many kinds of GHGs and pollutants *radically* in an order of seconds. Although OH is not a radiatively active agent, its role of oxidizing CH_4 has a substantial impact on the CH_4 radiative forcing, thus termed "an indirect radiative agent."

The primary source of OH is the photodissociation of O_3 by solar UltraViolet (UV) radiation in the troposphere.

$$O_3 + h\nu \rightarrow O(^1D) + O_2 \qquad (2.2.8)$$

$$O(^1D) + H_2O \rightarrow OH + OH \qquad (2.2.9)$$

$O(^1D)$ is an oxygen atom that is electronically excited while $O(^3P)$ is an oxygen atom at ground state (e.g. Seinfeld and Pandis, 2006, pp.84-85). OH is also produced from NO_x (equation (2.2.16)). The sink of OH is the depletion by the oxidation reactions mostly with CH_4 and CO and also with HFCs, HCFCs, and VOCs in the troposphere. The above mentioned nature of the OH sources and sinks leads to the high spatial and temporal variability of OH concentration and the short atmospheric lifetime in the order of minutes.[30]

There is a large uncertainty in the temporal evolution of the OH concentration. Although the decrease in the OH concentration for the past decade was shown based on the CH_3CCl_3 concentration (Prinn et al., 2001), other modelling studies currently indicate that the global-mean OH concentration has varied little since the preindustrial time because the anthropogenic emissions led to two opposite effects that inadvertently compensated each other (higher CO and CH_4 emissions leading to OH depletion vs. higher NO emission leading to OH formation) (Lelieveld et al., 2004). As for the future projection, the evidences point to a decrease in the OH concentration, but the uncertainty ranges in the projections are too large to reach anything conclusive (IPCC, 2001, p.263; Penkett et al., 2003, p.98). Recent relevant debates are summarized in IPCC (2005, Section 2.2.2).

In ACC2 the relative concentration of OH, $r(\mathrm{OH})$, rather than the absolute concentration, is defined as follows: $r(\mathrm{OH})_t = \dfrac{c(\mathrm{OH})_t}{c(\mathrm{OH})_{2000}}$, where $c(\mathrm{OH})_t$ and $c(\mathrm{OH})_{2000}$ are the absolute OH concentrations in the year t and 2000, respectively.

[30] The OH concentration is estimated based on the burden and the trend of CH_3CCl_3 (lifetime: 4.8 years (IPCC, 2001, Table 4.1a)), which reacts only with OH. The accuracy of the OH concentration estimates depends on the measurements calibration and proxy emission figures. The recent decline in the CH_3CCl_3 emission under the Montreal Protocol provided an opportunity to better constrain the OH concentration (Penkett et al., 2003, pp.96-97), but the illegal and unaccounted emissions preclude an accurate determination of the OH concentration (Lelieveld et al., 2004).

In earlier models (e.g. ICM and the model of Harvey et al. (1997)), the OH concentration is not explicitly defined and rather implicit in the definition of CH_4 lifetime as a positive feedback to its own. In ACC2, the relative concentration of OH is explicitly defined as a function of the concentration of CH_4 and the emissions of pollutants NO_x, CO, and VOC in the following.

$$\begin{aligned}
&\ln(r(\mathrm{OH})_t) \\
&= \ln(c(\mathrm{OH})_t) - \ln(c(\mathrm{OH})_{2000}) \\
&= -0.32\{\ln(c(\mathrm{CH_4})_t) - \ln(c(\mathrm{CH_4})_{2000})\} + 0.0042\left(e(\mathrm{NO}_x)_t - e(\mathrm{NO}_x)_{2000}\right) \\
&- 0.000105\left(e(\mathrm{CO})_t - e(\mathrm{CO})_{2000}\right) - 0.000315\left(e(\mathrm{VOC})_t - e(\mathrm{VOC})_{2000}\right)
\end{aligned} \tag{2.2.10}$$

As discussed in Section 2.2.1, the concentration of OH is not dynamically described as equation (2.2.1) because of the extremely fast turnover time. $c(\mathrm{CH_4})_{2000}$ in equation (2.2.10) is the posterior estimate of the atmospheric CH_4 concentration obtained from the ACC2 inverse calculation. This estimate is transferred from the past mode to the future mode and used in the future mode. The estimates of the pollutant emissions are provided as scenarios in both the past and future modes.[31] The role of O_3 in the OH production is implicitly expressed in the terms for pollutants. Equation (2.2.10) is derived from the OxComp workshop where 11 state-of-the-art chemistry transport models ran using a set of emission scenarios between 2000 and 2100 (Joos et al., 2001, p.893; IPCC, 2001, pp.267-268). The coefficients in equation (2.2.10) are obtained by applying various linear assumptions to the results of the OxComp workshop.[32] In ACC2, the relationship in equation (2.2.10) is also assumed to be valid during the historical period.

2.2.5. Halocarbons

Halocarbons are atmospheric halogen- (such as fluorine, chlorine, bromine, and iodine) containing carbon compounds. Halocarbons modelled in ACC2 (Table 2.2) are classified according to their molecular structures into the following categories: perfluorocarbons (PFCs), hydrofluorocarbons (HFCs), chlorofluorocarbons (CFCs), chlorocarbons (carbon tetrachloride (CCl_4) and methyl chloroform (CH_3CCl_3)), halons, hydrochlorofluorocarbons (HCFCs), and monomethyl halides (methyl chloride (CH_3Cl) and methyl bromide (CH_3Br)). CFCs, chlorocarbons, halons, HCFCs, and

[31] The estimates of pollutant emissions and SO_2 emission in the year 2000 are not consistent in EDGAR-HYDE 1.3 (van Aardenne et al., 2001) and SRES (Nakićenović et al., 2000). However, the literature values are directly adopted to ACC2 without modification.

[32] The coefficient of –0.32 in the first term of the right side of the equation was derived from the fact that a 10% increase in the CH_4 concentration in the year 2000 leads to a decrease in the tropospheric OH concentration by 3.0% in 2100 relative to the OH concentration in 2000 (IPCC, 2001, Table 4.11). The coefficient of 0.0042 in the second term of the right side of the equation was obtained from the fact that maintaining the NO_x emission level in the year 2000 throughout the model run leads to a decrease in the OH concentration by 40% in 2100 relative to that in 2000. The rates of the NO_x emission in 2000 and 2100 are 32.5 Tg(N)/yr and 110.0 Tg(N)/yr, respectively. Similarly, the coefficients of –0.000105 and –0.000315 in the third term of the right hand of the equation are obtained (see IPCC (2001, Table 4.11)).

monomethyl halides are Ozone-Depleting Substances (ODSs), which release chlorine and bromine[33] photochemically in the stratosphere, destroying the stratospheric O_3 in effect. The latest IPCC estimate of the radiative forcing of all the halocarbons is 0.34 W/m^2 in the year 2005 (IPCC, 2007, Figure SPM.2). CFC-12 is the third strongest GHG after CO_2 and CH_4 in terms of the radiative forcing. Although the radiative interference of each of the halocarbons is currently weak, several halocarbons have extremely long lifetimes on the order of thousands of years, suggesting a need for stringent emission measures. ACC2 describes a total of 29 halocarbon species (all the 27 halocarbons[34] in SRES, CH_3Cl, and CH_3Br), in contrast to the predecessor ICM describing only four halocarbon species (CFC-11, CFC-12, HCFC-22, and HFC-134a).

Most of the halocarbons are predominantly of industrial origin. The main source of PFCs is the anode effect during aluminum production (Fenhann, 2000). CFCs, HCFCs, and HFCs are emitted from various industrial usages such as semiconductor device fabrication, refrigerants, foam blowing agents, solvents, aerosol spray propellants, fire extinguishing agents, and chemical reagents (Haloalkane in Wikipedia, November 27, 2006). Halons are primarily used in fire extinction (WMO, 2003, 1.21). The principal source of CCl_4 is the CFC production (WMO, 2003, 1.21). CH_3CCl_3 is predominantly used as a solvent and cleansing agent (WMO, 2003, 1.62). CH_3Cl is predominantly of natural origin (ocean and biomass burning) and its main anthropogenic source is coal combustion (WMO, 2003, Table 1-10). CH_3Br is also mainly of natural origin (ocean, fumigation, and biomass burning) and its anthropogenic source is the combustion of leaded gasoline (WMO, 2003, Table 1-9).

The reductions in the emissions of PFCs and HFCs are addressed in the Kyoto Protocol. The emissions of ODSs are regulated by the Montreal Protocol.[35] The concentrations of CFCs have dropped abruptly since they are effectively controlled by the Montreal Protocol. The declines in the CFC concentrations are accompanied by rising HCFC concentrations. Under the Montreal Protocol,

[33] Fluorine is not released in the stratosphere because of its strong bond with carbon. Iodine is a more powerful O_3 depletion agent than chlorine and bromine, but iodine-containing gases are largely removed in the troposphere (WMO, 2003, questions, Q.12).

[34] The emission scenarios of halocarbons in SRES (Nakićenović, 2000, Section 5.4.3.) are based on Fenhann (2000). The particular set of 27 species are chosen from over 100 species discussed in WMO (2003) based on the contribution to climate forcing (Jörgen Fenhann, personal communication, November 27, 2006). Among the halocarbon species that should be included for future projection is trifluoromethyl sulphur pentafluoride (SF_5CF_3) (Sturges et al., 2000), a hybrid of SF_6 and halocarbon, which is still a minor forcing agent at present but has the largest radiative efficiency (W/m^2/ppt) ever found in the atmosphere (IPCC, 2001, p.254). Hydrofluoroethers (HFEs) are recently considered as replacements for CFCs (IPCC, 2005, p.151).

[35] The Montreal Protocol has been virtually ratified globally (191 countries as of November 14, 2006). The Protocol has been progressively strengthened with Adjustments and Amendments in London in 1990, Copenhagen in 1992, Vienna in 1995, Montreal in 1997, and Beijing in 1999. Substances banned in the Protocol are practically of purely anthropogenic origin except for monomethyl halides. Ultimately, the use of the major human-produced O_3-depleting gases will be phased out and effective stratospheric chlorine will slowly decay, reaching pre-ozone-hole values in the mid-21st century (WMO, 2003, Questions. p.28). The Montreal Protocol proves a resounding success with most of the states being compliant to it so far.

HCFCs are temporal replacements of CFCs. The Montreal Protocol requires the production and consumption of HCFCs to end in developed nations by 2030 and developing nations by 2040 (WMO, 2003, questions, p.29). HCFCs are 1 to 15% as effective as CFC-12 in depleting stratospheric O_3 because they are removed primarily by tropospheric OH. All HCFC emissions are eventually replaced with HFC emissions. The concentrations of HFCs are rising (WMO, 2003, Figure 1-20). Exceptionally, the concentration of HFC-23, by-product of HCFC-22, has already risen substantially (Oram et al., 1998). In all the six SRES cases, HFC-134a is expected to be the most radiatively important halocarbon in 2100 (0.129 W/m^2 under SRES A1b: IPCC, 2001, Table 6.14). The concentrations of halons are still increasing because of the substantial reserves in fire extinguishing equipment in spite of the cessation of their production in developed nations (WMO, 2003, questions, p.31). The concentrations of PFCs are rising (WMO, 2003, Figure 1-21).

The past mode of ACC2 uses the concentrations of the SRES 27 halocarbon species obtained from various station measurements and ice core records: CFCs, chlorocarbons, halons (except for halon2402), and HCFCs (except for HCFC-123) (Sturrock et al., 2002; WMO, 2003); Halon2402 (Fraser et al., 1999); CF_4 (Oram et al., 1998; Harnisch et al., 1999); C_2F_6 (Oram, unpublished); HFC-23 (Oram et al., 2000; WMO, 2003, Table 1-12); HFC-125 (WMO, 2003, Table 1-12); HFC-134a (Montzka et al. 1999; WMO, 2003, Table 1-12), and HFC-152a (IPCC, 2001, Figure 4.3; WMO, 2003, Table 1-12). The concentrations of the remaining halocarbon species (C_4F_{10}, HFC-32, HFC-43-10mee, HFC-143a, HFC-227a, HFC-236a, HFC-245a, and HCFC-123) are negligible. To validate the halocarbon concentration data, we extensively used the Carbon Dioxide Information Analysis Center (CDIAC) Data Set DB-1001 ALE (Prinn et al., 2000; http://cdiac.ornl.gov/).

For the future mode of ACC2, the concentrations of the 27 halocarbon species are dynamically calculated by using equation (2.2.1). The emission scenario (SRES)[36] and the unit conversion factors υ (Table 2.2) are prescribed to equation (2.2.1). The expression of the lifetime of a halocarbon τ depends on its molecular composition as explained below.

Generally, halocarbons containing one or more H atoms (HCFCs, HFCs, and monomethyl halides) are effectively removed by the reaction with OH in the troposphere (IPCC, 2001, p.245; Seinfeld and Pandis, 2006, p.48). Halocarbons not containing any H atom (PFCs, CFCs, and halons) do not react with OH and tend to be long-lived. They can only be destroyed in the stratosphere and above photochemically. Such a 'rule of thumb' is manifested (but not without exception) by the

[36] Noted that WMO (2003) discusses the projections of the mixing ratios for 16 species of halocarbon up to the year 2100 (Table 1-16 in p.1.66). However, these mixing ratios are only for the Ab baseline scenario defined in WMO (2003). These projections do not refer to Fenhann (2000). Projections of WMO (2003) and those of IPCC (2001) are not directly comparable; the emission scenarios to calculate the WMO concentration paths are not found. The new future emission estimates in IPCC (2005, Chapter 11) have not been considered in ACC2.

Arrhenius A-factors for the reactions of halocarbons with OH (Jet Propulsion Laboratory (JPL), 2003) expressing the reaction rates, showing that halocarbons with at least one H atom tend to react with OH slower than halocarbons without a H atom.

In ACC2 the lifetime of a halocarbon *k* containing at least one H molecule is defined as

$$\tau(\text{halo}_k)_t = \frac{\tau(\text{halo}_k)_{2000}}{r(\text{OH})_t}. \qquad (2.2.11)$$

For a fully halogenated halocarbon, its lifetime is not scaled with the OH concentration and is simply given as a constant (IPCC, 2005, p.167). Estimates for the halocarbon lifetimes are obtained from WMO (2003, Table 1.6), many of which have been updated from IPCC (2001, Table 6.7). In contrast, Joos et al. (2001) assume that the lifetimes of the fully fluorinated species (SF_6, CF_4, C_2F_6, and C_4F_{10}) are independent of the OH concentration whereas the lifetimes of other halocarbons are scaled with the OH concentration. In ICM, all the four halocarbons are independent of the OH concentration.

In the future mode of ACC2, the expression for the lifetime (equation (2.2.11)) or a constant lifetime is prescribed in equation (2.2.1) to calculate the halocarbon concentration. The value of the unit conversion factor υ in equation (2.2.1) for each of the halocarbons is shown in Table 2.2. In the past mode of ACC2, the concentration estimates for halocarbons are simply adopted to the model without dynamical calculations.

The radiative forcing of a halocarbon *l* is simply given as a linear function of its concentration as follows (IPCC, 2005, p.158 and 163):

$$RF(\text{halo}_l)_t = RE(\text{halo}_l) \cdot c(\text{halo}_l)_t. \qquad (2.2.12)$$

$RE(\text{halo})$ denotes the radiative efficiency of a particular halocarbon *l* (Table 2.2). The preindustrial concentration for each of the SRES 27 halocarbons is ignored in equation (2.2.12) as these halocarbons are practically of natural origins.

In addition to the 27 species, the concentrations of CH_3Cl and CH_3Br, primarily of natural origins, are calculated in the future mode of ACC2. The initial CH_3Cl and CH_3Br concentrations in 2000 are given as 536 ppt and 8.1 ppt, respectively (WMO, 2003, Table 1-1). The fixed natural emissions (3684.7 Gg for CH_3Cl; 192 Gg for CH_3Br) are optimized to explain the Ab mixing ratio scenario (WMO, 2003, Table 1-16) with the respective lifetimes (1.3 year for CH_3Cl; 0.7 year for CH_3Br (WMO, 2003, Table 1-6)). Inclusion of these two species is required to estimate the Effective Equivalent Stratospheric Chlorine (EESC), which is used to calculate the stratospheric O_3 forcing. CH_3Cl and CH_3Br are rather weak radiative forcing agents with a low radiative efficiency of 0.01 $W/m^2/ppb$ (WMO, 2003, Table 1-6) and thus are not included for the calculation of radiative forcing.

2.2.6. SF_6

SF_6 is a potent GHG characterized by its long atmospheric lifetime, the emission of which is

controlled by the Kyoto Protocol. SF_6 does not react with OH and its only sink is photolysis or ion reactions in the mesosphere (IPCC, 2001, p.254). The source of SF_6 is predominantly industrial: the use for insulation of high-voltage electrical equipment and oxidation prevention of molten magnesium (Maiss et al., 1996; Fenhann, 2000). A small amount of SF_6 is emitted naturally from the outgassing from fluorites (CaF_2), giving rise to the background concentration of 0.01 ppt (Harnisch and Eisenhauer, 1998). The anthropogenic emission of SF_6 began to increase in the 1950s. The rising emission trend has been reversed in 1996 in response to the rise in the market price (Maiss and Brenninkmeijer, 1999). The SF_6 concentration in 2000 was 4.7 ppt (WMO, 2003, 1.61). A global emission reduction by up to 90% is feasible if appropriate measures are taken for replacement and maintenance of relevant equipment (Maiss and Brenninkmeijer, 1998).

In the ACC2 past mode, we use the SF_6 concentration records based on Harnisch and Eisenhauer (1998) between the year 1750 and 1940, Maiss and Brenninkmeijer (1998) between 1953 and 1996, and the Climate Monitoring and Diagnostics Laboratory (CMDL) flask measurements between 1997 and 2000 (http://www.cmdl.noaa.gov/infodata/ftpdata.html). In the future mode of ACC2, the SF_6 concentration is dynamically calculated (equation (2.1.1)) on the basis of a SF_6 emission scenario in SRES. The SF_6 lifetime $\tau(\mathrm{SF}_6)$ is fixed at 3200 years (WMO, 2003, Table 1-6)). The unit conversion factor $\upsilon(\mathrm{SF}_6)$ is 25.1 (Table 2.2).

The radiative forcing of SF_6 is linearly related to its concentration as follows:

$$RF(\mathrm{SF}_6)_t = RE(\mathrm{SF}_6)\cdot c(\mathrm{SF}_6)_t\,, \qquad (2.2.13)$$

where the SF_6 radiative efficiency $RE(\mathrm{SF}_6)$ is 0.52 W/m^2/ppb (WMO, 2003, Table 1-6). The effect of the natural background SF_6 concentration is sufficiently small to be neglected in calculating the SF_6 radiative forcing.

2.2.7. Pollutants NO_x, CO, and VOC

Pollutants do not directly incur discernable changes in the atmospheric radiation budget but indirectly do so by in situ chemical reactions with GHGs, thus called "indirect GHGs." The direct forcings of CO and VOC are estimated to be merely 0.024 W/m^2 and 0.015 W/m^2, respectively (IPCC, 2001, pp.365-366). The emissions of pollutants cause climate and environmental problems (e.g. air quality degradation).

The major sources of NO_x are fossil fuel combustion, biomass burning, soil emission, and lightning (IPCC, 2001, Table 4.8). The sink of NO_x is the atmospheric oxidation of NO_2 by OH. NO is oxidized to NO_2 accompanied by OH production (equation (2.2.16)). NO_x catalyzes the O_3 formation in the troposphere (equations (2.2.14) – (2.2.18)). The sources of CO are CH_4 oxidation, biomass burning, fossil fuel combustion, Non-Methane HydroCarbons (NMHC) oxidation, vegetation, and ocean (IPCC, 2001, Table 4.6). The sinks of CO are predominantly the photochemical depletion involving OH (leading to O_3 formation) and the soil uptake (IPCC, 2001,

Table 4.6). The sources of VOC are vegetation, fossil fuel combustion, and biomass burning (IPCC, 2001, Table 4.7(a)). The sink of VOC is the oxidation by OH. NMHC, a class of VOC, include ethane (C_2H_4), propene (C_3H_6), isoprene (C_5H_8), and terpene ($C_{10}H_{16}$).

The emissions of pollutants are used to parameterize the OH concentration and the O_3 concentration in ACC2. The past pollutant emissions in ACC2 are based on EDGAR-HYDE 1.3 (van Aardenne et al., 2001). The emissions prior to 1890 are extrapolated on the basis of Bairoch (1995, pp.142-144), Klein Goldewijk (2001), United Nations (UN) Population Division (2002), and Houghton (2003). The future pollutant emissions in ACC2 are provided by SRES. The concentrations of the pollutants are not explicitly described because of their heterogeneous emission patterns and short lifetimes. Their direct radiative forcings are relatively small in magnitude and they are thus not included in the radiative forcing calculation in ACC2.

2.2.8. Tropospheric O_3

Tropospheric O_3 positively interferes the Earth's radiation and is a toxic agent in urban smog while stratospheric O_3 negatively interferes the radiation and plays a pivotal role in protecting human health against UV exposure. The IPCC estimate of the tropospheric O_3 radiative forcing in 2005 is 0.35 W/m^2 (IPCC, 2007, Figure SPM.2). Tropospheric O_3 is formed by the oxidation of CO with O_2 catalyzed by HO_x (H, OH, and HO_2) and NO_x (equations (2.2.14) – (2.2.18)).

$$OH + CO \rightarrow CO_2 + H \quad (2.2.14)$$

$$H + O_2 + M \rightarrow HO_2 + M \quad (2.2.15)$$

$$HO_2 + NO \rightarrow NO_2 + OH \quad (2.2.16)$$

$$NO_2 + h\nu \rightarrow NO + O(^3P) \quad (2.2.17)$$

$$O(^3P) + O_2 + M \rightarrow O_3 + M \quad (2.2.18)$$

In most instances, M is N_2 or O_2. The net reaction for the tropospheric O_3 formation pathway from CO oxidation is in the following.

$$CO + 2O_2 \rightarrow CO_2 + O_3 \quad (2.2.19)$$

Tropospheric O_3 is also formed by the oxidation of CH_4 in the presence of NO_x. CH_4 is oxidized to CO and then the reactions (equations (2.2.14) – (2.2.18)) proceed to produce O_3 (e.g. Jacob, 1999, pp.207-212). The net reaction the tropospheric O_3 formation pathway from CH_4 oxidation is the following.

$$CH_4 + 10O_2 \rightarrow CO_2 + H_2O + 5O_3 + 2OH \quad (2.2.20)$$

The foregoing two mechanisms are the dominant mode of tropospheric O_3 formation in the free troposphere. On the other hand, tropospheric O_3 formation near the surface is mainly occurred by the oxidation of NMHC (e.g. Brasseur et al., 2003, pp.472-473). O_3 is also transported from the stratosphere.

The sinks of O_3 are the photochemical depletion, vegetation uptake, and polar marine

boundary layer (IPCC, 2001, p.262). The nature of these sources and sinks and its turnover time of an order of weeks (IPCC, 2001, p.361) lead to so large spatial variability in the tropospheric O_3 concentration that no general trend can be extracted (IPCC, 2001, p.263). On the basis of the surface measurements, satellite measurements, and models, IPCC (2001, Table 4.9) recommends that the O_3 concentration increased from 25 DU in preindustrial time to 34 DU in 2000.

Similar to the OH concentration, the tropospheric O_3 concentration is parameterized based on the OxComp Workshop results (IPCC, 2001, Table 4.11).

$$\begin{aligned} &\mathrm{c(trp\_O_3)}_t - c(\mathrm{trp\_O_3})_{2000} \\ &= 5.0\{\ln(c(\mathrm{CH_4})_t) - \ln(c(\mathrm{CH_4})_{2000})\} + 0.125\left(e(\mathrm{NO}_x)_t - e(\mathrm{NO}_x)_{2000}\right) \\ &+ 0.0011\left(e(\mathrm{CO})_t - e(\mathrm{CO})_{2000}\right) + 0.0033\left(e(\mathrm{VOC})_t - e(\mathrm{VOC})_{2000}\right) \end{aligned} \quad (2.2.21)$$

The parameterization of the tropospheric O_3 concentration is similar to that of OH and related explanations are found in Section 2.2.4.

In the ACC2 past mode, the tropospheric O_3 radiative forcing uses the forcing of Hansen and Sato (2004). In the future mode, the radiative forcing due to tropospheric O_3 is parameterized as follows:

$$RF(\mathrm{trp\_O_3})_t = RE(\mathrm{trp\_O_3}) \cdot (c(\mathrm{trp\_O_3})_t - c(\mathrm{trp\_O_3})_{pre}) . \quad (2.2.22)$$

The radiative efficiency of tropospheric O_3 is 0.042 W/m^2/DU in ACC2 (Joos et al., 2001, p.904) based on the estimates in various models (IPCC, 2001, Table 6.3) ranges from 0.033 to 0.056 W/m^2/DU. $c(\mathrm{trp\_O_3})_{pre}$ is assumed to be 25 DU (IPCC, 2001, Table 4.9).

2.2.9. Stratospheric O_3

The stratospheric O_3 concentration had been substantially decreased mainly due to the industrial emissions of halogen-containing gases (Solomon, 1999).

$$\mathrm{O_3} + h\nu \rightarrow \mathrm{O_2} + \mathrm{O(^3P)} \quad (2.2.23)$$

$$\mathrm{Cl} + \mathrm{O_3} \rightarrow \mathrm{ClO} + \mathrm{O_2} \quad (2.2.24)$$

$$\mathrm{O(^3P)} + \mathrm{ClO} \rightarrow \mathrm{Cl} + \mathrm{O_2} \quad (2.2.25)$$

The net reaction is the following.

$$2\mathrm{O_3} \rightarrow 3\mathrm{O_2} \quad (2.2.26)$$

There are some signs of recovery in the stratospheric O_3 concentration due to the global adherence to the Montreal Protocol (Weatherhead and Andersen, 2006), which imposes the progressive reductions in halogen-containing gas emissions (Section 2.2.5).[37] Aside from the primary function of stratospheric O_3 shielding UV from the Earth's surface, stratospheric O_3 is a negative radiative agent, in contrast to tropospheric O_3 being a positive radiative agent. The decrease in the stratospheric O_3

[37] Note that the stratospheric O_3 concentration is also influenced by the NO emission, volcanic eruptions, solar cycle, and other meteorological conditions (Weatherhead and Andersen, 2006).

concentration allows more short-wave radiation to penetrate into the surface-troposphere system and less long-wave radiation to be absorbed. These two competing factors result in cooling for the surface-troposphere system (Brasseur et al., 1999, p.527; IPCC, 2001, p.359).

In ACC2, the concentration of stratospheric O_3 is not explicitly described. In the past mode, the stratospheric O_3 radiative forcing uses the forcing of Hansen and Sato (2004). In the future mode, the stratospheric O_3 radiative forcing is given as a function of EESC (Section 2.2.10) as follows (Joos et al., 2001):

$$RF(\text{str\_O}_3)_t = -0.07317(c(\text{EESC})_t - c(\text{EESC})_{1970}) . \quad (2.2.27)$$

The coefficient of –0.07317 was adopted from Joos et al. (2001) that assumes the present stratospheric O_3 forcing of –0.15 W/m^2 based on the estimate for the period between 1979 and 1997 (IPCC, 2001, p.360). The IPCC estimate of the stratospheric O_3 forcing is –0.05 W/m^2 in the year 2005 with a range between –0.15 W/m^2 and 0.05 W/m^2 (IPCC, 2007, Figure SPM.2). $c(\text{EESC})_{1970}$ is 1250 ppt (IPCC, 2001, Table II.2.10).

2.2.10. EESC

EESC is the chlorine-equivalent concentration of halogens in the lower stratosphere in terms of the O_3 destruction potential. The estimate of EESC is required to calculate the stratospheric O_3 radiative forcing. EESC is defined in the following (Daniel et al., 1995).

$$\begin{aligned}\text{EESC}_t = &\left\{\sum_i n_i \cdot c(\text{halo\_Cl}_i)_{t-3} \cdot \frac{FC_{\text{halo\_Cl}_i}}{FC_{\text{CFC-11}}}\right\} \cdot FC_{\text{CFC-11}} \\ &+ \left\{\sum_j n_j \cdot c(\text{halo\_Br}_j)_{t-3} \cdot \frac{FC_{\text{halo\_Br}_j}}{FC_{\text{CFC-11}}} \cdot \alpha\right\} \cdot FC_{\text{CFC-11}}\end{aligned} \quad (2.2.28)$$

halo_Cl_i and halo_Br_j denote a halocarbon containing chlorine and bromine, respectively (Table 2.2). n_i and n_j denote the number of chlorine and bromine contained in halo_Cl_i and halo_Br_j, respectively. $FC_{\text{halo\_Cl}_i}$ is the fractional release of chlorine from halo_Cl_i relative to CFC-11 (WMO, 2003, Table 1-4). Corresponding definitions hold for $FC_{\text{halo\_Br}_j}$. α denotes the enhanced chemical ability of a bromine atom to destroy O_3 relative to a chlorine atom. A constant value of 45 obtained from the work on mid-latitudes (WMO, 2003, 1.29 and 1.30) is used for EESC calculations in ACC2. The time lag of three years (Pollock et al., 1992) expresses an average travel time for halogens to reach the lower stratosphere from the emission source.[38] Note that the period of three years is generally used for EESC calculations although the travel time differs from a few

[38] Note that Equivalent Effective Chlorine (EECl) is identical with EESC except for the fact that EECl does not account for the 3-year time lag of halogen transportation (WMO, 2003, 1.19).

months to 6 years depending on the source locations (WMO, 2003, 1.19). The three-year travel time is not a valid assumption for the short-lived substances such as CH_3Br, the lifetime of which is merely 0.7 years.

EESC is calculated only in the future mode because the stratospheric O_3 radiative forcing is calculated only in the future mode. The estimates of the ODS concentrations between 1997 and 2000 (Section 2.2.5) are transferred from the past mode to the future mode in ACC2. The concentrations of CH_3Cl and CH_3Br are computed because of their significant contributions to EESC and do not enter the radiative forcing calculations. Among all the halocarbons described in ACC2, CFC-115 does not take part in the EESC calculation because the estimate of relative fractional release factor of CFC-115 was not found, but a significant change is not expected due to its omission.

The EESC estimate calculated in ACC2 is smaller than in IPCC (2001, Table II.2.10 in Appendix). The lifetimes and fractional release rates in ACC2 are updated with WMO (2003) and IPCC (2005). The EESC estimates in IPCC (2001) are actually taken from WMO (1999) based on the model of Daniel et al. (1995).

2.2.11. Stratospheric H_2O

Although water vapor is one of the two most important GHGs with CO_2, climate change due to water vapor is treated as a feedback rather than a forcing, in accordance with the definition of radiative forcing (IPCC, 2001, pp.405-406). Thus, changes in the H_2O concentration as a result of temperature change are considered as feedbacks. In fact, the representation of water vapor in climate models is a recurring theme of debate (e.g. Soden et al., 2002). The only exception is the stratospheric H_2O produced as a result of CH_4 oxidation. The direct anthropogenic H_2O emission in the troposphere and the H_2O emission from the high-flying aircrafts in the stratosphere[39] are insignificant in terms of climate forcing.

The radiative forcing of stratospheric H_2O is parameterized as a function of CH_4 concentration.

$$RF(\text{Stratospheric\_H}_2\text{O})_t = 0.035\left\{0.036\left(\sqrt{c(\text{CH}_4)_t} - \sqrt{c(\text{CH}_4)_{pre}}\right)\right\} \qquad (2.2.29)$$

The coefficient of 0.036 is the coefficient used in the CH_4 radiative forcing equation. 0.035 in equation (2.2.29) is based on the fact that the forcing contribution of stratospheric H_2O is 2 to 5% of the total CH_4 forcing (IPCC, 2001, p.366). Joos et al., (2001) uses a similar formulation but their coefficient is 0.05 rather than 0.035. The preindustrial CH_4 concentration in equation (2.2.29) is

[39] The radiative forcing due to contrails (with respect to only the formation of cirrus clouds) in 2005 is estimated to be 0.01 W/m^2 (IPCC, 2007, Figure SPM.2) with a large uncertainty.

assumed to be 700 ppb (IPCC, 2001, Table 6.1).

The concentration of stratospheric H_2O is not explicitly specified in ACC2. Observational records for almost half a century indicate a rising trend of stratospheric H_2O concentration of about 1% per year (Rosenlof et al., 2001). The forcing due to stratospheric H_2O is 0.2 W/m^2 since 1980 (IPCC, 2001, p.367). The estimate of the stratospheric H_2O forcing in the year 2005 is 0.07 W/m^2 with a range between 0.02 W/m^2 and 0.12 W/m^2 (IPCC, 2007, Figure SPM.2).

2.2.12. Aerosols

Aerosols are minute substances present in the atmosphere in a solid or liquid phase. Current scientific knowledge indicates that aerosols are strong negative radiative agents. However, the quantification of the aerosol forcing involves a large uncertainty due to the associated complex interactions with cloud formation and the resulting precipitation efficiency. The elucidation of the magnitude of the aerosol forcing is important to narrow down the uncertainties in climate projections.

Aerosols affect the Earth's radiation budget in the following three ways. First, aerosols generally scatter and absorb radiation, resulting in cooling and warming, respectively (direct effect of the aerosol forcing). Second, relevant to the warm (liquid-water) cloud formation is a role of aerosols in creating water droplets by functioning as cloud condensation nuclei, which leads to an increase in the droplet concentration and a decrease in the cloud albedo, resulting in cooling (first indirect effect). Third, the increase in the droplet concentration further leads to a reduction in the precipitation efficiency, resulting also in cooling (second indirect effect) (IPCC, 2001, p.375). The second indirect effect is regarded as a feedback rather than a forcing because it incurs changes in the tropospheric water vapor (IPCC, 2001, pp.405-406). The second indirect effect was not considered in the Second Assessment Report of IPCC (1996). Aerosols act also as ice nuclei for the formation of ice clouds. However, premature knowledge of the aerosol forcing in terms of ice cloud formation does not allow it to be taken into account in the aerosol forcing in ACC2 although the associated effect to the radiative forcing is estimated to be significant (IPCC, 2001, p.311).

Many species of aerosols are acting on the Earth's radiation budget differently. The representation of the aerosol forcing in the simple model framework requires coarse assumptions. In ACC2, aerosol forcings are divided into three types of forcings: 1) direct effect due to sulfate aerosols of anthropogenic origin, 2) direct effect due to OC and BC emitted from biomass burning and fossil fuel burning, and 3) indirect effect due to all the anthropogenic aerosols. This simplified scheme is used both in the ACC2 past and future mode and based on the following assumptions:

First, the direct effect of the sulfate aerosols is parameterized in the following way as described in Joos et al. (2001):

$$RF(\text{Sulfate\_Aerosols}^{direct})_t = RF(\text{Sulfate\_Aerosols}^{direct})_{2000} \cdot \frac{e(\text{SO}_2^{anthro})_t}{e(\text{SO}_2^{anthro})_{2000}}, \quad (2.2.30)$$

where $e(\text{SO}_2^{anthro})_t$ denotes anthropogenic SO_2 emission due to fossil fuel combustion at year *t*. The value of $e(\text{SO}_2^{anthro})_{2000}$ is given in each of the emission scenarios used in the past and future modes (EDGAR-HYDE 1.3 (van Aardenne et al., 2001) and SRES (Nakićenović et al., 2000)) (Footnote No.31). The emission prior to 1890 is extrapolated on the basis of Bairoch (1995, pp.142-144), Klein Goldewijk (2001), UN Population Division (2002), and Houghton (2003). The future anthropogenic SO_2 emission uses SRES. The estimate of the present sulfate aerosol forcing (direct effect only) $RF(\text{Sulfate\_Aerosols}^{direct})_{2000}$ is –0.4 W/m^2 with a range of –0.2 and –0.8 W/m^2 (IPCC, 2001, p.369 and Table 6.4). The central estimate has not been changed since the Second Assessment Report of IPCC (1996). Sulfate aerosols are formed through chemical reactions from sulfate precursors, which are mainly SO_2 originating from fossil fuel combustion, volcanic eruptions, and DiMethylSulphide (DMS) from marine plankton (e.g. Takemura et al., 2000; IPCC, 2001, Table 5.2). The sulfate forcing formulation above includes only the contribution from anthropogenic SO_2 emission.

Second, the direct effect of carbonaceous aerosols is represented in the following way (Joos et al., 2001):

$$RF(\text{Carbonaceous\_Aerosols}^{direct})_t = RF(\text{Carbonaceous\_Aerosols}^{direct})_{2000} \cdot \frac{e(\text{CO})_t}{e(\text{CO})_{2000}}. \quad (2.2.31)$$

The value of $e(\text{CO})_{2000}$ is provided from each of the emission scenarios in the past and future modes. Carbonaceous aerosols comprise OC and BC. OC is formed by atmospheric oxidation of biogenic hydrocarbons mainly with OH and takes a large fraction of carbonaceous aerosols. BC is soot and tarry substances originating from fossil fuel combustion and biomass burning. BC has a light absorbing character, which is of particular importance for the direct effect of the carbonaceous aerosols. The parameterization above uses CO emission to approximate various emissions leading to the formation of carbonaceous aerosols (Section 2.2.7 for emission data source). The radiative forcing of biomass burning carbonaceous aerosols is estimated to be –0.2 W/m^2 with an uncertainty range of –0.07 to –0.6 W/m^2 (IPCC, 2001, p.372). The radiative forcing of fossil fuel OC and BC aerosols is –0.1 W/m^2 with an uncertainty of a factor of 3 and 0.2 W/m^2 with an uncertainty of a factor of 2, respectively. The sum of the medians gives the estimate of –0.1 W/m^2 used for $RF(\text{Carbonaceous\_Aerosols}^{direct})_{2000}$. Note that the geographical distribution of carbonaceous aerosols is quite different from that of sulfate aerosols (IPCC, 2001, Figure 6.7 (d) and (e)).

Third, the indirect effect due to all the aerosols is parameterized as follows:

$$RF(\text{All\_Aerosols}^{indirect})_t = RF(\text{All\_Aerosols}^{indirect})_{2000}$$

$$\times \ln\left[\frac{e(\mathrm{SO}_2^{natur})_{const} + e(\mathrm{SO}_2^{anthro})_t}{e(\mathrm{SO}_2^{natur})_{const}}\right] \div \ln\left[\frac{e(\mathrm{SO}_2^{natur})_{const} + e(\mathrm{SO}_2^{anthro})_{2000}}{e(\mathrm{SO}_2^{natur})_{const}}\right]. \qquad (2.2.32)$$

The indirect forcing due to all the aerosols is assumed to be linearly linked to sulfate aerosol load of natural and anthropogenic origin. The logarithmic expression was taken from Harvey et al. (1997). The value of $e(\mathrm{SO}_2^{anthro})_{2000}$ is provided from each of the emission scenarios in the past and future modes. The natural SO_2 emission is assumed to be 42 Tg(S)/year (Harvey et al., 1997; Joos et al., 2001). $RF(\mathrm{All\_Aerosols}^{indirect})_{2000}$ is set to −0.8 W/m^2 based on the following estimates. Shine and Forster (1999) estimate that the indirect effect of all aerosols is −1.0 W/m^2 with an uncertainty of at least a factor of two. Joos' formulation similar to equation (2.2.32), the scaling coefficient is set to −0.8 W/m^2 is used for the year 1990 in the IS92a scenario. The GCM estimate of the indirect effect of aerosols has a large uncertainty because of considerable differences in the treatment of microphysical details (IPCC, 2001, p.377). The estimate of the indirect effect of all the aerosols in the year 2005 is −0.7 W/m^2 with an uncertainty range of –1.8 to –0.3 W/m^2 (IPCC, 2007, Figure SPM.2).

Aerosols that are not described in ACC2 are mineral dust, sea salt aerosols, industrial dust, primary biogenic aerosols, and nitrate aerosols. Mineral dust originates mainly from deserts but also from anthropogenic activities. Mineral dust scatters the incoming short-wave solar radiation while it also absorbs radiation over high albedo surface. The IPCC estimate of the radiative forcing of mineral dust is the range between –0.6 and 0.4 W/m^2 (IPCC, 2001, p.373). The mineral dust forcing (at present –0.6 to 0.4 W/m^2 (IPCC, 2001, p.373)) is not described in ACC2 because of the large uncertainty even in the present forcing estimate and also because of the lack of past and future forcing estimates. Sea salt aerosols are physically formed by bursting entrained air bubbles during whitecap formation on the ocean surface. Sea salt aerosols serve as both light scattering and cloud nuclei, which is important in particular over the ocean where wind speeds exceed a certain level (IPCC, 2001, p.297). No explicit estimate for the sea salt aerosol forcing is given in IPCC (2001) (see model-based estimate of Takemura et al., (2003)). Industrial dust is primary particles emitted from transportation, coal combustion, cement manufacturing, metallurgy, and waste incineration. Because of the direct relevance to environmental air quality, this type of aerosols have been well monitored and regulated, whose emissions have already been significantly reduced in developed countries (IPCC, 2001, p.299). On the other hand, the emission of industrial dust is rising in the advancement of emerging economy. Primary biogenic aerosols consist of plant debris, humic matter, and microbial particles and acts as both cloud nuclei and ice nuclei (IPCC, 2001, p.300). The abundance of nitrate aerosols is related to the relative abundances of ammonium and sulfate. The nitrate aerosol forcing is estimated to be merely –0.024 W/m^2 (IPCC, 2001, p.303). Finally, the interactions with aerosols with gases are not taken into account here.

2.3. CLIMATE COMPONENT – DOECLIM

In contrast to the earlier approach in NICCS where an IRF is used for calculating the temperature response to the radiative forcing (Hooss et al., 2001),[40] two different EBMs are available for the temperature calculation in ACC2. The first option is a global-mean EBM, which can be obtained by interpreting the Hooss' IRF as a physical box model (Kriegler, unpublished). Such a box-model representation overcomes a problem of the original IRF which was tied to the value of the climate sensitivity of the parent model used for the IRF calibration (2.39K in Hooss (2001, p.33)). The climate sensitivity is a measure of the asymptotic temperature change after doubling the preindustrial CO_2 concentration in AOGCM. The temperature pathway to reach the new equilibrium largely depends on the nonlinear thermal inertia of the ocean. Thus, the original IRF approach can be erroneous when the value of the climate sensitivity used in ACC2 departs largely from the reference value, and simply scaling the entire temperature response linearly with climate sensitivity would violate the energy conservation between heat flux into the earth system and net energy imbalance at the top of the atmosphere (Figure 2.6). Kriegler's global-mean EBM produces a temperature change projection that conforms to the energy conservation. The use of such an EBM is necessary for the inverse calculation where the climate sensitivity constitutes a tuning parameter to obtain a good fit of the 20th century temperature record. The second option for the temperature calculation in ACC2 is the Diffusion Ocean Energy balance CLIMate model (Acronym: DOECLIM), which is a land-ocean EBM used 'by default' in ACC2. Practically, DOECLIM should be used in all cases except for comparative analyses or solution checks. In this section, we will present the details of DOECLIM. Note that the sea level component in ACC2 is not actively used at this point,[41] and therefore not

[40] A strength of Hooss' approach is that a fixed spatial pattern of temperature anomalies (relative to the global mean) has been extracted *together* with annual-global-mean time characteristics of the temperature response to radiative forcing. The time-dependent part is computed separately in NICCS; however, the extraction procedure allows to approximate the spatially resolved temperature response by scaling the pattern with the global mean response. DOECLIM or the physical EBM interpretation of the IRF used for temperature calculations in ACC2 does not guarantee the validity of this approximation. Therefore, Hooss' spatial pattern is not actively used by the authors.

[41] The sea level component in ACC2 has been fully upgraded from ICM1.1 by implementing the parameterization of the sea level change summarized in IPCC (2001, Appendix 11.1). The IPCC approach takes account of the sea level rise due to thermal expansion, loss of mass of glaciers and ice caps, loss of mass of the Greenland ice sheet, loss of mass of the Antarctic ice sheet, loss of mass of the Greenland and Antarctic ice sheets due to the ongoing adjustment to past climate change, runoff from thawing of permafrost, and deposition of sediment on the ocean floor. The sea level change component in ACC2 produces a comparable projection to the corresponding IPCC projection up to 2100; however, some erroneous behavior was reported for the projection on a longer time scale. Hitherto, the sea level calculation 'by default' uses the global-annual-mean surface air temperature calculated from DOECLIM. However, since DOECLIM provides the temperature anomaly profile for the entire interior ocean water column, the estimation of sea level rise due to thermal expansion can be considerably improved. The extension of DOECLIM to the calculation of sea level rise is under way.

discussed here.

DOECLIM is used to calculate surface temperature change in response to radiative forcing of the earth system as computed by the carbon cycle and atmospheric chemistry components of ACC2. EBMs have found renewed interest in the 1980s for estimating the response of global surface temperature to a human-induced increase in atmospheric GHG concentrations (e.g., Hoffert et al. 1980; Harvey and Schneider, 1985; Schlesinger, 1985; Wigley and Schlesinger, 1985; Hansen et al. 1985; Wigley and Raper, 1992), and since then have been used as emulators for global mean response characteristics of AOGCM (e.g., Murphy, 1995; Raper and Cubasch, 1996; Raper et al., 2001) and as reduced-form climate models in integrated assessments of climate impacts and policies (e.g., Wigley et al., 1996; Nordhaus and Boyer, 2000). These EBMs are based on a linearised treatment of the climate response to small perturbations of the earth's energy balance. A discussion of the basic assumptions that underlie such a linearised treatment and their validity is beyond the scope of this section, but can be found elsewhere (e.g., Kriegler, 2005, Appendix A).

The model DOECLIM was originally constructed in a separate project (Kriegler, 2005) to estimate the joint uncertainty about climate sensitivity, vertical ocean heat diffusivity and sulphate aerosol forcing from a comparison of model response and 20th century surface temperature record. It was coupled to the carbon cycle and atmospheric chemistry components of ACC2 after that analysis was completed. The model structure and model parameter values are unchanged from Kriegler (2005), but the numerical implementation has been upgraded (Section 2.3.4) to eliminate artificial damped oscillations in the temperature response following volcanic spikes in the radiative forcing time series.

Section 2.3.1 motivates the particular model representation that was chosen for the specific purpose of comparing model response to the 20th century surface temperature record. Section 2.3.2 outlines the treatment of the interior ocean which dominates the transient model response. In Section 2.3.3, the model parameters are calibrated so that the set of free parameters is narrowed to climate sensitivity $T_{2\times}$ and effective vertical diffusivity κ_v of heat in the ocean. Section 2.3.4 describes the numerical implementation of DOECLIM. In Section 2.3.5, we discuss the coupling of the EBM to the upstream components of ACC2. Due to page constraints, we have tried to keep the model description as concise as possible. A more detailed description, particular of the model calibration and the analytical solution of the 1D-ocean model, can be found in Kriegler (2005, Section 2.1 and Appendices A and B).

2.3.1. Atmosphere – Land – Surface Ocean Model

EBMs of climate change try to assess the response of surface temperature to a perturbation of the (annual average) energy balance at the surface, i.e.,

$$\sigma T_{S,eq}^4 = F_{Sol} + G\,, \tag{2.3.1}$$

where $T_{S,eq}$ is the surface temperature in equilibrium, $\sigma = 5.67 \times 10^{-8}$ W/(m^{2}K^4) the Stefan-Boltzmann constant, F_{Sol} the portion of solar radiation that is absorbed by the earth system and G the additional net energy incident at the surface due to the natural greenhouse effect. If the incident energy $E = F_{Sol} + G$ is perturbed by a small amount ΔE, the first order Taylor approximation of the resulting heat flux into or out of the surface is given by

$$\dot{H}(t) = \Delta E(t) - rT_S(t)\,, \text{ with } r := 4\sigma(T_{S,eq})^3\,, \tag{2.3.2}$$

where T_S is the surface temperature anomaly with respect to the original equilibrium temperature. The main assumption underlying EBMs of climate change is that the perturbation of the incident energy can be approximated by the sum of a radiative forcing term (Q) capturing alterations of the energy balance due to changes in solar insolation, atmospheric aerosol load and GHG concentrations, and a temperature feedback term which scales with surface temperature anomaly T_S, i.e., $\Delta E := Q + rfT_S$. Under this assumption, the simplest EBM of temperature response to a radiative forcing Q is described by

$$\dot{H}(t) = Q(t) - \lambda T_S(t)\,, \tag{2.3.3}$$

where the climate feedback parameter $\lambda = r(1-f)$ amalgamates the effect of radiative damping and temperature feedback on the incident energy perturbation.

Equation (2.3.3) refers to annual average global mean quantities. Since the heat flux is dominated by the world's ocean, a more realistic model has to consider ocean and land masses separately. Most EBMs of climate change go a step further, and also separate Southern and Northern hemisphere (e.g., Wigley and Raper, 1992; Schlesinger et al., 1997). Two-hemisphere models are useful to capture the spatially inhomogeneous forcing from anthropogenic aerosols and tropospheric ozone, which are concentrated over the Northern hemisphere land masses. However, they come at the costs of additional uncertain parameters, because the inter-hemispheric heat fluxes need to be parameterized. Since the carbon cycle and atmospheric chemistry components of ACC2 provide only global mean quantities, we have decided to restrict ourselves to a separation of ocean and land masses only.

In its initial form, our EBM is constituted by four stylized boxes: land *L*, troposphere over land *AL*, troposphere over the ocean *AS*, and ocean mixed layer *S*. The model does not include the stratosphere, as it adjusts to a radiative perturbation within months, and these adjustment processes can be accounted for in the choice of radiative forcing (Harvey, 1999). The radiative heating is distributed among the boxes, before it diffuses into the interior ocean. Such a four box EBM is described by (compare Murphy, 1995):

Troposphere (land) $$C_A \dot{T}_{AL} = Q^*_{AL} - \lambda^*_{AL} T_{AL} - \frac{k^*}{f_L}\left(T_{AL} - T_{AS}\right) - k^*_L\left(T_{AL} - T_L\right) \quad (2.3.4)$$

Land $$C_L \dot{T}_L = Q^*_L - \lambda^*_L T_L - k^*_L\left(T_L - T_{AL}\right) \quad (2.3.5)$$

Troposphere (ocean) $$C_A \dot{T}_{AS} = Q^*_{AS} - \lambda^*_{AS} T_{AS} - \frac{k^*}{1 - f_L}\left(T_{AS} - T_{AL}\right) - k^*_S\left(T_{AS} - T_S\right) \quad (2.3.6)$$

Ocean mixed layer $$c_V z_S \dot{T}_S = Q^*_S - \lambda^*_S T_S - k^*_S\left(T_S - T_{AS}\right) - F_O \quad (2.3.7)$$

where $\lambda^*_{AL}, \lambda^*_L, \lambda^*_{AS}, \lambda^*_S$ are the climate feedback parameters in the respective boxes in W/(m^{2}K), k^* atmospheric land-sea heat exchange coefficient in W/(m^{2}K), k^*_L and k^*_S atmosphere-land and atmosphere-sea heat exchange coefficients in W/(m^{2}K), C_A and C_L heat capacity of atmosphere and land in W·yr/(m^{2}K), respectively, c_V specific heat capacity of a cubic meter of seawater in W·yr/(m^3 K), z_S depth of ocean mixed layer in m, F_O heat flux into the interior ocean in W/m^2, and f_L land fraction of earth surface.

Obviously, the differential equations (equations (2.3.4) – (2.3.7)) reflect the basic structure of equation (2.3.3), with temperature separated into T_{AL}, T_L, T_{AS}, T_S the effective temperature anomalies in the respective boxes, and global mean radiative forcing replaced by radiative forcings Q^*_{AL} and Q^*_{AS} of the troposphere over land and ocean, respectively (after stratospheric adjustments), and radiative forcings Q^*_L and Q^*_S at the troposphere-land/ocean interface. In addition, the model includes the anomalous heat transfer to the neighbouring boxes (no direct heat transfer is assumed between land and ocean box), which are assumed to scale with the temperature anomaly gradient between the boxes. Since we express the heat flux per unit area, we need to weigh the heat transfer coefficient between troposphere over land and sea by the land fraction of the earth surface.

The 4-Box model exhibits a variety of parameters, of which in particular the climate feedback parameters of the individual boxes will be difficult to estimate. Moreover, the partitioning of the radiative forcing onto the four boxes will depend on the forcing agent. To eliminate these complications, we take advantage of the fact that there exists a strong coupling between surface and troposphere due to large physical heat fluxes of latent and sensible heat. A perturbation of the radiation balance at the surface-troposphere interface equilibrates much faster due to readjustments of the surface-troposphere temperature gradient than a perturbation at the Top Of the Atmosphere (TOA) due to a change of the effective radiating temperature of the entire earth system (Harvey, 1999). Hence, for the sake of modelling the secular climate response to a radiative perturbation, we can assume that the tightly coupled Surface Air Temperatures (SAT) and troposphere temperatures increase in step ($dT_{AL}/dt = a_L\, dT_L^{SAT}/dt$, $dT_{AS}/dt = a_S\, dT_S^{SAT}/dt$). It is generally expected that the troposphere warms faster than the surface (on a global average; $a_L > 1$, $a_S > 1$) due to the decrease in lapse rate in moister air. The enhancement of effective troposphere warming relative to surface warming has been investigated in several AOGCM experiments, suggesting a globally averaged

value of $a = 1.2$ (Hansen et al., 2002). Radiosonde and satellite-borne measurements have shown the opposite trend with surface warming outpacing troposphere warming (Mears et al., 2003). Recently, these measurements have been corrected for residual errors which reconciled model projections with observations (Santer et al., 2005).

The proportionality between surface and troposphere warming allows us to simplify the 4-box model by expressing the increase in effective atmospheric temperatures T_{AL} and T_{AS} in terms of the corresponding increase in near surface air temperature. Over land, the increase in SAT is taken to be equal to the increase in land surface temperature itself. Over the ocean, the situation is more complex. The marine air warms faster than the sea surface due to a reduction in sea ice cover, hence we postulate $dT_S^{SAT}/dt = b_{SI}\, dT_S/dt$, where b_{SI} captures the air warming enhancement from retreating sea ice (compare Raper and Cubasch, 1996). In summary, we make the assumptions $dT_{AL}/dt = a\, dT_L/dt$ and $dT_{AS}/dt = a\, b_{SI} dT_S/dt$, where we have neglected any difference between troposphere warming enhancement over land and ocean ($a_L = a_S = a$). Under these assumptions, the model simplifies to a 2-box representation with a land-troposphere and ocean-troposphere box:

$$\text{Land + Troposphere} \quad C_{AL}\dot{T}_L = Q_L - \lambda_L T_L - \frac{k}{f_L}\left(T_L - b_{SI} T_S\right), \tag{2.3.8}$$

$$\text{Ocean + Troposphere} \quad C_{AS}\dot{T}_S = Q_S - \lambda_S T_S - \frac{k}{1-f_L}\left(b_{SI} T_S - T_L\right) - F_O\,. \tag{2.3.9}$$

The effective heat capacities of the two boxes are given by $C_{AL} \coloneqq aC_A + C_L$ and $C_{AS} \coloneqq ab_{SI}C_A + c_V z_S$, respectively. $\lambda_L \coloneqq a\lambda_{AL}^* + \lambda_L^*$ and $\lambda_S \coloneqq ab_{SI}\lambda_{AS}^* + \lambda_S^*$ denote the climate feedback parameters of the surface-troposphere system over land (relative to SAT) and ocean (relative to Sea Surface Temperature (SST)), respectively, and $k \coloneqq ak^*$ the effective land-sea heat exchange coefficient relative to the surface air temperature gradient. Finally, the radiative forcing terms are summed to radiative forcings $Q_L \coloneqq Q_{AL}^* + Q_L^*$ and $Q_S \coloneqq Q_{AS}^* + Q_S^*$ at the TOA after stratospheric adjustments.

2.3.2. Interior Ocean Model

The transient behavior of the EBM is dominated by the heat uptake of the ocean. Therefore, we need a reasonable model to calculate the heat flux F_O into the interior ocean. Most EBMs for the assessment of anthropogenic climate change utilize a 1-D upwelling-diffusion ocean model that describes the transfer of heat in the water column (e.g., Hoffert et al., 1980; Dickinson and Schaudt, 1998), i.e.,

$$\frac{\partial}{\partial t}T_O(z,t) = \frac{\partial}{\partial z}\left(\kappa_v(z)\frac{\partial}{\partial z}T_O(z,t)\right) + w\frac{\partial}{\partial z}T_O(z,t)\,, \tag{2.3.10}$$

where $z > 0$ denotes the depth of the interior ocean below the mixed layer, $T_O(z,t)$ the ocean

temperature at depth z and time t, κ_v the *effective vertical diffusivity* of heat in cm^2/s and w the upwelling velocity in the water column, which transports heat in the opposite direction of diffusion. The 1-D upwelling-diffusion model gained interest as a model of the globally averaged ocean column, because its equilibrium solution provides a good match to the observed global mean temperature profile in the ocean under reasonable values of upwelling velocity $w = 4$ m/yr and uniform vertical diffusivity $\kappa_v = 1$ cm^2/s (Munk, 1966).

Studies of climate change are interested in the penetration of a heat anomaly into the ocean due to rising sea surface temperatures (boundary condition: $T_O(0,t) = T_S(t)$). Since the upwelling-diffusion equation is linear, the anomalous heat fluxes are governed by equation (2.3.10) with initial condition $T_O(z,0) = 0$, where $T_O(z,t)$ represents now the temperature anomaly at depth z and time t relative to its equilibrium value at depth z and time $t = 0$. An analytical solution of this problem on the half line (case of an infinitely deep ocean) for constant vertical heat diffusivity can be found in Kriegler (2005, Appendix B). More realistic upwelling-diffusion ocean models with finite ocean depth include a heat source at the ocean floor which is hypothesized to represent downwelling polar water entering the main ocean column at the bottom. It was shown in Kriegler (2005, Appendix B) that a 'bucket' ocean with depth $z_B = 4000\,\text{m}$, and a uniform cross-section and vertical diffusivity throughout the water column yields a good approximation of upwelling-diffusion models with realistic depth-dependent cross-section and diffusivity profiles. This is due to the fact that the heat accumulation arising from the decrease of ocean cross-section with depth is counteracted by the increase of vertical diffusivity with depth (Simmons et al., 2004).

It is also discussed in Kriegler (2005, Appendix B) that a model with infinitely deep upwelling-diffusion ocean has difficulties to reproduce the temperature anomaly profiles from climate change experiments with AOGCMs, particularly at depths. The assumption of bottom heating from downwelling polar water seems to be an important prerequisite for upwelling-diffusion models to emulate the deep ocean warming in AOGCM simulations. However, a heat source at the bottom gives rise to “U-shaped” temperature anomaly profiles with greatest warming in the upper ocean and (to a lesser degree) at the bottom, leading to instability of the global mean ocean column. Some EBMs with upwelling-diffusion oceans try to resolve this instability by redistributing the warming with a simple convection algorithm (Raper et al., 2001). In our opinion, the physical interpretation of such a model of anomalous heat fluxes in the ocean becomes increasingly unclear. This point is reinforced by the finding that such upwelling-diffusion models are not in better agreement with the temperature anomaly profiles simulated by AOGCMs than pure diffusion models without upwelling (case $w = 0$; see Raper, 2001). Therefore, we restrict ourselves to a physically simpler pure diffusion model described by the following heat diffusion problem:

$$\text{for } 0 < z < z_B: \qquad \frac{\partial}{\partial t} T_O(z,t) = \kappa_v \frac{\partial^2}{\partial z^2} T_O(z,t)$$

$$\text{B.C.:} \qquad T_O(0,t) = T_S(t)\,, \quad \frac{\partial}{\partial z} T_O(z_B,t) = 0 \tag{2.3.11}$$

$$\text{I.C.:} \qquad T_O(z,0) = 0$$

The boundary conditions ensure that the interior ocean temperature at $z = 0$, i.e., the boundary to the mixed layer, equals the mixed layer temperature T_S, and that the heat flux into the ocean floor at $z = z_B$ vanishes. Kriegler (2005, Appendix B) derives an analytical solution for this problem which consists in an infinite series of solutions for the heat diffusion problem on the half line, i.e.,[42]

$$\begin{aligned} T_O(z,t) = T_S(t) - \int_0^t \dot{T}_S(t')\,\mathrm{Erf}\left(\frac{z}{2\sqrt{\kappa_v (t-t')}}\right) dt' \\ + \sum_{n=1}^{+\infty} (-1)^n \int_0^t \dot{T}_S(t') \left(\mathrm{Erf}\left(\frac{2nz_B - z}{2\sqrt{\kappa_v (t-t')}}\right) - \mathrm{Erf}\left(\frac{2nz_B + z}{2\sqrt{\kappa_v (t-t')}}\right)\right) dt' \end{aligned} \tag{2.3.12}$$

The series converges very fast, so that it will be sufficient for our application to just consider the zeroth order term describing the behaviour of an infinitely deep ocean and one to three next order bottom correction terms (depending on ocean heat diffusivity, surface warming and time span of model integration).

Equation (2.3.12) allows us to calculate the heat flux into the interior ocean as a function of the mixed layer temperature T_S, i.e.,

$$\begin{aligned} F_O(t) &= -f_{SO} c_V \kappa_v \frac{\partial}{\partial z} T_O(z,t)\Big|_{z=0} \\ &= f_{SO} c_V \sqrt{\frac{\kappa_v}{\pi}} \int_0^t \frac{\dot{T}_S(t')}{\sqrt{t-t'}} \left(1 + 2\sum_{n=1}^{+\infty} (-1)^n \exp\left(-\frac{n^2 z_B^2}{\kappa_v (t-t')}\right)\right) dt' \end{aligned} \tag{2.3.13}$$

The heat flux F_O (in W/m^2) has been scaled by a parameter $f_{SO} < 1$, which captures the reduction of ocean area at the bottom of the mixed layer relative to the ocean surface area. This accounts for the portion of shallow coastal water, where the heat cannot diffuse into the interior ocean.

Equation (2.3.13) can be inserted into equation (2.3.9) to close the EBM without having to model the entire ocean column explicitly. Such an approach for including a 1-D ocean model in an EBM of anthropogenic climate change was proposed by Wigley and Schlesinger (1985). They approximated the analytical solution of the problem (equation (2.3.11)) for the idealized case of an

---

[42] $\mathrm{Erf}(x)$ in equation (2.3.12) is the error function defined as $\mathrm{Erf}(x) = \frac{2}{\sqrt{\pi}} \int_0^x e^{-t^2} dt$. The error function is related to the cumulative normal distribution $\Phi(x) = \frac{1}{\sqrt{2\pi}} \int_{-\infty}^x e^{-\frac{x^2}{2}}$ by $\Phi(x) = \frac{1}{2}\left(1 + \mathrm{Erf}\left(\frac{x}{\sqrt{2}}\right)\right)$. $\Phi(x)$ is available under the name "errorf" in GAMS that was employed to implement DOECLIM numerically.

infinitely deep ocean to derive an ordinary differential equation for the mixed layer temperature T_S. The drawback of their approximation was that they had to introduce an artificial parameter which depended on the particular forcing scenario under consideration. In contrast, we consider the more realistic case of an ocean with finite depth, and do not approximate the resulting integro-differential equation by an ordinary differential equation, since we are seeking a general solution for arbitrary forcing trajectories. Due to the presence of an integro-differential equation for the sea surface temperature T_S, the model integration is complicated, but numerical solutions are still straightforward to obtain as discussed in Section 2.3.4. Once equations (2.3.8) and (2.3.9) are solved, we can recover the development of the entire temperature anomaly profile in the interior ocean by use of equation (2.3.12).

2.3.3. Model Calibration

Equations (2.3.8) and (2.3.9) (with the heat flux F_O into the interior ocean spelled out by equation (2.3.13)) constitute the dynamical core of DOECLIM. The model parameters are summarized in Table 2.3. Our goal is to limit the number of free model parameters to just two: the global climate sensitivity $T_{2\times}$, and the effective vertical diffusivity κ_v of heat in the ocean. The remaining parameter values have to be estimated, at least as a function of climate sensitivity, from comparing the model with empirical data and simulations with more complex climate models, or derived from physical properties of the earth system. The land fraction of the earth surface (f_L) and the fraction of ocean area with depth greater than 60 m (f_{SO}) (relative to surface ocean area) can be derived directly from the topography of the earth system. The interior ocean depth of $z_B = 4000$ m is close to the average ocean depth of 3800 m, and a frequent choice in 1D upwelling-diffusion ocean models (e.g., Schlesinger et al., 1997). As demonstrated in Kriegler (2005, Appendix B) a 'bucket' ocean with that depth and uniform vertical diffusivity yields a good approximation to 1D models with depth-dependent cross-section and diffusivity profiles. The specific heat capacity c_V of a cubic meter of seawater is well known from the literature (e.g., Dickinson, 1981).

We have used seasonal data to estimate the land-sea heat exchange coefficient k and the thermal inertia of the land-troposphere box C_{AL}. Admittedly, this constitutes a difficult choice since our highly aggregated EBM is better suited to simulate secular trends in response to a much smaller forcing modulation than is represented by the seasonal cycle. Nevertheless, simple EBMs have been successfully calibrated with seasonal data (e.g. Schlesinger et al., 1997), or even been used to deduce estimates for climate sensitivity from seasonal variations (Dutton, 1995). Therefore, we consider it a viable approach to calibrate those model parameters that influence the model response on monthly time scales (k, C_{AL}) with seasonal data.

The calibration procedure is detailed in Kriegler (2005, Appendix A). Here, we only recapitulate the basic approach and the results. In a first step, we have estimated the seasonal forcing

on land and ocean boxes by calculating the seasonal cycle of average solar insolation per box, and then using the climatology of monthly mean planetary albedo provided by the NASA Earth Radiation Budget Experiment (ERBE; data available at iridl.ldeo.columbia.edu/SOURCES/.NASA/) to estimate the amount of solar radiation that is absorbed in those boxes.

In a second step, we have constructed a climatology of monthly mean temperature anomalies (relative to the annual average) from the land and sea surface temperature time series provided by the US National Climatic Data Center (NCDC; data available at www.ncdc.noaa.gov/oa/climate/research/anomalies/anomalies.html). Seasonal anomalies showed no significant trend over the last 120 years, so that the mean anomaly averaged over the period 1880-2003 and its standard deviation could be directly estimated for each month. Due to the much smaller thermal inertia of the land-troposphere system, the amplitude of the seasonal cycle of temperature over land is much larger than over the oceans.

We then fitted equation (2.3.8) forced with the seasonal anomalies of absorbed solar radiation over land (Q_L; derived in Step 1) and sea surface temperature (T_S; from NCDC data) to the seasonal cycle of observed land surface air temperature anomalies as given in the NCDC data set. The fit estimated the maximum likelihood combination of land-sea heat exchange coefficient k and heat capacity C_{AL} (taking into account correlations between the data points) for fixed values of the climate feedback parameter λ_L. 95% confidence ellipsoids were obtained from the curvature of the likelihood function around the maximum likelihood estimate (k', C'_{AL}).

We found that the data strongly constrains the two parameters k and C_{AL}. The best estimate of the land-sea heat exchange coefficient scales strictly linear with the climate feedback parameter λ_L, i.e.,

$$k = b_k - a_k \lambda_L, \quad \text{with} \quad b_k = 1.59 \pm 0.063 \ \text{W/(m}^2\text{K)}, \quad a_k = 0.31. \qquad (2.3.14)$$

The relative error on the intersect (from the 95% confidence ellipsoids) is approximately 4%, and will be neglected in the following. The best estimate for the effective heat capacity of the land-troposphere system exhibits only a very small dependence on the climate feedback parameter λ_L. We find an overall value of $C_{AL} = 0.52 \pm 0.05$ W/(m^{2}K) (error bounds from the 95% confidence ellipsoids). For the purpose of our study, it suffices to choose the mean value of $C_{AL} = 0.52$ W/(m^{2}K). Such a heat capacity corresponds to a land column of approximately 8 m. Since the atmospheric heat capacity equals the heat capacity of a land column of approximately 5 m, the remaining 3 m are the effective depth of the land surface that contributes to the overall heat capacity of the land-troposphere system.

It would be desirable to estimate the effective heat capacity C_{AS} of the ocean mixed layer-troposphere system in the same manner. However, the seasonal global mean SST anomalies provide a much weaker signal and show a flat maximum during NH summer, when the global mean absorbed solar radiation over the oceans is at its minimum. The anti-correlation results from the

difference in land fraction between Northern and Southern hemisphere. Such a behavior can not be explained solely on the basis of heat fluxes between two aggregated land and ocean boxes. Its description would require, as a minimum, the resolution of Northern and Southern hemisphere.

Therefore, we do not try to estimate the effective mixed layer depth from seasonal data, but choose a value of 60 m that has been adopted in the EBM MAGICC for emulating the behavior of several AOGCMs (Raper et al., 2001). The effective mixed layer depth of 60 m includes the thermal inertia of the troposphere (which is equivalent to the inertia of a water column with approximately 2.5 m depth) and amounts to a heat capacity of the ocean mixed layer-troposphere system of $C_{AS} = 7.8$ W/(m^2 K). For comparison, Schlesinger et al. (1997) finds an effective depth of 55.9 m (53.9 m ocean mixed layer + 2 m tropospheric contribution) from a fit of their hemisphere resolving EBM to the seasonal cycle of land and sea surface temperatures in both hemispheres. Given the difficulty to constrain the effective heat capacity C_{AS} by seasonal data, it is fortunate that it does not influence markedly the model response to radiative perturbations on decadal to secular time scales. The transient temperature behaviour on these time scales is dominated by the heat flux into the interior ocean.

The remaining three parameters $\lambda_L, \lambda_S, b_{SI}$ refer to climate system properties on decadal to secular time scales and therefore cannot be estimated from seasonal data. We also refrain from utilizing the 20th century temperature record to avoid double counting, since these data will be used later to fit the fully coupled model ACC2 to observations. Instead, we rely on a data set of 2×CO_2 experiments with the model CLIMBER-2 (Schneider von Deimling et al., 2006). CLIMBER-2 is a 2.5-dimensional climate system model with a statistical-dynamical atmosphere module coupled to ocean, sea ice, and terrestrial vegetation modules (Petoukhov et al., 2000). The data set comprised 62 individual model runs with perturbed parameter values covering a wide range of climate sensitivities.

Concerning the marine air warming enhancement b_{SI}, i.e., the ratio between global mean marine surface (2m) air temperature anomaly and global mean SST, we find good agreement between individual model runs despite the heterogeneity of parameter settings relating to radiative transfer processes, heat transport in the ocean, atmospheric lapse rate, cloud cover, and water vapour. At the time of 2×CO_2 (year 70), all experiments showed ratios in the range $b_{SI} = 1.43 \pm 0.05$, which decreased to $b_{SI} = 1.32 \pm 0.05$ after 300 years, and remained constant (with narrowing range) thereafter. On the basis of these experiments, we choose a value of $b_{SI} = 1.3$. For comparison, Raper and Cubasch (1996) have estimated that retreating sea ice leads to a 20% larger warming of marine surface air than of the sea surface itself ($b_{SI} = 1.2$).

The climate feedback parameters λ_L and λ_S are directly related to the climate sensitivity $T_{L,2\times}$ over land (for 2m air temperature) and $T_{S,2\times}$ at the sea surface (which is lower than the climate sensitivity for 2m marine air temperature by the sea ice enhancement factor b_{SI}).

The functional dependence between these quantities can be identified from the equilibrium solution of equations (2.3.8) and (2.3.9), i.e., $dT_S/dt = dT_L/dt = 0$ and $F_O = 0$, for a doubling of the atmospheric CO_2 concentration relative to its preindustrial value (leading to a radiative forcing $Q_{2\times} = 3.7$ W/m^2):

$$\lambda_L = \frac{Q_{2\times}}{T_{L,2\times}} - \frac{k}{f_L}\frac{T_{L,2\times} - b_{SI}T_{S,2\times}}{T_{L,2\times}}, \quad \lambda_S = \frac{Q_{2\times}}{T_{S,2\times}} + \frac{k}{1-f_L}\frac{T_{L,2\times} - b_{SI}T_{S,2\times}}{T_{S,2\times}}. \qquad (2.3.15)$$

We have investigated the relationship between $T_{L,2\times}$ and $T_{S,2\times}$ with data from the ensemble of CLIMBER-2 2×CO_2 experiments, and found an almost strictly linear relationship $T_{L,2\times} = R_\lambda T_{S,2\times}$ with a land enhancement factor of $R_\lambda = 1.43 \pm 0.02$ (see Kriegler, 2005, Appendix A for details). This value is close to the land-sea ratio of climate sensitivity, $R_\lambda = 1.4$, employed in the EBM MAGICC (Raper et al., 2001). The larger climate sensitivity over land reflects the fact, inter alia, that temperatures at high latitudes will respond more strongly to an increase in atmospheric carbon dioxide concentrations than temperatures at low latitudes. Since the land fraction is highest at mid to high latitudes, this suggests a higher equilibrium temperature increase averaged over land than averaged over the sea (see, e.g., Murphy, 1995; Raper and Cubasch, 1996).

The proportionality between climate sensitivity over land and at the sea surface enables us to express these two parameters in terms of global mean climate sensitivity $T_{2\times} = f_L T_{L,2\times} + (1-f_L) b_{SI} T_{S,2\times}$, i.e.,

$$T_{L,2\times} = \frac{R_\lambda T_{2\times}}{R_\lambda f_L + (1-f_L) b_{SI}}, \quad T_{S,2\times} = \frac{T_{2\times}}{R_\lambda f_L + (1-f_L) b_{SI}}, \text{ with } R_\lambda = 1.43. \qquad (2.3.16)$$

By means of equation (2.3.14) describing the land-sea heat exchange coefficient k as a function of λ_L, together with equations (2.3.15) and (2.3.16) yielding the climate feedback parameters λ_L and λ_S as a function of $T_{2\times}$ and k, we can express all three parameters λ_L, λ_S, and k as functions of a single uncertain model parameter, global mean climate sensitivity $T_{2\times}$. Figure 2.7 shows the dependence of those parameters on climate sensitivity. In summary, we have calibrated the model DOECLIM described by equations (2.3.8), (2.3.9) and (2.3.13) so that it exhibits only two free parameters dominating the temperature response to anthropogenic forcing on secular time scales: the global mean climate sensitivity $T_{2\times}$ and the effective vertical diffusivity κ_v of heat in the ocean.

Figure 2.8 compares the behaviour of DOECLIM with a CO_2 quadrupling experiment conducted with the third version of the Hadley Centre Coupled Model (HadCM3) (Gordon et al., 2000). In this experiment, the Hadley centre model was run for 1040 years with a quadrupling of the atmospheric CO_2 concentration from 280 ppm to 1120 ppm in the first 70 years. The HadCM3 data was kindly provided by Simon Gosling from the UK MetOffice. Since HadCM3 overestimates the magnitude of land warming (compared to HadCM2, other GCMs and CLIMBER-2), we had to adjust the land-warming enhancement factor to $R_\lambda = 1.99$ in order to account for the large land-ocean temperature differential at the end of the HadCM3 simulation. The global mean climate

sensitivity in DOECLIM was set to $T_{2\times} = 4.1$ K, which is the effective climate sensitivity of HadCM3 at the end of the simulation period as identified by (Gregory et al., 2004). We have adjusted the vertical ocean heat diffusivity so that DOECLIM reproduces the temperature response of HadCM3 to a CO_2 quadrupling scenario. Figure 2.8 shows that DOECLIM can approximate the HadCM3 behaviour convincingly.

2.3.4. Numerical Implementation of DOECLIM

In order to choose an adequate numerical method for the integration of equations (2.3.8) and (2.3.9), we need to assess the range of time scales that are resolved by the model. DOECLIM contains six time scales,

$$\begin{aligned} &\tau_L \coloneqq \frac{C_{AL}}{\lambda_L},\ \tau_{LS} \coloneqq f_L \frac{C_{AL}}{k},\ \tau_{BO} \coloneqq \frac{z_B^2}{\kappa_v}, \\ &\tau_S \coloneqq \frac{C_{AS}}{\lambda_S},\ \tau_{SL} \coloneqq (1-f_L)\frac{C_{AS}}{k},\ \tau_{FO} \coloneqq \left(\frac{C_{AS}}{c_V}\right)^2 \frac{\pi}{\kappa_v}, \end{aligned} \tag{2.3.17}$$

which vary from 1-2 months (ocean-to-land heat exchange time scale τ_{LS}) and 3 months (temperature response time scale τ_L over land for low climate sensitivity of 1.5 K) to 2-6 years (ocean mixed layer temperature response time scales τ_S and τ_{SL}) to 10-30 years (average interior ocean heat uptake time scale $\sqrt{\tau_{FO} t}$ for a time horizon of $t = 100$ years and a heat diffusivity of $k_v = 0.5$ to 2 cm^2/s). By means of the timescales defined in equation (2.3.17), we can rewrite DOECLIM in compact form:

$$\dot{T}_L = \frac{Q_L}{C_{AL}} - \frac{T_L}{\tau_L} - \frac{T_L - b_{SI} T_S}{\tau_{LS}} \tag{2.3.18}$$

$$\dot{T}_S = \frac{Q_S}{C_{AS}} - \frac{T_S}{\tau_S} - \frac{b_{SI} T_S - T_L}{\tau_{SL}} - \frac{f_{SO}}{\sqrt{\tau_{FO}}} \int_0^t \frac{\dot{T}_S(t')}{\sqrt{t-t'}} \left(1 + 2\sum_{n=1}^{+\infty} (-1)^n \exp\left(-\frac{n^2 \tau_{BO}}{t-t'}\right)\right) dt'. \tag{2.3.19}$$

Since the time scales range over two orders of magnitude, equations (2.3.18) and (2.3.19) constitute a system of stiff differential equations. Therefore, if we want to choose a time step of the numerical integration (typically, $\Delta t = 1$ year) that is an order of magnitude larger than the fastest time scale in the model (τ_{LS} = 1-2 months), we need to turn to implicit numerical schemes to integrate the differential equations. To this end, Kriegler (2005) has employed the implicit midpoint rule, which can be derived as an implicit one-stage Runge-Kutta method with maximum order 2:

$$\dot{T}_i = \frac{T_{i+1} - T_i}{\Delta t} = f\left(t_i + \frac{\Delta t}{2}, \frac{T_i + T_{i+1}}{2}\right), \quad i: \text{time step index}, \tag{2.3.20}$$

where the function symbol f denotes the right-hand side of equations (2.3.18) and (2.3.19). The resulting difference equations are

$$\frac{T_{L,i+1}-T_{L,i}}{\Delta t}=\frac{Q_L\left(t_i+\frac{\Delta t}{2}\right)}{C_{AL}}-\frac{T_{L,i}+T_{L,i+1}}{2\tau_L}-\frac{\left(T_{L,i}+T_{L,i+1}\right)-b_{SI}\left(T_{S,i}+T_{S,i+1}\right)}{2\tau_{LS}}, \qquad (2.3.21)$$

$$\frac{T_{S,i+1}-T_{S,i}}{\Delta t}=\frac{Q_S\left(t_i+\frac{\Delta t}{2}\right)}{C_{AS}}-\frac{T_{S,i}+T_{S,i+1}}{2\tau_S}-\frac{b_{SI}\left(T_{S,i}+T_{S,i+1}\right)-\left(T_{L,i}+T_{L,i+1}\right)}{2\tau_{SL}}$$

$$-\frac{f_{SO}}{\sqrt{\tau_{SO}\Delta t}}\sum_{j=0}^{i}(T_{S,j+1}-T_{S,j})\int_j^{j+1}\frac{1+2\sum_{n=1}^{+\infty}(-1)^n\exp\left(-\frac{n^2\tau_{BO}}{\Delta t}\frac{1}{i+1-t'}\right)}{\sqrt{i+1-t'}}dt'. \qquad (2.3.22)$$

The coefficients in the sum on the right-hand side of equation (2.3.22) contain an integral, which can be solved analytically:

$$a_{i-j}:=\int_j^{j+1}\frac{1+2\sum_{n=1}^{+\infty}(-1)^n\exp\left(-\frac{n^2\tau_{BO}}{\Delta t}\frac{1}{i+1-t'}\right)}{\sqrt{i+1-t'}}dt'$$

$$=2\sqrt{i-j+1}\left(1+2\sum_{n=1}^{+\infty}(-1)^n\exp\left(-\frac{n^2\tau_{BO}}{\Delta t}\frac{1}{i-j+1}\right)\right)$$

$$-2\sqrt{i-j}\left(1+2\sum_{n=1}^{+\infty}(-1)^n\exp\left(-\frac{n^2\tau_{BO}}{\Delta t}\frac{1}{i-j}\right)\right)$$

$$+4\sum_{n=1}^{+\infty}(-1)^{n+1}n\sqrt{\pi\frac{\tau_{BO}}{\Delta t}}\left(\mathrm{Erf}\left(n\sqrt{\frac{\tau_{BO}}{\Delta t}\frac{1}{i-j}}\right)-\mathrm{Erf}\left(n\sqrt{\frac{\tau_{BO}}{\Delta t}\frac{1}{i-j+1}}\right)\right) \qquad (2.3.23)$$

We note that the coefficient a_0 is well defined, since $\lim_{x\to 0}e^{-c/x}=0$ and $\lim_{x\to 0}\mathrm{Erf}(c/x)=1$. The infinite sum in the expression for the a_{i-j} converges very fast, if the time scale of heat penetration to the ocean bottom, τ_{BO}, is on the order of magnitude of the time period $\Delta t(i-j)$ or smaller. For the case of interest here, i.e., the temperature response in the period 1750-2100, and realistic values of ocean heat diffusivity $\kappa_v<5$ cm^2/s, for which $\tau_{BO}>1000$ years, it is sufficient to consider just the first order bottom correction term. It the simulation is run longer until, e.g., the year 2500, the inclusion of the second and third order bottom correction terms will be more than sufficient for an accurate approximation of equations (2.3.21) and (2.3.22).

In order to allow a straightforward integration of the model by calculating the land and sea surface temperatures at time step $i+1$ from their predecessors at time step i, we reshuffle the terms in the difference equations (2.3.21) and (2.3.22) to yield the following numerical representation of the time-continuous model described by equations (2.3.18) and (2.3.19):

$$\boldsymbol{B}\cdot\begin{pmatrix} T_{L,i+1} \\ T_{S,i+1} \end{pmatrix} = \boldsymbol{Q} + \boldsymbol{A}\cdot\begin{pmatrix} T_{L,i} \\ T_{S,i} \end{pmatrix}, \tag{2.3.24}$$

$$\text{with} \quad \boldsymbol{B} := \begin{pmatrix} 1+\frac{1}{2}\frac{\Delta t}{\tau_L}+\frac{1}{2}\frac{\Delta t}{\tau_{LS}} & -\frac{1}{2}\frac{\Delta t}{\tau_{LS}} b_{SI} \\ -\frac{1}{2}\frac{\Delta t}{\tau_{SL}} & 1+\frac{1}{2}\frac{\Delta t}{\tau_S}+\frac{1}{2}\frac{\Delta t}{\tau_{SL}} b_{SI} + f_{SO}\sqrt{\frac{\Delta t}{\tau_{FO}}} a_0 \end{pmatrix},$$

$$\boldsymbol{Q} := \begin{pmatrix} \frac{\Delta t}{2}\frac{Q_L\left(t_i+\frac{\Delta t}{2}\right)}{C_{AL}} \\ \frac{\Delta t}{2}\frac{Q_S\left(t_i+\frac{\Delta t}{2}\right)}{C_{AS}} + f_{SO}\sqrt{\frac{\Delta t}{\tau_{FO}}}\sum_{j=1}^{i-1}(a_{i-j}-a_{i-j+1})T_{S,j} \end{pmatrix},$$

$$\boldsymbol{A} := \begin{pmatrix} 1-\frac{1}{2}\frac{\Delta t}{\tau_L}-\frac{1}{2}\frac{\Delta t}{\tau_{LS}} & \frac{1}{2}\frac{\Delta t}{\tau_{LS}} b_{SI} \\ \frac{1}{2}\frac{\Delta t}{\tau_{SL}} & 1-\frac{1}{2}\frac{\Delta t}{\tau_S}-\frac{1}{2}\frac{\Delta t}{\tau_{SL}} b_{SI} + f_{SO}\sqrt{\frac{\Delta t}{\tau_{FO}}}(a_0-a_1) \end{pmatrix}.$$

The weighted sum over the predecessor temperatures $T_{S,j}$ at all earlier times $j < i$ stems from the integral in the integro-differential equation (2.3.19), and reflects the memory of the interior ocean. Due to the presence of this sum, it is not possible to initialize the model at arbitrary times *t*, as would be the case for a system of ordinary differential equations, but only at a presumed idealised equilibrium state t_0 without radiative forcing ($T_{S,0} = Q_{L,0} = 0$) and temperature anomalies $T_{S,0} = T_{L,0} = 0$. Ocean memory about SST anomalies at earlier times $j < i$ comes into play at time step $i = 2$ for the first time, i.e. the sum over predecessor SSTs in the vector $\boldsymbol{Q}$ is only evaluated for $i \geq 2$. Note that we have omitted the term involving $T_{S,0}$ from this sum, since $T_{S,0} = 0$.

For time steps on the order of $t = 1$ year, Equation (2.3.24) yields a stable and accurate integration of the model DOECLIM in most instances of radiative forcing trajectories. However, if distinct forcing spikes due to volcanic aerosols are added to the forcing trajectory, small and quickly (within several years) dampening numerical oscillations occur in the temperature response following such spikes. In order to remove those artefacts, we have upgraded our numerical scheme to an implicit two-stage Runge-Kutta method with maximum order 4. Such a method was derived by Hammer and Hollingsworth (1955):

$$\dot{T}_i = \frac{T_{i+1}-T_i}{\Delta t} = \frac{p_i + q_i}{2} \quad i: \text{time step index},$$

$$\text{with} \quad p_i = f\left(t_i + \frac{3-\sqrt{3}}{6}\Delta t, \frac{T_i + T_{i+1}}{2} - \frac{\sqrt{3}}{6}\Delta t q_i\right),$$

$$q_i = f\left(t_i + \frac{3+\sqrt{3}}{6}\Delta t, \frac{T_i + T_{i+1}}{2} + \frac{\sqrt{3}}{6}\Delta t p_i \right), \tag{2.3.25}$$

To greatly simplify the implementation of the Hammer-Hollingsworth (HH) method, we do not apply it to the integral for the ocean memory, i.e., we retain the integration period ($t_0 = 0$ to $t_i + \Delta t/2$) from the implicit midpoint rule. This amounts to the assumption

$$\int_{t_i+\frac{3-\sqrt{3}}{6}\Delta t}^{t_i+\frac{3+\sqrt{3}}{6}\Delta t} \frac{\dot{T}_S(t')}{\sqrt{t-t'}}\left(1+2\sum_{n=1}^{+\infty}(-1)^n \exp\left(-\frac{n^2\tau_{BO}}{t-t'}\right)\right)dt' \approx$$

$$2\times \int_{t_i+\frac{3-\sqrt{3}}{6}\Delta t}^{t_i+\frac{\Delta t}{2}} \frac{\dot{T}_S(t')}{\sqrt{t-t'}}\left(1+2\sum_{n=1}^{+\infty}(-1)^n \exp\left(-\frac{n^2\tau_{BO}}{t-t'}\right)\right)dt', \tag{2.3.26}$$

which is an excellent approximation as long as the time step Δt (1 year) is an order of magnitude smaller than the time scale of heat uptake by the interior ocean (10-30 years). With this simplification, the HH method yields a numerical representation of DOECLIM that includes the terms from the implicit midterm rule plus additional correction terms:

$$(\boldsymbol{B}+\boldsymbol{C})\cdot\begin{pmatrix} T_{L,i+1} \\ T_{S,i+1} \end{pmatrix} = \boldsymbol{Q} + \boldsymbol{Q_C} + (\boldsymbol{A}+\boldsymbol{C})\cdot\begin{pmatrix} T_{L,i} \\ T_{S,i} \end{pmatrix},$$

$$\text{with } \boldsymbol{C} := \frac{\Delta t^2}{12}\begin{pmatrix} \frac{1}{\tau_L^2}+\frac{1}{\tau_{LS}^2}+\frac{2}{\tau_L\tau_{LS}}+\frac{b_{SI}}{\tau_{LS}\tau_{SL}} & -\frac{b_{SI}}{\tau_{LS}^2}-\frac{b_{SI}}{\tau_L\tau_{LS}}-\frac{b_{SI}}{\tau_S\tau_{LS}}-\frac{b_{SL}^2}{\tau_{LS}\tau_{SL}} \\ -\frac{b_{SI}}{\tau_{SL}^2}-\frac{1}{\tau_S\tau_{SL}}-\frac{1}{\tau_L\tau_{SL}}-\frac{1}{\tau_{LS}\tau_{SL}} & \frac{1}{\tau_S^2}+\frac{b_{SI}^2}{\tau_{SL}^2}+\frac{2b_{SI}}{\tau_S\tau_{SL}}+\frac{b_{SI}}{\tau_{LS}\tau_{SL}} \end{pmatrix}$$

$$\boldsymbol{Q_C} := \frac{\sqrt{3}}{12}\Delta t^2\begin{pmatrix} \frac{\Delta Q_{L,i}}{C_{AL}\tau_L}+\frac{\Delta Q_{L,i}}{C_{AL}\tau_{LS}}-b_{SI}\frac{\Delta Q_{S,i}}{C_{AS}\tau_{LS}} \\ \frac{\Delta Q_{S,i}}{C_{AS}\tau_S}+b_{SI}\frac{\Delta Q_{S,i}}{C_{AS}\tau_{SL}}-\frac{\Delta Q_{L,i}}{C_{AL}\tau_{SL}} \end{pmatrix},$$

$$\text{where } \Delta Q_{L/S,i} := Q_{L/S}\left(t_i+\frac{3+\sqrt{3}}{6}\Delta t\right) - Q_{L/S}\left(t_i+\frac{3-\sqrt{3}}{6}\Delta t\right), \tag{2.3.27}$$

where the matrices $\boldsymbol{A}$, $\boldsymbol{B}$ and the vector $\boldsymbol{Q}$ are the same as in equation (2.3.24). In order to separate the radiative forcing terms into a vector $\boldsymbol{Q}$ that emerged from the implicit midpoint rule and a correction $\boldsymbol{Q_C}$ from the two stage approach of the HH method we had to make the additional assumption

$$Q_{L/S}\left(t_i+\frac{\Delta t}{2}\right) \approx \frac{Q_{L/S}\left(t_i+\frac{3-\sqrt{3}}{6}\Delta t\right)+Q_{L/S}\left(t_i+\frac{3+\sqrt{3}}{6}\Delta t\right)}{2} \tag{2.3.28}$$

which is valid for climate change studies concerned with trends in annual mean radiative forcing, as

long as the time step Δt is of the order of 1 year.

The numerical representation (equation (2.3.27)) of the time-continuous equations (2.3.18) and (2.3.19) achieves the desired result of an accurate and oscillation-free model integration even for large spikes in the forcing trajectory due to volcanic aerosols. We have implemented equation (2.3.27) with a time step $\Delta t = 1$ year in GAMS (Brooke et al., 1992) (Section 4.1), where it can be used both in forward integrations and as a constraint for optimization problems. It is left to the discretion of the user, whether to activate only the numerical representation (2.3.24) derived from the implicit midpoint rule or to also include the correction terms in equation (2.3.27) derived from the HH method. In addition, the user can choose whether to include 1, 2 or 3 bottom-order correction terms in the calculation of the coefficients a_{i-j} (equation (2.3.23)), depending on the time period under consideration and the magnitude of the vertical ocean heat diffusivity. Final, the climate sensitivity and the vertical ocean heat diffusivity of the model DOECLIM can be adjusted freely, and the resulting values for the time scales and coefficients in equation (2.3.27) will be calculated automatically.

2.3.5. Coupling DOECLIM to the Other Components of ACC2

DOECLIM takes the total radiative forcing from anthropogenic and natural sources calculated by the carbon cycle and atmospheric chemistry modules of ACC2, and computes the response of land, sea surface and interior ocean temperature. The resulting temperature anomalies feed back on the carbon cycle module of ACC2.

ACC2 computes global-annual-mean radiative forcing values which need to be separated into forcing over land and ocean before they can be fed into DOECLIM. The derivation of these two forcings from the global mean radiative forcing proceeds as follows:

1) The forcing (in units of W/m^2) from well-mixed GHGs (CO_2, CH_4, N_2O, halocarbons, and SF_6) and from associated stratospheric ozone and water vapour anomalies is assumed to be equal over land and ocean, and thus equal to the global mean forcing from these sources.
2) The indirect forcing of anthropogenic aerosols is assumed to be roughly equal over land and ocean. Although the anthropogenic aerosol load over land is significantly larger, aerosol particles are more effective in acting as cloud condensation nuclei over the ocean (Harvey, 1999, Chapter 7.4).
3) We also assume that the forcing from volcanic aerosols in the stratosphere is roughly equal over land and ocean. This assumption is not unreasonable, since the volcanic cloud circles the globe rapidly.
4) The situation is different for the direct radiative forcing from sulphate and carbonaceous aerosols, which is concentrated over Central Europe, the Eastern United States, and Southeast Asia. We make the rough estimate that the direct sulphate forcing over land exceeds the forcing

over the ocean by a factor of 2 (Harvey, 1999, Figure 7.10, Plate 9). Taking into account the ratio of land to ocean surface area, this implies that the direct sulphate forcing per unit area over land is 155% of its global mean value, and over the ocean 78% of its global mean value. In the case of carbonaceous aerosols from fossil fuel and biomass burning, we assume that its direct forcing over land exceeds the forcing over the ocean by a factor 3 (Harvey, 1999, Figure 7.10). This implies that the direct forcing from carbonaceous aerosols over land is 190% of its global mean value, and over the ocean 63% of its global mean value.

5) The tropospheric ozone load is concentrated around metropolitan areas. Therefore, its abundance is higher over land than over the ocean, and higher in the Northern hemisphere than in the Southern hemisphere. We assume that the land-ocean ratio of its radiative forcing is of comparable magnitude as the NH:SH ratio, which has been estimated to range between 1.4 and 2 (Harvey, 1999, Table 7.3). Hence, we roughly estimate that the tropospheric ozone forcing over land exceeds the forcing over the ocean by a factor 1.5. This implies that the forcing over land is 131% of its global mean value, and over the ocean 87% of its global mean value.
6) The difference of solar forcing over land and ocean depends on the difference of annual mean insolation that the two areas receive, and the difference in annual mean albedo over these two areas. We have calculated these differences from the seasonal and latitudinal distribution of solar insolation and ERBE data (Section 2.3.3). The land surface receives 96% and the ocean 102% of the global mean solar insolation. At the same time, the annual mean albedo over land ($\alpha_L = 0.35$) is larger than over the ocean ($\alpha_O = 0.28$). This implies that the solar forcing over land is 89% of its global mean value, and over the ocean 105% of its global mean value.

The forcing contributions of the individual sources are summed to yield the total radiative forcing over land and the ocean which is then forwarded to DOECLIM. Predominantly due to the larger concentration of cooling aerosols over land, the radiative forcing over the ocean is slightly higher than over land.

Table 2.1. Summary of model equations in the carbon cycle and atmospheric chemistry components of ACC2

c and e denote the concentration and the emission of a gas, respectively. υ is the conversion factor between the emission unit and the concentration unit of a gas (values given in Table 2.2). τ denotes the atmospheric lifetime of a gas. RE is the radiative efficiency of a gas, that is, a radiative forcing per associated concentration unit. RF is a radiative forcing of a gas. The equations in this table are fully explained in the respective sections. The overlap function is explained in Section 2.2.2.

Forcing agent names	Concentration equations	Radiative forcing equations
CO_2 (carbon dioxide)	IRF-based ocean four-reservoir box model IRF-based land four-reservoir box model (Section 2.1.4)	$RF(\mathrm{CO_2})_t = \frac{RF_{2\times c(\mathrm{CO_2})_{pre}}}{\ln 2}\cdot\left(\ln\frac{c(\mathrm{CO_2})_t}{c(\mathrm{CO_2})_{pre}}\right)$
CH_4 (methane)	$\dot{c}(\mathrm{CH_4})_t = \frac{e(\mathrm{CH_4})_t}{\upsilon(\mathrm{CH_4})} - \frac{c(\mathrm{CH_4})_t}{\tau(\mathrm{CH_4})_t}$ $\frac{1}{\tau(\mathrm{CH_4})_t} = \frac{c(\mathrm{OH})_t / c(\mathrm{OH})_{2000}}{\tau(\mathrm{CH_4})^{\mathrm{OH}}} + \frac{1}{\tau(\mathrm{CH_4})^{stratosphere}} + \frac{1}{\tau(\mathrm{CH_4})^{soil}}$	$RF(\mathrm{CH_4})_t = 0.036\cdot\left\{\sqrt{c(\mathrm{CH_4})_t} - \sqrt{c(\mathrm{CH_4})_{pre}}\right\}$ $-Overlap\left(c(\mathrm{CH_4})_t, c(\mathrm{N_2O})_{pre}\right) - Overlap\left(c(\mathrm{CH_4})_{pre}, c(\mathrm{N_2O})_{pre}\right)$ $Overlap(M,N) = 0.47\cdot\ln\left\{1 + 2.01\times10^{-5}(M\cdot N)^{0.75} + 5.31\times10^{-15}M(M\cdot N)^{1.52}\right\}$
N_2O (nitrous oxide)	$\dot{c}(\mathrm{N_2O})_t = \frac{e(\mathrm{N_2O})_t}{\upsilon(\mathrm{N_2O})} - \frac{c(\mathrm{N_2O})_t}{\tau(\mathrm{N_2O})_t}$ $\tau(\mathrm{N_2O})_t = \tau(\mathrm{N_2O})_{2000}\left(\frac{c(\mathrm{N_2O})_t}{c(\mathrm{N_2O})_{2000}}\right)^{-0.046}$	$RF(\mathrm{N_2O})_t = 0.12\cdot\left\{\sqrt{c(\mathrm{N_2O})_t} - \sqrt{c(\mathrm{N_2O})_{pre}}\right\}$ $-Overlap\left(c(\mathrm{CH_4})_{pre}, c(\mathrm{N_2O})_t\right) - Overlap\left(c(\mathrm{CH_4})_{pre}, c(\mathrm{N_2O})_{pre}\right)$ $Overlap(M,N) = 0.47\cdot\ln\left\{1 + 2.01\times10^{-5}(M\cdot N)^{0.75} + 5.31\times10^{-15}M(M\cdot N)^{1.52}\right\}$
OH (hydroxyl radical)	$\ln(c(\mathrm{OH})_t) - \ln(c(\mathrm{OH})_{2000}) = -0.32\left\{\ln(c(\mathrm{CH_4})_t) - \ln(c(\mathrm{CH_4})_{2000})\right\}$ $+ 0.0042\left(e(\mathrm{NO_x})_t - e(\mathrm{NO_x})_{2000}\right) - 0.000105\left(e(\mathrm{CO})_t - e(\mathrm{CO})_{2000}\right)$ $- 0.000315\left(e(\mathrm{VOC})_t - e(\mathrm{VOC})_{2000}\right)$	Not defined
Halocarbons	Not defined (past mode) $\dot{c}(\mathrm{halo})_t = \frac{e(\mathrm{halo})_t}{\upsilon(\mathrm{halo})} - \frac{c(\mathrm{halo})_t}{\tau(\mathrm{halo})_t}$ (future mode)[43]	$RF(\mathrm{halo})_t = RE(\mathrm{halo})\cdot c(\mathrm{halo})_t$
SF_6	Not defined (past mode) $\dot{c}(\mathrm{SF_6})_t = \frac{e(\mathrm{SF_6})_t}{\upsilon(\mathrm{SF_6})} - \frac{c(\mathrm{SF_6})_t}{\tau(\mathrm{SF_6})}$ (future mode)	$RF(\mathrm{SF_6})_t = RE(\mathrm{SF_6})\cdot c(\mathrm{SF_6})_t$
CO, VOC, NOx	Not defined[44]	Not defined

[43] $\tau(\mathrm{halo})$ is a constant for halocarbons containing no hydrogen atom. For halocarbons containing at least one hydrogen atom, $\tau(\mathrm{halo})_t = \frac{\tau(\mathrm{halo})_{2000}}{c(\mathrm{OH})_t / c(\mathrm{OH})_{2000}}$. See Table 2.2.

[44] Emissions are used to define the concentrations of tropospheric O_3 and OH (thus, CH_4 and OH-reactive halocarbons) and the radiative forcing of the direct effect of carbonaceous aerosol.

Table 2.1. (Continued) Summary of model equations in the carbon cycle and atmospheric chemistry components of ACC2

Forcing agent names	Concentration equations	Radiative forcing equations
Tropospheric O_3	Not defined (past mode) $c(\text{trp\_O}_3)_t - c(\text{trp\_O}_3)_{2000} = 5.0\{\ln(c(\text{CH}_4)_t) - \ln(c(\text{CH}_4)_{2000})\}$ $+ 0.125(e(\text{NO}_x)_t - e(\text{NO}_x)_{2000}) + 0.0011(e(\text{CO})_t - e(\text{CO})_{2000})$ $+ 0.0033(e(\text{VOC})_t - e(\text{VOC})_{2000})$ (future mode)	Radiative forcing scenario (past mode) $RF(\text{trp\_O}_3)_t = RE(\text{trp\_O}_3) \cdot (c(\text{trp\_O}_3)_t - c(\text{trp\_O}_3)_{pre})$ (future mode)
Stratospheric O_3	Not defined	$RF(\text{str\_O}_3)_t = -0.07317(c(\text{EESC})_t - c(\text{EESC})_{1970})$
Stratospheric H_2O	Not defined	$RF(\text{Stratospheric\_H}_2\text{O})_t = 0.035\left\{0.036\left(\sqrt{c(\text{CH}_4)_t} - \sqrt{c(\text{CH}_4)_{pre}}\right)\right\}$
Sulfate aerosols (direct effect)	Not defined	$RF(\text{Sulfate\_Aerosols}^{direct})_t = RF(\text{Sulfate\_Aerosols}^{direct})_{2000} \cdot \frac{e(\text{SO}_2^{anthro})_t}{e(\text{SO}_2^{anthro})_{2000}}$
Carbonaceous aerosols (direct effect)	Not defined	$RF(\text{Carbonaceous\_Aerosols}^{direct})_t = RF(\text{Carbonaceous\_Aerosols}^{direct})_{2000} \cdot \frac{e(\text{CO})_t}{e(\text{CO})_{2000}}$
All aerosols (indirect effect)	Not defined	$RF(\text{All\_Aerosols}^{indirect})_t$ $= RF(\text{All\_Aerosols}^{indirect})_{2000} \times \ln\frac{e(\text{SO}_2^{natur})_{const} + e(\text{SO}_2^{anthro})_t}{e(\text{SO}_2^{natur})_{const}} \Big/ \ln\frac{e(\text{SO}_2^{natur})_{const} + e(\text{SO}_2^{anthro})_{2000}}{e(\text{SO}_2^{natur})_{const}}$

Table 2.2. Summary of the information on halocarbons (27 species in SRES, methyl chloride, and methyl bromide) and SF_6

ACC2 adopted the estimates of the unit conversion factors (denoted by υ in Table 2.1) that are linearly scaled with molecular weights (see text). In most of the cases, these estimates used in ACC2 are in good agreements with corresponding estimates in Fuglestvedt and Berntsen (1999, Table 2). The estimates of the lifetimes and the radiative efficiencies were taken from IPCC (2005, Table 2.6). Such estimates are in some cases slightly different from the corresponding earlier estimates in IPCC (2001, Table 6.7) and WMO (2003, Table 1-6). The lifetimes and the unit conversion factors are used in the concentration equations in ACC2 (Table 2.1). The radiative efficiencies are used in the radiative forcing equations in ACC2 (Table 2.1). The estimates of the relative fractional releases were taken from WMO (2003, Table 1-4) and Schauffler et al. (1999). The relative fractional releases are used to calculate EESC (Section 2.2.10).

Groups	Common names	Chemical formula	Molecular weights	Unit conversions	Lifetimes (year)	Radiative efficiencies ($W/m^2/ppb$)	Relative fractional releases
PFC Fully Fluorinated	FC-14	CF_4	88	15.1	50000	0.08	
PFC Fully Fluorinated	FC-116	C_2F_6	138	23.7	10000	0.26	
PFC Fully Fluorinated	FC-31-10	C_4F_{10}	238	40.8	2600	0.33	
HFC	HFC-23	CHF_3	70	12.0	270	0.19	
HFC	HFC-32	CH_2F_2	52	8.9	4.9	0.11	
HFC	HFC-43-10mee	$CF_3CHFCHFCF_2CF_3$	252	43.2	15.9	0.4	
HFC	HFC-125	CHF_2CF_3	120	20.6	29	0.23	
HFC	HFC-134a	CH_2FCF_3	102	17.5	14	0.16	
HFC	HFC-143a	CF_3CH_3	84	14.4	52	0.13	
HFC	HFC-152a	CH_3CHF_2	66	11.3	1.4	0.09	
HFC	HFC-227ea	CF_3CHFCF_3	170	29.2	34.2	0.26	
HFC	HFC-236fa	$CF_3CH_2CF_3$	152	26.1	240	0.28	
HFC	HFC-245ca	$CH_2FCF_2CHF_2$	134	23.0	6.2	0.23	
Fully fluorinated	Sulfur hexafluoride	SF_6	146	25.1	3200	0.52	
CFC	CFC-11 (Freon-11)	CCl_3F	137.35	23.6	45	0.25	1.00
CFC	CFC-12 (Freon-12)	CCl_2F_2	120.9	20.7	100	0.32	0.60
CFC	CFC-113	CCl_2FCClF_2	187.35	32.1	85	0.3	0.75
CFC	CFC-114	$CClF_2CClF_2$	170.9	29.3	300	0.31	0.28
CFC	CFC-115	CF_3CClF_2	154.45	26.5	1700	0.18	
Chlorocarbon	Carbon tetrachloride	CCl_4	153.8	26.4	26	0.13	1.06
Chlorocarbon	Methyl chloroform	CH_3CCl_3	133.35	22.9	5	0.06	1.08
Halon	Halon1211	$CBrClF_2$	165.35	28.4	16	0.3	1.18
Halon	Halon1301	$CBrF_3$	148.9	25.6	65	0.32	0.62
Halon	Halon2402	$CBrF_2CBrF_2$	259.8	44.6	20	0.33	1.22
HCFC	HCFC-22	$CHClF_2$	86.45	14.8	12	0.2	0.35
HCFC	HCFC-141b	CH_3CCl_2F	116.9	20.1	9.3	0.14	0.72
HCFC	HCFC-142b	CH_3CClF_2	100.45	17.2	17.9	0.2	0.36
HCFC	HCFC-123	CF_3CHCl_2	152.9	26.2	1.3	0.14	1.11
Monomethyl halide	Methyl chloride	CH_3Cl	50.45	8.7	1.3	0.01	
Monomethyl halide	Methyl bromide	CH_3Br	94.9	16.3	0.7	0.01	

Table 2.3. The parameters of the diffusion ocean energy balance model DOECLIM

The estimate of the global-mean climate sensitivity $T_{2\times}$ is taken from the result of the inverse calculation of ACC2. In the ACC2 inverse calculation, the effective vertical ocean heat diffusivity κ_v is fixed at 0.55 cm^2/s because κ_v and $T_{2\times}$ cannot be well-constrained simultaneously (Section 3.3). The value of $T_{2\times}$ influences the estimates of the climate feedback parameter over land $\lambda_L(T_{2\times})$ and over ocean $\lambda_S(T_{2\times})$ (equations (2.3.15) and (2.3.16)) and the land-ocean heat exchange coefficient $k(T_{2\times})$ (equation 2.3.14).

Topographical parameters		
Land fraction of earth surface	f_L	0.29
Ocean fractional area below 60 m depth	f_{SO}	0.95
Interior ocean depth	z_B	4000 m
Heat capacities		
Specific heat capacity of seawater	c_V	0.13 Wyr/(m^{3}K)
Effective troposphere-land heat capacity	C_{AL}	0.52 Wyr/(m^{2}K)
Effective troposphere-ocean mixed layer heat capacity	C_{AS}	7.80 Wyr/(m^{2}K)
Heat flux and climate feedback parameterisations		
Climate feedback parameter over land	$\lambda_L(T_{2\times})$	0.37 W/(m^{2}K)
Climate feedback parameter over ocean	$\lambda_S(T_{2\times})$	1.47 W/(m^{2}K)
Land-ocean heat exchange coefficient	$k(T_{2\times})$	1.48 W/(m^{2}K)
Marine surface air warming enhancement	b_{SI}	1.3
Free model parameters		
Global mean climate sensitivity	$T_{2\times}$	4.0 K
Effective vertical ocean heat diffusivity	κ_v	0.55 cm^2/s

Figure 2.1. Ocean IRF used to tune the ACC2 atmosphere-ocean box model (after Hooss (2001, Figure 2.1))

In the control run of HAMOCC3i, the atmospheric CO_2 concentration is perturbed at year 0. The three dashed lines from top to bottom show the perturbations in the magnitudes of 300%, 100%, and 1%, respectively. Solid lines are the IRFs fitted to the respective dotted curves. All the perturbation curves and IRFs are normalized. The IRF obtained from the 1% perturbation experiment (bottom) is adopted for ACC2 (equations (2.1.11) and (2.1.12)).

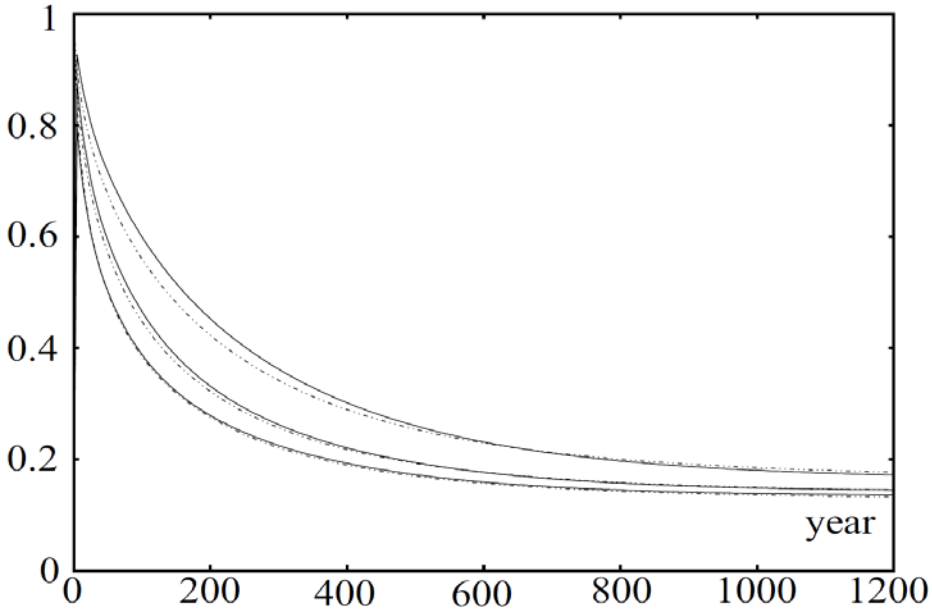

Figure 2.2. Shifts of the thermodynamic equilibria of $CO_2(aq)$, HCO_3^-, and CO_3^{2-} with the changes in pH and temperature

The equilibrated fractional concentrations are calculated by using the relationships of the equilibrium constants as functions of temperature (Millero, 1995; Millero et al., 2006). In the present day condition, HCO_3^- is the dominant form of DIC in the mixed layer. $CO_2(aq)$ is the quantity that is directly equilibrated with the atmospheric CO_2 concentration. The fractionation of the carbonate species is thus an important factor determining the carbon storage capacity in the mixed layer.

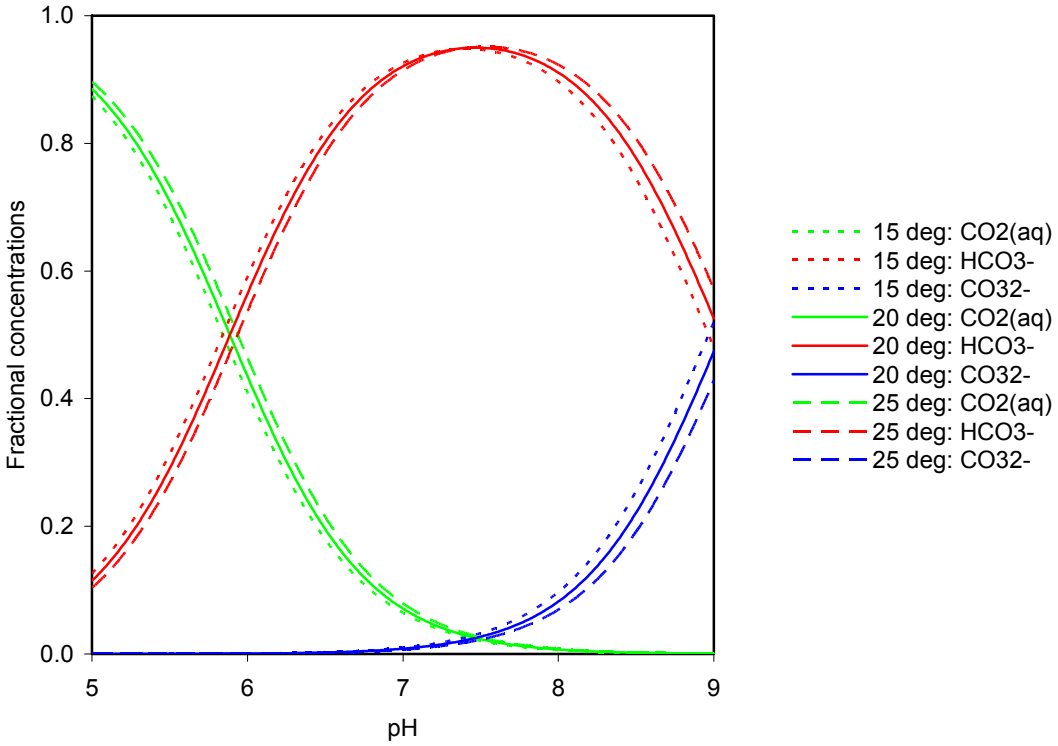

Figure 2.3. The CO_2 equilibrium between the atmosphere and the ocean mixed layer

This figure is aimed at demonstrating the importance of describing the thermodynamic equilibria for the marine carbonate species under a high atmospheric CO_2 concentration. The equilibrium between the atmospheric CO_2 concentration and the mixed layer carbon content computed by four different methods are shown. The first three methods are essentially scalings using the Revelle factor (10, 15, or 20). The last method is based on the explicit calculation of the thermodynamic equilibria of $CO_2(aq)$, HCO_3^-, and CO_3^{2-} in ACC2. In the last method, a constant alkalinity of 2.435×10^{-3} mol-equivalent/liter and a constant mixed layer temperature of 20°C are assumed.

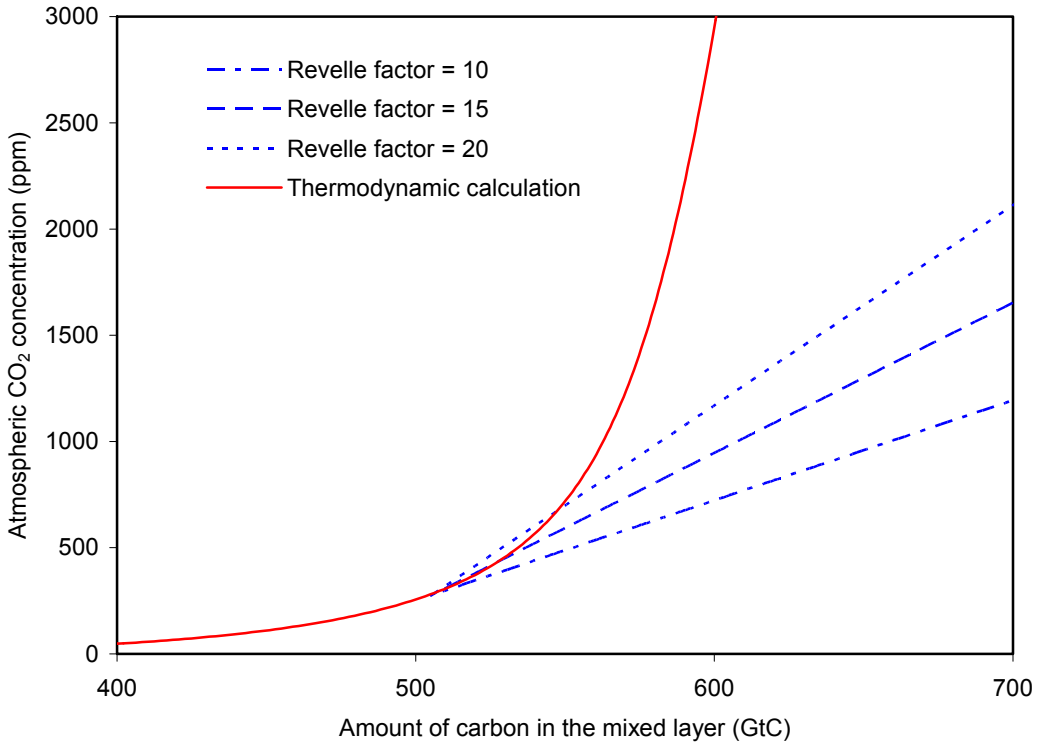

Figure 2.4. pH and the carbon content in the mixed layer under changing atmospheric CO_2 concentration

This figure shows the equilibrium of the CO_2 system in the atmosphere and the mixed layer computed from ACC2. The amount of carbon in the ocean mixed layer is practically saturated even under the present day condition, indicating that there is no significant fast ocean sink. Thus, the remaining ocean sink is primarily in the deep ocean, controlled by the rate of thermohaline circulation.

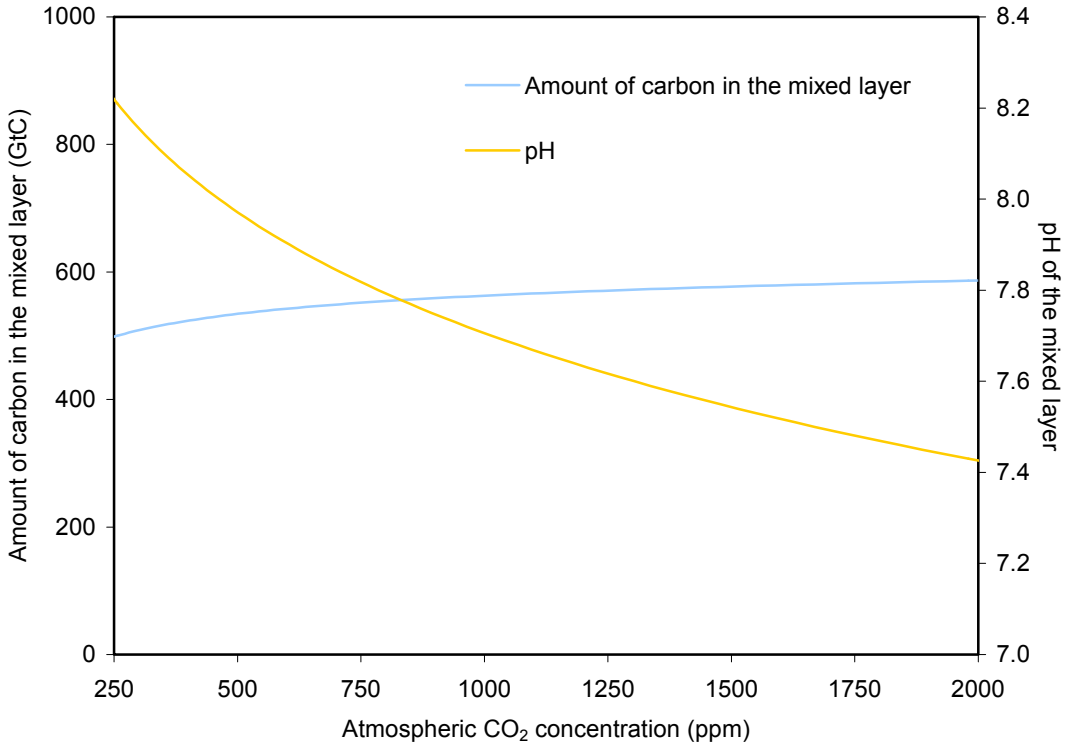

Figure 2.5. Land IRF used to tune the ACC2 land box model

The IRF (heterotrophic respiration flux) is obtained from Bern-CC (Joos et al., 1996).

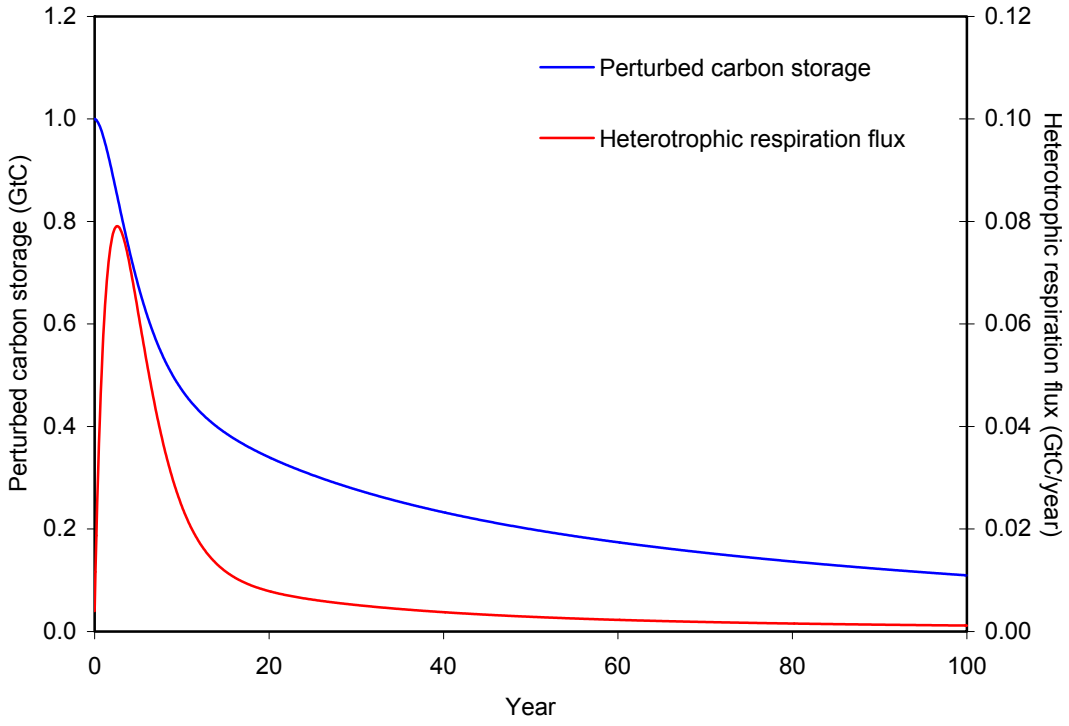

Figure 2.6. Surface air temperature response to the $2\times CO_2$ forcing

The performances of the IRF (Hooss, 2001) and the global-mean EBM (box-model interpretation of the Hooss' IRF) (Kriegler, unpublished) are evaluated for different climate sensitivity. The Hooss' IRF is linearly scaled with climate sensitivity. Kriegler's EBM accounts for the energy conservation between net radiation imbalance at the top of the atmosphere and heat flux into the earth system. It can be seen that the initial response of the two models are markedly different. The temperature responses of the two models agree when the climate sensitivity is fixed at the sensitivity of the parent model (2.39°C).

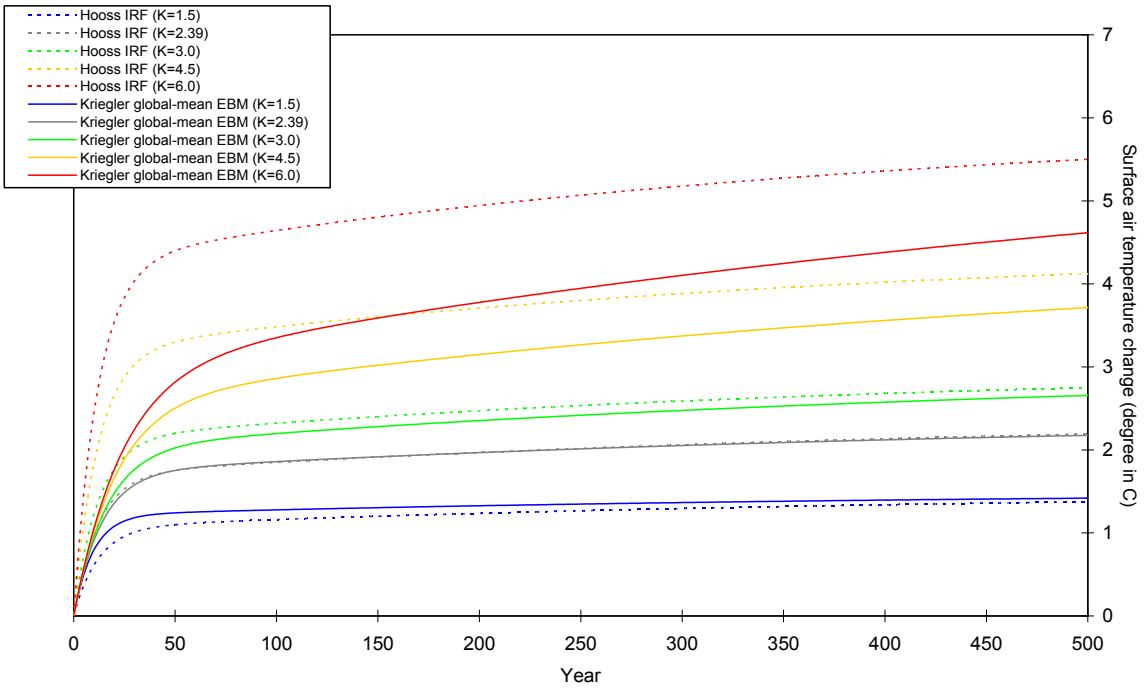

Figure 2.7. Dependence of λ_L and λ_S, and k on global mean climate sensitivity $T_{2\times}$

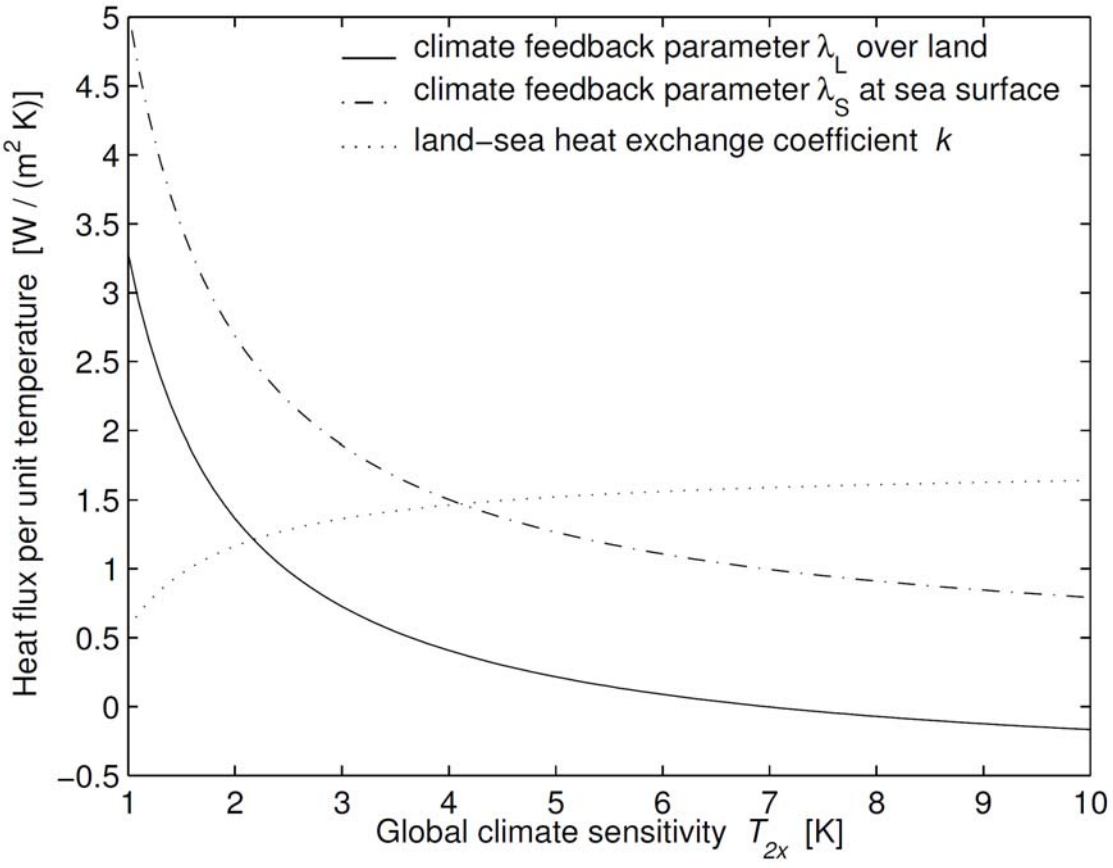

Figure 2.8. Comparison of DOECLIM with results from a CO_2 quadrupling experiment with HadCM3

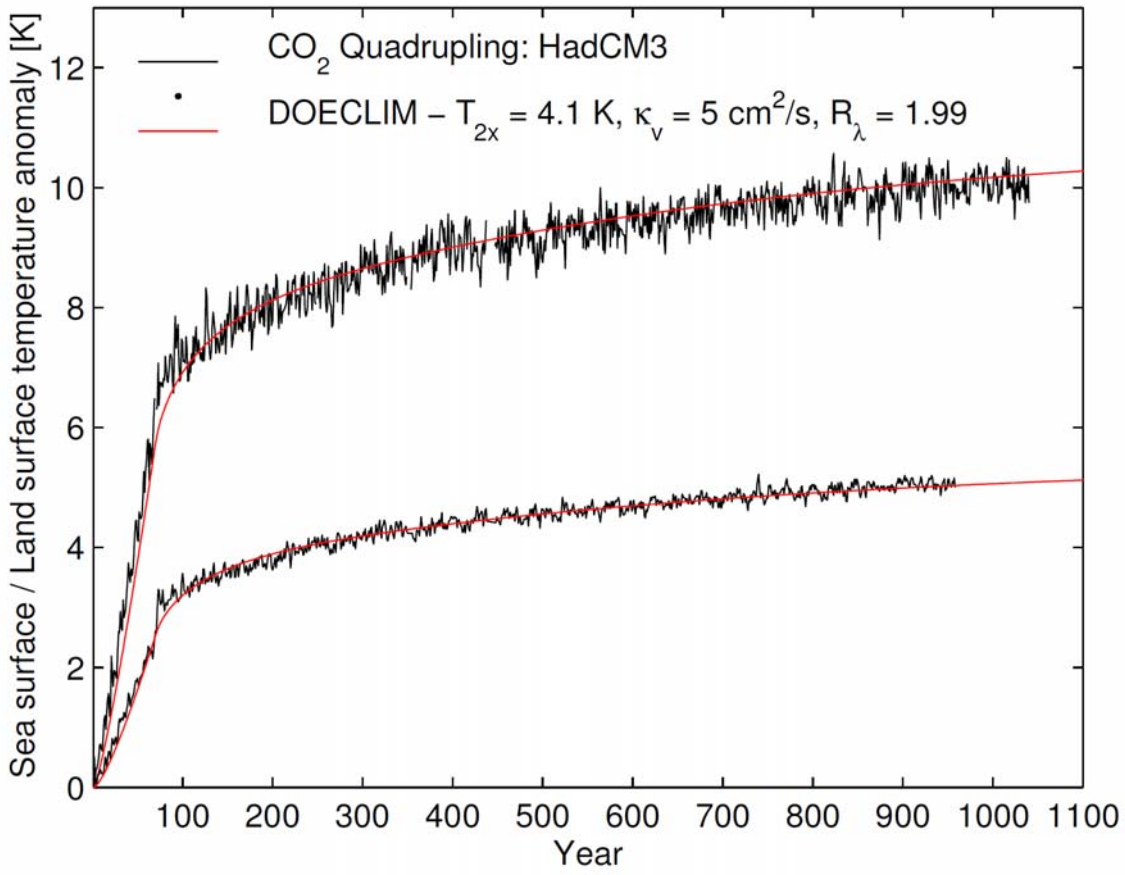

3. DESCRIPTION ON INVERSE MODELLING

3.1. BACKGROUND AND MOTIVATIONS

Uncertainties reside in virtually all the aspects of our knowledge on the Earth system. When one is interested in the uncertainty in a model projection of future climate, uncertainties in the emissions of radiative forcing agents propagate to the uncertainties in the processes associated with the carbon cycle, resulting in a larger combined uncertainty in the future climate projection. The more comprehensive a domain of the Earth system is modeled, the more multiplications and summations of uncertainties sequentially emerge, rendering the uncertainty in the future climate change uncontrollably large, as it is termed "uncertainty explosion" (Schneider, 2002; Schneider and Kuntz-Duriseti, 2002).

Uncertainty analyses of future climate projections fall into two categories: scenario approach and probabilistic approach. A typical example for the scenario approach is the future GHG emission estimates in SRES (Nakićenović et al., 2000), where various socioeconomic assumptions are made in accordance to the representing storylines for future evolution of globalization, population, economic growth, technological change, and energy system transformation. The scenario approach has an advantage of making underlying assumptions explicit, but the disadvantage is that attaching any probability to scenarios cannot be justified. In other words, one should treat all the projections spanning a wide spectrum equally plausible, posing a difficulty in extracting information for climate policy decision making. An example of the probabilistic approach is the inverse calculation method (e.g. Knutti et al., 2002), where probabilistic model projections are produced by using process descriptions, observations, and parameter estimates including their uncertainties.[45] A critical problem for the probabilistic approach is that the probabilistic climate projections are sensitive to the subjective choices of assumptions and methods employed (e.g. IPCC Working Group I, 2004b, p.1). In addition, application of the probabilistic approach is suited for the non-human dimensions because future human reflexivity cannot be innately expressed in terms of probability (Dessai and Hulme, 2003). The complementary nature of the two approaches calls for the multiplicity of the two approaches. In the past mode of ACC2 (Section 4.1), uncertainties are handled in the context of probabilities. The outcome of such a probabilistic uncertainty analysis is

[45] The optimal fingerprint detection method (e.g. Allen et al., 2000) would be another example of the probabilistic approach. The optimal fingerprint approach statistically distinguishes signals from noises in historical climate records and utilizes the maximum signal to noise ratio to estimate a future climate prediction.

combined with the future emission scenarios in the future mode of ACC2 (Section 4.2).

The inverse method has been applied to various components of the Earth system; however, none of those studies looked into uncertainties together in the Earth system. With respect to the carbon cycle, research efforts have been put into the uncertainty in the terrestrial biosphere feedback to climate change (e.g. Knorr and Heimann, 2001). As for the atmospheric chemistry, inversion studies have been carried out for CH_4 (e.g. Hein et al., 1997; Mikaloff Fletcher et al., 2004) and CFCs (Hartley and Prinn, 1993). With respect to the climate system, uncertainty analyses have been conducted for climate sensitivity, aerosol forcing, and deep ocean heat uptake (e.g. Forest et al., 2002). However, most of the uncertainty analyses treated one of the three systems in isolation and do not deal with the uncertainties in the Earth system simultaneously.[46]

Thus, a gap can be identified in the uncertainty analyses of the three Earth system components. The state-of-the-art Earth system model in a process of development (e.g. COSMOS project, http://cosmos.enes.org/) is, however, not likely to be used for a full-fledged uncertainty analysis in the near future. Prohibitively expensive computational requirement would arise if many uncertain parameters were to be constrained in such a complex model. The *climateprediction.net* project (Allen and Ingram, 2002; Murphy et al., 2004; Stainforth et al., 2005) presented one approach to this technical problem by distributing computational loads to volunteered computers in idle around the globe. Another approach is utilization of a neural network substituting a climate model, which increases the efficiency of ensemble runs by an order of magnitude (Knutti et al., 2003).

Uncertainty analyses often deal with the sources of uncertainties that are hotly debated, leaving the others unaddressed. The estimates of the CH_4 emission from wetlands and N_2O emission from agriculture have substantial uncertainties. The estimate of the *global*-annual-mean CO_2 concentration may actually has a larger uncertainty range than what is currently assumed based on *local* in situ or flask measurements of the monitoring network (e.g. Scripps Institution of Oceanography (SIO) network (Keeling and Whorf, 2005)); the current CO_2 concentration measurement network does not cover the Amazon rainforests and the countries with economy in transition, where the CO_2 concentration is expected to be high (Section 3.3). The estimates of the historical volcanic forcing based on various proxies are not in agreement (e.g. Bertrand et al., 2002;

[46] Webster et al. (2003) consolidated the two preceding works of (i) Webster et al. (2002) addressing emission uncertainties using a computable general equilibrium model and (ii) Forest et al. (2002) addressing climate system uncertainties using an intermediate complexity climate model. They discussed the relative contributions of uncertainties involving emissions parameters and climate parameters to the climate sensitivity; however, they do not address the uncertainties in the carbon cycle and, more critically, do not analyze the uncertainties simultaneously. Knutti et al. (2003) not only estimated the uncertainties in the aerosol forcing and the climate sensitivity but also the uncertainty in the temperature feedback on the ocean and land CO_2 uptake; however, it does not address the uncertainties in the CO_2 emissions and the CO_2 fertilization effect.

Ammann et al., 2003; Crowley et al., 2003; Jones and Mann, 2004, Figure 7).

The development of the inverse calculation scheme for ACC2 was inspired by the spinup scheme originally developed in ICM where the beta factor (controlling the CO_2 fertilization effect) is optimized to minimize the deviations from the historical CO_2 emission data and the atmospheric CO_2 concentration measurements. The inverse calculation for ACC2 simultaneously analyzes the chain of uncertainties in the Earth system. Our study is the first attempt to perform an inverse calculation in the coupled carbon cycle, atmospheric chemistry, and climate system. A model like ACC2 is not used in any of the previous inversion studies: simple climate models (e.g. Allen et al., 2000; Andronova and Schlesinger, 2001), intermediate complexity models (e.g. Forest et al., 2002; Knutti et al., 2002; Webster et al., 2002), GCMs (e.g. Murphy et al., 2004; Stainforth et al., 2005), Integrated Assessment models (Mastrandrea and Schneider, 2004), and statistical models (Tol and de Vos, 1998). Our approach deals with only global-annual-mean information. Thus, it can be restated that the novelty of the inversion scheme for ACC2 is the holistic treatment of the uncertainties in the Earth system as a *tradeoff* with the finer spatial and temporal resolutions.

The ACC2 inverse calculation scheme is based on the probabilistic inverse estimation theory of Tarantola (2005). The next section provides a general discussion on the inverse estimation theory. Then, Tarantola's theory is introduced along with assumptions that are made as it is applied to the ACC2 inversion.

3.2. INVERSE ESTIMATION THEORIES

3.2.1. Generalization of Inverse Estimation Theories

Inverse calculations are characterized differently depending on the fields of application. Enting (2002a, p.131) characterizes an inverse calculation as a chain of calculation or inference in the opposite direction to real-world causality where dissipative processes lead to a loss of information about details of causes. Wunsch (1996, p.13) states that an inverse problem is inverse to a corresponding forward or direct problem, interchanging the roles of at least some of the knowns and unknowns. An inverse modelling is also explained as a use of measurements to infer the values of model parameters (Tarantola, 2005, p.2) and as a mean of interpreting experimental data with uncertainties attached ("inverse problem" in Wikipedia, http://www.wikipedia.org/). In this paper, above all, an inversion is characterized as an information synthesis (Tarantola and Valette, 1982), which we demonstrate by the theoretical derivation in Section 3.2.2.

There are mainly two different theories that underpin inverse calculations: statistical least-square theory and probabilistic inverse estimation theory (including Tarantola's theory adopted for the ACC2 inversion). On the basis of the least-square theory, an inverse problem can be seen as a

minimization of the misfit between model projections and observations. It is advantageous that the least-square theory provides mathematical insights into the inverse problem for an explicit linear model such as large scale ocean circulation (e.g. Wunsch, 1996, p.12). However, a problem lies in the inherent subjectivity of the definition of the cost function (also termed penalty function or misfit function). If, instead, one rests on the probabilistic inverse estimation theory (Tarantola and Valette, 1982; Mosegaard and Tarantola, 2002; Tarantola, 2005), the form of a cost function is rigorously derived from the uncertainty ranges and distributions rather than weights are subjectively given. In Section 3.2.2 we demonstrate that, under some assumptions, a solution obtained from the least-square approach is a part of the solution obtained from the corresponding probabilistic inverse estimation approach (Tarantola, 2005, Chapter 3). Another advantage of the probabilistic inverse estimation theory is a wide-range of applications including an implicit nonlinear model.

An important issue is that the probabilistic inverse estimation theory presupposes the concept of Bayesian probabilities, which has long been disputed by the camp of the frequentists. For Bayesians a probability can signify a degree of subjective belief while for frequentists the interpretation of a probability is limited to objective and repeatable phenomena. For example, the frequentists would not attach a probability density to the global-annual-mean surface air temperature of a particular time because it cannot be repeatedly measured. Maximum likelihood estimation (discussed in subsection on particularization for ACC2 inverse estimation) falls into the frequentist method. Fundamentally, Tarantola's theory is based on the philosophy that a state of information is generally perceived as a probability density. Shafer (1992) discusses various ways of interpreting probabilities that arrive at different statistical inferences. The dispute is not settled and the jury is still out, but there is a general tendency that the probabilistic inverse estimation approach is increasingly popular across the Earth science disciplines[47] due to the recent trend of increasing computational power and the relevance to decision makings for climate and environmental policy. In fact, frequentist methods were by far favored twenty years ago due to the subjectivity entering in Bayesian methods (Efron, 1986).

3.2.2. Tarantola's Inverse Estimation Theory

Tarantola's approach to the inverse estimation theory is a probabilistic approach akin to the conventional Bayesian method but is more general. Tarantola (2005) formulates inverse estimation based on the probabilistic notion of conjunction, showing inverse estimation as an information synthesis. Descriptive and technical introductions to Tarantola's theory are given in Tarantola (2006) and Tarantola (2005, Chapter 1), respectively; Tarantola's theory developed for more special settings

[47] Various applications of inverse estimations are summarized in Enting (2002a, Part B) and Enting (2002b).

is provided in Mosegaard and Tarantola (2002). In this section, we first introduce the most general form of inverse estimation (equation (3.2.1)). This is then transformed to a specific form for the ACC2 application (equation (3.2.14)). Assumptions that are made with the particularization are explicitly discussed at length. Such discussion is useful to clarify how the ACC2 inversion deviates from the theory and what their implications are. Most of the notations are consistent with Tarantola (2005) for the convenience of comparison.

- General Expression of Inverse Estimation

An inverse estimation is a synthesis of information associated with data and parameters. Data and parameters are denoted as $\mathbf{d}$ and $\mathbf{m}$ defined in a finite-dimensional data space $\mathcal{D}$ and a finite-dimensional parameter space $\mathcal{M}$, respectively.[48] *Data* are properties that a model gives projections to; *parameters* are direct inputs to a model.[49,50] In Tarantola's philosophy of the inverse calculation formulation, all the information is expressed as probability densities in the most general settings. All the knowledge on data derived from observations, measurements, reconstructions, other independent modelling studies, and expert elicitation including their uncertainties (or errors) is termed *measurement information on data* (or simply *measurements*), while all the knowledge on parameters including their uncertainties is termed *prior information on parameters* (or simply *prior*).[51] Measurements and prior are collectively called as *prior information*, denoted as a joint *prior* probability density $\rho(\mathbf{d},\mathbf{m})$ defined in the space $(\mathcal{D},\mathcal{M})$. *A theoretical relationship of data and parameters* (or simply *theoretical information*), similarly denoted as a joint *theoretical* probability density $\Theta(\mathbf{d},\mathbf{m})$, consists of functional relationships on the basis of scientific laws and statistical estimations including their modelling uncertainties between data and parameters.[52] The conjunction (corresponding to logical "and" operation) of prior information and theoretical information is *posterior information*, denoted as a joint *posterior* probability density $\sigma(\mathbf{d},\mathbf{m})$

[48] The discussion here is limited to the cases with a finite number of parameters and data. Such a discrete approach is sufficient for the inverse calculation for ACC2. For the infinite-dimensional functional approach, see Tarantola (2005, Chapter 5).

[49] The beta factor for the CO_2 fertilization effect is a *parameter* in ACC2 but a *datum* in complex models such as Lund-Potsdam-Jena Dynamic Global Vegetation Model (LPJ-DGVM) (Sitch et al. 2003), which include process-based phonological descriptions. In non-inversion settings, it would be rather called a *higher order parameter* in LPJ-DGVM.

[50] We adhere to such definitions of data and parameters in this paper. The meanings of data and parameters used in inversion modelling are different from those used in forward modelling. The definition of a parameter in GAMS is different from an inverse estimation. The terminologies are in some cases even not consistent in inversion studies. Data and parameters are alternatively called observational parameters and model parameters (Tarantola, 2005) and dependent parameters and independent parameters (Tarantola and Mosegaard, 2000).

[51] Note that the terminologies here are not symmetrically defined (Table 3.3).

[52] Generally, theoretical relationships encompass modelling uncertainties; however, in actual applications, models are often treated as being exact with an implicit assumption that modelling uncertainties are negligible compared to other sources of uncertainties (Figure 3.2).

defined in the space $(\mathcal{D},\mathcal{M})$. It is theoretically demonstrated that joint posterior probability density $\sigma(\mathbf{d},\mathbf{m})$ can be given as the product of the joint prior probability density $\rho(\mathbf{d},\mathbf{m})$ and the joint theoretical probability density $\Theta(\mathbf{d},\mathbf{m})$ in the following (Tarantola and Valette, 1982; Mosegaard and Tarantola, 2002, Section 4.6.2; Tarantola, 2005, Appendix 6.17):[53]

$$\sigma(\mathbf{d},\mathbf{m}) = k\frac{\rho(\mathbf{d},\mathbf{m})\Theta(\mathbf{d},\mathbf{m})}{\mu(\mathbf{d},\mathbf{m})}. \tag{3.2.1}$$

$\mu(\mathbf{d},\mathbf{m})$ is a joint *homogeneous* probability density representing *homogeneous information* defined in the space $(\mathcal{D},\mathcal{M})$ (Tarantola, 2005, Section 1.2.4 and Appendix 6.2).[54] k is a normalization constant $\left(\iint_{(\mathcal{D},\mathcal{M})}\frac{\rho(\mathbf{d},\mathbf{m})\Theta(\mathbf{d},\mathbf{m})}{\mu(\mathbf{d},\mathbf{m})}d\mathbf{d}\,d\mathbf{m}\right)^{-1}$.

Equation (3.2.1) is the general expression of inverse estimation (Tarantola, 2005, p.32), where measurement information on data and prior information on parameters are combined with theoretical information, to produce posterior information. Such a concept is illustrated in Figure 3.1. Equation (3.2.1) shows that posterior information depends on prior and theoretical information that is put into an inverse estimation, supporting the general principle that one must include all the relevant information at hand in the right side of equation (3.2.1).[55] Another point is that a forward calculation (that is, a projection using functional relationships) is embedded in an inverse calculation, in spite of the contrastive terms of "forward" and "inverse."

Now, the posterior information of parameters is given as a marginal posterior probability density with respect to data

$$\sigma_{\mathrm{M}}(\mathbf{m}) = \int_{\mathcal{D}}\sigma(\mathbf{d},\mathbf{m})d\mathbf{d}, \tag{3.2.2}$$

and the posterior information of data as

$$\sigma_{\mathrm{D}}(\mathbf{d}) = \int_{\mathcal{M}}\sigma(\mathbf{d},\mathbf{m})d\mathbf{m}. \tag{3.2.3}$$

The solution of an inverse problem is equation (3.2.2). Equation (3.2.2) corresponds to the more restricted Bayesian theorem: $p(\mathbf{m}\,|\,\mathbf{d}) = \frac{p(\mathbf{d}\,|\,\mathbf{m})\,p(\mathbf{m})}{p(\mathbf{d})}$, where $p(\cdot)$ denotes a probability distribution or a probability density. The Bayesian theorem is conventionally used to derive the probabilistic inverse estimation theory; however, we think that the Tarantola's derivation is more intuitive as an inverse estimation can be formulated as a synthesis of information. In the following

[53] Although it is easier to derive equation (3.2.1) by assuming the Cartesian product of the data space and the parameter space $\mathcal{D}\times\mathcal{M}$ (equivalent to an independent assumption between data and parameters), the theoretical development here is based on a more general space $(\mathcal{D},\mathcal{M})$ in order to maintain the description of the inverse estimation at a very general level.

[54] This term is required except for a linear space represented by a Cartesian coordinate system.

[55] It is problematic that one can practically 'pick and choose' prior information to obtain the posterior information that one wishes (Scales and Tenorio, 2001).

section, we shall obtain the expression for $\sigma_{\mathrm{M}}(\mathbf{m})$ in more specific settings.

- Particularization for ACC2 Inverse Estimation

The following development tailors the general inverse estimation (equation (3.2.1)) to our needs for ACC2 by making simplifying assumptions. The assumptions that are numbered are discussed extensively in the next subsection.

First of all, we assume that the data and parameter spaces are linear (termed *linear space* or *vector space*), denoted as $\mathbb{D}$ and $\mathbb{M}$, respectively (Assumption No.1). Under the linear space assumptions, data and parameters can be expressed with components such as $\mathbf{d} = \{d_1, d_2, \ldots, d_a\}$ and $\mathbf{m} = \{m_1, m_2, \ldots, m_b\}$, respectively. a and b are the total numbers of data and parameters, respectively. Here, for a further simplification, we choose (quasi-)Cartesian coordinates to represent the data space and the parameter space. With Cartesian coordinates, the homogeneous probability density reduces to a constant (Tarantola, 2005, Example 1.15). In addition, we restrict ourselves to the circumstances where the relationship between $\mathbf{m}$ and $\mathbf{d}$ is (approximately) linear (Assumption No.2) (Figure 3.2).

A joint probability density can be expressed as the product of a conditional probability density and a marginal probability density. Theoretical information can be broken down as follows:[56]

$$\Theta(\mathbf{d},\mathbf{m}) = \theta(\mathbf{d}\,|\,\mathbf{m})\theta_{\mathrm{M}}(\mathbf{m}). \tag{3.2.4}$$

$\theta_{\mathrm{M}}(\mathbf{m})$ does not have an information content on parameters themselves. Thus, equation (3.2.4) is simplified to

$$\Theta(\mathbf{d},\mathbf{m}) = \theta(\mathbf{d}\,|\,\mathbf{m})\mu_{\mathrm{M}}(\mathbf{m}). \tag{3.2.5}$$

$\mu_{\mathrm{M}}(\mathbf{m})$ is a constant in assumed Cartesian coordinates. Then, we further assume that the uncertainty in theoretical information is negligible (in other words, exact theoretical relationships hold) (Figure 3.3) (Assumption No.3). The conditional theoretical probability density can be described with the delta function as follows:[57]

$$\theta(\mathbf{d}\,|\,\mathbf{m}) = \delta(\mathbf{d} - \mathbf{g}(\mathbf{m})). \tag{3.2.6}$$

$\mathbf{g}(\cdot)$ is a forward operator representing a model projection.

If we assume that prior information on parameters is independent of measurement information on data (Assumption No.4), a joint prior probability density can be broken down to the product of two marginal prior probability densities as follows:

$$\rho(\mathbf{d},\mathbf{m}) = \rho_{\mathrm{D}}(\mathbf{d})\rho_{\mathrm{M}}(\mathbf{m}). \tag{3.2.7}$$

A similar relationship holds for the homogeneous probability density as follows:

[56] Note that mathematical complication arises in the expression of the conditional probability if the relationship between $\mathbf{m}$ and $\mathbf{d}$ is strongly nonlinear (Mosegaard and Tarantola, 2002, Sections 2.5, 4.5.2, and B.1; Tarantola, 2005, p.22).

[57] Note that, without the linear space assumption, the simple delta function above cannot be used here (Tarantola, 2005, p.34 footnote).

$$\mu(\mathbf{d},\mathbf{m}) = \mu_{\mathrm{D}}(\mathbf{d})\mu_{\mathrm{M}}(\mathbf{m}). \tag{3.2.8}$$

Using equations (3.2.1), (3.2.2), (3.2.5) – (3.2.8), the marginal posterior probability density with respect to parameters $\sigma_{\mathrm{M}}(\mathbf{m})$ can be expressed in the following simplified form:

$$\sigma_{\mathrm{M}}(\mathbf{m}) = k'\rho_{\mathrm{M}}(\mathbf{m})\rho_{\mathrm{D}}(\mathbf{g}(\mathbf{m})), \tag{3.2.9}$$

where k' is the normalization constant. In statistics, $\rho_{\mathrm{D}}(\mathbf{g}(\mathbf{m}))$ in equation (3.2.9) is usually called a likelihood function.[58] Then, a maximum likelihood point is the maximum of a likelihood function. A likelihood function expresses the ability of a model in explaining data.[59] Equation (3.2.9) shows a salient point that prior information on parameters plays no part in a likelihood function, indicating that a use of a likelihood function falls into the frequentist approach rather than the Bayesian approach (e.g. Ulrych et al., 2001). In fact, if $\rho_{\mathrm{M}}(\mathbf{m})$ is a uniform probability density, $\sigma_{\mathrm{M}}(\mathbf{m})$ is equal to the likelihood function $\rho_{\mathrm{D}}(\mathbf{g}(\mathbf{m}))$. Thus, with the lowest content in the prior information, a solution obtained from the Bayesian approach is equivalent to a solution obtained from the frequentist approach (Ulrych et al., 2001).

Assuming that measurements $\mathbf{d}_{mes}$ follow Gaussian distributions[60] characterized by a covariance matrix $\mathbf{C}_{\mathrm{D}}$ (Assumption No.5), the marginal prior probability density of the data can be written as

$$\rho_{\mathrm{D}}(\mathbf{d}) = \frac{1}{\sqrt{(2\pi)^a \det \mathbf{C}_{\mathrm{D}}}} \exp\left(-\frac{1}{2}(\mathbf{d}-\mathbf{d}_{mes})^T \mathbf{C}_{\mathrm{D}}^{-1}(\mathbf{d}-\mathbf{d}_{mes})\right). \tag{3.2.10}$$

Similarly, by assuming Gaussian uncertainty distributions for prior $\mathbf{m}_{prior}$ characterized by covariance matrix $\mathbf{C}_{\mathrm{M}}$ (Assumption No.5), the marginal prior probability density of the parameters is

$$\rho_{\mathrm{M}}(\mathbf{m}) = \frac{1}{\sqrt{(2\pi)^b \det \mathbf{C}_{\mathrm{M}}}} \exp\left(-\frac{1}{2}(\mathbf{m}-\mathbf{m}_{prior})^T \mathbf{C}_{\mathrm{M}}^{-1}(\mathbf{m}-\mathbf{m}_{prior})\right). \tag{3.2.11}$$

Then, the marginal posterior probability density of the parameters (equation (3.2.9)) can be expressed in the following form (Tarantola, 2005, Example 1.37):

$$\sigma_{\mathrm{M}}(\mathbf{m}) = k'' \exp(-S(\mathbf{m})). \tag{3.2.12}$$

k'' is a normalization constant. $S(\mathbf{m})$ is defined as

$$S(\mathbf{m}) = \frac{1}{2}\left((\mathbf{g}(\mathbf{m})-\mathbf{d}_{mes})^T \mathbf{C}_{\mathrm{D}}^{-1}(\mathbf{g}(\mathbf{m})-\mathbf{d}_{mes}) + (\mathbf{m}-\mathbf{m}_{prior})^T \mathbf{C}_{\mathrm{M}}^{-1}(\mathbf{m}-\mathbf{m}_{prior})\right). \tag{3.2.13}$$

When cross-correlations are assumed negligible (in other words, uncertainties are assumed

---

[58] A likelihood function is mathematically defined as a probability density divided by the associated homogeneous probability density (not a probability density itself) (Tarantola, 2005, Section 1.6.4).

[59] $\rho_{\mathrm{D}}(\mathbf{g}(\mathbf{m}))$ is a concise expression of $\rho_{\mathrm{D}}(\mathbf{d})\cdot\delta(\mathbf{d}-\mathbf{g}(\mathbf{m}))$. Without the assumption on negligible modelling uncertainties, it is $\int_{\mathbb{D}} \frac{\rho_{\mathrm{D}}(\mathbf{d})\cdot\theta(\mathbf{d}\,|\,\mathbf{m})}{\mu_D(\mathbf{d})} d\mathbf{d}$.

[60] Gaussian distributions can be generalized by using different norms (Tarantola, 2005, Section 6.6) as discussed later. $l_2 - norm$ is assumed here.

independent) (Assumption No.6), $S(\mathbf{m})$ reduces to (Tarantola, 2005, Example 1.39) equation (3.2.14) as off-diagonal elements in $\mathbf{C}_\mathrm{D}$ and $\mathbf{C}_\mathrm{M}$ are zero.

$$S(\mathbf{m}) = \frac{1}{2}\left(\sum_{i=1}^{a} \left(\frac{g_i(\mathbf{m}) - d_{mes,i}}{\sigma_{d,i}} \right)^2 + \sum_{j=1}^{b} \left(\frac{m_j - m_{prior,j}}{\sigma_{m,j}} \right)^2 \right) \tag{3.2.14}$$

$\sigma_{d,i}$ and $\sigma_{m,j}$ are one-sigma uncertainty ranges for measurement i and for the prior estimate of parameter j, respectively.

Equation (3.2.14) is the cost function in the ACC2 inverse calculation. Although the residual terms for parameters and data appear symmetrical in the model code, they are fundamentally of different origins as demonstrated above. To summarize, the cost function is the sum of the arguments of the exponential functions representing the marginal posterior probability density of all the parameters, which are in essence derived from the conjunction of the joint prior probability density and the joint theoretical probability density. Although the preceding theoretical derivation has taken all the way from a fundamental level, it demonstrates how the parameter term enters in the cost function. This is often questioned and can be intuitively shown from the foregoing theoretical perspective. Note that frequentists would not, in contrast, include the residual terms associated with parameters in the cost function due to the inherent subjectivity in the prior information on the parameters (discussion on equation (3.2.9)).

The ACC2 inversion scheme determines only a particular solution $\hat{\mathbf{m}}$ that corresponds to the maximum of the marginal posterior probability density of all the parameters $\sigma_\mathrm{M}(\mathbf{m})$ (equation (3.2.12)); in other words, full posterior probability densities are not produced. Numerically the optimal parameter values that minimize the cost function $S(\mathbf{m})$ (equation (3.2.14)) are the solution for the ACC2 inversion. Our approach is in contrast to several other inversion studies (Forest et al., 2002; Gregory et al., 2002; Knutti et al., 2002; Hegerl et al., 2006) that estimated the marginal probability densities of each of the uncertain climate properties (e.g. climate sensitivity), which provide valuable insights into the extents of unknowns. In fact, there is a technical advantage to adhere to the one-point estimates because of the use of the state-of-the-art nonlinear optimization solver CONOPT3 provided in the GAMS programming environment. Yet, the one-point estimates obtained from the ACC2 inversion add a distinct value on the basis of the following arguments:

First, our approach computes the best estimates of the uncertain parameters in the coupled carbon cycle, atmospheric chemistry, and climate system interactively whereas the other inversion studies treat the individual systems in isolation. The interactions among different Earth system components have been so far neglected in inversion studies.

Second, our one-point estimates allow straightforward interpretation, given the interdependencies in the estimates of uncertain parameters. It is important to stress that the maximum value of each of the posterior probability densities of the parameters derived separately is

different from each of the associated parameter estimates that correspond to the cost function minimum when the parameter estimates are not independent each other.[61]

Third, our optimization approach can exhaustively account for a large number of uncertain parameters even in each point of time series whereas the probability density approach can consider only a small number of uncertain parameters because of the computational requirement. For example, in many probability density studies, the uncertainty in radiative forcing is expressed just by one parameter that scales a fixed time evolution of radiative forcing (e.g. Knutti et al., 2002).

Based on the arguments above, we contend that our optimization approach is complementary to the probability density approach. The arguments here are crucial when we interpret our inversion results in comparison with the results of the probability density studies (Chapter 5 of this thesis; Tanaka et al., 2008).

We have not checked the validity of the particular solution by computing the Hessian matrix to look around the neighborhood of the solution. The Hessian matrix provides an indication of the curvature of the cost function at the minimum. According to Amemiya's theorem (Amemiya, 1977; Amemiya, 1985), the outer product of a Jacobian matrix is a consistent estimator of a Hessian matrix. The elements of the Jacobian can be obtained by using the GAMS options LIMCOL and LIMROW or by solving the model with the GAMS solver CONVERT. The Hessian is internally calculated by the GAMS solver CONOPT3 but is not available to GAMS users (Arne Stolbjerg Drud, personal communication, April 21, 2008). At this point, evidences to support the validity of the inversion solution are limited to empirical ones. First, the inversion solutions are checked by performing the inversions with different initial points. Second, the sensitivity of the solution to the change in the prior assumptions has not presented any abrupt behavior.

The argument of the exponential function in the posterior parameter estimates (equation (3.2.12)) is equivalent to the cost function typically assumed in the least square approach. Thus, the least square approach with such a cost function can be interpreted as a special case of the probabilistic inversion approach. One should be aware of the fact that the least square method does not provide apriori criteria to decide upon the values of the weighting coefficients. In the probabilistic inversion approach, covariance matrices are theoretically drawn from the assumptions on the prior probability densities. In the least square approach covariance matrices or standard deviations are not necessarily required from the theoretical point of view; they are rather subjectively chosen even for the convenience of the studies. Thus, although the least square method indeed allows a greater freedom in determining the form of the cost function, the results obtained from the least square approach are less rigorous in the absence of theoretical underpinning for the cost

[61] A relevant point is that the peaks of the posterior probability densities are different from the corresponding maximum likelihood points, which do not account for the prior information on the parameters.

function form.

- Assumptions in ACC2 Inverse Estimation

A total of six assumptions have been made to arrive at the formulation of the cost function in ACC2 (equation (3.2.14)) from the general inversion solution (equation (3.2.1)). What follows discusses the implications and issues relevant to such assumptions. Numbering below corresponds to Assumptions No.1 to 6.

1) The assumption of the linearity in the data and parameter spaces requires all the data and parameters to follow the eight axioms associated with addition and scalar multiplication (e.g. Bretscher, 2001, pp.149-150). Positive parameters such as gas lifetime (year) and positive data such as atmospheric gas concentrations (ppb or ppm) do not satisfy the linearity axioms. In theory, they must be expressed in the logarithmic scale (Mosegaard and Tarantola, 2002, pp.8-9; Tarantola, 2005, Examples 1.30 and 1.31): $\ln\frac{x}{x_0}$. x and x_0 are a positive parameter or datum and its arbitrary positive constant, respectively. However, such a logarithmic conversion is practically not needed for the ACC2 inversion because none of the prior information on the parameters and the data is sufficiently close to zero.
2) Linearity or mild nonlinearity in the neighborhood of the inversion solution is assumed (equation (3.2.4)). Such an assumption fairly reduces the complexities in the inverse calculation formulation. At a global-annual-mean level, the natural Earth system has behaved as a mildly nonlinear system during the Anthropocene. A strong nonlinear response of the Earth system to human perturbation has not been observed for the past hundred years[62] although process-based model studies give projections of strong nonlinear responses such as ocean circulation reorganization in the next century. The mild nonlinearity as a whole is partly brought about from the offset of nonlinearities; the amplifying nonlinearity due to the reduction in the ocean CO_2 uptake with rising atmospheric CO_2 concentration is nearly cancelled out with the damping nonlinearity due to the decrease in the CO_2 radiative forcing increment (owing to the saturation of CO_2 absorption bands).
3) In many applications, modelling (or theoretical) uncertainties are simply overlooked and only parameter and data uncertainties are addressed. Or they assume that modelling uncertainties are sufficiently small to address only parameter and data uncertainties. Note that, as long as Gaussian distributions are assumed for errors, theoretical uncertainties can be viewed as being

[62] This argument is valid only for the processes relevant to the temporal and spatial scale of the ACC2 inversion. Outside of the particular temporal and special time scale, abrupt changes in ecosystem species have been observed, for example (e.g. the widespread amphibian extinction (Boyd and Doney, 2003)). Small sale dynamics in the ocean and the atmosphere are highly nonlinear.

included in data uncertainties (Tarantola, 2005, Example 1.36).

4) It is assumed that the prior information on parameters is independent of the measurement information on data. Such an assumption is justifiable for the ACC2 application because the information used for the prior parameter estimates does not contain the measurements. However, one cannot expect in a strict sense a separation of prior from measurements. An example would be the prior information of the beta factor (parameterization of the CO_2 fertilization effect) obtained from other inversion studies. Such information is derived from the historical carbon budgetary calculation using the atmospheric CO_2 concentration records, which are, however, used as measurements in the ACC2 inverse calculation.

5) Gaussian distributions are assumed for errors in the inverse calculation for ACC2. The central limit theorem states that a Gaussian distribution can be used for a phenomenon where one suspects the presence of a large number of small effects acting additively and independently even though each of the small effects is not believed to behave normally. Because the data uncertainties in the ACC2 inversion express all the secondary processes that the model does not explain, it is reasonable to assume that the data uncertainties follow Gaussian distributions. On the other hand, even if the ACC2 inversion stands on the Bayesian probabilistic approach, using Gaussian distributions for the parameter uncertainties should be regarded as a strong assumption. The parameter uncertainties such as that in beta factor typically express the imperfectness of our scientific knowledge and are best expressed as intervals. Applying Gaussian distributions to such intervals can be argued as an overspecification.[63]

   A Gaussian distribution used for the ACC2 inverse calculation and most of the other inverse calculations is a special case of a general Gaussian distribution defined as $\frac{p^{1-1/p}}{2\sigma_p\Gamma(1/p)}\exp\left(-\frac{1}{p}\frac{|x-x_0|^p}{(\sigma_p)^p}\right)$, where $\Gamma(\cdot)$ denotes the gamma function. p corresponds to $l_p - norm$ that is selected in a particular application (Tarantola, 2005, Sections 6.5 and 6.6). The cost function is then more generally defined as

$$S(\mathbf{m}) = \frac{1}{p}\left(\sum_i \frac{\left|g(m_i) - d_{mes,i}\right|^p}{(\sigma_{d,i})^p} + \sum_j \frac{\left|m_j - m_{prior,j}\right|^p}{(\sigma_{m,j})^p}\right). \qquad (3.2.15)$$

   When $p = 2$ (or $l_2 - norm$), equation (3.2.15) is equivalent to the cost function used in the ACC2 inversion (equation (3.2.14)). With $p = 1$ (or $l_1 - norm$), the assumed probability densities (also called Laplace distributions) have longer tails. Thus, an inverse estimation with a

[63] New approaches of hierarchical Bayes and empirical Bayes are proposed in an attempt to establish a methodology to relax the treatment of prior information that is only poorly known (Malinverno and Briggs, 2004). Another approach is the imprecise probability theory (e.g. Kriegler, 2005), which can handle prior information that cannot be expressed as probability distributions.

$l_1 - norm$ assumption ensures more robustness to outliers than with a $l_2 - norm$ assumption (Tarantola, 2005, Section 4.4.3). In fact, it is a methodological weakness that the solution for an inverse calculation with $l_2 - norm$ is sensitive to outliers. However, the computation to find out a solution with $l_1 - norm$ norm (or generally $l_{odd} - norm$) has a technical problem for the solver CONOPT3 in GAMS caused by the non-smooth absolute functions. In the opposite extreme case of $p = \infty$ (or $l_\infty - norm$), the assumed probability densities are boxcar functions. Such an assumption would allow strict control on errors, but nonexistence of a solution could result. As a whole, these particular cases of the generalized Gaussian distributions provide the perspective that the least square approach is a special class of the probabilistic inverse estimation approach.

Practically, choices are $l_1 - norm$, $l_2 - norm$, or $l_\infty - norm$. Making use of a $l_2 - norm$ is supported from the fact that the Gaussian distribution ($l_2 - norm$) has the lowest information content or the highest entropy (Tarantola, 2005, Section 1.2.5 and p.173). The computational easiness and the relevance to the least square methods are also factors favoring the $l_2 - norm$. The employment of a Gaussian assumption ($l_2 - norm$) is a common approach in solving inverse estimation problems – the validity of such an assumption is, however, often even not questioned, masked by the popularity.

6) The assumption of the independent uncertainties (zero off-diagonal elements in $\mathbf{C}_\mathrm{D}$ and $\mathbf{C}_\mathrm{M}$) is introduced to the ACC2 inverse calculation. The independent error assumption is problematic for time series data and parameters such as the atmospheric CO_2 concentration and the CO_2 emission. Such independent assumptions for time series imply excess weights on time series in the cost function. Making such an assumption is not theoretically correct also in other applications. However, independent uncertainties are often assumed due to the difficulty in estimating off-diagonal elements of the covariant matrices $\mathbf{C}_\mathrm{D}$ and $\mathbf{C}_\mathrm{M}$.

   One approach to tackle this problem is to establish hyperparameters that represent the time series (e.g. parameterized CO_2 emission model). Another approach is to implement an AutoRegressive (AR) process. These approaches are useful to alleviate the problem here but they cannot completely solve it because the interdependencies of the large number of uncertainty estimates are extremely complex. Moreover, an AR models cannot be interpreted in the context of probabilistic inverse estimation theory. The other approach is to compute the off-diagonal elements of the covariant matrices directly. Various estimation techniques are proposed in the field of data assimilation. Data assimilation, a variant of inverse estimation, is widely applied in short-term weather forecasting and atmospheric retrieval methods. As a method in data assimilation, error covariance is computed from an ensemble of forecasts obtained by perturbing the observations (Houtekamer et al., 1996). Similarly, stochasticity can be introduced to the ACC2 inversion as model errors. The ensemble run results provide a statistics to compute the

covariances although an efficient setup needs to be revised for computational feasibility.

A related issue associated with time series is the quality of the data and parameters. For example, the atmospheric CO_2, CH_4, and N_2O concentration records consist of ice core measurements in early periods and station measurements in the last few decades (Section 3.4). Ice core measurements are coarser than the annually-resolved model time step and are interpolated by spline curves with different cutoff lengths. On the other hand, station measurements are the compilations of in-situ measurements, which are continuously sampled, and flask measurements, which are discretely (hourly at Mauna Loa) sampled in glass flasks to be analyzed in respective laboratories. Thus, the information content of the station measurements is denser than that of ice core measurements. To circumvent this problem, it is often proposed to add artificial weights to the residual terms of the ice core data. However, such operations would not possibly be justified under the probabilistic inverse estimation theory (equation (3.2.12)). The problem that the quality of information cannot be entered into an inverse estimation is inherent to the probabilistic inverse estimation theory. This is a problem for the uncertainty in the uncertainty. In the ACC2 inversion, all the annual measurements are assumed to have equal information content regardless of their quality. Here is where the probability inverse estimation theory hits a limit in dealing with information with a low level of confidence. IPCC recommends that probability densities should be shown only when the level of confidence in the underlying science is high (IPCC Workshop Group I, 2004b, p.2).

The assumptions in the ACC2 inversion have been fundamentally discussed above. Below, the data and parameters used in the ACC2 inverse calculation are discussed.

3.3. DATA IN ACC2 INVERSE CALCULATION

Data in the ACC2 inverse calculation (Table 3.1) are the atmospheric CO_2, CH_4, and N_2O concentration, ocean and land CO_2 uptake, and surface air temperature change, which are all time series. The relationships between the data and the parameters in the ACC2 inversion are shown in Figure 3.4. The data in the ACC2 inversion are discussed in the following.

In many studies (e.g. Jones and Cox, 2001; Jones et al., 2001), the global-mean atmospheric CO_2 concentration is represented by the station measurements at Mauna Loa, Hawaii. The isolated location of the Mauna Loa station makes the CO_2 concentration measurements less susceptible to local CO_2 fluxes and dampens the seasonable oscillations, making it ideal for interannual or decadal studies. Gammon et al. (1985) suggest, based on the inspection of the CO_2 concentration measured in the SIO air sampling network (Keeling and Whorf, 2005), that the Mauna Loa record or the Mauna Loa record minus 0.2 ppm can be used as a proxy for the global-mean CO_2 concentration for modelling purposes. However, the SIO air sampling stations are distributed mainly

over the Pacific and the adjacent land area, without covering the rainforests in Amazon and industrial areas of the countries with economy in transition, where the CO_2 concentration is expected to be significantly higher than the global average. Within the SIO network, the CO_2 concentration difference between Mauna Loa and South Pole measurements had became larger in the second half of the 20th century and has been stabilized around 2.5 ppm for the past 10 years. The increasing parity in the CO_2 concentration measurements can be explained by the trend and locations of the anthropogenic CO_2 emission time series, which, however, poses a question on the representative nature of the Mauna Loa measurements. On an intraannual time scale, the amplitude of the seasonal oscillation in the CO_2 concentration over Alaska is large (approximately 15 ppm at the Point Barrow station in contrast to 5 ppm at the Mauna Loa station), which may corrupt the Mauna Loa measurements that depend on the seasonal atmospheric circulation. The satellite measurements of the atmospheric CO_2 concentration would be an important input for this issue,[64] but they have not had a global coverage yet. Given the arguments above, Mauna Loa records are still used for the data in the ACC2 inverse calculation, but we apply the uncertainty range larger than the station measurement errors (= 0.2 ppm for all station measurements) by a factor of four. Similar arguments are applicable to the global-mean concentrations of CH_4 and N_2O when station measurements are available. The data uncertainties of the CH_4 concentration are the estimates of the instrumental precision and experimental uncertainty in Table 1 of Masarie et al. (2001). The data uncertainties of the N_2O concentration are larger than the corresponding estimates by a factor of four.

Data for the anthropogenic ocean and land CO_2 uptake are based on the results of C^4MIP, which includes a total of 11 carbon cycle-climate GCMs and EMIC worldwide (Friedlingstein et al., 2006). The results of two models (CSM-1 and UMD) have been excluded from our analysis as they simulate a global atmospheric CO_2 concentration in the year 2000 different from the observed value by more than 10 ppm. The average of the remaining model runs in each year between 1861 and 2000 is used as the measurements in the inverse calculation. The largest deviation from the mean is used to form the 2σ Gaussian uncertainty range in each year. The measurements including the uncertainties prior to 1860 are linearly extrapolated from those after 1860 to zero in 1750. The estimates of the ocean and land CO_2 uptake based on atmospheric $\delta^{13}C$ and O_2 measurements (IPCC, 2001, Table 3.4) and CFC tracers (e.g. Wetzel, 2004, Table 6.1) are not used here.

Direct instrumental measurements of the surface air temperature (Jones et al., 2006) (http://www.cru.uea.ac.uk/cru/data/temperature/) are available from 1856 and are used for the ACC2 inverse calculation. These estimates are frequently updated with new measurements as well as additional past information. Prior to 1855, the temperature reconstruction of Jones et al. (1998)

[64] Chèdin et al. (2003) demonstrate that tropospheric CO_2 concentration measurements between 20°N and 20°S are in a good agreement with the corresponding station measurements and aircraft measurements. The Orbiting Carbon Observatory (OCO) mission (http://oco.jpl.nasa.gov/) launching a satellite dedicated to atmospheric CO_2 concentration measurements is underway.

(http://www.ncdc.noaa.gov/paleo/recons.html) is used for the ACC2 inversion. Temperature reconstructions are obtained from regression analyses between instrumental temperature records and multi-proxy variables such as tree-rings, ice cores, marine sediments, corals, and historical documents. Proxies are unevenly distributed on the globe. The reconstructions of the southern hemisphere temperature should be regarded with caution because of the scarcity in the proxies (Phil Jones, personal communication, March 14, 2006). Most of the temperature reconstructions represent only the northern hemisphere. Time resolution is another problem: reconstructions such as Mann and Jones (2003) are decadally averaged, where short-term signals from volcanic eruptions are largely smoothed out. The reconstructions of Jones et al. (1998) are the only reconstructions available for both of the hemispheres with an annual resolution. Thus, the average of Jone's reconstructions for the northern and southern hemispheres is used as measurements in the ACC2 inverse calculation. The ranges of the data uncertainties are based on Mann and Jones (2003). It is possible that the uncertainty ranges are larger because of the considerable disagreements among various temperature reconstructions (Jones and Mann, 2004; Moberg et al., 2005).

3.4. PARAMETERS IN ACC2 INVERSE CALCULATION

The parameters in the ACC2 inverse calculation are summarized in Table 3.2. The following time series are parameters in the ACC2 inverse calculation: the emissions of CO_2, CH_4, and N_2O and the missing forcing. The relationships between the parameters and the data in the ACC2 inversion are shown in Figure 3.4. Here we discuss the details of the parameters in the ACC2 inversion.

The CO_2 emission due to fossil fuel combustion is relatively well-known because of the availability of the historical energy statistics, whereas the CO_2 emission due to land use change is subject to a large uncertainty. The literature estimate of the 2σ uncertainty ranges of the fossil fuel CO_2 emission is ±8% of the prior mean (Marland et al., 2006) and that of the land use CO_2 emission is ±50% of the prior mean (Houghton, 2003).

The historical carbon budget is still not well-known because of the uncertainty in the land use CO_2 emission and in the response of the terrestrial biosphere to the atmospheric CO_2 change, climate change, and fertilizer applications. These uncertainties are all linked to balance the historical carbon budget. An additional complexity is speculation on missing carbon cycle processes such as soil erosion (Lal, 2005).

The estimate of the land use CO_2 emission of Houghton (2003) is used as the prior estimates in the ACC2 inverse calculation. Houghton's estimates are available only from 1850 so we extrapolate them linearly to a zero emission in the year 1750 on the basis of the preindustrial quasi-steady state assumption. However, some inversion studies (e.g. Gurney et al., 2002) indicate that Houghton overestimates the amount of land use CO_2 emission, which emerge mostly from

deforestation in the tropics (Houghton, 2003, Table 3). The emission estimate due to deforestation is based on FAO's Forest Resource Assessments and their datasets are subject to large uncertainties. Another problem is that Houghton's estimates do not account for wild fire (except for the US) as well as the forest and agricultural management such as changes in species, thinning, and fertilizer application. In inversion results, the land use CO_2 emission may account for missing carbon cycle processes such as soil erosion. Given these arguments, the uncertainty range originally stated by Houghton is doubled for the ACC2 inversion (that is, ±100% of the prior mean).

In models such as ACC2, the CO_2 fertilization effect is parameterized as a logarithmic dependence of NPP on the atmospheric CO_2 concentration. Such a dependency is scaled with the beta factor (equation (2.1.50)). The CO_2 fertilization effect is a major uncertainty in the global carbon cycle, according to the diversity of literature estimates of the beta factor: 0.287 (Meyer et al., 1999; Kicklighter et al., 1999), 0.4 (Gitz and Ciais, 2003), 0.45 (Brovkin et al., 1997), and 0.15 to 0.6 (Kohlmaier et al., 1987). The estimates of the beta factor obtained from inversion studies tend to be higher than those from field experiments (section 2.1.3). Based on the foregoing literature estimates, the prior estimate of the beta factor in the ACC2 inverse calculation is 0.4 with the 2σ uncertainty range between 0.1 and 0.7. When the beta factor is 0.4, doubling atmospheric CO_2 concentration leads to approximately 28% increase in NPP.

The prior mean of Q10 is 2.0 in the ACC2 inversion, which is commonly assumed as a rule of thumb in many biological studies although such a Q10 value is valid under restricted conditions (Davidson and Janssens, 2006). Jones and Cox (2001) estimate that Q10 of the global terrestrial biosphere is 2.1 ± 0.7 by constraining with observations. In this study, the 2σ uncertainty range of Q10 is assumed to be between 1.5 and 2.5. For further discussion on the Q10 parameterization, see subsection on the limitations for the land model in ACC2.

The preindustrial CO_2 degassing from the ocean and the preindustrial land CO_2 uptake are addressed to modify the preindustrial equilibrium assumption (Section 2.1.1).

The prior information of the anthropogenic CH_4 and N_2O emissions is based on van Aardenne et al. (2001). The data of van Aardenne et al. comprise the mean estimates between 1890 and 2000. On the basis of the curvatures of these emission profiles, the prior mean of the CH_4 emission is nonlinearly extrapolated from 1890 to 1750 by using a quadratic function. The prior mean of the N_2O emission is linearly extrapolated. Both of the CH_4 and N_2O emissions are fixed at zero in 1750 in accordance with the preindustrial quasi-steady state assumption. The associated uncertainty ranges shown in Table 3.2 are based on van Aardenne (personal communication, February 22, 2006). The global emission estimate of CH_4 dating back to 1860 (Stern and Kaufmann, 1998) is not used in this study.

The prior estimates of the natural CH_4 and N_2O emissions are based on Table 4.2 and Table 4.4 in IPCC (2001), respectively. The main source of uncertainty in the natural CH_4 emission

is the emission from the wetland because of the lack of knowledge on the global wetland distribution (Section 2.2.2). The main source of uncertainty in the natural N_2O emission is the agricultural emission (Section 2.2.3).

The uncertainties in the atmospheric CH_4 and N_2O lifetimes are derived from the compilations of the corresponding lifetimes in major Chemistry-Transport Models (CTMs) (IPCC, 2001, Tables 4.3 and 4.5).

The estimate of the radiative forcing associated with doubling the atmospheric CO_2 concentration is based on various radiative transfer calculations. It is estimated to be 4.37 W/m^2 in the Second Assessment Report and is revised to be 3.7 W/m^2 in the Third Assessment Report (IPCC, 2001, pp.356-357). The old estimate does not account for the stratospheric temperature adjustment and the short-wave forcing. IPCC (2001, pp.356-357) shows the range between 3.5 W/m^2 and 4.1 W/m^2 for $2\times CO_2$ forcing uncertainty. However, the $2\times CO_2$ forcing cannot be estimated simultaneously with the climate sensitivity in the ACC2 inversion as their influences to the model projections are not clearly distinguished. In ACC2, the $2\times CO_2$ forcing is fixed at 3.7 W/m^2. The similar problem can be seen in constraining the ocean vertical diffusivity.

The missing forcing is defined as the sum of all the radiative forcings that are not accounted for by the other radiative forcings in ACC2. For example, the missing forcing includes the albedo forcing and the remaining aerosol forcings, which are not parameterized in the three classes of the aerosol forcings in ACC2 (Section 2.2.12). Thus, the uncertainty in the missing forcing essentially includes the uncertainty in the total radiative forcing. In the inversion, the missing radiative forcing also in part explains the natural variability of the temperature records (except for the El Niño-Southern Oscillation (ENSO)-induced change after 1930 (Section 3.5.1)). The 2σ prior uncertainty range is assumed to be constantly 0.5 W/m^2 before 1900 primarily to explain the natural variability in the temperature change. Then the uncertainty range increases linearly to 1.0 W/m^2 in 2000 to account for the uncertainty in the aerosol forcing, which is consistent with the corresponding range in IPCC (2007, Figure SPM.2).

The rationales for such uncertainty ranges for the missing forcing before 1900 are as follows. Attribution/detection studies have not so far agreed upon whether the surface temperature rise in the first half of the 20th century is due to natural variability or anthropogenic interference. If the 0.5°C rise in the surface air temperature in that period were to be decadal variability, the missing radiative forcing with a magnitude of about 0.5 W/m^2 would constantly be required to drive such a temperature rise in ACC2 with climate sensitivity in the range 0.5–6.5°C (Table 3.2 and Figure B.5). The range of 0.5°C is also indicated in the temperature variability in the 1000-year control run of Community Climate System Model (CSM-1.4) (a coupled carbon cycle-climate GCM) (Doney et al., 2006, Figure 4a). Furthermore, the initial state of the system is not well-known and it is not completely equilibrated due to various natural forcings and internal dynamics. The problem of the

equilibrium assumption in 1750 can be alleviated by the uncertainty of the missing forcing in such a magnitude.

Here we mention the estimates of solar forcing and volcanic forcing. The associated uncertainties are not addressed individually and are collectively included in the missing forcing uncertainty. The solar forcing in ACC2 is based on the solar irradiance reconstruction of Krivova et al. (2007). Solar irradiance reconstructions rely on the statistical analysis of the sunspot numbers recorded by historical documents and isotopic information recorded in tree rings (^{14}C) and in ice cores (^{10}Be). Krivova's solar irradiance reconstruction is estimated to be smaller than the earlier solar irradiance reconstructions such as Lean et al. (1995) and Lean (2000). The scaling of the proxies to the total solar irradiance is subject to a large uncertainty and has recently been revised. In Krivova's reconstruction, the statistical analysis is combined with the underlying solar physics of Solanki et al. (2002). Krivova's reconstruction shows that the 11-year cycle produces the fluctuations of merely 0.1% of the total solar irradiance, leading to a minor climate response. The volcanic forcing used in ACC2 is adopted from Ammann et al. (2003) and discussed further in Section 3.5.2.

The climate sensitivity is always central to the discussion on the uncertainties in climate projections. The radiative transfer processes involving CO_2 are relatively well-known. However, the climatic feedback such as cloud formation is substantially different across models, resulting in the uncertainty in climate sensitivity (http://www.met.rdg.ac.uk/~radiation/includes/radforc.html). Throughout the first three IPCC reports, the estimate of the climate sensitivity (between 1.5°C and 4.5°C) has not been changed. The current GCMs around the world indicate the range of the climate sensitivity between 2.5°C and 4.0°C (IPCC Working Group I, 2004a). On the other hand, the inversion studies indicate that the peaks of the probability densities for the climate sensitivity range between 2°C and 3.5°C (Forest et al., 2002; Gregory et al., 2002; Knutti et al., 2002; Hegerl et al., 2006). The most recent summary of the climate sensitivity estimates from inversion approaches is in Räisänen (2007). In the inversion approach, the uncertainty in climate sensitivity depends on the uncertainties in the aerosol forcing and the vertical ocean diffusivity. Probability densities derived from the inversion approach vary widely from less than 1°C to more than 6°C (e.g. Hegerl et al., 2006). Earlier inversion studies produce a long tail toward high climate sensitivity. GCM ensemble runs also produce a long tail reaching over 10°C (Stainforth et al., 2005). IPCC (2007) gives the best estimate of about 3°C in the range of 2.0°C to 4.5°C. Based on the literature cited above, the 2σ prior uncertainty range of the climate sensitivity is assumed to be between 0.5°C and 6.5°C (prior mean: 3.5°C) in the ACC2 inversion.

The vertical ocean diffusivity is subject to a large uncertainty. In the framework of the ACC2 inversion, the climate sensitivity and the vertical ocean diffusivity cannot be constrained simultaneously. It would require an explicit process description of the heat diffusion in each layer of the ocean to be constrained by the associated observation (Levitus et al., 2000). The ocean

diffusivity is estimated to be 1 $cm^2\ s^{-1}$ (Munk, 1966; Simmons et al., 2004). For the ACC2 inversion, the ocean diffusivity is fixed at 0.55 $cm^2\ s^{-1}$ (Elmar Kriegler, personal communication, March 1, 2006).

3.5. FACTORS INFLUENCING THE INTERANNUAL VARIABILITY

Two important factors that influence the interannual variability are the ENSO and volcanic eruptions. Their influences need to be removed from the measurements because the model does not provide the driving mechanisms. The influences of ENSO on the surface air temperature and the atmospheric CO_2 concentration are statistically taken into account in the ACC2 inversion; The Southern Oscillation Index (SOI) and NINO3 index are used to identify ENSO-induced anomalies in the surface air temperature and the atmospheric CO_2 concentration, respectively. The uncertainty ranges of the CO_2, CH_4, and N_2O concentrations, missing forcing, and surface air temperature measurements are assumed to be larger in the ACC2 inversion when the Earth system is under the influence of large volcanic eruptions. Details are discussed in the following.

3.5.1. ENSO

ENSO is the dominant internal oscillation among others (e.g. North Atlantic Oscillation (NAO) and Pacific Decadal Oscillation (PDO)); ENSO is an oscillation in the coupled atmosphere-ocean system in the equatorial Pacific, which has a far reaching effect to the global carbon cycle and climate system through atmospheric teleconnections (McPhaden et al., 2006).

ENSO has a periodicity of three to seven years, with El Niño, a phase of ENSO, persisting usually one to three years. The opposite phase is termed La Niña. During El Niño years, the surface water of the eastern equatorial Pacific is relatively warm. The zonal SST gradient across the equatorial Pacific becomes less pronounced, weakening the tradewind over the equatorial Pacific. The thermocline is suppressed in the eastern Pacific, resulting in the depression or paucity of upwelling, which would fuel the Peruvian coastal ocean with cold and nutrient-rich water during the normal years. The reduction in the upwelling leads to higher SST in the eastern Pacific, further weakening the tradewind. Such positive feedback is termed Bjerknes feedback (e.g. Neelin et al., 1998; Cane, 2005), which also holds for the La Niña phase. These amplifying loops are counteracted by internal ocean waves such as Kelvin waves and Rossby waves, which are generated in concurrence with the initiation of El Niño. They initially support the growth of El Niño but subsequently counteract it after being reflected at the boundaries (Neelin et al., 1998). The Bjerknes feedback in the atmosphere-surface ocean and the internal wave feedback in the subsurface ocean are combined to control the duration of the ENSO phases (McPhaden et al., 2006).

El Niño usually begins near the end of the year when the SST anomaly becomes largest.

During El Niño years, as a result of the complex atmosphere-ocean processes, the global-mean surface air temperature is relatively high (Ropelewski, 1992). The responses of carbon cycle processes to El Niño are two folds (Jones et al., 2001; McPhaden et al., 2006). In the early stage of an El Niño, the CO_2 degassing from the equatorial Pacific, the largest ocean carbon source, decreases because of the depression of the upwelling off the Peruvian coast. In the later stage, the global terrestrial GPP decreases due to the temperature rise in the tropics and the precipitation decrease in tropical Asia and Australia. The plant and soil respiration increases due to the temperature rise in most parts of the globe (Jones et al., 2001). More prominently, the droughts and elevated temperature in the tropics increase the extent of wild fires (e.g. forest fire in Indonesia during the El Niño in 1997 and 1998). Overall, during El Niño the atmospheric CO_2 concentration initially drops due to the suppression of upwelling but subsequently rises due to the terrestrial carbon release. Jones and Cox (2001) demonstrates that the interannual variability in the atmospheric CO_2 concentration is largely controlled by ENSO during the period of 1967-1981, which has been free from large volcanic eruptions.

The intensity and phase of ENSO is captured by the two widely-used atmospheric and oceanic indices: SOI and NINO3. SOI is defined as the difference in the sea level pressure anomalies between Tahiti (17°S, 149°W, French Polynesia) and Darwin (12°S, 131°E, Australia) (http://www.cru.uea.ac.uk/cru/data/soi.htm). NINO3 is defined as the average of the mean sea surface temperature anomaly in the area of 150°W-90°W and 5°S-5°N (Kaplan reconstruction between 1856 and 1949; CPC (Reynolds OI SST) from 1950 to present, http://climexp.knmi.nl/). These ENSO indices are used to infer the influences of ENSO to the measurements of the surface air temperature and the atmospheric CO_2 concentration in the ACC2 inversion.

With regard to the influence of ENSO to the surface air temperature records, the SOI index is multiplied with the scaling factor (-0.063 for the ocean surface air temperature; -0.148 for the land surface air temperature (Kriegler, 2005, p.32) and then the scaled SOI indices are added to the ocean and land surface air temperature calculated from ACC2 so that the ENSO-related interannual variability in the temperature measurements is explained. Such an ENSO adjustment for temperature records is applied after 1930. The SOI index exists as early as 1867, but the credibility of the SOI index is thought to be sufficiently high only after 1930. The SOI index requires a three- to six-month lead (Kriegler, 2005, Figure 2.4) or a four- to seven-month lead (Smith et al., 2003) to explain the surface air temperature change. Kriegler (2005) estimates that the optimum lead is four months. The pre-analysis of the ACC2 inversion results also indicate the optimum lead of four months. Thus, the lead of four months is adopted to calculate the annualized SOI index used for the ACC2 inversion.

With regard to the influence of ENSO to the atmospheric CO_2 concentration records, the relationship between NINO3 and the atmospheric CO_2 concentration records is statistically calculated in the model. Our approach is similar to Jones and Cox (2001), which obtained a

regression line that explains the natural change in the atmospheric CO_2 concentration as a function of NINO3. In ACC2, the natural change in the atmospheric CO_2 concentration is computed as the total (anthropogenic and natural) change in the atmospheric CO_2 concentration (prior information) subtracted from the anthropogenic CO_2 emission (posterior information) and ocean and land CO_2 uptake (posterior information). The *y*-intercept and the slope of such a linear regression line are estimated concurrently with the inversion. Our approach uses the posterior information to be consistent with other parts of the model. In the pre-analysis of the ACC2 inversion, it was found that the optimum lead of NINO3 relative to the natural change in the atmospheric CO_2 concentration is seven months. Such a time lead is used to calculate the annualized NINO3 index used for the ACC2 inverse estimation. The ENSO adjustment for the atmospheric CO_2 concentration above is applied from 1960 onward although the NINO3 index exists in as early as 1857. Prior to 1960, the atmospheric CO_2 concentration measurements used in the ACC2 inversion are based on ice core sampling (Etheridge et al., 1996), where the interannual variability due to ENSO is largely smoothed out by spline fitting. The atmospheric CO_2 records are highly perturbed by large volcanic eruptions. Thus, we exclude the period from the line fitting calculation when the absolute magnitudes of the volcanic forcings are less than 0.5 W/m^2.

Our predictive capability for ENSO cycle is still limited (Cane, 2005; van Oldenborgh et al., 2005). Dynamical models do not produce significantly better forecasts than statistical models (McPhaden et al., 2006). The interaction between the future warming and ENSO is currently under debate (e.g. Neelin et al., 2003; Cane, 2005; van Oldenborgh et al., 2005). The association of volcanic eruptions with ENSO is debated (Robock, 2000; de Silva, 2003; Adams et al., 2003).[65] Thus, the effect of ENSO is accounted for in the future mode of ACC2.

3.5.2. Volcanic Eruptions

The second half of the 20th century saw some major volcanic eruptions (Agung, Indonesia in 1963; El Chichón, Mexico in 1982; Pinatubo, The Philippines in 1991). The largest eruptions for the past 250 years are those of Tambora, Indonesia in 1815 and Krakatau, Indonesia in 1883. The document-based records of past large volcanic eruptions[66] are given by Siebert and Simkin (2006)

[65] The paleoclimate information of ENSO dating back to 130,000 years ago (Tudhope et al., 2001) statistically supports the hypothesis that volcanic eruptions produce a state in the atmosphere-ocean system in the equatorial Pacific that triggers El Niño-like conditions (de Silva, 2003; Adams et al., 2003).

[66] Volcanic Explosivity Index (VEI) is an integrated index for the size of a volcanic eruption based on the compilation of various qualitative data and subjective descriptions of observers in the Smithsonian catalogue. VEI should not be directly taken as the indication for climatic influence from volcanic eruptions, which should also depend on the location, quality of the magma, eruption heights, and other factors. A more climate-relevant index is Ice-core Volcanic Index (IVI), which is based on the amount of sulfate aerosols found in the ice cores in the both pole.

(http://www.volcano.si.edu/world/largeeruptions.cfm). Several indices of the size of volcanic eruptions are discussed in Zielinski (1995).

Large volcanic eruptions left footprints in global climate records (Robock, 2000). They emit SO_2 to the stratosphere where SO_2 is converted into sulfate aerosols, shading the Earth surface. A recent remarkable example is the Pinatubo eruption, which was followed by the drop in the global-mean temperature and the slowdown in the atmospheric CO_2 concentration rise (Jones and Cox, 2001). The other climatic relevance of volcanic eruptions is their possible association with the ENSO cycle (Section 3.5.1).

Volcanic eruptions add 'dips' to past records of the Earth system, influencing the uncertainty estimates derived from the inverse calculation. Wigley et al. (2005) inferred the climate sensitivity using observations during periods influenced by major volcanic eruptions.

Problems and issues associated with the estimate of the past volcanic forcing are discussed in the following. The climatic influence due to large volcanic eruptions typically lasts one to three years. Given the short time scale of the volcanic forcing, the volcanic forcing is not well resolved in ACC2. Additionally, the temporal evolution of the volcanic forcing depends on the locations of the eruptions (Oman et al., 2005). Such regional features of the volcanic forcing cannot be resolved in ACC2.

The estimate of the past volcanic forcing is based on the sulfate aerosol concentration in ice cores in Greenland (e.g. the GISP2 and Crete ice cores) and Antarctica, instrumental and satellite radiation measurements, and the volcanic eruption catalogue (Siebert and Simkin, 2006). It is generally assumed that, when sulfate signals are found in the ice cores of both poles simultaneously, the corresponding volcanic eruptions are considered markedly influencing the global climate. The estimate of the volcanic forcing (e.g. Bertrand et al., 2002; Ammann et al., 2003; Crowley et al., 2003) depends on the choice of ice cores (Jones and Mann, 2004, Figure 7). Uncertainties in the volcanic forcing arise from the uncertain relationship between the stratospheric sulfate aerosol load and the sulfate aerosol deposited at the surface and also the uncertain relationship between the stratospheric aerosol optical depth and the radiative forcing. The volcanic forcing is affected by the seasonably changing stratospheric transport, which is accounted for only in Ammann et al. (2003). ACC2 uses the volcanic forcing of Ammann et al. (2003).

There are some apparent contradictions between historical temperature reconstructions and volcanic eruption records; temperature does not drop after some large volcanic eruptions (e.g. Tambora and Krakatau eruptions). To explain such puzzling records, the diffuse radiation hypothesis (Robock, 2005) has been put forward. Diffuse radiation is produced from the enhanced forward scattering of the solar radiation due to the stratospheric sulfate aerosols. The photosynthesis of terrestrial plants is more efficient under diffuse radiation than direct radiation because of the reduction in shade area and the saturation level with respect to light intensity (e.g. Farquhar and

Roderick, 2003). Thus, the drop in the atmospheric CO_2 buildup after volcanic eruptions (Jones and Cox, 2001) can be attributed to the increase in the land carbon storage due not only to the temperature-driven terrestrial respiration reduction (Lucht et al., 2002) but also to the diffuse radiation-driven photosynthesis enhancement (Gu et al., 2003). As the terrestrial biosphere shows enhanced growth due to high diffuse radiation during volcanic eruptions, temperature reconstructions based on tree rings are possibly biased upward, underestimating the temperature drop after eruptions.

The atmospheric CH_4 concentration growth increased after the Pinatubo eruption (Dlugokencky et al., 1998). This is caused by a reduction in the atmospheric OH concentration, as the reaction with OH is the main sink of CH_4. The production of OH depends on the photodissociation of O_3 by solar UV. Solar UV is scattered by sulfate aerosols after the volcanic eruption (Dlugokencky et al., 1996). The rate of the atmospheric N_2O concentration change decreased after the Pinatubo eruptions due to the enhanced exchange between the troposphere and the stratosphere driven by the heating from the volcanic aerosols (Schauffler and Daniel, 1994). The mechanisms to control the CH_4 and N_2O concentration changes due to volcanic eruptions are not parameterized in ACC2.

Given the foregoing arguments associated with the different volcanic forcing estimates and far reaching effects of volcanic eruptions in the Earth system, we quadruple the uncertainty ranges of the CO_2, CH_4, and N_2O concentrations, the missing forcing, and the surface air temperature measurements when the absolute magnitude of the volcanic forcing is larger than 0.5 W/m^2.[67] Numerically, such modifications of the uncertainty ranges decrease the weights for the associated misfits caused by major volcanic eruptions. This treatment partly alleviates the problems discussed above.

[67] The treatment of the Earth system influence from volcanic eruptions here is just one approach. Kriegler (2005) halves the magnitudes of the volcanic forcing because of the time scale problem of the fast-converging volcanic forcing.

Table 3.1. Data in the ACC2 coupled inversion

* Four times larger uncertainty ranges are assumed when volcanic forcing is stronger than -0.5 W/m^2 (Section 3.5.2). The total number of degrees of freedom for data is 1,498.

Names (degrees of freedom)	Periods	Measurement types	Temporal resolutions	2σ measurement uncertainties	Data sources
Ocean CO_2 uptake (df=250)	1750-1860	N/A	Linear extrapolation to the origin from 1860 to 1750	Average uncertainties between 1865 and 2000	N/A
	1861-2000	C^4MIP GCMs/EMIC	10-year moving average	Maxima and minima of GCMs runs (=1σ)	Friedlingstein et al. (2006)
Land CO_2 uptake (df=250)	1750-1860	N/A	Linear extrapolation to the origin from 1860 to 1750	Average uncertainties between 1865 and 2000	N/A
	1861-2000	C^4MIP GCMs/EMIC	10-year moving average	Maxima and minima of GCMs runs (=1σ)	Friedlingstein et al. (2006)
Atmospheric CO_2 concentration (df=250)	1750-1968	Ice core sampling (Law Dome, Antarctica)	75-year cutoff spline fit with 5-year intervals (1750-1830) 25-year cutoff spline fit with 1-year intervals (1832-1968) Linear interpolations between the data points	*1.2 ppm	Etheridge et al. (1996)
	1969-2000	Station measurements (Mauna Loa, Hawaii)	Annual fit	*0.8 ppm (0.2 ppm in the literature)	Keeling et al. (2005)
Atmospheric CH_4 concentration (df=249)	1750-1850	Ice core sampling (Law Dome, Antarctica; Summit, Greenland)	75-year cutoff spline fit with 10-year intervals (1750-1900) 12.5-year cutoff spline fit with 2-year intervals (1900-1984) Linear interpolations between the data points	*5 ppb	Etheridge et al. (1998)
	1851-1983				Etheridge data compiled by Hansen and Sato (2004) Etheridge et al. (1998)
	1984-2000	Station measurements (CMDL global air sampling network)	Annual fit	*12 ppb (3 ppb in the literature)	Dlugokencky data compiled by Hansen and Sato (2004) for mean estimates Masarie et al. (2001, Table 1) for uncertainties
Atmospheric N_2O concentration (df=249)	1750-1961	Ice core sampling (Summit, Greenland)	300-year cutoff spline fit with 1-year intervals	*Time variant	Flueckiger (personal communication)
	1962-1977			*Interpolation	Hansen and Sato (2004)
	1978-2000	Station measurements (CMDL global air sampling network)	Annual fit	*2.0 ppb (0.5 ppb in the literature)	Hansen and Sato (2004) for mean estimates Masarie et al. (2001, Table 1) for uncertainties
Surface air temperature change (df=250)	1750-1855	Multi-proxy	1-year intervals	*0.36°C	Jones et al. (1998) for mean estimates Mann and Jones (2003) for uncertainties
	1856-2000	Instrumental measurements	Annual fit	*0.20°C (1856-1860) *0.05°C (2000) *Linear interpolation between the periods	Jones et al. (2006)

Table 3.2. Parameters in the ACC2 coupled inversion

* Four times larger uncertainty ranges are assumed when volcanic forcing is stronger than -0.5 W/m^2 (Section 3.5.2). The total number of degrees of freedom for parameters is 1,266.

Names (degrees of freedom)	Prior estimates	2σ prior uncertainties
Anthropogenic CO_2 emission due to fossil fuel combustion (df=251)	Marland et al. (2006) between 1750 and 2000	±8% of the prior mean (Marland et al., 2006)
Anthropogenic CO_2 emission due to land use change (df=251)	Houghton (2003) between 1850 and 2000 Linear extrapolation between 1750 and 1849 Zero emission in 1750	±100% of the prior mean (±50% in Houghton (2003))
Anthropogenic CH_4 emission (df=251)	van Aardenne et al. (2001) between 1890 and 2000 Nonlinear extrapolation between 1750 and 1890 Zero emission in 1750	±50% in 2000, ±100% in 1970 ±150% between 1890 and 1950 Linear interpolations between the periods Absolute uncertainty ranges assumed constant before 1890 (John van Aardenne, personal communication)
Anthropogenic N_2O emission (df=251)	van Aardenne et al. (2001) between 1890 and 2000 Linear extrapolation between 1750 and 1890 Zero emission in 1750	±50% in 2000, ±100% in 1970 ±150% between 1890 and 1950 Linear interpolations between the periods Absolute uncertain ranges assumed constant before 1890 (John van Aardenne, personal communication)
Missing forcing (df=251)	Zero forcing between 1750 and 2000	*±0.5 W/m^2 between 1750 and 1900 *±1.0 W/m^2 in 2000 *Linear interpolation between 1900 and 2000
Preindustrial mixed layer temperature (df=1)	19.59°C (Hoffert et al., 1981, pp.290-291; Sundquist and Plummer, 1981, p.267)	Between 13.59 and 25.59°C
Atmosphere-mixed layer temperature scaling factor (df=1)	0.5	Between 0.0 and 1.0
Beta factor for CO_2 fertilization (df=1)	0.4 (0.287 (Meyer et al., 1999; Kicklighter et al., 1999), 0.4 (Gitz and Ciais, 2003), 0.45 (Brovkin et al., 1997), and 0.15 to 0.6 (Kohlmaier et al., 1987))	Between 0.1 and 0.7 (references in left column)
Q10 for heterotrophic respiration (df=1)	2.0 (Jones and Cox, 2001; Tjoelker et al., 2001)	Between 1.5 and 2.5 (references in left column)
Preindustrial ocean CO_2 uptake (df=1)	-0.24 GtC/year (net degassing) (-0.48 GtC/year in Mackenzie and Lerman (2006))	Between -0.48 and 0.0 GtC/year
Preindustrial land CO_2 uptake (df=1)	0.30 GtC/year (net uptake) (0.36 - 0.6 GtC/year in Mackenzie and Lerman (2006))	Between 0.0 and 0.60 GtC/year
Natural CH_4 emission (df=1)	210 Mt(CH_4)/year (IPCC, 2001, Table 4.2)	Between -30 and 450 Mt(CH_4)/year (IPCC, 2001, Table 4.2)
Natural N_2O emission (df=1)	10.2 Mt(N)/year (IPCC, 2001, Table 4.4)	Between 7.8 and 12.6 Mt(N)/year (IPCC, 2001, Table 4.4)
CH_4 lifetime with respect to OH depletion (df=1)	9.6 year (IPCC, 2001, Table 4.3)	Between 5.4 and 13.8 year (IPCC, 2001, Table 4.3)
N_2O lifetime (df=1)	110 year (IPCC, 2001, Table 4.5)	Between 83 and 137 year (IPCC, 2001, Table 4.5)
Climate sensitivity (df=1)	3.5°C (Forest et al., 2002; Gregory et al., 2002; Knutti et al., 2002; IPCC Working Group I, 2004; Kriegler, 2005; Stainforth et al., 2005; Forest et al., 2006; Hegerl et al., 2006; IPCC, 2007; Räisänen, 2007)	Between 0.5 and 6.5°C (references in left column)

Table 3.3. Terminologies used in inverse estimation for ACC2

The terminologies referring to the information on parameters and data before/after an inverse calculation are not symmetrically defined. Nevertheless, such terminologies are commonly used and thus adopted in this study (Section 3.3.2).

	Information on parameters	Information on data	Information on both parameters and data
Before inversion	Prior information (or prior)	Measurement information (or measurements)	Prior information (or prior)
After inversion	Posterior information	Posterior information	Posterior information

Figure 3.1. Two-dimensional illustration of inverse estimations (after Tarantola (2005, Figure 1.12))

This figure illustrates the concept of the Tarantola's inverse estimation theory. The joint probability density, $\rho(\mathbf{d},\mathbf{m})$, in left panel shows the prior information on parameters and data. Its marginal probability densities with respect to parameters, $\rho_{\mathrm{M}}(\mathbf{m})$, and data, $\rho_{\mathrm{D}}(\mathbf{d})$, are also shown along the respective axes. The probability density, $\Theta(\mathbf{d},\mathbf{m})$, in middle panel shows the theoretical information between parameters and data. Note that, in the theoretical probability density, there is no information on parameters and data by themselves. The conjunction of the prior information, $\rho(\mathbf{d},\mathbf{m})$, in left panel and the theoretical information, $\Theta(\mathbf{d},\mathbf{m})$, in middle panel gives the joint posterior information on parameters and data, $\sigma(\mathbf{d},\mathbf{m})$. The marginal posterior information with respect to parameters, $\sigma_{\mathrm{M}}(\mathbf{m})$, shown along the horizontal axis is generally the solution of an inverse estimation. See Section 3.2.2.

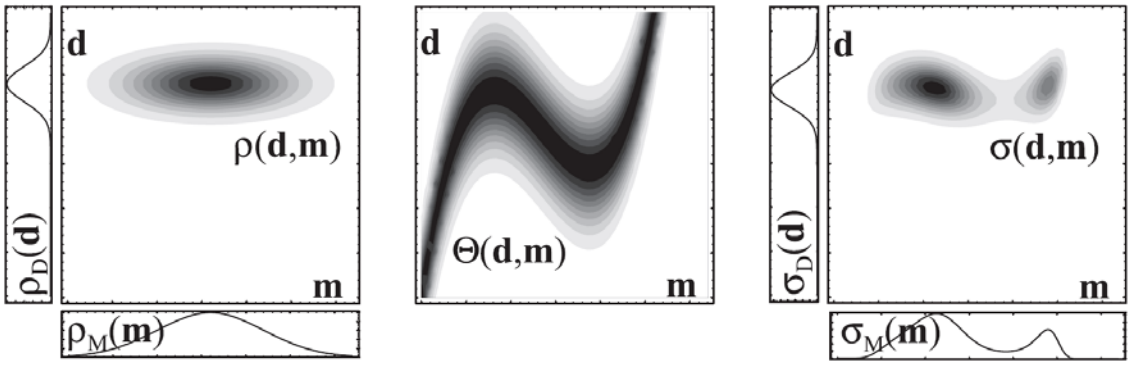

Figure 3.2. Two-dimensional illustration of theoretical information and modelling uncertainties (after Tarantola (2005, Figure 1.4)).

When no modelling uncertainties are assumed (as many practical applications use exact functional relationships), the theoretical information between parameters and data is represented by a line, $\mathbf{d} = \mathbf{g}(\mathbf{m})$, (left panel). In more general settings where modelling uncertainties are explicitly taken into account, the theoretical information is expressed in a form of the probability density, $\theta(\mathbf{d} \mid \mathbf{m})$, (right panel), which corresponds to the middle panel in Figure 3.1. See Section 3.2.2.

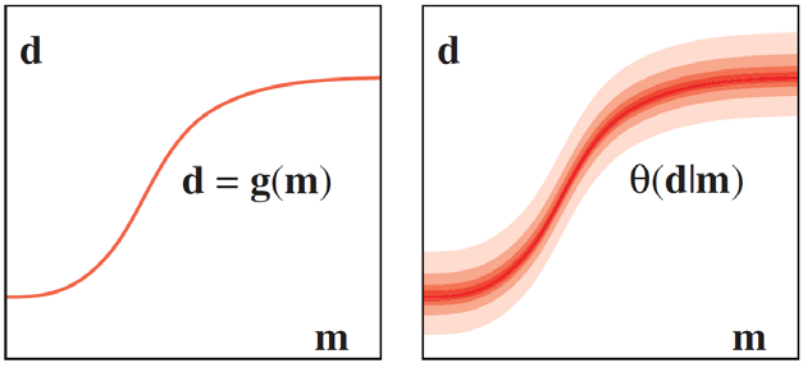

Figure 3.3. Two-dimensional illustration of the nonlinearities in the theoretical relationship between parameters and data (after Tarantola (2005, Figure 3.2)).

Different degrees of nonlinearity are shown in five steps. In top left panel, only the prior information on parameters and data are shown. In top middle panel, the theoretical information (or the functional relationship in a model) is linear and exact. In top right panel, the functional relationship in the model can be linearly approximated around the peak of the prior probability density of parameters. Such an approximation is not valid in bottom left panel as no measurement information would enter. Thus, the functional relationship is linearly approximate linearly around the peak of the measurement probability density (the maximum likelihood estimate). Neither of the linear approximation is possible in bottom middle panel. The bottom right panel shows the most extreme case of nonlinearity where the theory discussed in Section 3.2.2 cannot apply.

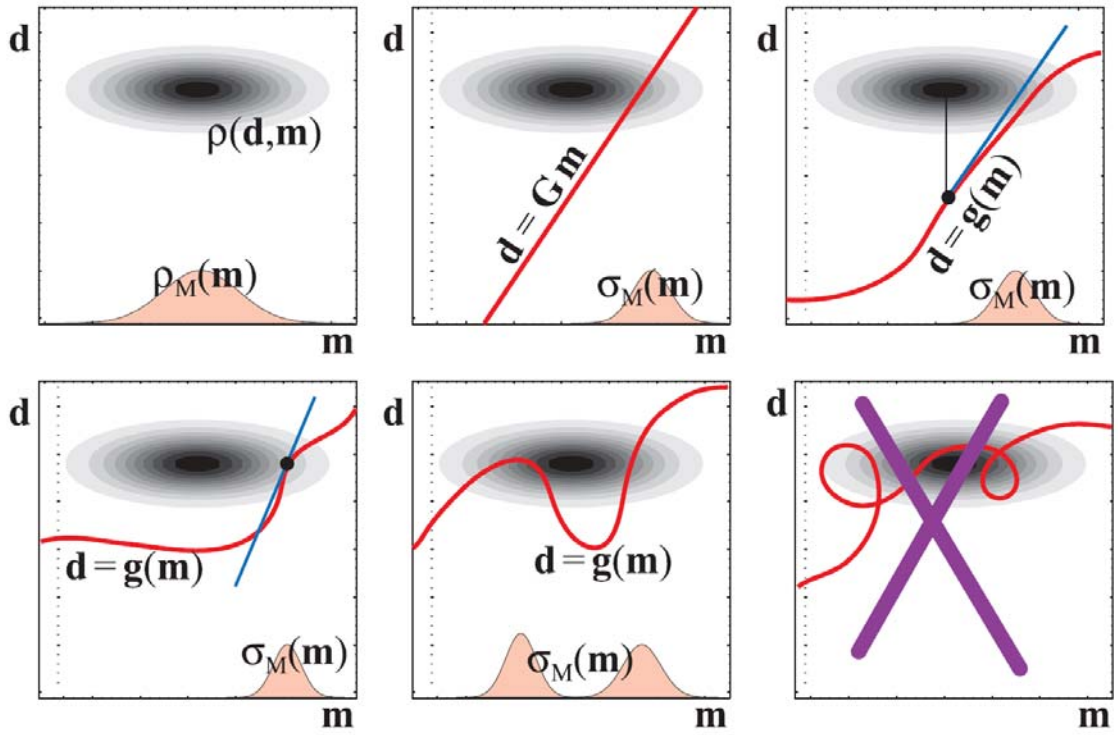

Figure 3.4. The relationships between parameters and data in the ACC2 inverse estimation

Red and blue boxes represent parameters and data, respectively. Solid and dotted boxes represent time series and constants, respectively.

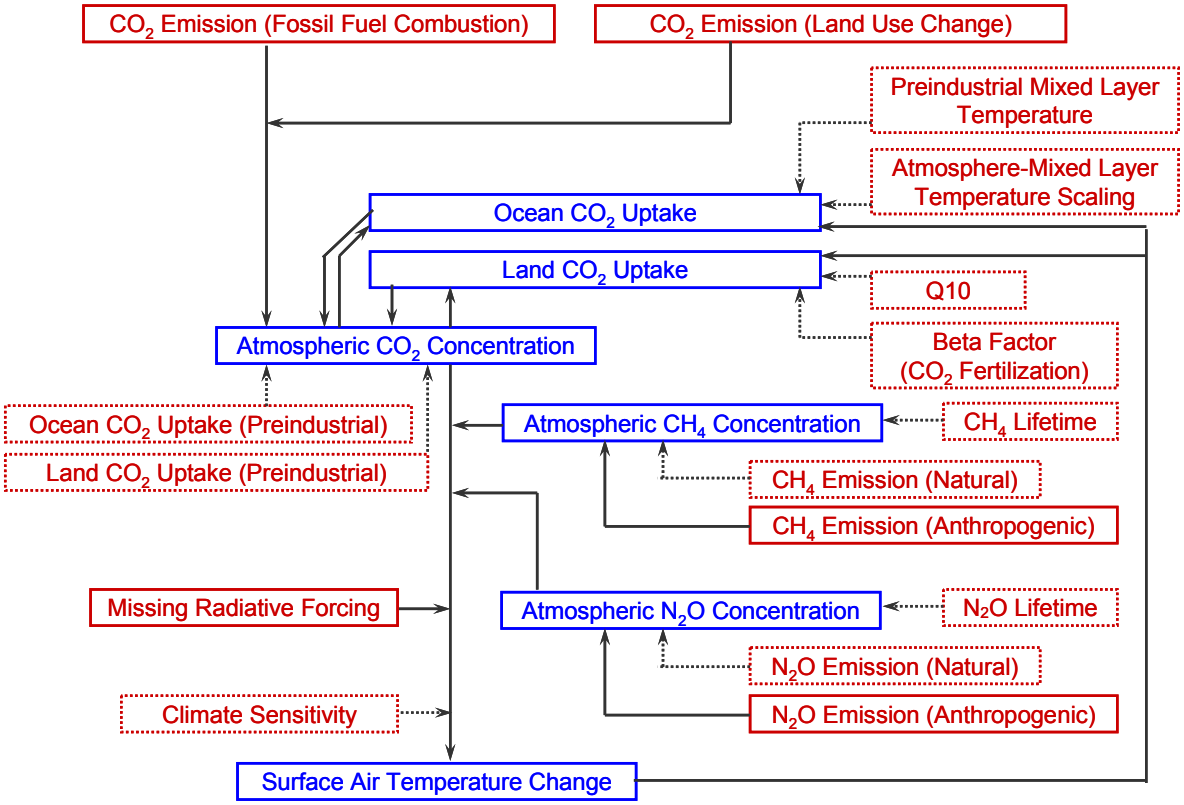

4. PAST AND FUTURE SIMULATION RESULTS

In this section, the results and findings are only highlighted within the scope of model description. Section 4.1 provides to-the-point discussion of the results of the ACC2 past mode run. More details of the inversion results are shown in Appendix A. Examination of the inversion results are discussed in Chapter 5 and Appendix B. In Section 4.2, the results of the ACC2 future mode run are compared with the corresponding results in IPCC (2001) for six emission scenarios (SRES (Nakićenović et al., 2000)) (Figures 4.2 to 4.5). This section is concluded with future perspectives for the development of ACC2.

4.1. RESULTS FOR PAST MODE SIMULATION

The inverse estimation for ACC2 has been set up as it is described in Section 3. Specifically, all the parameters and data in Tables 3.1 and 3.2 are put into the inverse estimation. The inverse calculation takes care of the ENSO-induced changes in the atmospheric CO_2 concentration and the surface air temperature (Section 3.5.1). The prior uncertainty ranges for various time series are adjusted during the periods influenced by large volcanic eruptions (Section 3.5.2). The inverse calculation results are shown in comparison with the forward calculation results in which all the parameters are fixed at the respective prior values.

Visual inspection of Figure 4.1 shows that most of the posterior estimates are contained within their 2σ prior uncertainty ranges. Comparison between the inverse and forward projections demonstrates how the ACC2 inverse calculation effectively synthesizes various information on the parameter estimates, measurements, and physical-biogeochemical laws.

The posterior estimates of the land use CO_2 emission (Figure 4.1.2) are substantially lower than the corresponding prior estimates for the last 60 years. Similar results can be seen in the posterior estimates of the fossil fuel CO_2 emission (Figure 4.1.1). The reduction in the CO_2 emission is larger for the land use part because the same amount of emission reduction can be attained with a less penalty in the land use part than in the fossil fuel part. The posterior estimates of the ocean and land CO_2 uptake and the atmospheric CO_2 concentration are relatively close to the respective measurements. The posterior value of the beta factor is estimated to be 0.59, which is high in the prior range between 0.1 and 0.7. The results above are in line with Friedlingstein et al. (2006). The estimates of the land use CO_2 emission (Houghton, 2003) are so high that, to explain the observed atmospheric CO_2 concentration, the terrestrial biosphere has to take up excessive carbon by strong CO_2 fertilization. Keep in mind that, in view of the previous inversion studies, the prior uncertainty

ranges of the land use CO_2 emission in ACC2 are taken twice as large as the ranges suggested in Houghton (2003). However, the results here should not be regarded just as an indication for lower estimates of the land use CO_2 emission. The knowledge on the response of the global terrestrial biosphere to the changes in the atmospheric CO_2 concentration and climate are not well-established (Friedlingstein et al., 2006). Some missing carbon cycle processes are under debate – it is not known whether soil erosion leads to net carbon release or uptake (Lal, 2005). Therefore, the indication from the inversion results should rather be that the substantially low land use CO_2 emission reflects the overall uncertainties in the historical carbon budget.

The posterior value of Q10 is estimated to be 1.18, which is beyond the 2σ prior uncertainty range between 1.5 and 2.5 (Sections 2.1.3 and 3.4; Table 3.2). However, such a posterior estimate is not necessarily unrealistic. The prior estimate of Q10 is based on a compilation of field measurements (Tjoelker et al., 2001). The value of Q10 on the global scale can only be speculated although global modelling studies typically assume the value of 2.0. It can be argued that the low Q10 value obtained from the ACC2 inversion reflects the biospheric response to not only the temperature change but also the soil moisture change, which is not described in ACC2. With global warming the contrast between wet and dry regions will increase as virtually all GCMs have demonstrated (Wang, 2005). Precipitation and probably also soil moisture will increase in most of the presently wet regions and decrease in the subtropical regions. More water in presently wet soils will decrease heterotrophic respiration because of the oxygen limitation while less water in presently dry soils will also reduce heterotrophic respiration because of the water limitation. Thus, the temperature effect and the soil moisture effect on the heterotrophic respiration cancel out each other, providing an argument for the low Q10 estimate in the ACC2 inversion results.

The residuals for the atmospheric CO_2 concentration (Figure 4.1.3) show decadal variability. There is a plateau in the rise of the atmospheric CO_2 concentration between 1940 and 1960. The temperature rise also stalls during this time and even thereafter. Mechanisms that led to the 'stagnation' are in dispute. An inversion study (Trudinger et al., 2002) shows that the slowdown in the atmospheric CO_2 concentration rise is caused by the change in the large-scale ocean circulation. Such a halt does not appear in the prior estimates of the ocean CO_2 uptake based on the C^4MIP runs (Section 3.3).

The drop in the forward estimates of the atmospheric CO_2 concentration around 1810 is caused by the extremely large terrestrial CO_2 uptake (Figure 4.1.5) when the heterotrophic respiration is drastically reduced by the temperature drop after large volcanic eruptions (Figures A.4 and A.6 for inversion estimates). In the forward run, the heterotrophic respiration is more sensitive to the temperature change since the value of Q10 is fixed at the prior value of 2.0.

The forward projections of the CH_4 and N_2O concentrations (Figures 4.1.8 and 4.1.9) are incorrectly low primarily because the prior estimates of their natural emissions are too low to explain

the trend of the concentration measurements. The results here point to a need for better knowledge on the natural CH_4 and N_2O emissions (Table 3.2).

The large downward spikes in the total radiative forcing are the signatures of volcanic eruptions (Figure 4.1.10). The inverse calculation shows that some strong volcanic forcing signals between 1750 and 1850 are offset by positive missing forcing because the reconstructed temperature does not sufficiently drop during the same periods (Figure 4.1.11). This is partly due to a problem in the model time step in which the fast-converging volcanic forcing is not well resolved (Section 3.5.2). Further discussion and analysis of the missing forcing is in Chapter 5 and Appendix B.

It is still a mystery why there are no large temperature drops after the Tambora eruption in 1815. A diffuse radiation hypothesis (Robock, 2005) put forward to explain such seemingly contradicted records is that the tree ring proxies used for the temperature reconstruction are biased by the plant growth enhanced by the diffuse radiation (Section 3.5.1). If this hypothesis is true, the temperature would have actually been lower after the eruption than what the proxies directly suggest. The growth of the atmospheric CO_2 concentration indeed slowed down after the Pinatubo eruption in 1991. The inverse calculation indicates that, because the suppression of the heterotrophic respiration due to the cooling after the eruption was not sufficient to explain the observed CO_2 concentration (Figures 4.1.3 and 4.1.5), the land use CO_2 emission are drastically reduced after the eruption (Figure 4.1.2). The unusually low land use CO_2 emission can be explained by the enhanced plant growth due to diffuse radiation. However, evidences are not yet conclusive as there are large discrepancies among different volcanic forcings and temperature reconstructions (Jones and Mann, 2004, Figures 7 and 8).

The foregoing analysis of the ACC2 inversion results not only reaffirms the existing large uncertainties in the parameters and data but also raises the problem of possible ill-representation of the processes. Given that, parameter estimates and the model state in 2000 obtained from the inversion are used to make future projections.

4.2. RESULTS FOR FUTURE MODE SIMULATION

Results of the ACC2 future mode runs using six different emission scenarios (SRES (Nakićenović et al., 2000)) are shown in Figures 4.2 to 4.5 and Table 4.1. Visual inspection of the figures shows that the projections of the ACC2 future mode run are compatible with the corresponding projections in IPCC (2001, Appendix II) and WMO (2003, Table 1-16). Differences between the ACC2 projections and the IPCC/WMO projections can be well explained as follows.

The atmospheric CO_2 concentration projections simulated from ACC2 are in the middle ranges of the corresponding IPCC projections using Integrated Science Assessment Model (ISAM) and Bern-CC for all the six emission scenarios (Figure 4.2). ACC2 uses a relatively high CO_2

fertilization (beta = 0.59), relatively weak ocean CO_2 uptake (1.59 GtC/yr in 1980s), and a low temperature sensitivity to the heterotrophic respiration (Q10 = 1.18) as obtained from the inverse calculation (Table 3.2). Such parameter settings in ACC2 roughly correspond to the settings for the reference case simulations of ISAM and Bern-CC. Thus, the ACC2 projections are compatible with the projections of ISAM and Bern-CC.

The atmospheric CH_4 concentration projections obtained from ACC2 (Figure 4.3.2) are systematically lower than the corresponding IPCC projections, which are based on the OxComp workshop CTMs (IPCC, 2001, Table 4.10). The dynamics between CH_4 and OH are similar because the parameterizations for CH_4 and OH in ACC2 are tuned to the outputs of such CTMs (Section 2.2.2). The relatively low CH_4 concentration projections in ACC2 can be attributed to the combined effect of the lower CH_4 lifetime with respect to OH depletion (= 8.5 years) and the higher natural CH_4 emission (= 320 Mt(CH_4)/year) obtained from the ACC2 inverse calculation (IPCC, 2001, Tables 4.2 and 4.3). As a result of the lower CH_4 concentration projections, the relative OH concentration projections (Figure 4.3.35) are higher in ACC2 than in IPCC (2001).

Conversely, the N_2O concentration projections simulated from ACC2 (Figure 4.3.3) are higher than the corresponding IPCC projections. The feedback of the N_2O concentration to its own lifetime in ACC2 is similar to the feedbacks in the CTMs (Section 2.2.3). The relatively high N_2O concentration projection in ACC2 can be attributed to the combined effect of the higher N_2O lifetime (= 114 years) and the higher natural N_2O emission (= 11.3 Mt(N)/year) obtained from in the inverse calculation (IPCC, 2001, Tables 4.4 and 4.5).

The differences in the projections for the halocarbon concentrations between ACC2 and IPCC/WMO (Figures 4.3.5 to 4.3.33) are mainly due to the differences in the atmospheric lifetimes. The lifetimes in ACC2 are up-to-date with respect to WMO (2003, Table 1-6) and IPCC (2005, Table 2.6).

For non-ODS halocarbons and SF_6 (Figures 4.3.4 to 4.3.17), same emission scenarios are used for the A1B, A1T, and A1FI scenarios (A1 family). However, the differences in the concentration projections for the A1 family scenarios exist because of the differences in the relative OH concentration projections. The lifetimes of halocarbons containing at least one hydrogen atom are defined as functions of the relative OH concentration (Section 2.2.5). For ODS halocarbons (Figures 4.3.18 to 4.3.33), the same emission scenario is used for all the six scenarios. Because ODS halocarbons are not removed by OH, there are no differences in the concentration projections of ODS halocarbons for the six scenarios.

The mismatch in the projections of the tropospheric O_3 concentration (Figure 4.3.36) are owing to the fact that errors in the IPCC calculation of the tropospheric O_3 concentration projection are not properly corrected even though the modification for error corrections is suggested (IPCC, 2001, Table 4.11).

The basic relationships in the concentration projections between ACC2 and IPCC/WMO hold for the radiative forcing projections (Figure 4.4). The radiative forcings of most of the agents (except for CO_2, CH_4, and N_2O) are defined linearly with the respective concentrations scaled with the individual radiative efficiencies. The radiative efficiencies in ACC2 are up-to-date with respect to WMO (2003, Table 1-6) and IPCC (2005, Table 2.6), which give rise to slight differences for the radiative forcing projections of some halocarbons. As for the solar forcing (Figure 4.4.38), from 2030 onward it is assumed to be equal to the average solar forcing of the 20th century. The solar forcing between 2000 and 2030 is linearly interpolated.

The total radiative forcing projected from ACC2 (Figure 4.5.1) is lower than the corresponding IPCC total radiative forcing for the six scenarios primarily because the CO_2 radiative forcing projected from ACC2 is in the low IPCC ranges as can be inferred from the CO_2 concentration projections (Figure 4.2). On the other hand, the temperature change projections calculated from ACC2 (Figure 4.5.2) are estimated to be higher than the IPCC projections also for the six scenarios. It is not possible to identify exact reasons for the discrepancy because the IPCC results are the averages of the outputs from several simple models with different parameter setups (IPCC 2001, Table 9.A1). Nevertheless, we speculate that the primary reason is the climate sensitivity calculated by ACC2 (= 4.0^{o}C) as the outcome from the inverse calculation, which is substantially higher than the average of the estimates of the climate sensitivity used in the ensemble of simple models.

Clarification of the differences between IPCC projections and the present results is an important requirement for the practical application of ACC2. The differences between the ACC2 projections and the IPCC/WMO projections are all explained above. In particular for the atmospheric CO_2 concentration and temperature change, the differences in the projections emerge directly from the differences in the approaches. While the IPCC projections are based on some representative parameter values, the ACC2 projections consistently uses the parameter values obtained from the inverse calculation.

4.3. CONCLUDING REMARKS AND FUTURE PERSPECTIVES

ACC2 is the third generation of the simple models developed in Germany with various international collaborations. ACC2 is fully up-to-date with respect to the current literature and refined with detailed processes compared to the two predecessor models (NICCS (Hooss, 2001); ICM (Bruckner et al., 2003)). ACC2 could serve as a prototype for complex Earth system models, in particular as a tool to explore uncertainties in the Earth system.

The most notable achievement for the development of ACC2 is the implementation of the inversion scheme. Our inversion approach is the first attempt to perform an inversion for the

integrated Earth system. The ACC2 inversion approach limits itself to the global-annual-mean information and produces one-point estimates for the parameters and data (corresponding to the cost function minimum). Our approach is complementary to the approach computing probability densities (e.g. Forest et al., 2002; Gregory et al., 2002; Knutti et al., 2002; Hegerl et al., 2006). Although the probability densities show the extent of the knowledge on uncertainties, the number of uncertainties considered in the probability density approach is limited to several due to the computational requirement. On the other hand, our inversion approach exhaustively accounts for a large number of uncertainties even in each point of time series independently although the associated interdependencies of the large number of uncertainty estimates give bias to the inversion solution and are extremely complex to analyze. Nevertheless, our best guess of the uncertain parameter estimates provides straightforward interpretation, appealing to further scientific applications (e.g. Chapters 5 and 6 of this thesis; Tanaka et al., 2007b; Tanaka et al., 2008).

Under the probabilistic inverse estimation theory (Tarantola, 2005; Figure 3.1), we have synthesized the existing scientific evidences comprising various observational databases, parameter estimates, and physical-biogeochemical laws. The ACC2 inverse calculation successfully reproduces a plausible evolution of the Earth system between the year 1750 and 2000 and generates the best guess of parameters (Figure 4.1 and Tables 3.1 and 3.2). The comparison between the inverse calculation and the forward calculation shows how effectively various pieces of information are integrated. Under the Tarantola's theory, assumptions in the ACC2 inverse calculation are thoroughly extracted and discussed (Section 3.2.2).

At the present level of the development and analysis of our inverse estimation, the ACC2 approach achieves the attainable limits of our knowledge of the Earth system. The estimate of the land use CO_2 emission is not well-known as the bottom-up approach (Houghton, 2003) and the inversion approach (including ours) point to different magnitudes in particular for the past 50 years. Missing carbon cycle processes such as soil erosion (Lal, 2005) need to be investigated further to balance the historical carbon budget. We confirm that the uncertainties in the natural CH_4 and N_2O emissions are substantial. Both the radiative forcing and temperature reconstructions are subject to large uncertainties. Some contradictions between the volcanic forcing and temperature drops may be explained by the diffuse radiation hypothesis (Robock, 2005).

The results of the inverse calculation contain the parameter estimates and model state for the year 2000, on the basis of which the future evolutions of the Earth system are projected up to 2100 (Figures 4.2 to 4.5). On the ground of our consistent treatment of the uncertainties from the past to the future, we contend that our approach is more rigorous than IPCC (2001), where the ranges of future projections are produced by picking representative parameter values in simple models.

The current stage of the development of ACC2 is sufficient for various applications.

However, ACC2 encompasses only limited aspects of natural Earth system processes. Further improvements in the inversion methodology are possible. We conclude this document with the following future tasks:

- Analyze the interdependencies of residuals for parameters and data. Stochasticity can be introduced to the inversion as model errors. The ensemble results can be used to estimate covariances.
- Consider isotopic data to provide an additional constraint for the carbon budget. $\delta^{13}C$, the relative concentrations of two isotopes ^{12}C and ^{13}C, can discriminate ocean and land CO_2 uptake (e.g. IPCC, 2001, p.207). A further constraint for ocean CO_2 uptake can be provided by ^{14}C (e.g. Enting, 2002a, p.241).
- Couple with the carbon cycle with other element cycles (nitrogen, phosphorus, sulfur, and oxygen). Interactions between different element cycles are becoming an important research topic (Ver et al., 1999; Mackenzie et al., 2002; Mackenzie and Lerman, 2006, Chapter 11; Gruber and Galloway, 2008). Nitrogen and phosphorus cycles possibly provide additional constraints for the carbon cycle because primary productivity of various ecosystems is limited by the availability of these elements.
- Constrain ocean diffusivity by using ocean heat diffusion data (Levitus et al., 2000). Kriegler (2005) applied the imprecise probability theory to constrain climate sensitivity, ocean diffusivity, and aerosol forcing by using DOECLIM as a standalone model.
- Complete the development of the sea level component. The thermal expansion calculation by DOECLIM can be combined with the parameterization of sea level rise (IPCC, 2001, Appendix 11.1).

Table 4.1. The results of the ACC2 future mode run

The results of the ACC2 future mode runs for the six emission scenarios (SRES) are shown below. The temperature change refers to the global-mean surface air temperature change relative to the level in 1990.

	A1B scenario					**A1T scenario**				
Year	CO_2 concentration (ppm)	CH_4 concentration (ppb)	N_2O concentration (ppb)	Total radiative forcing (W/m^2)	Temperature change (°C)	CO_2 concentration (ppm)	CH_4 concentration (ppb)	N_2O concentration (ppb)	Total radiative forcing (W/m^2)	Temperature change (°C)
2000	370	1752	317	1.48	0.06	370	1752	317	1.48	0.06
2005	380	1783	322	1.55	0.21	379	1778	322	1.70	0.25
2010	392	1836	327	1.66	0.30	389	1820	326	1.93	0.40
2015	405	1901	332	1.81	0.41	400	1876	330	2.16	0.56
2020	419	1971	337	1.97	0.51	411	1946	334	2.39	0.72
2025	435	2049	341	2.27	0.66	423	2030	337	2.60	0.88
2030	452	2133	345	2.58	0.84	437	2127	341	2.84	1.04
2035	469	2203	350	2.97	1.05	452	2217	344	3.17	1.23
2040	487	2248	354	3.37	1.29	466	2288	347	3.50	1.44
2045	505	2278	358	3.64	1.52	480	2347	350	3.76	1.65
2050	524	2299	361	3.90	1.73	493	2400	353	4.00	1.84
2055	543	2300	365	4.25	1.96	505	2431	355	4.21	2.02
2060	561	2276	368	4.58	2.19	517	2433	358	4.40	2.19
2065	579	2237	372	4.84	2.41	527	2417	360	4.53	2.34
2070	597	2191	374	5.10	2.62	536	2387	362	4.64	2.47
2075	614	2140	377	5.28	2.81	543	2349	364	4.73	2.58
2080	631	2087	380	5.45	2.98	549	2307	366	4.80	2.68
2085	646	2035	382	5.57	3.13	553	2260	367	4.83	2.76
2090	661	1984	385	5.68	3.26	556	2206	368	4.84	2.82
2095	676	1936	387	5.78	3.38	558	2144	370	4.85	2.87
2100	689	1892	389	5.87	3.49	558	2074	371	4.84	2.91

Table 4.1. (Continued) The results of the ACC2 future mode run

	A1FI scenario					**A2 scenario**				
Year	CO_2 concentration (ppm)	CH_4 concentration (ppb)	N_2O concentration (ppb)	Total radiative forcing (W/m^2)	Temperature change (°C)	CO_2 concentration (ppm)	CH_4 concentration (ppb)	N_2O concentration (ppb)	Total radiative forcing (W/m^2)	Temperature change (°C)
2000	370	1752	317	1.48	0.06	370	1752	317	1.48	0.06
2005	379	1777	322	1.59	0.22	379	1780	322	1.63	0.23
2010	390	1814	328	1.71	0.32	389	1825	328	1.80	0.35
2015	402	1866	334	1.90	0.44	401	1880	334	1.85	0.45
2020	416	1933	341	2.10	0.57	415	1941	341	1.93	0.53
2025	433	2013	348	2.32	0.71	430	2011	348	2.09	0.62
2030	452	2106	355	2.57	0.86	447	2091	355	2.28	0.73
2035	474	2210	363	2.94	1.06	465	2176	362	2.58	0.89
2040	499	2324	371	3.34	1.29	484	2266	370	2.89	1.07
2045	527	2441	380	3.85	1.56	504	2358	377	3.19	1.26
2050	558	2557	390	4.37	1.88	524	2451	385	3.50	1.47
2055	591	2657	400	4.95	2.23	546	2548	392	3.90	1.70
2060	626	2736	409	5.53	2.60	569	2650	400	4.30	1.95
2065	661	2804	418	6.01	2.97	593	2756	407	4.71	2.23
2070	698	2870	427	6.49	3.32	619	2864	415	5.14	2.51
2075	736	2935	436	6.87	3.66	647	2973	423	5.53	2.80
2080	775	3001	445	7.23	3.97	677	3083	431	5.93	3.08
2085	815	3063	453	7.54	4.25	709	3192	439	6.29	3.37
2090	854	3120	461	7.82	4.52	745	3299	448	6.67	3.65
2095	892	3171	469	8.10	4.77	782	3407	456	7.05	3.94
2100	931	3212	477	8.35	5.01	823	3514	464	7.43	4.23

Table 4.1. (Continued) The results of the ACC2 future mode run

	B1 scenario					B2 scenario				
Year	CO_2 concentration (ppm)	CH_4 concentration (ppb)	N_2O concentration (ppb)	Total radiative forcing (W/m^2)	Temperature change (°C)	CO_2 concentration (ppm)	CH_4 concentration (ppb)	N_2O concentration (ppb)	Total radiative forcing (W/m^2)	Temperature change (°C)
2000	370	1752	317	1.48	0.06	370	1752	317	1.48	0.06
2005	379	1769	322	1.63	0.23	379	1773	322	1.68	0.24
2010	389	1787	328	1.78	0.35	388	1801	326	1.88	0.39
2015	400	1808	333	1.95	0.47	397	1838	330	2.08	0.53
2020	411	1833	338	2.12	0.59	407	1882	334	2.27	0.67
2025	423	1850	344	2.26	0.71	416	1934	337	2.43	0.80
2030	435	1854	349	2.39	0.82	426	1992	341	2.60	0.93
2035	447	1848	354	2.54	0.93	437	2055	344	2.79	1.07
2040	459	1837	359	2.70	1.05	448	2123	347	2.99	1.21
2045	471	1819	363	2.91	1.18	460	2196	350	3.19	1.35
2050	482	1796	368	3.10	1.32	471	2273	353	3.40	1.50
2055	492	1773	372	3.30	1.46	483	2345	356	3.59	1.65
2060	501	1754	375	3.49	1.60	495	2406	359	3.77	1.80
2065	509	1737	379	3.65	1.74	507	2463	361	3.96	1.94
2070	515	1721	382	3.80	1.87	519	2523	364	4.15	2.09
2075	520	1700	384	3.91	1.98	531	2581	367	4.32	2.23
2080	524	1669	386	4.00	2.09	544	2636	369	4.50	2.37
2085	527	1634	388	4.06	2.17	557	2686	372	4.67	2.51
2090	529	1597	390	4.12	2.25	571	2731	374	4.84	2.65
2095	530	1558	391	4.15	2.31	585	2775	377	5.02	2.79
2100	530	1516	392	4.17	2.36	599	2823	379	5.19	2.93

Figure 4.1. The results of the ACC2 past mode run

The series of figures show the results of the ACC2 inverse calculation. Posterior estimates of the parameters and data (red lines) are shown in comparison with the respective prior estimates and measurements (thick black lines) including their 2σ prior and measurement uncertainty ranges (thin black lines). Also shown are the results of forward run in which all the parameters are fixed at the respective prior estimates (blue lines). Large spikes in the prior and measurement uncertainty ranges are their adjustments for large volcanic eruptions (Section 3.5.2). In inserts, residuals (red lines in inserts) are shown with their 2σ prior and measurement uncertainty ranges (black lines in inserts). Prior and posterior parameter values are shown in Table 3.2.

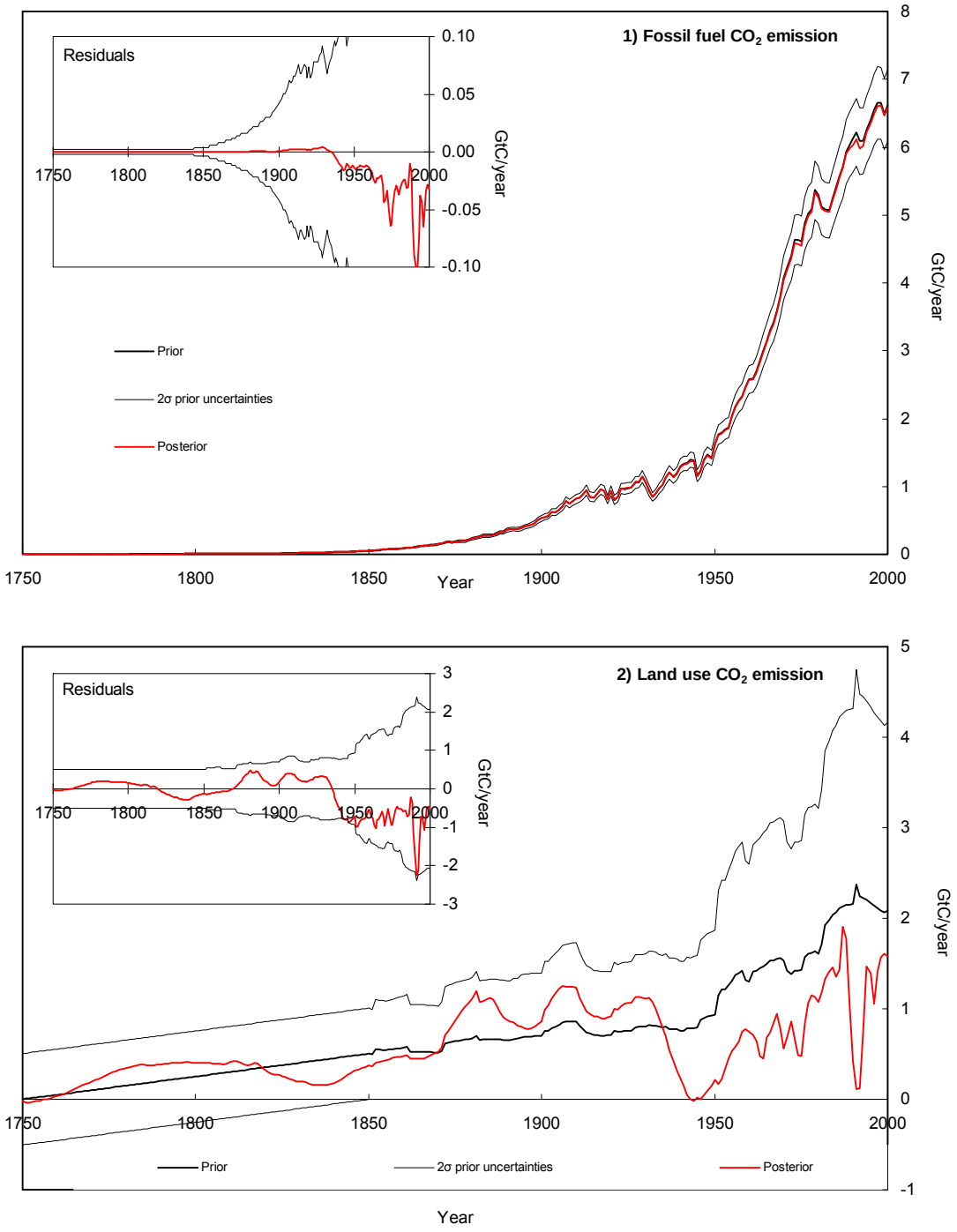

Figure 4.1. (Continued) The results of the ACC2 past mode run

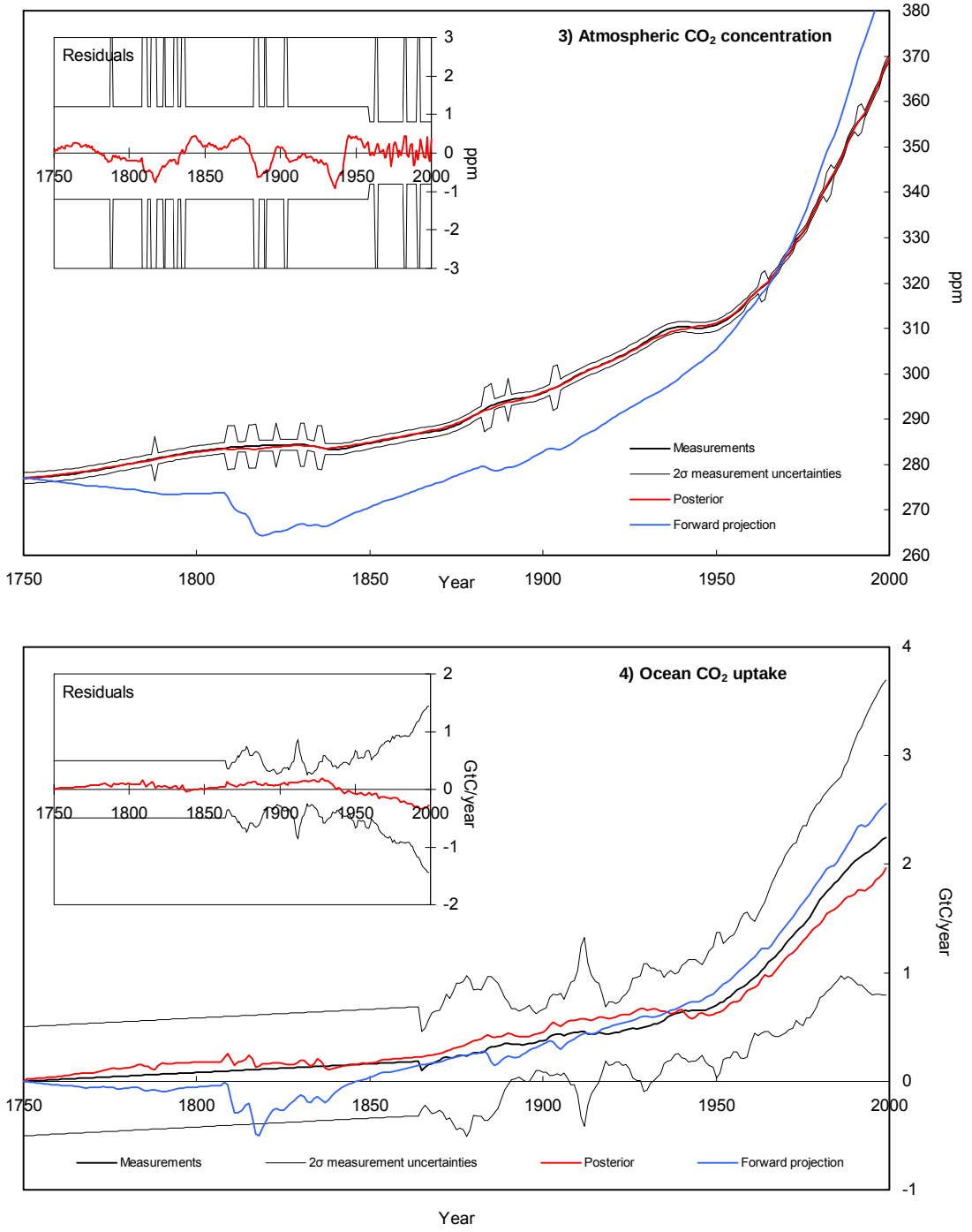

Figure 4.1. (Continued) The results of the ACC2 past mode run

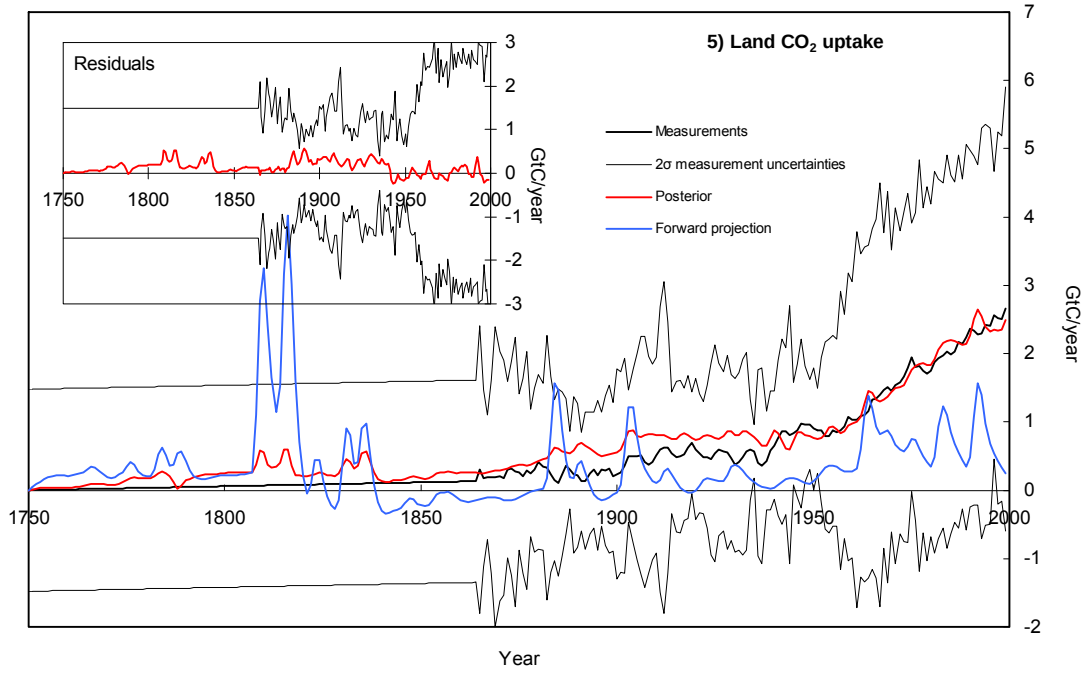

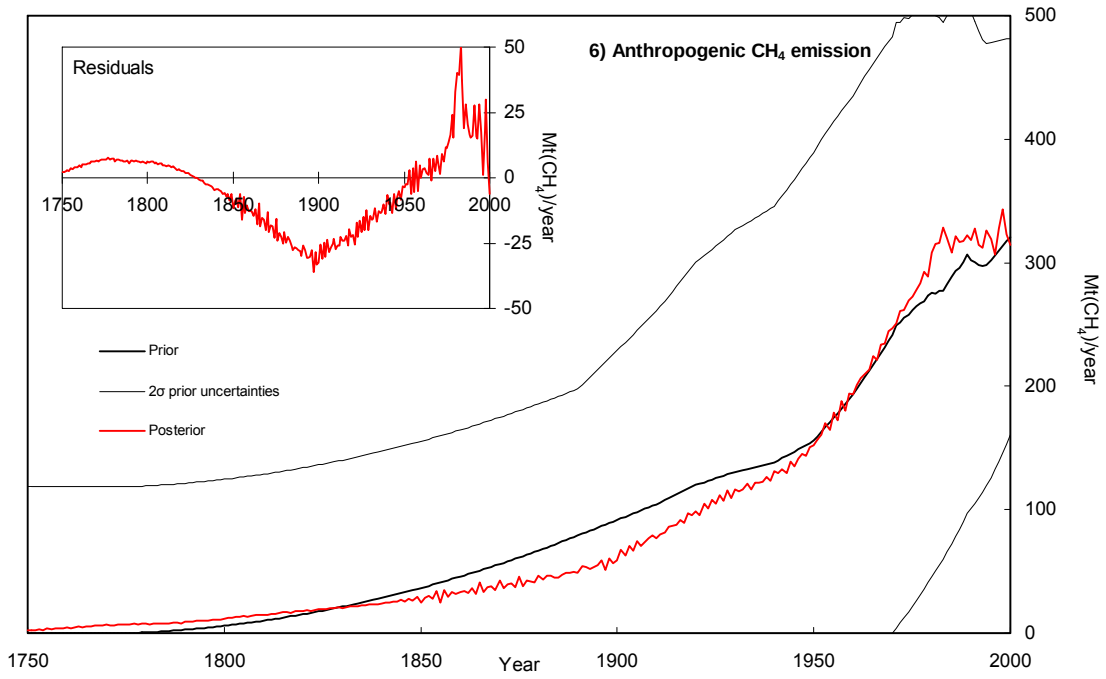

Figure 4.1. (Continued) The results of the ACC2 past mode run

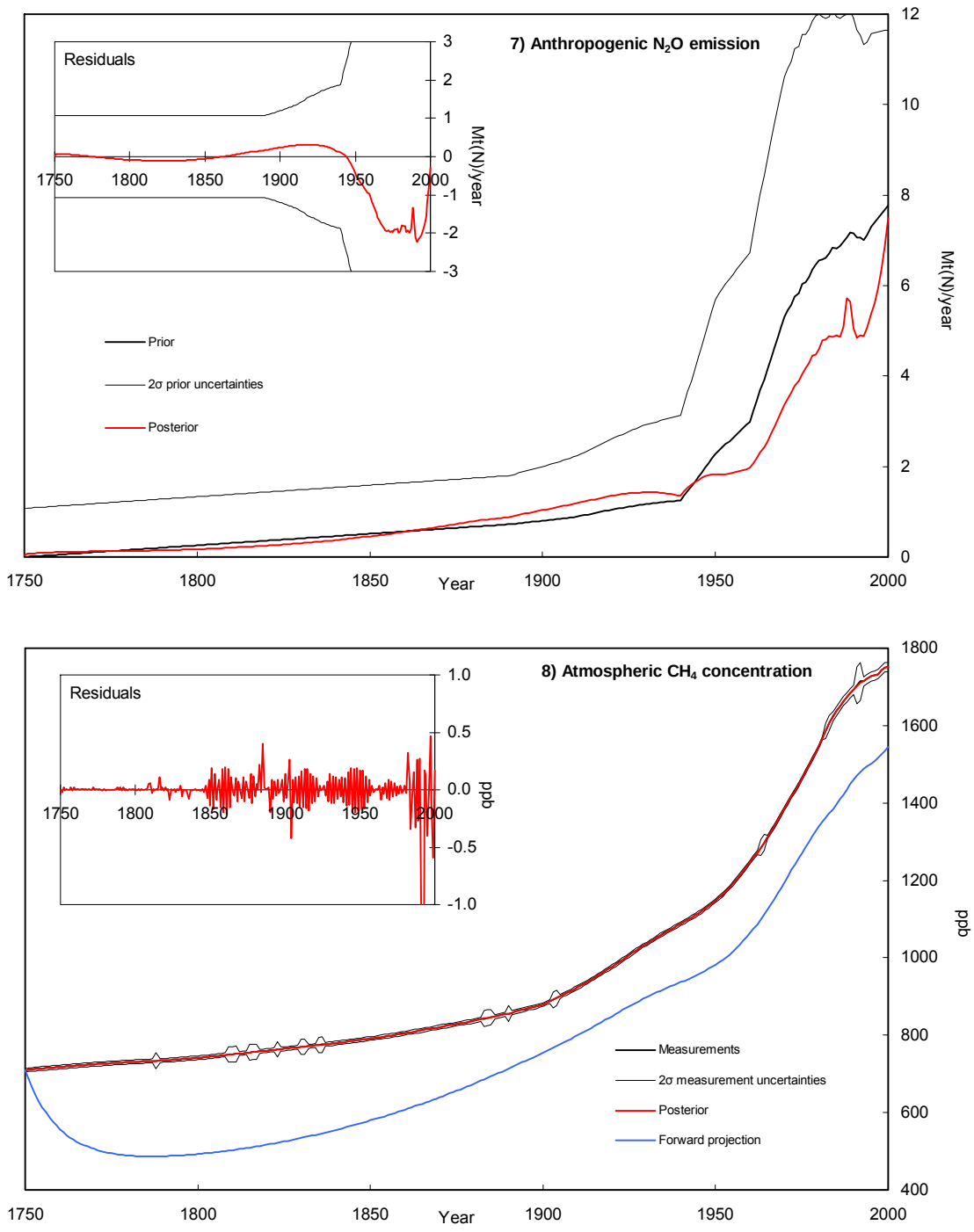

Figure 4.1. (Continued) The results of the ACC2 past mode run

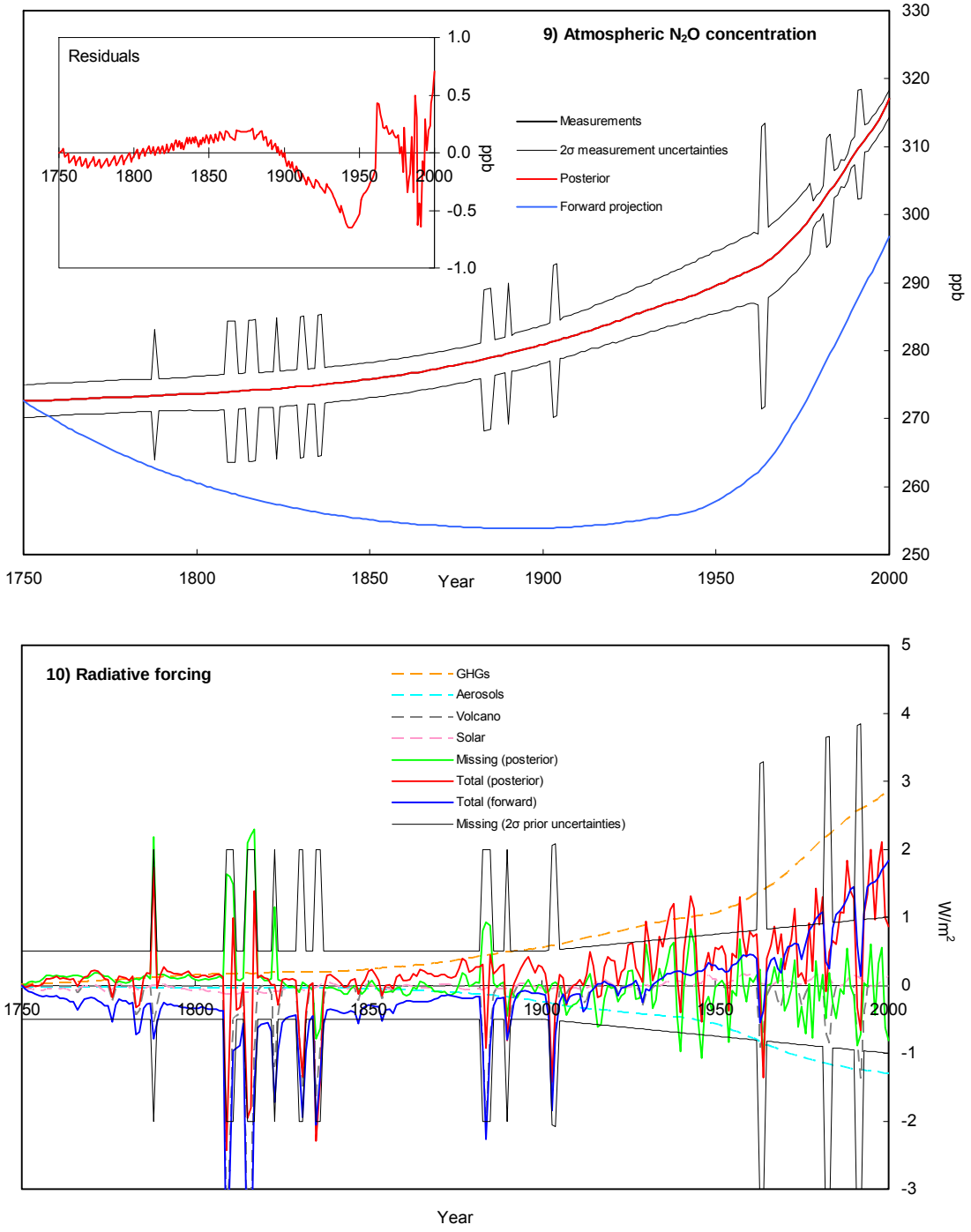

Figure 4.1. (Continued) The results of the ACC2 past mode run

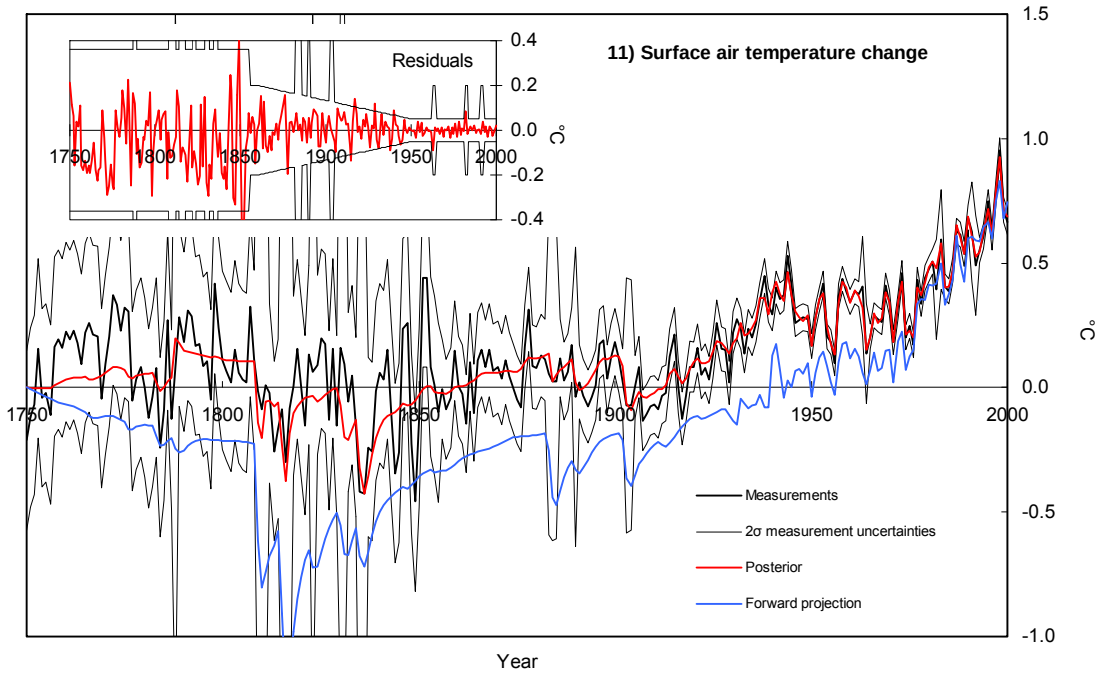

Figure 4.2. The atmospheric CO_2 concentration projections of the ACC2 future run

The CO_2 concentration projections of the ACC2 future runs for the six emission scenarios (SRES) are shown in comparison with the corresponding projections of ISAM and the Bern-CC model (IPCC, 2001, Appendix II). Both ISAM and the Bern-CC model are simple carbon cycle-climate models (IPCC, 2001, Box 3.7). ISAM is tuned to mimic the ranges of projections for the carbon cycle processes shown by several process-based models (IPCC, 2001, Figure 3.10), producing the projections of the "ISAM low, reference, and high" cases. In the "Bern-CC low" case, the transport parameters in the ocean are increased by 50% relative to those in the reference case and no temperature sensitivity is assumed for the heterotrophic respiration. In the "Bern-CC high" case, the ocean transport parameters are decreased by 50% and the CO_2 fertilization effect is capped at the level in 2000.

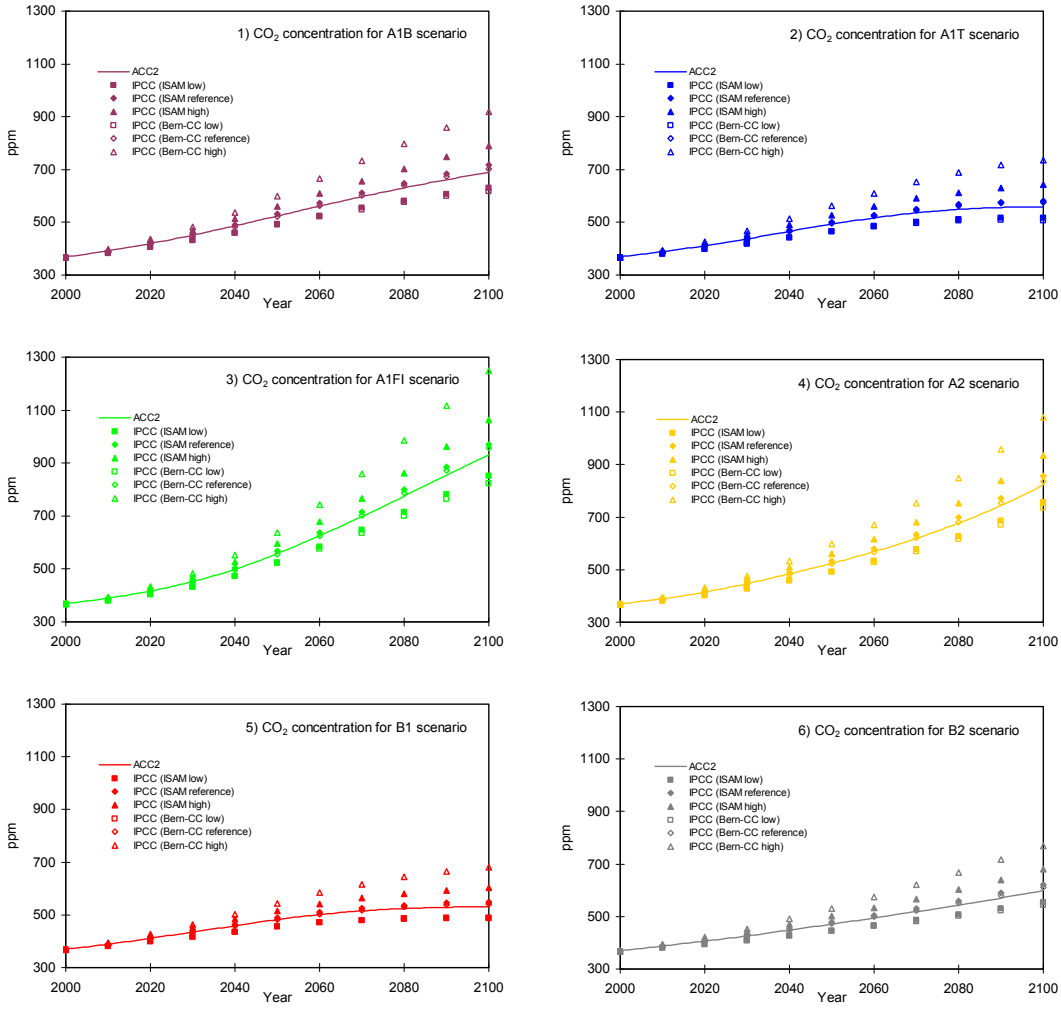

Figure 4.3. The results of the ACC2 future mode run – atmospheric concentrations of radiative agents

The concentration projections of the ACC2 future mode runs for the six emission scenarios (SRES) are shown in comparison with the corresponding projections in IPCC (2001, Appendix II) and WMO (2003, Table 1-16). The emissions of C_4F_{10}, HFC152a, and HFC236fa are kept zero throughout the projection horizon in the six scenarios.

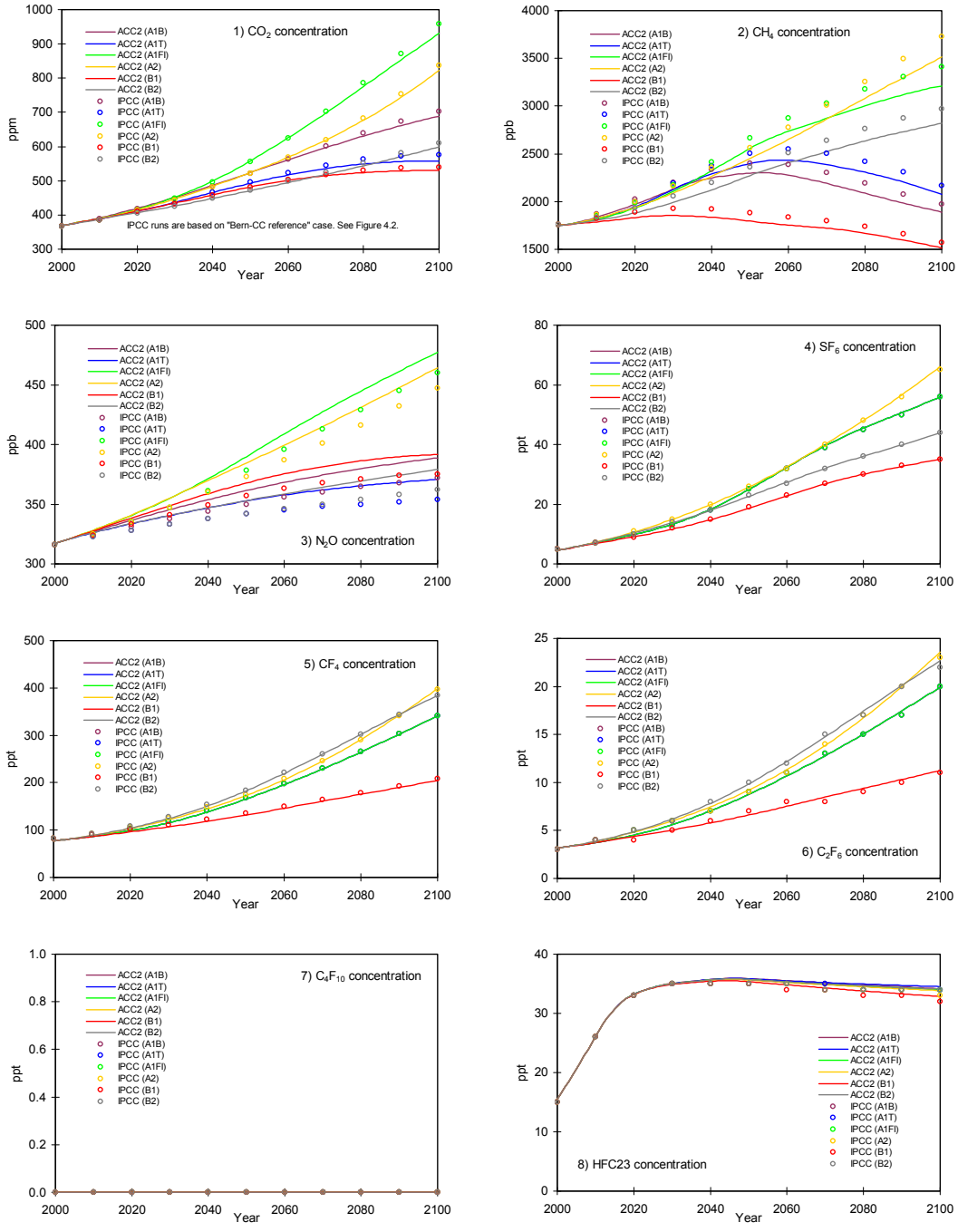

Figure 4.3. (Continued) The results of the ACC2 future mode run – atmospheric concentrations of radiative agents

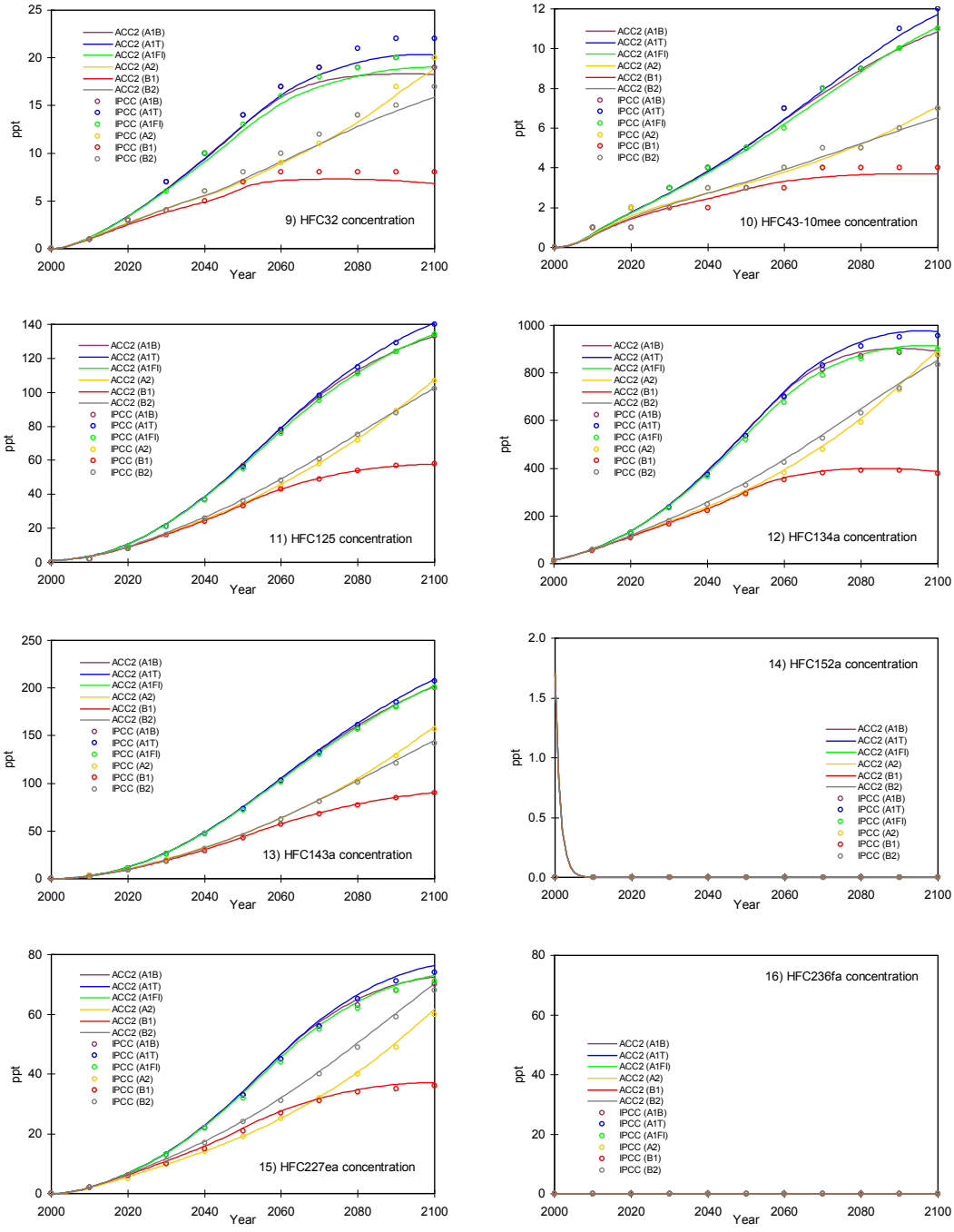

Figure 4.3. (Continued) The results of the ACC2 future mode run – atmospheric concentrations of radiative agents

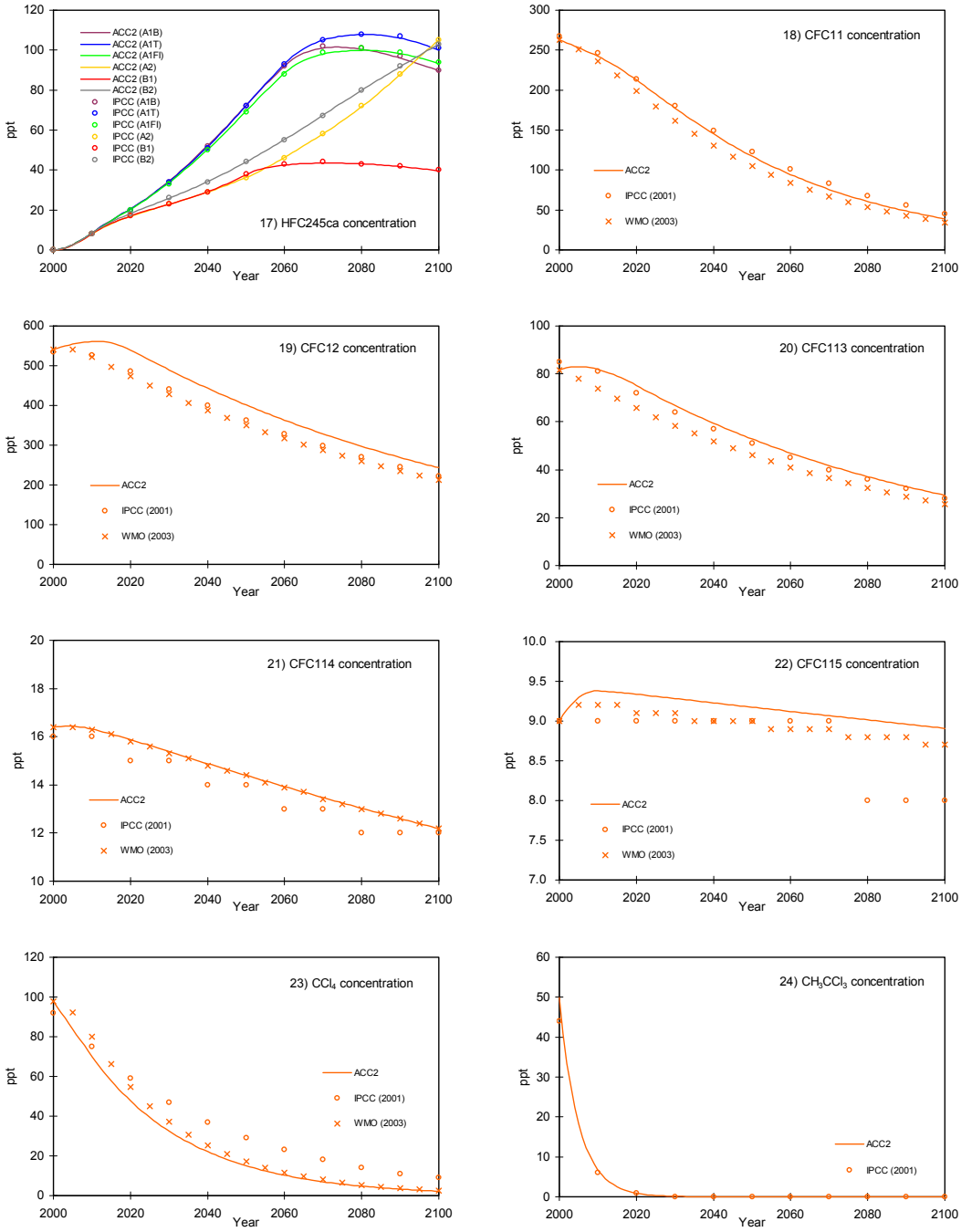

Figure 4.3. (Continued) The results of the ACC2 future mode run – atmospheric concentrations of radiative agents

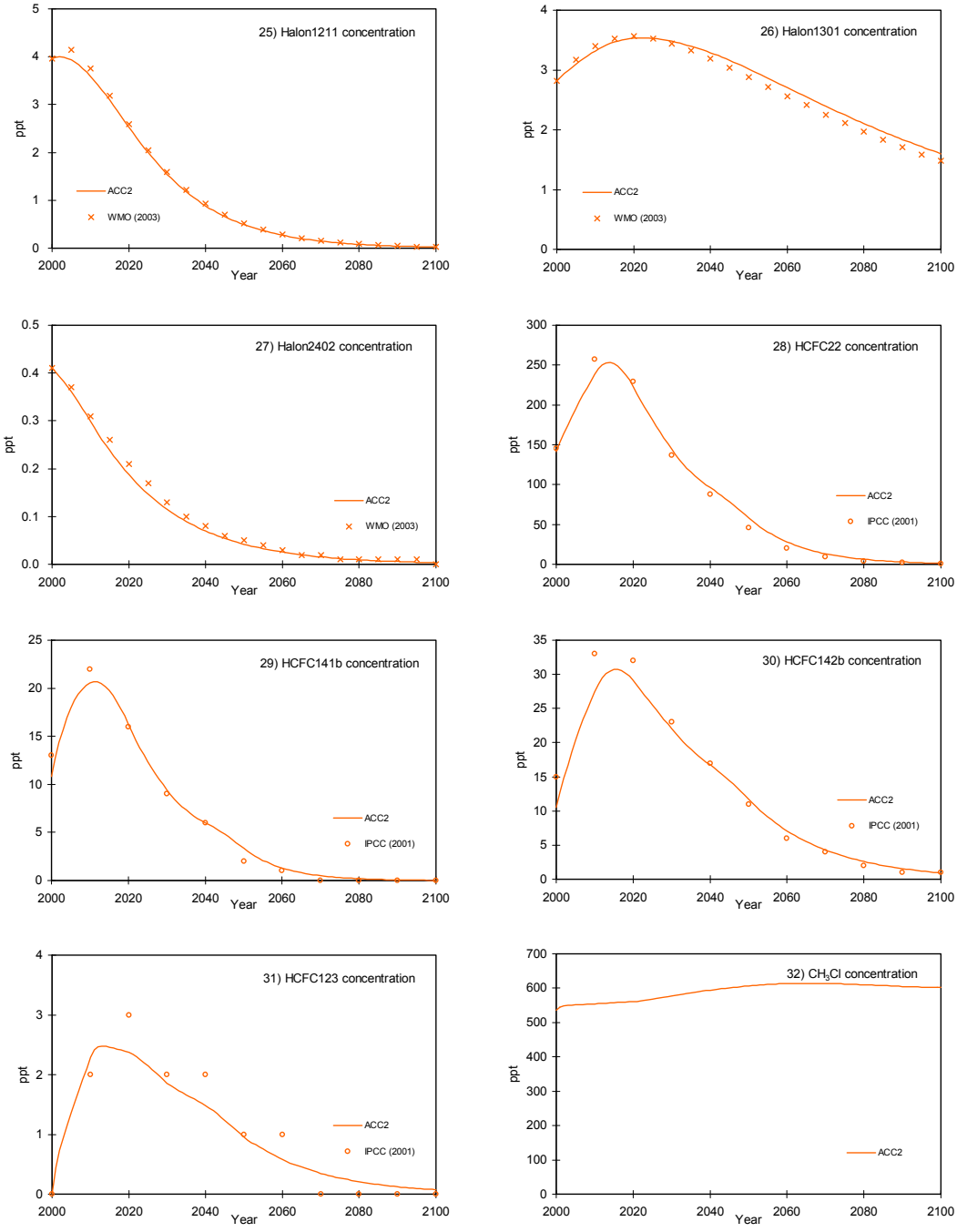

Figure 4.3. (Continued) The results of the ACC2 future mode run – atmospheric concentrations of radiative agents

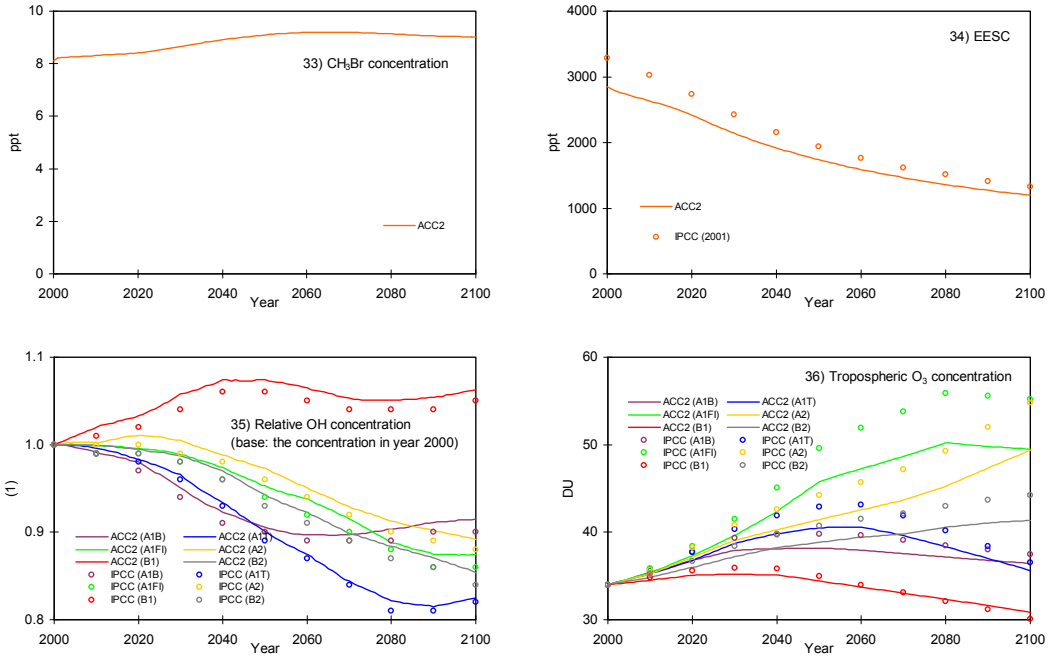

Figure 4.4. The results of the ACC2 future mode run – individual radiative forcings

The radiative forcing projections of the ACC2 future mode runs for the six emission scenarios (SRES) are shown in comparison with the corresponding projections in IPCC (2001, Appendix II). The figures for C_4F_{10}, HFC152a, and HFC236fa are presented here for completeness.

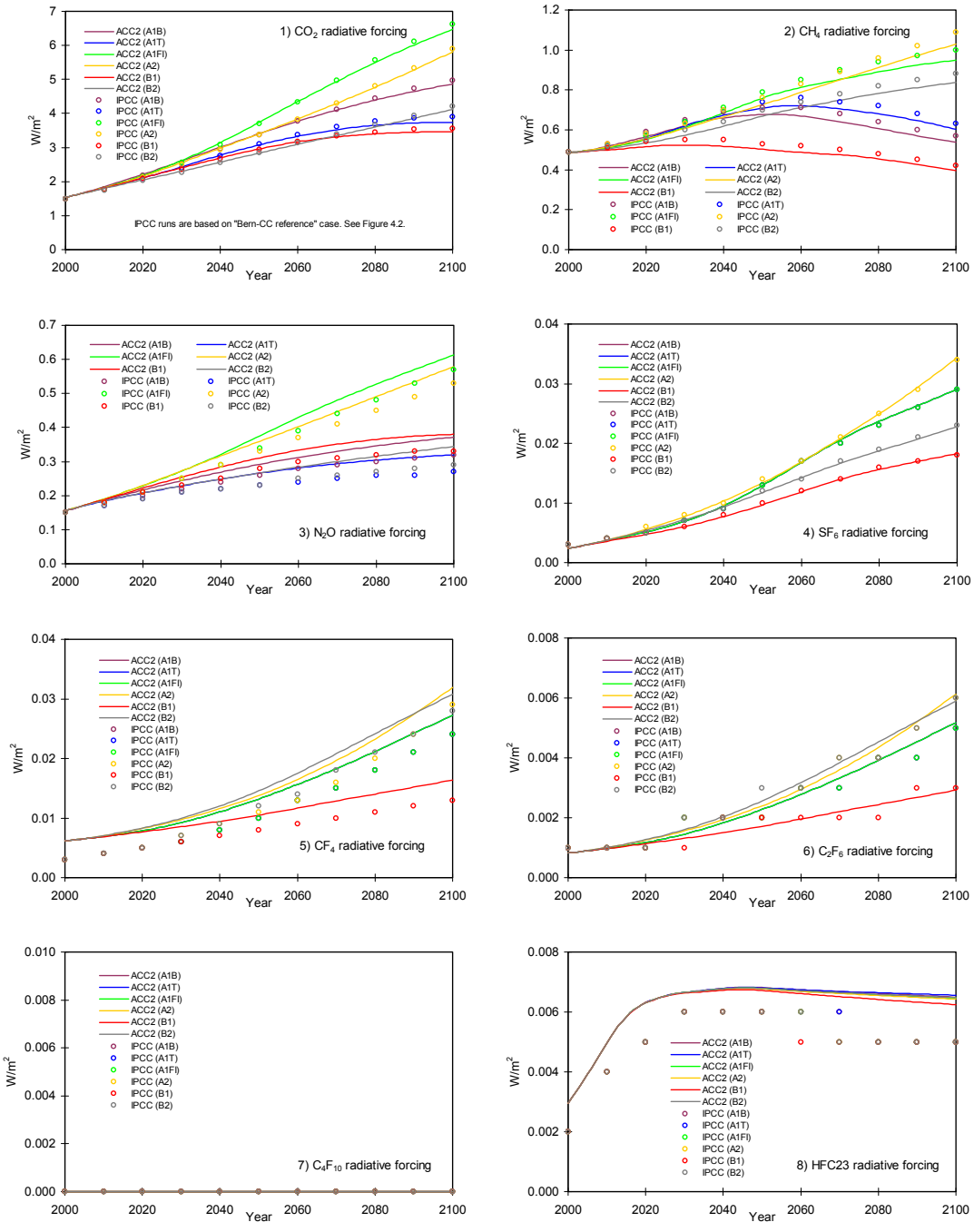

Figure 4.4. (Continued) The results of the ACC2 future mode run – individual radiative forcings

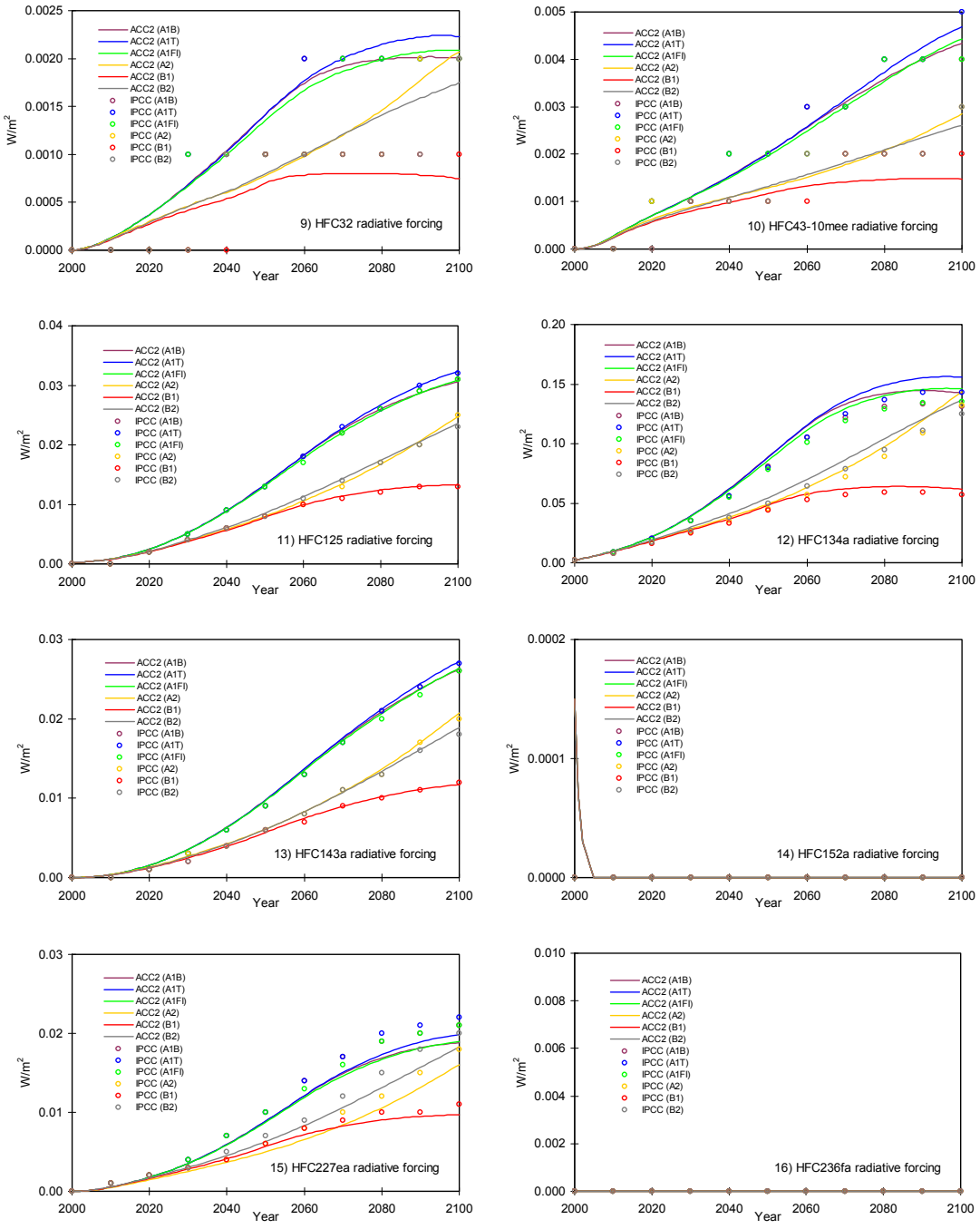

Figure 4.4. (Continued) The results of the ACC2 future mode run – individual radiative forcings

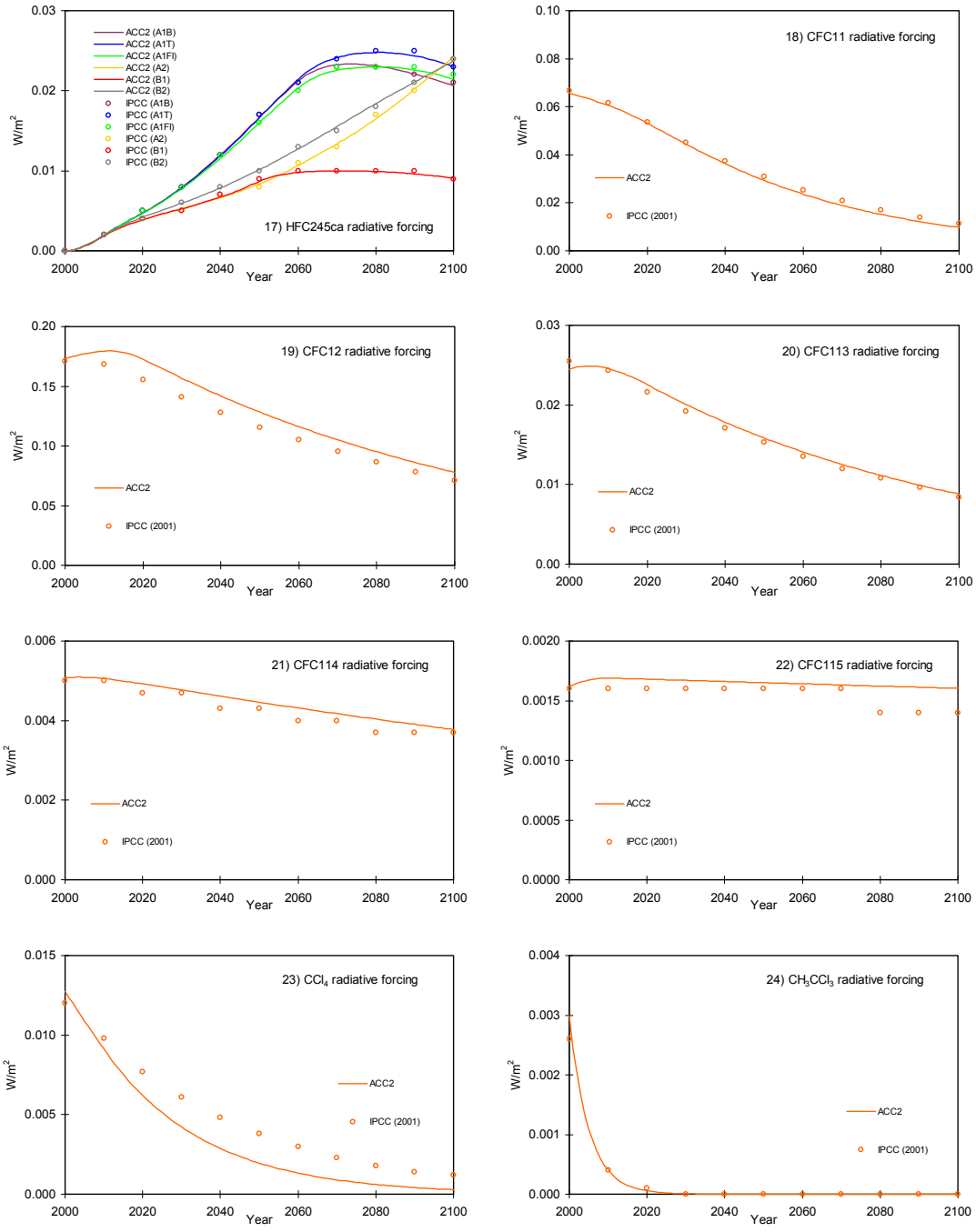

Figure 4.4. (Continued) The results of the ACC2 future mode run – individual radiative forcings

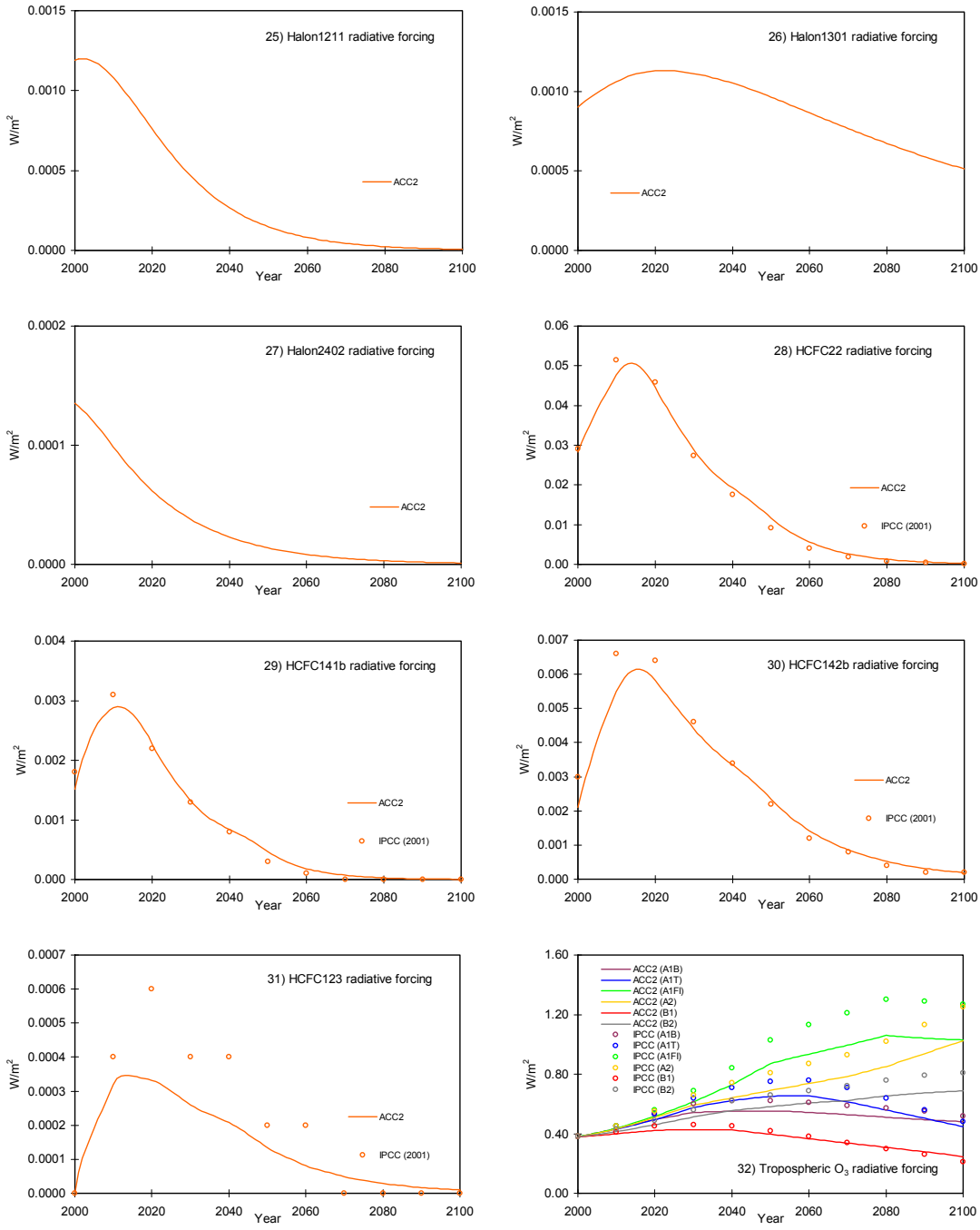

Figure 4.4. (Continued) The results of the ACC2 future mode run – individual radiative forcings

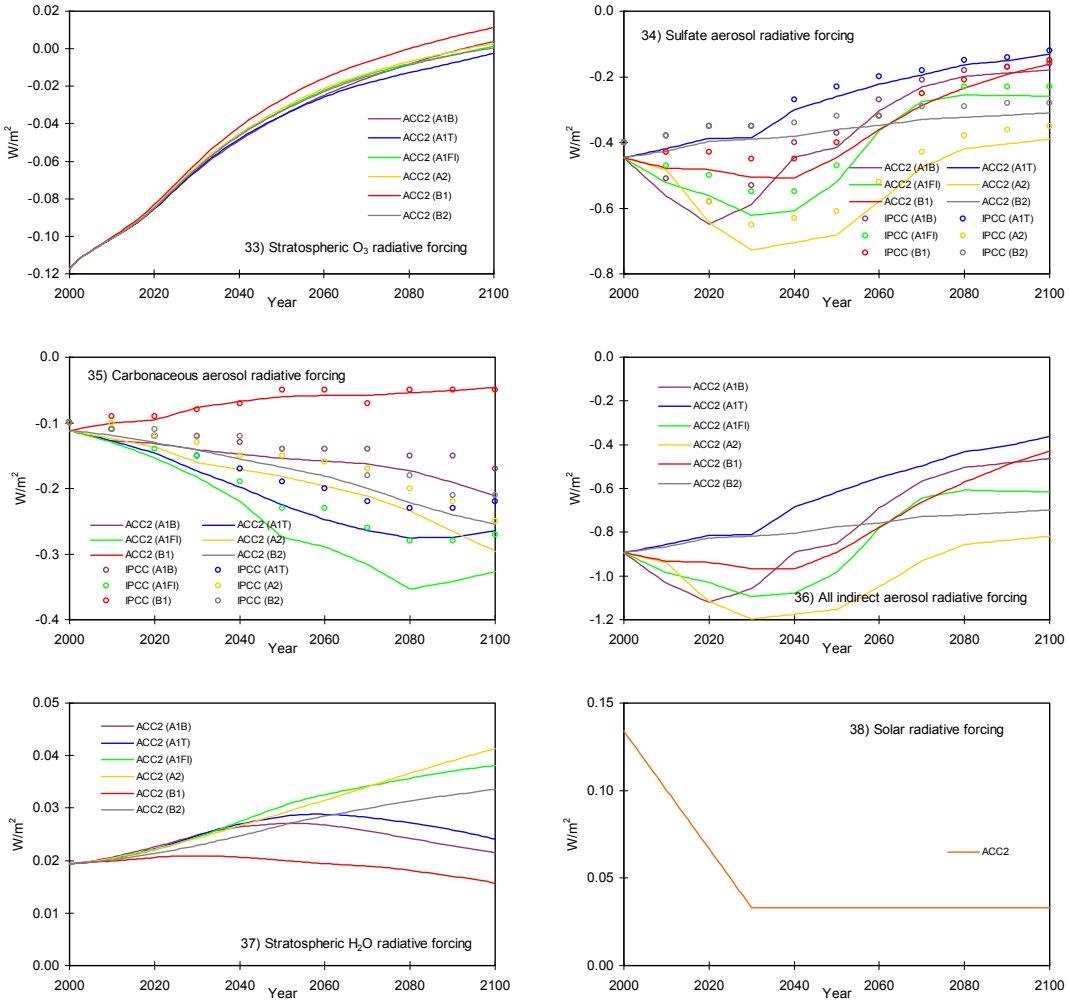

Figure 4.5. The results of the ACC2 future mode run – total radiative forcing and surface air temperature change

The ACC2 projections of the total radiative forcing and global-mean surface air temperature for the six emission scenarios (SRES) are shown in comparison with the corresponding projections in IPCC (2001, Appendix II).

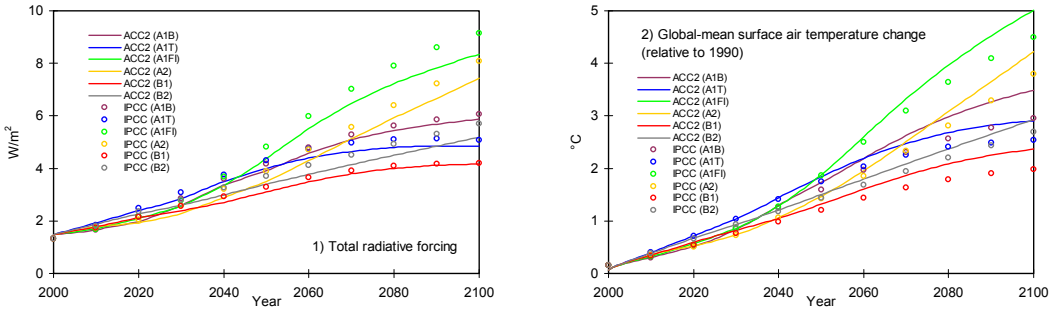

5. IS THE CLIMATE SENSITIVITY EVEN MORE UNCERTAIN? — APPLICATION I

5.1. MAIN TEXT

Uncertainty in climate sensitivity is a fundamental problem for projections of the future climate. Climate sensitivity is defined as the equilibrium response of global-mean surface air temperature to a doubling of the atmospheric CO_2 concentration from the preindustrial level (≈ 280 ppm). In spite of various efforts to estimate its value, climate sensitivity is still not well constrained (IPCC, 2007, pp.718-727 and pp.798-799; Gerard and Baker, 2007), posing a difficulty to informing climate change policy. Here we show that the climate sensitivity is in fact even more uncertain than has been found by earlier studies (Andronova and Schlesinger, 2001; Gregory et al., 2002; Knutti et al., 2002; Forest et al., 2006; Hegerl et al., 2006). Our results suggest that uncertainty in historical radiative forcing has not been sufficiently considered and that including a carbon cycle feedback, which in principle offers an additional constraint on climate sensitivity, does not reduce the uncertainty in climate sensitivity due to the poor knowledge of the global carbon budget before the year 1850.

Atmosphere-Ocean General Circulation Models (AOGCMs) show different climate sensitivity ranging from 1.9°C to 4.6°C (IPCC, 2007, pp.798-799), reflecting our poor understanding of the Earth's radiation budget and the response of the hydrological cycle and the biosphere to climate change.

Climate sensitivity can also be estimated by an inversion approach using historical observations over various periods and time scales. The uncertainties in existing inversion estimates are dominated by uncertainties in reconstructions of historical surface air temperature. Uncertainty in historical radiative forcing has received much less attention. Previous inversion studies express this uncertainty by introducing an additional parameter to scale a presumed time-evolution of the aerosol forcing, with the exception of one study (Hegerl et al., 2006) that also uses different realizations of volcanic and solar forcings. This scaling approach does not fully capture radiative forcing uncertainty, because the influence of its temporal structure on climate may also be relevant for estimating climate sensitivity. Previous inversion studies also have not considered interactions of the climate system with the other aspects of the Earth system (e.g. carbon cycle feedbacks and anthropogenic changes in land albedo), despite the recognized importance of these feedbacks for future climate projections (Cox et al., 2000; IPCC, 2007, p.13).

Here we investigate the effect of radiative forcing uncertainty and carbon cycle feedback on the estimation of climate sensitivity using an inversion setup of the Aggregated Carbon Cycle, Atmospheric Chemistry, and Climate model (ACC2) (Tanaka and Kriegler et al., 2007a) (see Section 5.2.1) for the period 1750-2000. In ACC2, the carbon cycle, atmospheric chemistry, and the climate system are linked via feedbacks and therefore jointly affect the estimation of various uncertain parameters in each of these components (Tables B.1 and B.2).

Radiative forcing is represented as the sum of three types of forcing: calculated radiative forcing subject to uncertainties (CO_2, CH_4, and N_2O forcing), prescribed/parameterized radiative forcing without uncertainties (other GreenHouse Gas (GHG), aerosol, volcanic, and solar forcing), and "missing forcing." This missing forcing term accounts for the uncertainty in the prescribed/parameterized radiative forcing and also represents forcings that are not included in other forcing terms in ACC2 (e.g. albedo forcing and mineral dust forcing). Furthermore, it reflects the interannual and decadal variability in the temperature records (except for the ENSO-induced change after 1930) (Section 3.5.1). Missing forcing is treated as a parameter in each year. Further discussion on missing forcing is found in Section 5.2.3.

We obtain a best estimate of the uncertain parameters corresponding to the minimum of the cost function (equation (5.2.1)), in contrast to previous inversion studies which compute the PDF of climate sensitivity. Calculating a PDF can be done for a problem addressing a small number of uncertainties but is infeasible for our approach, which includes more than one thousand uncertain parameters, including those representing missing forcing.

We conduct two sets of simulations:

1) We compare the standard ACC2 inversion (i.e., expressing radiative forcing uncertainty as missing forcing) with two other ACC2 inversions with alternative representations of radiative forcing uncertainty: one in which, similar to previous studies, it is expressed by an uncertain forcing scaling factor applied to the aerosol forcing, and a second that assumes no forcing uncertainty at all. We do not consider the climate-carbon cycle feedback in these cases in order to focus on the effect of radiative forcing uncertainty.
2) We use the standard radiative forcing representation, but carry out two inversions in which the climate-carbon cycle feedback is either included or not, termed coupled or uncoupled inversion experiment, respectively. For further details, see Section 5.2.4.

For all setups, we calculate the relationship between the cost function and the value of climate sensitivity by performing a series of inversions by which the climate sensitivity is fixed at values between 1°C and 10°C at intervals of 0.25°C. The shape of this relationship indicates both the best estimate of climate sensitivity and the robustness of such an estimate.

Figure 5.1 (unfilled plots) shows these cost function values for the first set of simulations. It indicates that the climate sensitivity is unlikely to be smaller than 2°C, in line with the results of

the PDF studies (e.g. Tol and de Vos, 1998). More importantly, if the forcing uncertainty is fully addressed as missing forcing, the cost function curve is almost completely flat at values of climate sensitivity above about 2°C. In this case, the inversion indicates little preference for any value of climate sensitivity in the range 2°C–10°C. In contrast, if the forcing uncertainty is represented as an uncertain scaling factor applied to a fixed temporal trend of aerosol forcing as in the PDF studies, the climate sensitivity appears far better constrained, particularly at high values. It is even better constrained if the uncertainty in the radiative forcing is not considered at all. Therefore, our analysis suggests that the well-defined peak of the PDF of climate sensitivity in former studies is a consequence of insufficient treatment of radiative forcing uncertainty. Including these uncertainties implies that climate sensitivity is less constrained at the high end than previously thought.

We can draw this conclusion even though our results are not expressed as PDFs as in previous studies. According to probabilistic inverse estimation theory (Tarantola, 2005), our best estimate for climate sensitivity can be interpreted as the *peak* of the marginal posterior PDF with respect to *all the parameters*. The previous studies cited above, on the other hand, present the marginal posterior PDF with respect to *climate sensitivity* (obtained by integrating our marginal posterior PDF with respect to the parameters other than climate sensitivity). Thus, the two approaches reduce the full joint posterior PDF differently. Nevertheless, in our case, differences in the value of the cost function indicate differences in relative likelihood because the cost function changes monotonically with respect to parameters (Figure B.14). In other words, cost function curves are qualitatively comparable to PDFs.

More in detail, Figure 5.2 presents radiative forcing and temperature time series resulting from missing forcing-based and forcing scaling-based inversions. Figure 5.2.1 shows that low climate sensitivity is not supported even with the missing forcing approach because of the difficulty in explaining the warming in the late 20th century. On the other hand, Figure 5.2.2 demonstrates that high climate sensitivity is acceptable with the missing forcing approach but not with the forcing scaling approach because the forcing scaling approach results in excessively strong cooling after large volcanic eruptions in the 19th century. Such results indicate that the forcing scaling approach is too inflexible to deal with the complexity in forcing uncertainty.

If considering temperature and radiative forcing is insufficient to constrain climate sensitivity, including feedbacks with other Earth system components in the inversion may provide an upper limit on its value, a possibility addressed by the second set of simulations.

The cost function curves of the coupled and uncoupled inversions are both nearly flat at high values of climate sensitivity (two lower curves in Figure 5.1). So, despite the addition of climate-carbon cycle feedback, our optimization still almost equally accepts a wide range of high climate sensitivity.

This result can be explained by examining the relative contributions of different sources of

uncertainty to the cost function (Figure 5.3). Almost all sources display the same flat shape toward high climate sensitivity, with two exceptions: missing forcing in both coupled and uncoupled cases, which has a distinct minimum at a climate sensitivity of 2.5–3.0°C, and land use CO_2 emissions in the coupled case, which decreases monotonically toward high climate sensitivity. Thus, Figure 5.3 suggests that in the uncoupled case, the robustness of the climate sensitivity estimate is low because about 80% of the cost function is derived from variables that do not contribute to discriminating among higher values of climate sensitivity. In the coupled case, the robustness of the climate sensitivity estimate is even slightly lower because, although the missing forcing and land use emission terms do discriminate among climate sensitivity values to some extent, they act in opposite directions.

Based on the inspection on the coupled inversion results (Figure 5.4), the robustness of climate sensitivity estimation is not improved by the coupling as a consequence of poor data quality before 1850. In the early 19th century, the atmospheric CO_2 concentration stabilized (Figure 5.4.2) due to the suppression of heterotrophic respiration at the low surface temperatures caused by large volcanic eruptions. The episodic net increase in the land CO_2 uptake following volcanic eruptions (Figure 5.4.3) is smaller with lower climate sensitivity. With low climate sensitivity, in order to curb the rise in the atmospheric CO_2 concentration, the land use CO_2 emission is reduced more, resulting in a larger cost function value.

The key to this result is the prior estimate of land use CO_2 emissions for the first 100 years of the inversion, which is highly uncertain – the prior (Houghton, 2003) is linearly extrapolated to zero from the year 1850 to 1750. Other relevant data such as volcanic forcing and temperature reconstruction are also uncertain. An improvement of data quality before 1850 would be necessary to improve the effectiveness of climate sensitivity estimation with a coupled model.

We have not discussed ocean CO_2 uptake as it turned out to be nearly insensitive to the temperature change in our simulations (Figure B.1). Also we have not discussed the atmospheric chemistry component because no temperature feedbacks to the atmospheric chemistry processes are included in the model and it therefore did not affect the results of our analysis. We assume a fixed estimate for the vertical ocean heat diffusivity because constraining the ocean diffusivity requires oceanic heat diffusion processes, which are not explicitly modelled in ACC2. Our estimate of the prior range for missing forcing is also uncertain, but the sensitivity analysis in Section B.3 demonstrates that our overall conclusions hold under various possible assumptions. Our methodology uses independent assumptions for parameters and data (Section 5.2.2). Thus, the 'true' inversion solution lies somewhere between the missing forcing-based results and forcing scaling-based results. Our results are based on only one temperature reconstruction (Jones et al., 1998; Mann and Jones, 2003) as our emphasis lies in considering radiative forcing uncertainty.

Further analysis lies ahead to understand the Earth system inversion results from the

perspectives of other parameters. The question still remains as to how to appropriately represent the forcing uncertainty, although it may ultimately depend on the specific research question. The idea of using the carbon cycle for climate sensitivity estimation and, moreover, of considering additional information for uncertainty estimation (e.g. isotopic data) should still be pursued, as the interplay among the uncertainty estimates in the carbon cycle and climate systems is observed. The spirit of constraining uncertainties in the Earth system should be maintained toward a holistic uncertainty analysis using an Earth system model with more complexity.

5.2. METHODS

5.2.1. Model

We use ACC2, a global-annual-mean Earth system model comprising carbon cycle, atmospheric chemistry, and climate components. The ocean and land carbon cycle processes are represented by the respective four-reservoir box models tuned to the Impulse Response Function models (Hooss et al., 2001; Joos et al., 1996). Thermodynamic equilibria for marine carbonate species ($CO_2(aq)$, HCO_3^-, and CO_3^{2-}) are dynamically computed and are sensitive to the mixed layer temperature, providing temperature effect on ocean CO_2 uptake. The temperature sensitivity of large scale ocean circulation is not accounted for, which is acceptable on the time scale of our model projections. CO_2 fertilization for Net Primary Production and temperature-dependency of heterotrophic respiration are parameterized with the beta factor and Q10, respectively. ACC2 incorporates parameterizations of atmospheric chemistry processes (Joos et al., 2001; WMO, 2003; IPCC, 2005) involving direct radiative forcing agents (CO_2, CH_4, N_2O, O_3, SF_6, 29 species of halocarbons, sulfate aerosols (direct effect), carbonaceous aerosols (direct effect), all aerosols (indirect effect), and stratospheric H_2O) and indirect radiative forcing agents (OH, NO_x, CO, and VOC), including feedbacks of CH_4 and N_2O concentrations on their lifetimes. Volcanic (Ammann et al., 2003) and solar (Krivova et al., 2007) forcings are prescribed. Calculation of the surface air temperature is based on the Diffusion Ocean Energy balance CLIMate model (DOECLIM) (Kriegler, 2005), a land-ocean energy balance model. Note that ACC2 version 3.1 (this thesis) that we use in this paper slightly differs from ACC2 version 3.0 (Tanaka and Kriegler et al., 2007a) mainly in its treatment of Q10. Differences in the inversion results are not significant.

5.2.2. Inversion

The ACC2 inversion derives a best estimate of major uncertain parameters by synthesizing various knowledge on the Earth system including parameter estimates, observations, and physical-biogeochemical laws on the basis of the probabilistic inverse estimation theory (Tarantola,

2005). The parameters and data used in the ACC2 inversion are summarized in Tables B.1 and B.2. We assume normal distributions for all the prior uncertainties of the parameters and data.

Our approach is concerned with only the single estimates obtained by optimization, corresponding to the minimum of the cost function $S(\mathbf{m})$ as follows:

$$S(\mathbf{m}) = \frac{1}{2}\left(\sum_{i=1}^{a} \left(\frac{g_i(\mathbf{m}) - d_{mes,i}}{\sigma_{d,i}} \right)^2 + \sum_{j=1}^{b} \left(\frac{m_j - m_{prior,j}}{\sigma_{m,j}} \right)^2 \right) \tag{5.2.1}$$

$g_i(\mathbf{m})$ is the forward model projection for data i based on a set of parameter $\mathbf{m}$. a and b are the total numbers of data and parameters, respectively. $d_{mes,i}$ and $m_{prior,j}$ denote measurement i and prior estimate of parameter j, respectively. $\sigma_{d,i}$ and $\sigma_{m,j}$ are one-sigma uncertainty ranges for measurement i and for prior estimate of parameter j, respectively. In the framework of the probabilistic inverse estimation theory, the cost function is the negative of the argument of the exponential function expressing the marginal posterior PDF for all the parameters.

It should be noted that all the parameters and data in the ACC2 inversions are treated independently, implying that fits for time series having strong autocorrelations are over-emphasized. Using AR models would only partially account for the autocorrelations because of their complexity. There is a theoretical problem in estimating an AR propagator in the context of inverse estimation (Section B.8). A full solution would be to introduce stochasticity to the model as model errors (Houtekamer et al., 1996) and the ensemble results can be used to estimate the off-diagonal elements of the covariance matrices.

Inverse calculations are performed using the local optimization solver CONOPT3 implemented in GAMS. The solutions for inversions are confirmed by performing the same inversions from different initial points.

Inversions are performed from the year 1750 to 2000. Although the system is not completely equilibrated due to various natural forcings and internal dynamics, we made a steady-state assumption in 1750 on the ground that the energy-intensive machinery, the key driver for the global warming, emerged in the early 18th century and also that the land use CO_2 emission has already been substantial in magnitude by mid 19th century.

5.2.3. Missing Forcing

The prior estimate of the missing forcing is assumed to be 0.0 W/m^2 throughout the inversion period. The 2σ prior uncertainty range is assumed to be constant at 0.5 W/m^2 before 1900 primarily to explain the natural variability in the temperature (rationales explained below). Then the uncertainty range increases linearly to 1.0 W/m^2 in 2000 to account mainly for the uncertainty in the aerosol forcing, which is consistent with the corresponding IPCC range (IPCC, 2007, Figure SPM.2). The prior uncertainty range of the missing forcing is assumed to be larger by four-fold when volcanic

forcing is stronger than -0.5 W/m^2 in consideration of associated processes not resolved in the model (Section 3.5.2).

Below are the rationales for the 2σ prior missing forcing range before 1900 (±0.5 W/m^2). Our model simulations indicate that a constant radiative forcing of at least 0.5 W/m^2 is required to produce a temperature rise of 0.5°C on a decadal time scale with various climate sensitivity (Figure B.5). We assume that natural variability of the global-mean temperature is at most 0.5°C, based on the followings: 1) The global-mean surface temperature has risen about 0.5°C in the first half of the 20th century. It can be assumed that this was caused by natural variability as attribution/detection studies have so far not agreed upon whether such warming was due to natural variability or anthropogenic interference. 2) The temperature projection in the 1000-year control run of Community Climate System Model (CSM-1.4) (a coupled GCM) indicates a temperature variability of about 0.5°C (Doney et al., 2006).

5.2.4. Coupled/Uncoupled Inversion Setup

The coupled inversion experiment uses the standard inversion setup, where the climate component is fully coupled with the ocean and land carbon cycle components, so that the feedback between these Earth system components is fully accounted for. More specifically, in ACC2 this feedback is acting via the following two loops: a) Thermodynamic equilibria for the marine carbonate species ($CO_2(aq)$, HCO_3^-, and CO_3^{2-}) depend on the ocean mixed layer temperature (linearly related to the ocean surface air temperature), which in turn controls the CO_2 uptake from the atmosphere, thereby influences indirectly the ocean surface air temperature. b) The land surface air temperature influences heterotrophic respiration of the soil, and thus the land CO_2 flux to the atmosphere, thereby indirectly feeding back on the land surface air temperature. In the second experiment, uncoupled inversion experiment, this climate-carbon cycle feedback has been suppressed, by setting artificially the temperature as seen by ocean and land carbon cycle fixed to its preindustrial value. CO_2 exchange between the three compartments atmosphere, ocean, and land is thus uncoupled from changes in surface air temperature in this second type of experiment.

Figure 5.1. Cost function in the ACC2 inversions under different treatments to radiative forcing uncertainty and climate-carbon cycle feedback

Final values of the cost function are computed by optimizations with climate sensitivity fixed at values between 1°C and 10°C at intervals of 0.25°C. Each plot represents a unique inversion result. In square brackets, best estimates of climate sensitivity are shown.

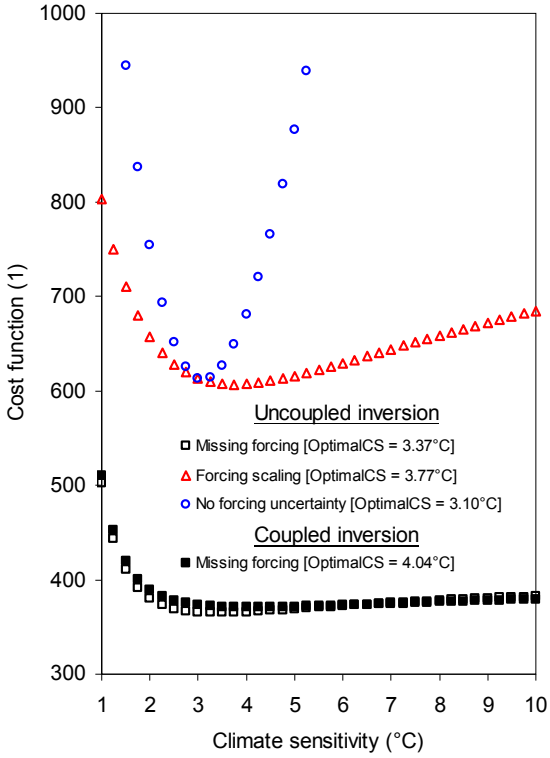

Figure 5.2. ACC2 uncoupled inversion results for the climate component (missing forcing- and forcing scaling-approach)

Below are obtained from the inversions using the missing forcing- and forcing scaling-approach with climate sensitivity of 1, 3, 5, and 10°C. The prior missing forcing is 0 W/m^2 over the entire period. The forcing scaling factor is estimated to be 0.045, 0.999, 1.214, and 1.398 in the forcing scaling-based inversions with climate sensitivity of 1, 3, 5, and 10°C, respectively. Insert of Figure 5.2.2 shows the "residuals," i.e. the difference between prior and posterior values. The residuals are calculated by vertically shifting the measurements such that their average during the period 1961-1990 is equal to the corresponding posterior average. Measurements shown are for the missing forcing-based inversion with climate sensitivity of 3°C. Note that the prior uncertainty ranges for the missing forcing and temperature change are assumed four times larger when volcanic forcing is stronger than -0.5 W/m^2.

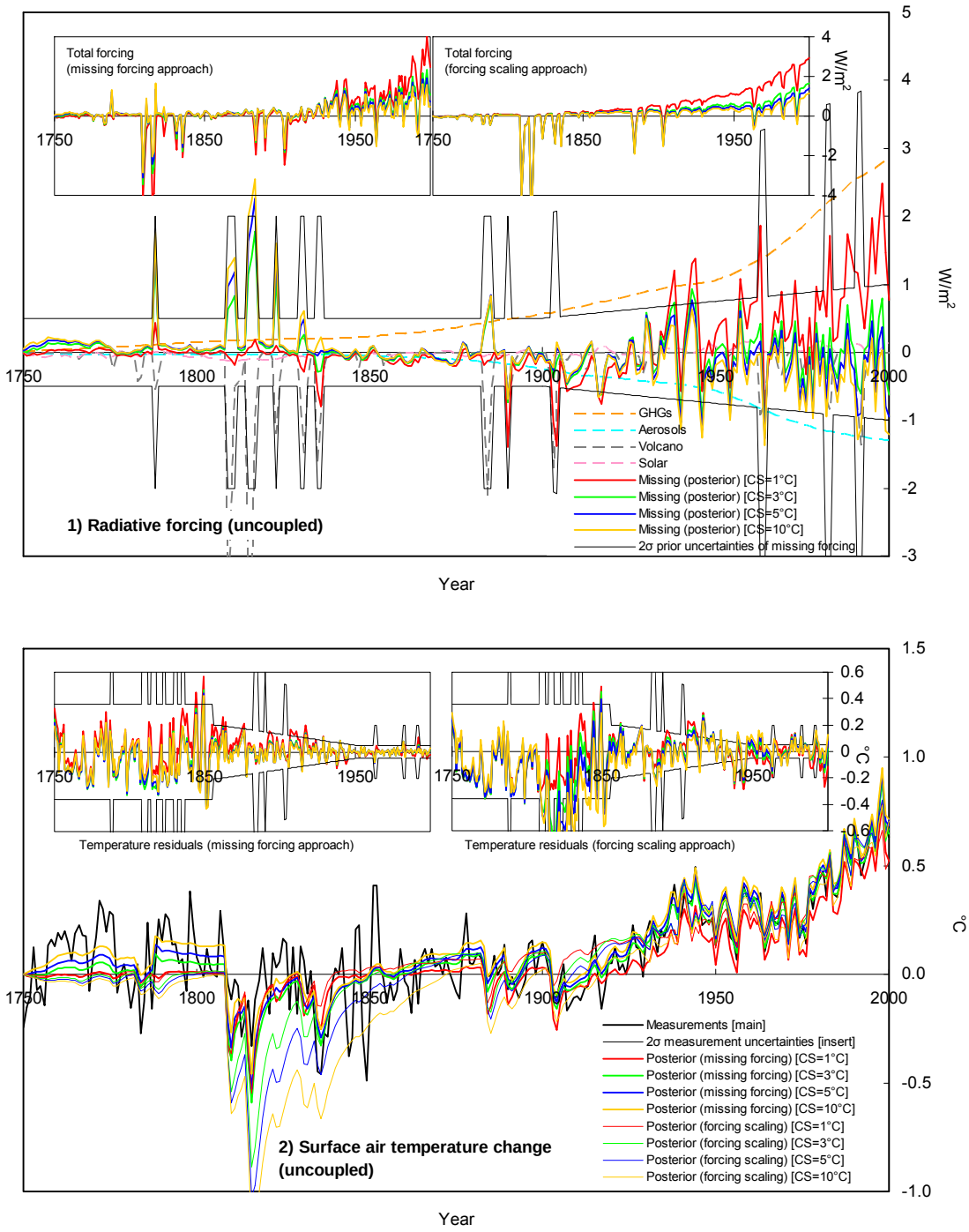

Figure 5.3. Squared weighted residuals in the coupled and uncoupled ACC2 inversions

Squared weighted residuals shown below are the temporal sum of the squares of the residuals weighted by the associated prior uncertainties (σ). They are obtained from the inversions with climate sensitivity fixed at values between 1°C and 10°C at intervals of 0.25°C. Each plot represents a unique inversion result.

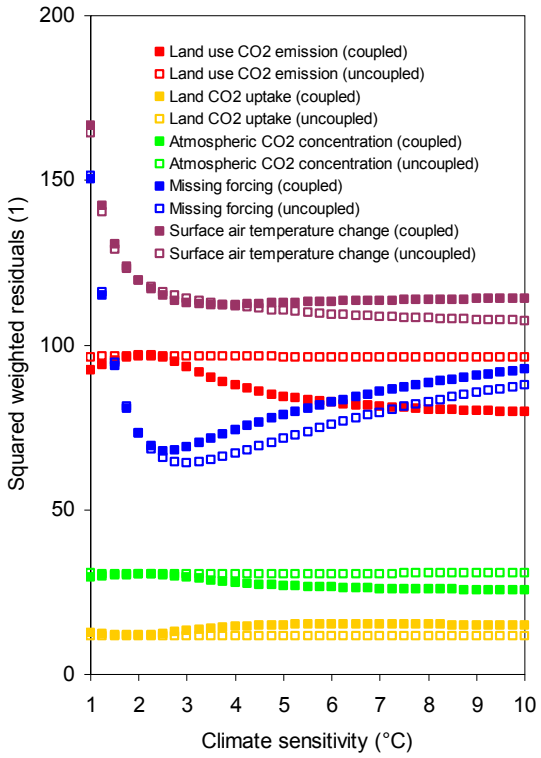

Figure 5.4. ACC2 coupled and uncoupled inversion results for the carbon cycle component

Shown below are the coupled and uncoupled inversion results for optimal climate sensitivity (4.04°C and 3.37°C, respectively). Note that the prior uncertainty range for the atmospheric CO_2 concentration is assumed four times larger when volcanic forcing is stronger than -0.5 W/m^2.

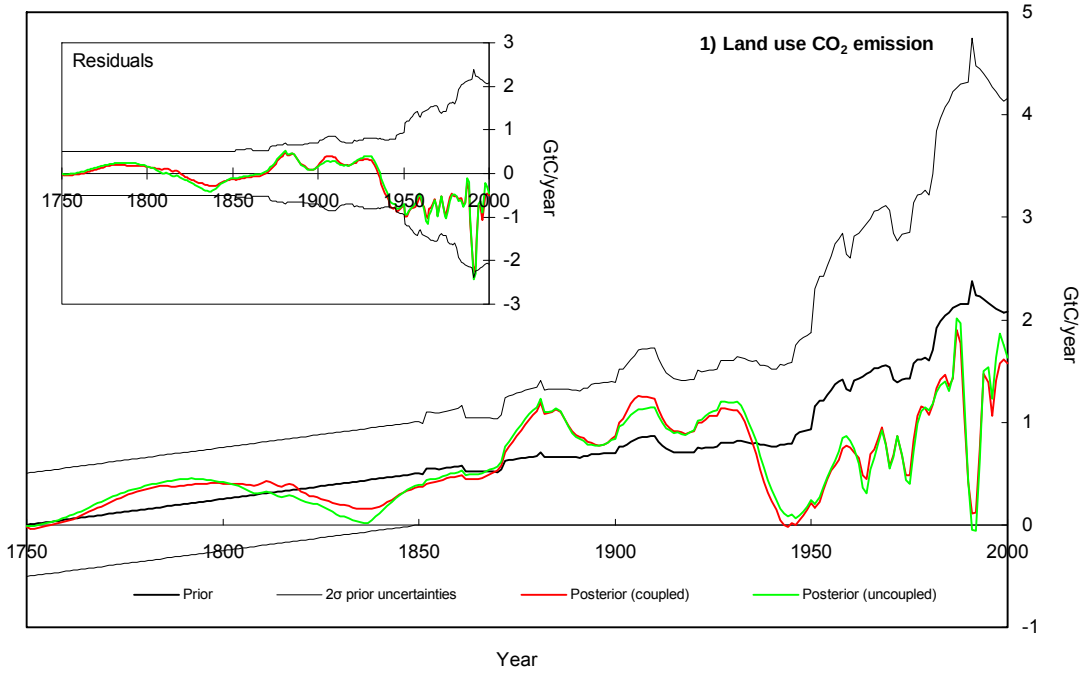

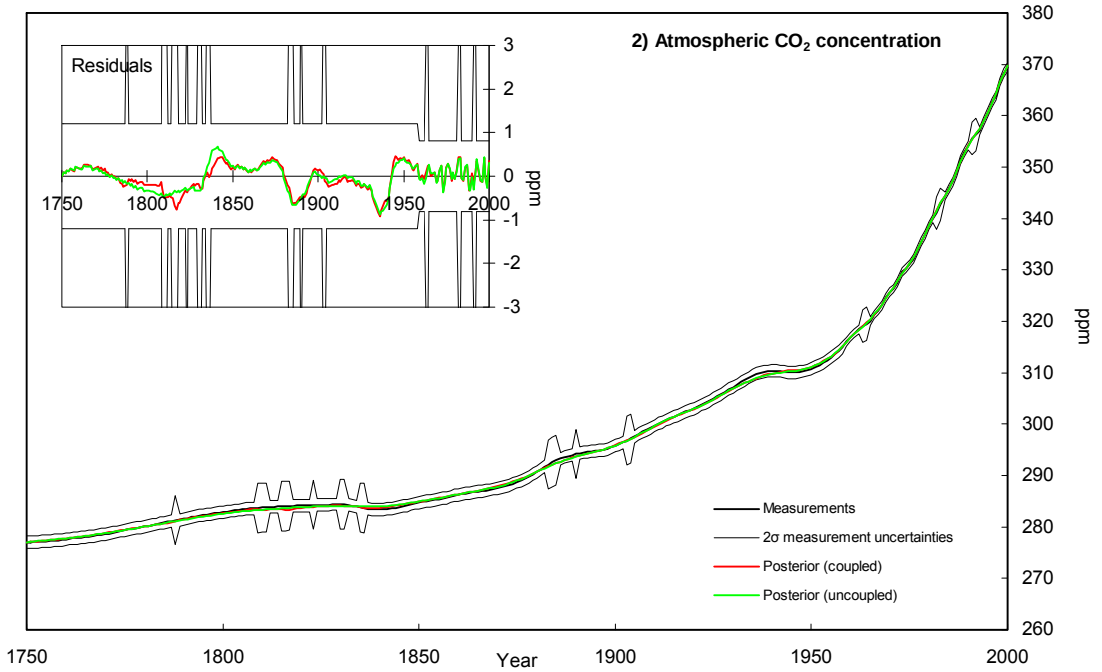

Figure 5.4. (Continued) ACC2 coupled and uncoupled inversion results for the carbon cycle component

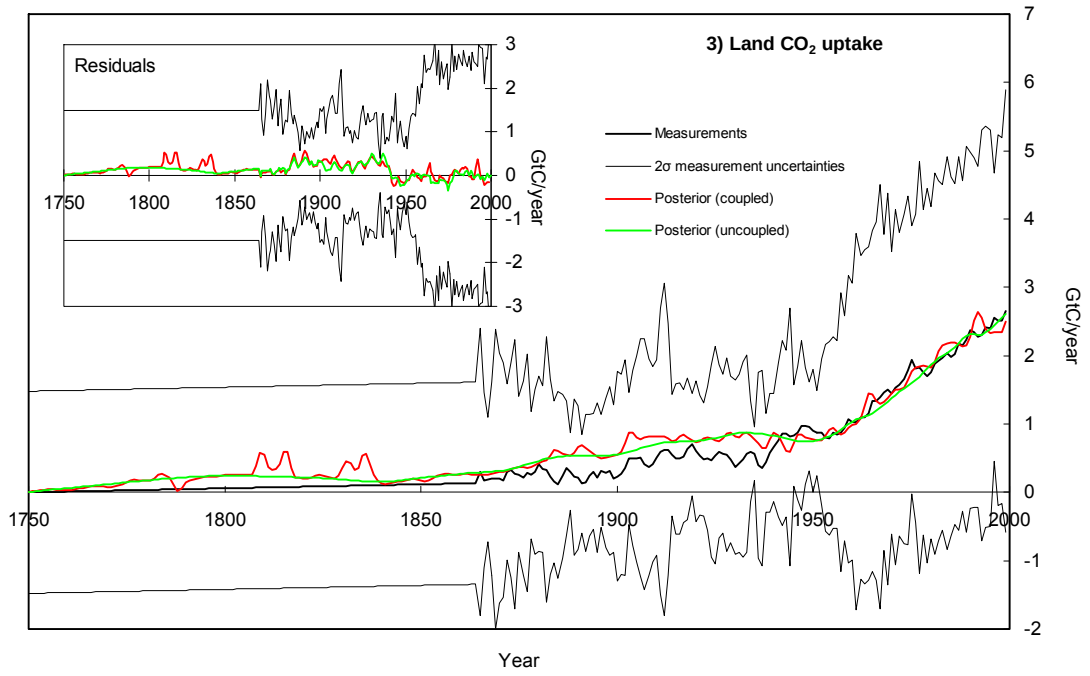

6. EVALUATING GLOBAL WARMING POTENTIALS — APPLICATION II

6.1. INTRODUCTION

Global climate change during the Anthropocene (Crutzen, 2002) is largely triggered by the human-driven perturbation of the atmospheric composition of various radiative agents. These agents have different physical and biogeochemical properties, interfering with the Earth system distinctively. Due to the complexities and uncertainties in the Earth system processes, finding a common ground to compare different GreenHouse Gas (GHG) emissions is a challenging task. As a simple measure, the concept of Global Warming Potentials (GWPs) has been introduced. The GWP of a particular GHG is defined as the ratio of the integrated radiative forcing of the GHG over a time horizon to that of CO_2 after their instantaneous releases to the atmosphere in the amounts of 1 kg (IPCC, 1990). GWPs are used to convert the emissions of non-CO_2 GHGs to 'equivalent' CO_2 emissions, allowing policy-makers to consider and compare multiple options for GHG emission reduction.

However, since the conception of GWPs, they have been a subject of dispute in the research community (Fuglestvedt et al., 2003). One fundamental shortcoming in the concept of GWPs is the arbitrariness in the length of the time horizon over which to integrate the radiative forcings. Time horizons of 20, 100, and 500 years are representatively used in Table 6.7 of IPCC (2001).[68] A time horizon of 100 years is selected for the GWPs implemented in the Kyoto Protocol without any clear scientific argumentation. Generally, for a GHG with a lifetime shorter than that of CO_2, the GWP will be larger for shorter time horizons, although this comparison is complicated by the range of timescales with which CO_2 is removed (O'Neill et al., 1997). Figures 6.1a-b show the GWPs of CH_4 and N_2O for time horizons of 0-500 years, calculated using the lifetimes and other parameter values given in Table 6.1. Various alternatives to GWPs have been proposed (Fuglestvedt et al., 2003; Shine et al., 2005). However, no general consensus has been reached yet among researchers as to which metrics should replace the GWPs in spite of the urgent need for the post-Kyoto regime.

There are natural science-oriented and economics-oriented interpretations to GWPs (Fuglestvedt et al., 2003). Although theoretically under idealized conditions the two coincide (O'Neill, 2003), in practice different evaluation methodologies result in different conclusions. From

[68] We evaluate the GWPs shown in IPCC (2001, Table 6.7). The values of GWPs have been slightly changed in IPCC (2007, Table 2.14) because a different CO_2 response function has been employed. However, these changes are minor and there would be no change in our conclusions.

a natural science perspective, GWPs are an instrument designed to compare the relative effects on climate of various GHGs (Wigley, 1998; O'Neill, 2000; Smith and Wigley, 2000; Smith, 2003; Shine et al., 2005) while, from an economic perspective, GWPs are an instrument to weight GHG emissions to achieve optimal mitigation either in a cost-effectiveness framework (Reilly et al., 1999; Manne and Richels, 2001; Godal and Fuglestvedt, 2002; Johansson et al., 2006) or a cost-benefit framework (Eckaus, 1992; Reilly and Richards, 1993; Schmalensee, 1993; Fankhauser, 1995; Kandlikar, 1996; Tol, 1999). Our study takes the natural science approach without exploring economic implications.

Here we evaluate GWPs as a proxy for the historical surface air temperature. Our study is the first to apply GWPs to historical data. GWPs by concept aim to be applied to future scenarios and have been tested only within the context of modeled futures. However, it is worth investigating the performance of GWPs for the one available "real" scenario – namely, past history. Such a test may help improve our understanding of how well GWPs work and under what circumstances.
This test leads us to propose a new metric, TEMperature Proxy index (TEMP) which is designed to reproduce optimally the historical temperature change, and we compare its behavior to that of GWPs.

A factor hampering the application of GWPs or other indices to historical data is the mismatch among the estimates of the GHG emissions, their concentrations, and the surface air temperature when the associated dynamic relationships are considered. This problem can be solved by adopting the inversion results for the Aggregated Carbon Cycle, Atmospheric Cycle, and Climate Model (ACC2) (Tanaka and Kriegler et al., 2007a) that provide a best guess for the historical Earth system evolution since 1750 by considering the associated uncertainties. In fact, it is the crucial novel aspect of the ACC2 methodology to perform an inversion for the interactive carbon cycle, atmospheric chemistry, and climate system *albeit* at a global-and-annual-mean level. Currently inversions for more complex Earth system models are not operational because of the prohibitively expensive computation requirements.

The next section summarizes the ACC2 model and its inversion to be used as a base for the GWP evaluations. In Section 6.3, we evaluate the IPCC GWPs for CH_4 and N_2O as historical temperature proxies. In Section 6.4, we propose TEMP and evaluate it relative to GWPs. To better understand the evaluation results, the influences of the key assumptions in the IPCC GWP calculations are investigated in Section 6.5. The conclusions are summarized in Section 6.6.

6.2. MODEL AND ITS INVERSION

6.2.1. The Model ACC2

ACC2 is developed for first-order understanding of the interactions in the Earth system processes and uncertainties on a global-and-annual-mean basis. ACC2 calculates the concentrations of various GHGs, their radiative forcings, and the surface air temperature as a consequence of the emissions of GHGs and relevant agents. ACC2 version 3.1 (this thesis) is used in this study.[69] The origins of ACC2 are traced back to the Nonlinear Impulse-response representation of the coupled Carbon cycle-Climate System (NICCS) (Hooss, 2001; Hooss et al., 2001) and the ICLIPS Climate Model (ICM) (Bruckner et al., 2003).

The functional relationships and physical and biogeochemical constants in ACC2 (Tables 2.1 and 2.2) are mostly consistent with IPCC (2001), WMO (2003), IPCC (2005), and other recent literature. No major updates are necessary according to IPCC (2007). Each of the ocean and land CO_2 uptake is represented by a four-reservoir box model tuned to the respective impulse response functions (Maier-Reimer and Hasselmann, 1987; Hooss, 2001; Joos et al., 1996). Saturation in the ocean CO_2 uptake with rising CO_2 concentration is modelled by calculating dynamically the thermodynamic equilibria of the marine carbonate species ($CO_2(aq)$, HCO_3^-, and CO_3^{2-}). The temperature feedback to ocean CO_2 uptake is provided with the equilibrium constants for marine carbonate species that are given as functions of the seawater temperature (Millero, 1995; Millero et al., 2006). The CO_2 fertilization of the terrestrial biosphere is parameterized by the beta factor (Gifford, 1980; Friedlingstein et al., 1995), which logarithmically scales the preindustrial Net Primary Production (NPP) with the fractional increase in the atmospheric CO_2 concentration. The temperature feedback to the land CO_2 uptake is modeled with a Q10 parameter, which indicates how much the rate of terrestrial respiration increases with a temperature increase of 10°C. ACC2 incorporates the parameterizations of atmospheric chemistry processes involving direct radiative forcing agents (CO_2, CH_4, N_2O, SF_6, 29 species of halocarbons, tropospheric and stratospheric O_3, and stratospheric water vapor) and indirect radiative forcing agents (OH, NO_x, CO, and VOC) (Joos et al., 2001), including the feedbacks of the CH_4 and N_2O concentrations to their lifetimes. The radiative forcings of the individual agents are calculated by the respective parameterizations. The saturations and overlaps of the CH_4 and N_2O absorption bands change with the CH_4 and N_2O concentrations, affecting the CH_4 and N_2O radiative forcing. The radiative forcings due to various aerosols are reduced to the following three types: the direct effect of sulfate aerosols, the direct effect

[69] ACC2 version 3.1 (this thesis) differs from ACC2 version 3.0 (Tanaka and Kriegler et al., 2007a) in their treatments of Q10. ACC2 version 3.1 assumes a constant Q10 value whereas ACC2 version 3.0 adopts the temperature dependency of the Q10 value (Tjoelker et al., 2001). Changes in the inversion results are not significant.

of carbonaceous aerosols (black carbon and organic carbon), and the indirect effect of all aerosols (involving cloud processes). The total radiative forcing is used to calculate the surface air temperature by the Diffusion Ocean Energy balance CLIMate model (DOECLIM) (Kriegler, 2005), a land-ocean energy balance model.

6.2.2. Inversion for ACC2

In the inverse estimation for ACC2, various geophysical observational databases and functional relationships of the Earth system processes including the associated uncertainties are synthesized based on the probabilistic inverse estimation theory (Tarantola, 2005). Parameters in the inverse calculation include the annual CO_2, CH_4, and N_2O emissions, the beta factor, the CH_4 and N_2O lifetimes, the climate sensitivity, and more (Table 3.2). Data in the inverse calculation are annual time series of the atmospheric CO_2, CH_4, and N_2O concentrations, the ocean and land CO_2 uptake, and the surface air temperature (Table 3.1). The GHG forcing and the aerosol forcing are based on model calculation, and the volcanic forcing (Ammann et al., 2003) and the solar forcing (Krivova et al., 2007) are prescribed to the model. The types of radiative forcings that are not explicitly represented in ACC2 (e.g. albedo forcing) are lumped together and represented as the "missing forcing." The missing forcing has a degree of freedom in every year and is treated as parameters. The uncertainties in the GHGs, aerosol, volcanic, and solar forcings are also contained in the missing forcing term. Gaussian distributions are assumed for all the prior parameter and measurement uncertainties. Our inversion setup produces particular posterior estimates of the parameters and the data corresponding to the minimum of the cost function and does not provide associated posterior probability distributions. Numerically, we optimize the parameter values to minimize the following cost function:

$$S(\mathbf{m}) = \frac{1}{2}\left(\sum_{i=1}^{a} \left(\frac{g_i(\mathbf{m}) - d_{mes,i}}{\sigma_{d,i}} \right)^2 + \sum_{j=1}^{b} \left(\frac{m_j - m_{prior,j}}{\sigma_{m,j}} \right)^2 \right). \qquad (1)$$

$g_i(\mathbf{m})$ is the forward model projection for data i based on a set of parameter $\mathbf{m}$. a and b are the total numbers of data and parameters, respectively. $d_{mes,i}$ and $m_{prior,j}$ denote measurement and prior estimate of parameter j, respectively. $\sigma_{d,i}$ and $\sigma_{m,j}$ are one-sigma uncertainty ranges for measurement i and for prior estimate of parameter j, respectively. Note that all of the errors in the parameters and the data are treated independently. The optimization is performed using CONOPT3 in GAMS (Rev 148).

The inverse calculation results are shown in Figures 6.2a-e. The posterior estimates of the CH_4 and N_2O concentrations turned out to be almost identical to the corresponding measurements because of the adjustments in the CH_4 and N_2O emissions that have much larger prior uncertainties. The full inversion results are shown and discussed in Section 4. All in all, the ACC2 inversion

generated a best guess of the historical Earth system evolution from the year 1750 to 2000, which we use as the basis for the GWP evaluation in the following sections.

6.3. EVALUATION OF GWPS

We take the Earth system evolution obtained from the ACC2 inversion as our 'baseline.' We replace the baseline anthropogenic CH_4 and N_2O emissions (separately) with their equivalent CO_2 emissions using GWPs as conversion coefficients. Then, by fixing all the other parameter values at the respective baseline levels, we calculate the surface air temperature and compare with the baseline temperature. We use temperature to compare outcomes, although results are similar for radiative forcing, a measure closer to the GWP definition, which can be inferred from the results in Appendix A.1. The GWP-based emission conversions are applied beginning in 1890, the earliest year in which estimates of the anthropogenic CH_4 and N_2O emissions are available (van Aardenne et al., 2001). Even if we apply the GHG conversion from a later start year, the overall results hold (as can be inferred from Appendix A.2). We deal with only CH_4 and N_2O in this paper as CH_4 and N_2O are distinct GHGs in terms of their lifetimes and feedbacks, from which the essence of this paper can be derived. Testing for HFCs, which currently account for a significant share of the Clean Development Mechanism (CDM) market, would be an extension of our study.

Figure 6.3a shows the temperature projections when the CH_4 emissions are converted to equivalent CO_2 emissions based on the IPCC GWPs with the 20-, 100-, and 500-year time horizons. In all three cases, the temperature projection is not well reproduced and the deviations are up to 0.30°C in the year 2000. In particular, the temperature projection using the 100-year CH_4 GWP is lower than the baseline temperature projection by 0.13°C, suggesting that a GWP with a shorter time would perform better. This is qualitatively in line with the results of Smith and Wigley (2000), who demonstrate that the 100-year time horizon is too long for CH_4 GWP in a more idealized setting. Also in the case of N_2O (Figure 6.3b), the three IPCC GWPs do not reproduce the historical temperature, leaving a deviation of up to 0.05°C in the year 2000. The temperature projection using the 100-year N_2O GWP underestimates the baseline by 0.012°C. The deviations are larger in the CH_4 experiment than in the N_2O experiment because the CH_4 radiative forcing is larger and also because the CH_4 GWP is more sensitive to the time horizon due to its short lifetime (Figures 6.1a-b). Although the absolute temperature deviations for the N_2O GWP are small, they are important because N_2O is currently the second most important non-CO_2 GHG with respect to radiative forcing. The results of the IPCC GWP evaluations suggest that in the context of the historical scenario, non-CO_2 gases should be valued more than they currently are by the 100-year GWPs.

Could it be that the baseline temperature projections are not reproduced well with GWPs because we use three arbitrary time horizons? To find out, we optimized the time horizon for CH_4

and N_2O GWPs such that the baseline temperature projection is best explained (that is, the sum of the squared distances between the GWP-based temperature and the baseline temperature during the period 1890 – 2000 is minimized) (Figures 6.3a-b). Note that this is different from testing the effect of using a time dependent GWP (e.g. Wigley, 1998). Here we find the single, constant GWP value that would perform best over the historical period. The optimal time horizons for CH_4 and N_2O GWPs are approximately 44 years and 70 years, respectively. However, while in the CH_4 case the temperature projection using the optimal-horizon GWP appears to be a good fit to the baseline temperature projection (insert for Figure 6.3a), in the N_2O case the temperature projection using the optimal-horizon GWP still lies considerably below the baseline projection (insert for Figure 6.3b).

These results, puzzling at first sight, are related to the fact that the GWP values cover only a restricted range as a function of the assumed time horizon (Figures 6.1a-b). The CH_4 GWP reaches its maximum with an extremely short time horizon of approximately 1.5 years and decreases thereafter due to its short lifetime. The N_2O GWP is maximized with the time horizon of approximately 70 years and falls off on both sides. This occurs because of the nature of the removal timescale for CO_2, which is relatively fast for several decades and then slows considerably. Thus, CO_2 is removed faster than N_2O at first, and then later is removed more slowly, which produces first a rising and then a falling value of N_2O GWP as the time horizon lengthens. The range of values covered by the N_2O GWP does not include the optimal value for reproducing historical temperature.

6.4. TEMPERATURE PROXY INDEX (TEMP)

Now we introduce new GHG exchange metrics, TEMPs. A TEMP is a non-physical quantity that provides a best fit to the baseline temperature projection when it is used to convert non-CO_2 GHG emissions to their CO_2-equivalents. The CH_4 TEMP for emissions over the 1890-2000 period is approximately 39, equal to the optimal-horizon CH_4 GWP (44-year time horizon). On the other hand, the N_2O TEMP is 355 whereas the optimal-horizon N_2O GWP (70-year time horizon) is 310, equal to the maximum N_2O GWP. The disparity between the N_2O TEMP and the optimal-horizon N_2O GWP indicates that the range for the N_2O GWP does not contain the value for the optimal temperature proxy.

The TEMP is related in spirit to the Forcing Equivalence Index (FEI) proposed by Wigley (1998) in that it is a value calculated in order to produce equal outcomes from two different mixes of emissions. The FEI is an instantaneous, time-varying index that produces identical radiative forcing pathways over time. In contrast, the TEMP is an index that remains constant over a specified time horizon, and is calculated to produce an optimal (although not necessarily identical) temperature pathway over time.

Nonetheless, it is useful to investigate how the value of the TEMP depends on the

optimization period. We therefore repeat the same optimization exercise for different periods. First, we maintain a start year of 1890 while progressively changing the end year from 1891 to 2000 in one-year steps. This version of the TEMP can be described as backward-looking: one looks back from a constantly updated end year to the start year to determine the optimal value over the period that has passed. The results (Figure 6.4a) show that the backward-looking TEMP for CH_4 declines with increasing length of the optimization period, consistent with behavior of the FEI for CH_4 calculated by Wigley (1998) for several future scenarios. Given the short lifetime of CH_4 compared to CO_2, its value is highest when optimization occurs over the shortest period, and declines as the optimization period lengthens. The backward-looking TEMP value begins outside the range of possible GWP values, and then falls within it for optimization periods that are greater than 13 years.

In contrast, the results for N_2O (Figure 6.4b) show that the backward-looking TEMP increases with increasing length of the optimization period, and begins within the range of possible GWP values but exceeds this range for optimization periods longer than 40 years. The increasing trend is a result of the fact that, as discussed above, the removal rate of a pulse emission of N_2O is slower than that of CO_2 for many decades, and faster only much later when CO_2 uptake slows (O'Neill et al., 1997). Thus at least initially, the N_2O TEMP value behaves as it would for a gas with a lifetime longer than that of CO_2: it rises as the optimization period lengthens. As the optimization period grows longer yet, the emissions being traded off slowly shift from recent emissions (for which N_2O removal is slower than CO_2) to a growing fraction of older emissions (for which N_2O removal is faster than CO_2). For the particular emissions pathways over the historical period, this leads to a N_2O TEMP that grows more and more slowly over time, but does not decline.

While these results provide insight into the effect of the optimization period on the value of the TEMP, they are less useful for insight into how a TEMP value might be applied within a forward-looking policy setting. For example, from the perspective of the year 1890, an index aimed at equating the effect of different gases over the period 1890-2000 would want to begin with the value that was optimal over that entire period. In the next year, the relevant TEMP would be the optimal value over the period 1891-2000, and so on through time, at each point looking forward from an updated start year to a common end year. Figures 6.4a-b show these forward-looking TEMP values calculated by maintaining the end year of the optimization period at 2000, and progressively changing the start year from 1890-2000 in one-year steps.

In contrast to the backward-looking TEMP, the forward-looking TEMP for CH_4 rises over time, rather than falls. The reasoning is the same: with a short lifetime, CH_4 reductions early in the period, when the optimization period is long, are not valuable relative to reductions later in the period, when the optimization period is short. This rising value of CH_4 reductions is opposite to the trend in the FEI (Wigley, 1998), but similar to that found by Manne and Richels (2001) in their calculation of the economic value of reductions of different gases using price ratios and by Shine et

al. (2005) in their calculation of Global Temperature Potentials (GTPs). The trends in the forward-looking TEMP, price ratios, and GTPs share a common cause: as the overall temperature scenario approaches a temperature target or the end of the optimization period, the relative contribution of short-lived gases increases and is reflected in the rising index.

The results for N_2O are also the opposite of the backward-looking calculation, showing a declining (rather than rising) TEMP value over time. N_2O reductions are more valuable early on because of the expectation that N_2O emissions over the full optimization period will on balance be more slowly removed than CO_2. Thus the earlier the optimization period begins, the more valuable reductions in N_2O will be. In fact, the forward-looking TEMP for N_2O lies outside the range of possible GWP values for nearly the entire period. In the next section, we explore the reasons for this mismatch.

6.5. ASSUMPTIONS IN THE IPCC GWP CALCULATIONS

The IPCC GWP calculations use a simplified approach to representing carbon cycle processes, CH_4 and N_2O atmospheric chemistry, and associated concentration-forcing relationships. As the different process representations lead to different index values, we compute TEMPs under the assumptions used in the IPCC GWP calculations. This exercise is useful to gain an insight into the disparity between the N_2O TEMP and GWP ranges. Namely, we assume a low CO_2 fertilization (beta = 0.287) as in the Bern Carbon Cycle Model (Joos et al., 1996) adopted for the IPCC GWP calculations (IPCC, 2001, p.386), the CH_4 lifetime of 12 years (IPCC, 2001, Table 6.7) equivalent to the CH_4 lifetime with respect to OH depletion of 14.5 years (Appendix B.2), the N_2O lifetime of 114 years (IPCC, 2001, Table 6.7), linear marine carbonate chemistry by fixing the Revelle factor at the present level (Revelle and Munk, 1977; Mackenzie and Lerman, 2006, p.265), no CH_4 and N_2O concentration feedbacks to their own lifetimes, linear CH_4 and N_2O concentration-forcing relationships (no change in the saturations and overlaps of the CH_4 and N_2O absorption bands), and no climate-carbon cycle feedback by keeping the temperature seen by the carbon cycle at the preindustrial level. Note that the other parameters not mentioned above are adjusted in the inverse calculation according to the change in assumptions for IPCC GWP calculations.

The TEMP calculation results under the IPCC assumptions are compared with the reference results in Figures 6.5a-b. With the assumptions used in the IPCC GWP calculations, both the CH_4 and N_2O TEMPs stay below their respective maximum GWPs. A sensitivity analysis with respect to each of the assumptions (Appendix B.1 to B.3) shows that the ones having the largest effect are the low beta factor and the linearization of the CH_4 and N_2O concentration-forcing relationships. Unlike our high beta factor (= 0.59), the low beta factor assumed in the IPCC GWP calculations is not supported by most of the recent process-based terrestrial biosphere models

(Friedlingstein et al., 2006). The linear CH_4 and N_2O concentration-forcing relationships assumed in the IPCC GWP calculations are an oversimplification as the background system dynamics are expected to change on the time scale of global climate policy, a well-known problem with GWPs. In the context of the Earth system history, the assumptions used in the IPCC GWP calculations would not be satisfied, indicating that the current GWPs are detached from how the Earth system has actually behaved. The mismatch between the N_2O GWP range and the optimal TEMP value is caused by the IPCC GWP calculation methodology not representing sufficient complexity in the system dynamics and also not rigorously treating uncertain parameters.

6.6. CONCLUSIONS

We have demonstrated that the CH_4 and N_2O GWPs used in the Kyoto Protocol, when applied to historical emissions, lead to an underestimation of historical temperature change. We show however that a single constant index can in principle reproduce this history well, and we introduce a new index, the TEMperature Proxy (TEMP) that is designed to do so. The optimal TEMP value for CH_4 is equivalent to a GWP calculated with a 44-year time horizon, but the optimal TEMP for N_2O is not consistent with any time horizon used to calculate a GWP. We show that this discrepancy is due to the simplified earth system dynamics used to calculate GWPs, as well as parameter estimates in the models on which GWPs are based that are inconsistent with other data from the historical period.

We also show that the value of the TEMP index depends on the time period over which it is calculated. Although our analysis is restricted to the historical period, we calculate a forward-looking version of the TEMP that is indirectly relevant to policy considerations. We show that it has some key features that are similar to other indices based on, or motivated by, economic considerations. In particular, the value of reductions of short-lived gases rises over time as a constraint, or the end of the optimization period, is approached.

These results suggest that it would be worthwhile to further explore the potential for a purely geophysically based index such as the TEMP to be usefully applied to climate policy. First in order would be to assess its behavior under a variety of alternative future scenarios, and to evaluate its performance as compared to economic indices.

Figure 6.1. GWPs of CH_4 and N_2O with the change in time horizon

The estimates of the lifetimes and IPCC GWPs are taken from Table 6.7 of IPCC (2001). The GWP curves are calculated based on Table 6.1.

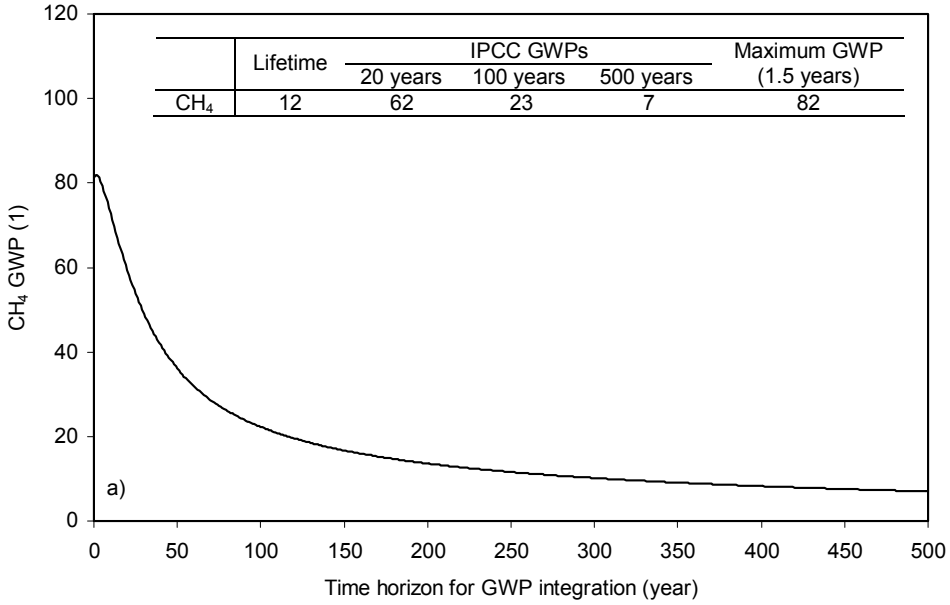

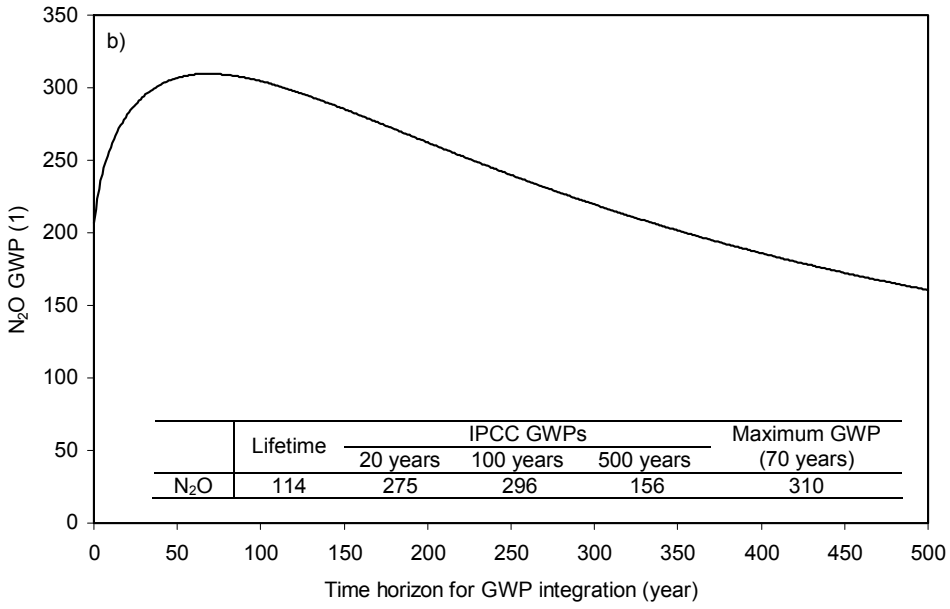

Figure 6.2. ACC2 inverse calculation results

The posterior estimates of the parameters and data (red lines) are shown in comparison with the respective prior estimates and measurements (black thick lines) including their 2σ prior and measurement uncertainty ranges (black thin lines). The prior for the CH_4 and N_2O emissions are based on van Aardenne et al. (2001). Data for the CH_4 and N_2O concentrations are based on Etheridge et al. (1998), Jacqueline Flückiger (personal communication), Hansen and Sato (2004), and Masarie et al. (2001, Table 1). Data for the surface air temperature are the compilation of Jones et al. (1998), Jones et al. (2006), and Mann and Jones (2003). The large spikes in the prior parameter and data uncertainties are due to the adjustments for large volcanic eruptions (Section 3.5.2). The residuals of the posterior estimates from their corresponding prior estimates (red lines in inserts) are separately shown in inserts with their 2σ prior and measurement uncertainty ranges (black lines in inserts). The full inversion results are shown in Section 4.

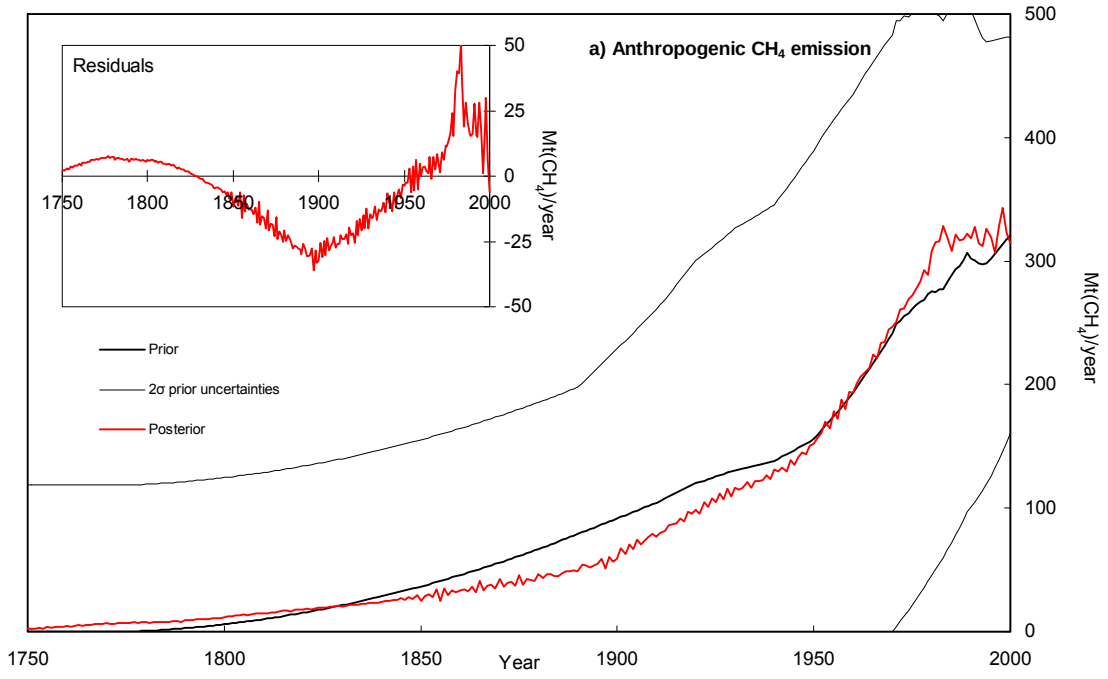

Figure 6.2. (Continued) ACC2 inverse calculation results

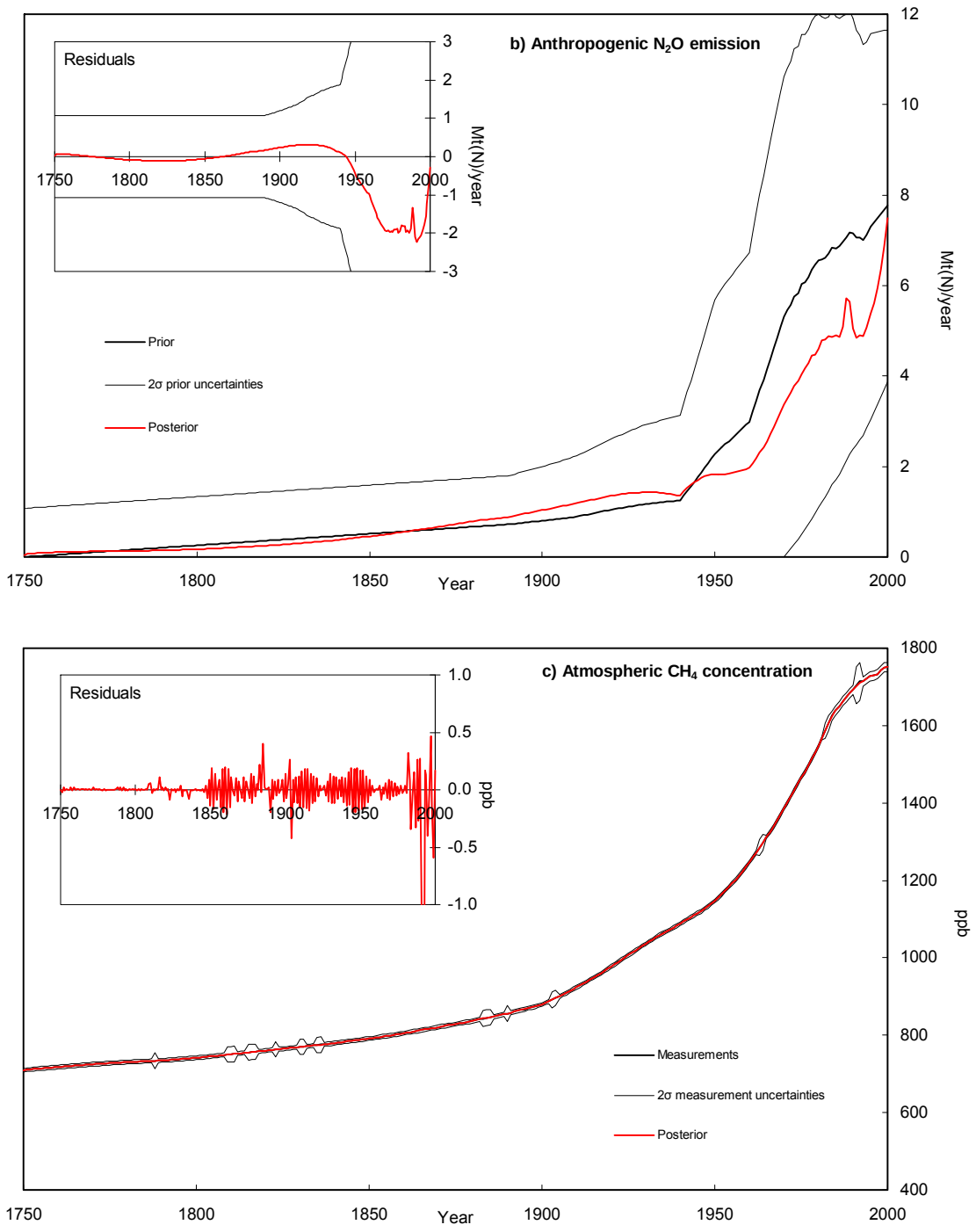

Figure 6.2. (Continued) ACC2 inverse calculation results

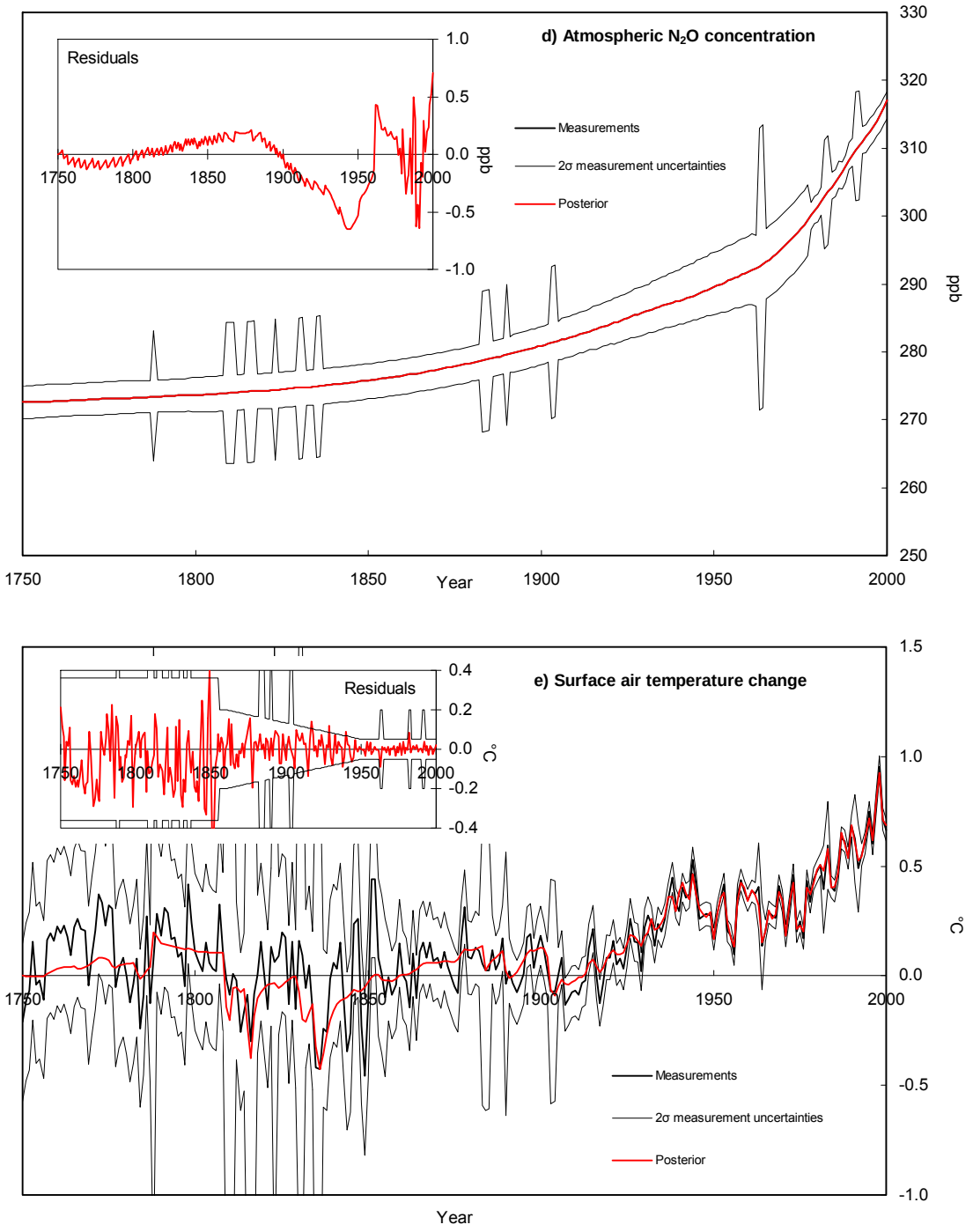

Figure 6.3. Temperature projections with CH_4 or N_2O emissions converted using GWPs and TEMPs

The conversions are applied from the year 1890 onward. Baselines are the posterior estimates obtained from the ACC2 inverse calculation. The temperature projection using the CH_4 TEMP is identical with the projection using the optimal-horizon CH_4 GWP.

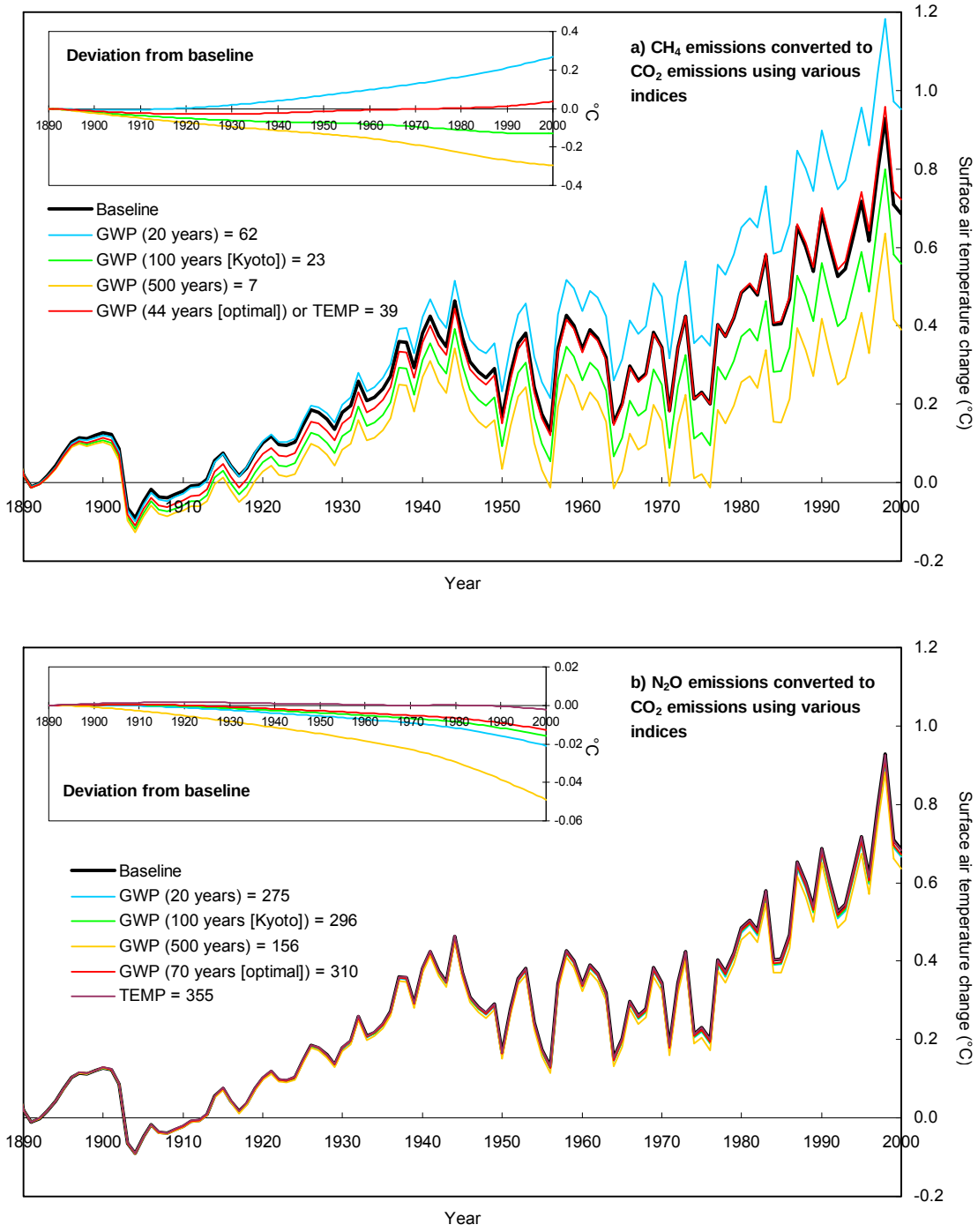

Figure 6.4. CH_4 and N_2O TEMPs calculated over different time periods

In the backward-looking calculations, TEMPs are optimized with respect to their fits to the baseline temperature between the year 1890 and the end year shifting from 1900 to 2000. In the forward-looking calculations, TEMPs are optimized between starting years ranging from 1890 to 2000 and the year 2000. The backward-looking calculation results serve as a reference for the rest of our analysis.

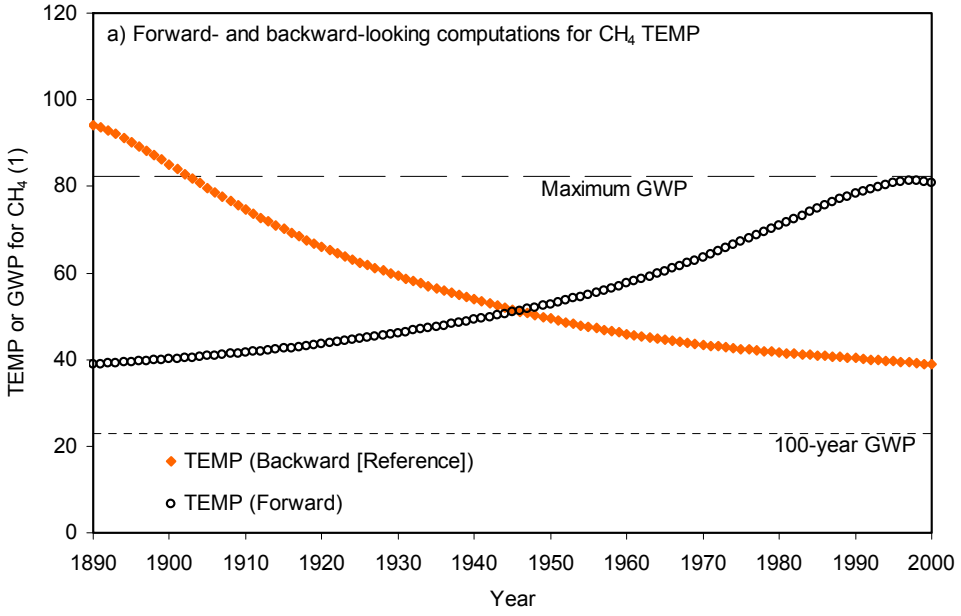

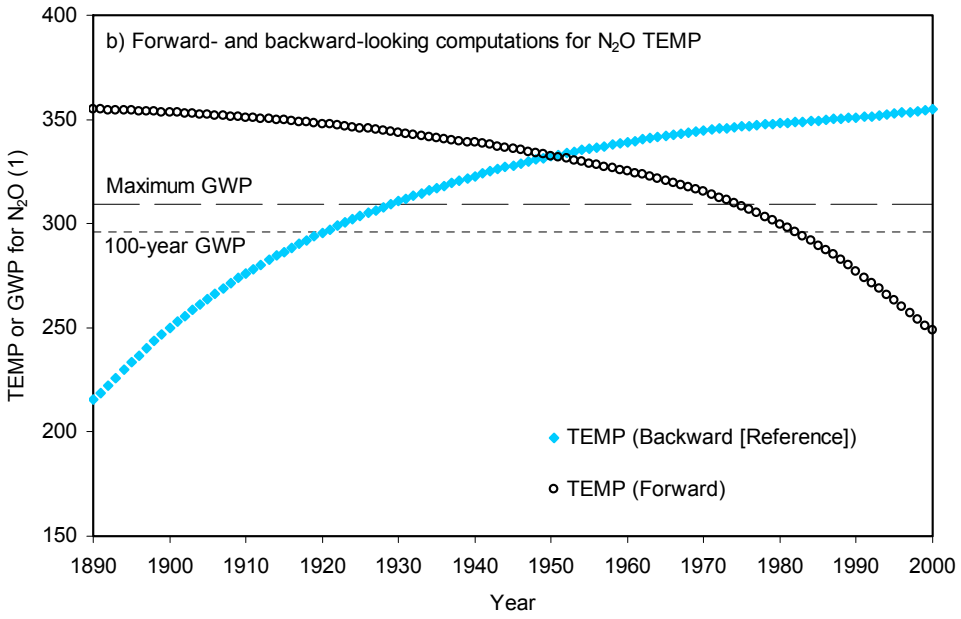

Figure 6.5. Updating CH_4 and N_2O TEMPs under the assumptions used for IPCC GWP calculations

Backward-looking TEMPs are calculated for every year from 1890 to 2000.

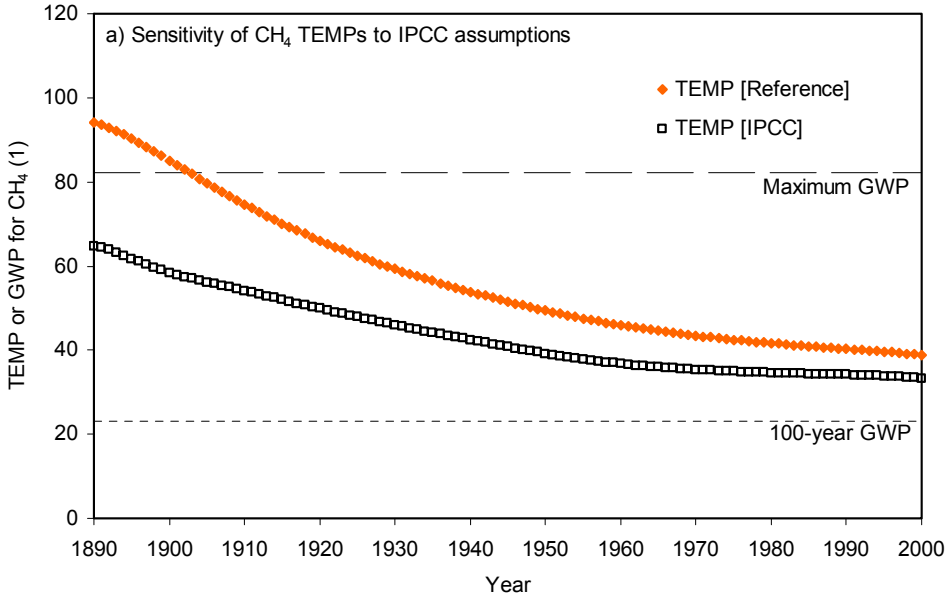

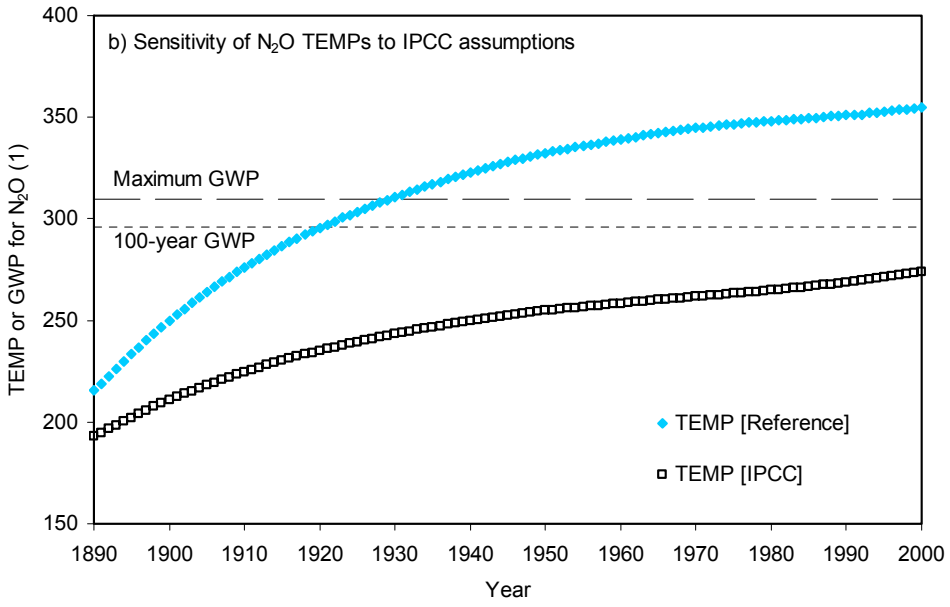

Table 6.1. Information used for GWP calculations

The estimates of the lifetimes and radiative efficiencies are taken from Table 6.7 of IPCC (2001). The CO_2 lifetime is merely nominal; the complex removal processes of CO_2 from the atmosphere cannot be represented by a single lifetime. In the GWP calculations, the CO_2 uptake is described by the impulse response function $R(T)$ (equation 10-6 of WMO (1999)) as follows: $R(T) = \frac{279400 + 72240T + 730.4T^2}{279400 + 107000T + 3367T^2 + T^3}$, where T denotes the time in years. The estimates of the conversion units are taken from Table 2 of Fuglestvedt and Berntsen (1999). They are linearly correlated with the associated molecular weights. We made an upward correction on our CH_4 GWP estimates by 25% as the indirect contribution to be in an agreement with the corresponding IPCC estimates.

* The denominator is ppm in the case of CO_2 and ppb in the cases of CH_4 and N_2O.

Names of GHGs	Molecular Weights	Conversion Units *(kg/ppb or ppm)	Lifetimes (year)	Radiative Efficiencies *(W/m^2/ppb or ppm)
CO_2	44	0.471×10^{12}	(150)	0.01548
CH_4	16	2.75×10^{9}	12	0.00037
N_2O	44	4.80×10^{9}	114	0.0031

7. CONCLUDING REMARKS

This thesis covers a wide range of natural Earth system processes and deals with two distinct problems having policy implications. The underlying theme throughout this thesis is the simplified integrated perspective. The usefulness of this approach is shown based on the following arguments and results. First, the uncertain parameters in the carbon cycle, atmospheric chemistry, and climate system are simultaneously estimated by considering the interdependencies of their estimates. Second, the ACC2 inversion approach addresses a large number of uncertainties in the inversion, demonstrating the importance of the uncertainty in radiative forcing for climate sensitivity estimation. Third, the integrated inversion allows a new attempt to climate sensitivity estimation by considering the contribution from climate-carbon cycle feedback that had been overlooked previously. Fourth, it is made possible to evaluate GWPs and compute TEMPs on the basis of the past Earth system evolution obtained from the inversion. There are dominant processes and uncertainties on each spatial and time scale, providing the usefulness of this perspective. I hope that this thesis serves as a step forward within the series of integrated studies (Hooss, 2001).

Possible future developments of the model and its inversion were discussed at the end of Chapter 4. Further research perspectives related to the two applications are stated at the end of Chapters 5 and 6, respectively. This section looks out for other applications for ACC2 and its inversion to utilize fully its potential.

1) Further studies related to ocean acidification are possible (e.g. Kriegler et al., 2007) as ACC2 explicitly estimates the state of carbonate chemistry including pH and their temperature dependency. This treatment of carbonate chemistry has so far been utilized only to calculate the saturation effect of ocean CO_2 uptake under rising atmospheric CO_2 concentration.
2) TEMPs for halocarbons can be calculated in addition to those for CH_4 and N_2O (Chapter 6 of this thesis; Tanaka et al., 2007b). ACC2 implemented the parameterized atmospheric chemistry for 29 species of halocarbons. The individual treatment of halocarbons has just been used to reflect each of their emission scenarios to climate projections.
3) The ACC2 future mode can be used to answer questions related to learning (O'Neill et al., 2006): a) How is the future climate policy altered if our understanding on climate sensitivity is changed at some point in the future? b) How should the current climate policy be formulated in consideration of learning in the future?
4) The ACC2 past and future mode can be used to demonstrate how it is important to consider the interdependency of the estimates of uncertain parameters for the projections of future climate. Taking account of such interdependency was one of the motivations for the development of the ACC2 inversion.

5) The ACC2 past and future mode can be used to illustrate the concept of a "climate trap" (Raddatz and Tanaka, 2008) as explained below. If all anthropogenic GHG and aerosol emissions are abruptly suspended, rapid warming would follow, because cooling by aerosols would cease within days whereas the warming by CO_2 would persist for years. Such warming would be stronger for higher climate sensitivity because stronger aerosol forcing would be implied. If in the near future the climate sensitivity turned out to be high, a rapid emission reduction would result in a dangerously large abrupt warming.
6) The ACC2 future mode can be used to compute the emission corridors for multi-GHGs. The original model ICM has been extensively used for the emission corridors for CO_2 (Toth et al., 2003).
7) A low-order thermohaline circulation model (Zickfeld et al., 2004) can be coupled with ACC2. The risk of thermohaline circulation collapse can be included in the analysis of future climate change.
8) One can ask which uncertainties and feedbacks play a large role in the inversion results by examining residuals. Two extreme results are shown in Chapter 4: inversion run vs forward run. Such a study provides insight into which knowledge is useful to increase the overall knowledge in the Earth system evolution.

This Ph.D. thesis is concluded with some general views on uncertainties that I acquired throughout my doctoral study. The inversion exercise for ACC2 taught me that an inversion lets a model confront the reality so faithfully that one faces with structural uncertainties. Departure of a theory from reality cannot be noticed when parameter spaces are simply sampled. The inversion exercise also made me realize that the way of thinking for inverse modelling is complementary to the thinking for forward modelling. In forward modelling, the approach of adding more complexity to a model can be justified as it is generally assumed that the more detailed the processes, the better the model projections. However, in inverse modelling, adding complexity to a model is not worth the effort when the associated uncertainties are not well-constrained. This thought is linked to the claim of Enting (2002b) that an inversion is a revival of a reductionist approach for holistic system studies, which once emerged as a replacement of a reductionist approach. In other words, I learned a tradeoff between the level of complexity and the degree of uncertainties. Finally, I realize that uncertainty in the uncertainty gives rise to a major problem upon practical application of the inverse estimation theory – quality of uncertainty is beyond the scope of the theory. As a whole, the problem of uncertainties in the Earth system is deeper than what I initially thought.

APPENDIX A. SUPPLEMENTARY INFORMATION I — CHAPTER 4

In this appendix, details of the ACC2 inverse calculation results are shown: carbon storage in the ocean and land reservoirs (Figures A.1, A.3, and A.4), the concentrations of marine carbonate species (Figure A.2), historical evolutions of the individual radiative forcings (Figure A.6), the land-ocean separations of the radiative forcing and the surface air temperature (Figure A.7), and the influence of ENSO to the atmospheric CO_2 concentration (Figure A.5) as well as the surface air temperature (Figure A.8). Explanations for the figures are provided in the respective notes.

Figure A.1. Carbon accumulations in the reservoirs of the ACC2 atmosphere-ocean box model

The two figures below show the cumulative (1) and annual (2) carbon inputs to the reservoirs of the ACC2 atmosphere-ocean box model. In the composite reservoir, the atmosphere and the ocean mixed layer are equilibrated at every time step. The partition of the carbon between the atmosphere and the ocean mixed layer is determined by the atmospheric CO_2 concentration, the chemical state of the ocean mixed layer, the ocean surface air temperature, and the mixed layer temperature. The fluctuations in the annual amount of carbon input are largest in the composite layer, which gradually propagate to the subsequent ocean reservoirs.

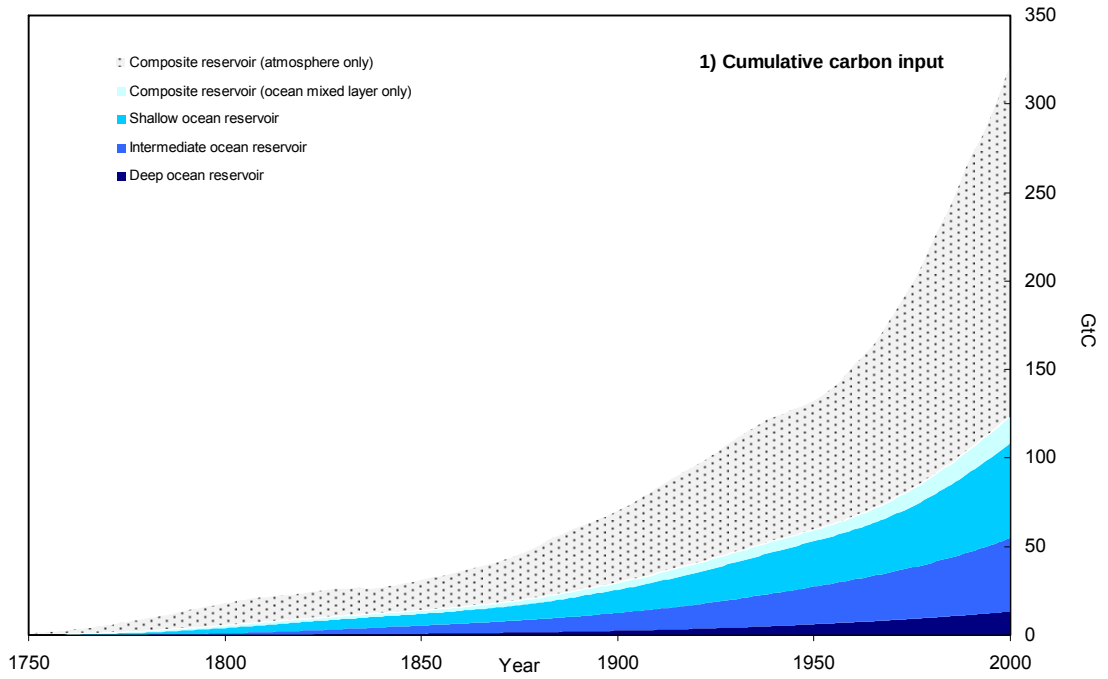

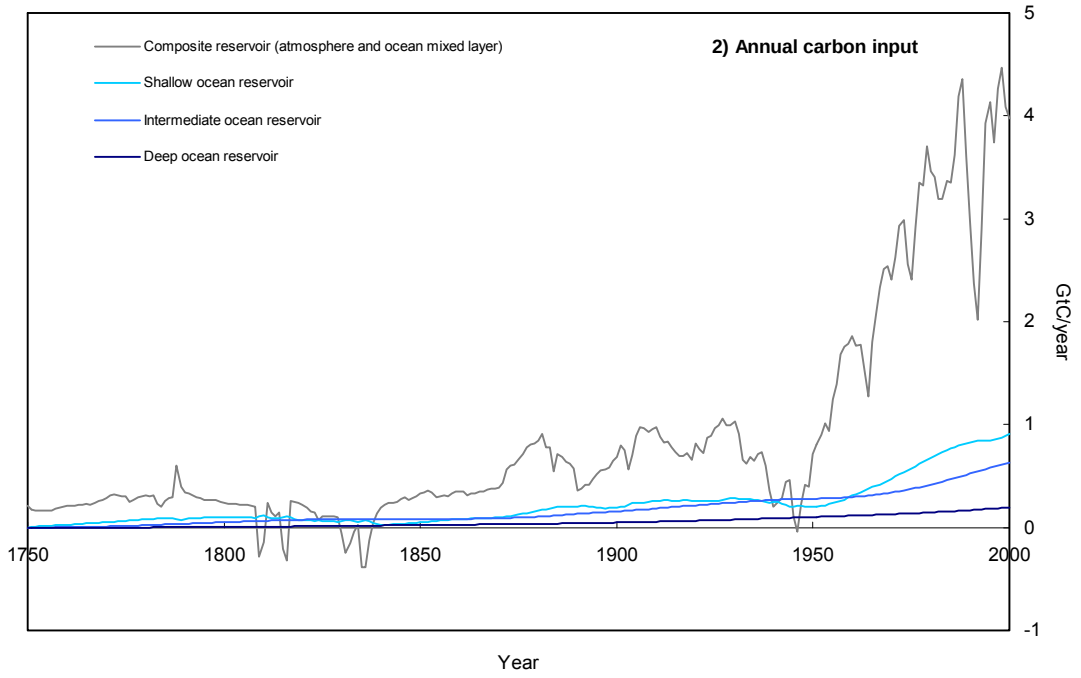

Figure A.2. Changes in the chemistry of the ocean mixed layer

The ACC2 inverse calculation indicates that pH has dropped by about 0.1 during the last 250 years, accompanied by the changes in the composition of the carbonate species ($CO_2(aq)$, HCO_3^- , and CO_3^{2-}) (compare Figure 2.2).

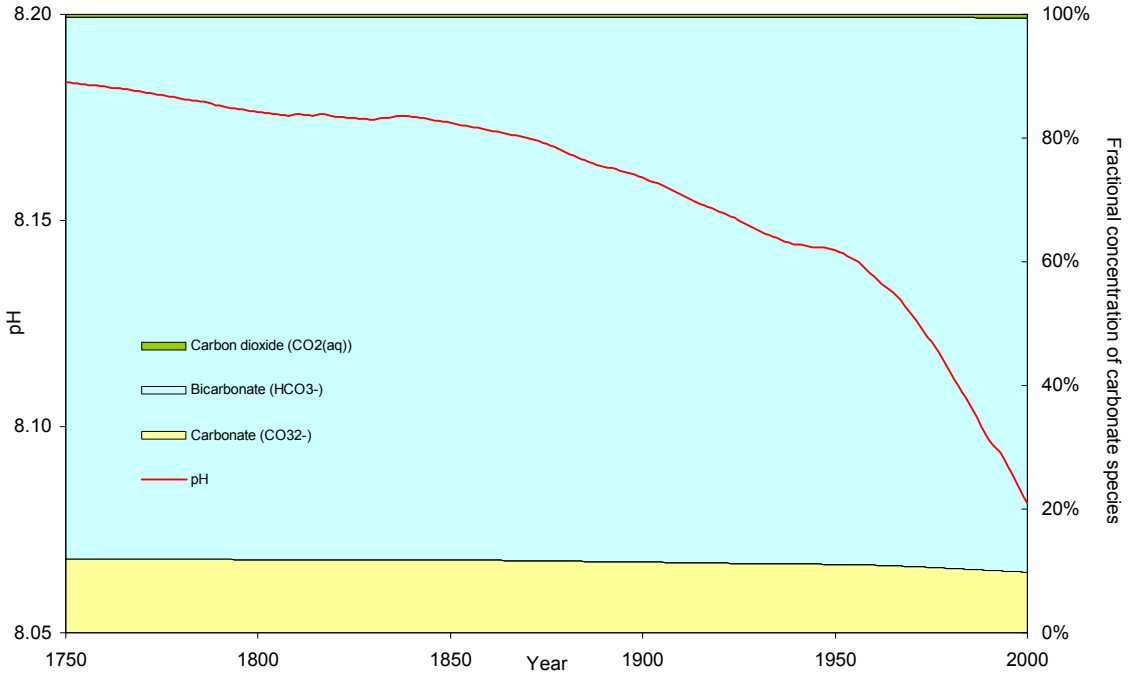

Figure A.3. Carbon accumulations in the reservoirs of the ACC2 land box model

The cumulative (1) and annual (2) carbon inputs to the reservoirs of the ACC2 land box model are shown. The numbers in the brackets correspond to the time constants of the reservoirs ($\tau_{ter,i}$ in equation (2.1.54)). Note that the reservoirs cannot be directly interpreted as physical reservoirs even though the time constants are chosen to be the same with the parent Bern-CC model (Joos et al., 1996). In fact, the land reservoir D *negatively* accumulates carbon ($A_{ter,i}$ in equation (2.1.54)). This counterintuitive phenomenon occurs because of reservoir configuration – in ACC2, all the four reservoirs are directly connected to the atmosphere (more precisely, the composite reservoir) whereas in the parent model, the reservoirs of detritus, ground vegetation, wood, and soil organic carbon are directly connected each other (subsection on IRF for CO_2 Uptake in Section 2.1.3).

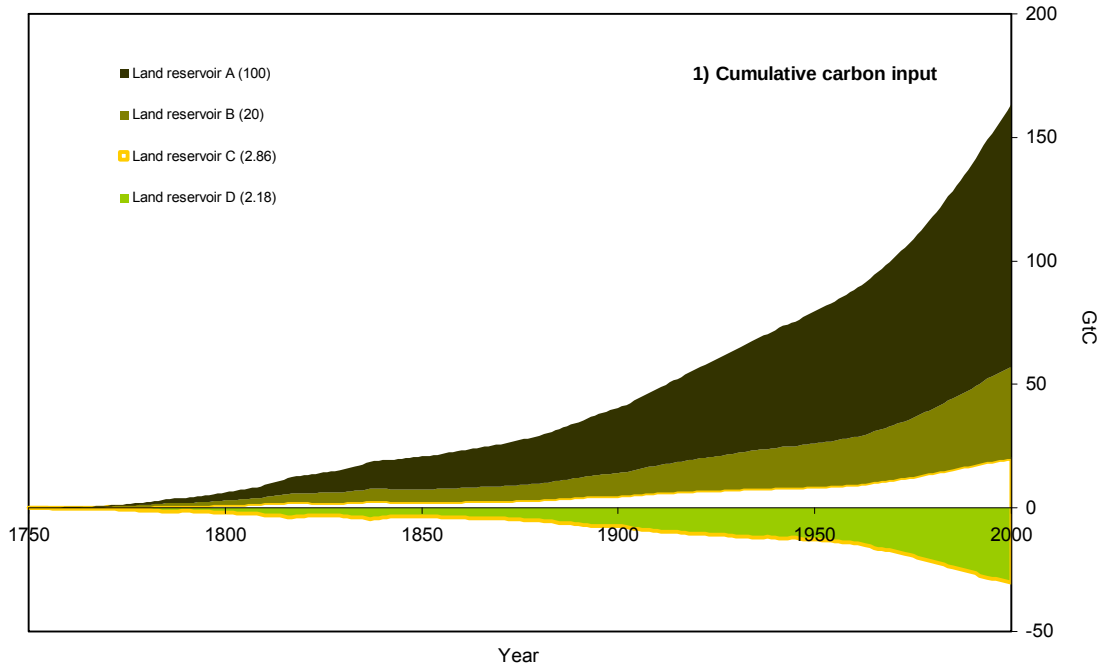

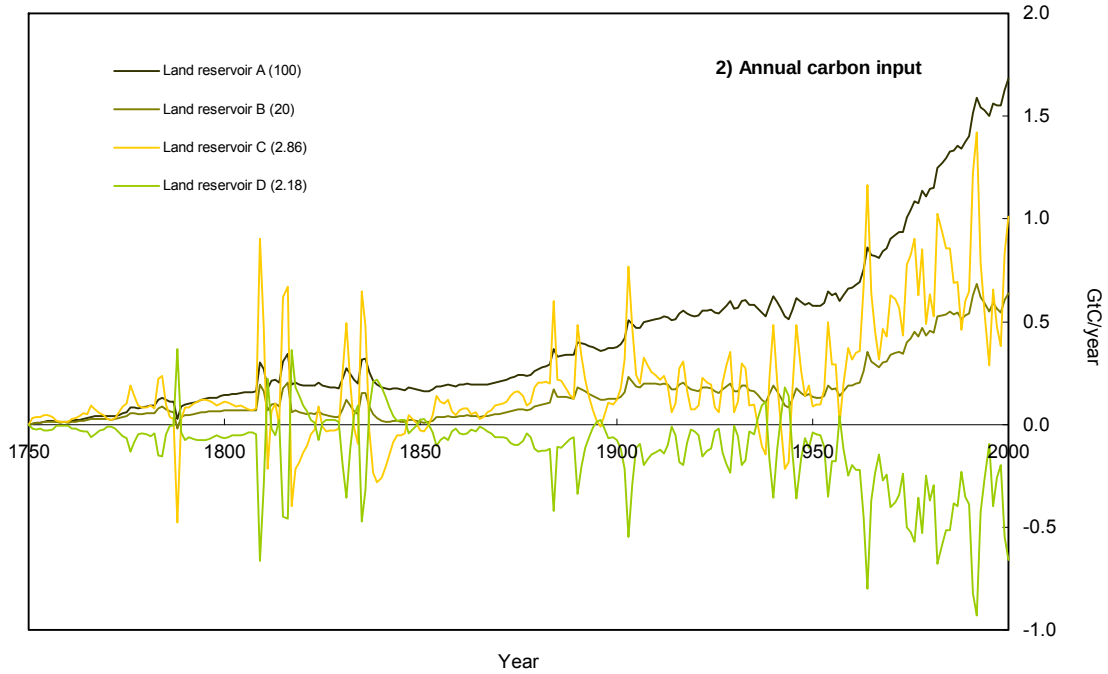

Figure A.4. Changes in NPP and heterotrophic respiration

The total NPP and the heterotrophic respiration for the sum of all the four land reservoirs in ACC2 are shown. The NPP and the heterotrophic respiration are initially balanced under the quasi-steady state assumption (Section 2.1.1) and change thereafter by reflecting the atmospheric CO_2 concentration and the land surface air temperature change, respectively. The difference between the NPP and the heterotrophic respiration gives the carbon accumulation in the land reservoirs.

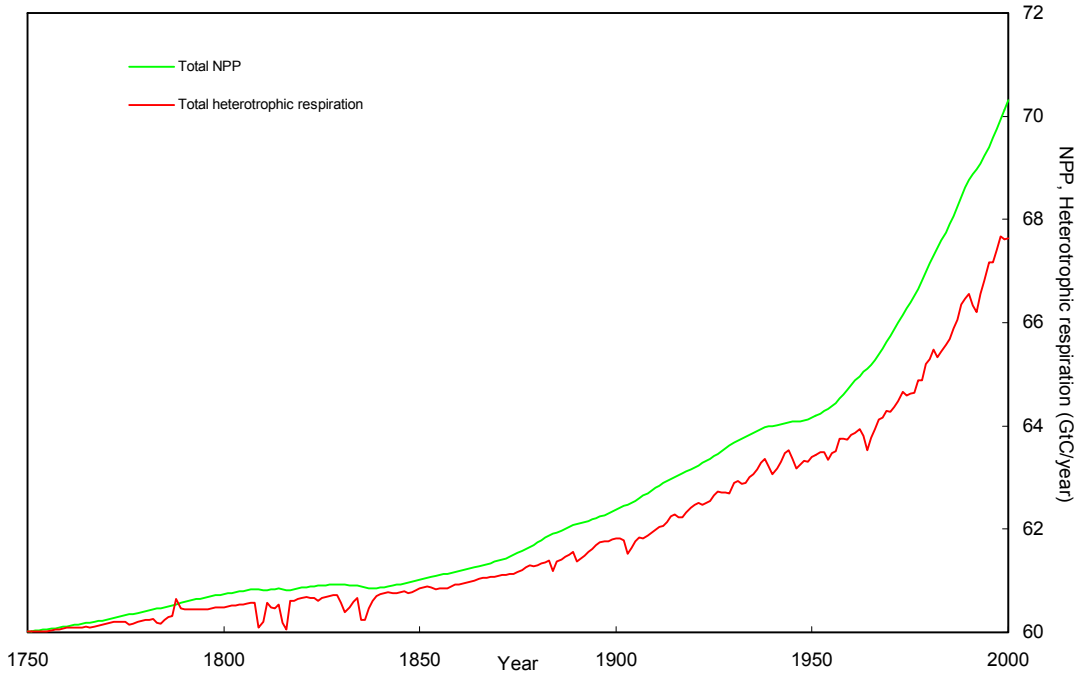

Figure A.5. ENSO-induced anomalies in the atmospheric CO_2 concentration

The ACC2 inverse calculation uses a regression line that explains the natural change in the atmospheric CO_2 concentration as a function of NINO3 (Section 3.5.1). The result of such a statistical inference is the blue line. Although the associated R^2 value is a merely 0.30, the significance test in correlation still rejects the null hypothesis that the two variables are uncorrelated. The low R^2 value is due to the fact that the ENSO-induced variation in the atmospheric CO_2 concentration is also explained by the land use CO_2 emission in the inverse calculation results. The effect of large volcanic eruptions can be seen in the large discrepancies between the statistically inferred change and the natural change in 1981 and 1992.

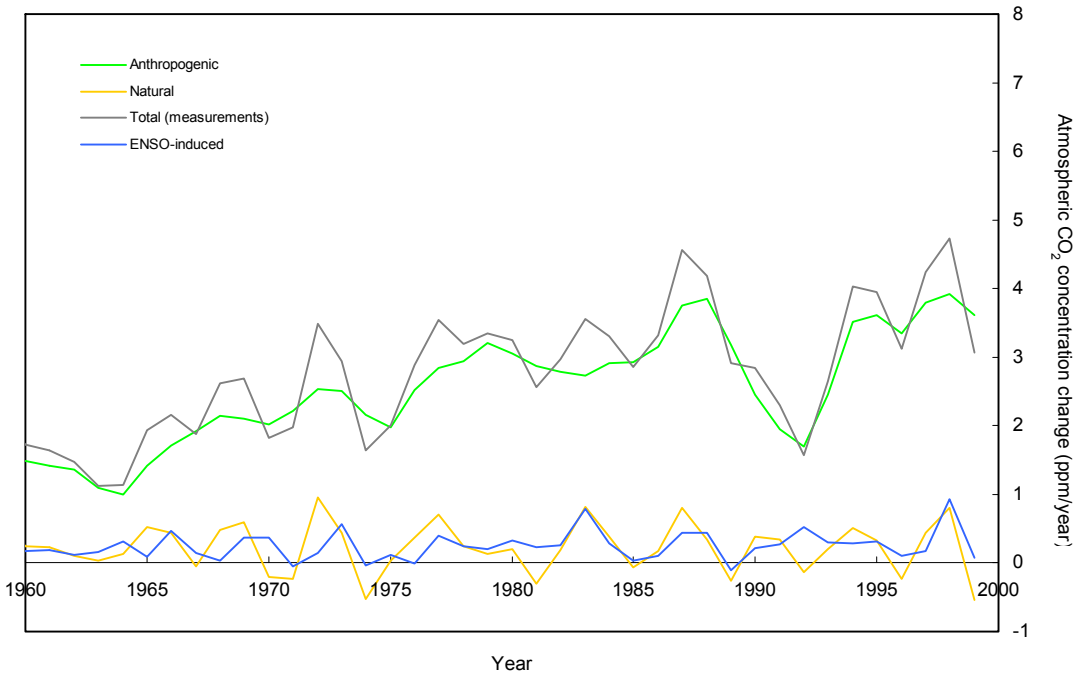

Figure A.6. Evolutions of the individual radiative forcings in the ACC2 inverse calculation

The CO_2 radiative forcing is nearly cancelled out by the sum of the three aerosol forcings. Missing forcing is a parameter in each year. The missing forcing tends to be positive for the last 50 years, except for the periods under the influence of large volcanic eruptions. In the earlier period, large downpeaks of the volcanic forcing are in some cases counteracted by large positive missing forcing. There is one instance around 1780 when a large positive in the missing forcing occurs not in concurrent to a large volcanic forcing to explain the rise in the temperature records.

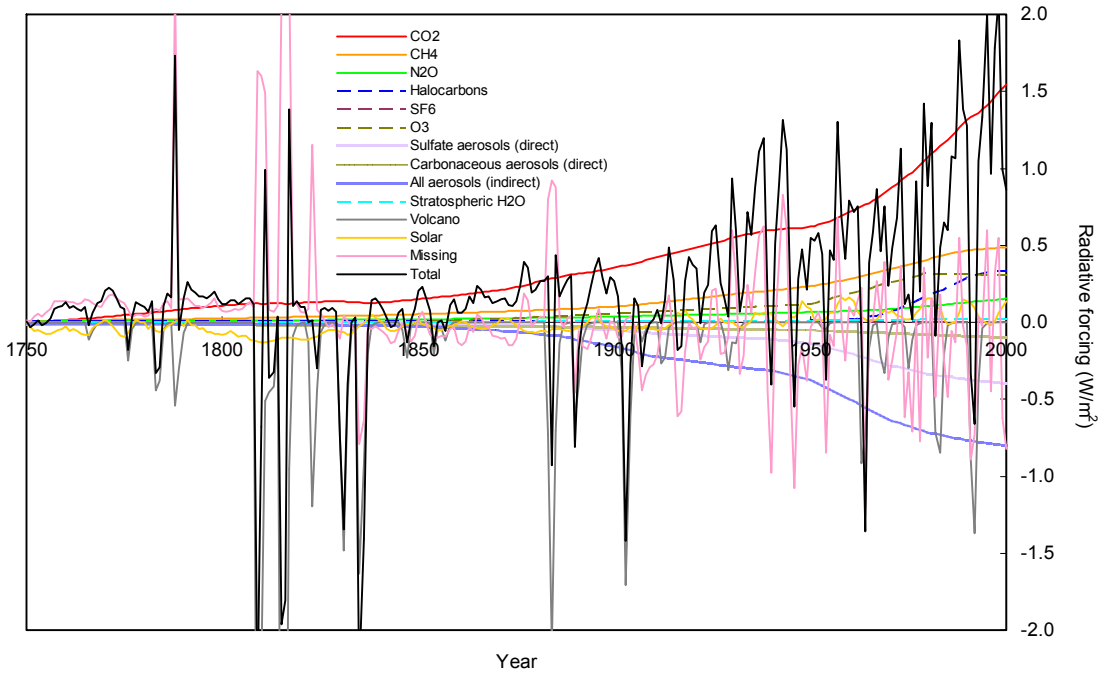

Figure A.7. Radiative forcing and the surface air temperature change over land and the ocean

Temperature change is calculated in DOECLIM by considering the ocean and the land separately. Individual forcing (Figure A.6) is separately scaled for land and the ocean (Section 2.3.5). The anthropogenic radiative forcing over land is smaller than that over the ocean primarily because the aerosol forcing is overweighed over land. On the contrary, the climate sensitivity over land is larger than the sensitivity over the ocean by 43%. As a combined effect, the trend and the variability in the surface air temperature are amplified over land relative to those over the ocean. Note that the effect of ENSO is excluded in the temperature projections to allow for better comparison between the radiative forcing and the temperature change.

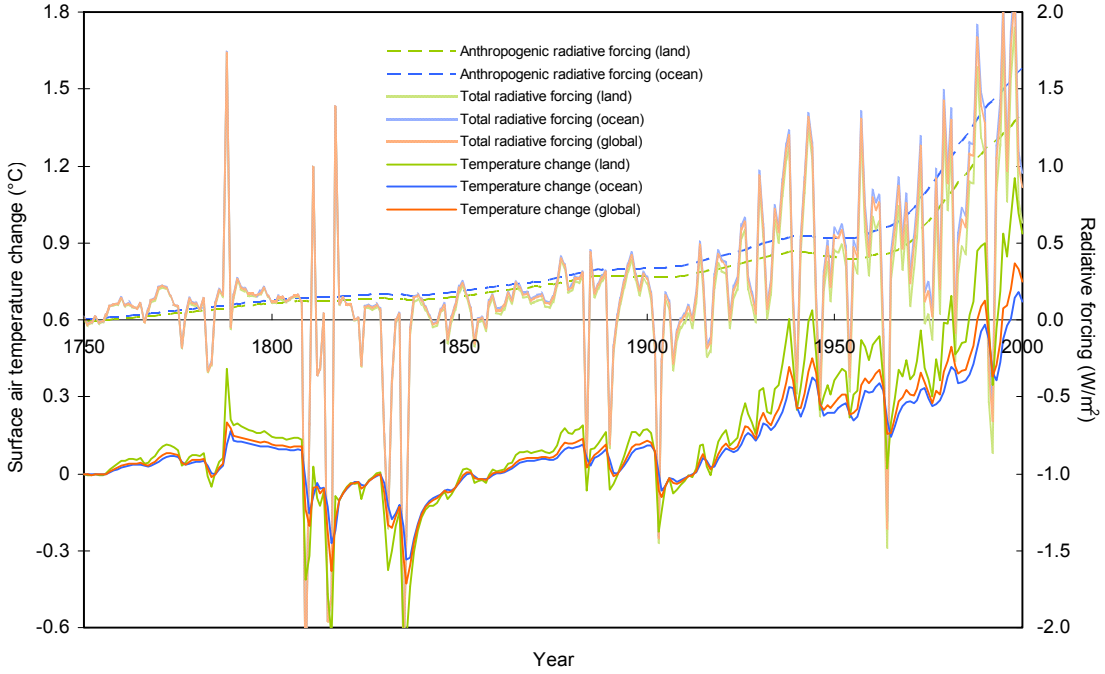

Figure A.8. ENSO-induced anomalies in the surface air temperature change

The influence of ENSO on the surface air temperature is taken into account in the ACC2 inverse calculation between 1930 and 2000. A fixed regression line is used to explain the natural variability in the surface air temperature as a function of SOI (Section 3.5.1). The figure shows that the variability in the posterior temperature estimates accounting for ENSO is closer to the variability in the temperature records.

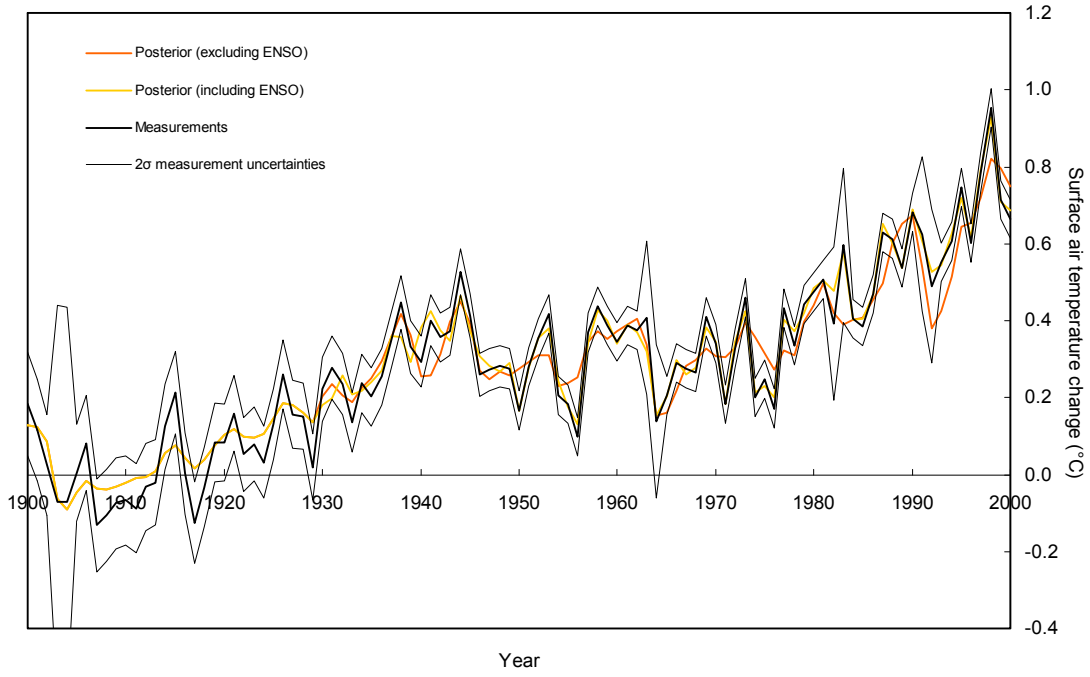

APPENDIX B. SUPPLEMENTARY INFORMATION II — CHAPTER 5

B.1. INTRODUCTION AND SUMMARY

This appendix provides in-depth analyses to support our inversion methodology and conclusions in Chapter 5. First, we show the validity of the ACC2 inversion results based on their qualitative interpretation. Second, we demonstrate that the conclusions in Chapter 5 hold under various assumptions.

Two conclusions in Chapter 5 are the followings: 1) It is of paramount importance to reconsider how to deal with forcing uncertainty in inversion-based climate sensitivity estimation. 2) Even when the carbon cycle feedback is provided in the inversion, the uncertainty in the historical global carbon budget makes it difficult to produce a tighter constraint on climate sensitivity estimation.

The conclusions above rest on several assumptions. We assess the influence of such assumptions to the main conclusions. Assumptions that we explicitly look at are as follows. First, the prior missing forcing uncertainty presumed in the ACC2 inversion is established based on the early 20th-century warming and the natural variability of a GCM control run (Doney et al., 2006), but this is an assumption as uncertainty ranges in various radiative forcings are not yet well-established (IPCC, 2007, p.4). Second, we assume that the prior uncertainty range for land use CO_2 emission is twice as large as the corresponding estimate of Houghton (2003). This is because the estimate of land use CO_2 emission is different depending on the approach (bottom-up vs. inversion) and also influenced by the uncertainty in the global carbon budget (e.g. missing carbon flux such as soil erosion (Lal, 2005)). Third, ACC2 employs the volcanic forcing of Ammann et al. (2003) among others (e.g. Bertrand et al., 2002; Crowley et al., 2003). The estimate of volcanic forcing depends on the ice cores used, interpretation of the records, and estimation methodology (e.g. scaling from aerosol optimal depth to radiative forcing).

Furthermore, some statements in Chapter 5 can be checked with additional analyses. For example, regarding the composition of missing forcing, relevant sensitivity analyses provide some insight. Also, further sensitivity analyses can substantiate our claim that the cost function curves are qualitatively comparable with PDFs.

This appendix is organized as follows. In Section B.2, we discuss the main ACC2 inversion results in more detail. Section B.3 aims to strengthen the first main conclusion by looking at the influence of prior forcing uncertainty to the inversion results. Section B.4 is to support the second

main conclusion by investigating how the inversion results are affected by the presupposed prior land use CO_2 emission range and volcanic forcing. In Section B.5, we discuss the implications of other key assumptions to the main conclusions: namely, presupposed ocean diffusivity and prior climate sensitivity. In Section B.6, a brief discussion on the posterior missing forcing is provided. Then we look at how the missing forcing is affected by prescribed aerosol forcing, prescribed volcanic forcing, and ENSO-driven temperature variability. Section B.7 aims to show the relevancy of our cost function curves to PDFs on the basis of the sensitivity of the cost function value to major parameters (beta, Q10, and forcing scaling factor). Lastly in Section B.8, we analyze the implications of the independence assumption of the residuals – specifically, our analysis investigate how the autocorrelations in temperature residuals influences the first main conclusion.

B.2. FULL RESULTS OF THE MAIN ACC2 INVERSIONS

In this section, full results of the main ACC2 inversions are shown. We demonstrate that the inversion results can be meaningfully interpreted, supporting the validity of the inversion results. We begin with overall discussion of the inversion results (Section B.2.1) and explain problems for statistical tests (Section B.2.2). This is followed by detailed accounts for the land use CO_2 emission in the late 20th century (Section B.2.3), global estimate of Q10 (Section B.2.4), temporal suspension of the atmospheric CO_2 concentration rise in the mid 20th century (Section B.2.5), terrestrial biosphere response to volcanic eruptions (Section B.2.6), and optimal climate sensitivity (Section B.2.7).

B.2.1. Overall Discussion

Visual inspection of the time series (Figure B.1) indicates that in the coupled and uncoupled inversion results, the overall fits to the observations are fairly good in view of the associated prior uncertainty ranges. All the posterior parameter estimates (Table B.4) do not substantially depart from their prior estimates, supporting the validity of the inversion results. Exceptions are the land use CO_2 emission around 1991 and Q10, which are discussed in Sections B.2.3 and B.2.4, respectively. It had also been demonstrated that the fits for various time series has been drastically improved, compared to the results of forward simulation in which all the parameters are fixed at their prior estimates (Figure 4.1).

The final values of the cost function are nearly the same in the coupled and uncoupled inversions (371.1 and 365.1, respectively (Table B.3)) – however, it is substantially larger in the forcing scaling-based inversion (607.0 (Table B.3)). Such a large cost function value stems from the poor temperature misfit, in particular the short-term changes due to the natural variability and volcanic cooling (Figure B.2). In the forcing scaling-based inversion, the squared weighted residuals

for temperature account for nearly 70% of the cost function. The result here indicates that the forcing scaling approach is not sufficient to explain the observed temperature change.

B.2.2. Problems with Statistical Tests

Validation for the ACC2 inversion results relies only on qualitative examinations. A χ^2 test, which is designed to evaluate the size of residuals, is not a proper statistical validation for our problem due to the following two reasons:

First, a χ^2 test can be used only for a linear model. Our model ACC2 is moderately nonlinear as a whole, as a result of the combined effect of several nonlinear processes such as CO_2 fertilization, temperature feedback to the ocean and land CO_2 uptake, concentration-radiative forcing relationships for CO_2, CH_4, and N_2O, and ocean heat uptake. While CO_2 fertilization dampens the rising atmospheric CO_2 concentration, the temperature feedback to the ocean and land CO_2 uptake further amplifies it. The CO_2 concentration-radiative forcing relationship has a damping effect for CO_2-induced warming as relevant absorption bands are filled with rising CO_2 concentration. Ocean heat uptake delays the warming (Figure B.5). The entire warming effect emerges after several hundred years.

Second, a large number of correlations among the residuals (inserts for Figures B.1 and B.2; Figure B.3) is a problem for a χ^2 test. All the parameters and data are assumed to be independent in the ACC2 inversions (Section 5.2). A χ^2 test would not produce a meaningful result.

B.2.3. Land Use CO_2 Emission in the Late 20th Century

To explain the observed atmospheric CO_2 concentration in the late 20th century, the posterior estimates of the land use CO_2 emission (Houghton, 2003) are substantially smaller than the prior even with strong terrestrial biospheric uptake. The posterior land use CO_2 emission (Figure B.1.2) is lower than the corresponding prior for the last 60 years. The posterior estimate of the beta factor is 0.59, which is high in the prior range between 0.1 and 0.7. The high beta factor is in line with Friedlingstein et al. (2006) showing strong CO_2 fertilization in most process-based terrestrial biosphere models.

It is important to point out that such inversion results should not be regarded merely as an indication for low land use CO_2 emission – they should rather be taken as an overall uncertainty in the historical carbon budget. Structural uncertainty in the carbon cycle is reflected to the posterior land use CO_2 emission because of its relatively large prior uncertainty range.

It should be noted that the prior uncertainty range of the land use CO_2 emission is assumed to be twice as large as the range suggested in Houghton (2003). Without such an adjustment, the inversion produces large residuals (beyond the 2σ prior uncertainty ranges) for land use CO_2

emission around 1991 (Figure B.7.2a) and for the atmospheric CO_2 concentration between 1930 and 1940 (Figure B.7.3a). The reasons for such an adjustment are three-fold: 1) Previous inversion studies (e.g. Gurney et al., 2002) indicate smaller estimates of land use CO_2 emission than Houghton's estimates. 2) In the inversion results, the land use CO_2 emission reflects the imbalance of the carbon budget due to the missing carbon cycle processes such as soil erosion, which is estimated to be -1.5 to +1.0 GtC/year (Lal, 2005). 3) Processes related to water cycle are not described in ACC2 (Section B.2.4).

B.2.4. Global Estimate of Q10

The posterior estimate of Q10 is 1.18, lying outside of the 2σ prior uncertainty range between 1.5 and 2.5 (Table B.2), which is based on the compilation of field measurements (Table 2 in Tjoelker et al. (2003)) and the observational constraint for GCM (Jones and Cox, 2001). It is also significantly lower than 2.0, which is typically assumed in biosphere models.

The low Q10 points to structural uncertainty – the low Q10 reflects the biospheric response not only to the temperature change but also to the soil moisture change, which is not described in ACC2. With global warming, the contrast between wet and dry regions will increase as all GCMs demonstrate (Wang, 2005). Precipitation and probably also soil moisture will increase in most of the presently wet regions and decrease in the subtropical regions. More water in presently wet soils will decrease heterotrophic respiration because of the oxygen limitation while less water in presently dry soils will also reduce heterotrophic respiration because of the water limitation. Thus, the temperature effect and the soil moisture effect on the heterotrophic respiration cancel out each other, resulting in the low Q10.

B.2.5. Temporal Suspension of the Atmospheric CO_2 Concentration Rise

The influence of decadal variability shows up in the residuals for the atmospheric CO_2 concentration. An example is the plateau between 1940 and 1960. During this period and thereafter, the temperature rise also stalls. Mechanisms that led to this phenomenon are in dispute. An inversion study (Trudinger et al., 2002) shows that the slowdown of the atmospheric CO_2 concentration rise is caused by the change in the large-scale ocean circulation. However, such a halt does not appear in the prior ocean CO_2 uptake based on C^4MIP runs (Figure B.1.4).

B.2.6. Terrestrial Biosphere Response to Volcanic Eruptions

Several strong volcanic forcing between 1750 and 1850 are offset by positive missing forcing when the corresponding temperature drops in reconstruction are relatively small (Figures B.1.10 to B.1.12).

The mismatch between the volcanic forcing and reconstructed temperature is explained by the diffuse radiation hypothesis (Robock, 2005): Photosynthesis is enhanced by diffuse radiation produced from the forward scattering of the solar radiation due to stratospheric sulfate aerosols. However, evidences for the diffuse radiation hypothesis are not yet conclusive as there are large discrepancies among different volcanic forcings (Section B.4.2) and temperature reconstructions (Jones and Mann, 2004, Figures 7 and 8).

We discuss two examples below. After the Tambora eruption in 1815, no temperature drop appears in the reconstruction. If the diffuse radiation hypothesis is true, tree ring proxies used for the temperature reconstruction would be biased by the plant growth enhanced by the diffuse radiation. Then, the temperature would have actually been lower after the eruption than what is directly indicated by the proxies.

Following the Pinatubo eruption in 1991, the growth of the atmospheric CO_2 concentration slowed down. Our inversion results indicate that the suppression of the heterotrophic respiration due to the cooling was not sufficient to explain the observed CO_2 concentration trend, resulting in a drastic reduction in the land use CO_2 emission (Figure B.1.2). If the diffuse radiation hypothesis is true, the unusually low land use CO_2 emission can be attributed to the photosynthesis enhancement due to increased diffuse radiation (Gu et al., 2003).

B.2.7. Optimal Climate Sensitivity

Differences in the optimal climate sensitivity obtained from different approaches can be explained by looking at residuals.

The best estimate of climate sensitivity is larger in the coupled inversion (4.04°C) than in the uncoupled inversion (3.37°C). The higher optimal climate sensitivity in the coupled inversion is due to the declining trend in the residuals for land use CO_2 emission toward high climate sensitivity (Figure 5.3).

The optimal climate sensitivity is higher in the forcing-scaling inversion (3.77°C) than in the missing forcing-based inversion (3.37°C). Figure B.4 shows that this is primarily caused by the residual curve for the surface air temperature change, which dominates the change in the cost function. The temperature residual curve has a distinct minimum at climate sensitivity of 3.5–4.0°C.

B.3. ASSUMPTIONS FOR PRIOR FORCING UNCERTAINTY

The prior uncertainty of radiative forcing is uncertain (a problem of uncertainty's uncertainty). In this section, we first discuss numerical simulations that indicate the standard prior uncertainty range for missing forcing. And then we look at the sensitivity of the inversion results to the prior uncertainty range of missing forcing.

The prior forcing uncertainty range assumed in the ACC2 inversion can be supported by model calculations. The 2σ prior missing forcing range of 0.5 W/m^2 is assumed before 1900 in order to account for the temperature variability of 0.5°C under various climate sensitivity (up to 6.5°C as in its 2σ prior range). Such temperature variability is indicated from the early 20th-century warming and the natural variability of a GCM control run (Doney et al., 2006). Figure B.5 shows that, if the climate sensitivity is 6.5°C, a sustained perturbation of 0.5 W/m^2 leads to a warming of about 0.5°C over 50 years.

Cost function curves are sensitive to the prior range for missing forcing (Figure B.6). If we reduce the prior missing forcing range by 50%, the cost function curve is not only shifted up over the entire range of climate sensitivity, but also tilted up toward high climate sensitivity (Figure B.6.1). The temperature time series (Figure B.6.3) show that such a tilt stems mainly from the growing misfit for the temperature after volcanic eruptions in the early 19th century. The slope toward high climate sensitivity is coincidentally similar to those for the forcing scaling approach. With smaller prior forcing uncertainty range, the slope eventually converges to that for no forcing uncertainty. The cost function curve for the forcing scaling approach is not sensitive to the prior uncertainty range for the forcing scaling factor, indicating that the single parameter of forcing scaling factor does not have a significant impact on the cost function.

B.4. ASSUMPTIONS RELATED TO CARBON CYCLE FEEDBACK

The second main conclusion on carbon cycle feedback rests on the prior assumptions for the land use CO_2 emission and also on the prescribed volcanic forcing selected among others. Volcanic eruptions have a non-negligible perturbation to the global carbon cycle. In this section, we demonstrate that the inversion results are influenced by the prior land use CO_2 emission – nonetheless, the conclusions remain the same.

B.4.1. Prior Uncertainty in Land Use CO_2 Emission

The uncertainty range for land use CO_2 emission is uncertain and is assumed twice as large as the uncertainty range suggested by Houghton (2003) (Section B.2.3). We discuss the sensitivity of the inversion results to prior uncertainty range for land use CO_2 emission.

When a 50% smaller prior range for land use CO_2 emission (equivalent to Houghton's estimate) is assumed, the cost function value of the coupled inversion becomes substantially smaller than that of the uncoupled inversion over the entire range of climate sensitivity (Figure B.7.1). The larger difference between the coupled and uncoupled results stems from the carbon cycle in the early 19th century. The cessation of the CO_2 concentration rise during the period 1800-1850 is explained by the suppression of soil respiration during the cooling periods following large volcanic eruptions.

Without the climate-carbon cycle feedback, the slump of the CO_2 concentration rise is reproduced by the reduction in the land use CO_2 emission. This results in a larger penalty in the cost function particularly when the prior range of the land use CO_2 emission is assumed 50% smaller than the standard (Figure B.7.2a). The opposite but less pronounced results are found when the prior uncertainty of land use CO_2 emission is assumed 50% larger than the standard (Figure B.7.2c).

Using 50% smaller prior range for land use CO_2 emission is problematic. This is indicated from the large residuals for land use CO_2 emission around 1991 (Figure B.7.2a) and for the atmospheric CO_2 concentration between 1930 and 1940 (Figure B.7.3a). Under such an assumption, the inversion is forced to resolve prior information in conflict. In light of the overall uncertainty in the global carbon budget (Section B.2.3), it is fair to assume the standard prior range (twice as large as the Houghton's range).

It is worth noting that in the uncoupled inversion results the best estimate of the climate sensitivity is nearly unaffected from the change in the prior uncertainty range for land use CO_2 emission. The inversion in the carbon cycle component hardly influences the inversion in the climate component in the absence of the climate-carbon cycle feedback. This result itself is interesting as it suggests that uncertainty in the carbon cycle system can hardly be seen as a problem from the climate system – the uncertainties in radiative forcing and climate sensitivity dwarfs the uncertainties in the carbon cycle. This is so unless a feedback from climate to carbon cycle is provided.

B.4.2. Volcanic Forcing

Estimates of volcanic forcing depend on the ice cores used, interpretation of the records, and estimation methodology (e.g. scaling from aerosol optimal depth to radiative forcing) as indicated by the inconsistency among different volcanic forcing estimates (e.g. Ammann et al., 2003; Bertrand et al., 2002; Crowley et al., 2003). We investigate whether our finding based on Ammann's volcanic forcing is still valid when different volcanic forcing is used.

Inversion results based on the three different volcanic forcings are compared in Figure B.8. Missing forcing shows marked differences before 1930 (Figures B.8.5 and B.8.6), but this does not affect our conclusions on forcing uncertainty. Similar results can be seen in the carbon cycle (Figures B.8.2 to B.8.4), supporting our conclusion on carbon cycle feedback. The trend of the cost function curve is similar among all the inversion results (Figure B.8.1). The climate sensitivity is estimated higher for the coupled inversion in all the three cases. The best guess of climate sensitivity is diverse in particular in the coupled cases, ranging from 3.37°C to 4.44°C.

B.5. OTHER KEY ASSUMPTIONS IN THE ACC2 INVERSION

In the previous sections we have analyzed how the inversion results are influenced by the prior missing forcing range, the prior land use CO_2 emission range, and the prescribed volcanic forcing. In this section, we discuss the influences from remaining key assumptions: namely, the presupposed ocean diffusivity and the prior climate sensitivity.

B.5.1. Ocean Diffusivity

Ocean diffusivity is a major uncertainty in the climate system. However, we assume a fixed estimate for ocean diffusivity (0.55 cm^2/s) based on Kriegler (2005, Figure 2.8) because ocean diffusivity cannot be well-constrained simultaneously with climate sensitivity in our inversion setup, which does not utilize ocean heat distribution data (Levitus et al., 2000). We look into how our results are affected when assuming different ocean diffusivity (1.0 cm^2/s and 2.0 cm^2/s).

The results of such a sensitivity analysis are shown in Figure B.9. The influence of the ocean diffusivity to the inversion results is systematic and small (Figure B.9.1). Time series in Figures B.9.2 and B.9.3 are nearly the same. Thus, our main findings are not affected by the treatment of ocean diffusivity.

B.5.2. Prior Climate Sensitivity

It has been argued that prior assumptions highly influence inversion results (Tol and de Vos, 1998; Frame et al., 2005). We investigate the sensitivity of the inversion results to different prior assumptions for climate sensitivity. The prior 2σ uncertainty range adopted in the standard inversion is 0.5°C–6.5°C. The prior mean is 3.5°C as normal distributions are assumed for all the parameters and data in the ACC2 inversion. We try our inversion for the 2σ uncertainty range of 1.5°C–4.5°C, a conventional range indicated by GCMs (IPCC, 2001, Chapter 9). The 2σ uncertainty range of 0.5°C–10.5°C is also tested, a conservative range emphasizing the long tail indicated by PDFs for climate sensitivity (e.g. IPCC, 2007, pp.798-799).

The resulting change in the best estimate of climate sensitivity is, however, not substantial (Figure B.10). One reason is that in our approach the time-variant parameters are dominant in the cost function over constant parameter such as climate sensitivity. The analysis here suggests that our main conclusions are not significantly influenced by the prior climate sensitivity.

B.6. MISSING FORCING

Missing forcing is “catch-all” forcing, comprising mainly three elements as discussed in Chapter 5.

First, we provide a brief discussion on the posterior missing forcing. Then we investigate how the missing forcing is influenced by aerosol forcing, volcanic forcing, ENSO-induced temperature variability to get an insight into the composition of missing forcing.

B.6.1. Posterior Missing Forcing

The missing forcing is punctuated by large spikes corresponding to volcanic eruptions. Most of these spikes are positive and some others negative, depending on how are the mismatches between the volcanic forcing and the reconstructed temperature. The missing forcing after 1900 is highly variable, reflecting the interannual variability of the temperature records. The fluctuation becomes larger toward present as the prior temperature uncertainty gets smaller with extensive observation network put into place and also as the prior uncertainty of the missing forcing becomes larger to reflect aerosol forcing uncertainty. The average missing forcing over the last 50 years is about -0.12 W/m^2, an indication that the aerosol forcing used in ACC2 is slightly underestimated in magnitude.

B.6.2. Influence from Aerosol Forcing

We look at how the uncertainty in aerosol forcing is reflected to missing forcing. The aerosol forcing is a major uncertainty in the climate system (IPCC, 2007, p.32). In ACC2, the aerosol forcing is represented by the following three types: sulfate aerosol forcing (direct effect), carbonaceous aerosol forcing (direct effect), and all aerosol forcing (indirect effect) (Table 2.1). The direct sulfate aerosol forcing and indirect aerosol forcing are calculated based on the respective parameterizations given as a function of SO_2 emission. The carbonaceous aerosol forcing is given as a function of CO emission. These three types of aerosol forcings are summed up to 1.3 W/m^2 in year 2000. We perform a sensitivity analysis of the inversion results by assuming 50% weaker total aerosol forcing over the entire period and also by assuming 50% stronger total aerosol forcing.

The results of such a sensitivity analysis are in Figure B.11, showing that the missing forcing acts to cancel out the hypothesized change in the magnitude of aerosol forcing. The offset between the aerosol forcing and the missing forcing is only partial – there are large differences in the posterior estimates of climate sensitivity (1.95°C for 50% weaker aerosol forcing; 3.37°C for standard aerosol forcing; and 6.71°C for 50% stronger aerosol forcing). Final values of the cost function are, however, similar (368.8 for 50% weaker aerosol forcing; 371.7 for standard aerosol forcing; and 386.9 for 50% stronger aerosol forcing).

B.6.3. Influence from Volcanic Forcing

We check how the uncertainty in volcanic forcing (Section B.4.2) is reflected to the missing forcing.

We perform a sensitivity analysis of the inversion results to volcanic forcing (Ammann et al., 2003; Bertrand et al., 2002; Crowley et al., 2003).

The results of the sensitivity analysis are in Figure B.12. It is demonstrated that the missing forcing is highly influenced by the volcanic forcing. It is evident in particular before 1900, but for the last 100 years it is less explicit as it is superimposed by the influence from the interannual variability in the temperature records. Mostly missing forcing turns strongly positive, contemporaneous with volcanic eruptions, which can be interpreted as corrections for the volcanic forcing to reproduce the reconstructed temperature. Note that such corrections are not always positive (e.g. 1890 in Ammann's volcanic forcing). The insert of Figure B.12.1 shows that the missing forcing is all contained within the 2σ prior boundary, except for the period influenced by the Tambora eruption in 1815 in Crowley's volcanic forcing.

B.6.4. Influence from ENSO-driven Temperature Variability

We look into how the missing forcing is influenced by interannual variability in the temperature data. In the standard ACC2 inversion setup, the ENSO-induced interannual variability in the temperature records is removed by using a linear regression as a function of an annualized Southern Oscillation Index (SOI) (Section 3.5.1). The annualization includes a 4-month lead because the temperature variability is statistically best explained by SOI with 4-month lead (Kriegler, 2005, Figure 2.4; our pre-analysis). The ENSO-related correction on the temperature records is applied only after 1930 due to the credibility of the index. We perform an inversion without using the ENSO-related correction on the temperature records and compare it with the standard results.

The two inversion results are compared in Figure B.13, showing that the missing forcing reflects the interannual variability of the temperature records. The insert of Figure B.13.2 demonstrates that, when a strong El Niño or La Niña event occurs, the temperature fit is better with the correction for ENSO-induced temperature variability. Without the ENSO-related correction, the missing forcing is adjusted such that it artificially produces the ENSO-induced temperature variability (insert of Figure B.13.1).

B.7. COST FUNCTION CURVE VS PDF

In Chapter 5, we argue that the cost function curves for climate sensitivity (consisting of different optimization results) are qualitatively indicative of PDFs for climate sensitivity in literature because the cost function changes monotonically with parameters and it does not show other local optima or extreme irregularity. We now demonstrate this by a sensitivity analysis of the cost function curves with respect to major influential parameters.

The results in Figures B.14.1 to B.14.4 show that the changes in the cost function curves

are not so drastic or irregular for middle to high climate sensitivity. These results suggest that cost function curves are comparable to PDFs for middle to high climate sensitivity. Although rigorous proofs for the statements above require extensive parameter sampling and mathematical derivations, our sensitivity analysis provides a first-order indication that the cost function curves are qualitatively comparable to PDFs for climate sensitivity.

Furthermore, we check how the cost function curves appear on the scale of probability density $\sigma_{\mathrm{M}}(\mathbf{m})$ and whether the main conclusions can still be drawn. Equation (3.2.12) shows that the cost function $S(\mathbf{m})$ is the negative argument of the exponential function representing the marginal posterior PDF of all the parameters $\sigma_{\mathrm{M}}(\mathbf{m})$.

$$\sigma_{\mathrm{M}}(\mathbf{m}) = k'' \exp\big(-S(\mathbf{m})\big) \tag{3.2.12}$$

We convert the cost function curves on an exponential scale and renormalize them.

The conversion results are shown in Figure B.15, suggesting that, although the same conclusion on the importance of forcing uncertainty is still indicated from the converted curves, the clarity of the finding certainly depends on how the results are expressed. The curve for the forcing scaling approach is sharper than the curve for the missing forcing approach although the difference appears less drastic. The slopes toward high climate sensitivity are not as clearly distinguishable in Figure B.15 as in Figure 5.1. On the contrary, the difference between the curve for the coupled inversion and that for the uncoupled inversion is now more distinctive.

The converted curves in Figure B.15 should be interpreted with caution similar to the original cost function curves in Figure 5.1 because these converted curves are still not exactly PDFs of climate sensitivity. As discussed in Section 5.1, the cost function curves are the series of peaks of the marginal posterior PDF for all the parameters. The PDFs for climate sensitivity shown in literature are obtained by integrating our marginal PDFs with respect to the parameters other than climate sensitivity. The comparison of different cost function curves or those converted only qualitatively indicates PDFs.

B.8. AUTOCORRELATIONS

The residuals for the data and parameters in the ACC2 inversion are assumed to be independent without accounting for their autocorrelations. Although such an assumption implies that fits for time series having strong autocorrelations are over-emphasized, the autocorrelations are neglected altogether in the ACC2 inversion because of the difficulty in fully estimating them (Section 5.2.2). However, Ricciuto et al. (2008) demonstrate that neglecting autocorrelations result in overconfidence in parameter estimation by using an inversion setup for a simple global carbon cycle and climate model. It is also statistically known that the ignorance of autocorrelations biases the estimation (e.g. Zellner and Tiao, 1964). Thus, in this section, we quantitatively assess how the

solutions of the ACC2 inversions are biased due to the ignorance of autocorrelations. Our analysis focuses on the autocorrelations in the surface air temperature residuals and their impacts on the cost function curves in Figure 5.1.

B.8.1. Implementing AR(1) Model in the Cost Function

The following explains how the autocorrelations in temperature residuals can be taken into account in the ACC2 inversion. The solution of the ACC2 inversion corresponds to the minimum of the cost function $S(\mathbf{m})$:

$$S(\mathbf{m}) = \frac{1}{2}\left(\sum_{i=1}^{a} \left(\frac{g_i(\mathbf{m}) - d_{mes,i}}{\sigma_{d,i}} \right)^2 + \sum_{j=1}^{b} \left(\frac{m_j - m_{prior,j}}{\sigma_{m,j}} \right)^2 \right). \qquad (3.2.14)$$

$g_i(\mathbf{m})$ is the forward model projection for data i based on a set of parameter $\mathbf{m}$. a and b are the total numbers of data and parameters, respectively. $d_{mes,i}$ and $m_{prior,j}$ denote measurement i and prior estimate of parameter j, respectively. $\sigma_{d,i}$ and $\sigma_{m,j}$ are one-sigma uncertainty ranges for measurement i and for prior estimate of parameter j, respectively. In terms of "residuals," i.e. the differences between prior and posterior values, equation (3.2.14) can be expressed as

$$S(\mathbf{m}) = \frac{1}{2}\left(\sum_{i=1}^{a} \left(\frac{r_{d,i}}{\sigma_{d,i}} \right)^2 + \sum_{j=1}^{b} \left(\frac{r_{m,j}}{\sigma_{m,j}} \right)^2 \right), \qquad (B.8.1)$$

where $r_{d,i}$ and $r_{m,j}$ are the residuals for data *i* and parameter *j*.

In order to account for the autocorrelations in temperature residuals, we use an AR model of 1st-order (AR(1)), a simplest method to describe an AR process. Collins et al. (2001) demonstrate that the global-mean surface air temperature variability of the 1000-year control run of HadCM3 can be described as an AR(1) process. Kriegler (2005, p.43) concludes that based on several statistical tests, an AR(1) model is sufficient to describe the weather-driven variability of SST residuals during the period 1870-2002 except for ENSO. However, it is not clear how the decadal variability appeared in the residuals can be explained just with an AR(1) model. Eden et al. (2002) demonstrate that AR(5) provides a best fit to explain the variability in the mix layer temperature of the North Atlantic. Nevertheless, we use the AR(1) representation as a first cut and check the residual spectrums to see whether the AR(1) model removes the autocorrelations in temperature residuals.

An AR(1) model (e.g. Box and Jenkins, 1970, pp.56-58; von Storch and Zwiers, 1999, p.204) between temperature residuals can be described as

$$r_{d,k+1} = \alpha \cdot r_{d,k} + \beta + \varepsilon_{d,k}, \quad k = 1,2,\cdots,250 \qquad (B.8.2)$$

where α and β are the propagator and constant, respectively. $r_{d,k}$ and $r_{d,k+1}$ are temperature residuals. Index numbers 1-251 are assigned to temperature residuals in years 1750–2000. $\varepsilon_{d,k}$ is Independently and Identically Distributed (IID) (thus, white noise) and follows a normal distribution

with a mean of zero and a standard deviation of σ_ε. By further assuming $\beta = 0$, the AR(1) model is simplified to

$$r_{d,k+1} = \alpha \cdot r_{d,k} + \varepsilon_{d,k} . \tag{B.8.3}$$

The AR(1) model is implemented to the cost function $S(\mathbf{m})$ as follows:

$$S(\mathbf{m}) = \frac{1}{2}\left(\left(\frac{r_{d,1}}{\sigma_\varepsilon} \right)^2 + \sum_{i=1}^{250} \left(\frac{r_{d,i+1} - \alpha \cdot r_{d,i}}{\sigma_\varepsilon} \right)^2 + \sum_{l=251}^{a} \left(\frac{r_{d,l}}{\sigma_{d,l}} \right)^2 + \sum_{j=1}^{b} \left(\frac{r_{m,j}}{\sigma_{m,j}} \right)^2 + \left(\frac{r_{m,b+1}}{\sigma_{m,b+1}} \right)^2 \right). \tag{B.8.4}$$

The first term on the right side of equation (B.8.4) account for the squared weighted residual for the temperature residual in 1750. The autocorrelation for this start year is not considered, but this does not significantly affect the results because the time series are relatively long in our inversion. For the temperature residuals from 1751 onward, the autocorrelations are taken into account (second term in equation (B.8.4)). The standard deviation σ_ε is used for all the temperature residuals instead of the prior uncertainty for temperature change, e.g. $\sigma_{d,k}$. The residual terms of the other parameters and data are unchanged (third and fourth terms). The last term on the right side of equation (B.8.4) is introduced for the new parameter α. The implementation here is similar to the form of the likelihood function for an AR(1) process (e.g. Box and Jenkins, 1970, pp.274-284; von Storch and Zwiers, 1999, pp.257-258).

B.8.2. Estimation of AR(1) Propagator

The previous section shows how an AR(1) model is implemented in the cost function. In this section, we discuss the estimation problem of the propagator α and the standard deviation σ_ε in equation (B.8.3). For this exercise, we assume a fixed value of 0.45 for propagator α. Such a value is the maximum likelihood estimate for the SST residuals (except for ENSO) during the period 1870-2002 (Kriegler, 2005, p.40). We also assume a value of 0.078°C for the standard deviation σ_ε. This estimate is also taken from Kriegler (2005, p.36). This set of estimates is assumed for all the ACC2 inversion cases when the AR(1) model is introduced. As a result of such an assumption, the propagator α is no longer considered as a new parameter in the inversion. Thus, the last term in the cost function (equation (B.8.4)) is dropped and the cost function can be rewritten as

$$S(\mathbf{m}) = \frac{1}{2}\left(\left(\frac{r_{d,1}}{\sigma_\varepsilon} \right)^2 + \sum_{i=1}^{250} \left(\frac{r_{d,i+1} - \alpha \cdot r_{d,i}}{\sigma_\varepsilon} \right)^2 + \sum_{l=251}^{a} \left(\frac{r_{d,l}}{\sigma_{d,l}} \right)^2 + \sum_{j=1}^{b} \left(\frac{r_{m,j}}{\sigma_{m,j}} \right)^2 \right). \tag{B.8.5}$$

Our approach stated above is in contrast to other studies in which the propagator for the AR(1) model is treated similar to other parameters and optimized in the inversion (e.g. Ricciuto et al., 2008). The value of propagator is indeed specific to the specific inversion result. However, we dare to take this approach due to an interpretational problem discussed below.

To interpret the AR(1) model from the perspective of inverse estimation, equation (B.8.4) is reformulated as follows:

$$S(\mathbf{m}) = \frac{1}{2}\left(\cdots + \left(\frac{r_{d,k}}{\sigma_\varepsilon / \sqrt{1+\alpha^2}} \right)^2 - \frac{1}{\sigma_\varepsilon / 2\alpha} r_{d,k-1} \cdot r_{d,k} - \frac{1}{\sigma_\varepsilon / 2\alpha} r_{d,k} \cdot r_{d,k+1} + \cdots \right) + \frac{1}{2}\left(\frac{r_{m,b+1}}{\sigma_{m,b+1}} \right)^2 \tag{B.8.6}$$

Only the changes related to temperature residual $r_{d,k}$ are explicitly shown in equation (B.8.6). In all the three terms on the right side of equation (B.8.6), the propagator α appears. If the propagator α is optimized in the inversion, equation (B.8.6) shows that the prior uncertainty for $r_{d,k}$ (and also the associated covariances), which must be fixed before the inversion, is optimized to minimize the cost function. This is not theoretically compatible with inverse estimation even though numerical computation is feasible. Therefore, in this exercise, a fixed value is assigned for propagator α. Note that this problem is rarely discussed in the field of econometrics (Jesus Crespo Cuaresma, personal communication, April 19, 2008). Further research is required to clarify this problem.

B.8.3. Experimental Design

By using the AR(1) model discussed above, we re-calculate the results of the three types of inversions shown in Figure 5.1: namely, the missing forcing-based inversion, the forcing scaling-based inversion, and the inversion assuming no forcing uncertainty. Similar to other sensitivity analyses, the relationship between the cost function and the value of climate sensitivity is calculated by performing a series of inversions by which the climate sensitivity is fixed at values between 1°C and 10°C at intervals of 0.25°C. By comparing with the original inversion results without the AR(1) model, we investigate how the ignorance of temperature residuals affects the conclusion of the importance of forcing uncertainty that is drawn from Figure 5.1.

Except for the AR(1) model implementation, other parts of the model and inversion are kept the same. Some detailed notes for the methodology follow. We apply the similar treatment for the standard deviation σ_ε during the periods under the influence of large volcanic eruptions (Section 3.5.2). Namely, the standard deviation σ_ε is assumed to be larger by a factor of 4 when volcanic forcing is stronger than -0.5 W/m^2. The ENSO-driven temperature variability is also statistically considered as in the standard inversion without the AR(1) model (Section 3.5.1). The Kriegler's estimate of σ_ε is obtained for the period of instrumental temperature, but the same estimate is assumed for all the period in our exercise. The autocorrelations for missing forcing are still neglected because the estimate of the associated propagator is not available. The autocorrelations for atmospheric CO_2 concentration is also not included in our analysis as we focus on the autocorrelations in temperature residuals and clarify how the ignorance of temperature autocorrelations affects the main conclusion on the importance of forcing uncertainty. It should be

noted that the estimate of associated AR(1) propagator is available (0.83 in Ricciuto et al. (2008)) with the standard deviation of whitened residuals of 0.43 ppm.

B.8.4. Results and Discussion

In Figure B.16.1, the results of the three types of inversions including the AR(1) model are compared with the results of the corresponding standard inversions without the AR(1) model. The associated residuals in several selected time series are shown in Figure B.16.2. In more detail, Figures B.16.3 to B.16.6 show the radiative forcing and temperature change for such inversions with the climate sensitivity fixed at 1, 3, 5, and 10°C. The histograms and spectrums of the temperature residuals are shown in Figure B.17.

Visual inspection of the cost function curves in Figure B.16.1 suggests that on the whole the cost function curves based on the inversions including the AR(1) model are wider than those based on the standard inversions. This result suggests that the ignorance of autocorrelations leads to an overconfidence of climate sensitivity estimation, which is in line with the carbon cycle results obtained by Ricciuto et al. (2008).

Looking into this result in more details, the influence of the AR(1) model to the cost function curves is different for low and high climate sensitivity. Toward high climate sensitivity, the slopes of the cost function curves are hardly influenced by the inclusion of the AR(1) model in all the three inversion cases. This result suggests that our conclusion on the importance of forcing uncertainty is unaffected even if the autocorrelations in temperature residuals are neglected.

On the contrary, in low climate sensitivity, the slopes of the cost function curves become much flatter by the inclusion of the AR(1) model. This is particularly so in the forcing scaling case. The flatter curve for the forcing scaling case stems from the trend in the temperature residuals (right panel of Figure B.16.2). Figure B.16.6 furthermore shows that in the forcing scaling case with climate sensitivity of 1°C, the temperature residuals during the period 1940-1950 and 1980-2000 are less penalized than in the case without the AR(1) model. This results in the flatter curve toward low climate sensitivity in the forcing scaling case. Note that this also causes the best estimate of climate sensitivity to be merely 1.60°C. But these results are highly influenced by the assumption for the value of standard deviation σ_ε.

The best estimate of climate sensitivity for the missing forcing approach is slightly lowered from 3.37°C to 3.06°C when the AR(1) model is considered (Figure B.16.1). This is primarily caused by the flatter shape of missing forcing residuals (left panel of Figure B.16.2). This can be seen in the time series in Figure B.16.3, which shows that the missing forcing becomes substantially smaller for the last 50 years of the inversion (climate sensitivity fixed at 1°C). The smaller missing forcing in combination of small climate sensitivity results in an apparent systematic underestimation of the recent temperature (Figure B.16.4). However, this turns out to be the ‘best

estimates' because the systematic errors are partly explained as autocorrelations. This result points to the necessity of careful interpretation of the inversion results when the autocorrelations are considered because removing autocorrelations can mask wrong results.

The other noteworthy result is that the cost function curve for the missing forcing approach in Figure B.16.1 is lifted up by the inclusion of the AR(1) model whereas those for the other two cases are lowered. The left panel of Figure B.16.2 indicates that the increase in the cost function values for the missing forcing approach is primarily due to the increase in the temperature residuals over the entire range of climate sensitivity. Furthermore, Figure B.16.6 shows that the temperature residuals before 1850 are more penalized due to the smaller standard deviation. Thus this result also depends on the presupposed value of standard deviation σ_ε.

To check the validity of using the AR(1) model, visual inspection of the spectrums in Figure B.17 indicates that in all the cases the residuals appear as white noise when the AR(1) is implemented.

In conclusion, our analysis confirms the fact that the ignorance of autocorrelations leads to an overconfidence of parameter estimation (e.g. Zellner and Tiao, 1964; Ricciuto et al., 2008). In our results, however, this does apply to low climate sensitivity but not high climate sensitivity. By neglecting the autocorrelations in temperature residuals, the confirmation of ruling out the low climate sensitivity becomes excessively strong. On the contrary, the main conclusion on the importance of forcing uncertainty holds irrespective of the treatment of the autocorrelations in temperature residuals. The best estimate of climate sensitivity is overestimated when the temperature autocorrelations are not considered.

The analysis presented here considers only the autocorrelations in temperature residuals described as the AR(1) model, leaving out all the other autocorrelations including those remaining in the residuals of temperature and those in other parameters and data. In particular, the autocorrelations for the missing forcing residuals are important for our analysis. To account for them, the theoretical problem of estimating the propagator α (Section B.8.2) needs to be worked out. The results here are also sensitive to the presupposed value of standard deviation σ_ε. Furthermore, it is problematic in our results that systematic errors in time series are also explained as autocorrelations. The memory of the nonlinear system makes this problem even severe.

In considering the caveats and problems stated above, our present analysis of autocorrelations is preliminary. More work lies ahead to properly consider the autocorrelations in the ACC2 inversions.

Table B.1. Data in the ACC2 coupled inversion (after Table 3.1)

* Four times larger uncertainty ranges are assumed when volcanic forcing is stronger than -0.5 W/m^2 (Section 3.5.2). The total number of degrees of freedom for data is 1,498.

Names (degrees of freedom)	Periods	Measurement types	Temporal resolutions	2σ measurement uncertainties	Data sources
Ocean CO_2 uptake (df=250)	1750-1860	N/A	Linear extrapolation to the origin from 1860 to 1750	Average uncertainties between 1865 and 2000	N/A
	1861-2000	C^4MIP GCMs/EMIC	10-year moving average	Maxima and minima of GCMs runs (=1σ)	Friedlingstein et al. (2006)
Land CO_2 uptake (df=250)	1750-1860	N/A	Linear extrapolation to the origin from 1860 to 1750	Average uncertainties between 1865 and 2000	N/A
	1861-2000	C^4MIP GCMs/EMIC	10-year moving average	Maxima and minima of GCMs runs (=1σ)	Friedlingstein et al. (2006)
Atmospheric CO_2 concentration (df=250)	1750-1968	Ice core sampling (Law Dome, Antarctica)	75-year cutoff spline fit with 5-year intervals (1750-1830) 25-year cutoff spline fit with 1-year intervals (1832-1968) Linear interpolations between the data points	*1.2 ppm	Etheridge et al. (1996)
	1969-2000	Station measurements (Mauna Loa, Hawaii)	Annual fit	*0.8 ppm (0.2 ppm in the literature)	Keeling et al. (2005)
Atmospheric CH_4 concentration (df=249)	1750-1850	Ice core sampling (Law Dome, Antarctica; Summit, Greenland)	75-year cutoff spline fit with 10-year intervals (1750-1900) 12.5-year cutoff spline fit with 2-year intervals (1900-1984) Linear interpolations between the data points	*5 ppb	Etheridge et al. (1998)
	1851-1983				Etheridge data compiled by Hansen and Sato (2004) Etheridge et al. (1998)
	1984-2000	Station measurements (CMDL global air sampling network)	Annual fit	*12 ppb (3 ppb in the literature)	Dlugokencky data compiled by Hansen and Sato (2004) for mean estimates Masarie et al. (2001, Table 1) for uncertainties
Atmospheric N_2O concentration (df=249)	1750-1961	Ice core sampling (Summit, Greenland)	300-year cutoff spline fit with 1-year intervals	*Time variant	Flueckiger (personal communication)
	1962-1977			*Interpolation	Hansen and Sato (2004)
	1978-2000	Station measurements (CMDL global air sampling network)	Annual fit	*2.0 ppb (0.5 ppb in the literature)	Hansen and Sato (2004) for mean estimates Masarie et al. (2001, Table 1) for uncertainties
Surface air temperature change (df=250)	1750-1855	Multi-proxy	1-year intervals	*0.36°C	Jones et al. (1998) for mean estimates Mann and Jones (2003) for uncertainties
	1856-2000	Instrumental measurements	Annual fit	*0.20°C (1856-1860) *0.05°C (2000) *Linear interpolation between the periods	Jones et al. (2006)

Table B.2. Parameters in the ACC2 coupled inversion (after Table 3.2)

* Four times larger uncertainty ranges are assumed when volcanic forcing is stronger than -0.5 W/m^2 (Section 3.5.2). The total number of degrees of freedom for parameters is 1,266.

Names (degrees of freedom)	Prior estimates	2σ prior uncertainties
Anthropogenic CO_2 emission due to fossil fuel combustion (df=251)	Marland et al. (2006) between 1750 and 2000	±8% of the prior mean (Marland et al., 2006)
Anthropogenic CO_2 emission due to land use change (df=251)	Houghton (2003) between 1850 and 2000 Linear extrapolation between 1750 and 1849 Zero emission in 1750	±100% of the prior mean (±50% in Houghton (2003))
Anthropogenic CH_4 emission (df=251)	van Aardenne et al. (2001) between 1890 and 2000 Nonlinear extrapolation between 1750 and 1890 Zero emission in 1750	±50% in 2000, ±100% in 1970 ±150% between 1890 and 1950 Linear interpolations between the periods Absolute uncertainty ranges assumed constant before 1890 (John van Aardenne, personal communication)
Anthropogenic N_2O emission (df=251)	van Aardenne et al. (2001) between 1890 and 2000 Linear extrapolation between 1750 and 1890 Zero emission in 1750	±50% in 2000, ±100% in 1970 ±150% between 1890 and 1950 Linear interpolations between the periods Absolute uncertain ranges assumed constant before 1890 (John van Aardenne, personal communication)
Missing forcing (df=251)	Zero forcing between 1750 and 2000	*±0.5 W/m^2 between 1750 and 1900 *±1.0 W/m^2 in 2000 *Linear interpolation between 1900 and 2000
Preindustrial mixed layer temperature (df=1)	19.59°C (Hoffert et al., 1981, pp.290-291; Sundquist and Plummer, 1981, p.267)	Between 13.59 and 25.59°C
Atmosphere-mixed layer temperature scaling factor (df=1)	0.5	Between 0.0 and 1.0
Beta factor for CO_2 fertilization (df=1)	0.4 (0.287 (Meyer et al., 1999; Kicklighter et al., 1999), 0.4 (Gitz and Ciais, 2003), 0.45 (Brovkin et al., 1997), and 0.15 to 0.6 (Kohlmaier et al., 1987))	Between 0.1 and 0.7 (references in left column)
Q10 for heterotrophic respiration (df=1)	2.0 (Jones and Cox, 2001; Tjoelker et al., 2001)	Between 1.5 and 2.5 (references in left column)
Preindustrial ocean CO_2 uptake (df=1)	-0.24 GtC/year (net degassing) (-0.48 GtC/year in Mackenzie and Lerman (2006))	Between -0.48 and 0.0 GtC/year
Preindustrial land CO_2 uptake (df=1)	0.30 GtC/year (net uptake) (0.36 - 0.6 GtC/year in Mackenzie and Lerman (2006))	Between 0.0 and 0.60 GtC/year
Natural CH_4 emission (df=1)	210 Mt(CH_4)/year (IPCC, 2001, Table 4.2)	Between -30 and 450 Mt(CH_4)/year (IPCC, 2001, Table 4.2)
Natural N_2O emission (df=1)	10.2 Mt(N)/year (IPCC, 2001, Table 4.4)	Between 7.8 and 12.6 Mt(N)/year (IPCC, 2001, Table 4.4)
CH_4 lifetime with respect to OH depletion (df=1)	9.6 year (IPCC, 2001, Table 4.3)	Between 5.4 and 13.8 year (IPCC, 2001, Table 4.3)
N_2O lifetime (df=1)	110 year (IPCC, 2001, Table 4.5)	Between 83 and 137 year (IPCC, 2001, Table 4.5)
Climate sensitivity (df=1)	3.5°C (Forest et al., 2002; Gregory et al., 2002; Knutti et al., 2002; IPCC Working Group I, 2004; Kriegler, 2005; Stainforth et al., 2005; Forest et al., 2006; Hegerl et al., 2006; IPCC, 2007; Räisänen, 2007)	Between 0.5 and 6.5°C (references in left column)

Table B.3. Cost function values and squared weighted residuals in the main ACC2 inversions

The final values of the cost function are shown in the top row. Other entries show the contributions to the cost function arising from time-dependent parameters and data and also from constant parameters. These are equivalent to the squares of the residuals weighted by the associated prior uncertainty ranges (σ). Squared weighted residuals from time series are summed up over the time horizon of simulation. Units for all the quantities shown here are 1. Parameters marked with "—" are not included for the corresponding inversion setup. For example, in the uncoupled experiment, the preindustrial mixed layer temperature, the atmosphere-mixed layer temperature scaling factor, and Q10 for heterotrophic respiration are not included in the cost function as carbon cycle processes are not influenced by temperature change.

	Coupled Missing forcing	Uncoupled Missing forcing	Uncoupled Forcing scaling	Uncoupled No forcing uncertainty
Total	371.1	365.1	607.0	612.5
Parameters (time series)				
Fossil fuel CO_2 emission	1.5	1.4	1.5	1.5
Land use CO_2 emission	87.6	96.5	98.8	98.9
Anthropogenic CH_4 emission	5.8	5.8	5.8	5.8
Anthropogenic N_2O emission	16.6	16.5	16.5	16.8
Missing forcing	74.3	64.8	—	—
Parameters (constants)				
Preindustrial mixed layer temperature	0.01	—	—	—
Atmosphere-mixed layer temperature scaling factor	0.21	—	—	—
Beta factor for CO_2 fertilization	0.83	0.35	0.35	0.34
Q10 for heterotrophic respiration	5.58	—	—	—
Preindustrial ocean CO_2 uptake	0.46	0.39	0.39	0.39
Preindustrial land CO_2 uptake	0.71	0.60	0.60	0.60
Natural CH_4 emission	0.42	0.42	0.42	0.42
Natural N_2O emission	0.45	0.45	0.46	0.45
CH_4 lifetime	0.13	0.13	0.13	0.13
N_2O lifetime	0.05	0.05	0.05	0.05
Forcing scaling factor	—	—	0.02	—
Climate sensitivity	0.06	0.00	0.02	0.04
Data (time series)				
Ocean CO_2 uptake	18.8	19.4	19.4	19.5
Land CO_2 uptake	14.6	11.7	11.8	11.8
Atmospheric CO_2 concentration	27.9	30.6	28.7	28.6
Atmospheric CH_4 concentration	0.2	0.2	0.2	0.2
Atmospheric N_2O concentration	2.7	2.7	2.9	2.8
Surface air temperature change	112.3	113.1	418.9	424.3

Table B.4. Prior and posterior parameter estimates in the main ACC2 inversions

2σ prior uncertainty ranges are shown in brackets in the column for prior. Parameters marked with "—" are not included in the corresponding inversion setup.

	Posterior Coupled Missing forcing	Posterior Uncoupled Missing forcing	Posterior Uncoupled Forcing scaling	Posterior Uncoupled No forcing uncertainty	Prior For all cases
Preindustrial mixed layer temperature (°C)	19.9	—	—	—	19.6 (13.6 ~ 25.6)
Atmosphere-mixed layer temperature scaling factor (1)	0.34	—	—	—	0.5 (0.0 ~ 1.0)
Beta factor for CO_2 fertilization (1)	0.59	0.53	0.53	0.52	0.4 (0.1 ~ 0.8)
Q10 for heterotrophic respiration (1)	1.17	—	—	—	2.0 (1.5 ~ 2.5)
Preindustrial ocean CO_2 uptake (GtC/year)	-0.36	-0.35	-0.35	-0.35	-0.24 (0 ~ -0.48)
Preindustrial land CO_2 uptake (GtC/year)	0.12	0.14	0.14	0.14	0.3 (0 ~ 0.6)
Natural CH_4 emission (Mt(CH_4)/year)	320	320	320	320	210 (-30 ~ 450)
Natural N_2O emission (Mt(N)/year)	11.3	11.3	11.3	11.3	10.2 (7.8 ~ 12.6)
CH_4 lifetime (year)	8.54	8.54	8.54	8.54	9.6 (5.4 ~ 13.8)
N_2O lifetime (year)	114	114	114	114	110 (83 ~ 137)
Forcing scaling factor (1)	—	—	1.106	—	1.0 (0.0 ~ 2.0)
Climate sensitivity (°C)	4.04	3.37	3.77	3.10	3.5 (0.5 ~ 6.5)

Figure B.1. Time series in the ACC2 coupled and uncoupled inversions

Shown below are the results of the coupled and uncoupled inversions with optimal climate sensitivity (4.04°C and 3.37°C, respectively). Forcing uncertainty is expressed as missing forcing. Unless noted otherwise, inserts show the "residuals," i.e. the differences between prior and posterior values. For the anthropogenic CH_4 and N_2O emissions and atmospheric CH_4 and N_2O concentrations in Figures B.1.6 to B.1.9, the posterior estimates for the coupled inversion are indistinguishable from those for the uncoupled inversion. In Figures B.1.10 and B.1.11, prior for missing forcing is 0 W/m^2 over the entire period. In Figures B.1.3 and B.1.8 to B.1.12, prior uncertainty ranges are assumed four times larger when volcanic forcing is stronger than -0.5 W/m^2. In Figures B.1.10 and B.1.11, individual forcings in the coupled and uncoupled inversions are nearly the same except for the missing forcing and the total forcing. Measurements shown in Figure B.1.12 are vertically shifted for the coupled inversion.

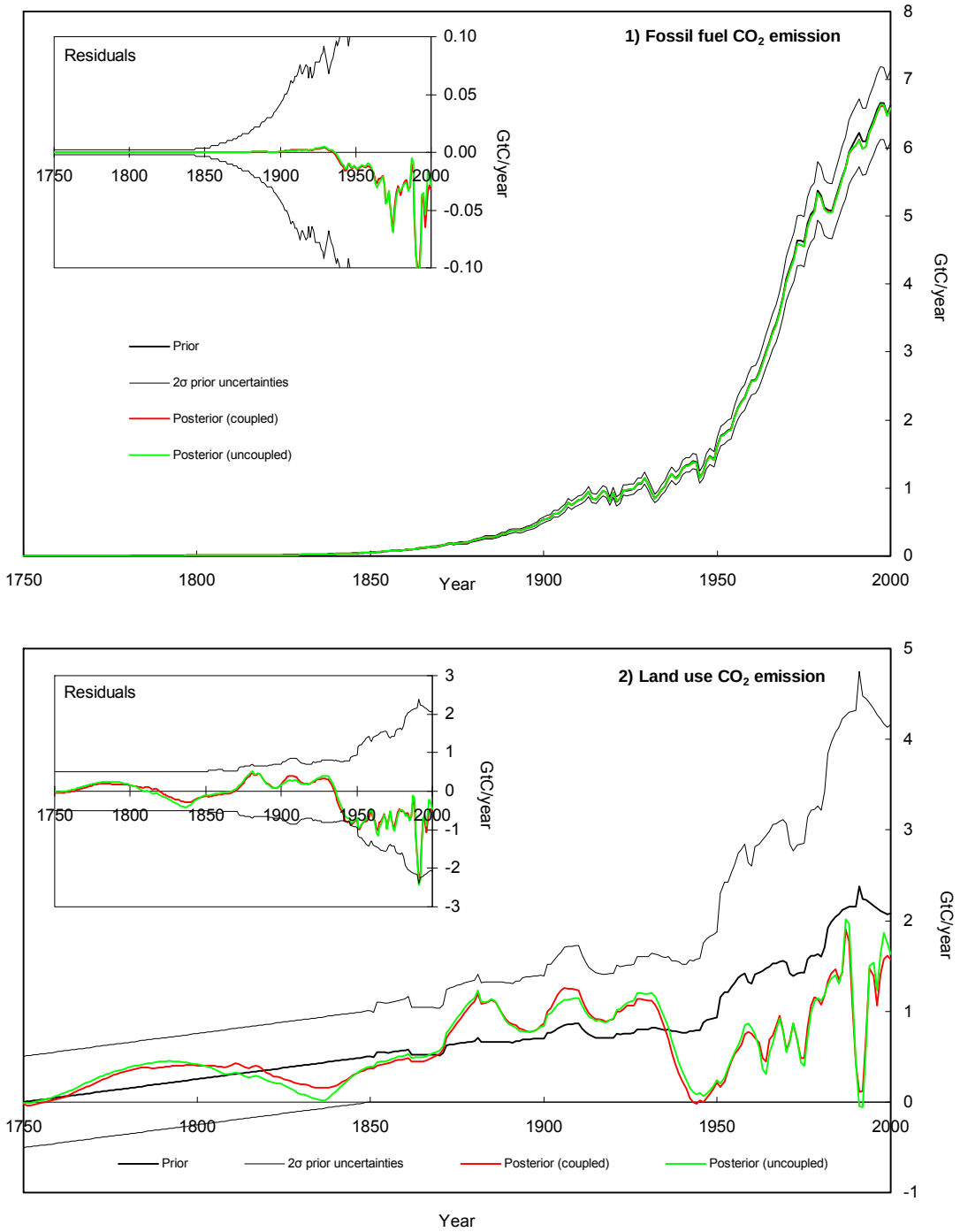

Figure B.1. (Continued) Time series in the ACC2 coupled and uncoupled inversions

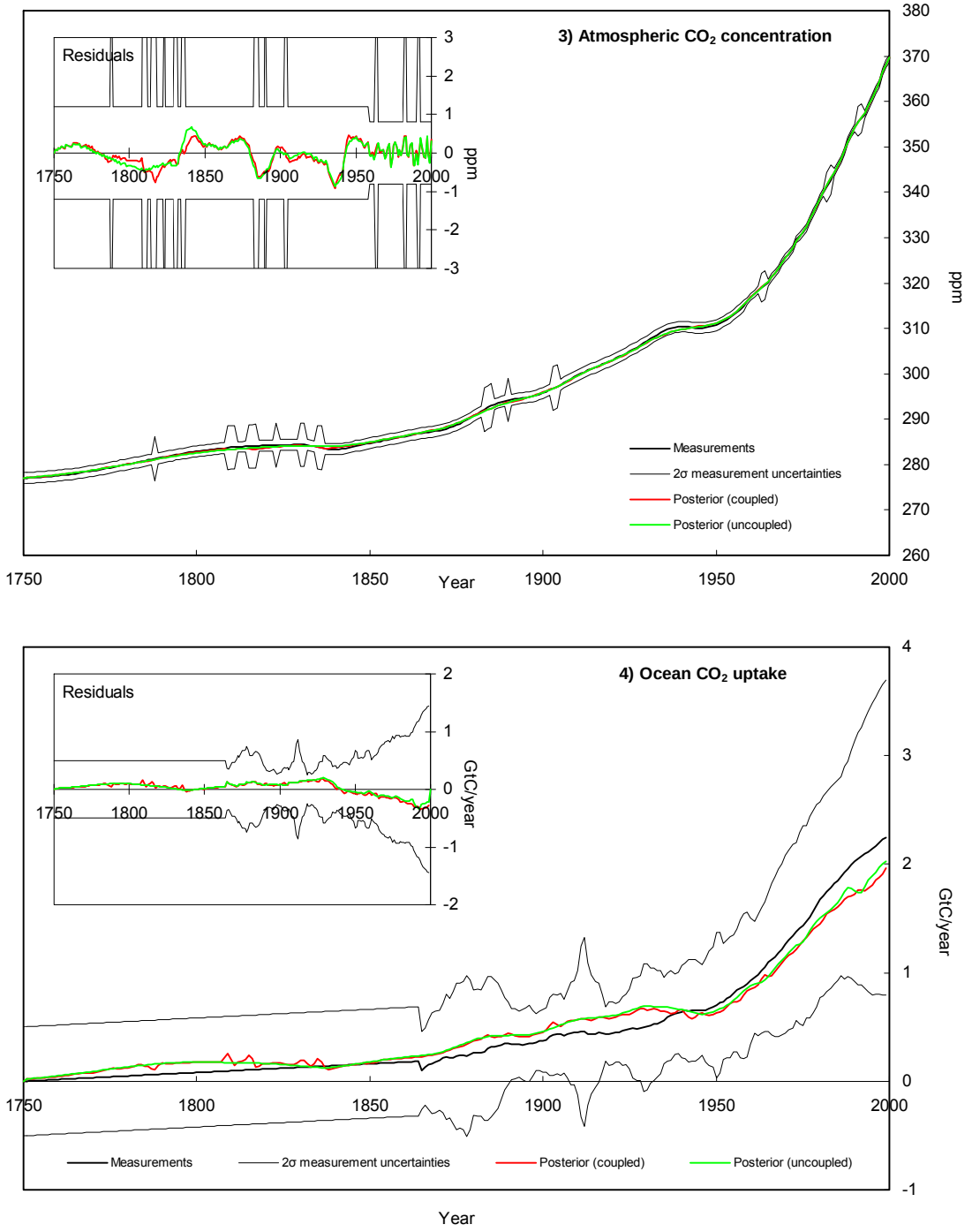

Figure B.1. (Continued) Time series in the ACC2 coupled and uncoupled inversions

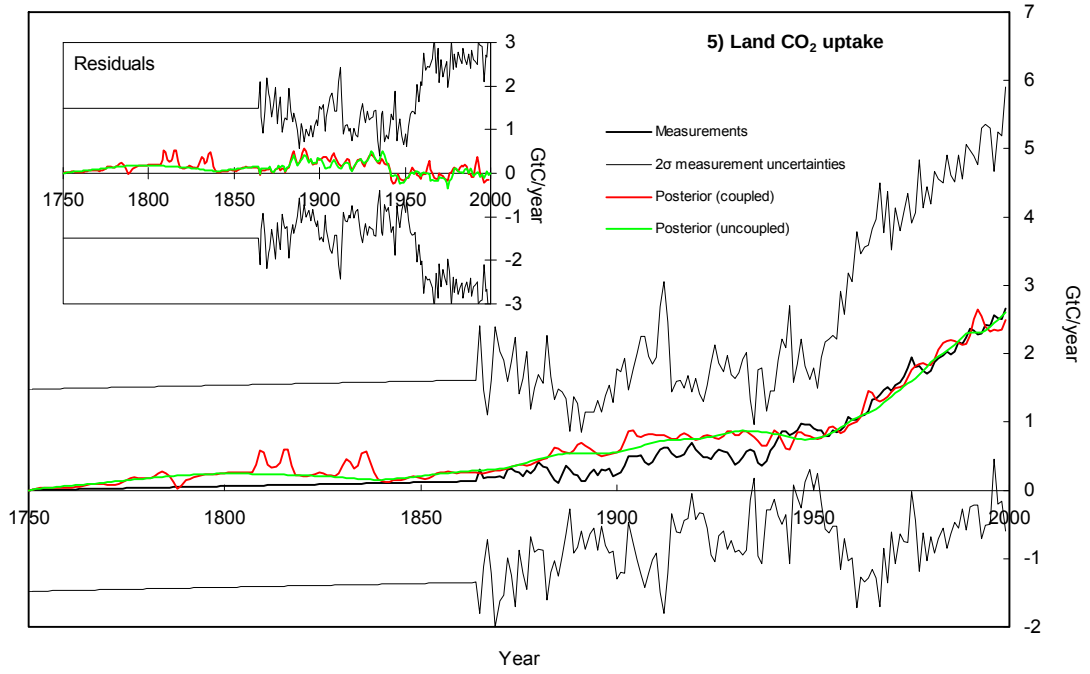

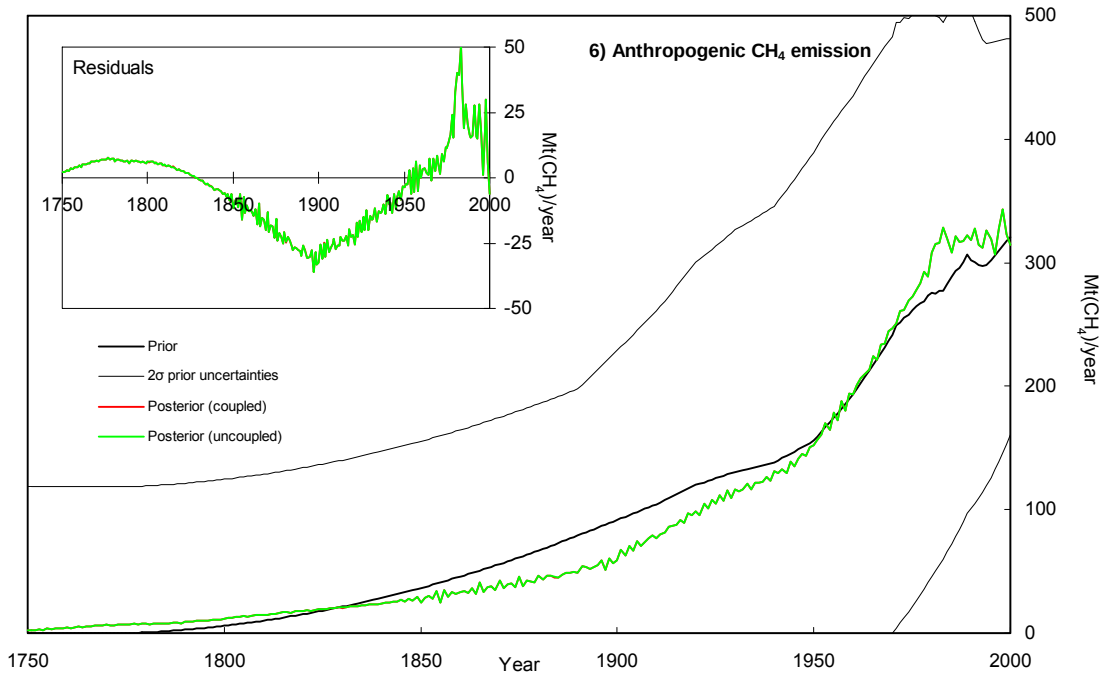

Figure B.1. (Continued) Time series in the ACC2 coupled and uncoupled inversions

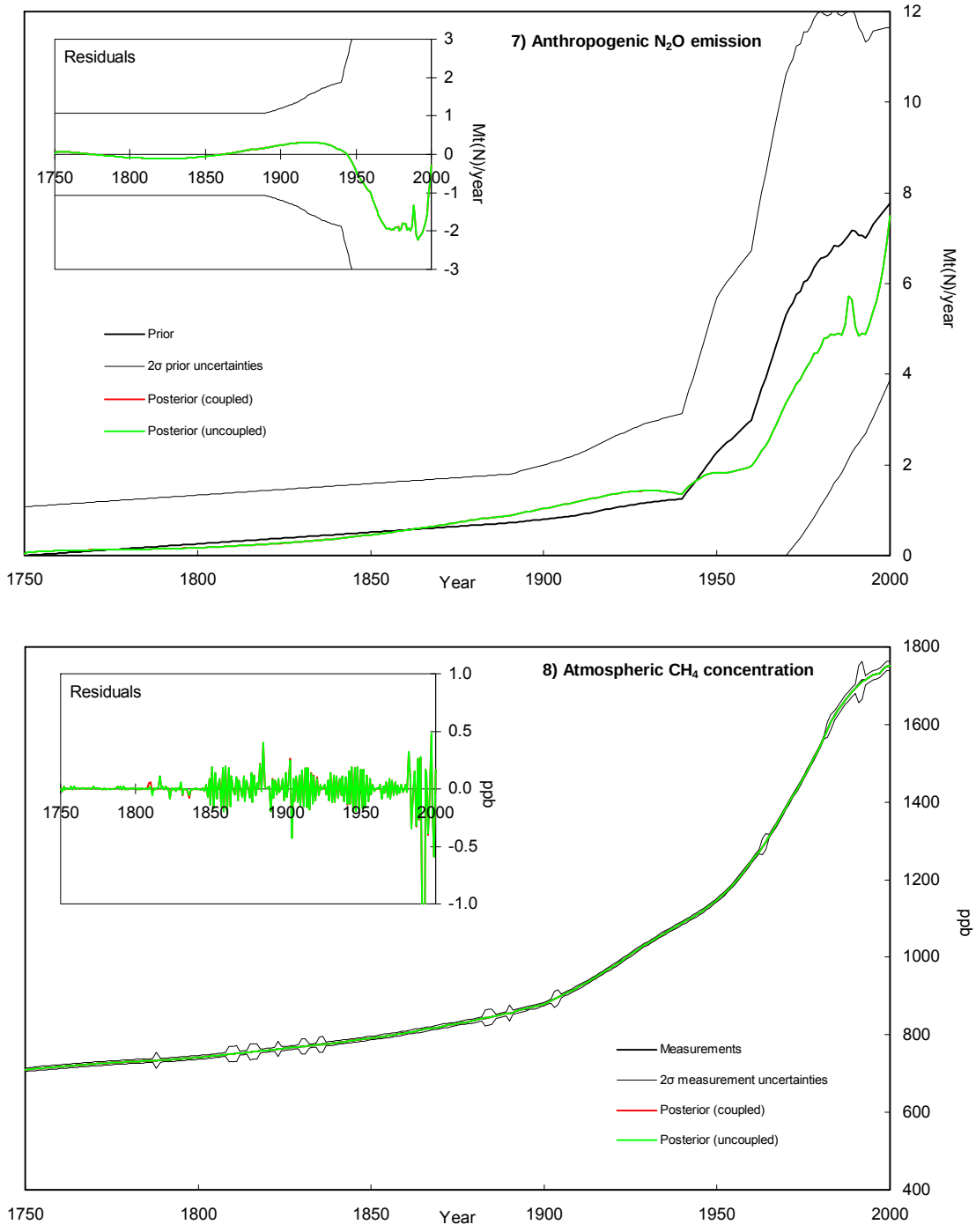

Figure B.1. (Continued) Time series in the ACC2 coupled and uncoupled inversions

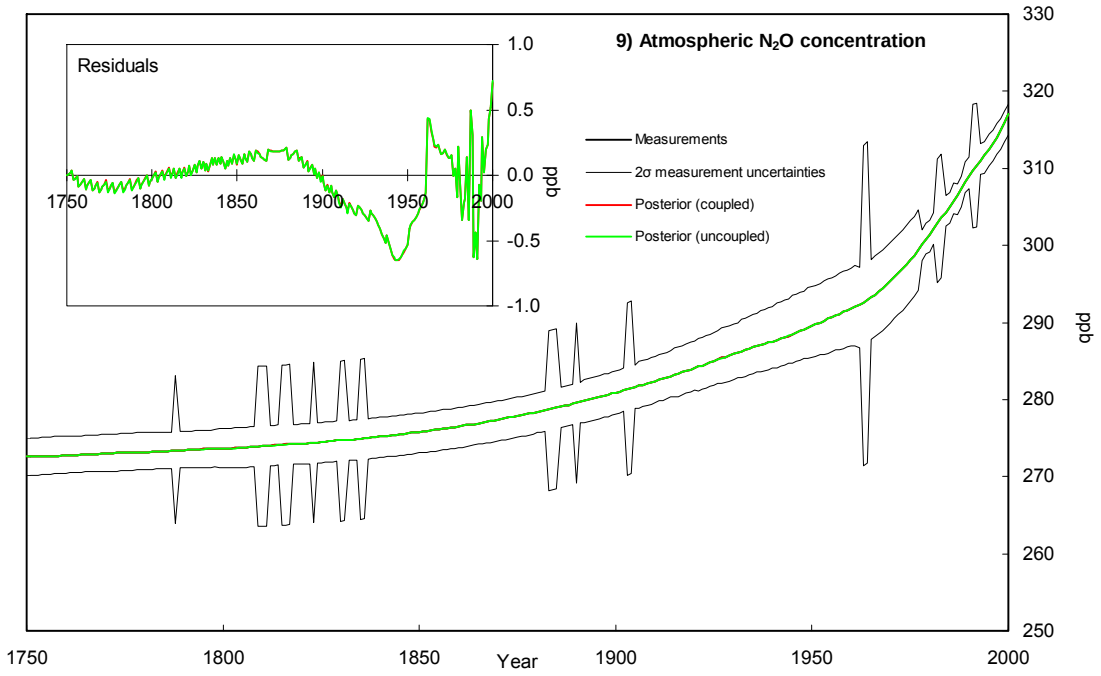

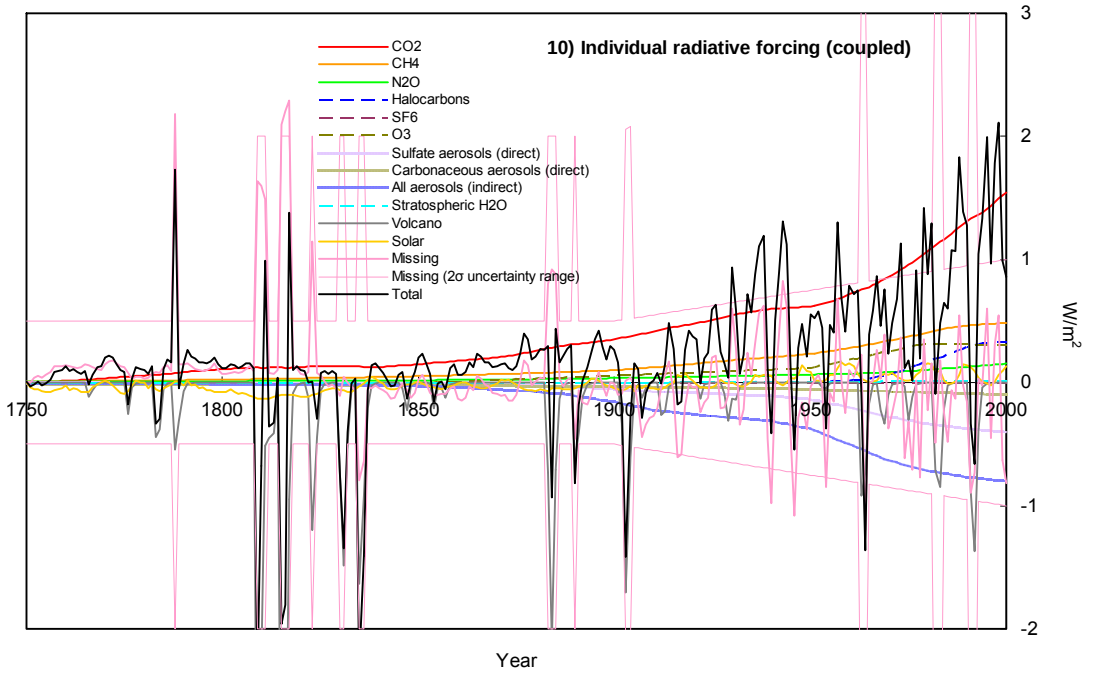

Figure B.1. (Continued) Time series in the ACC2 coupled and uncoupled inversions

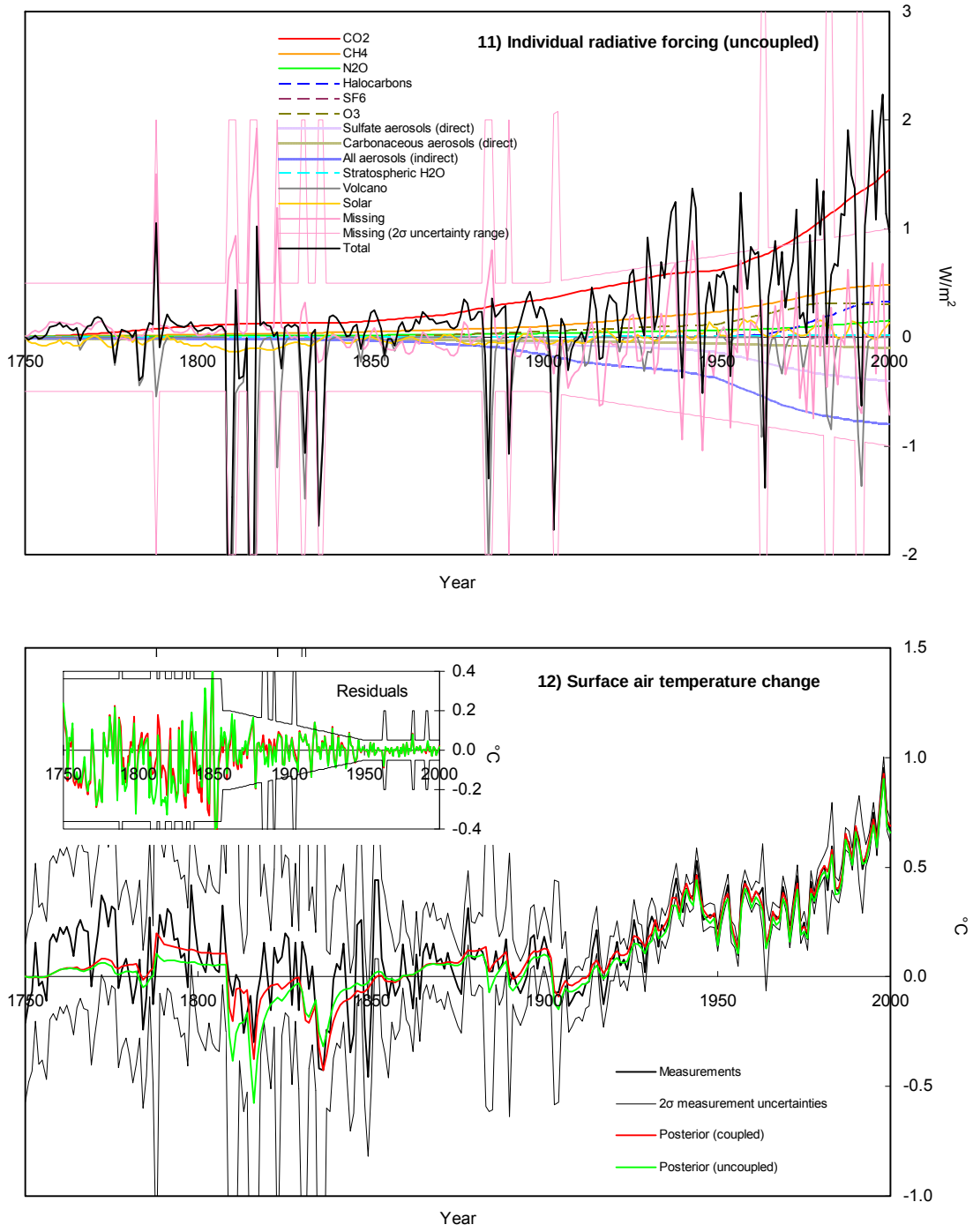

Figure B.2. Time series in the ACC2 uncoupled inversions giving different treatments to forcing uncertainty

Only the results for the climate component are shown as the other components are insensitive to the treatment of forcing uncertainty. The main figure of B.2.1 shows the total forcing, which is the sum of the GHG, aerosol, volcanic, solar, and missing forcing. Note that in the inversion setup using forcing scaling or assuming no forcing uncertainty, missing forcing is fixed at 0 W/m^2 over the entire period. Insert in Figure B.2.1 shows missing forcing and "additional forcing by scaling," i.e. additional aerosol forcing that are added by scaling the prescribed total aerosol forcing according to the forcing scaling factor obtained from the inversion (=1.106, that is 10.6% of the prescribed total aerosol forcing). In Figures B.2.1 and B.2.2, prior uncertainty ranges are assumed four times larger when volcanic forcing is stronger than -0.5 W/m^2. Measurements shown in Figure B.2.2 are vertically shifted for the inversion using the missing forcing approach. Values in the square brackets are the best estimates of climate sensitivity for the respective inversions.

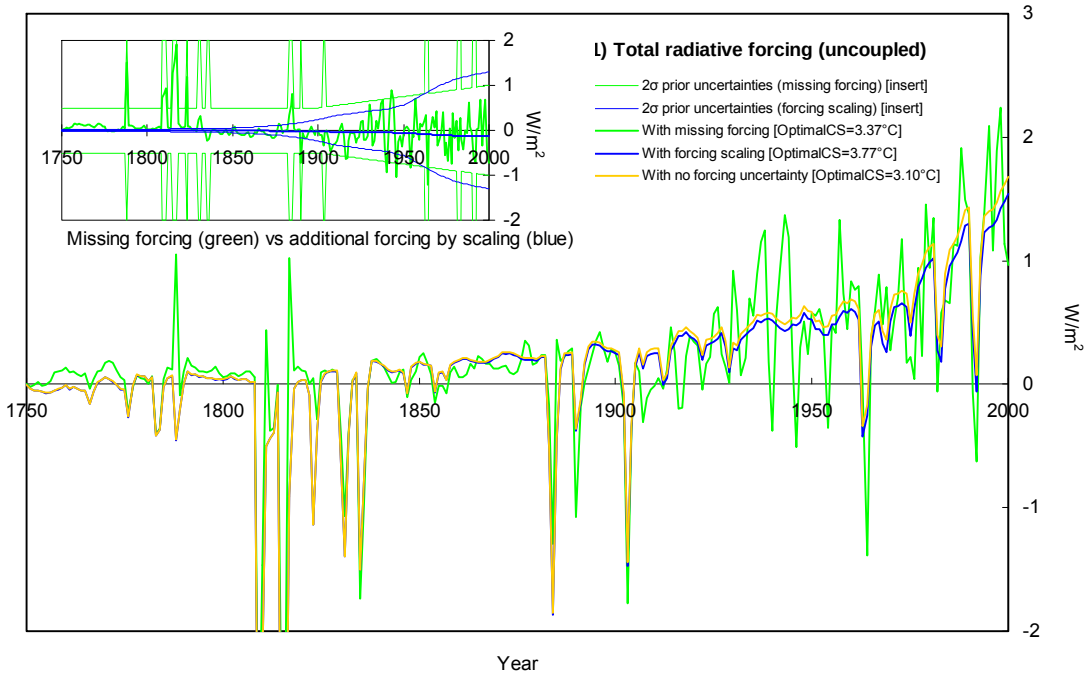

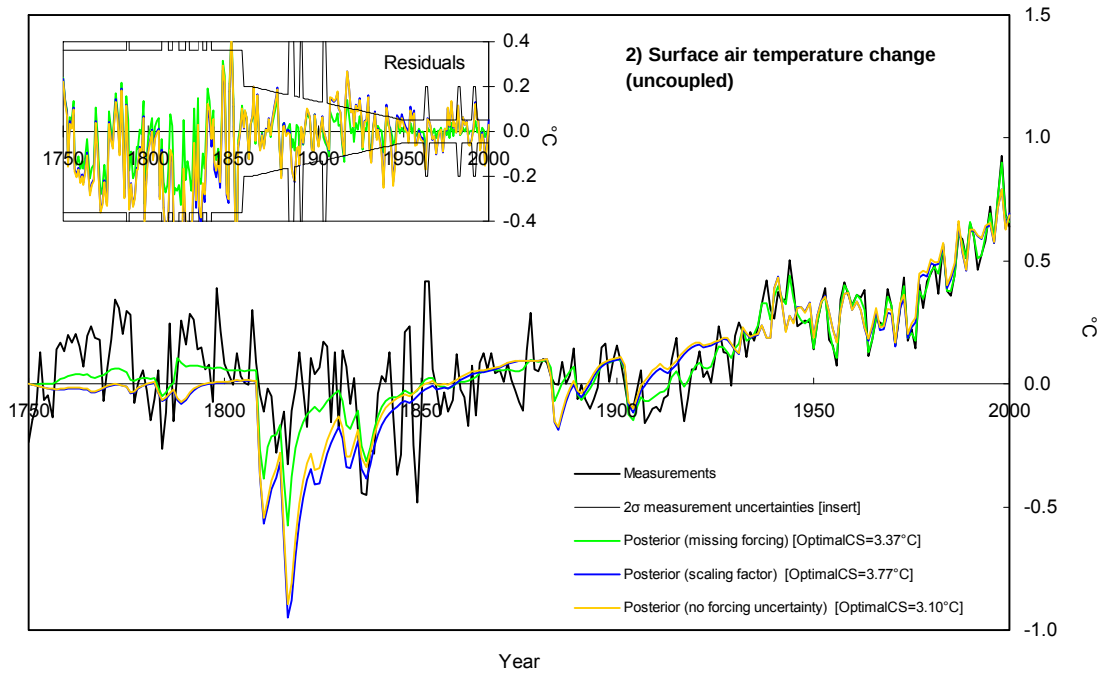

Figure B.3. Squared weighted residuals in time series of the main ACC2 inversions

Squared weighted residuals shown below are the squares of the residuals weighted by the associated prior uncertainty ranges (σ). Not that they are shown on a logarithmic scale. Explanations for acronyms follow. EMICO2FF: fossil fuel CO_2 emission, EMICO2LU: land use CO_2 emission, EMICH4ANT: anthropogenic CH_4 emission, EMIN2OANT: anthropogenic N_2O emission, MISFOR: missing forcing, UPCO2OCN: ocean CO_2 uptake, UPCO2LND: land CO_2 uptake, CONCO2: atmospheric CO_2 concentration, CONCH4: atmospheric CH_4 concentration, CONN2O: atmospheric N_2O concentration, TEMP: surface air temperature change, SUM: sum of the squared weighted residuals for all the time series.

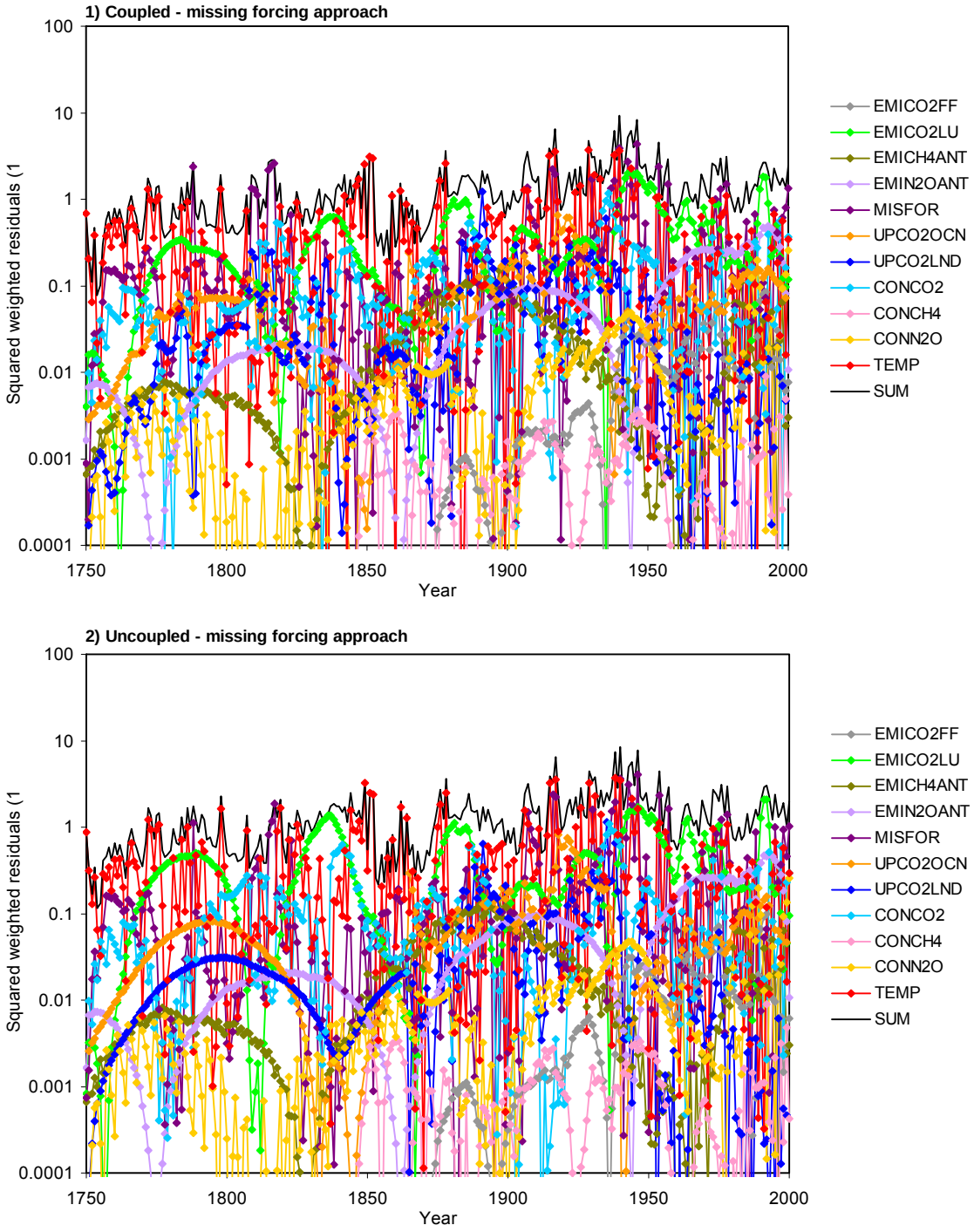

Figure B.3. (Continued) Squared weighted residuals in time series of the main ACC2 inversions

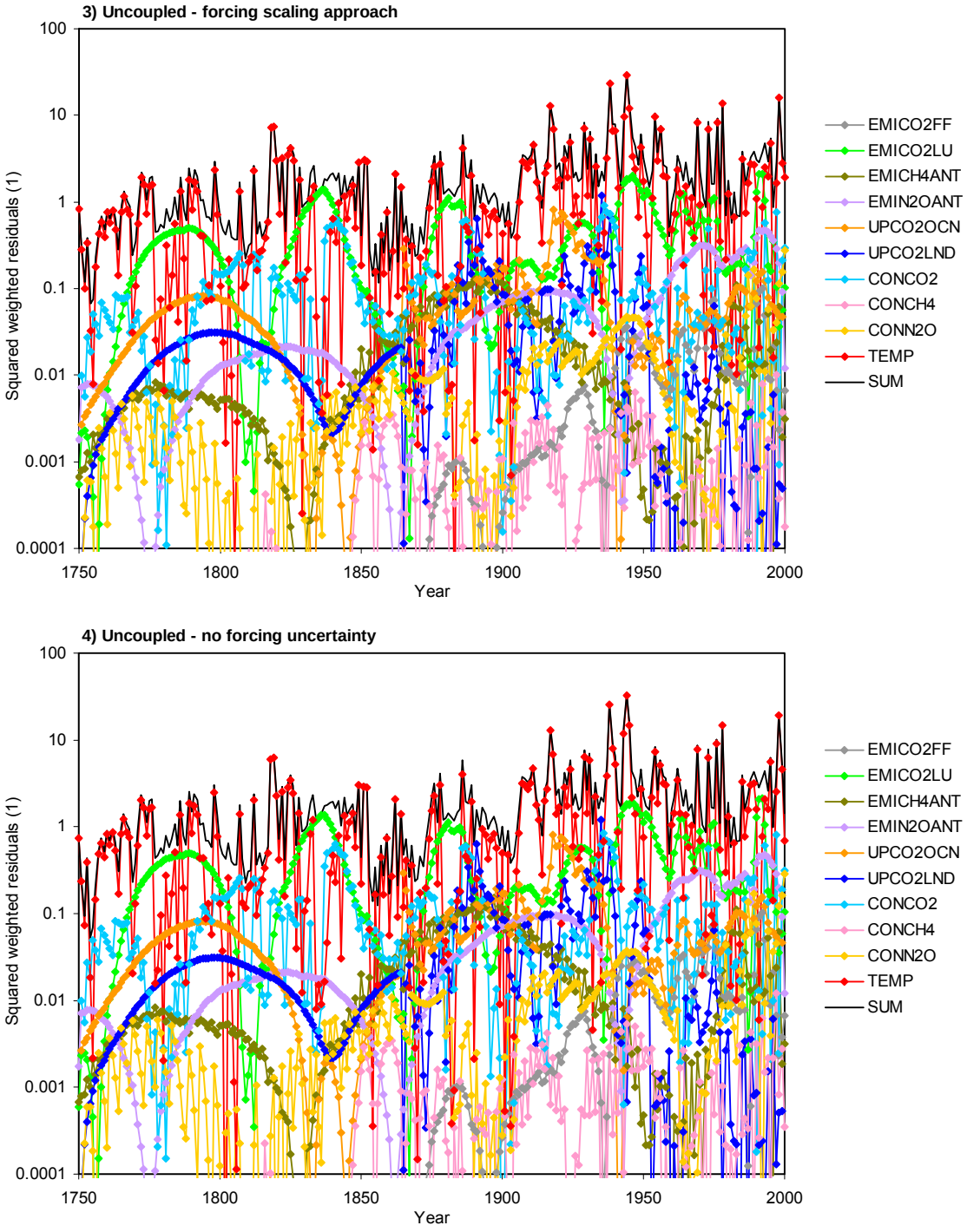

Figure B.4. Squared weighted residuals in the ACC2 uncoupled inversions giving different treatments to forcing uncertainty

Squared weighted residuals summed over the entire time horizon are shown for the missing forcing- and forcing scaling-based uncoupled inversions with climate sensitivity fixed at values between 1°C and 10°C at intervals of 0.25°C. Except for temperature change, squared weighted residuals from the two approaches are hardly distinguishable.

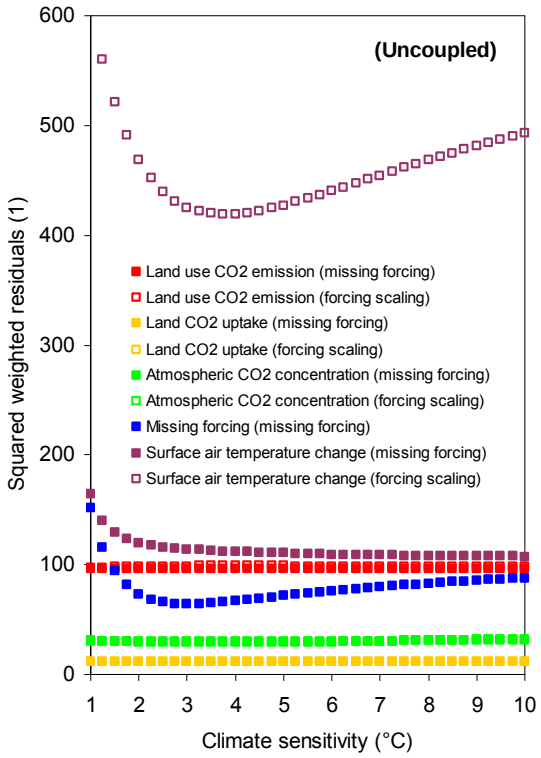

Figure B.5. Global-mean surface air temperature response to constant radiative forcing perturbation

Temperature response to sustained perturbation in radiative forcing (0.25, 0.50, and 0.75 W/m^2) is computed under different assumptions on climate sensitivity (1, 4, 7, and 10°C). The forcing perturbation starts in the year 0. The initial state is equivalent to the preindustrial state assumed for the year 1750. Calculations are performed by using DOECLIM (Kriegler, 2005; Section 2.3 of this thesis), the climate component of ACC2. No climate-carbon cycle feedback is provided.

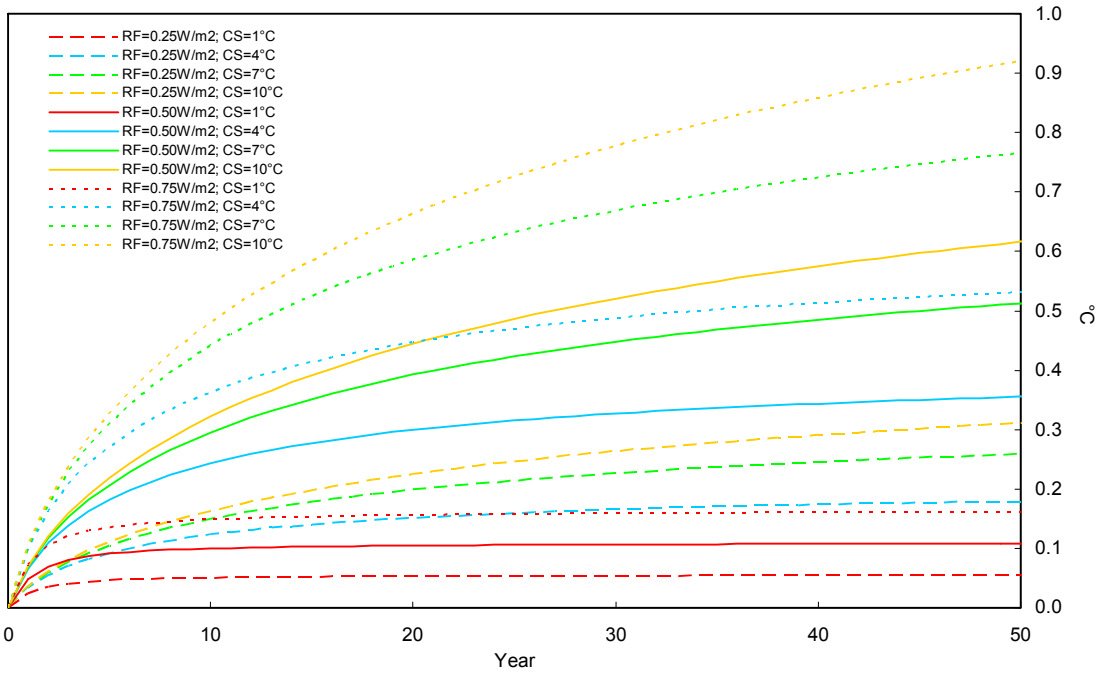

Figure B.6. Sensitivity of the ACC2 inversion results to the prior forcing uncertainty

Missing forcing- and forcing scaling-based ACC2 uncoupled inversions are performed by assuming 50% smaller, standard, and 50% larger prior uncertainty ranges for missing forcing and forcing scaling factor with climate sensitivity fixed at values between 1°C and 10°C at intervals of 0.25°C. Figure B.6.1 shows the changes in the final value of the cost function. Values in the square brackets are the best estimates of climate sensitivity for the respective inversion setups. Cost functions values for the different forcing scaling cases are indistinguishable. In Figures B.6.2 and B.6.3, forcing residuals (that is, posterior missing forcing and additional forcing by scaling) and temperature residuals are compared for different climate sensitivity (1, 3, 5, and 10°C) and different prior forcing uncertainty (50% smaller, standard, and 50% larger ranges). Thick red and blue lines in Figure B.6.2 are the posterior missing forcing and additional forcing by scaling, respectively. Thin lines represent the respective 2σ prior uncertainty ranges. In Figure B.6.3, thick red and blue lines represent the temperature residuals for the missing forcing- and forcing scaling-based inversions, respectively. Thin black line is the 2σ prior uncertainty ranges used for both types of inversions.

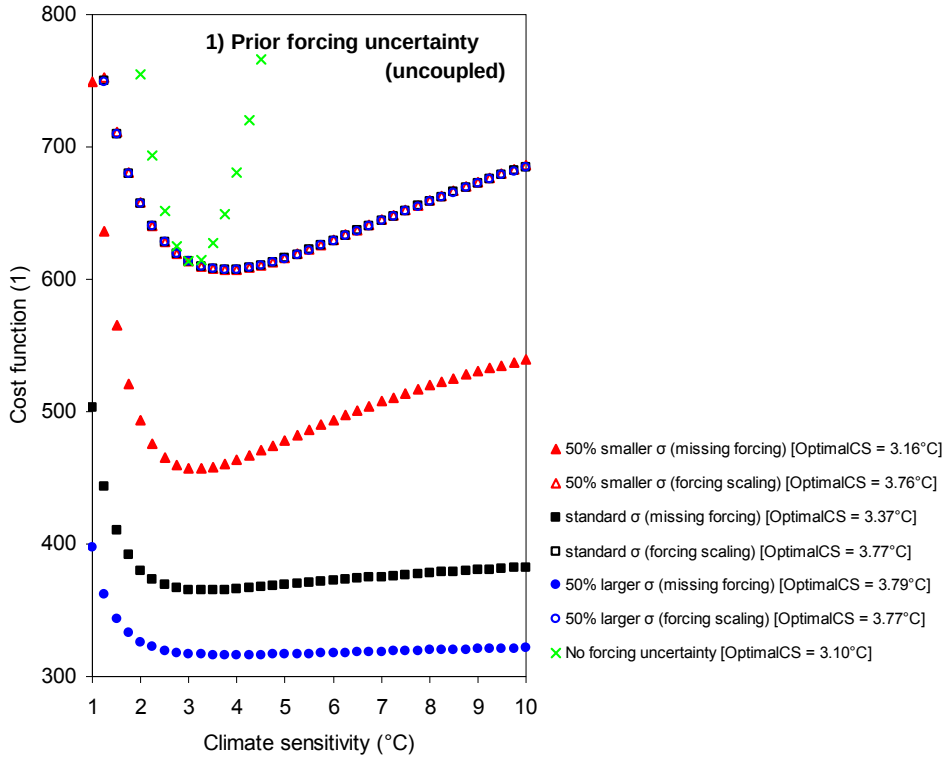

Figure B.6. (Continued) Sensitivity of the ACC2 inversion results to the prior forcing uncertainty

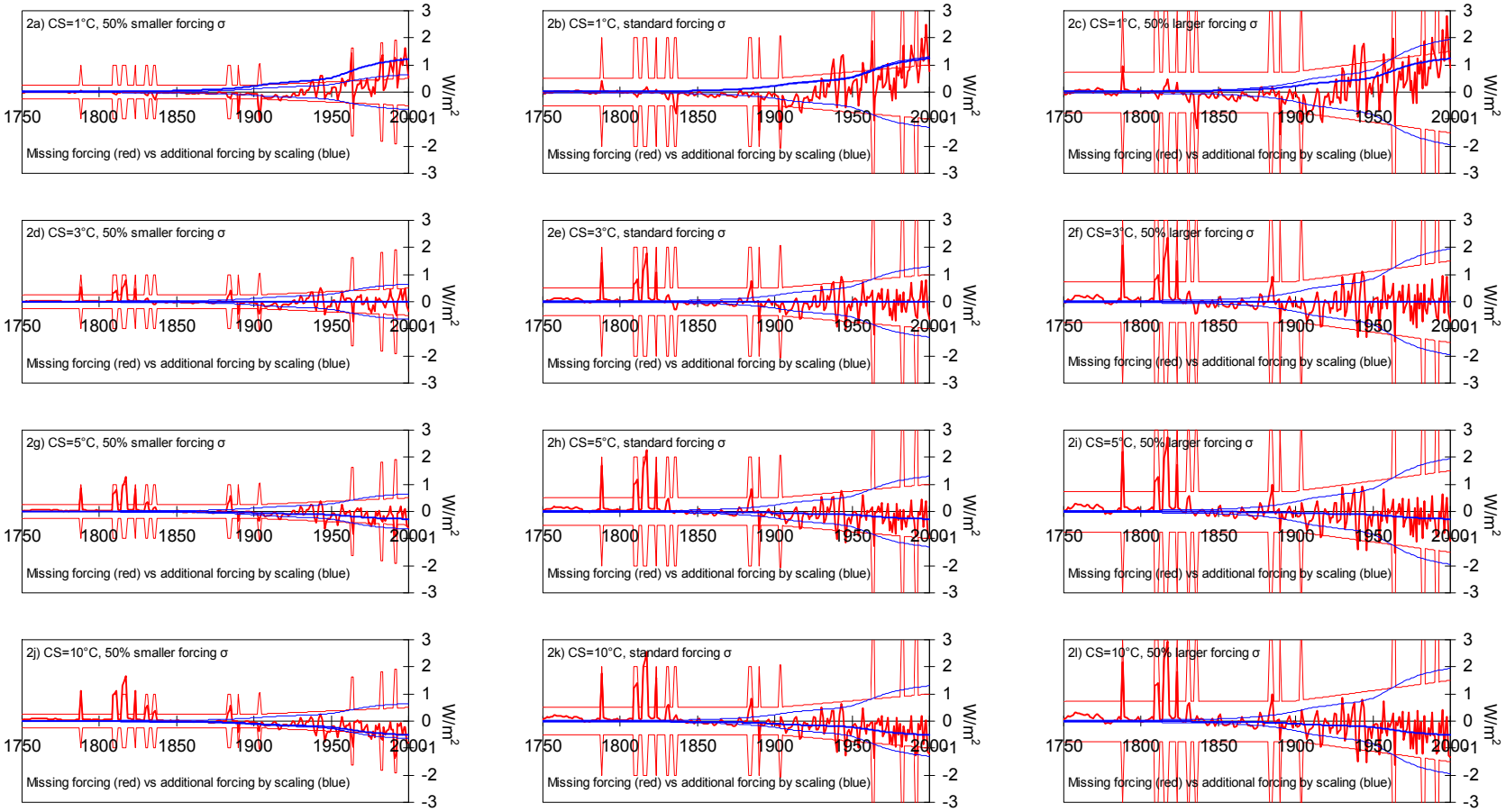

Figure B.6. (Continued) Sensitivity of the ACC2 inversion results to the prior forcing uncertainty

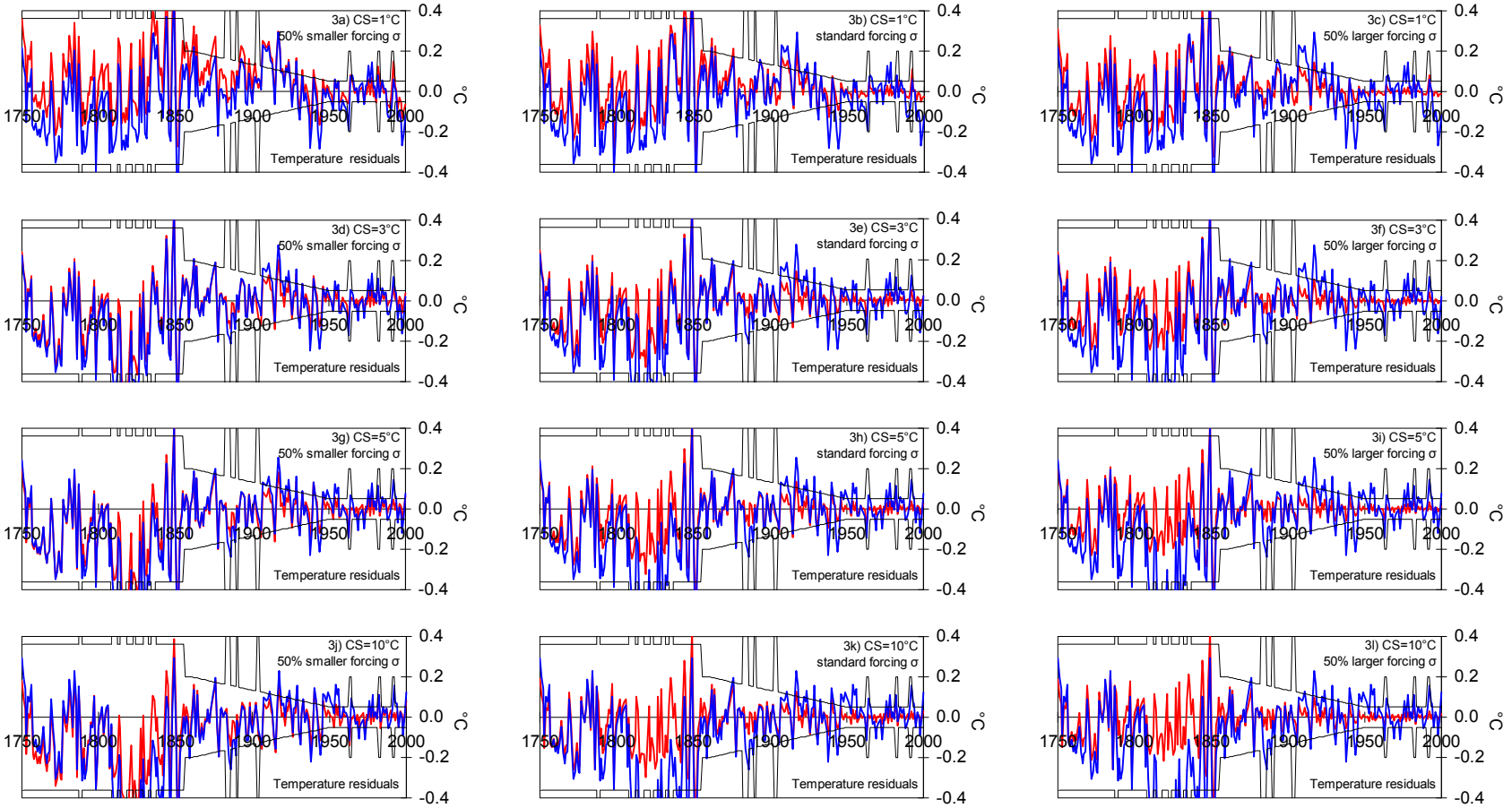

Figure B.7. Sensitivity of the ACC2 inversion results to prior land use CO_2 emission uncertainty

Figure B.7.1 shows the changes in the final value of the cost function when the prior uncertainty in land use CO_2 emission is assumed to be larger/smaller than the standard by 50%. The ACC2 coupled and inversions are performed with climate sensitivity fixed at values between 1°C and 10°C at intervals of 0.25°C. Black plots are identical with those shown in Figure 5.1. Values in the square brackets are the best estimates of climate sensitivity for the respective inversion setups. Figures B.7.2 to B.7.4 shows the associated coupled inversion results in the carbon cycle using respective optimal climate sensitivity.

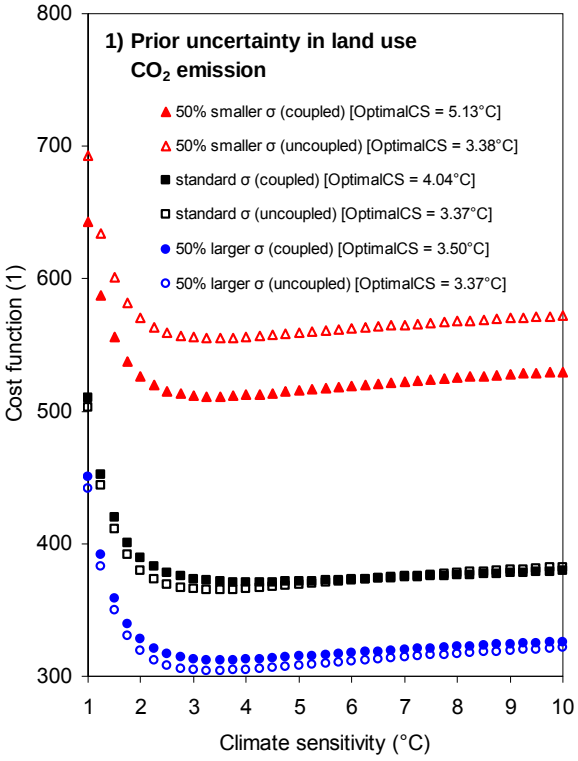

Figure B.7. (Continued) Sensitivity of the ACC2 inversion results to prior land use CO_2 emission uncertainty

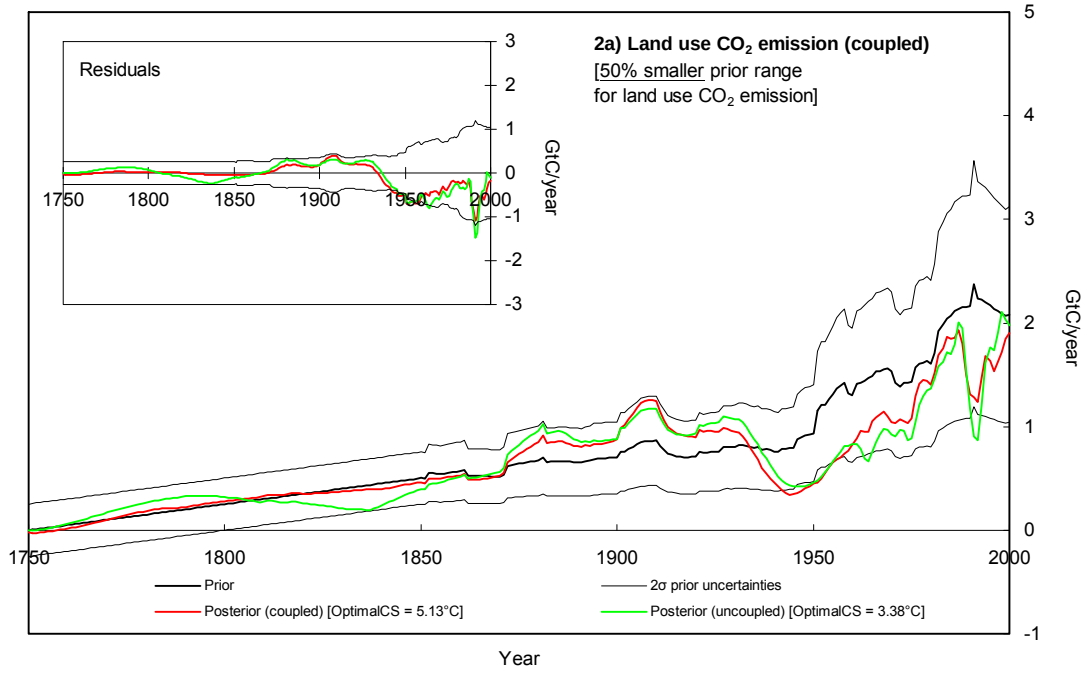

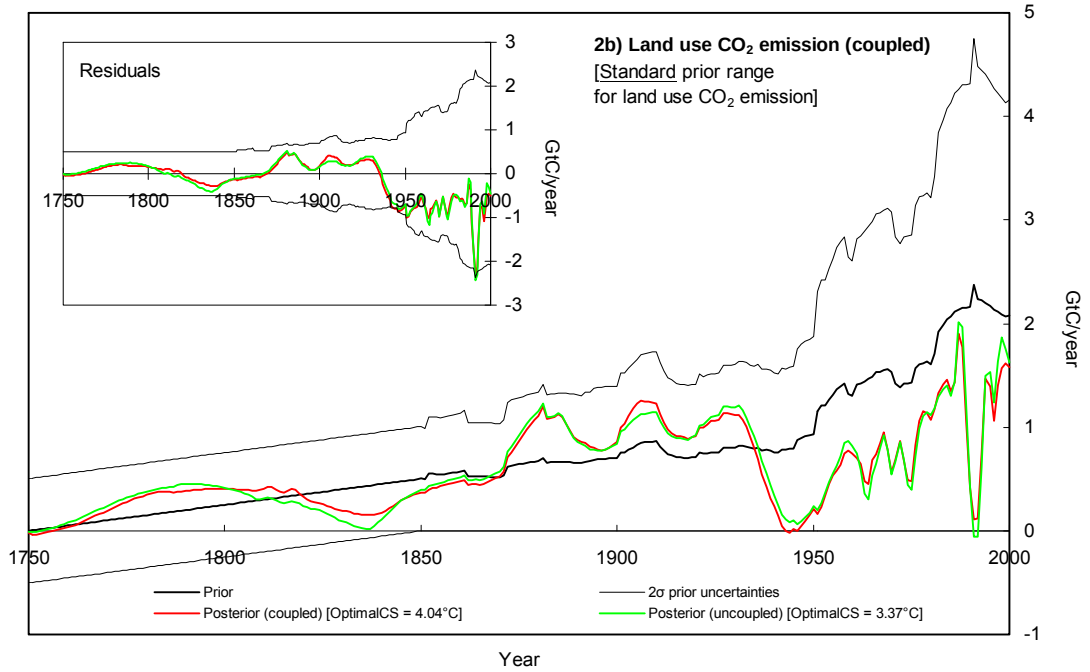

Figure B.7. (Continued) Sensitivity of the ACC2 inversion results to prior land use CO_2 emission uncertainty

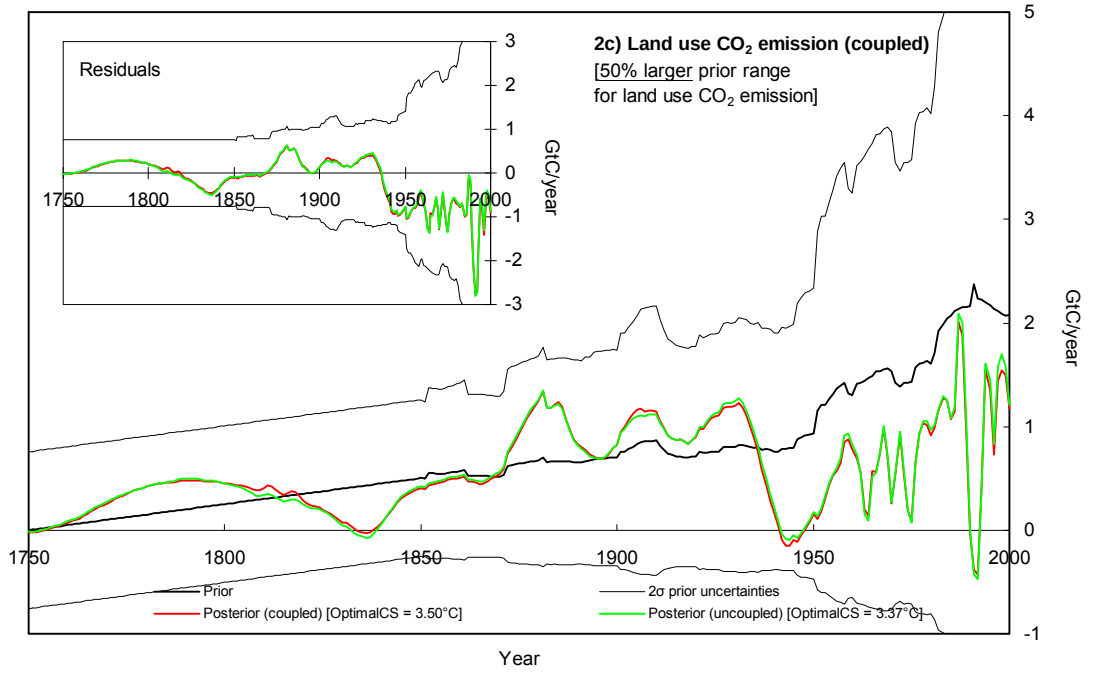

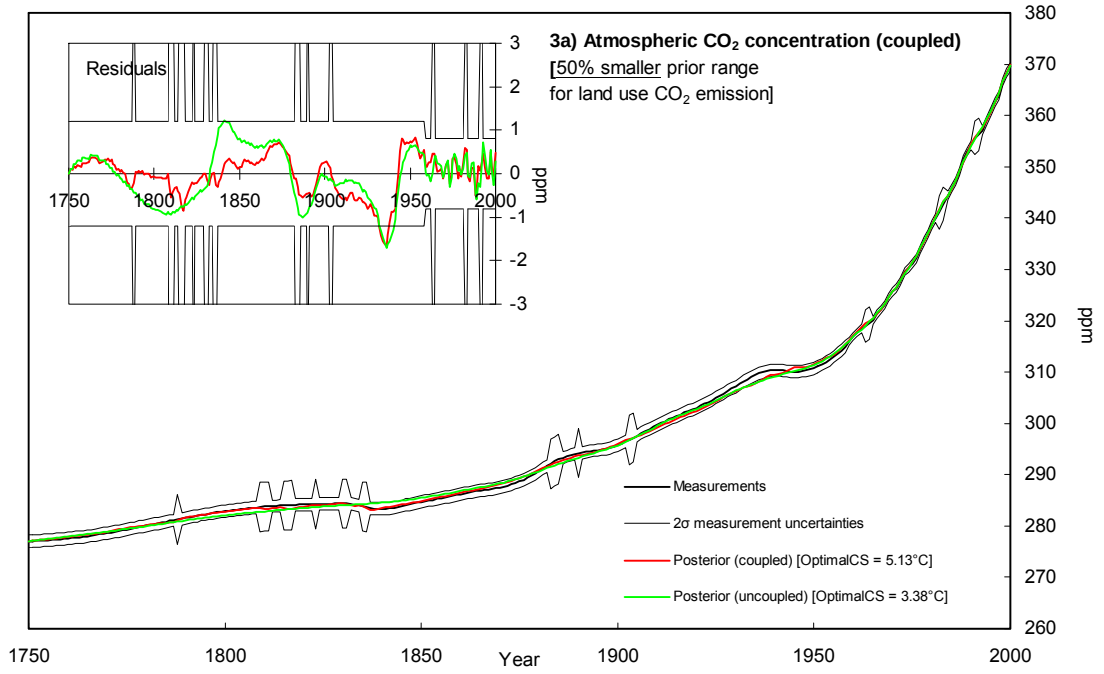

Figure B.7. (Continued) Sensitivity of the ACC2 inversion results to prior land use CO_2 emission uncertainty

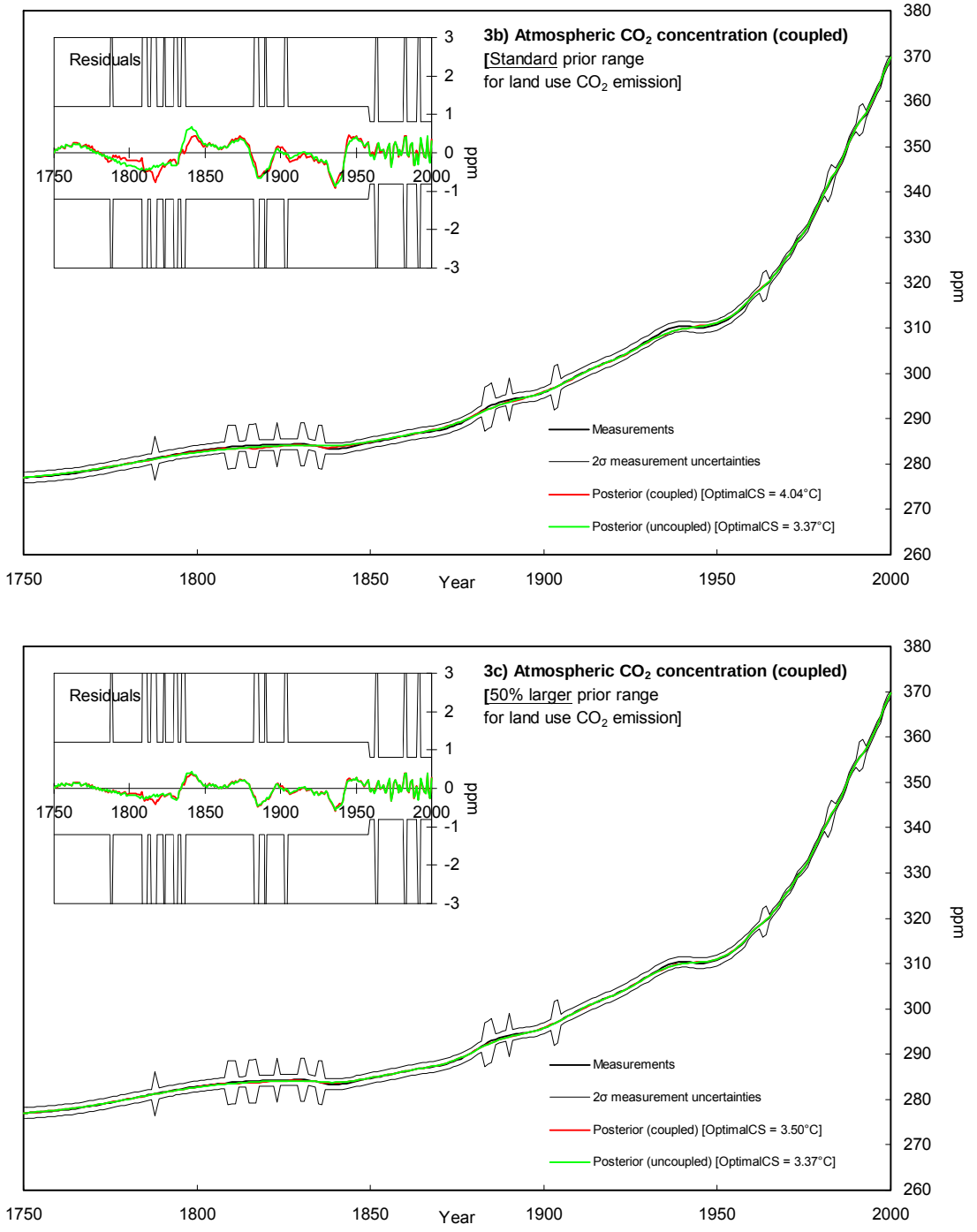

Figure B.7. (Continued) Sensitivity of the ACC2 inversion results to prior land use CO_2 emission uncertainty

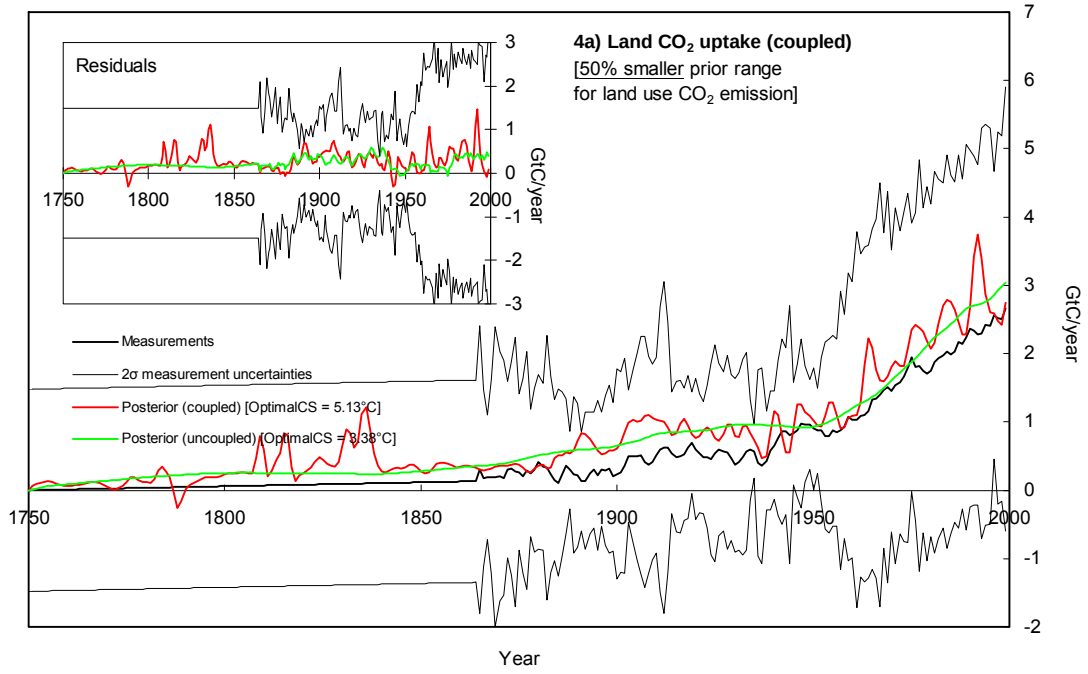

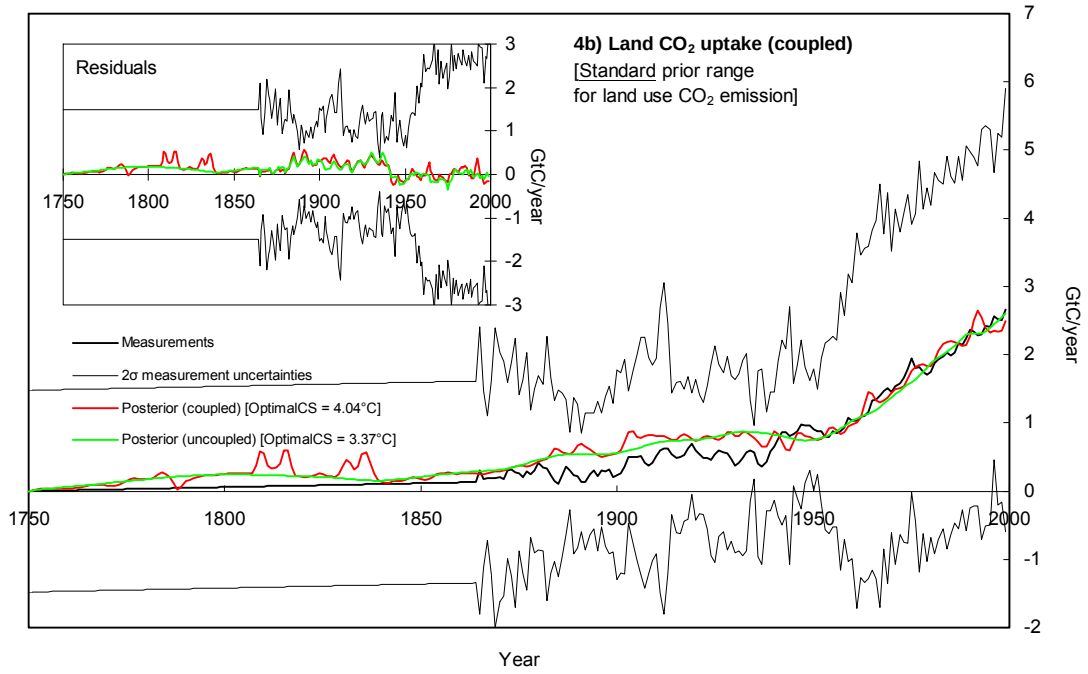

Figure B.7. (Continued) Sensitivity of the ACC2 inversion results to prior land use CO_2 emission uncertainty

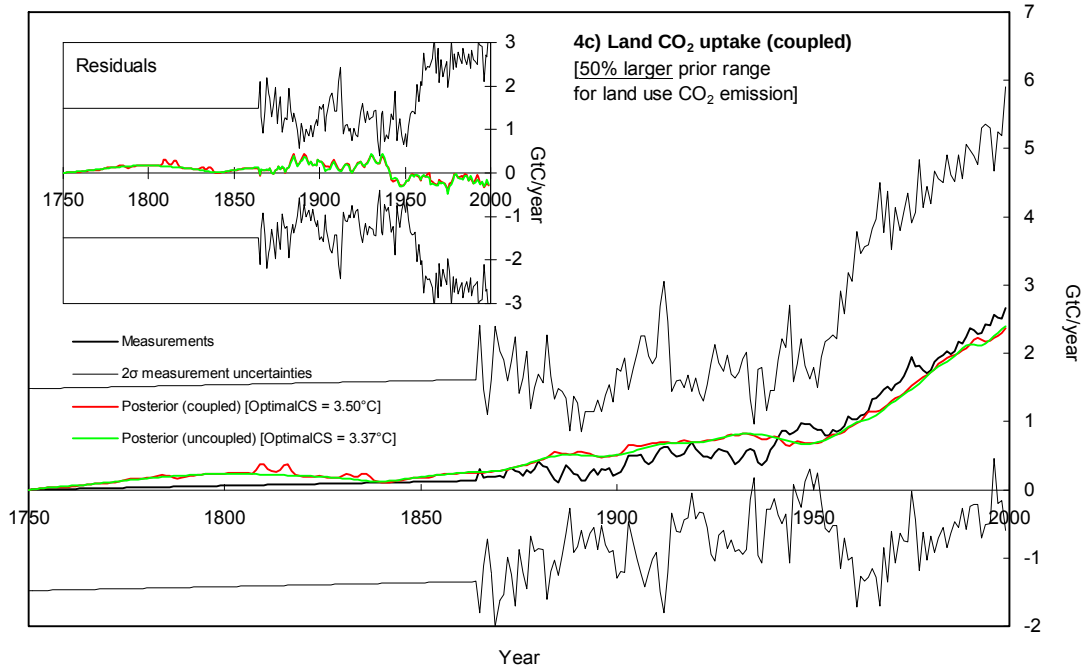

Figure B.8. Sensitivity of the ACC2 inversion results to volcanic forcing

Figure B.8.1 shows the changes in the final value of the cost function when different volcanic forcing is used (Ammann et al., 2003; Bertrand et al., 2002; Crowley et al., 2003). Inversions are performed with climate sensitivity fixed at values between 1°C and 10°C at intervals of 0.25°C. Black plots are identical with those shown in Figure 5.1. Values in the square brackets are the best estimates of climate sensitivity for the respective inversion setups. Figures B.8.2 to B.8.8 show the associated coupled inversion results with respective optimal climate sensitivity. In Figures B.8.3, B.8.6, and B.8.8, prior uncertainty ranges are assumed four times larger when volcanic forcing is stronger than -0.5 W/m^2. Measurements shown in Figure B.8.8 are vertically shifted for the coupled inversion using Ammann's volcanic forcing.

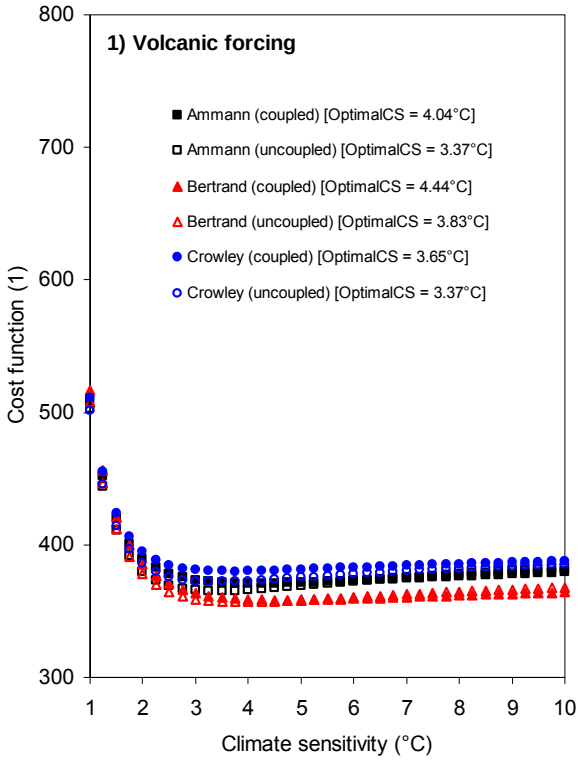

Figure B.8. (Continued) Sensitivity of the ACC2 inversion results to volcanic forcing

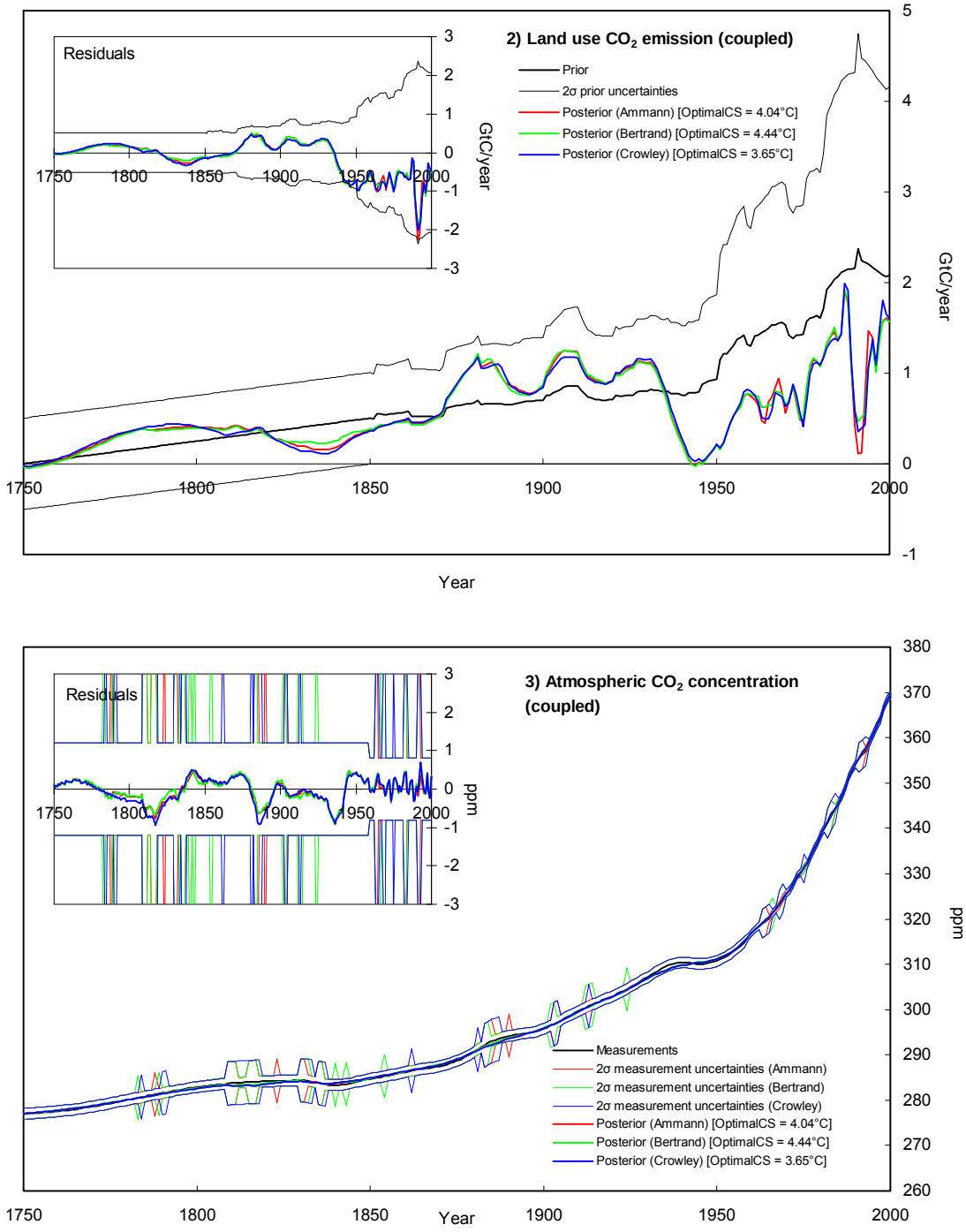

Figure B.8. (Continued) Sensitivity of the ACC2 inversion results to volcanic forcing

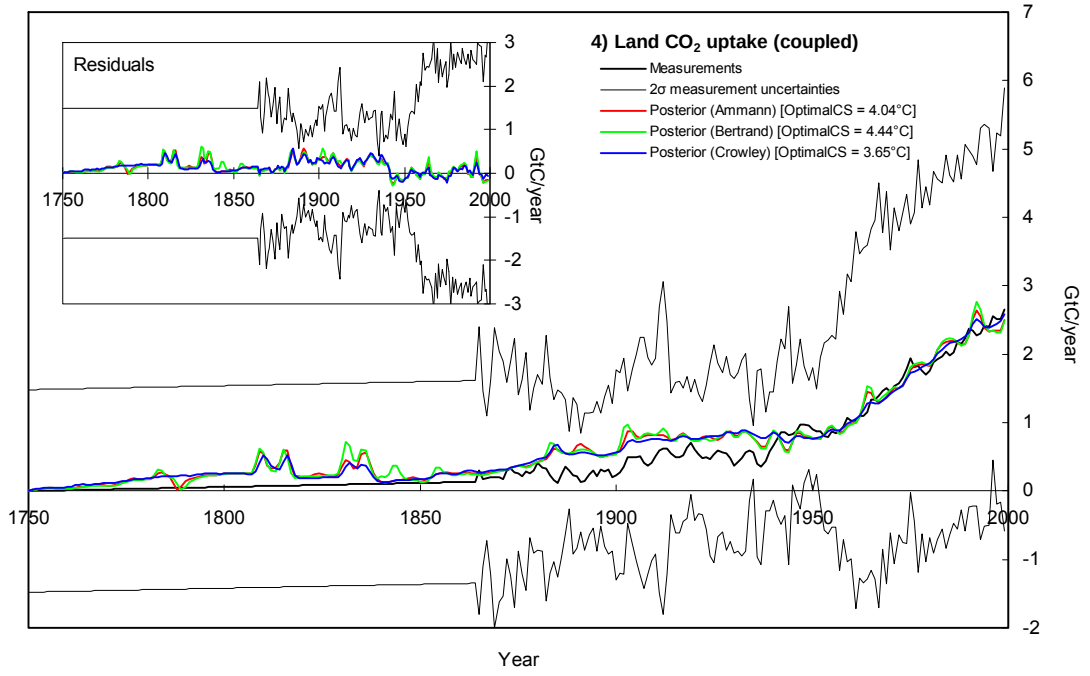

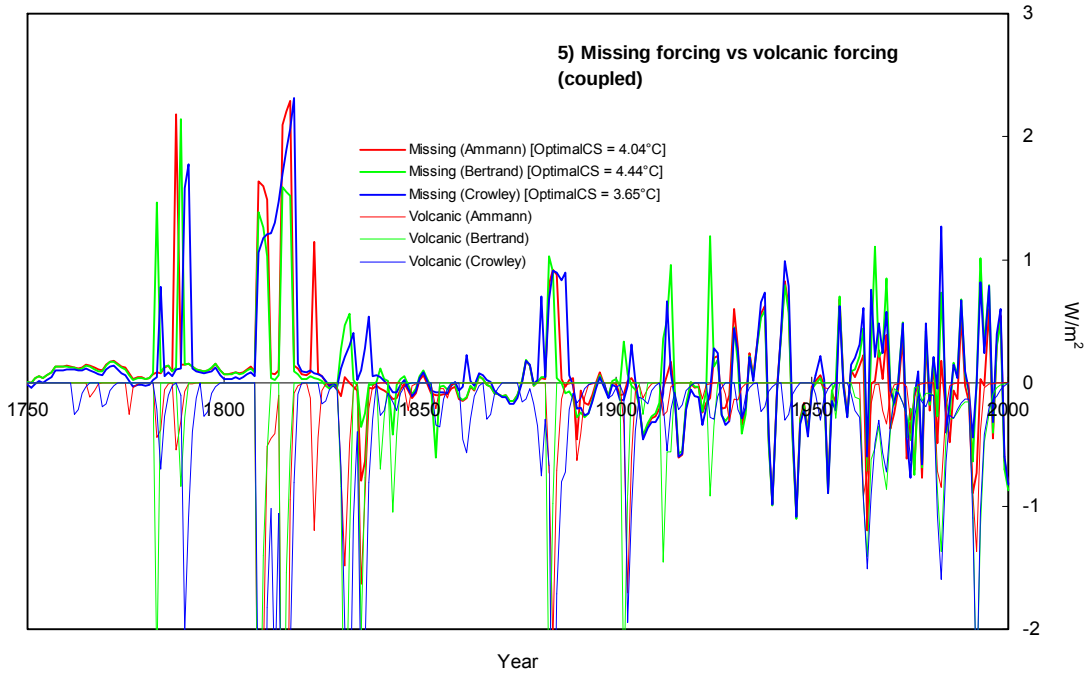

Figure B.8. (Continued) Sensitivity of the ACC2 inversion results to volcanic forcing

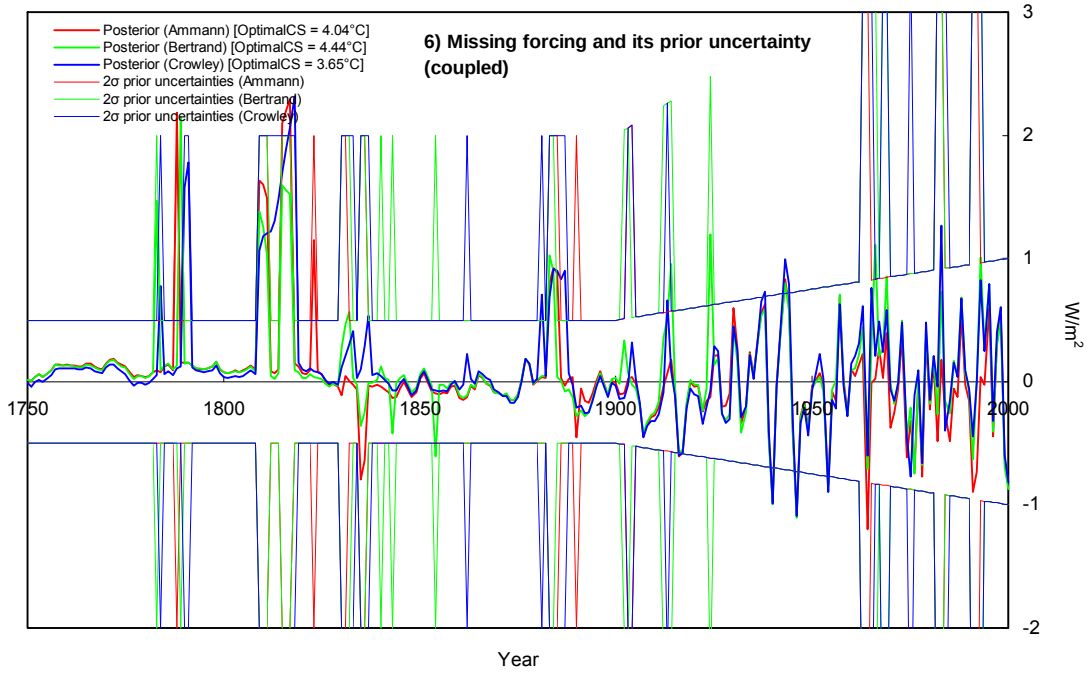

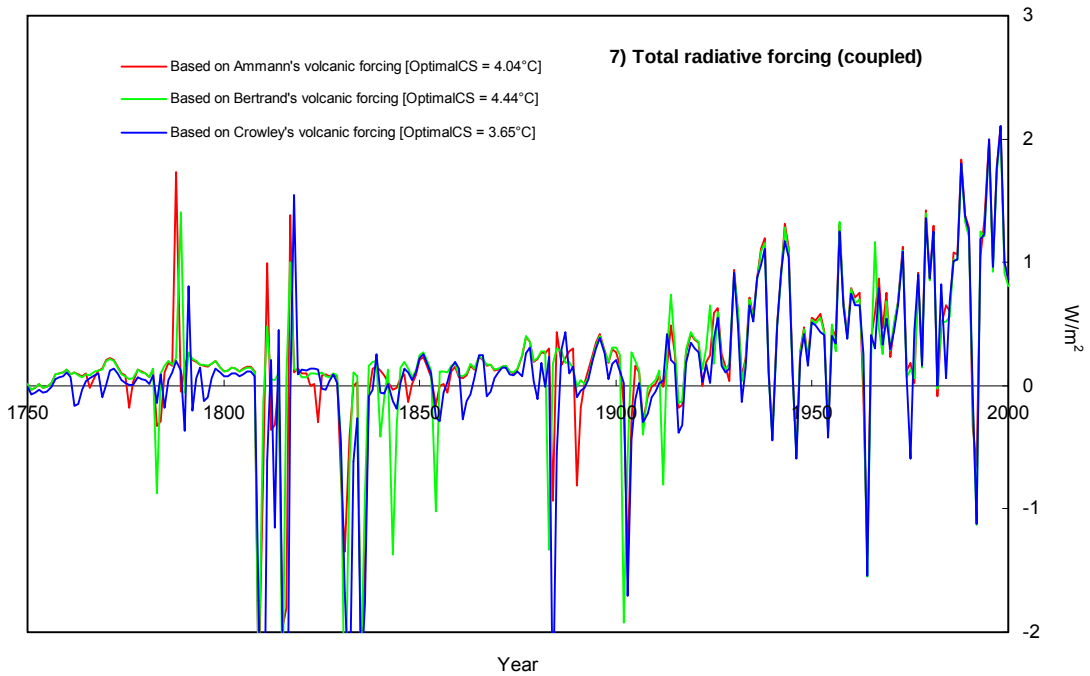

Figure B.8. (Continued) Sensitivity of the ACC2 inversion results to volcanic forcing

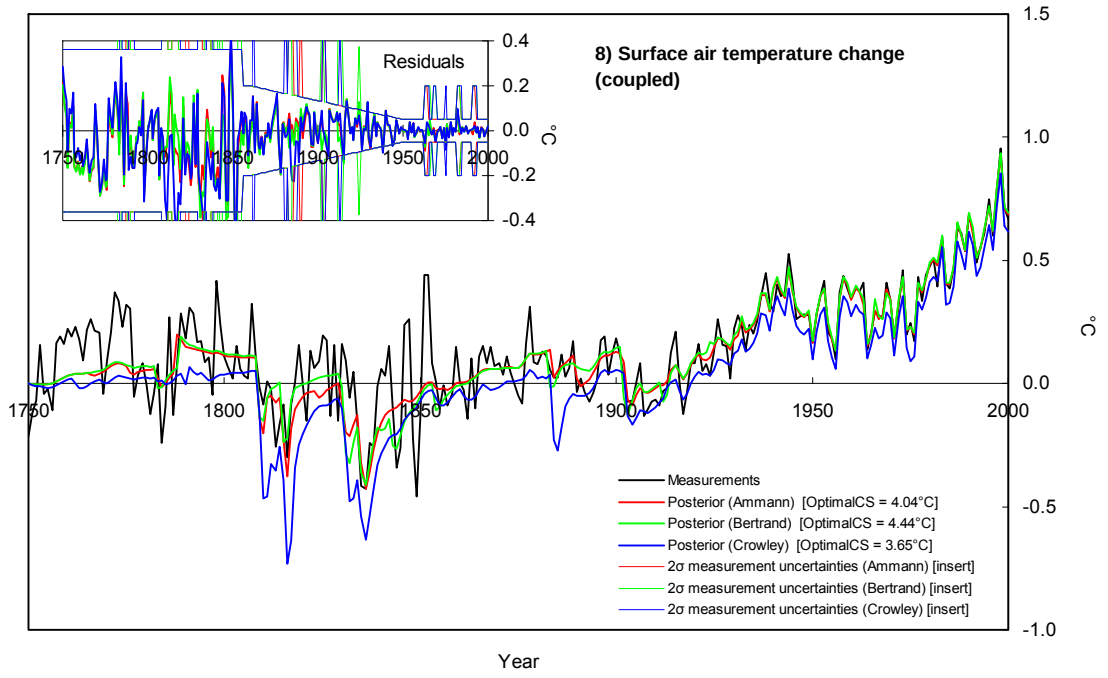

Figure B.9. Sensitivity of the ACC2 inversion results to ocean diffusivity

Figure B.9.1 shows the changes in the final value of the cost function when ocean diffusivity is assumed to be 0.55 cm^2/s (standard), 1 cm^2/s, and 2 cm^2/s. The uncoupled inversions are performed with climate sensitivity fixed at values between 1°C and 10°C at intervals of 0.25°C. Black plots are identical with those shown in Figure 5.1. Values in the square brackets are the best estimates of climate sensitivity for the respective inversion setups. Figures B.9.2 and B.9.3 show the associated uncoupled inversion results of radiative forcing and temperature change with respective optimal climate sensitivity indicated in the square brackets. Measurements shown in Figure B.9.3 are vertically shifted for the uncoupled inversion with ocean diffusivity of 0.55 cm^2/s.

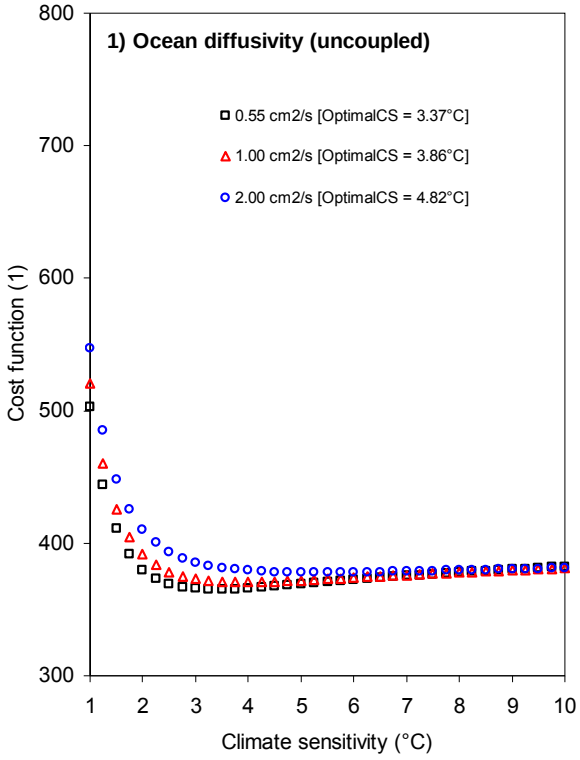

Figure B.9. (Continued) Sensitivity of the ACC2 inversion results to ocean diffusivity

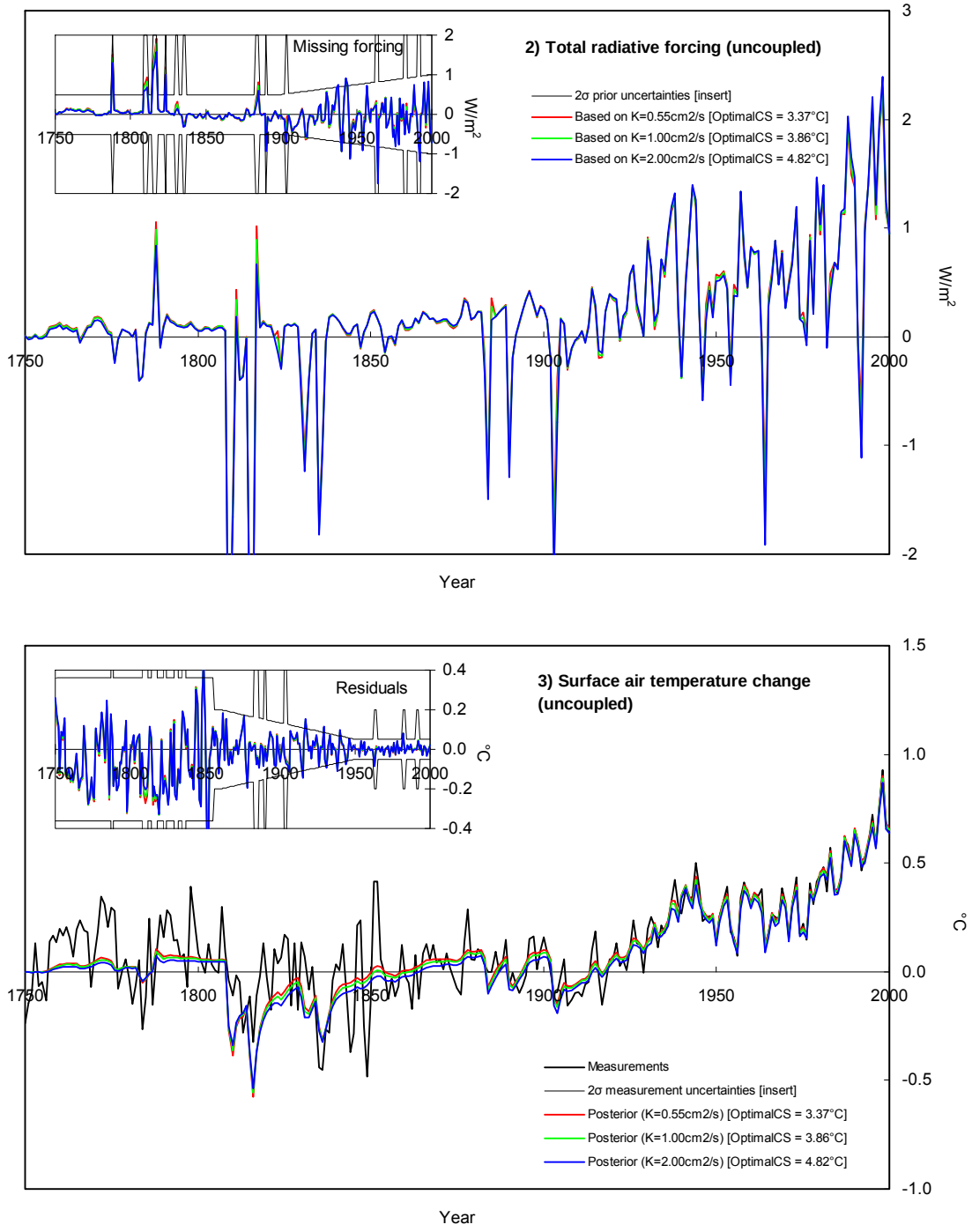

Figure B.10. Sensitivity of the ACC2 inversion results to prior climate sensitivity

Shown below are the ACC2 uncoupled inversion results for radiative forcing and temperature change under different assumptions on prior climate sensitivity. The 2σ prior range of 0.5°C–6.5°C is the standard assumption adopted in the ACC2 inversion. The 2σ prior range of 1.5°C–4.5°C (IPCC, 2001, Chapter 9) is a conventional range. The 2σ prior range of 0.5°C–10.5°C is a conservative range (e.g. IPCC, 2007, pp.798-799). The inversion results are nearly indistinguishable each other. Values in the square brackets are the best estimates of climate sensitivity for the respective inversion setups. Measurements shown in Figure B.10.2 are vertically shifted for the uncoupled inversion with the standard prior range for climate sensitivity.

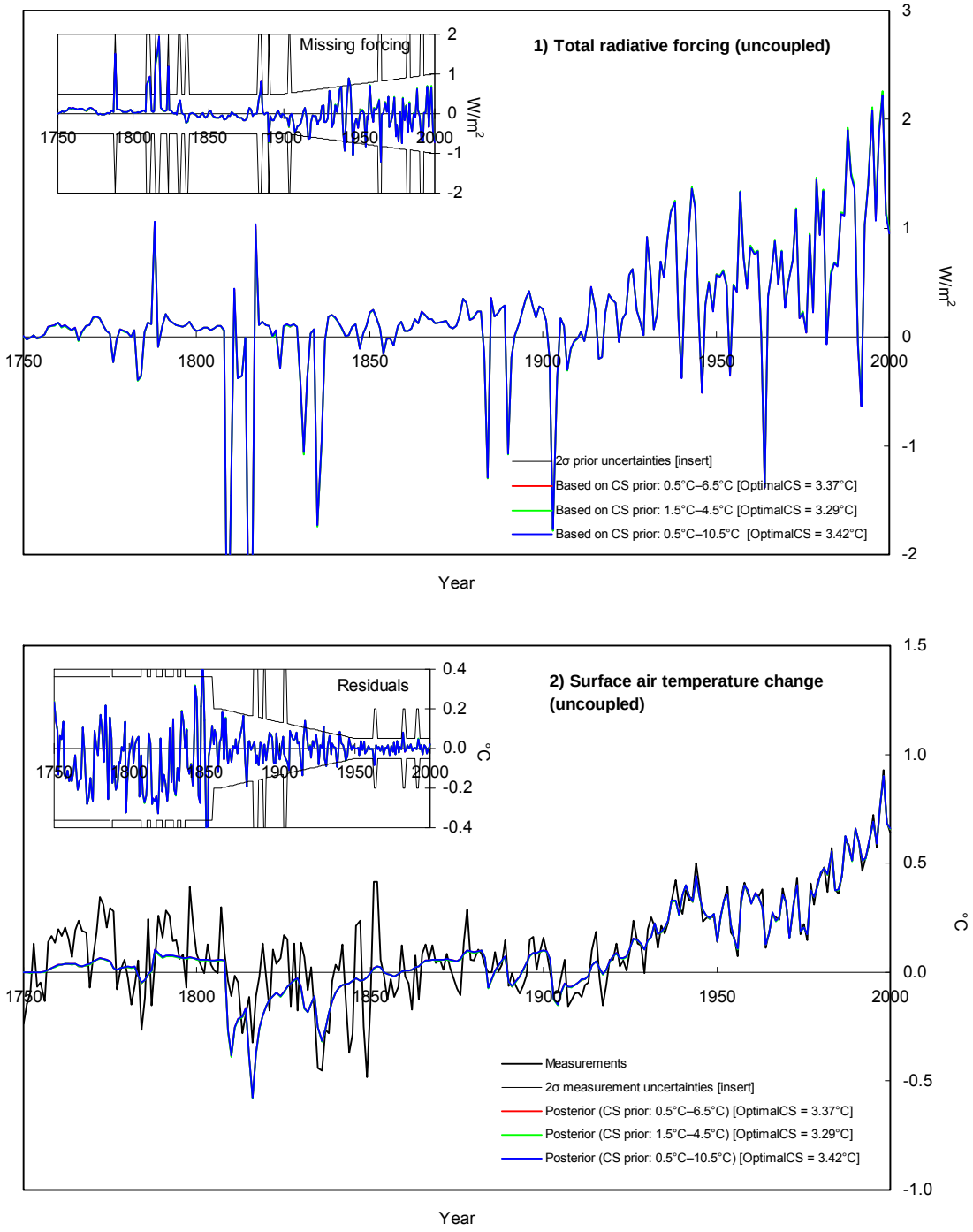

Figure B.11. Influence of prescribed aerosol forcing to missing forcing

Shown below are the results of ACC2 uncoupled inversions when 50% smaller, standard, and 50% larger total aerosol forcing are assumed. In Figure B.11.3, measurements are vertically shifted for the standard uncoupled inversion. Values in the square brackets are the best estimates of climate sensitivity for the respective inversion setups.

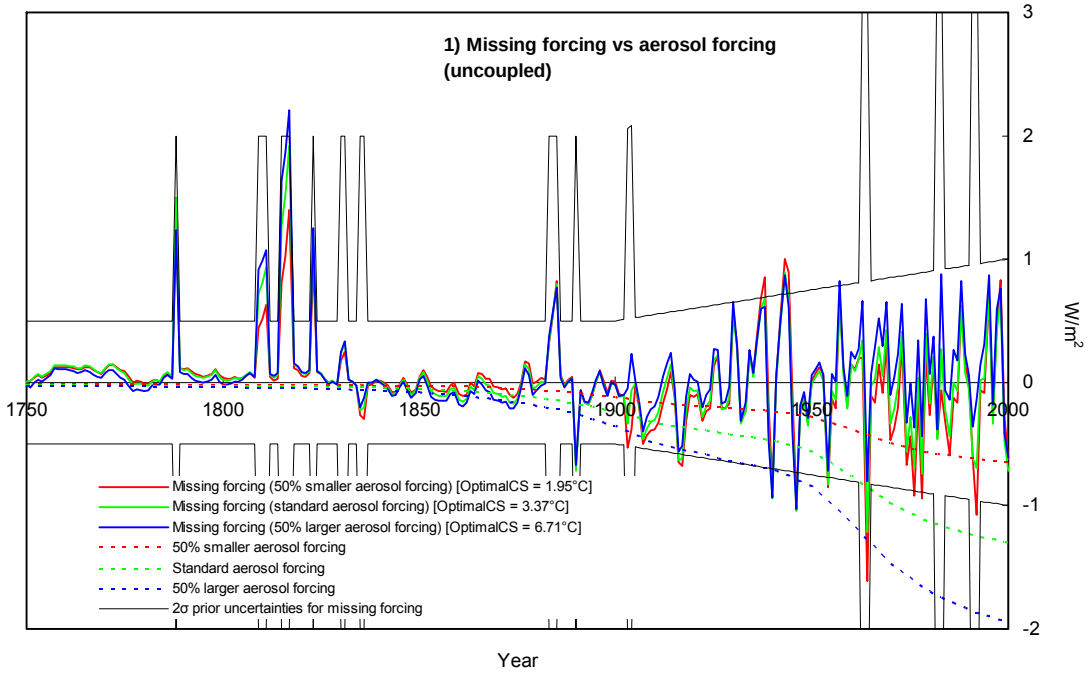

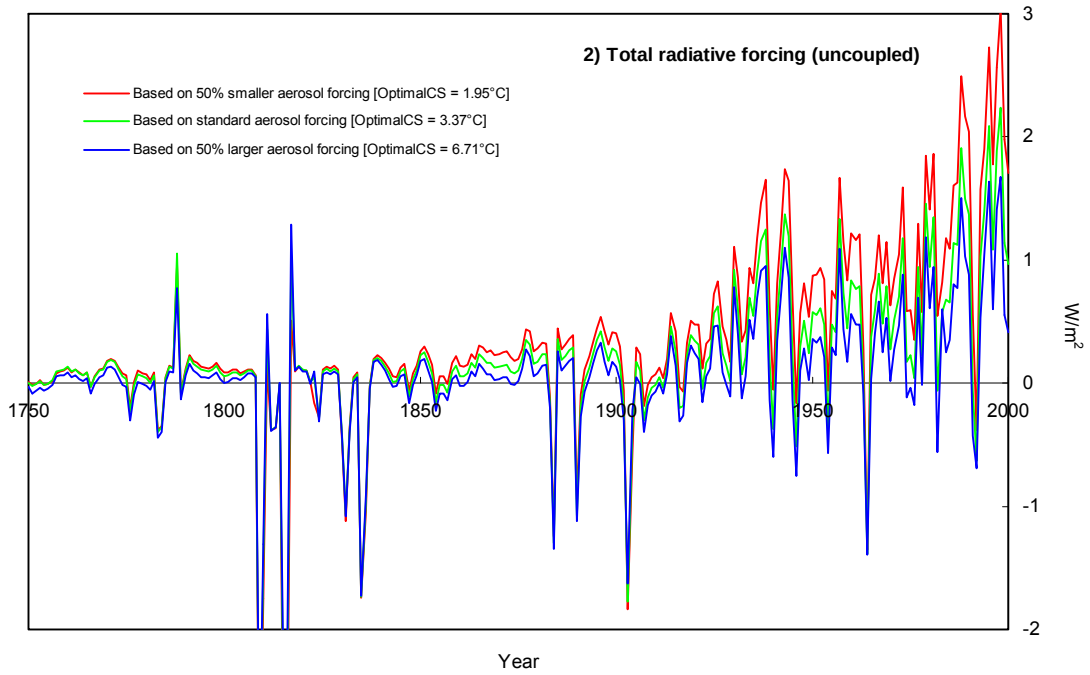

Figure B.11. (Continued) Influence of prescribed aerosol forcing to missing forcing

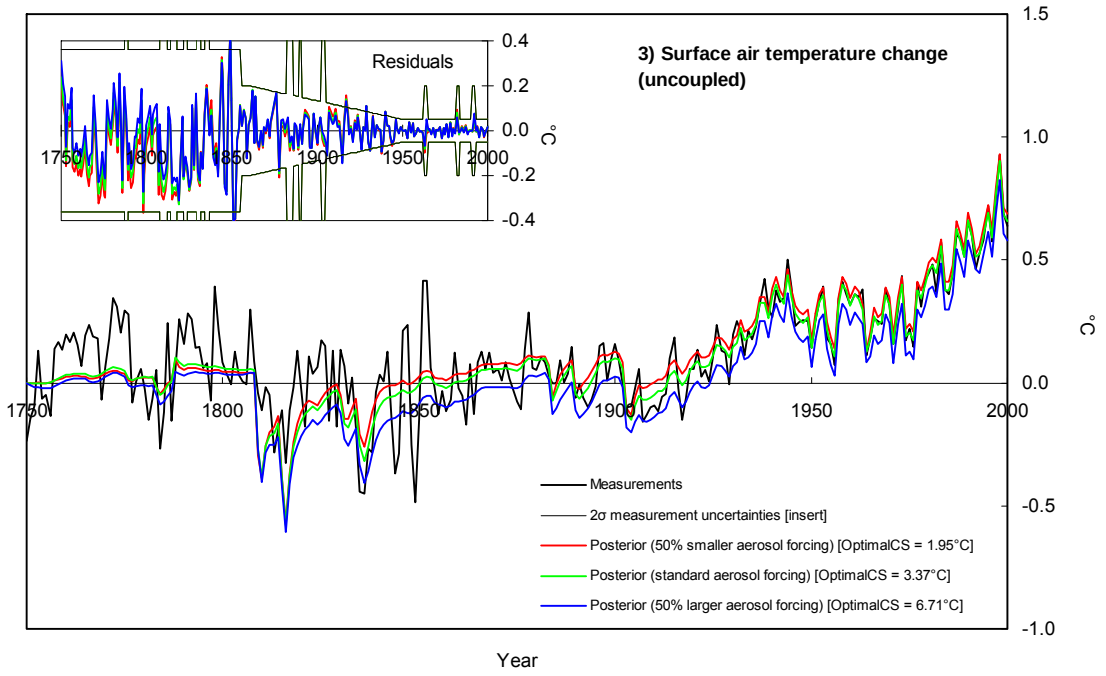

Figure B.12. Influence of prescribed volcanic forcing to missing forcing

Shown below are the results of the ACC2 uncoupled inversions with different volcanic forcing prescribed (Ammann et al., 2003 (standard setup); Bertrand et al., 2002; Crowley et al., 2003). Values in the square brackets in the legends are the best estimates of climate sensitivity for the respective inversion setups. In Figure B.12.3, measurements are vertically shifted for the uncoupled inversion using Ammann's volcanic forcing.

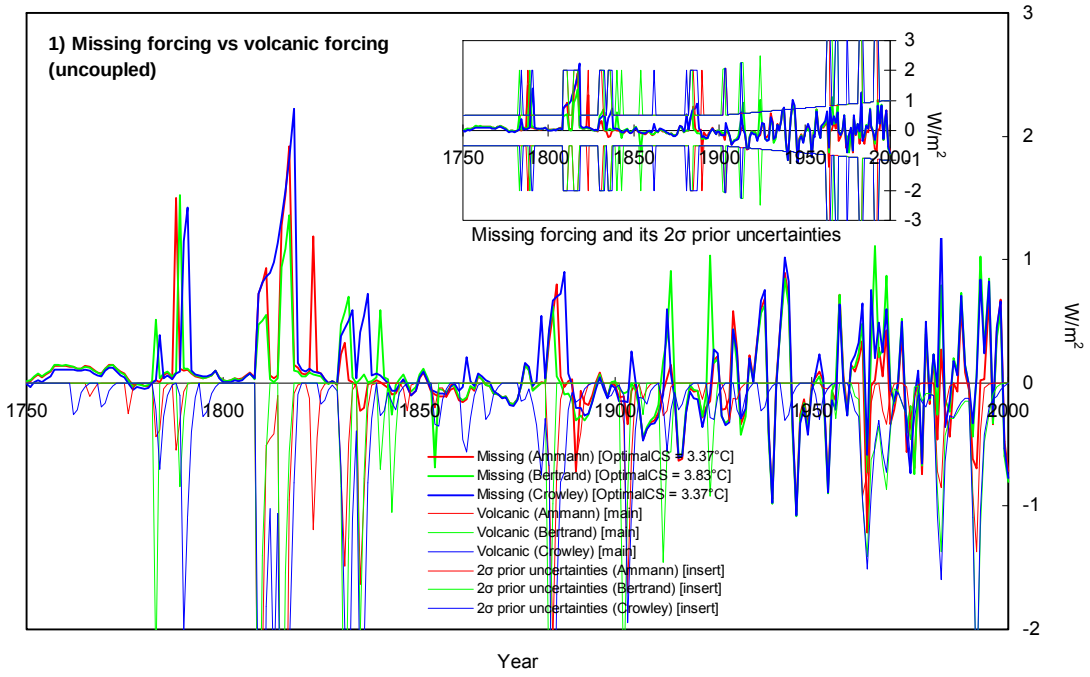

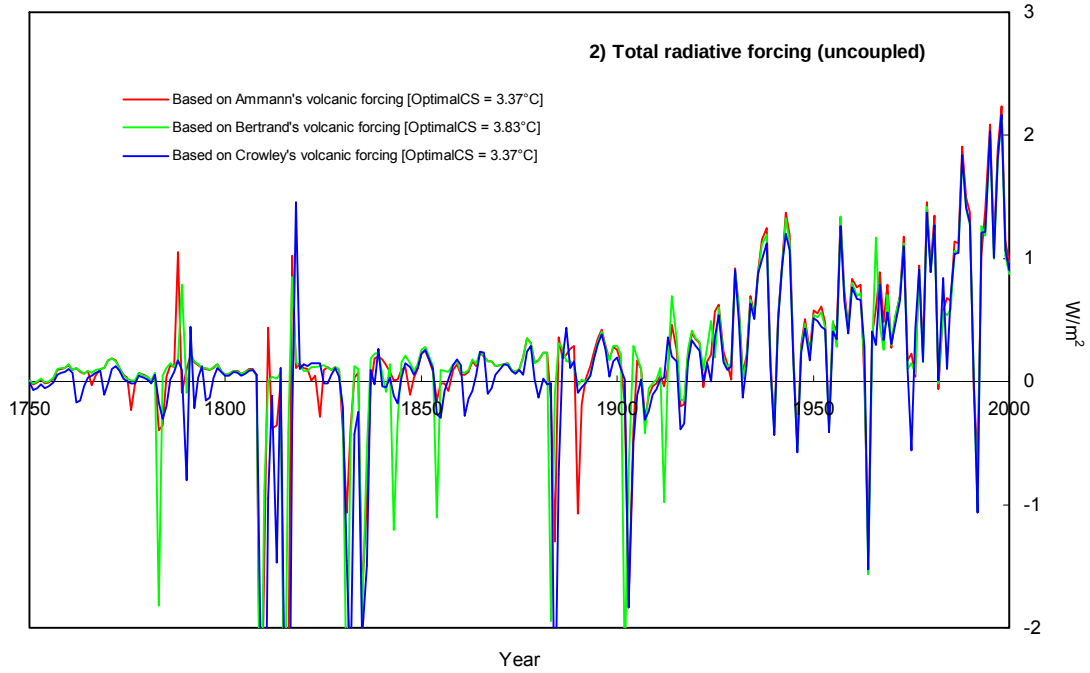

Figure B.12. (Continued) Influence of prescribed volcanic forcing to missing forcing

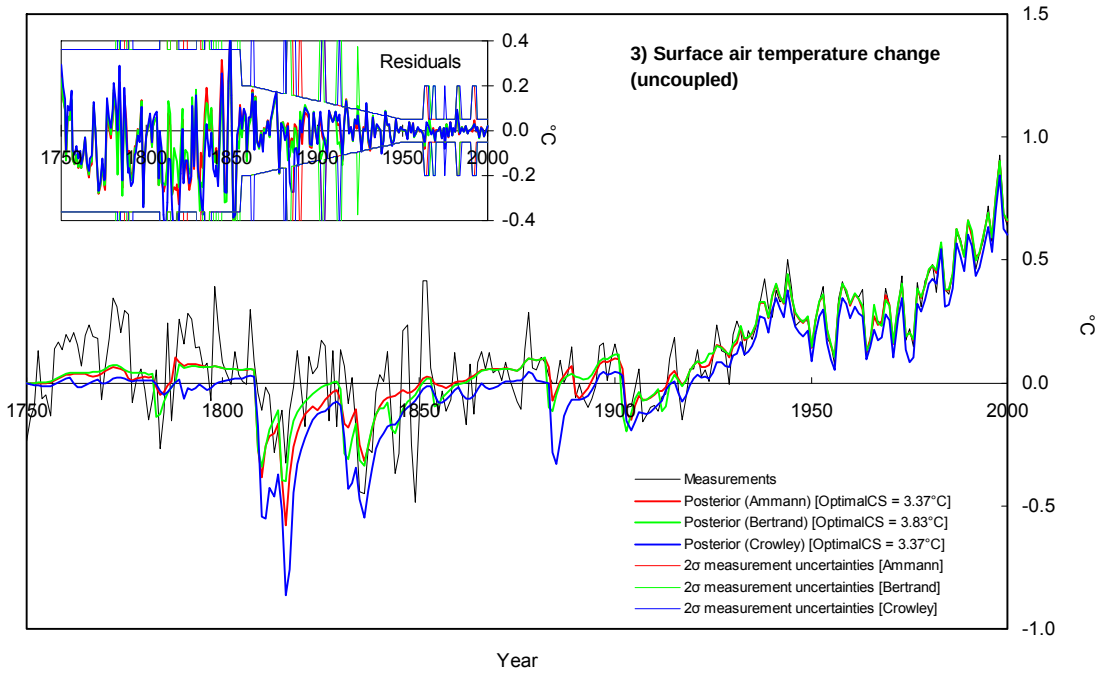

Figure B.13. Influence of ENSO-driven temperature variability to missing forcing

The standard ACC2 uncoupled inversion is compared with an uncoupled inversion without accounting for the ENSO-driven variability in the temperature records. Values in the square brackets in the legends are the best estimates of climate sensitivity for the respective inversion setups. Measurements shown in Figure B.13.2 are vertically shifted for the standard uncoupled inversion.

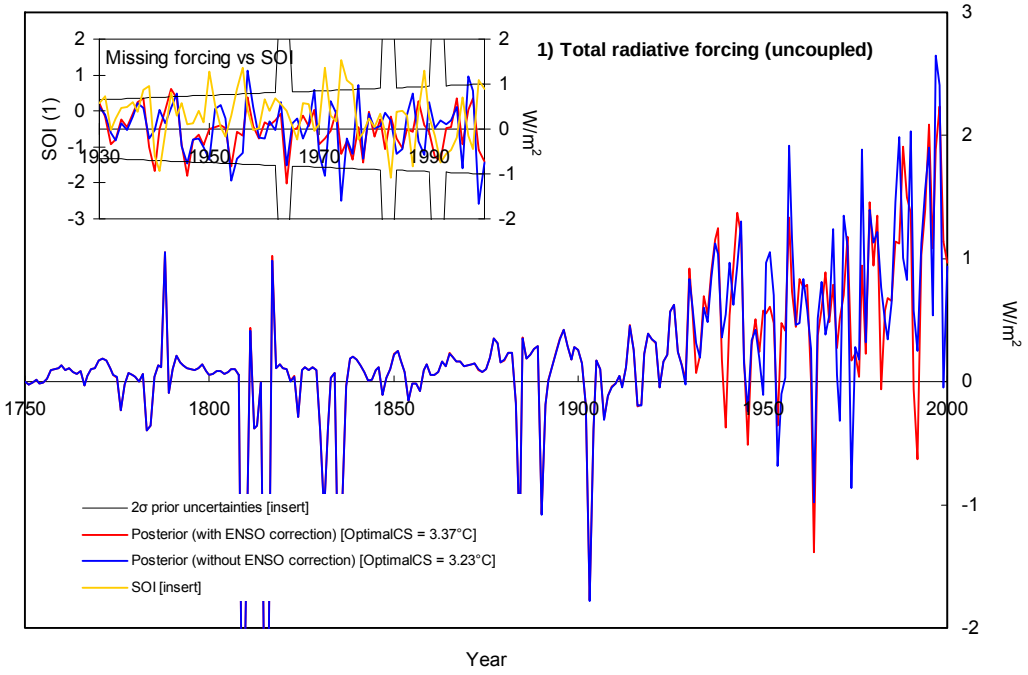

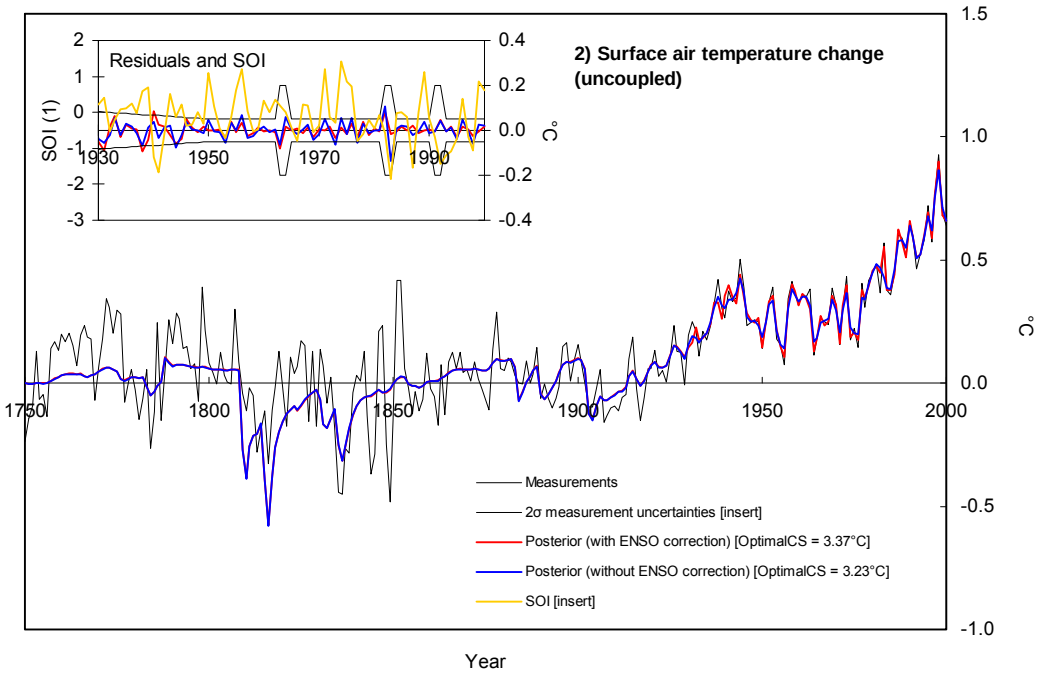

Figure B.14. Changes in the cost function value with the changes in parameter values

Shown below are the final values of the cost function when inversions are performed with some key parameters fixed at different values. These experiments are done for fixed climate sensitivity (1, 3, 5, and 10°C). Note that the vertical scale for Figure B.14.4 is different from others.

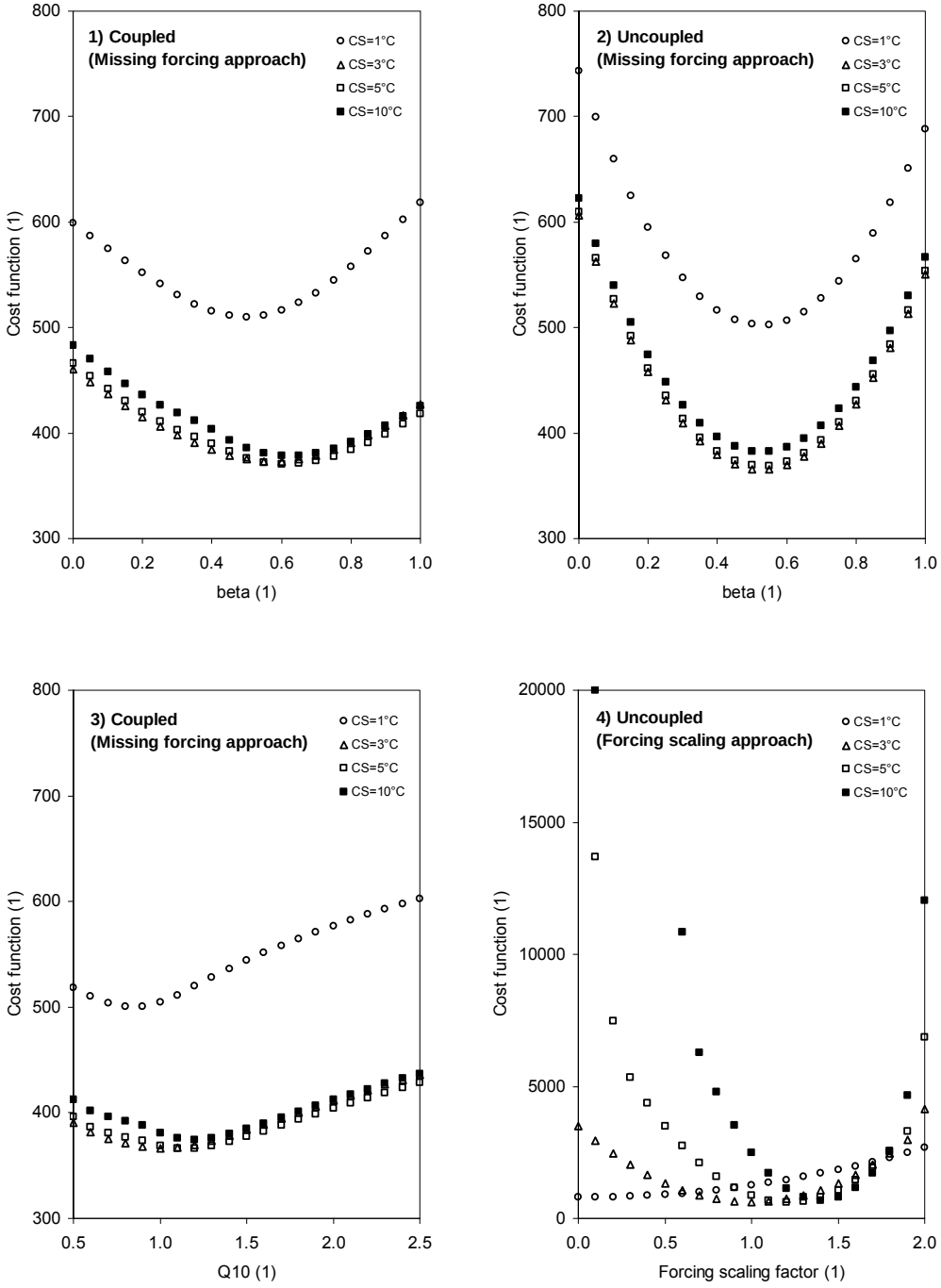

Figure B.15. Normalized cost function curves plotted on an exponential scale

The cost function curves in Figure 5.1 are converted on an exponential scale and renormalized. Lines between the plots are shown to clarify the sequences of plots. The insert scales up the main figure to allow a close comparison between the cost function curves for the missing forcing- and forcing scaling-based inversion.

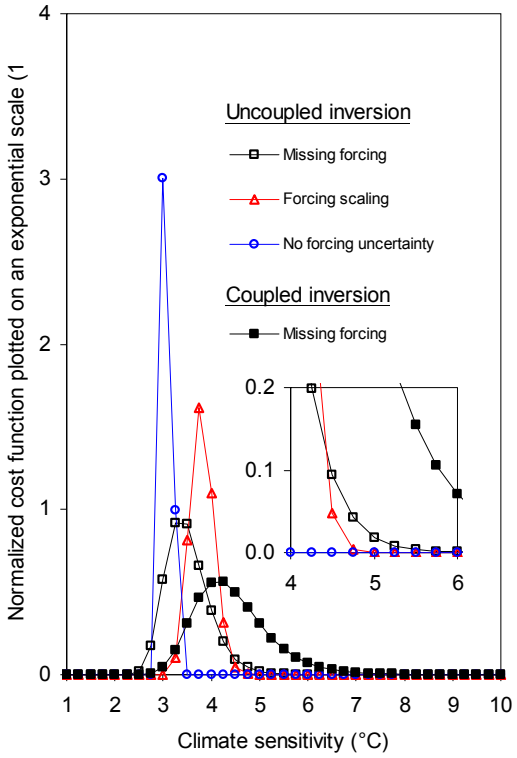

Figure B.16. Influence of the AR(1) model to the inversion results

Figure B.16.1 shows how the cost function curves in Figure 5.1 are influenced by the implementation of the AR(1) model for temperature residuals. The associated squared weighted residuals of selected time series are shown in Figure B.16.2. Figures B.16.3 to B.16.6 are the radiative forcing and temperature change in the missing forcing-based and forcing scaling-based inversions with the climate sensitivity fixed at 1, 3, 5, and 10°C.

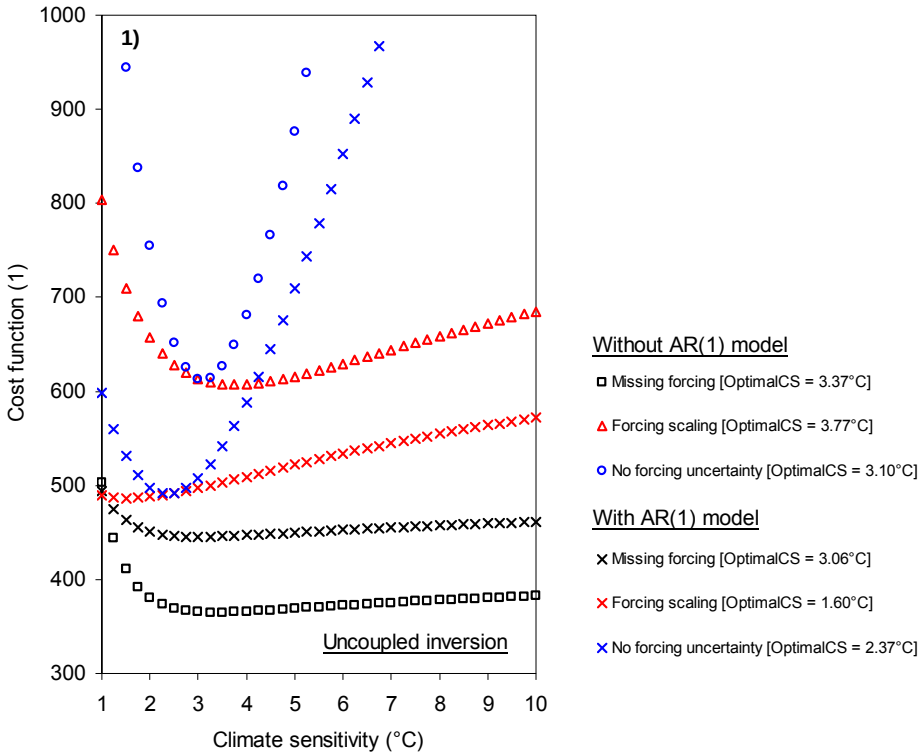

Figure B.16. (Continued) Influence of the AR(1) model to the inversion results

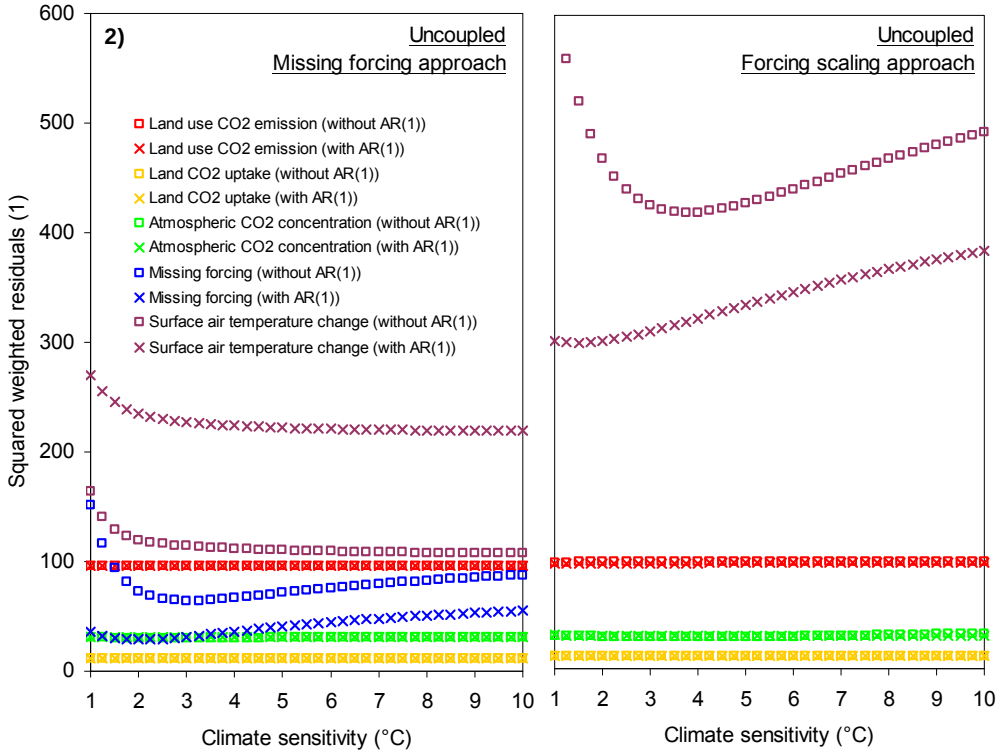

Figure B.16. (Continued) Influence of the AR(1) model to the inversion results

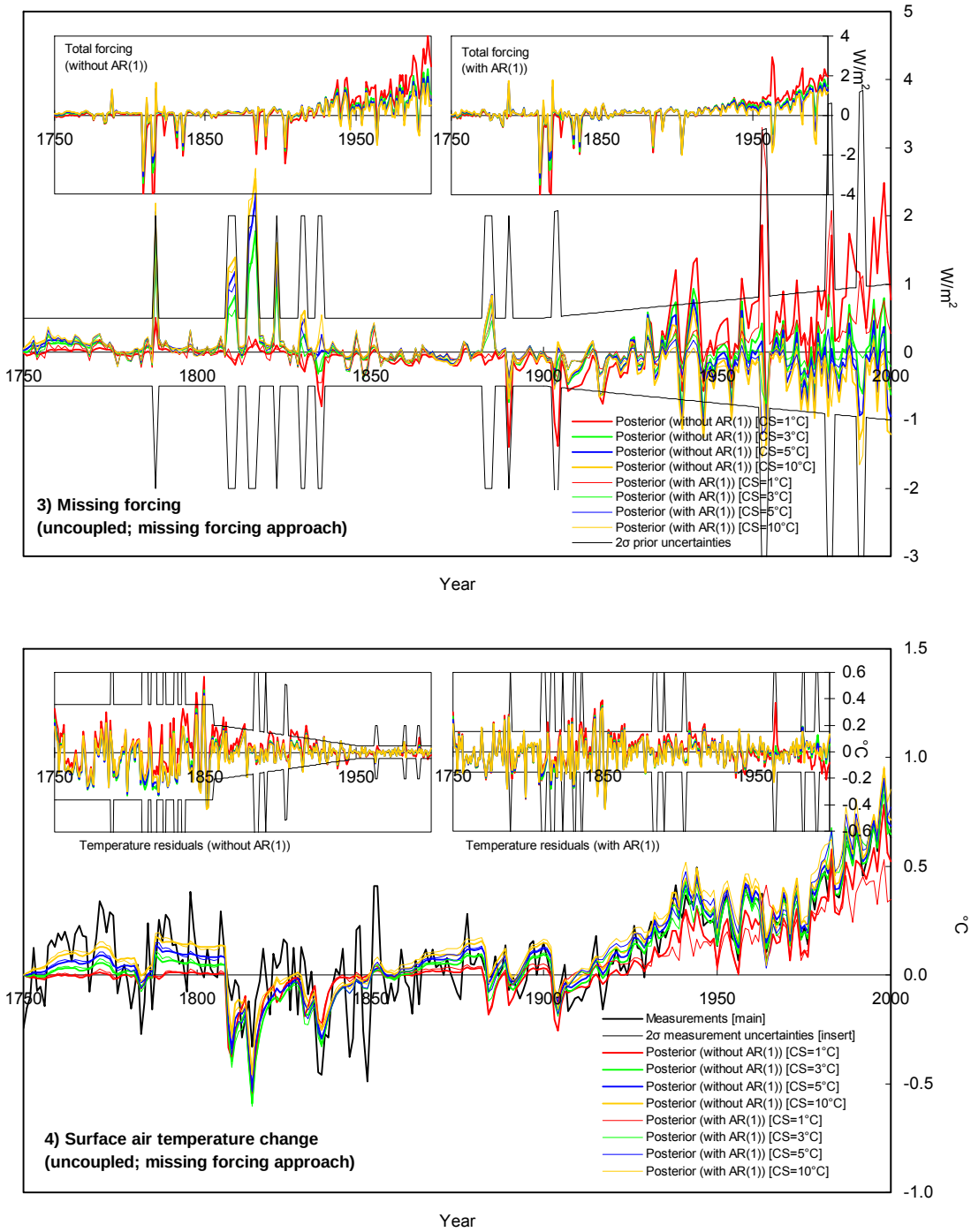

Figure B.16. (Continued) Influence of the AR(1) model to the inversion results

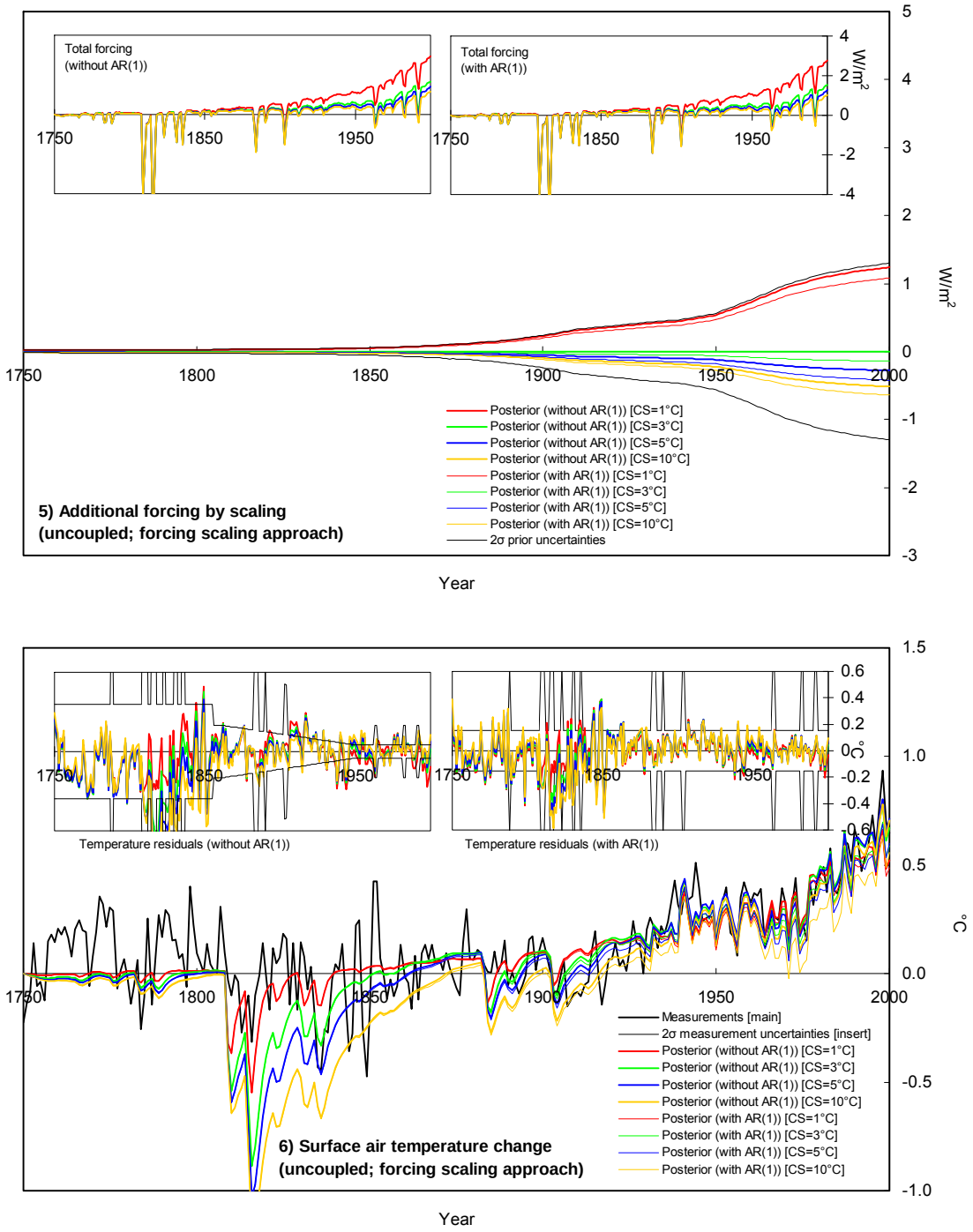

Figure B.17. Influence of the AR(1) model to the temperature residuals

Figures B.17.1a-p are the histograms of the temperature residuals in various ACC2 inversion results (missing forcing- and forcing scaling-based approach; climate sensitivity fixed at 1, 3, 5, 10°C; with/without the AR(1) model for temperature residuals). The bin width is determined by computing 40% of the standard deviation (e.g. Laws, 1997, p.215). Figures B.17.2a-p show the corresponding spectrums of the temperature residuals.

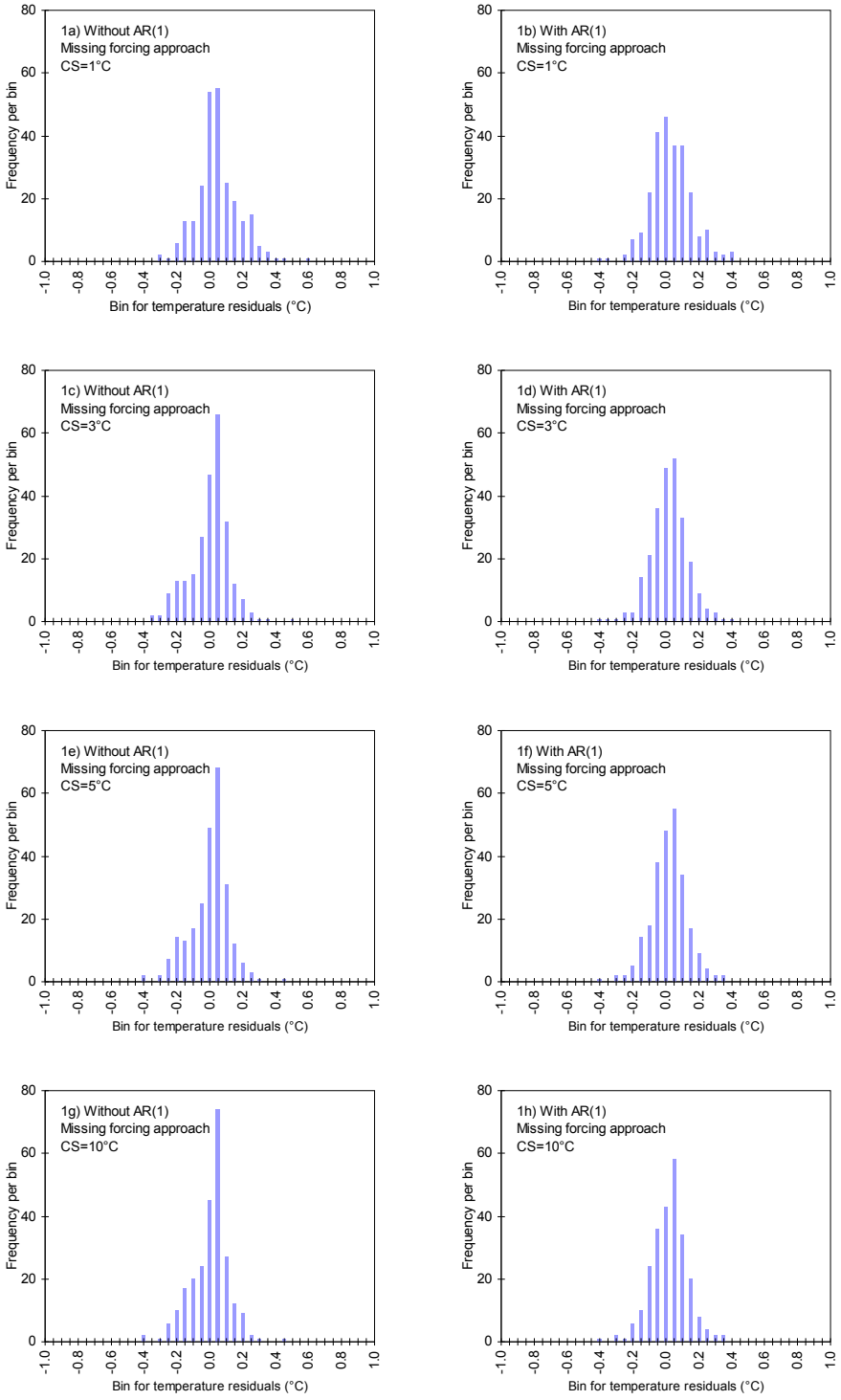

Figure B.17. (Continued) Influence of the AR(1) model to the temperature residuals

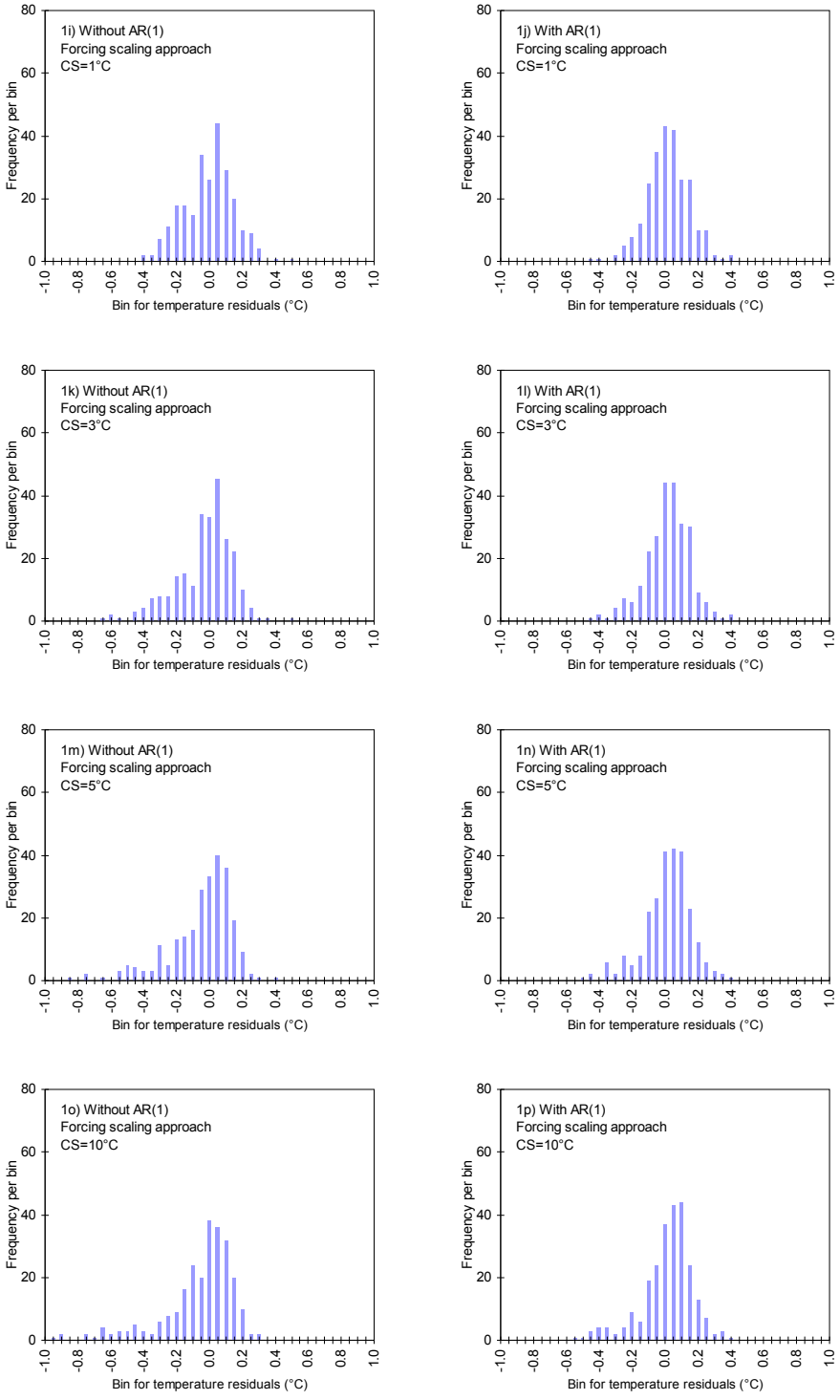

Figure B.17. (Continued) Influence of the AR(1) model to the temperature residuals

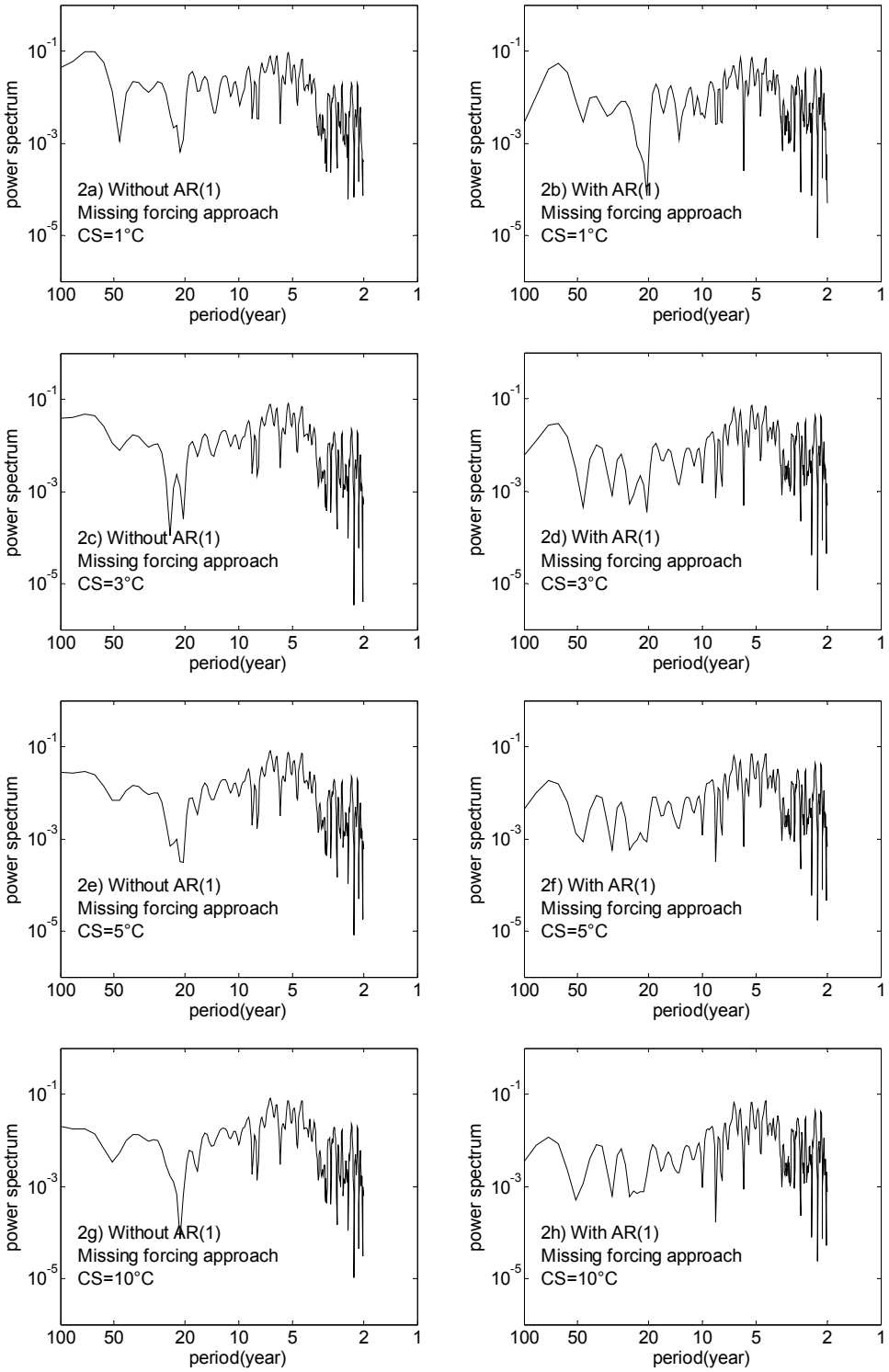

Figure B.17. (Continued) Influence of the AR(1) model to the temperature residuals

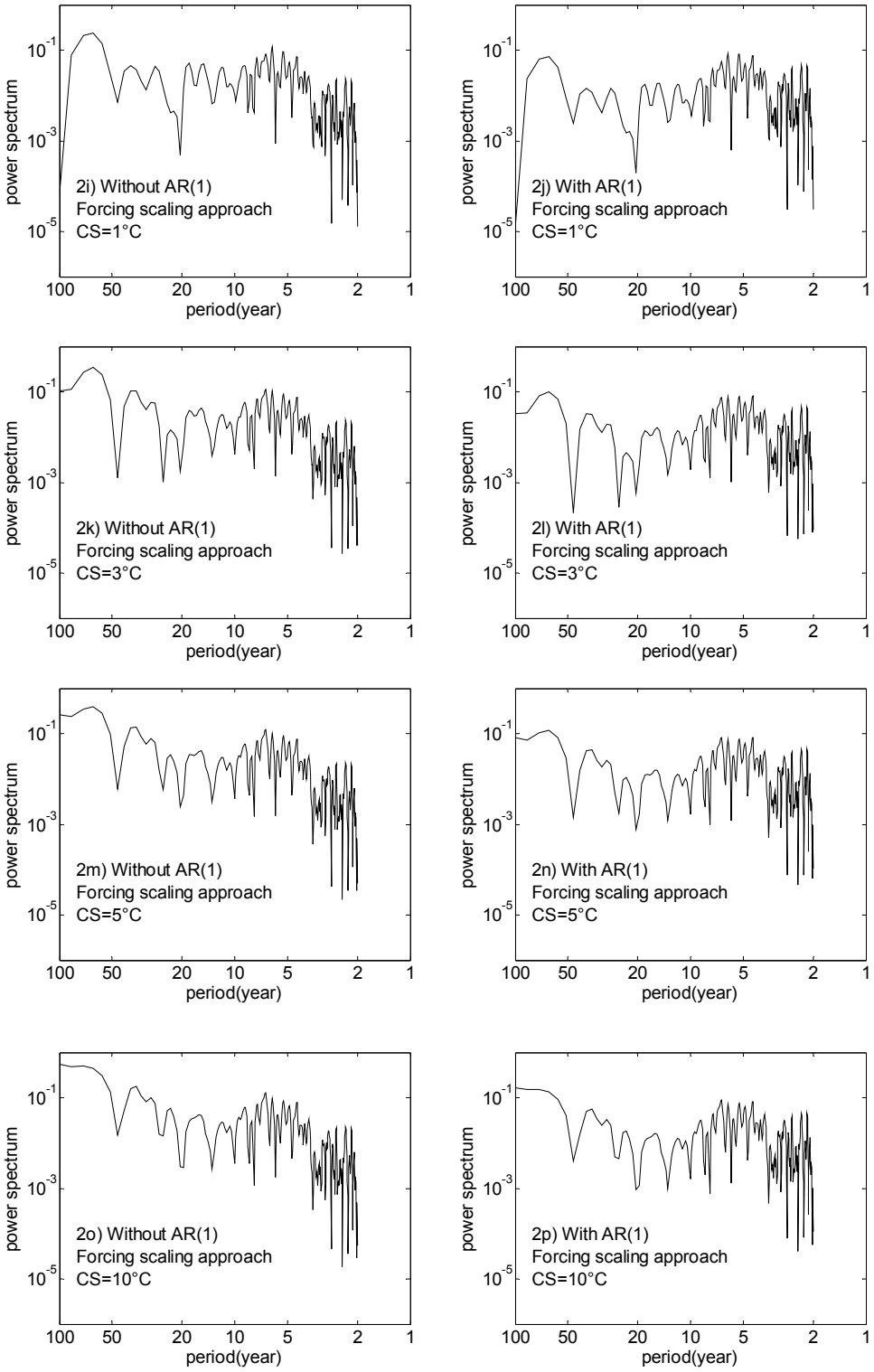

APPENDIX C. SUPPLEMENTARY INFORMATION III — CHAPTER 6

C.1. GWP EVALUATION METHODOLOGY

We first show a further analysis of our GWP evaluation methodology in terms of the reference for TEMP computation (Section C.1.1) and the start year for TEMP computation (Section C.1.2).

C.1.1. Reference for TEMP Computation

Here the effect of using temperature as the reference for TEMP computation is looked into. We similarly compute TEMPs by using radiative forcing as a reference (Figures C.1a-b). The results are nearly identical except for the slight delay in the standard TEMPs due to the inertia of the temperature response to a change in radiative forcing. The finding here also indicates that the GWP evaluation results would also be similar if using radiative forcing reference.

C.1.2. Start Year for TEMP Computation

We investigate the influence of the start year of 1890 to apply the GHG conversion by performing similar TEMP updating computations for different start years (Figures C.1c-d). The general trend of the CH_4 TEMPs does not change. As for the N_2O TEMPs, some irregular structures emerge in the early stage of updating, but the overall quasi-logarithmic trend remains the same. The problem of having the N_2O TEMP above the maximum N_2O GWP persists. Irrespective of the start year, it appears that the CH_4 and N_2O TEMPs follow similar paths and converge to certain values.

C.2. INDIVIDUAL ASSUMPTIONS IN IPCC GWP CALCULATIONS

In Section 6.5, we show the effect of all the IPCC assumptions to TEMPs. Here we investigate the influences of the individual IPCC assumptions, namely, CO_2 fertilization (Section C.2.1), CH_4 and N_2O lifetimes (Section C.2.2), and process simplifications (Section C.2.3).

C.2.1. CO_2 Fertilization

The literature estimates of the beta factor substantially vary between 0.15 and 0.6 (e.g. Kohlmaier et al., 1987). We fix the beta factor at a very low level (= 0.15) and the IPCC level (= 0.287) and

perform inverse calculations for the respective cases. The results of these inversions provide their respective best guess of the parameter estimates to be used for TEMP computations. It should be noted that the TEMP computations for the lower beta factors are based on different inversion results because the best guess of all the parameter estimates has to be re-computed to reflect the assumption on the beta factor. Figures C.2a-b show the respective TEMP updating experiments, indicating that the weaker the CO_2 fertilization, the lower the TEMPs. A low CO_2 fertilization means less carbon storage in the terrestrial biosphere, implying a longer CO_2 lifetime in the atmosphere. As a result, the influence of the CO_2 emissions to the temperature is enhanced, lowering the TEMP for CH_4 and N_2O. When the CO_2 fertilization is assumed to be at the level for the IPCC GWP calculations, the TEMP projection is substantially lowered. In the case of very low CO_2 fertilization, the N_2O TEMP stays below the maximum N_2O GWP throughout the updating exercise. Our inverse calculation indicates that assuming the very low CO_2 fertilization of 0.15 is not realistic because the CO_2 emissions have to be unacceptably low to counteract the atmospheric CO_2 build-up owing to the very low CO_2 fertilization. The results of the sensitivity analysis here suggest that the low beta factor assumed in the IPCC GWP in part explains why the N_2O GWP does not function as a historical temperature proxy.

C.2.2. CH_4 and N_2O Lifetimes

In the IPCC GWP calculations, the CH_4 and N_2O lifetimes adopt the adjustment times of 12 and 114 years, respectively (IPCC, 2001, Table 6.7). In contrast, in the TEMP calculations, the CH_4 lifetime with respect to OH depletion and N_2O lifetimes use the baseline estimates of 8.5 and 114 years obtained from the ACC2 inversion, respectively (Table 3.2) and the CH_4 lifetimes with respect to stratospheric loss and soil uptake are 120 and 160 years, respectively (IPCC, 2001, p.248). The chemistry-transport models show the CH_4 lifetime with respect to OH varying from 6.5 to 13.8 years (IPCC, 2001, Table 4.3) and N_2O lifetime from 97 to 137 years (IPCC, 2001, Table 4.5). The total CH_4 lifetime of 12 years assumed in the IPCC GWP calculation is equivalent to the CH_4 lifetime with respect to OH depletion of 14.5 years when the CH_4 lifetimes with respect to stratospheric loss and soil uptake are the IPCC estimates above.

We perform inversions by fixing the CH_4 and N_2O lifetimes at the values discussed above and then calculate TEMPs. Figures C.2c-d indicate that a longer lifetime of CH_4 or N_2O leads to a higher TEMP. This is due to the fact that an increase in the CH_4 or N_2O lifetime enhances the influence of the CH_4 or N_2O emissions to the temperature, resulting in a higher TEMP.

C.2.3. Process Simplifications

The IPCC GWP calculations simplify the nonlinear dynamics in the background system. We

investigate the implications of such simplifications in the following three parts:

1) The rate of ocean CO_2 uptake in ACC2 saturates with increasing atmospheric CO_2 concentration due to the shift in the thermodynamic equilibrium of the marine carbonate system. In contrast, the IPCC GWP calculation implicitly assumes a fixed equilibrium implied in the impulse response function for the Bern Carbon Cycle Model (Joos et al., 1996). To mimic the IPCC setting for the ocean CO_2 uptake, we perform an inverse calculation by assuming a present Revelle factor (= 10.34 (Revelle and Munk, 1977; Mackenzie and Lerman, 2006, p.265)) throughout the historical period and compute TEMPs on the basis of such an inversion result.
2) A positive feedback for the CH_4 concentration to its own lifetime occurs as a result of various chemical processes involving tropospheric OH (Seinfeld and Pandis, 2006, pp.1048-1049). In contrast, there is a smaller but negative feedback for the N_2O concentration to its own lifetime brought about by chemical reactions in the N_2O-NO_y-O_3 system (Seinfeld and Pandis, 2006, p.1048). Such concentration feedbacks to the lifetimes are accounted for in the IPCC GWP calculations as it uses the adjustment times for the lifetimes (IPCC, 2001, Table 6.7). However, unlike ACC2 (Table 2.1), the IPCC GWP calculations assume the feedbacks as being fixed and independent of the concentrations. We hypothetically perform an inverse calculation by removing the concentration feedbacks to the lifetimes and then calculate TEMPs.
3) In ACC2, the CH_4/N_2O radiative forcing is formulated as a square root function of the CH_4/N_2O concentration to account for the saturation effect with an additional term to account for the overlap effect (IPCC, 2001, Table 6.2; this thesis, Table 2.1). In the IPCC GWP calculations, the saturation and overlap effects are kept constant, irrespective of the associated concentrations. To test the effect of such linearization, we perform an additional inverse calculation with linear concentration-forcing relationships using associated radiative efficiencies (IPCC, 2001, Table 6.7) and then compute TEMPs.

The results of the three experiments are shown in Figures C.2e-f. It is indicated that the differences in the functional forms of the concentration-forcing relationships in particular go some way in explaining the disparity between N_2O TEMPs and GWPs. The other two simplifications are not as important as the linearization of the concentration-forcing relationships to explain the departure of N_2O GWPs from the TEMP. Thus, the linear assumptions in the concentration-forcing functional relationships in the IPCC GWP calculations is another factor (besides the low beta factor) explaining the fact that N_2O GWP does not follow the temperature change history with any time horizon.

Figure C.1. Sensitivities of TEMPs to the different system dynamics and uncertain parameter estimates: a,b) beta factor; c,d) CH_4 lifetime with respect to OH depletion and N_2O lifetime; and e,f) process simplifications

Backward-looking TEMPs are calculated for every year from 1890 to 2000.

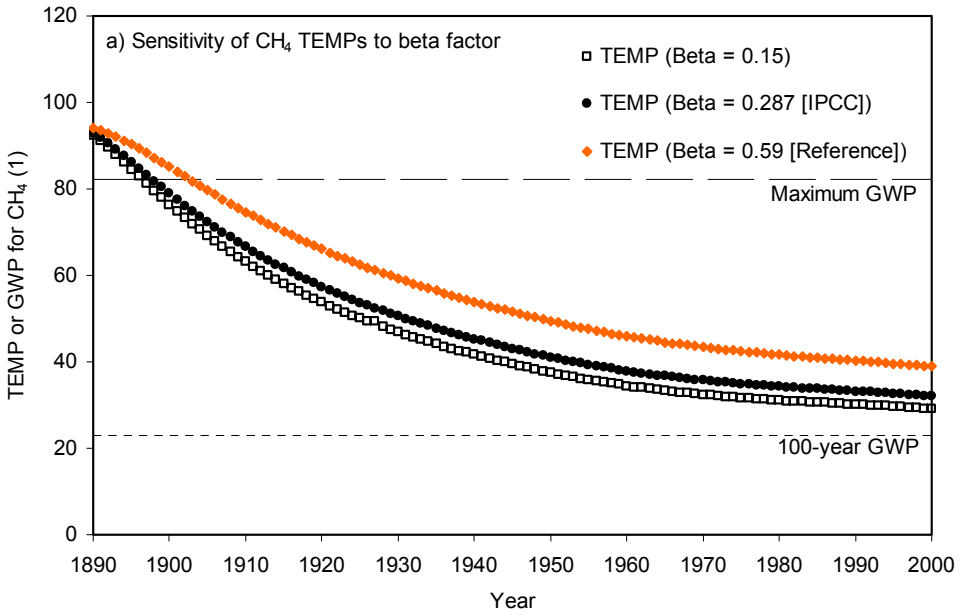

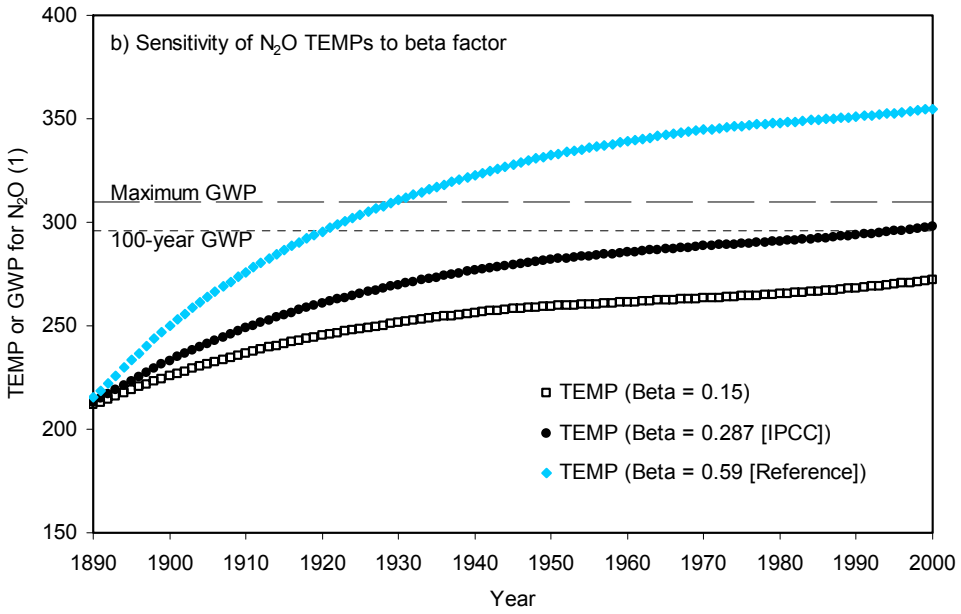

Figure C.1. (Continued) Sensitivities of TEMPs to the different system dynamics and uncertain parameter estimates: a,b) beta factor; c,d) CH_4 lifetime with respect to OH depletion and N_2O lifetime; and e,f) process simplifications

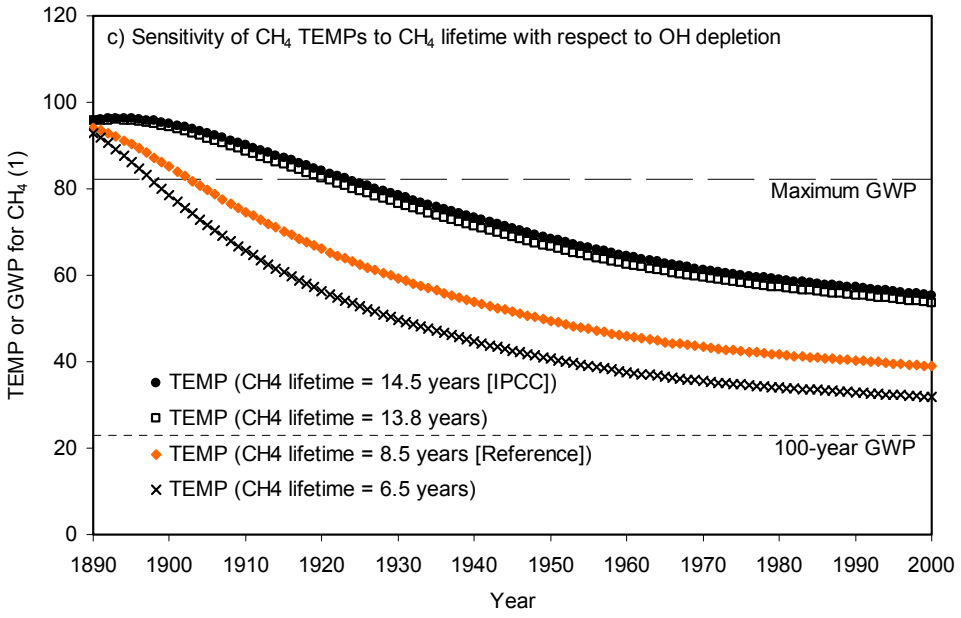

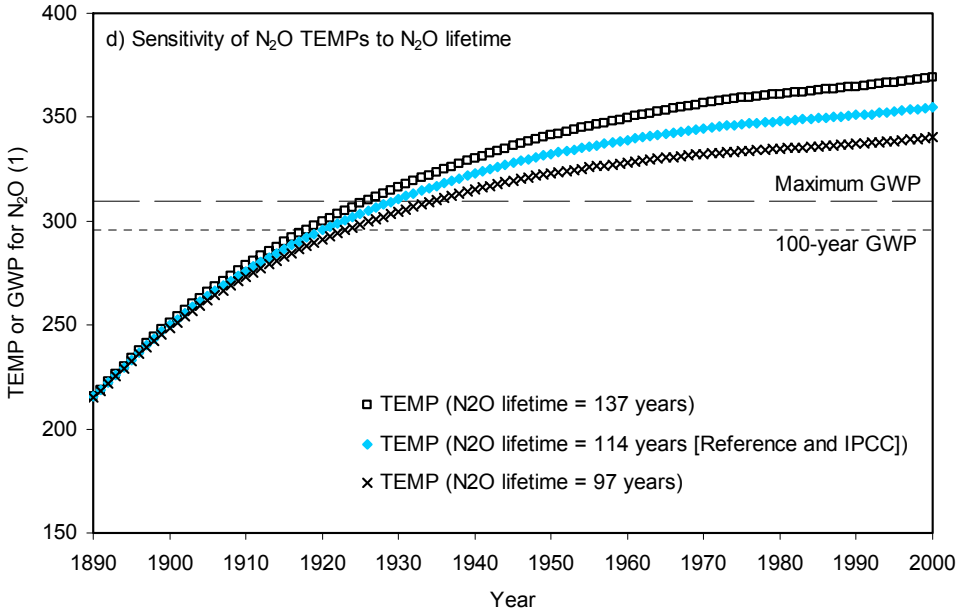

Figure C.1. (Continued) Sensitivities of TEMPs to the different system dynamics and uncertain parameter estimates: a,b) beta factor; c,d) CH_4 lifetime with respect to OH depletion and N_2O lifetime; and e,f) process simplifications

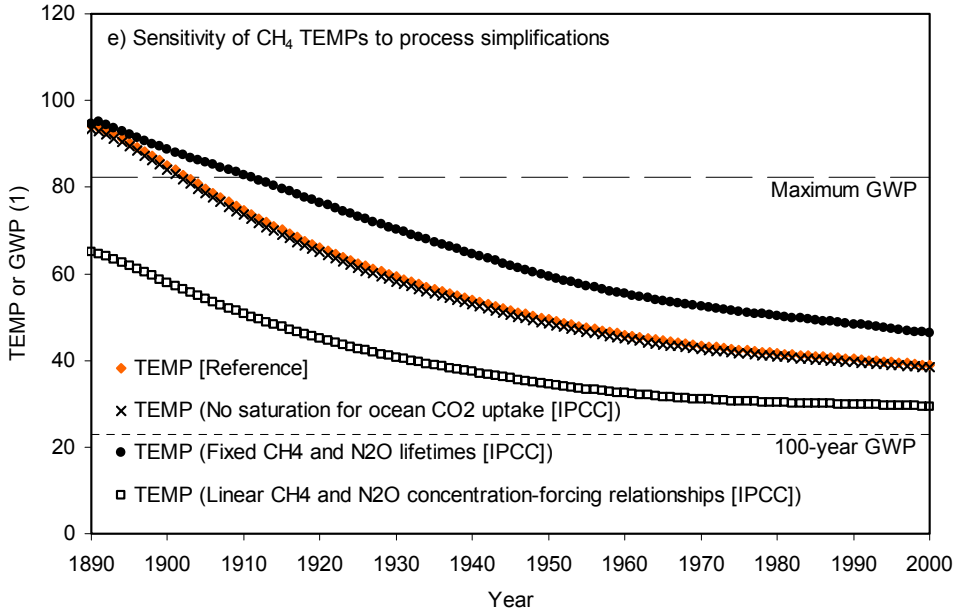

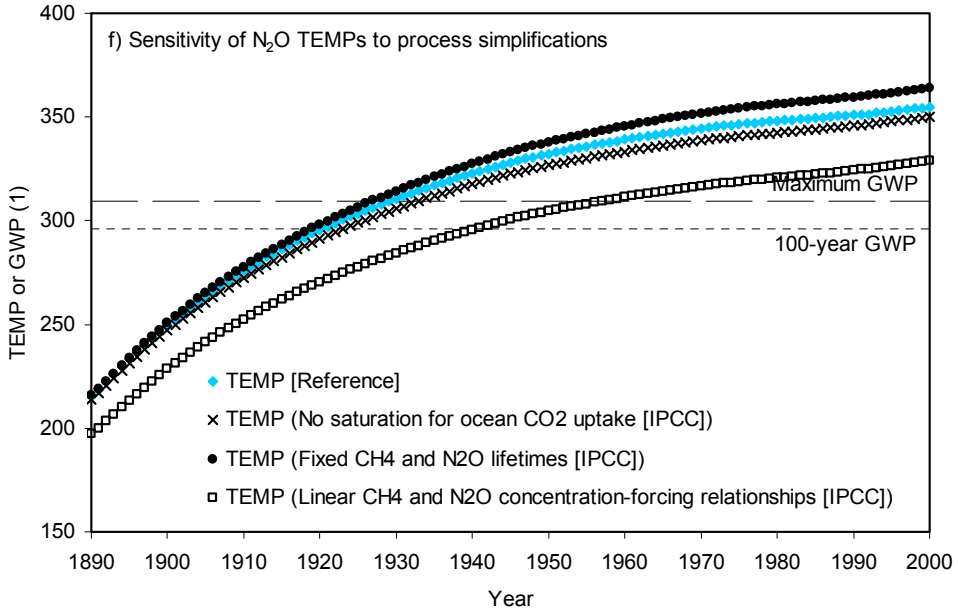

APPENDIX D. TECHNICALITIES

D.1. PROGRAMMING LANGUAGE AND SOLVERS

ACC2 is programmed in GAMS (Distribution 22.6, released on December 14, 2007, http://www.gams.com). GAMS is a language designed for mathematical programming and optimization. It is used for various model applications (GAMS Model Library in the GAMS software package) including economic models (e.g. Dynamic Integrated model of Climate and the Economy (DICE) (Nordhaus and Boyer, 2000)). Descriptions on GAMS (including tutorial and some advanced materials) are provided in the GAMS software package.

GAMS falls into the category of fifth-generation programming language, which requires the programmers only to describe particular problems (e.g. functional relationships and boundary conditions) without building up their algorithms and specifying machine-related matters such as address calculations ("fifth-generation programming languages" in Wikipedia). GAMS is easier for humans to read than the third-generation programming languages such as C and Fortran. GAMS is available for various operation systems – the 32-bit Windows version is used for the development of ACC2. ACC2 has been partly tested on the 64-bit Windows version and has not shown any difference from the 32-bit Windows version in the model calculation results. We have seen small numerical differences between the Windows-based GAMS and the Unix-based GAMS in the model calculation results, but such differences are sufficiently small and can thus be disregarded in practical applications.

One of the strengths of the ACC2 approach is its compactness; the model is small enough to run on a laptop PC. It takes about one hour to run the ACC2 past mode on a Windows XP machine (Intel® Core™2 2.4GHz). The future mode needs only some minutes to complete (from the year 2000 to 2100 for one emission scenario) as it has no nasty optimization. The past mode of ACC2 heavily relies on the optimization capability of GAMS while the future mode of ACC2 uses GAMS just as a simulator. In the future mode, the cost function is set to a trivial constant (zero) because a cost function is formally required in a GAMS-based model. The multivariable equations describing inorganic carbonate chemistry (Section 2.1.2) and the implicit numerical integration method (Sections 2.3.4 and 4.2) are solved by utilizing iterative computation algorithm in GAMS.

The GAMS software package comprises a *compiler* to convert from the high-level language to a low-level machine-readable language and a suite of *solvers* for various mathematical

problems such as linear, nonlinear and mixed integer optimization problems (e.g. Winston, 1994) (for general information on GAMS solvers, http://www.gams.com/solvers/solvers.htm). All of the individual solvers are explained in detail in the solver manual contained in the GAMS software package. The GAMS software package offers three local optimization solvers for NonLinear Programming (NLP): CONOPT, MINOS, and SNOPT. The choice of a solver is model-dependent as each of the solvers has strengths and weaknesses. Some guidelines for choosing between CONOPT and MINOS are available at http://www.gams.com/docs/minosvsconopt.htm. ACC2 uses only CONOPT for its past and future modes. CONOPT and MINOS are complementary in terms of their algorithms. ACC2 cannot be solved with MINOS. ACC2 is too large to be dealt with SNOPT.

One could use solvers EXAMINER and GAMSCHK to check the feasibility of the solution. BARON, the *global* optimization solvers for NLP, should be useful to check the solution obtained from the *local* optimization solver CONOPT. However, BARON cannot be used for ACC2 at this point because BARON does not support a model solved with CONOPT (extension in progress (Nick Sahinidis, personal communication, February 14, 2007)) and also because ACC2 is beyond the capacity of BARON. BARON can deal with up to some thousand of variables (Nick Sahinidis, personal communication, February 23, 2007) whereas ACC2 has about 50,000 variables. The time for BARON to parse and reformulate the model is significant, depending on the nonlinearity and the size of a model. Furthermore, BARON does not support the "errorf" functions used in the DOECLIM component in ACC2.

The optimization for the ACC2 inverse estimation is performed by using solver CONOPT3 developed by Arne Stolbjerg Drud, ARKI Consulting and Development (http://www.conopt.com/). CONOPT3 is the third version of the CONOPT series and is occasionally updated. Both CONOPT2 and CONOPT3 were required during some development phases of ACC2. We currently use only the latest CONOPT3 (version 3.14r) for ACC2 for all model settings. Performances of different solvers can be compared by utilizing a solver BENCH (better with EXAMINER and PAVER options), which is also included in the GAMS software package. CONOPT3 is said to be the most advanced solver designed for nonlinear programming in the IA community. Switching to different solvers only requires a change in one option statement on the solver assignment.

CONOPT3 is designed for large and sparse models and has been proved to solve models with over 20,000 equations and variables. It is suitable for models with functions depending on a small number of variables (Drud, 2006, p.2). ACC2 has over 50,000 equations and variables, according to model statistics in GAMS. CONOPT3 is designed for the class of models that are declared as "NLP" in GAMS. Such models must contain only smooth functions (or without any discontinuous first derivative). It can still be used with models containing non-smooth functions, which are declared as "Dynamic NonLinear Programming (DNLP)" in GAMS – however, the DNLP mode is not recommended for CONOPT3 (Drud, 2006, Section 7; Rosenthal, 2007, p.72).

CONOPT3 is based on the Generalized Reduced Gradient (GRG) algorithm (Drud, 2006, p.22); that is, CONOPT3 first tries to find a feasible solution (satisfying all the constraints), from which CONOPT3 then tries to look for an optimal solution on the feasible pathways (Drud, 2006, p.30). Scaling of variables and equations are automatically done by default. A major change in CONOPT3 over the previous CONOPT2 is that CONOPT3 uses second derivatives (Hessian matrix if computationary feasible) to determine search directions more efficiently in nonlinear models.

The algorithms in CONOPT3 are technically described in Drud (2006, Appendix A). Here, the flow of the CONOPT3 algorithms is briefly introduced. During the first phase of feasible solution search (Phase 0 in CONOPT3), the Newton's method and the Linear Programming (LP) techniques are used. During the second phase of feasible solution search and the phase of optimal solution search (Phase 1 to 4 in CONOPT3), if the model is linear or approximately linear around the current point, CONOPT3 basically uses a steepest descend algorithm (Press, 2001, Figure 10.6.1; http://www.nr.com/nronline_switcher.php). When the evaluations of nonlinear constraints are costly, the Sequential Linear Programming (SLP) techniques are employed for a linear approximation of the model at a current point by using the first-order Taylor expansion (Greenberg, 2006, "Sequential Linear Programming") to look for good search directions. CONOPT3 also offers the steepest edge algorithm alternatively. When the model is nonlinear, the Sequential Quadratic Programming (SQP) procedures are adopted for a quadratic approximation of the model at a current point by using the second-order Taylor expansion (Greenberg, 2006, "Sequential Quadratic Programming"). The second-order Taylor expansion requires a Hessian matrix, which can be computed by CONOPT3 (neither CONOPT1 nor CONOPT2). If the whole Hessian matrix cannot be computed due to technical reason, the Broyden-Fletcher-Goldfarb-Shanno (BFGS) algorithm is used to obtain approximately the second order information without computing the Hessian matrix directly. Then the conjugate gradient algorithm is used to determine solution search directions.

Although CONOPT3 is designed to adjust its own performance to the characteristics of a model, it can be 'fine-tuned' through the statements in an associated option file. The option files for CONOPT3 used in ACC2 are named "conopt.opt" and "conopt3.opt". Both of these CONOPT option files are identical. As only one of them is read depending on the version of GAMS, two identical files are prepared. This file is recognized at the beginning of the model run (both the past and future modes). Note that, even if an option file is not successfully recognized, the process goes anyway without prompting the user to check, except for delivering hardly noticeable error lines in the file with an extension "*.lst." The technical explanation of the option files is provided in pdf files called "Basic Solver Usage" and "CONOPT" in the GAMS software package. Use of the solver options requires specific knowledge and experiences on numerical algorithms. The solver options for ACC2 are set under a guidance of Arne Stolbjerg Drud. Further explanations on the solver options are provided directly in the option files.

Features of GAMS are controlled through option statements. The GAMS option statements for ACC2 are directly written in the main files. The option for automatic scaling is activated. In ACC2, the variables and the equations are also individually scaled by using "scale" suffixes. The BAS option (McCarl, 1996) is no longer used because of some reported errors – it does not work with all the variables and equations (Arne Stolbjerg Drud, personal communication, February 15, 2008). Instead, SAVEPOINT/LOADPOINT options are used. With these options, basis information such as equation marginals, variable levels, and variable marginals is used to provide an initial point for the subsequent past mode run, leading to an improvement in the efficiency for solution convergence. This feature has been highly exploited when the model is solved repeatedly with slightly different initial conditions. Lastly, GAMS is a commercial software package; a license is required to run ACC2. Demo-version GAMS limits the size of models to be solved and cannot be used for ACC2.

D.2. NUMERICAL INTEGRATION

The time dependent differential equations of the carbon cycle and atmospheric chemistry components in ACC2 are numerically solved by using a variant of Heun's Predictor-Corrector method. The climate component DOECLIM uses the HH method (Section 2.3.4). The multiplicity of the numerical integration methods in ACC2 is not a problem because suitable numerical methods should be chosen in accordance with the characteristics of dynamic equations and the precisions required. This section begins with the general ideas of numerical integration methods. Then, the discussion of Heun's Predictor-Corrector method follows.

The Predictor-Corrector method is one of the methods to solve Ordinary Differential Equations (ODEs) numerically. An ODE includes only one dependent variable and should be distinguished from Partial Differential Equations (PDEs), which have more than one dependent variable. When one wishes to advance from t_n to $t_n + \Delta t$ (Δt : a model time step) for an ODE $y'(t) = f(t, y)$, one can use the following calculus theorem:

$$y(t_n + \Delta t) = y(t_n) + \int_{t_n}^{t_n + \Delta t} f(t', y)dt' . \qquad \text{(D.2.1)}$$

Note that, if function $f(\cdot)$ is independent of y, the problem reduces to a function integration.

ACC2 uses the following numerical integration scheme:

$$y(t_n + \Delta t) = y(t_n) + \Delta t \cdot \left\{ \frac{y'(t_n + \Delta t) + y'(t_n)}{2} \right\} . \qquad \text{(D.2.2)}$$

The estimate of $y(t_n + \Delta t)$ is obtained by interactive computation algorithms in CONOPT3. The initial value of $y'(t_n + \Delta t)$ is a specific pre-defined value in some cases (specified in the initial value files) or zero by default otherwise.

Equation (D.2.2) corresponds to the predictor step in the standard Heun's Predictor-Corrector method. But it is used differently in ACC2 as explained above. Heun's Predictor-Corrector method is one of the simplest Predictor-Corrector methods. More sophisticated numerical integration methods are exemplified by the Adams-Bashforth-Moulton scheme (Press et al., 2001, Section 16.7), the Runge-Kutta method (Press et al., 2001, Sections 16.1 and 16.2)[70], and the Bulirsch-Stoer method (Press et al., 2001, Section 16.4). However, these methods are not suitable for GAMS implementation because of the complications in their formulations.

The numerical integration method used in ACC2 is implicit in a sense that there is no explicit analytical expression because of the iterative scheme. An explicit method such as the Euler method is unstable for stiff problems where the scales of variables are not entirely in a same range (Press et al., 2001, Section 16.6). Thus, an implicit method is required for models such as ACC2.

Furthermore, the numerical integration of equation (D.2.2) is suitable for the estimation of the ENSO-driven CO_2 concentration change. In ACC2, the natural change in the atmospheric CO_2 concentration is statistically explained by the NINO3 index (Section 3.5.1). The natural CO_2 change in ACC2 is defined as the average of the slopes for the previous time step and for the following time step, to be compatible to the numerical integration of equation (D.2.2). An explicit Euler method would complicate the treatment for time derivatives. This method would bring in a time lead or time lag because it considers the derivative only for one side.

D.3. MODEL OPERATIONS AND FILE STRUCTURE

ACC2 succeeded to the framework of model operation in the predecessor model ICM. The two modes of operation in ACC2 are

1) Past mode: estimation of the uncertain parameters and the projection of the historical evolution of the carbon cycle, atmospheric chemistry, and climate system (years 1750 – 2000)
2) Future mode: projection of the future evolution of the carbon cycle, atmospheric chemistry, and

[70] The fourth-order Runge-Kutta method is frequently used in other applications. This method evaluates derivatives four times at each step:

$$y(t_n + \Delta t) = y(t_n) + \frac{k_1}{6} + \frac{k_2}{3} + \frac{k_3}{3} + \frac{k_4}{6}, \tag{D.2.3}$$

$$k_1 = \Delta t \cdot f\left(t_n, y(t_n)\right), \tag{D.2.4}$$

$$k_2 = \Delta t \cdot f\left(t_n + \frac{h}{2}, y(t_n) + \frac{k_1}{2}\right), \tag{D.2.5}$$

$$k_3 = \Delta t \cdot f\left(t_n + \frac{h}{2}, y(t_n) + \frac{k_2}{2}\right), \tag{D.2.6}$$

$$k_4 = \Delta t \cdot f\left(t_n + h, y(t_n) + k_3\right). \tag{D.2.7}$$

climate system (years 2000 – 2100).

The inverse estimation is performed in the ACC2 past mode. The results of the inverse calculation provide the model state for the year 2000 to be used for subsequent future mode runs. The future mode also uses a future emission scenario as a driver (SRES (Nakićenović et al., 2000)). The past and future modes were separated in year 1990 in ICM, but it has been shifted to 2000 in ACC2. An advantage of the separation of the past and future modes is that multi-scenario runs need only one common past mode run.[71] Notice that, whenever any part of the model (constant values and functional relationships) is altered, the past mode has to be performed again to reflect such a change to the estimates of the parameter values and model state for 2000.

The model code is contained separately in several files, the names of which always start with ACC2 (e.g. ACC2_equations_common.inc) (Table D.1). The names of the files used for the past mode are coded as "past" (e.g. ACC2_bounds_spinup.inc). Similarly, those for the future mode are coded as "future." Those coded as "common" (e.g. ACC2_equations_common.inc) are used for both the past and future modes.

The main program for the past mode is in the file "ACC2_main_past.gms." Files used for two modes of operation above are called through INCLUDE command lines in the respective main files (ACC2_main_past.gms and ACC2_main_future.gms). The outputs of a past mode run such as emissions, concentrations, radiative forcings, and temperature change are exported in several files named with "out" (e.g. "out_past_1.dat"). The past mode also generates the file "ACC2_init_future.inc," which contains the estimates of uncertain parameters and model state for 2000. This file is then called from the main program for the ACC2 future mode "ACC2_main_future.gms." Once the initial file for the future mode is generated, the past mode needs not to be performed unless changes are made to the model as discussed above. The outputs of a future mode run are exported in several files named "out" (e.g. "out_future_1.dat").

After a past mode run, a file "PAST_p.gdx" is produced as the SAVEPOINT/LOADPOINT option is activated. In this file, the basis information such as the equation marginals, variable levels, and variable marginals is contained in a binary format. This file is read next time the past mode run is performed. This option is also used for the future mode.

"conopt.opt" and "conopt3.opt" provide options for CONOPT3 in both the past and future modes. As discussed earlier, these CONOPT option files are identical and only one of them is read depending on the version of GAMS.

One change in the file structure from ICM to ACC2 is the addition of 'switchboard' contained in the file "ACC2_switchboard_common.inc," which allows one to select data and

[71] The six emission scenarios (SRES) are stored in GAMS tables ENGSCN and NEGSCN, which contain the energy-related and non-energy-related GHG emissions, respectively. Multi-scenario runs require only the changes in the set assignments for ENGSCN and NEGSCN in the file "ACC2_main_future.gms."

parameters to be included in the inverse estimation. Flags are assigned in each of (or each time series of) the parameters or data for the inverse calculation. ACC2 users can assign "1" to a flag to include a particular parameter or datum in the inverse estimation. Otherwise, "0" should be assigned to the flag. The switchboard also contains flags to control feedbacks and other features of the model. For example, the flags to control the temperature feedback to the ocean and terrestrial carbon cycle allow one to turn on/off the climate-carbon cycle feedback. The complex calculation to obtain the thermodynamic carbonate equilibria can be replaced with a simpler calculation using the Revelle factor by changing the relevant flag assignment. One could look into how the inverse calculation result changes when the ENSO-induced variability on the atmospheric CO_2 concentration and the temperature records are not accounted for just by changing the relevant flag assignments. More switchboard features are directly explained in the switchboard file.

When an ACC2 model run is completed, it is desirable that no variables be stuck at their bounds. After the completion of the ACC2 past and future runs, the model produces files "out_past_alert.dat" and "out_future_alert.dat," respectively, where variables are listed if they are stuck at their bounds. Users should check the content of the alert file after a model run. When variables are found to be stuck, the relevant bounds should be changed and/or model equations need to be looked into. Specifics are shown in the SolVAR section in "ACC2_past_main.lst" or "ACC2_future_main.lst." An alert system such as above is not provided with the GAMS software package, so the codes to generate alerts are explicitly written at the ends of "ACC2_past_main.gms" and "ACC2_future_main.gms". Any addition or removal in upper or lower bounds in "ACC2_past_bounds.inc" or "ACC2_future_bounds.inc" should be reflected in the associated codes for the alert in the ACC2 main files. Furthermore, squared weighted residuals are stored in the file "out_past_residuals.dat."

ICM has been extensively used for emission corridor calculations (Zickfeld and Bruckner, 2003).[72] ACC2 can also be used for emission corridor calculations. Limits of tolerability can be specified in the file called ACC2_settings_future.inc, which are taken as additional optimization constraints for GAMS. The separation of the past and future modes is a technical advantage for corridor calculations.

D.4. PRACTICAL TIPS ON RUNNING ACC2

Running ACC2 requires not only understanding on the model but also some practical experience on GAMS. Here are practical tips that should be emphasized:

[72] An emission corridor is the domain of admissible emissions to achieve a certain climatic goal. The emission corridors are used for studies that seek cost-effective mitigation strategies and admissible emissions corridors that would keep the system within a domain of tolerable climate change.

1) The pathways to reach a solution are in some cases sensitive to the structures of model equations – in particular, those contain multiplications and divisions of variables and exponential/logarithmic functions. The behavior of the model should be checked when the model equations are altered.
2) When a model run is aborted, GAMS does not erase the "225 directory" (within the ACC2 folder) where temporary files are stored. The unerased 225 directories need to be removed periodically as GAMS can hold only up to twenty six 225 directories. When the model no longer runs after many executions and abortions, 225 directories should be erased.
3) When two different bounds are set for one variable in GAMS, the bound appearing earlier in the code is ignored. Upon the addition of a new bound, users should check if another bound has already been set elsewhere.
4) In the ACC2 model, conditional statements cannot be used for variables as the model is declared as "NLP" in GAMS. The conditional statements in GAMS involve only set elements, coefficients, and scalars.
5) There are cases when, even after a feasible solution has been found and the program has stopped, a better solution can still be found with an additional execution of the program. Thus, we recommend that the users confirm the solution by executing the program twice.
6) The solution convergence process may run into a phase where very small changes in the cost function are made at every iteration. When this happens for so long, one could try a different starting point by using a PAST_p.gdx file from another run. One could also try without using the LOADPOINT option.
7) It is generally more difficult to fix an error due to equation infeasibilities than variable infeasibilities. When one encounters an equation infeasibility error, a good starting point is to check "out_past_alert.dat" or "out_future_alert.dat." showing variables stuck at their bounds.

Table D.1. Lists of files used for the ACC2 past and future modes

The model code for the ACC2 past and future modes are contained in several files. The main files, "ACC2_main_past.gms" and "ACC2_main_future.gms," call the other subsequent files at the beginnings of the respective model runs. "ACC2_init_future.inc" is generated after a past mode run and used in a subsequent future mode run to provide parameter values and model state for the year 2000. See Section D.3 for further explanations on the file structure.

Past mode	Future mode
ACC2_main_past.gms	ACC2_main_future.gms
ACC2_set_common.inc	ACC2_set_common.inc
ACC2_constants_common.inc	ACC2_coefficients_common.inc
ACC2_variables_common.inc	ACC2_variables_common.inc
ACC2_bounds_past.inc	ACC2_bounds_future.inc
ACC2_scenarios_past.inc	ACC2_scenarios_future.inc
ACC2_switchboard_common.in	ACC2_switchboard_common.inc
ACC2_settings_past.inc	ACC2_settings_future.inc
ACC2_init_past.inc	ACC2_init_future.inc
ACC2_equations_common.inc	ACC2_equations_common.inc
PAST_p.gpx	FUTURE_p.gpx
conopt.opt	conopt.opt
conopt3.opt	conopt3.opt
out_past_1.dat	out_future_1.dat
out_past_2.dat	out_future_2.dat
out_past_1a.dat	out_future_3.dat
out_past_1b.dat	out_future_4.dat
out_past_1c.dat	out_future_alert.dat
out_past_2a.dat	
out_past_inv.dat	
out_past_alert.dat	
out_past_residuals.dat	

APPENDIX E. ACRONYMS AND ABBREVIATIONS

Table E.1. List of acronyms and abbreviations

Acronyms and abbreviations	Full names
ACC2	Aggregated Carbon Cycle, Atmospheric Chemistry, and Climate model
AOGCM	Atmosphere-Ocean General Circulation Model
AR	AutoRegressive (process or model)
BC	Black Carbon
Bern-CC	Bern Carbon Cycle model
BFGS	Broyden-Fletcher-Goldfarb-Shanno
CDIAC	Carbon Dioxide Information Analysis Center
CDM	Clean Development Mechanism
CFC	ChloroFluoroCarbon
CMDL	(NOAA) Climate Monitoring and Diagnostics Laboratory
CSM	Community Climate System Model
CTBM	Community Terrestrial Biosphere Model
CTM	Chemistry-Transport Model
C^4MIP	Coupled Carbon Cycle Climate Model Intercomparison Project
DIC	Dissolved Inorganic Carbon
DICE	Dynamic Integrated model of Climate and the Economy
DMS	DiMethylSulphide
DNLP	Dynamic NonLinear Programming
DOECLIM	Diffusion Ocean Energy balance CLIMate model
EBM	Energy Balance Model
ECHAM	European Centre HAmburg Model
ECOBICE	Economy-Biosphere-Climate project
EECl	Equivalent Effective Chlorine
EESC	Equivalent Effective Stratospheric Chlorine
EMIC	Earth system Models of Intermediate Complexity
ENSO	El Niño-Southern Oscillation
ERBE	Earth Radiation Budget Experiment
EOF	Empirical Orthogonal Function
FACE	Free-Air CO_2 Enrichment
FEI	Forcing Equivalence Index
GAMS	General Algebraic Modeling System
GCM	General Circulation Model
GHG	GreenHouse Gas
GPP	Gross Primary Production
GRG	Generalized Reduced Gradient (algorithm)
GTP	Global Temperature Potential
GWP	Global Warming Potential
HadCM3	Third version of Hadley Centre Coupled Model
HAMOCC	HAmburg Model of the Ocean Carbon Cycle
HCFC	HydroChloroFluoroCarbon
HFC	HydroFluoroCarbon
HFE	Hydrofluoroether
HH	Hammer-Hollingsworth method
HRBM	High-Resolution terrestrial Biosphere Model
IA	Integrated Assessment
ICLIPS	Integrated assessment of CLImate Protection Strategies
ICM	ICLIPS Climate Model
IIASA	International Institute for Applied Systems Analysis
IID	Independently and Identically Distributed
IMPRS-ESM	International Max Planck Research School on Earth System Modelling
IPCC	Intergovernmental Panel on Climate Change
IRF	Impulse Response Function
ISAM	Integrated Science Assessment Model
IVI	Ice-core Volcanic Index
JPL	Jet Propulsion Laboratory
LP	Linear Programming
LPJ-DGVM	Lund-Potsdam-Jena Dynamic Global Vegetation Model
LSG	Large-Scale Geostrophic ocean model
MADIAM	Multi-Actor Dynamic Integrated Assessment Model

Table E.1. (Continued) List of acronyms and abbreviations

Acronyms and abbreviations	Full names
MIND	Model of INvestment and technological Development
NAO	North Atlantic Oscillation
NCAR	National Center for Atmospheric Research
NCDC	National Climatic Data Center
NEP	Net Ecosystem Production
NICCS	Nonlinear Impulse-response representation of the coupled Carbon cycle-Climate System model
NLP	NonLinear Programming
NMHC	Non-Methane HydroCarbon
NPP	Net Primary Production
OC	Organic Carbon
OCO	Orbiting Carbon Observatory
ODE	Ordinary Differential Equation
ODS	Ozone-Depleting Substance
PAR	Photosynthetically Active Radiation
PDE	Partial Differential Equation
PDF	Probability Density Function
PDO	Pacific Decadal Oscillation
PFC	PerFluoroCarbon
PIK	Potsdam-Institut für Klimafolgenforschung
POC	Particulate Organic Carbon
SAT	Surface Air Temperature
SIAM	Structural Integrated Assessment Model
SIO	Scripps Institution of Oceanography
SLP	Sequential Linear Programming
SOI	Southern Oscillation Index
SPM	Summary for PolicyMakers
SQP	Sequential Quadratic Programming
SRES	Special Report on Emissions Scenarios
SSS	Sea Surface Salinity
SST	Sea Surface Temperature
TA	Total Alkalinity
TEMP	TEMperature Proxy index
TOA	Top Of the Atmosphere
VOC	Volatile Organic Compound
UN	United Nations
UV	UltraViolet (solar radiation)
VEI	Volcanic Explosivity Index
YSSP	Young Scientists Summer Program

REFERENCES

Adams, J. B., M. E. Mann, C. M. Ammann (2003) Proxy evidence for an El Niño-like response to volcanic forcing. *Nature*, **426**, 271-278.

Ainsworth, E. A., S. P. Long (2004) What have we learned from 15 years of free-air CO_2 enrichment (FACE)? – A meta-analysis review of the responses of photosynthesis, canopy properties and plant production to rising CO_2. *New Phytologist*, **165**, 351-372.

Allen, M. R., P. A. Stott, J. F. B. Mitchell, R. Schnur, T. L. Delworth (2000) Quantifying the uncertainty in forecasts of anthropogenic climate change. *Nature*, **407**, 617-620.

Allen, M. R., W. J. Ingram (2002) Constraints on future changes in climate and the hydrologic cycle. *Nature*, **419**, 224-232.

Amemiya, T. (1977) The maximum likelihood and the nonlinear three-stage least squares estimator in the general nonlinear simultaneous equation model. *Econometrica*, **45**, 955-968.

Amemiya, T. (1985) Advanced econometrics. Harvard University Press, Cambridge, Massachusetts, USA. 521 pp.

Ammann, C. M., G. A. Meehl, W. M. Washington, C. S. Zender (2003) A monthly and latitudinally varying volcanic forcing dataset in simulations of 20th century climate. *Geophysical Research Letters*, **30**(12), 1657, doi:10.1029/2003GL016875.

Andersson, A. J., F. T. Mackenzie, A. Lerman (2006) Coastal ocean CO_2–carbonic acid–carbonate sediment system of the Anthropocene. *Global Biogeochemical Cycles*, **20**, doi:10.1029/2005GB002506

Andronova, N. G., M. E. Schlesinger (2001) Objective estimation of the probability density function for climate sensitivity. *Journal of Geophysical Research*, **106,** D9, 22605-22611.

Bacastow, R. (1981) Numerical evaluation of the evasion factor. In (ed.) B. Bolin. *Carbon cycle modelling (SCOPE 16)*. pp.95-101. John Wiley & Sons. 390 pp.

Bairoch, P. (1995) Economics and world history: myths and paradoxes. University of Chicago Press, Chicago, USA. 200 pp.

Behrenfeld, M. J., R. T. O'Malley, D. A. Siegel, C. R. McClain, J. L. Sarmiento, G. C. Feldman, A. J. Milligan, P. G. Falkowski, R. M. Letelier, E. S. Boss (2006) Climate-driven trends in contemporary ocean productivity. *Nature*, **444**, 752-755.

Bernard, S., T. Röckmann, J. Kaiser, J.-M. Barnola, H. Fischer, T. Blunier, J. Chappellaz (2006) Constraints on N_2O budget changes since pre-industrial time from new firn air and ice core isotope measurements. *Atmospheric Chemistry and Physics*, **6**, 493-503.

Berner, R. A. (1991) A model for atmospheric CO_2 over Phanerozoic time. *American Journal of*

Science, **291**, 339-376.

Berner, R. A. (1997) The rise of plants and their effect on weathering and atmospheric CO_2. *Science*, **276**, 544-546.

Bertrand C., M.-F. Loutre, M. Crucifix, A. Berger (2002) Climate of the last millennium: a sensitivity study. *Tellus A*, **54**, 221-244.

Bouwman, A. F. (1996) Direct emission of nitrous oxide from agricultural soils. *Nutrient Cycling in Agroecosystem*, **46**, 53-70.

Box, G. E. P., G. M. Jenkins (1970) Time series analysis – forcasting and control. Holden-Day, San Francisco, California, USA. 553 pp.

Boyd, P. W., S. C. Doney (2003) The impact of climate change and feedback processes on the ocean carbon cycle. In (ed.) M. J. R. Fasham. *Ocean biogeochemistry*. pp.157-193. Springer, Berlin, Germany. 297 pp.

Brasseur, G., J. J. Orlando, G. S. Tyndall (eds.) (1999) Atmospheric chemistry and global change. Oxford University Press, Oxford, United Kingdom. 654 pp.

Brasseur, G. P., P. Artaxo, L. A. Barrie, R. J. Delmas, I. Galbally, W. M. Hao, R. C. Harriss, I. S. A. Isaksen, D. J. Jacob, C. E. Kolb, M. Prather, H. Rodhe, D. Schwela, W. Steffen, D. J. Wuebbles (2003) An integrated view of the causes and impacts of atmospheric changes. In (eds.) G. P. Brasseur, R. G. Prinn, A. A. P. Pszenny. *Atmospheric chemistry in a changing world. The IGBP Series*. pp.207-271. Springer, Berlin, Germany. 300 pp.

Bretscher, O. (2001) Linear algebra with applications. 2nd edition. Prentice Hall, Upper Saddle River, New Jersey, USA. 478 pp.

Brooke, A., D. Kendrick, A. Meeraus (1992) GAMS: a user's guide, release 2.25. Scientific Press, San Francisco, USA.

Brovkin, V., A. Ganopolski, Y. Svirezhev (1997) A continuous climate-vegetation classification for use in climate-biosphere studies. *Ecological Modelling*, **101**, 251-261.

Bruckner, T., G. Hooss, H.-M. Füssel, K. Hasselmann (2003) Climate system modeling in the framework of the Tolerable Windows Approach: the ICLIPS climate model. *Climatic Change*, **56**, 119-137.

Burbidge, E. M., G. R. Burbidge, W. A. Fowler, F. Hoyle (1957) Synthesis of the elements in stars. *Reviews of Modern Physics*, **29**, 547-640.

Caldeira, K., M. E. Wickett (2003) Anthropogenic carbon and ocean pH. *Nature*, **425**, 365.

Cane, M. A. (2005) The evolution of El Niño, past and future. *Earth and Planetary Science Letters*, **230**, 227-240.

Chen, H., H.-Q Tian (2005) Does a general temperature-dependent Q_{10} model of soil respiration exist at biome and global scale? *Journal of Integrative Plant Biology*, **47**, 1288-1302.

Chèdin, A., S. Serrar, N. A. Scott, C. Crevoisier, R. Armante (2003) First global measurement of

midtropospheric CO_2 from NOAA polar satellites: tropical zone. *Journal of Geophysical Research*, **108**, D18, 4581, doi:10.1029/2003JD003439.

Collins, M., S. F. B. Tett, C. Cooper (2001) The internal climate variability of HadCM3, a version of the Hadley Centre coupled model without flux adjustments. *Climate Dynamics*, **17**, 61-81.

Conrad, R. (1996) Soil microorganisms as controllers of atmospheric trace gases (H_2, CO, CH_4, OCS, N_2O, and NO). *Microbiological Review*, **60**, 609-640.

Cox, P. M., R. A. Betts, C. D. Jones, S. A. Spall, I. J. Totterdell (2000) Acceleration of global warming due to carbon-cycle feedbacks in a coupled climate model. *Nature*, **408**, 184-187.

Crowley, T. J., S. K. Baum, K.-Y. Kim, G. C. Hegerl, W. T. Hyde (2003) Modeling ocean heat content changes during the last millennium. *Geophysical Research Letters*, **30**(18), 1932, doi:10.1029/2003GL017801.

Crutzen, P. J., E. F. Stoermer (2000) The "Anthropocene". *International Geosphere–Biosphere Programme (IGBP) Newsletter*, **41**, 17-18.

Crutzen, P. J. (2002) Geology of mankind. *Nature*, **415**, 23.

Daniel, J. S., S. Solomon, D. L. Alibritton (1995) On the evaluation of halocarbon radiative forcing and global warming potentials. *Journal of Geophysical Research*, **100**, D1, 1271-1285.

Davidson, E. A., I. A. Janssens (2006) Temperature sensitivity of soil carbon decomposition and feedbacks to climate change. *Nature*, **440**, 165-173.

Denman, K. L., M. A. Pena (2000) Beyond JGOFS. In (eds.) R. B. Hanson, H. W. Ducklow, J. G. Field. *The changing ocean carbon cycle: a midterm synthesis of the Joint Global Carbon Flux Study*. pp.469-490. Cambridge University Press, Cambridge, United Kingdom. 528 pp.

de Silva, S. (2003) Eruptions linked to El Niño. *Nature*, **426**, 239-241.

Dessai, S., M. Hulme (2003) Does climate policy need probabilities? Working Paper 34 at Tyndall Centre for Climate Change Research, United Kingdom. 42 pp.

Dickens, G. R. (2001) On the fate of past gas: what happens to methane released from a bacterially mediated gas hydrate capacitor? *Geochemistry, Geophysics, Geosystems* (*G3*), **2**, 2000GC000131.

Dickens, G. R. (2004) Hydrocarbon-driven warming. *Nature*, **429**, 513-515.

Dickinson, R. E. (1981) Convergence rate and stability of ocean-atmosphere coupling schemes with a zero-dimensional climate model. *Journal of Atmospheric Science*, **38**, 2112-2120.

Dickinson, R. E., K. J. Schaudt (1998) Analysis of timescales of response of a simple climate model. *Journal of Climate*, **11**, 97-107.

Dirmeyer, P. A., A. J. Dolman, N. Sato (1999) The pilot phase of the Global Soil Wetness Project. *Bulletin of the American Meteorological Society*, **80**, 851-878.

Dlugokencky, E. J., E. G. Dutton, P. C. Novelli, P. P. Tans, K. A. Masarie, K. O. Lantz, S. Madronich (1996) Changes in CH_4 and CO growth rates after the eruption of Mt. Pinatubo and their link

with changes in tropical tropospheric UV flux. *Geophysical Research Letters*, **23**, 2761-2764.

Dlugokencky, E. J., K. A. Masarie, P. M. Lang, P. P. Tans (1998) Continuing decline in the growth rate of the atmospheric methane burden. *Nature*, **393**, 447-450.

Doney, S. C. (2006) Plankton in a warmer world. *Nature*, **444**, 695-697.

Doney, S. C., K. Lindsay, I. Fung, J. John (2006) Natural variability in a stable, 1000-yr global coupled climate–carbon cycle simulation. *Journal of Climate*, **19**, 3033-3054.

Drud, A. (2006) CONOPT. Available in the GAMS software package. 45 pp.

Dutton, J. A. (1995) An analytical model of atmospheric feedback and global temperature change. *Journal of Climate*, **8**, 1122-1139.

Eckaus, R. S. (1992) Comparing the effects of greenhouse gas emissions on global warming. *Energy Journal*, **13**, 25-35.

Eden, C., R. J. Greatbatch, J. Lu (2002) Prospects for decadal prediction of the North Atlantic Oscillation (NAO). *Geophysical Research Letters*, **29**, 10, 1466, doi;10.1029/2001GL014069.

Edenhofer, O., N. Bauer, E. Kriegler (2005) The impact of technological change on climate protection and welfare: insights from the model MIND. *Ecological Economics*, **54**, 277-292.

Efron, B. (1986) Why isn't everyone a Bayesian? *The American Statistician*, **40**, 1-5.

Enting, I. G. (2002a) Inverse problems in atmospheric constituent transport. Cambridge University Press, Cambridge, United Kingdom. 392 pp.

Enting, I. G. (2002b) Inverse problems in earth system science: a complex systems perspective. CSIRO Atmospheric Research Technical Paper no. 62. 32 pp.

Etheridge, D. M., L. P. Steele, R. L. Langenfelds, R. J. Fransey (1996) Natural and anthropogenic changes in atmospheric CO_2 over the last 1000 years from air in Antarctic ice and firn. *Journal of Geophysical Research*, **101**, D2, 4115-4128.

Etheridge, D. M., L. P. Steele, R. J. Francey, R. L. Langenfelds (1998) Atmospheric methane between 1000 AD and present: evidence of anthropogenic emissions and climatic variability. *Journal of Geophysical Research*, **103**, D13, 15979-15993.

Falkowski, P., R. J. Scholes, E. Boyle, J. Canadell, D. CanÞeld, J. Elser, N. Gruber, K. Hibbard, P. Högberg, S. Linder, F. T. Mackenzie, B. Moore III, T. Pedersen, Y. Rosenthal, S. Seitzinger, V. Smetacek, W. Steffen (2000) The global carbon cycle: a test of our knowledge of Earth as a system. *Science*, **290**, 291-296.

Fankhauser, S. (1995) Valuing climate change: the economics of the greenhouse. EarthScan, London, United Kingdom. 176 pp.

Farquhar, G. D., M. L. Roderick (2003) Pinatubo, diffuse light, and the carbon cycle. *Science*, **299**, 1997-1998.

Fasham, M. J. R. (ed.) (2003) Ocean biogeochemistry: the role of the ocean carbon cycle in global change. Springer, Berlin, Germany. 297 pp.

Fenhann, J. (2000) Industrial non-energy, non-CO_2 greenhouse gas emissions. *Technological Forecasting and Social Change*, **63**, 313-334.

Field, C. B., M. J. Behrenfeld, J. T. Randerson, P. Falkowski (1998) Primary production of the biosphere: integrating terrestrial and oceanic components. *Science*, **281**, 237-240.

Fisher, A. G. (1984) Two Phanerozoic supercycles. In (eds.) W. A. Berggren, J. A. Van Couvering. *Catastrophes and Earth history*. pp.129-150. Princeton University Press, Princeton, New Jersey, USA.

Forest, C. E., P. H. Stone, A. P. Sokolov, M. R. Allen, M. D. Webster (2002) Quantifying uncertainties in climate system properties with the use of recent climate observations. *Nature*, **295**, 113-117.

Forest, C. E., P. H. Stone, A. P. Sokolov (2006) Estimated PDFs of climate system properties including natural and anthropogenic forcings. *Geophysical Research Letters*, **33**, L01705, doi:10.1029/2005GL023977.

Frame, D. J., B. B. B. Booth, J. A. Kettleborough, D. A. Stainforth, J. M. Gregory, M. Collins, M. R. Allen (2005) Constraining climate forecast: the role of prior assumptions. *Geophysical Research Letters*, **32**, L09702, doi: 10.1029/2004GL022241.

Fraser, P. L., D. E. Oram, C. E. Reeves, S. A. Penkett, A. McCulloch (1999) Southern hemispheric halon trends (1978-1998) and global halon emissions. *Journal of Geophysical Research*, **104**, D13, 15985-15999.

Friedlingstein, P, I. Fung, E. Holland, J. John, G. Brasseur, D. Erickson, D. Schimel (1995) On the contribution of CO_2 fertilization to the missing biospheric sink. *Global Biogeochemical Cycles*, **9**, 541-556.

Friedlingstein, P., P. Cox, R. Betts, L. Bopp, W. von Bloh, V. Brovkin, P. Cadule, S. Doney, M. Eby, I. Fung, G. Bala, J. John, C. Jones, F. Joos, T. Kato, M. Kawamiya, W. Knorr, K. Lindsay, H. D. Matthews, T. Raddatz, P. Rayner, C. Reick, E. Roeckner, K.-G. Schnitzler, R. Schnur, K. Strassmann, A. J. Weaver, C. Yoshikawa, N. Zeng (2006) Climate–carbon cycle feedback analysis: results from the C^4MIP model intercomparison. *Journal of Climate*, **19**, 3337-3353.

Fuglestvedt, J. S., T. Berntsen (1999) A simple model for scenario studies of changes in global climate Version 1.0. CICERO Working Paper 1999:2. University of Oslo, Norway. 59 pp.

Fuglestvedt, J. S., T. K. Berntsen, O. Godal, R. Sausen, K. P. Shine, T. Skodvin (2003) Metrics of climate change: assessing radiative forcing and emission indices. *Climatic Change*, **58**, 267-331.

Gammon, R., E. Sundquist, P. Fraser (1985) History of carbon dioxide in the atmosphere. In (ed.) T. Trabalka. *Atmospheric carbon dioxide and the global carbon cycle*. pp.25-62. Rep. DOE/ER-0239. US Department of Energy, Washington, D.C., USA.

Garrels, R. M., F. T. Mackenzie, C. Hunt (1975) Chemical cycles and the global environment: assessing human influences. William Kaufmann, Inc., Los Altos, California, USA. 206 pp.

Gerard, H. R., M. B. Baker (2007) Why is climate sensitivity so unpredictable? *Science*, **318**, 629-632.

Gifford, R. M. (1980) Carbon storage by the biosphere. In (ed.) G. I. Pearman. *Carbon dioxide and climate.* pp.167-181. Australian Academy of Science, Canberra, Australia.

Gitz, V., P. Ciais (2003) Amplifying effects of land-use change on future atmospheric CO_2 levels. *Global Biogeochemical Cycles*, **17**, 1024, doi:10.1029/2002GB001963.

Godal, O., J. Fuglestvedt (2002) Testing 100-year Global Warming Potentials: impacts on compliance costs and abatement profile. *Climatic Change*, **52**, 93-127.

Goldewijk, K. K., J. G. van Minnen, G. J. J. Kreileman, M. Vloedbeld, R. Leemans (1994) Simulating the carbon flux between the terrestrial environment and the atmosphere. *Water, Air, & Soil Pollution*, **76**, 199-230.

Gordon, C., C. Cooper, C. A. Senior (2000) The simulation of SST, sea ice extents and ocean heat transports in a version of the Hadley Centre coupled model without flux adjustments. *Climate Dynamics*, **16**, 147-168.

Greenberg, H. J. (2006) Mathematical Programming Glossary. (ed.) INFORMS Computing Society. http://glossary.computing.society.informs.org/

Gregory, J. M., R. J. Stouffer, S. C. B. Raper, P. A. Stott, N. A. Rayner (2002) An observationally based estimate of the climate sensitivity. *Journal of Climate*, **15**, 3117-3121.

Gregory, J. M., W. J. Ingram, M. A. Palmer, G. S. Jones, P. A. Stott, R. B. Thorpe, J. A. Lowe, T. C. Johns, K. D. Williams (2004) A new method for diagnosing radiative forcing and climate sensitivity. *Geophysical Research Letters*, **31**, doi:10.1029/2003GL018747.

Gruber, N., J. N. Galloway (2008) An Earth-system perspective of the global nitrogen cycle. *Nature*, **451**, 293-296.

Gu, L., D. D. Baldocchi, S. C. Wofsy, J. W. Munger, J. J. Michalsky, S. P. Urbanski, T. A. Boden (2003) Response of a deciduous forest to the Mount Pinatubo eruption: enhanced photosynthesis. *Science*, **299**, 2035-2038.

Gurney, K. R., R. M. Law, A. S. Denning (2002) Towards robust regional estimates of CO_2 sources and sinks using atmospheric transport models. *Nature*, **415**, 626-630.

Hall, S. J., P. A. Matson (1999) Nitrogen oxide emissions after nitrogen additions in tropical forests. *Nature*, **400**, 152-155.

Hammer, P. C., J. W. Hollingsworth (1955) Trapezoidal methods of approximating solutions of differential equations. *Mathematical Tables and Other Aids to Computation*, **9**, 92-96.

Hansen, J., G. Russell, A. Lacis, I. Fung, D. Rind, P. Stone (1985) Climate response times: dependence on climate sensitivity and ocean mixing. *Science*, **229**, 857-859.

Hansen, J., M. Sato, L. Nazarenko, R. Ruedy, A. Lacis, D. Koch, I. Tegen, T. Hall, D. Shindell, B. Santer, P. Stone, T. Novakov, L. Thomason, R. Wang, Y. Wang, D. Jacob, S. Hollandsworth, L.

Bishop, J. Logan, A. Thompson, R. Stolarski, J. Lean, R. Willson, S. Levitus, J. Antonov, R. Rayner, D. Parker, J. Christy (2002). Climate forcings in Goddard Institute for Space Studies SI2000 simulations. *Journal of Geophysical Research*, **107**, D18, 4347, doi:10.1029/2001JD001143, 2002.

Hansen J., M. Sato (2004) Data sets used in GISS 2004 GCM. http://www.giss.nasa.gov/data/simodel/ghgases/GCM.html

Harnisch, J., A. Eisenhauer (1998) Natural CF_4 and SF_6 on Earth. *Geophysical Research Letters*, **25**, 2401-2404.

Harnisch J., R. Borchers, P. Fabian, M. Maiss (1999) CF_4 and the age of mesospheric and polar vortex air. *Geophysical Research Letters*, **26**, 295-298.

Harriss, R. C. (1969) Boron regulation in the oceans. *Nature*, **223**, 290-291.

Hartley, D., R. Prinn (1993) Feasibility of determining surface emissions of trace gases using an inverse method in a three-dimensional chemical transport model. *Journal of Geophysical Research*, **98**, D3, 5183-5197.

Harvey, L. D. D., S. H. Schneider (1985) Transient climate response to external forcing on 100-104 year time scales. part 2: sensitivity experiments with a seasonal, hemispherically averaged, coupled atmosphere, land, and ocean energy balance model. *Journal of Geophysical Research*, **90**, D1, 2207-2222.

Harvey, D., J. Gregory, M. Hoffert, A. Jain, M. Lai, R. Leemans, S. Raper, T. Wigley, J. de Wolde (1997) An introduction to simple climate models used in the IPCC Second Assessment Report. IPCC Technical Paper II. 39 pp.

Harvey, L. D. D. (1999) Global warming: the hard science. Prentice Hall, Harlow. 408 pp.

Hasselmann, K., S. Hasselmann, R. Giering, V. Ocana, H. V. Storch (1997) Sensitivity study of optimal CO_2 emission paths using a simplified Structural Integrated Assessment Model (SIAM). *Climatic Change*, **37**, 345-386.

Hegerl, G. C., T. J. Crowley, W. T. Hyde, D. J. Frame (2006) Climate sensitivity constrained by temperature reconstructions over the past seven centuries. *Nature*, **440**, 1029-1032.

Hein, R., P. J. Crutzen, M. Heimann (1997) An inverse modelling approach to investigate the global atmospheric methane cycle. *Global Biogeochemical Cycles*, **11**, 43-76.

Hoffert, M. I., A. J. Callegari, C. T. Hsieh (1980) The role of deep sea heat storage in the secular response to climate forcing. *Journal of Geophysical Research*, **85**, C11, 6667-6679.

Hoffert, M. I., A. J. Callegari, C.-T. Hsieh (1981) A box-diffusion carbon cycle model with upwelling, polar bottom water formation and a marine biosphere. In (ed.) B. Bolin. *Carbon cycle modelling (SCOPE 16)*. pp.287-305. John Wiley & Sons. 390 pp.

Holland, H. D. (1978) The chemistry of the atmosphere and oceans. Wiley, New York. USA. 351 pp.

Hooss, G., V. Reinhard, K. Hasselmann, E. Maier-Reimer, F. Joos (1999) A nonlinear impulse

response model of the coupled carbon cycle-ocean-atmosphere climate system. Max Planck Institute for Meteorology, Hamburg, Germany. Report No. 290. 62 pp.

Hooss, G. (2001) Aggregate models of climate change: development and applications. Ph.D. thesis. Hamburg Universität, Germany. 113 pp. http://www.schoepfung-und-wandel.de/

Hooss, G., R. Voss, K. Hasselmann, E. Maier-Reimer, F. Joos (2001) A nonlinear impulse response model of the coupled carbon cycle-climate system (NICCS). *Climate Dynamics*, **18**, 189-202.

Hooss, K. G. (2004) Modelle der globalen Umwelt und Gesellschaft. *promet*, **30**, 213-224.

Houghton, R. A., J. L. Hackler (2002) Carbon flux to the atmosphere from land-use changes. In *Trends: a compendium of data on global change.* Carbon Dioxide Information Analysis Center, Oak Ridge National Laboratory, US Department of Energy, Oak Ridge, Tennessee, USA. http://cdiac.ornl.gov/

Houghton, R. A. (2003). Revised estimates of the annual net flux of carbon to the atmosphere from changes in land use and land management 1850-2000. *Tellus B*, **55**, 378-390.

Houtekamer, P. L., L. Lefaivre, J. Derome, H. Ritchie, H. L. Mitchell (1996) A system simulation approach to ensemble prediction. *Monthly Weather Review*, **124**, 1225-1242.

IPCC (1990) Scientific assessment of climate change – report of Working Group I. [Houghton, J. T., G. J. Jenkins, J. J. Ephraums (eds.)]. Cambridge University Press, Cambridge, United Kingdom and New York, New York, USA. 365 pp.

IPCC (1996) Climate change 1995: the science of climate change. [Houghton, J. T., L. G. Meira Filho, B. A. Callander, N. Harris, A. Kattenberg, K. Maskell (eds.)]. Cambridge University Press, Cambridge, United Kingdom and New York, New York, USA. 572 pp.

IPCC (2001) Climate change 2001: the scientific basis. Contribution of Working Group I to the Third Assessment Report of the Intergovernmental Panel on Climate Change [Houghton, J.T.,Y. Ding, D.J. Griggs, M. Noguer, P.J. van der Linden, X. Dai, K. Maskell, and C.A. Johnson (eds.)]. Cambridge University Press, Cambridge, United Kingdom and New York, New York, USA. 881 pp.

IPCC Working Group I (2004a) Workshop report on climate sensitivity. École Normale Supérieure Paris, France. July 26 – July 29, 2004. 177 pp.

IPCC Working Group I (2004b) IPCC Workshop on describing scientific uncertainties in climate change to support analysis of risk and of options. National University of Ireland, Maynooth, Co. Kildare, Ireland. May 11-May 13, 2004. 138 pp.

IPCC (2005) IPCC special report on safeguarding the ozone layer and the global climate system: issues related to hydrofluorocarbons and perfluorocarbons. Cambridge University Press, Cambridge, United Kingdom and New York, New York, USA, 486 pp.

IPCC (2007) Climate change 2007: the physical science basis. Contribution of Working Group I to the Fourth Assessment Report of the Intergovernmental Panel on Climate Change [Solomon, S.,

D. Qin, M. Manning, Z. Chen, M. Marquis, K.B. Averyt, M. Tignor and H.L. Miller (eds.)]. Cambridge University Press, Cambridge, United Kingdom and New York, New York, USA. 996 pp.

Jacob, D. (1999) Introduction to atmospheric chemistry. Princeton University Press, Princeton, New Jersey, USA. 264 pp.

Jet Propulsion Laboratory (JPL) (2003) Chemical kinetics and photochemical data for use in atmospheric studies: evaluation number 14.

Johansson, D. J. A., U. M. Persson, C. Azar (2006) The cost of using global warming potentials: analyzing the trade off between CO_2, CH_4 and N_2O. *Climatic Change*, **77**, 291-309.

Jones, C. D., P. M. Cox (2001) Modeling the volcanic signal in the atmospheric CO_2 record. *Global Biogeochemical Cycles*, **15**, 453-465.

Jones, C. D., M. Collins, P. M. Cox, S. A. Spall (2001) The carbon cycle response to ENSO: a coupled climate-carbon cycle model study. *Journal of Climate*, **14**, 4113-4129.

Jones, P. D., K. R. Briffa, T. P. Barnett, S. F. B. Tett (1998) Millennial temperature reconstructions. IGBP PAGES/World Data Center-A for Paleoclimatology Data Contribution Series #1998-039. NOAA/NGDC Paleoclimatology Program, Boulder, Colorado, USA.

Jones, P. D., M. E. Mann (2004) Climate over past millennia. *Review of Geophysics*, **42**, RG2002.

Jones, P. D., D. E. Parker, T. J. Osborn, K. R. Briffa (2006) Global and hemispheric temperature anomalies – land and marine instrumental records. In *Trends: a compendium of data on global change.* Carbon Dioxide Information Analysis Center, Oak Ridge National Laboratory, US Department of Energy, Oak Ridge, Tennessee, USA. http://cdiac.ornl.gov/

Joos, F., M. Bruno, R. Fink, U. Siegenthaler, T. F. Stocker (1996) An efficient and accurate representation of complex oceanic and biospheric models of anthropogenic carbon uptake. *Tellus B*, **48**, 397-417.

Joos, F., C. Prentice, S. Sitch, R. Meyer, G. Hooss, G.-K. Plattner, S. Gerber, K. Hasselmann (2001) Global warming feedbacks on terrestrial carbon uptake under the Intergovernmental Panel on Climate Change (IPCC) emission scenarios. *Global Biogeochemical Cycles*, **15**, 891-907.

Kandlikar, M. (1996) Indices for comparing greenhouse gas emissions: integrating science and economics. *Energy Economics*, **18**, 265-281.

Kaplan, J. O. (2001) Geophysical applications of vegetation modeling. Ph.D. thesis at Lund University, Sweden. 128 pp.

Kaplan, J. O. (2002) Wetlands at the Last Glacial Maximum: distribution and methane emissions. *Geophysical Research Letters*, **29**, 1079, doi:10.1029/2001GL013366, 2002.

Keeling, C. D. (1973) The carbon dioxide cycle: reservoir models to depict the exchange of atmospheric carbon dioxide with the oceans and land plants. In (ed.) S. Rasool. *Chemistry of the lower atmosphere*. pp.251-329. Plenum Press, New York, New York, USA.

Keeling, C. D., T. P. Whorf (2005) Atmospheric CO_2 records from sites in the SIO air sampling network. In *Trends: a compendium of data on global change.* Carbon Dioxide Information Analysis Center, Oak Ridge National Laboratory, US Department of Energy, Oak Ridge, Tennessee, USA. http://cdiac.ornl.gov/

Kemfert, C., W. Knorr (2006) Bewertung des Klimawandels anhand von gekoppelten, global vernetzten Ökonomie-Biosphäre-Klima-Modellen ECOBICE (Economy-Biosphere-Climate). 114 pp.

Keppler, F., J. T. G. Hamilton, M. Brass, T. Röckmann (2006) Methane emissions from terrestrial plants under aerobic conditions. *Nature*, **439**, 187-191.

Kicklighter, D. W., M. Bruno. S. Dönges, G. Esser, M. Heimann, J. Helfrich, F. Ift, F. Joos, J. Kaduk, G. H. Kohlmaier, A. D. Mcguire, J. M. Melillo, R. Meyer, B. Moore III, A. Nadler, I. C. Prentice, W. Sauf, A. L. Schloss, S. Sitch, U. Wittenberg, G. Würth (1999) A first-order analysis of the potential role of CO_2 fertilization to affect the global carbon budget: a comparison of four terrestrial biosphere models. *Tellus B*, **51**, 343-366.

Klein Goldewijk, K. (2001) Estimating global land use change over the past 300 years: the HYDE database. *Global Biogeochemical Cycles*, **15**, 417-433.

Kleypas, J. A., R. W. Buddemeier, D. Archer, J.-P. Gattuso, C. Langdon, B. N. Opdyke (1999) Geochemical consequences of increased atmospheric carbon dioxide on coral reefs. *Science*, **284**, 118-120.

Knorr, W., M. Heimann (2001) Uncertainties in global terrestrial biosphere modeling, part II: global constraints for a process-based vegetation model. *Global Biogeochemical Cycles*, **15**, 227-246.

Knutti, R., T. F. Stocker, F. Joos, G.-K. Plattner (2002) Constraints on radiative forcing and future climate change from observations and climate model ensembles. *Nature*, **416**, 719-723.

Knutti, R., T. F. Stocker, F. Joos, G.-K. Plattner (2003) Probabilistic climate change projections using neural networks. *Climate Dynamics*, **21**, 257-272.

Kohlmaier, G. H., H. Brohl, E. O. Siré, M. Plőchl, R. Reville (1987) Modelling stimulation of plants and ecosystem response to present levels of excess atmospheric CO_2. *Tellus B*, **39**, 155-179.

Körner, C. (2006) Plant CO_2 responses: an issue of definition, time and resource supply. *New Phytologist*, **172**, 393-411.

Kriegler, E. (2005) Imprecise probability analysis for Integrated Assessment of climate change. Ph.D. thesis. Potsdam Universität, Germany. 256 pp. http://www.pik-potsdam.de/~kriegler/

Kriegler, E., O. Edenhofer, K. Lessmann (2006) On the link between mitigation of and damages from climate change. Solicited oral presentation at the EGU General Assembly 2006, Vienna, Austria. April 2 – April 7, 2006.

Kriegler E., K. Tanaka, H. Held (2007) What is binding when? comparing targets for greenhouse gas concentration, ocean pH, temperature and sea level rise. Oral presentation at International

Energy Workshop. Stanford University, California, USA. June 25, 2007.

Krivova, N. A., L. Balmaceda, S. K. Solanki (2007) Reconstruction of solar total irradiance since 1700 from the surface magnetic flux. *Astronomy and Astrophysics*, **467**, 335-346.

Lal, R. (2005) Soil erosion and carbon dynamics. *Soil and Tillage Research*, **81**, 137-142.

Laws, E. A., (1997) Mathematical methods for oceanographers: an introduction. Wiley, New York, New York, USA. 343 pp.

Lean, J. (2000) Evolution of the Sun's spectral irradiance since the Maunder Minimum. *Geophysical Research Letters*, **27**, 16, 2425-2428.

Lean, J., J. Beer, R. Bradley (1995) Reconstruction of solar irradiance since 1610: implications for climate change. *Geophysical Research Letters*, **22**, 23, 3195-3198.

Lee, K., L. T. Tong, F. J. Millero, C. L. Sabine, A. G. Dickson, C. Goyet, G.-H. Park, R. Wanninkhof, R. A. Feely, R. M. Key (2006) Global relationships of total alkalinity with salinity and temperature in surface waters of the world's oceans. *Geophysical Research Letters*, **33**, L19605, doi:10.1029/2006GL027207.

Lelieveld, J., P. J. Crutzen, F. J. Dentener (1998) Changing concentration, lifetime and climate forcing of atmospheric methane. *Tellus B*, **50**, 128-150.

Lelieveld, J., F. J. Dentener, W. Peters, M. C. Krol (2004) On the role of hydroxyl radicals in the self-cleansing capacity of the troposphere. *Atmospheric Chemistry and Physics*, **4**, 2337-2344.

Levitus, S., J. I. Antonov, T. P. Boyer, C. Stephens (2000) Warming of the world ocean. *Science*, **287**, 2225-2229.

Li, Y.-H. (2000) A compendium of geochemistry. Princeton University Press, Princeton, New Jersey, USA. 475 pp.

Libes, S. M. (1992) An introduction to marine biogeochemistry. Wiley, New York, New York, USA. 734 pp.

Long, S. P., E. A. Ainsworth, A. Rogers, D. R. Ort (2004) Rising atmospheric carbon dioxide: plants FACE the future. *Annual review of plant biology*, 55, 591-628.

Lowe, D. C. (2006) A green source of surprise. *Nature*, **439**, 148-149.

Lucht, W., I. C. Prentice, R. B. Myneni, S. Sitch, P. Friedlingstein, W. Cramer, P. Bousquet, W. Buermann, B. Smith (2002) Climatic control of the high-latitude vegetation greening trend and Pinatubo effect. *Science*, **296**, 1687-1689.

Mackenzie, F. T. (2002) Our changing plant: an introduction to earth system science and global environmental change. 3rd edition. Prentice Hall, New Jersey, USA. 580 pp.

Mackenzie, F. T., L. M. Ver, A. Lerman (2002) Century-scale nitrogen and phosphorus controls of the carbon cycle. *Chemical Geology*, **190**, 13-32.

Mackenzie, F. T., A. Lerman, A. Andersson (2004) Past and present of sediment and carbon biogeochemical cycling models. *Biogeosciences*, **1**, 11-32.

Mackenzie, F. T., A. Lerman (2006) Carbon in the geobiosphere: Earth's outer shell. Springer, Dordrecht, The Netherlands. 402 pp.

Maier-Reimer, E., K. Hasselmann (1987) Transport and storage of CO_2 in the ocean – an inorganic ocean-circulation carbon cycle model. *Climate Dynamics*, **2**, 63-90.

Maier-Reimer, E., U. Mikolajewicz, A. Winguth (1996) Future ocean uptake of CO_2: interaction between ocean circulation and biology. *Climate Dynamics*, **12**, 711-721.

Maiss, M., L. P. Steele, R. J. Francey, P. J. Fraser, R. L. Langenfelds, N. B. A. Trivett, I. Levin (1996) Sulfur hexafluoride — a powerful new atmospheric tracer. *Atmospheric Environment*, **30**, 1621-1629.

Maiss, M., C. A. M. Brenninkmeijer (1998) Atmospheric SF_6: trends, sources, and prospects. *Environmental Science and Technology*, **32**, 3077-3086.

Maiss, M., C. A. M. Brenninkmeijer (1999) A reversed trend in emissions of SF_6 to the atmosphere? In (eds.) J. Van Ham, A. P. M. Baede, L. A. Meyer, and R. Ybema. *Non-CO_2 greenhouse gases: scientific understanding, control and implementation*, Proceedings of the 2nd International Symposium, Noordwijkerhout, The Netherlands. September 8 – September 10, 1999. p.199-204. Kluwer Academic Publishers, Dordrecht, The Netherlands.

Malinverno, A., V. A. Briggs (2004) Expanded uncertainty quantification in inverse problems: hierarchical Bayes and empirical Bayes. *Geophysics*, **69**, 1005-1016.

Mann, M. E., P. D. Jones (2003) Global surface temperatures over the past two millennia. *Geophysical Research Letters*, **30**(15), 1820, doi:10.1029/2003GL017814.

Manne, A. S., R. G. Richels (2001) An alternative approach to establishing trade-offs among greenhouse gases. *Nature*, **410**, 675-677.

Marland, G., T. A. Boden, R. J. Andres (2006) Global, regional, and national CO_2 emissions. In *Trends: a compendium of data on global change.* Carbon Dioxide Information Analysis Center, Oak Ridge National Laboratory, US Department of Energy, Oak Ridge, Tennessee, USA. http://cdiac.ornl.gov/

Masarie, K. A., R. L. Langenfelds, C. E. Allison, T. J. Conway, E. J. Dlugokencky, R. J. Francey, P. C. Novelli, L. P. Steele, P. P. Tans, B. Vaughn, J. W. C. White (2001) NOAA/CSIRO flask intercomparison project: a strategy for directly assessing consistency among atmospheric measurements made by independent laboratories. *Journal of Geophysical Research*, **106**, D17, 20445-20464.

Mastrandrea, M. D., S. H. Schneider (2004) Probabilistic integrated assessment of "dangerous" climate change. *Science*, **304**, 571-575.

Matthews, E., I. Fung (1987) Methane emission from natural wetlands: global distribution, area, and environmental characteristics of sources. *Global Biogeochemical Cycles*, **1**, 61-86.

McCarl, B. (1996) GAMBAS: a program for saving an advanced basis for GAMS. Version 1.

Accompanied in the GAMS software package.

McPhaden, M. J., S. E. Zebiak, M. H. Glantz (2006) ENSO as an integrating concept in Earth science. *Science*, **314**, 1740-1745.

Mears, C. A., M.C. Schabel, F. J. Wentz (2003) A reanalysis of the MSU channel 2 tropospheric temperature record. *Journal of Climate*, **16**, 3650-3664.

Melillo, J. M., A. D. McGuire, D. W. Kicklichter, B. Moore III, C. J. Vorosmarty, A. L. Schloss (1993) Global climate change and terrestrial net primary production. *Nature*, **363**, 234-240.

Meyer, R., F. Joos, G. Esser, M. Heimann, G. Hooss, G. Kohlmaier, W. Sauf, R. Voss, U. Wittenberg (1999) The substitution of high-resolution terrestrial biosphere models and carbon sequestration in response to changing CO_2 and climate. *Global Biogeochemical Cycles*, **13**, 785-802.

Mikaloff Fletcher, S. E., P. P. Tans, L. M. Bruhwiler, J. B. Miller, M. Heimann (2004) CH_4 sources estimated from atmospheric observations of CH_4 and its $^{13}C/^{12}C$ isotopic ratios: 1. inverse modeling of source processes. *Global Biogeochemical Cycles*, **18**, GB4004, doi:10.1029/2004GB002223.

Millero, F. J. (1995) Thermodynamics of the carbon dioxide system in the oceans. *Geochimica et Cosmochimica Acta*, **59**, 661-677.

Millero, F. J. (2006) Chemical oceanography. 3rd edition. CRC Press, Taylor & Francis Group. Boca Raton, Florida, USA. 496 pp.

Millero, F. J., T. B. Graham, F. Huang, H. Bustos-Serrano, D. Pierrot (2006) Dissociation constants of carbonic acid in seawater as a function of salinity and temperature. *Marine Chemistry*, **100**, 80-94.

Moberg, A., D. M. Sonechkin, K. Holmgren, N. M. Datsenko, W. Karlén (2005) Highly variable Northern Hemisphere temperatures reconstructed from low- and high-resolution proxy data. *Nature*, **433**, 613-617.

Montzka, S. A., J. H. Butler, J. W. Elkins, T. M. Thompson, A. D. Clarke, L. T. Lock (1999) Present and future trends in the atmospheric burden of ozone-depleting halogens. *Nature*, **398**, 690-694.

Mosegard, K., A. Tarantola (2002) Probabilistic approach to inverse problems. In (eds.) W. H. K. Lee, H. Kanamori, P. Jennings, C. Kisslinger. *International handbook of earthquake & engineering seismology, part A*. pp.237-265. Academic Press, Amsterdam, The Netherlands. http://www.ipgp.jussieu.fr/~tarantola/

Munk, W. (1966) Abyssal recipes. *Deep Sea Research*, **13**, 707-730.

Murphy, J. M. (1995) Transient response of the Hadley Centre coupled ocean-atmosphere model to increasing carbon dioxide. part III: analysis of global mean response using simple models. *Journal of Climate*, **8**, 496-514.

Murphy, J. M., D. M. H. Sexton, D. N. Barnett, G. S. Jones, M. J. Webb, M. Collins, D. A. Stainforth (2004) Quantification of modelling uncertainties in a large ensemble of climate change

simulation. *Nature*, **430**, 768-772.

Myhre, G., E. J. Highwood, K. P. Shine, F. Stordal (1998) New estimates of radiative forcing due to well mixed greenhouse gases. *Geophysical Research Letters*, **25**, **14**, 2715-2718.

Nakićenović, N., R. Swart (eds.) (2000) Special report on emissions scenarios. Cambridge University Press, Cambridge, United Kingdom. 612 pp.

Neelin, J. D., D. S. Battisti, A. C. Hirst, F.-F. Jin, Y. Wakata, T. Yamagata, S. E. Zebiak (1998) ENSO theory. *Journal of Geophysical Research*, **103**, C7, 14261-14290.

Neelin, J. D., C. Chou, H. Su (2003) Tropical drought regions in global warming and El Niño teleconnections. *Geophysical Research Letters*, **30**, doi:10.1029/2003GL018625.

Nisbet, E. G., D. J. W. Piper (1998) Giant submarine landslides. *Nature*, **392**, 329-330.

Nordhaus, W. D., J. Boyer (2000) Warming the world: economic models of global warming. MIT Press, Massachusetts Institute of Technology, Cambridge, Massachusetts, USA. 232 pp.

Oman, L., A. Robock, G. Stenchikov, G. A. Schmidt, R. Ruedy (2005) Climatic response to high-latitude volcanic eruptions. *Journal of Geophysical Research*, **110**, D13103, doi:10.1029/2004JD005487.

O'Neill, B. C., M. Oppenheimer, S. R. Gaffin (1997) Measuring time in the greenhouse. *Climatic Change*, **37**, 491-503.

O'Neill, B. C. (2000) The jury is still out on Global Warming Potentials. *Climatic Change*, **44**, 427-443.

O'Neill, B. C. (2003) Economics, natural science, and the costs of Global Warming Potentials. *Climatic Change*, **58**, 251-260.

O'Neill, B. C., P. Crutzen, A. Grübler, M. Ha Duong, K. Keller, C. Kolstad, J. Koomey, A. Lange, M. Obersteiner, M. Oppenheimer, W. Pepper, W. Sanderson, M. Schlesinger, N. Treich, A. Ulph, M. Webster, C. Wilson (2006) Learning and climate change. *Climate Policy*, **6**, 585-589.

Oram, D. E., W. T. Sturges, S. A. Penkett (1998) Growth of fluoroform (CHF_3, HFC-23) in the background atmosphere. *Geophysical Research Letters*, **25**, 35-38.

Oram, D. E., W. T. Sturges, S. A. Penkett, A. McCulloch, P. J. Fraser (2000) Atmospheric fluoroform (CHF_3, HFC-23) at Cape Grim, Tasmania. In *Trends: a compendium of data on global change.* Carbon Dioxide Information Analysis Center, Oak Ridge National Laboratory, US Department of Energy, Oak Ridge, Tennessee, USA. http://cdiac.ornl.gov/

Orr, J. C., V. J. Fabry, O. Aumont, L. Bopp, S. C. Doney, R. A. Feely, A. Gnanadesikan, N. Gruber, A. Ishida, F. Joos, R. M. Key, K. Lindsay, E. Maier-Reimer, R. Matear, P. Monfray, A. Mouchet, R. G. Najjar, G.-K. Plattner, K. B. Rodgers, C. L. Sabine, J. L. Sarmiento, R. Schlitzer, R. D. Slater, I. J. Totterdell, M.-F. Weirig, Y. Yamanaka, A. Yool (2005) Anthropogenic ocean acidification over the twenty-first century and its impact on calcifying organisms. *Nature*, **437**, 681-686.

Park, K. (1969) Oceanic CO_2 system: an evaluation of ten methods of investigation. *Limnology and*

Oceanography, **14**, 179-186.

Penkett, S. A., K. S. Law, T. Cox, P. Kasibhatla (2003) Atmospheric photooxidants. In (eds.) G. P. Brasseur, R. G. Prinn, A. A. P. Pszenny. *Atmospheric chemistry in a changing world. The IGBP Series*. pp.73-124. Springer, Berlin, Germany. 300 pp.

Petit, J. R., J. Jouzel, D. Raynaud, N. I. Barkov, J.-M. Barnola, I. Basile,M. Bender, J. Chappellaz, M. Davisk, G. Delaygue, M. Delmotte, V. M. Kotlyakov, M. Legrand, V. Y. Lipenkov, C. Lorius, L. Pépin, C. Ritz, E. Saltzmank, M. Stievenard (1999) Climate and atmospheric history of the past 420,000 years from the Vostok ice core, Antarctica. *Nature*, **399**, 429-436.

Petoukhov, V., A. Ganopolski, V. Brovkin, M. Claussen, A. Eliseev, C. Kubatzki, S. Rahmstorf (2000) CLIMBER-2: a climate system model of intermediate complexity. part I: model description and performance for present climate. *Climate Dynamics*, **16**, 1-17.

Pilson, M. E. Q. (1998) An introduction to the chemistry of the sea. Prentice Hall, Upper Saddle River, New Jersey, USA. 431 pp.

Plattner, G.-K., F. Joos, T. F. Stocker, O. Marchal (2001) Feedback mechanisms and sensitivities of ocean carbon uptake under global warming. *Tellus B*, **53**, 564-592.

Pollack, H. N. (2005) Uncertain science … uncertain world. Cambridge University Press, Cambridge, United Kingdom. 243 pp.

Pollock, W. H. L. E. Heidt, R. A. Lueb, J. F. Vedder, M. J. Mills, S. Solomon (1992) On the age of stratospheric air and ozone depletion potential in polar region. *Journal of Geophysical Research*, **97**, D12, 12993-12999.

Prather, M. J. (1998) Time scales in atmospheric chemistry: coupled perturbations to N_2O, NO_y, and O_3. *Science*, **279**, 1339-1341.

Press, W. H., S. A. Teukolsky, W. T. Vetterling, B. P. Flannery (2001) Numerical recipes in Fortran: the art of scientific computing. volume 1. Cambridge University Press, Cambridge, United Kingdom. 934 pp. http://www.nr.com/nronline_switcher.php

Prinn, R. G., R. F. Weiss, P. J. Fraser, P. G. Simmonds, D. M. Cunnold, F. N. Alyea, S. O'Doherty, P. Salameh, B. R. Miller, J. Huang, R. H. J. Wang, D. E. Hartley, C. Harth, L. P. Steele, G. Sturrock, P. M. Midgely, A. McCulloch (2000) A history of chemically and radiatively important gases in air deduced from ALE/GAGE/AGAGE. *Journal of Geophysical Research*, **105**, D14, 17751-17792.

Prinn, R. G., J. Huang, R. F. Weiss, D. M. Cunnold, P. J. Fraser, P. G. Simmonds, A. McCulloch, C. Harth, P. Salameh, S. O'Doherty, R. H. J. Wang, L. Porter, B. R. Miller (2001) Evidence for substantial variations of atmospheric hydroxyl radicals in the past two decades. *Science*, **292**, 1882-1888.

Raddatz, T. J., C. H. Reick, W. Knorr, J. Kattge, E. Roeckner, R. Schnur, K.-G. Schnitzler, P. Wetzel, J. Jungclaus (2007) Will the tropical land biosphere dominate the climate-carbon cycle feedback

during the 21st century? *Climate Dynamics*, **29**, 565-574.

Raddatz, T., K. Tanaka (2008) On the risk of abrupt warming after a shutdown of all emissions. Poster presentation at EGU General Assembly 2008, Vienna, Austria. April 13 – April 18, 2008.

Räisänen, J. (2007) How reliable are climate models? *Tellus A*, **59**, 2-29.

Raper, S. C. B., U. Cubasch (1996) Emulation of the results from a coupled general circulation model using a simple climate model. *Geophysical Research Letters*, **23**, 1107-1110.

Raper, S. C. B., J. M. Gregory, T. J. Osborn (2001) Use of an upwelling-diffusion balance climate model to simulate and diagnose A/OGCM results. *Climate Dynamics*, **17**, 601-613.

Reilly, J. M., K. R. Richards (1993) Climate change damage and the trace gas index issue. *Environmental and Resource Economics*, **3**, 41-61.

Reilly, J., R. Prinn, J. Harnisch, J. Fitzmaurice, H. Jacoby, D. Kicklighter, J. Melillo, P. Stone, A. Sokolov, C. Wang (1999) Multi-gas assessment of the Kyoto Protocol. *Nature*, **401**, 549-555.

Revelle, R., W. Munk (1977) The carbon dioxide cycle and the biosphere. In *Energy and climate, studies in geophysics.* pp.140-158. National Academy Press, Washington, D,C., USA.

Ricciuto, D. M., K. J. Davis, K. Keller (2008) A Bayesian synthesis inversion of carbon cycle observations: How can observations reduce uncertainties about future sinks? *Global Biogeochemical Cycles*, doi:10.1029/2006GB002908, in press.

Ridgwell, A. J., S. J. Marshall, K. Gregson (1999) Consumption of atmospheric methane by soils: a process-based model. *Global Biogeochemical Cycles*, **13**, 59-70.

Ridgwell, A, I. Zondervan, J. C. Hargreaves, J. Bijma, T. M. Lenton (2006) Significant long-term increase of fossil fuel CO_2 uptake from reduced marine calcification. *Biogeosciences Discussion*, **3**, 1763-1780. SRef-ID: 1810-6285/bgd/2006-3-1763.

Riebesell, U., I. Zondervan, B. Rost, P. D. Tortell, R. E. Zeebe, F. M. M. Morel (2000) Reduced calcification of marine plankton in response to increased atmospheric CO_2. *Nature*, **407**, 364-367.

Robock, A. (2000) Volcanic eruptions and climate. *Reviews of Geophysics*, **38**, 191-219.

Robock, A. (2005) Cooling following large volcanic eruptions corrected for the effect of diffuse radiation on tree rings. *Geophysical Research Letters*, **32**, L06702, doi: 10.1029/2004GL022116.

Ropelewski, C. F. (1992) Predicting El Niño events. *Nature*, **356**, 476-477.

Rosenlof, K., S. J. Oltmans, D. Kley, J. M. Russell III, E.-W. Chiou, W. P. Chu, D. G. Johnson, K. K. Kelly, H. A. Michelsen, G. E. Nedoluha, E. E. Remsberg, G. C. Toon, M. P. McCormick (2001) Stratospheric water vapor increases over the past half-century. *Geophysical Research Letters*, **28**, 1195-1198, 10.1029/2000GL012502.

Rosenthal, R. E. (2007) GAMS – a user's guide. GAMS Development Corporation, Washington, DC, USA. 271 pp.

Ruddiman, W. F. (2003) The anthropogenic greenhouse era began thousands of years ago. *Climatic*

Change, **61**, 261-293.

Ruttimann, J. (2006) Sick seas. *Nature*, **442**, 978-980.

Santer, B. D., T. M. L. Wigley, C. Mears, F. J. Wentz, S. A. Klein, D. J. Seidel, K. E. Taylor, P. W. Thorne, M. F. Wehner, P. J. Geckler, J. S. Boyle, W. D. Collins, K. W. Dixon, C. Doutriaux, M. Free, Q. Fu, J. E. Hansen, G. S. Jones, R. Ruedy, T. R. Karl, J. R. Lazarante, G. A. Meehl, V. Ramaswamy, G. Russel, G. A. Schmidt (2005) Amplification of surface temperature trends and variability in the tropical atmosphere. *Science*, **309**, 1551-1556.

Scales J. A., L. Tenorio (2001) Prior information and uncertainty in inverse problems. *Geophysics*, **66**, 389-397.

Schauffler, S. M., J. S. Daniel (1994) On the effects of stratospheric circulation changes on trace gas trends. *Journal of Geophysical Research*, **99**, D12, 25747-25754.

Schauffler, S. M., E. L. Atlas, D. R. Blake, F. Flocke, R. A. Lueb, J. M. Lee-Taylor, V. Stroud, W. Travnicek (1999) Distributions of brominated organic compounds in the troposphere and lower stratosphere. *Journal of Geophysical Research*, **104**, D17, 21513-21535.

Schlesinger, M. E. (1985) Appendix A: analysis of results from energy balance and radiative convective models. In (eds.) M.C. MacCracken, F. M. Luther. *Projecting the climate effects of increasing carbon dioxide*. pp.281-319. US Department of Energy, DOE/ER-0237.

Schlesinger, M. E., N. G. Andronova, B. Entwistle, A. Ghanem, N. Ramankutty, W. Wang, F. Yang (1997) Modeling and simulation of climate and climate change. In *Proceedings of the International School of Physics Enrico Fermi CXXXIII*. pp.389-429. IOS Press, Amsterdam, The Netherlands.

Schlesinger, W. H. (1997) Biogeochemistry: an analysis of global change. Academic Press, San Diego, California, USA. 588 pp.

Schmalensee, R. (1993) Comparing greenhouse gases for policy purposes. *Energy Journal*, **14**, 245-255.

Schneider (2002) Can we estimate the likelihood of climatic changes at 2100?: an editorial comment, *Climatic Change*, **52**, 441-451.

Schneider, S. H., K. Kuntz-Duriseti (2002) Uncertainty and climate change policy. In (eds.) S. H. Schneider, A. Rosencranz, J. O. Niles. *Climate change policy: a survey.* pp.53-87. Island Press, Washington, D.C., USA. 563 pp.

Schneider von Deimling, T., H. Held, A. Ganopolski, S. Rahmstorf (2006) Climate sensitivity estimated from ensemble simulations of glacial climate. *Climate Dynamics*, **27**, 149-163.

Seinfeld, J. H., S. N. Pandis (2006) Atmospheric chemistry and physics: from air pollution to climate change. 2nd edition. Wiley, New York, USA. 1203 pp.

Shafer, G. (1992) What is probability? In (eds.) David C. Hoaglin and David S. Moore. *Perspectives on Contemporary Statistics*. pp.93-105. Mathematical Association of America, MAA Notes

Number 21.

Shaffer, G., U. Rönner (1984) Denitrification in the Baltic proper deep water. *Deep Sea Research*, **31**, 197-220.

Shine, K., P. Forster (1999) The effect of human activity on radiative forcing of climate change: a review of recent developments. *Global and Planetary Change*, **20**, 205-225.

Shine, K. P., J. S. Fuglestvedt, K. Hailemariam, N. Stuber (2005) Alternatives to the Global Warming Potential for comparing climate impacts of emissions of greenhouse gases. *Climatic Change*, **68**, 281-302.

Siebert, L., T. Simkin (2006). Volcanoes of the world: an illustrated catalog of holocene volcanoes and their eruptions. Smithsonian Institution, Global Volcanism Program Digital Information Series, GVP-3. http://www.volcano.si.edu/world/

Simmons, H. L., S. R. Jayne, L. C. S. Laurent, A. J. Weaver (2004) Tidally driven mixing in a numerical model of the ocean circulation. *Ocean Modelling*, **6**, 245-263.

Sitch, S., B. Smith, I. C. Prentice, A. Arneth, A. Bondeau, W. Cramer, J. O. Kaplan, S. Levis, W. Lucht, M. T. Sykes, K. Thonicke, S. Venevsky (2003) Evaluation of ecosystem dynamics, plant geography and terrestrial carbon cycling in the LPJ dynamic global vegetation model. *Global Change Biology*, **6**, 161-185.

Smith, R. L., T. M. L. Wigley, B. D. Santer (2003) A bivariate time series approach to anthropogenic trend detection in hemispheric mean temperatures. *Journal of Climate*, **16**, 1228-1240.

Smith, S. J., T. M. L. Wigley (2000) Global Warming Potentials: 1. climatic implications of emissions reductions. *Climatic Change*, **44**, 445-457.

Smith, S. J. (2003) The evaluation of greenhouse gas indices. *Climatic Change*, **58**, 261-265.

Smith, S. V., F. T. Mackenzie (1987) The ocean as a net heterotrophic system: implications from the carbon biogeochemical cycle. *Global Biogeochemical Cycles*, **1**, 187-198.

Soden, B. J., R. T. Wetherald, G. L. Stenchikov, A. Robock (2002) Global cooling after the eruption of Mount Pinatubo: a test of climate feedback by water vapor. *Science*, **296**, 727-730.

Solanki, S. K., M. Schüssler, M. Fligge (2002) Secular variation of the Sun's magnetic flux. *Astronomy and Astrophysics*, **383**, 706-712.

Solomon, S. (1999) Stratospheric ozone depletion: a review of concepts and history. *Reviews of Geophysics*, **37**, 275-316.

Stainforth, D. A., T. Aina, C. Christensen, M. Collins, N. Faull, D. J. Frame, J. A. Kettleborough, S. Knight, A. Martin, J. M. Murphy, C. Piani, D. Sexton, L. A. Smith, R. A. Spicer, A. J. Thorpe, M. R. Allen (2005) Uncertainty in predictions of the climate response to rising levels of greenhouse gases. *Nature*, **433**, 403-406.

Stern, D. I., R. K. Kaufmann (1998) Annual estimates of global anthropogenic methane emissions: 1860-1994. In *Trends: a compendium of data on global change.* Carbon Dioxide Information

Analysis Center, Oak Ridge National Laboratory, US Department of Energy, Oak Ridge, Tennessee, USA. http://cdiac.ornl.gov/

Stocker, T. F., A. Schmittner (1998) Influence of CO_2 emission rates on the stability of the thermohaline circulation. *Nature*, **388**, 862-865.

Sturges, W. T., T. J. Wallington, M. D. Hurley, K. P. Shine, K. Sihra, A. Engel, D. E. Oram, S. A. Penkett, R. Mulvaney, C. A. M. Brenninkmeijer (2000) A potent greenhouse gas identified in the atmosphere: SF_5CF_3. *Science*, **289**, 611-613.

Sturrock, G. A., D. M. Etheridge, C. M. Trudinger, P. J. Fraser, A. M. Smith (2002) Atmospheric histories of halocarbons from analysis of Antarctic firn air: major Montreal Protocol species. *Journal of Geophysical Research*, **107**, D24, 4765, doi:10.1029/2002JD002548.

Suess, E., G. Bohrmann, J. Greinert, E. Lausch (1999) Flammable ice. *Scientific American*, **November 1999**, 52-59 and 76-83.

Sundquist, E. T., L. N. Plummer (1981) Carbon dioxide in the ocean surface layer: some modelling considerations. In (ed.) B. Bolin. *Carbon cycle modelling (SCOPE 16)*. pp.259-269. John Wiley & Sons. 390 pp.

Svensen, H., S. Planke, A. Malthe-Sørenssen, B. Jamtveit, R. Myklebust, T. R. Eidem, S. S. Rey (2004) Release of methane from a volcanic basin as a mechanism for initial Eocene global warming. *Nature*, **429**, 542-545.

Takahashi, T. (1989) The carbon dioxide puzzle. *Oceanus*, **32**, 22-29.

Takemura, T., H. Okamoto, Y. Maruyama, A. Numaguti, A. Higurashi, T. Nakajima (2000) Global three-dimensional simulation of aerosol optical thickness distribution of various origins. *Journal of Geophysical Research*, **105**, D14, 17853-17873.

Takemura, T., T. Nakajima, A. Higurashi, S. Ohta, N. Sugimoto (2003) Aerosol distributions and radiative forcing over the Asian Pacific region simulated by Spectral Radiation-Transport Model for Aerosol Species (SPRINTARS). *Journal of Geophysical Research*, **108**, D23, 8659, doi:10.1029/2002JD003210.

Tanaka, K., T. Bruckner, W. Knorr, R. S. J. Tol, G. Hooss (2005) Uncertainty analysis of carbon cycle and climate parameters using a simple climate model. Poster presentation at EGU General Assembly 2005, Vienna, Austria. April 25 – April 31, 2005.

Tanaka, K., F. T. Mackenzie (2005) Ecosystem behavior of southern Kaneohe Bay, Hawaii: a statistical and modelling approach. *Ecological Modelling*, **188**, 296-326.

Tanaka, K., R. S. J. Tol, W. Knorr, T. Bruckner, E. Kriegler, T. Raddatz (2006a) Uncertain analysis using Aggregated Carbon Cycle, Atmospheric Chemistry, and Climate Model (ACC2). Poster presentation at the EGU General Assembly 2006, Vienna, Austria. April 2 – April 7, 2006.

Tanaka, K., R. S. J. Tol, D. Rokityanskiy, B. C. O'Neill, M. Obersteiner (2006b) Evaluating Global Warming Potentials as historical temperature proxies: an application of ACC2 inverse

calculation. FNU-118, Hamburg University and Centre for Marine and Atmospheric Science, Hamburg, Germany.
http://www.uni-hamburg.de/Wiss/FB/15/Sustainability/Working_Papers.htm

Tanaka, K., E. Kriegler, T. Bruckner, G. Hooss, W. Knorr, T. Raddatz (2007a) Aggregated Carbon Cycle, Atmospheric Chemistry, and Climate Model (ACC2): description of the forward and inverse modes. Reports on Earth System Science No. 40. Max Planck Institute for Meteorology, Hamburg, Germany. 188 pp.
http://www.mpimet.mpg.de/wissenschaft/publikationen/erdsystemforschung.html

Tanaka, K., R. S. J. Tol, D. Rokityanskiy, B. C. O'Neill, M. Obersteiner (2007b) Evaluating Global Warming Potentials with historical temperature: an application of ACC2 inversion. Interim Report at International Institute for Applied Systems Analysis (IIASA) IR-07-035. 29 pp. Also re-submitted to *Climatic Change*.
http://www.iiasa.ac.at/Research/PCC/research-proj/uncer-learn.html

Tanaka, K. T. Raddatz, B. C. O'Neill, C. H. Reick (2008) Is the climate sensitivity even more uncertain? Submitted to *Nature*.

Tarantola, A., B. Valette (1982) Inverse problems = quest for information. *Journal of Geophysics*, **50**, 159-170. http://www.ipgp.jussieu.fr/~tarantola/

Tarantola, A., K. Mosegaard (2000) Mathematical basis of physical inference. *Mathematical Physics*, arXiv:math-ph/0009029. http://arxiv.org/

Tarantola, A. (2005) Inverse problem theory and methods for model parameter estimation. Society for Industrial and Applied Mathematics (SIAM), Philadelphia, US. 342 pp.
http://www.ipgp.jussieu.fr/~tarantola/

Tarantola, A. (2006) Popper, Bayes and the inverse problem. *Nature Physics*, **2**, 492-494.

Tjoelker, M. G., J. Oleksyn, P. B. Reich (2001) Modelling respiration of vegetation: evidence for a temperature-dependent Q10. *Global Change Biology*, **7**, 223-230.

Tol, R. S. J, A. F. de Vos (1998) A Bayesian statistical analysis of the enhanced greenhouse effect. *Climatic Change*, **38**, 87-112.

Tol, R. S. J. (1999) The marginal costs of greenhouse gas emissions. *Energy Journal*, **20**, 61-81.

Tomczak, M., J. S. Godfrey (1994) Regional oceanography: an introduction. Pergamon, Elsevier Science, Oxford, England. 422 pp.

Toth, F. (2003) Integrated assessment of climate protection strategies. *Climatic Change*, **56**, 1-5.

Toth, F. L., T. Bruckner, H.-M. Füssel, M. Leimbach, G. Petschel-Held (2003) Integrated assessment of long-term climate policies: part 2 – model results and uncertainty analysis. *Climatic Change*, **56**, 57-72.

Trudinger, C. M. Trudinger, I. G. Enting, P. J. Rayner, R. J. Francey (2002) Kalman filter analysis of ice core data 2: double deconvolution of CO_2 and $\delta^{13}C$ measurements. *Journal of Geophysical*

Research, **107**, D20, 4423-4446, doi:10.1029/2001JD001112.

Tudhope, A. W., C. P. Chilcott, M. T. McCulloch, E. R. Cook, J. Chappell, R. M. Ellam, D. W. Lea, J. M. Lough, G. B. Shimmield (2001) Variability in the El Niño – Southern Oscillation through a glacial-interglacial cycle. *Science*, **291**, 1511-1517.

Tyrrell, T., A. H. Taylor (1996) A modelling study of *Emiliania huxleyi* in the NE Atlantic. *Journal of Marine Systems*, **9**, 83-112.

Ulrych, T. J., M. D. Sacchi, A. Woodbury (2001) A Bayes tour of inversion. *Geophysics*, **66**, 55-69.

United Nations (UN) Population Division (2002) World urbanization prospects: the 2001 revision. 182 pp.

van Aardenne, J. A., F. J. Dentener, J. G. J. Olivier, C. G. M. Klein Goldewijk, J. Lelieveld (2001) A 1 x 1 degree resolution dataset of historical anthropogenic trace gas emissions for the period 1890-1990. *Global Biogeochemical Cycles*, **15**, 909-928.

van Oldenborgh, G. J., S. Y. Philip, M. Collins (2005) El Niño in a changing climate: a multi-model study. *Ocean Science*, **1**, 81-95.

Ver, L. M. B., F. T. Mackenzie, A. Lerman (1999) Biogeochemical responses of the carbon cycle to natural and human perturbations: past, present, and future. *American Journal of Science*, **299**, 762-801.

von Storch, H., F. W. Zwiers (1999) Statistical analysis in climate research. Cambridge University Press, Cambridge, United Kingdom. 484 pp.

Wang, G. (2005) Agricultural drought in a future climate: results from 15 global climate models participating in the IPCC 4th assessment. *Climate Dynamics*, **25**, 739-753.

Weatherhead, E. C., S. B. Andersen (2006) The search for signs of recovery of the ozone layer. *Nature*, **441**, 39-45.

Weber, M., V. Barth, K. Hasselmann (2005) A multi-actor dynamic integrated assessment model (MADIAM) of induced technological change and sustainable economic growth. *Ecological Economics*, **54**, 306-327.

Webster, M. D., M. Babiker, M. Mayer, J. M. Reilly, J. Harnisch, R. Hyman, M. C. Sarofim, C. Wang (2002) Uncertainty in emissions projections for climate models. *Atmospheric Environment*, **36**, 3659-3670.

Webster, M., C. Forest, J. Reilly, M. Babiker, D. Kicklighter, M. Mayer, R. Prinn, M. Sarofim, A. Sokolov, P. Stone, C. Wang (2003) Uncertainty analysis of climate change and policy response. *Climatic Change*, **61**, 295-320.

Wetzel, P. (2004) Interannual and decadal variability in the air-sea exchange of CO_2 – a model study. Reports on Earth System Science No.7. Max Planck Institute for Meteorology, Hamburg, Germany. 112 pp.
http://www.mpimet.mpg.de/wissenschaft/publikationen/erdsystemforschung.html

Wigley, T. M. L., M. E. Schlesinger (1985) Analytical solution for the effect of increasing CO_2 on global mean temperature. *Nature*, **315**, 649-652.

Wigley, T. M. L., S. C. B. Raper (1992) Implications for climate and sea level of revised IPCC emissions scenarios. *Nature*, **357**, 293-300.

Wigley, T. M. L., R. Richels, J. A. Edmonds (1996) Alternative emissions pathways for stabilizing concentrations. *Nature*, **379**, 240-243.

Wigley, T. M. L. (1998) The Kyoto Protocol: CO_2, CH_4 and climate implications. *Geophysical Research Letters*, **25**, 2285-2288.

Wigley, T. M. L., C. M. Ammann, B. D. Santer, S. C. B. Raper (2005) Effect of climate sensitivity on the response to volcanic forcing. *Journal of Geophysical Research*, **110**, D09107, doi:10.1029/2004JD005557.

Winston, W. L. (1994) Operations research: applications and algorithm. 3rd edition. International Thomson Publishing, Belmont, California, USA. 1318 pp.

World Meteorological Organization (WMO) (1999) Scientific assessment of ozone depletion: 1998, Global Ozone Research and Monitoring Project—Report No. 44, Geneva. 650 pp.

World Meteorological Organization (WMO) (2003) Scientific assessment of ozone depletion: 2002, Global Ozone Research and Monitoring Project—Report No. 47, Geneva. 498 pp.

Wunsch, C. (1996) The ocean circulation inverse problem. Cambridge University Press, Cambridge, United Kingdom. 442 pp.

Zeebe, R., D. Wolf-Gladrow (2001) CO_2 in seawater: equilibrium, kinetics, isotopes. Elsevier, Amsterdam, The Netherlands. 346 pp.

Zellner, A., G. C. Tiao (1964) Bayesian analysis of the regression model with autocorrelated errors. *Journal of the American Statistical Association*, **59**, 763-778.

Zhao, M., P. A. Dirmeyer (2003) Production and analysis of GSWP-2 near-surface meteorology data sets. Technical Report No. 159, Center for Land-Ocean-Atmosphere Studies, Calverton, Maryland, USA. 38 pp. http://www.iges.org/gswp/

Zickfeld, K., T. Bruckner (2003) Reducing the risk of abrupt climate change: emissions corridors preserving the Atlantic Thermohaline Circulation. *Integrated Assessment*, **4**, 106-115.

Zickfeld, K. T. Slawig, S. Rahmstorf (2004) A low-order model for the response of the Atlantic thermohaline circulation to climate change. *Ocean Dynamics*, **54**, 8-26.

Zielinski, G. A. (1995) Stratospheric loading and optical depth estimates of explosive volcanism over the last 2100 years derived from the Greenland Ice Sheet Project 2 ice core. *Journal of Geophysical Research*, **100**, D10, 20937-20956.